Transactions of the ASME, Journal of Heat Transfer (ISSN 0022-1481) is published monthly by The American Society of Mechanical Engineers, Three Park Avenue, New York, NY 10016. Periodicals postage paid at New York, NY and additional mailing offices. POSTMASTER: Send address changes to Transactions of the ASME, Journal of Heat Transfer, c/o THE AMERICAN SOCIETY OF MECHANICAL ENGINEERS, 22 Law Drive, Box 2300, Fairfield, NJ 07007-2300. **CHANGES OF ADDRESS** must be received at Society headquarters seven weeks before they are to be effective. Please send old label and new address. **STATEMENT from By-Laws.** The Society shall not be responsible for statements or opinions advanced in papers or ... printed in its publications (B7.1, Para. 3).

Journal of Heat Transfer

Published Monthly by ASME

VOLUME 132 • NUMBER 9 • SEPTEMBER 2010

RESEARCH PAPERS

(Contents continued on inside back cover)

This journal is printed on acid-free paper, which exceeds the ANSI Z39.48-1992 specification for permanence of paper and library materials. ♾™
♻ 85% recycled content, including 10% post-consumer fibers.

Journal of Heat Transfer Volume 132, Number 9 SEPTEMBER 2010

TECHNICAL BRIEFS

The ASME Journal of Heat Transfer is abstracted and indexed in the following:

Applied Science and Technology Index, Chemical Abstracts, Chemical Engineering and Biotechnology Abstracts (Electronic equivalent of Process and Chemical Engineering), Civil Engineering Abstracts, Compendex (The electronic equivalent of Engineering Index), Corrosion Abstracts, Current Contents, E & P Health, Safety, and Environment, Ei EncompassLit, Engineered Materials Abstracts, Engineering Index, Enviroline (The electronic equivalent of Environment Abstracts), Environment Abstracts, Environmental Engineering Abstracts, Environmental Science and Pollution Management, Fluidex, Fuel and Energy Abstracts, Index to Scientific Reviews, INSPEC, International Building Services Abstracts, Mechanical & Transportation Engineering Abstracts, Mechanical Engineering Abstracts, METADEX (The electronic equivalent of Metals Abstracts and Alloys Index), Petroleum Abstracts, Process and Chemical Engineering, Referativnyi Zhurnal, Science Citation Index, SciSearch (The electronic equivalent of Science Citation Index), Theoretical Chemical Engineering

Limiting Length, Steady Spread, and Nongrowing Flames in Concurrent Flow Over Solids

Ya-Ting Tseng
e-mail: yating@case.edu

James S. T'ien
e-mail: jst2@case.edu

Department of Mechanical and Aerospace Engineering,
Case Western Reserve University,
10900 Euclid Avenue, 418 Glennan Building,
Cleveland, OH 44106

A detailed two-dimensional transient model has been formulated and numerically solved for concurrent flames over thick and thin solids in low-speed forced flows. The processes of flame growth leading to steady states are numerically simulated. For a thick solid, the steady state is a nongrowing stationary flame with a limiting length. For a thin solid, the steady state is a spreading flame with a constant spread rate and a constant flame length. The reason for a nongrowing limiting flame for the thick solid is the balance between the flame heat feedback and the surface radiative heat loss at the pyrolysis front, as first suggested by Honda and Ronney. The reason for achieving a steady spread for thin solids is the balance between the solid burnout rate and the flame tip advancing rate. Detailed transient flame and thermal profiles are presented to illustrate the different flame growth features between the thick- and thin-solid fuel samples. [DOI: 10.1115/1.4001645]

Keywords: solid flame spread, fire growth, limiting flame length, microgravity

1 Introduction

Flame spread over a solid surface in concurrent flows has two limiting cases: upward spread in a buoyant flow in a gravitational field and downstream forced flow spread in zero gravity in a ventilated cabin. For thick solids, the conventional notion of upward flame spread in normal gravity is that it is an accelerating process. For example, Fernandez-Pello [1] suggested that the pyrolysis length is proportional to the square of time in the model and proportional to the 1.7 power of time in the experiment. However, a constant flame growth rate has been observed in upward flame spread experiments conducted by Orloff et al. [2] and predicted by Carrier et al. [3] using a fast kinetic model without radiation loss. In the experiment of Orloff et al., 41 cm-wide, 157 cm-long, and 4.5 cm-thick polymethyl-methacrylate (PMMA) samples were used. In another upward spread experiment, Brehob and Kulkarni [4] showed that for several wood samples of thickness ranging from 3.2 mm to 25.4 mm and length of 120 cm, the flame stops growing before burnout. These are seemingly quite different observations. We suspect that in buoyant flame spread over thick solids, the flame may initially accelerate but later slow down. If burnout does not occur quickly, the flame will reach its ultimate length limit and stop growing. In normal gravity air at one atmosphere, depending on the materials and sample width, this ultimate length can be quite large so it may not be observed in short samples. We also note that, unlike the downward case where flame spread is steady and well-defined, the longer flame and the more complex transient growing process in the concurrent flow configuration introduces ambiguities that complicate the descriptions of the flame spread. As an example, Tewarson [5] divided the flame propagation behaviors of thick-solid fuel into four groups according to the "flame propagation index," i.e., nonpropagating, decelerating propagation, nonaccelerating propagation, and accelerating propagation.

In microgravity, the forced flow in a spacecraft cabin can produce a concurrent flame. The typical low-speed flows in this environment result in a low-intensity flame that grows slowly with time after ignition. There is almost no study of flame spread over thick solids in forced concurrent flow in microgravity. The only experiment we are aware of is the one conducted in the Mir space station [6]. In this collaborative Russian/NASA effort, several polymer rods with an initial diameter of 0.45 cm were tested with the ignition source placed at the end, facing the approaching flow ($0 \sim 8.5$ cm/s). Upon ignition, the polymer melted, and a ball-shaped liquid melt was formed near the leading end under the flame. The flame was short but extended downstream. The testing condition was not maintained long enough to determine whether a steady state (i.e., limiting flame length) can be reached. However, it is noted that at the end of the test, the flame growth rate is very small.

For a thin solid in a concurrent flow, the solid may burn out quickly at the upstream end and the flame base begins to move. In many situations, a constant length flame with a steady spread rate (i.e., both the flame base and tip move with identical constant speeds) is achieved. The majority of concurrent flame spread studies over thermally thin solids is for steady, constant length spread. These include, for example, experiments using narrow samples in normal gravity [7,8], experiments and models of buoyant flames in reduced gravity [9–11], and models in forced flow in zero gravity [12,13]. To explain why steady spread occurs, Honda and Ronney theorized two mechanisms based on heat transfer considerations [7]. They argued that a limiting flame length is achieved when the net heat flux at the pyrolysis front becomes zero. In a two-dimensional (wide) sample, radiative losses are essential. In a narrow sample, transverse heat and momentum losses are essential. It should be noted here that there is a subtle difference between a moving (spreading) flame reaching a limiting length and a stationary (nonspreading) flame reaching a limiting length. The former applies to thin fuels with burnout, while the latter applies to thick solids without burnout. Although the argument of Honda and Ronney [7], i.e., zero net heat flux at the pyrolysis front, appears to be correct for stationary nonspreading flames as we shall see from the result of this investigation, their application to steady spreading flames over thin solids may need to be modified.

The purpose of the present paper is to obtain a thorough understanding of limiting flame spread/growth. Using a transient numerical model over solids in concurrent flow, we investigate the detailed time history of the flame growth leading to the limiting states for both thick (without solid burnout) and thin (with burnout) solids, and to determine why limiting flame lengths are attained. The computation is performed in a zero-gravity low-speed

Contributed by the Heat Transfer Division of ASME for publication in the JOURNAL OF HEAT TRANSFER. Manuscript received October 7, 2009; final manuscript received April 19, 2010; published online June 28, 2010. Assoc. Editor: Walter W. Yuen.

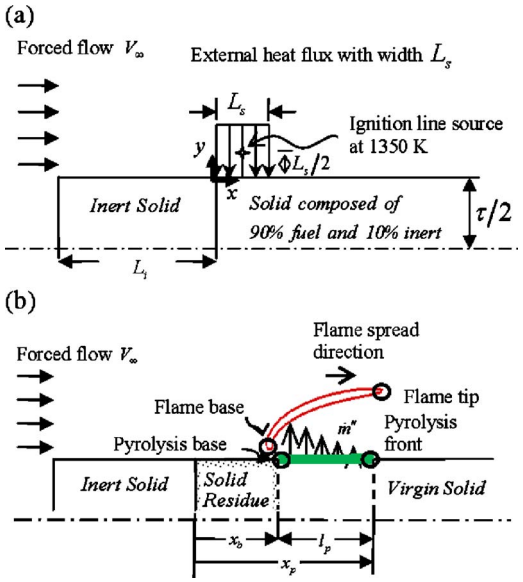

Fig. 1 Configuration in the computational model: schematic (*a*) of the ignition method and (*b*) of a spreading flame

forced flow. The flames are relatively short so that a laminar flame model can be used. This requires fewer approximations than a turbulent flame model. In practice, flame behavior in low-speed forced flow can be important for spacecraft fire safety. Although the present computation is performed for forced laminar flow, many of the qualitative features found here should be extendable to upward buoyant spread.

2 Model Description

2.1 Flow and Fuel Configurations. The fuel and flow configurations considered in the mathematical model are shown in Fig. 1(*a*). A semi-infinitely long solid of thickness τ composed of 90% combustible fuel and 10% inert is placed to the right of a block of pure inert solid (of the same thickness as the fuel block). A uniform approaching flow with velocity V_∞ is imposed at the end of the inert block ($x=-L_i$ with the origin $x=y=0$ located at the fuel-inert interface on the top surface). The atmosphere above the solid is unbounded in extent. For thin-solid samples, it is assumed that a symmetric flame is located on the lower side of the sample. This symmetry enables us to apply the gradient free boundary conditions at the center line and perform computation only over half of the flow domain, as shown in Figs. 1(*a*) and 1(*b*). For (infinitely) thick samples, gradient-free boundary conditions are also valid deep inside the solid far from the surface. The flow configuration is assumed to be two-dimensional. In the computations to be presented, L_i is chosen to be 6.3 cm. In a previous paper, we have shown that flame radiation feedback to the solid can reach up to 5 cm upstream [14]. So L_i is chosen to be greater than this value. Although other values of L_i can be used, it will not alter the basic physics of the present problem.

Solid ignition is achieved by applying an external uniform heat flux (2.09 W/cm^2 for thick fuel and 0.418 W/cm^2 for thin fuel) onto a strip of the solid fuel surface with strip width L_s (0.4 cm for thick fuel and 0.2 cm for thin fuel), as shown in Fig. 1(*a*). With this imposed heat flux, the solid fuel is heated up and pyrolyzed with vapor fuel diffusing into the gas phase. A hot ignition "wire" at 1350 K (a point source in the two-dimensional picture) is placed very close to the solid surface to serve as an ignition pilot (as shown in Fig. 1(*a*)). When there is sufficient fuel vapor in the gas phase, reaction is induced in the immediate neighborhood of the ignition wire. Both the external heat flux and the ignition wire are maintained steadily until a gaseous flame is formed and reaches 1 cm in length (judged using the fuel vapor reaction rate contour of value 10^{-4} $g/cm^3/s$). The ignition wire is then terminated abruptly, and the external heat flux is gradually turned down with a constant rate (0.105 $W/cm^2/s$ for thick fuel and 3.22 $W/cm^2/s$ for thin fuel). The flame then begins a self-sustained growth process. Note that there are conditions that the solid cannot self-sustain a flame [15] after the removal of the imposed radiative flux. However, this will not be discussed in this article.

Figure 1(*b*) shows a schematic of a propagating flame over a solid. In this paper, the visible flame is defined by the fuel vapor consumption rate contour with a value of $\dot{\omega}_F=10^{-4}$ $g/cm^3/s$ (suggested in Ref. [12]). The downstream edge of the contour is referred to as the flame tip, and the upstream edge is referred to as the flame base. Beneath the flame, solid fuel is pyrolyzed. According to the zeroth order pyrolysis relation (to be defined later) the mass rate of fuel vapor evolved $\dot{m}''$ decreases downstream with the decreasing solid surface temperature. In the upstream, $\dot{m}''$ is cut off when the pyrolyzable fuel there is spent. A pyrolysis region can be defined if $\dot{m}''$ exceeds a prescribed value (we use $\dot{m}'' \geq 10^{-5}$ $g/cm^2/s$). Thus, a pyrolysis front and a pyrolysis base can be defined as illustrated in Fig. 1(*b*). In this illustration, the flame base has moved downstream from the ignition region after the solid fuel is consumed.

During combustion, the mass of solid fuel under the flame decreases. However, because the solid consists of one phase of combustible (90%) and another phase of an inert matrix (10%), its structural integrity is retained, and the solid surface remains flat and is located in the $y=0$ plane during the computational period. For thick solids, it is assumed that no local burnout occurs in the computational time interval. So the flame base will not move (staying close to $x=0$), while the flame tip may move downstream and the flame length grows in the process. For thin solids, once the solid fuel beneath the flame has been completely spent, the flame base will move downstream and leave the solid residue as pure inert solid.

2.2 Theoretical Formulation

2.2.1 Quasi-Steady Gas-Phase Approximation. Although flame growth is intrinsically an unsteady process, a quasi-steady gas-phase approximation will be adopted in this paper. This is possible because the controlling process in flame growth over solids is in the solid phase. By comparing the gas residence time in the flame zone and the heat-up time of the solid, one can deduce the conditions when the gas-phase time is much smaller. For normal operating conditions, the quasi-steady gas-phase approximation is a valid one except for ultrathin solids. In the example computations to be presented, the solid thicknesses are chosen so that this approximation holds. A detailed derivation of the criterion for the quasi-steady gas-phase approximation can be found in the Appendix.

The gas phase is coupled to the solid phase through interfacial energy and mass conservation boundary conditions. In this unsteady solid-phase and quasi-steady gas-phase formulations, the resolved time scale is that of the solid.

2.2.2 Solid-Phase Model. The time-dependent energy (heat conduction) equation is employed to solve for the transient solid temperature distribution

$$\rho_s C_s \frac{\partial T_s}{\partial t} = \frac{\partial}{\partial x}\left(k_s \frac{\partial T_s}{\partial x}\right) + \frac{\partial}{\partial y}\left(k_s \frac{\partial T_s}{\partial y}\right) \quad (1)$$

At the interface of the solid- and gas-phases, the energy conservation boundary condition is imposed

$$\dot{q}''_{c,\text{in}} - \dot{q}''_{r,\text{out}} - \dot{m}''L = k_s \frac{\partial T_s}{\partial y} \tag{2}$$

In this equation, $\dot{q}''_{c,\text{in}}$ is obtained from the quasi-steady gas-phase solution, $\dot{q}''_{r,\text{out}}$ is equal to solid surface radiation heat loss minus the flame radiation feedback, and $\dot{m}''L$ is the energy consumed in pyrolyzing the solid fuel. Note that both the left and right hand sides of Eq. (2) represent the net heat flux entering the interior of the solid, thus related to the heat-up of the solid fuel. To facilitate our discussion, we use $\dot{q}''_{\text{net,in}}(=\dot{q}''_{c,\text{in}} - \dot{q}''_{r,\text{out}} - \dot{m}''L)$ to denote this quantity.

To relate the mass burning rate to the surface temperature, a zeroth order pyrolysis relation is assumed at the fuel surface

$$\dot{m}'' = A_s \exp(-E_s/R_u T_{s,w}) \tag{3}$$

This is a major assumption for the solid combustion. Not all solids obey the zeroth order pyrolysis. In other works for cellulose, a first order pyrolysis relation has been assumed. The differences between the computed results for these two pyrolysis relations will be presented in a later paper [16]. Either form of the pyrolysis relation suffices for the purpose of this paper, i.e., understanding why and how the limiting states are reached. Note that Eq. (3) indicates that the solid burning rate is very sensitive to the surface temperature for a reasonable value of E_s/R_u (i.e., $\gg 1$).

In the computations, the solid fuel properties are assumed constant. They are based on cellulose. The solid fuel thermal conductivity is taken from Ref. [17] (fir in the cross-grain direction). The properties of the inert solid upstream of the solid fuel are set to be the same as those of the solid fuel for simplicity (except its density). The inert density is 10% of the virgin solid density. The virgin solid consists of 90% of combustibles and 10% of noncombustibles (inert). The solid fuel properties can be found in Ref. [15].

2.2.3 Gas-Phase Model. Because of the quasi-steady gas-phase approximation, the governing differential equations in the gas phase are the same as those used in the previous steady model [18]. The essential features in the model are summarized here.

Fully elliptic Navier–Stokes mass and momentum equations are employed together with energy and species equations. A one-step, second-order overall Arrhenius gas-phase reaction is adopted. The gas-phase codes have two-dimensional and three-dimensional versions with the option whether to include flame radiation and gravity. In this paper, two-dimensional, purely forced (zero-gravity) concurrent, laminar flow is modeled with flame and surface radiation. The radiation transfer equation is solved using the S-N discrete ordinates method [19,20]. The radiation participating species are CO_2 and H_2O. Soot is assumed to be absent. This is justified by the experimental observation that many of the near-limit flames in low-speed flow are blue in color [21]. In order to account for the absorption effect in the gas layer, total absorption coefficients are modified from the Plank-mean values. Detailed description on the correction procedure of the absorption coefficients can be found in Refs. [19,22]. The solid surface radiation is assumed to be gray with emissivity and absorption coefficients equal to 0.92. The treatment of the flame radiation using the S-N discrete ordinates method facilitates the detailed study of heat-flux distributions over the solid surface to be given later.

In the gas phase, variable specific heat and thermal conductivities, and constant Lewis numbers for every species (but different for each species) are assumed. For the transport properties, it is assumed that μ, k/C_p, and ρD_i are all proportional to $T^{0.7}$. The gas density is evaluated from the ideal-gas equation of state. Again, all values of the gas-phase properties used in the computation can be found in Ref. [15].

2.3 Numerical Scheme. The system of governing differential equations, and initial and boundary conditions are solved numerically. Time marching is performed by integration of Eq. (1) over the solid phase. After each time step, the solid provides new boundary conditions for the gas at the interface. The gas-phase equations are then iterated to a new steady state. This, in turn, gives a new gas-phase input to the solid, and the integration cycle in time is then repeated.

The computation starts from the ignition sequence. As mentioned earlier, a prescribed external heat flux to the solid and an ignition wire in the gas phase were employed. Once solid ignition is achieved with a flame over 1-cm long, these external stimuli are turned off and a self-sustained flame growth process begins.

In the numerical algorithm, an unsteady solid-phase code has been written. The temperature gradient is obtained by central differencing. The transient conduction governing equation is discretized using the general finite-difference technique and is solved by the alternating-directions-implicit (ADI) method. For grid points on the solid surface, the explicit scheme is chosen in order to linearize the discretization equation. The solid-phase code is written using FORTRAN in order to be compatible with the gas-phase code.

To solve the quasi-steady gas-phase equations iteratively, the computational code previously established in Refs. [9,13,18] is used. Here, the convection-diffusion fluxes are discretized using the power-law scheme. The system of the coupled elliptic partial differential equations is solved by the SIMPLER algorithm [23] and by a sweeping line-by-line procedure, which is a combination of Gauss–Seidel and the tridiagonal matrix algorithm (TDMA).

A nonuniform grid structure is adopted in this model. To resolve the flame structure in the stabilization zone (located at the flame base), the chosen characteristic length used to nondimensionalize the gas-phase equations is the thermal-diffusional distance in the flame stabilization zone α_g/V_∞. This length is relatively large in low-speed flow. For example, $\alpha_g/V_\infty = 0.426$ cm for $V_\infty = 5$ cm/s in this paper. Finer grids are specified in the region close to the flame where the temperature and species gradients are large. In the region $0 < x < 50.2$ and $0 < y < 8$, the nondimensional grid size in both x- and y-directions is 0.2. The minimum grid size for $x < 0$ is 0.1. Away from the abovementioned region, the grids are expanded by factors of 1.1 upstream and downstream, and of 1.2 in the y-direction. In the solid phase, the grid size in the x-direction is the same as that for the gas phase. In the y-direction, the grid pattern is in the same fashion as in the gas phase, i.e., expanded away from the solid surface, except the smallest grid size is one fifth (thick solid) or one fiftieth (thin solid) of that of the gas-phase.

The time steps used are different for the thick- and thin-solid cases. For the thick fuel (i.e., without solid burnout), after ignition, the flame grows along the fuel surface while the base remains stationary around the interface between the solid fuel and the inert solid. To resolve the initial flame growth, the required time steps are small, especially near ignition, to prevent divergence of the gas-phase iteration by the large changes in the solid. However, using small time steps for the entire simulation is not economical, especially near the steady state. Hence, various time steps are used at different stages of the flame growth process. The time steps used in the example case to be shown in Sec. 3 are as follows:

$$\Delta t = \begin{cases} 0.02 \text{ (s)} & \text{for } t \le \text{ignition time} + 20 \text{ s (during and right after igniton)} \\ 0.05 \text{ (s)} & \text{for ignition time} + 20 \text{ s} < t \le 20 \text{ min (during flame growth)} \\ t \times 10^{-4} & \text{for } t > 20 \text{ min (near quasi-steady state)} \end{cases}$$

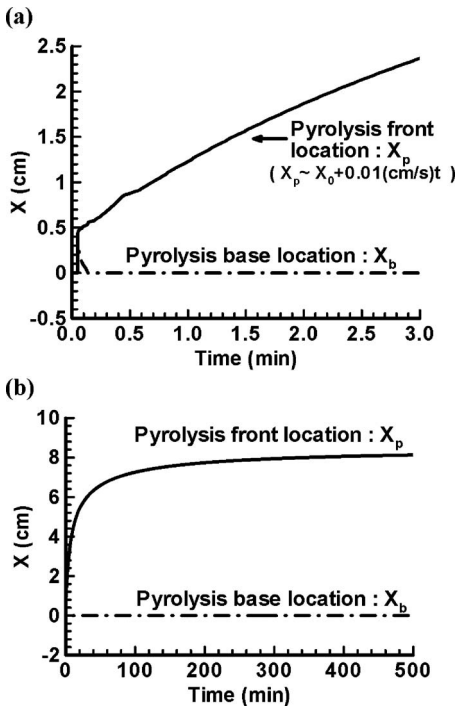

Fig. 2 Locus of pyrolysis front and base over the infinitely thick solid with flow condition: $X_{O_2,\infty}=21\%$, $V_\infty=5$ cm/s

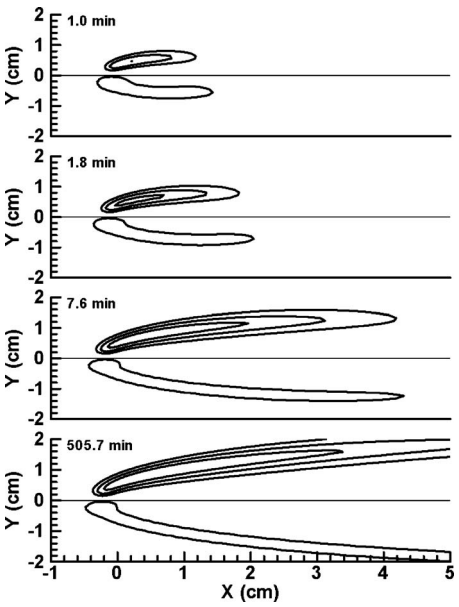

Fig. 3 Flame growth process over the thick solid. Upper half-plane: gas-phase temperature contour. The outermost contour has a value of 1350 K, and the difference between two adjacent contours is 150 K. Lower half-plane: vapor fuel reaction rate contour of $\dot{\omega}_F=10^{-4}$ g/cm^3/s.

For this thick fuel case, the computational time is about 15 h on the high performance computer cluster of Case Western Reserve University.

For a thin solid, the flame also grows in length initially. After solid burnout, however, the flame base spreads downstream along the solid surface. Although a steady spread rate and a limiting length can be reached, with the present coordinate system fixed with the laboratory, the mathematical system is always unsteady. Consequently, the time step cannot be large. In the present computation, a uniform solid time step (0.0013 s) is adopted for the thin fuel. The computational time is about 50 h, much longer than that of the thick fuel case in which an expanding solid time step is employed.

3 Computed Results and Discussion

Computed results for the two cases will be given in detail. The first case is for a very thick solid where no solid fuel burnout is assumed (thick-solid case). The second case is for a thin solid ($\rho_s\tau=28.4$ mg/cm^2) where solid burnout occurs (thin-solid case).

3.1 Flame Growth and Stopping Over a Thick Solid. To illustrate how a self-sustained flame grows over a thick-solid fuel, a representative case in low-speed forced flow in zero gravity is used for illustration with upstream flow velocity $V_\infty=5$ cm/s and 21% oxygen. Figure 2(*a*) shows the *x*-locus of the pyrolysis front (x_p) and pyrolysis base (x_b) of this flame versus time in the early stage of the simulation (the first 3 min). The solid is ignited and the flame starts a self-sustained growth process after 0.5 min. During the flame growth, the pyrolysis base stays close to the interfacial position between the solid fuel and the inert ($x=0$) at all times since there is no burnout. The pyrolysis front moves downstream with time, resulting in a flame growing in length. In this figure, x_p is only slightly curved and can be approximated by a linear fit with time after the ignition period with pyrolysis front velocity $V_p\sim0.01$ cm/s. This result of an approximately constant flame growth rate agrees both with the experimental observations in Refs. [2,24] and with the modeling result without radiative loss in Ref. [3]. Because a low-speed forced flow is used in this paper, the computed V_p is smaller than those in Refs. [2,24]. In addition, the qualitative agreement of a constant V_p is only valid in the initial period of the flame growth process.

The simulation is continued. Figure 2(*b*) shows x_p and x_b versus time up to 500 min. The pyrolysis front growth rate slows down with time. After about 100 min, a nearly constant limiting length is reached, and the flame practically no longer grows in length. At the end of the simulation, the flame reaches a quasi-steady state with a limiting flame length. A flame with a decelerating growth rate is found in this simulation.

3.1.1 Why Does the Flame Stop Growing? To explain why the flame stops growing, the flame profiles and the various heat-flux distributions over the solid are examined.

In Fig. 3, the gas-phase temperature contours at several times are shown in the upper half-plane and, for ease of reading, the corresponding visible flame (contour of $\dot{\omega}''_F=10^{-4}$ g/cm^3/s) is plotted in the lower half-plane. As the flame lengthens, the flame tip standoff distance δ (perpendicular distance from the solid surface to the temperature contour tip) increases as expected in a boundary layer flow over a flat surface, resulting in a decrease in the convective heat flux at the flame tip.

In Fig. 4, the heat fluxes over the solid surface are shown in the upper half-plane, and the nondimensional solid temperature contours are shown in the lower half-plane. These include heat flux into the solid by gas-phase convection $\dot{q}''_{c,\text{in}}$, net radiative heat flux leaving the solid (outward solid surface radiation minus inward flame radiation) $\dot{q}''_{r,\text{out}}$, and the energy of the phase transition (solid to vapor) $\dot{m}''L$. The net heat flux $\dot{q}''_{\text{net,in}}$ entering the solid interior is equal to $(\dot{q}''_{c,\text{in}}-\dot{q}''_{r,\text{out}}-\dot{m}''L)$, as stated in Eq. (2). Figure 4(*a*) shows that the $\dot{q}''_{c,\text{in}}$ decreases downstream. However, $\dot{q}''_{r,\text{out}}$ and $\dot{m}''L$ also decrease downstream (in accordance with the decreasing surface temperature). This results in an almost uniform $\dot{q}''_{\text{net,in}}$ in the pyrolysis zone ($l_p=1.2$ cm). This uniform $\dot{q}''_{\text{net,in}}$ provides the energy to heat up the interior of the solid. The bottom of Fig. 4(*a*), for the nondimensional solid temperature distribution, shows that at this instance, only a shallow layer of the solid is heated. At a later time ($t=1.8$ min), Fig. 4(*b*) shows that the flame lengthens with $l_p=1.74$ cm. Here, $\dot{q}''_{\text{net,in}}$ is still uniform in the pyrolysis region but

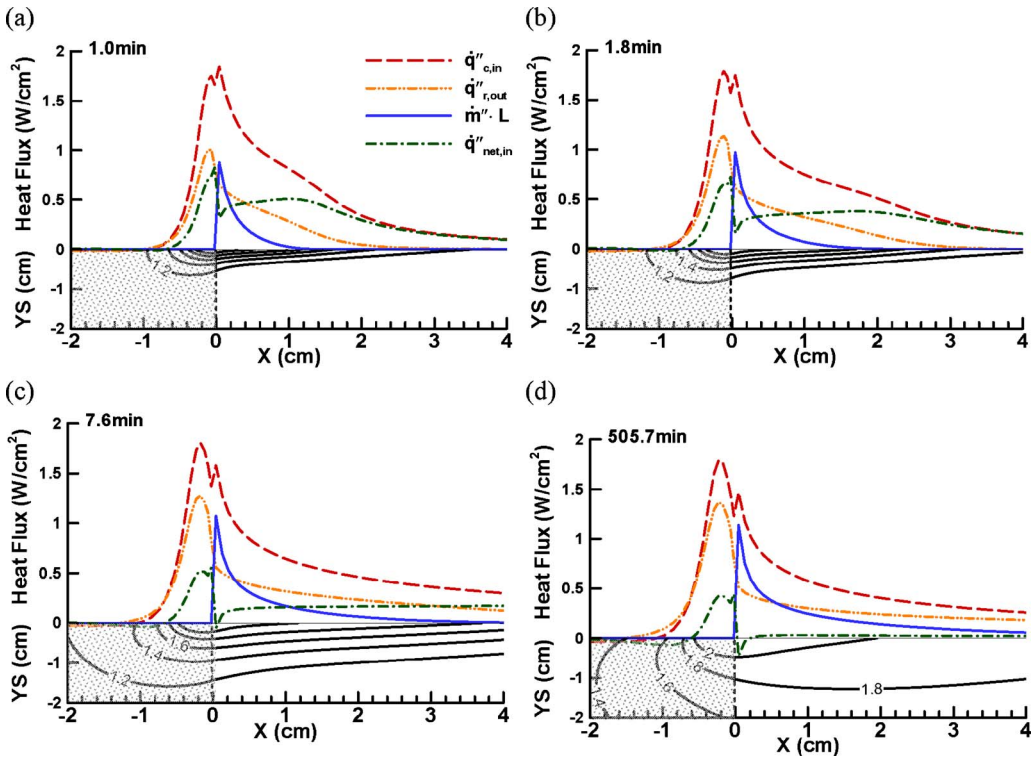

Fig. 4 Solid heat transfer process over the thick solid. Upper half-plane: heat fluxes over the solid surface; lower half-plane: solid-phase temperature contour. Difference between two adjacent contours is 0.2. Temperature is nondimensionalized by 300 K. The shaded portion of the solid is inert.

its magnitude has decreased compared with that at $t=1$ min. The decrease is due to a combined effect of the decrease in convective heat feedback from the flame and the solid surface heat-up. This requires discussion. At a fixed location (say $x=1$ cm) within the pyrolysis zone for both times, $\dot{q}''_{c,\text{in}}$ at these two instances are close. This is consistent with the boundary layer concept (a small difference between the two is due to different solid temperatures and downstream influences.). The solid surface temperature, however, is higher at $t=1.8$ min by the additional heating received from the flame. Consequently, both $\dot{q}''_{r,\text{out}}$ and $\dot{m}''L$ are higher, causing a lower $\dot{q}''_{\text{net,in}}$. From another point of view, we examine the pyrolysis front heat fluxes at these two times. The pyrolysis front for the flame at $t=1.8$ min is at $x=1.74$ cm. At this location, the surface temperature, $\dot{q}''_{r,\text{out}}$, and $\dot{m}''L$ are close to those at the pyrolysis front (at $x=1.2$ cm) for the $t=1$ min flame. $\dot{q}''_{c,\text{in}}$ at the pyrolysis front for the $t=1.8$ min flame is, however, much lower because of the larger flame standoff distance, as mentioned earlier (shown in Fig. 3). The result is again a lower $\dot{q}''_{\text{net,in}}$. This phenomenon is also shown in Fig. 5. Figure 5 is the time history of heat fluxes at the pyrolysis front. Please note that $\dot{m}''L$ at the pyrolysis front is always constant, by definition. Also, $\dot{q}''_{r,\text{out}}$ decreases slightly with time due to an increase in the radiation flame feedback to the solid surface as the flame lengthens. With $\dot{q}''_{c,\text{in}}$ decreasing with time, and $\dot{m}''L$ and $\dot{q}''_{r,\text{out}}$ remaining almost constant, the net pyrolysis front heat flux $\dot{q}''_{\text{net,in}}$ decreases over time.

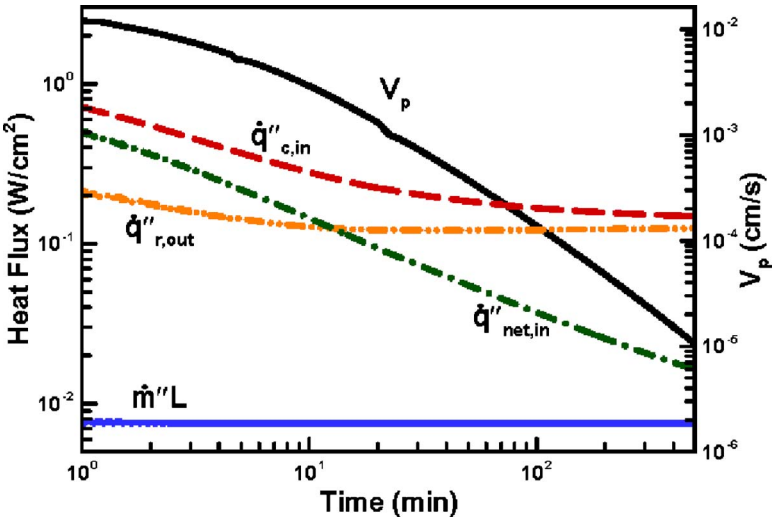

Fig. 5 Time history of heat fluxes at x_p and V_p for the thick solid

Figures 4(*c*) and 4(*d*) show that this trend continues. At $t=7.6$ min, in the pyrolysis zone, $\dot{q}''_{\text{net,in}}$ is 34.6% of that at $t=1$ min. At $t=505.7$ min, $\dot{q}''_{\text{net,in}}$ is nearly zero (3.3% of that at $t=1$ min). Since $\dot{q}''_{\text{net,in}}$ in the preheat zone is always lower than at the pyrolysis front, a nearly zero $\dot{q}''_{\text{net,in}}$ at the pyrolysis front implies a near zero pyrolysis front speed. This is further illustrated by the flame front velocity (V_p) time history in Fig. 5. Therefore, it is concluded that the flame stops growing because of the vanishing of the net heat input at the pyrolysis front. For the two-dimensional sample (i.e., the case modeled here), this is the result of an approximate balance between the net surface radiative heat loss and the convective heat gain, as previously suggested by Honda and Ronney using heuristic reasoning [7].

3.1.2 A Remark on Limiting Flame Length. The flame deceleration phenomena discussed above appears to be an asymptotic process. For a theoretically infinitely thick solid, i.e., no local burnout in finite time, the limiting length and zero spreading velocity may take an infinitely long time to reach. Although we cannot determine the exact limiting length using the present numerical approach, Fig. 2 shows that a practical limiting length is attained at the end of computation (500 min). Also, the time scale must be discussed. In low-speed forced flow with an air velocity of only 5 cm/s, the heat flux is weak, and the burning and spread rates are low. That is why it requires such a long time (500 min) to reach a quasi-converged state. This time scale and the limiting flame length depend on many parameters. Reference [15] shows that the limiting flame length increases monotonically with increasing ambient oxygen percentage and flow velocity, as expected.

3.2 Flame Growth and Steady Spread Over a Thin Solid. In this paper, it should be noted that by "a thin solid" we mean a solid will experience local burnout (or burn through) during the computational period. The solid can either be "thermally" thick, thin, or in-between. In the computation, the thermally thin assumption is not imposed since solid heat conduction is included. However, for the chosen solid fuel area density (mass per unit area) $\rho_s\tau=28.4$ mg/cm^2, the computed solid temperature profiles show that this solid is approximately thermally thin. In addition, for this chosen value of area density, the quasi-steady gas-phase approximation is valid (see Appendix).

For the thin solid, the same flow condition as the previous thick fuel case is used ($V_\infty=5$ cm/s, $X_{O_2,\infty}=21\%$). It should be noted that in the previous thick fuel case, the flow entrance length remains constant. However, for the thin fuel case, the flow entrance length increases with time when the flame base moves downstream. As we shall see later, this variable entrance length influences the flame growth process. In order to isolate this flow entrance length effect, we first present a case in which we artificially keep the entrance length fixed in the computation. To do that, we vary the position where we impose the forced plug-flow according to the pyrolysis base (i.e., the burnout point) location. Uniform 5 cm/s flow velocity is always imposed 6.3 cm upstream of the pyrolysis base. By doing so, the flame base "sees" the same flow pattern during the whole flame growth process. To realize a constant entrance length experimentally, a special setup is required as demonstrated in Ref. [25].

3.2.1 Flame Growth Process With a Constant Flow Entrance Length. The *x*-locus of the pyrolysis front and base versus time are shown in Fig. 6. The solid fuel is ignited at $t\sim5$ s. After ignition, the flame begins a self-sustained growth process. As shown in Fig. 6, solid burnout occurs, and the pyrolysis base begins to move around $t\sim10$ s. After that, both the pyrolysis front and the pyrolysis base propagate downstream. Figure 7 shows the velocities of pyrolysis front (V_p) and base (V_b) versus time. In the early stage of flame growth, both V_p and V_b increase with time; V_p is larger than V_b, and the flame lengthens (as shown in Fig. 6, l_p increases at the beginning). At $t\sim29$ s, V_p reaches a maximum value, then decreases, and eventually approaches V_b. This unusual nonmonotonic flame tip speed variation will be explained later.

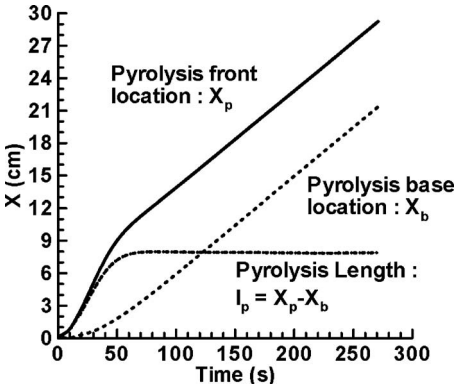

Fig. 6 Pyrolysis front, pyrolysis base locus, and pyrolysis length versus time for the thin solid with $\rho_s\tau=28.4$ mg/cm^2. The flow entrance length=6.3 cm. Flow condition: $X_{O_2,\infty}=21\%$, $V_\infty=5$ cm/s.

When $t\sim80$ s, V_p becomes identical to V_b. l_p reaches a constant limiting length, as shown in Fig. 6. Steady flame spread is observed, in which the flame propagates downstream at a constant rate with a constant flame length. In a coordinate system attached to the moving solid burnout point, we see a steady flame and a steady flow field. It is this steady limit that has been pursued in previous concurrent flame spread models for thin solids in Refs. [9,10,12,13,18,20,26,27]. In these previous modeling works, steady solutions were obtained iteratively, thus yielding no information on the transient processes leading to the steady limit.

3.2.1.1 Heat flux distributions. Various heat-flux distributions over the solid are examined in a time sequence. In Fig. 8, the heat-flux distributions $\dot{q}''_{c,\text{in}}$, $\dot{q}''_{r,\text{out}}$, $\dot{m}''L$, and $\dot{q}''_{\text{net,in}}$ are shown in the upper plane, and the nondimensional solid temperature is shown in the lower plane. The gas temperature contour corresponding to 1350 K is also inserted in the upper plane to show the flame shape and length at that moment (it is aligned with the *x*-coordinate). The flame tip also serves as an indicator of the pyrolysis front position. Note that we have aligned the base of the flame profiles at different times to facilitate plotting and reading; the solid burnout point (or the flame base) moves as indicated by the values in the *x*-axis (different scales in each instance).

First, we examine $\dot{q}''_{c,\text{in}}$, $\dot{q}''_{r,\text{out}}$, and $\dot{m}''L$ in the upper plane in Fig. 8. The shapes of their spatial distribution are similar to those in the thick-solid case (Fig. 4). $\dot{q}''_{c,\text{in}}$ is largest near the flame base, and decays in the downstream direction over both the pyrolysis and the preheat zones. The maximum value at ~1.8 W/cm^2 is

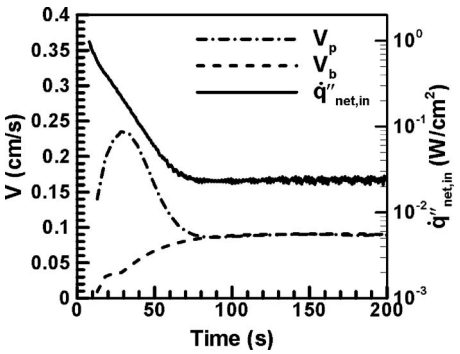

Fig. 7 Velocities of pyrolysis front and base and $\dot{q}''_{\text{net,in}}$ at x_p versus time for the thin solid with a constant flow entrance length

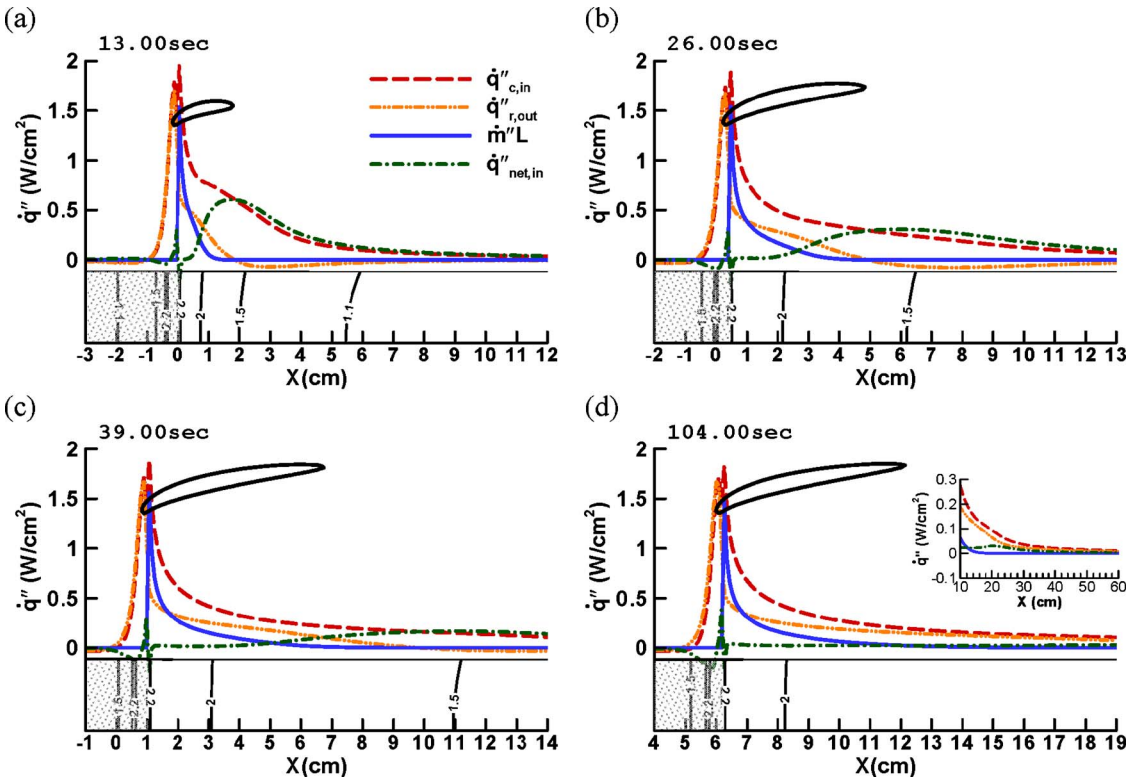

Fig. 8 Transient solid heat transfer process for the thin solid with a constant flow entrance length. Upper plane: Heat fluxes over the solid surface. Temperature contour of value 1350 K is also shown on the upper plane. Lower plane: solid-phase temperature contour. The vertical axis is from the surface to the center of the sample. Temperature is nondimensionalized by 300 K. The shaded portion of the solid is inert or leftover inert residue.

also close to that for the thick case. $\dot{q}''_{r,\text{out}}$ has its maximum located slightly upstream of the fuel-inert interface. At the interface (i.e., the upstream end of pyrolysis zone), it is slightly larger for the thin solid. Note, however, that the negative value of $\dot{q}''_{r,\text{out}}$ in the flame front region (see Figs. 8(*a*) and 8(*b*)) indicates that the flame radiative feedback can exceed the surface loss. The nonzero region of $\dot{m}''L$ defines the pyrolysis zone ($\dot{m}'' \geq 10^{-5}$ g/cm^2/s in this paper). The peak of $\dot{m}''L$, occurring at the pyrolysis base, is larger than that for the thick case by 50%. Because the amount of heat needed to heat up a thin solid is less than that for a thick solid, more heat feedbacks from the flame can go to vaporizing the solid. This produces a larger $\dot{m}''$.

The above comparisons of $\dot{q}''_{c,\text{in}}$, $\dot{q}''_{r,\text{out}}$, and $\dot{m}''L$ help to explain the large qualitative difference in $\dot{q}''_{\text{net,in}}$ distributions between the thin and thick samples. Recall that in the thick-solid case, $\dot{q}''_{\text{net,in}}$ is nearly uniform over the pyrolysis zone and monotonically decreases downstream in the preheat zone. Figure 8 shows that in the thin solid, the $\dot{q}''_{\text{net,in}}$ distribution is quite different. It is nearly zero around the flame base region and peaks at a location slightly downstream of the pyrolysis front (e.g., at ~1.5 cm and 6 cm in Figs. 8(*a*) and 8(*b*), respectively). Near the flame base, the solid temperature is near its maximum value so no heat is needed to raise the temperature, and little heat goes into the interior and along the surface directions since it is thermally thin. This is consistent with the heat balance equation $\dot{q}''_{\text{net,in}} = \dot{q}''_{c,\text{in}} - \dot{q}''_{r,\text{out}} - \dot{m}''L$. At the flame base, $\dot{m}''L$ is much larger for the thin solid, while $\dot{q}''_{c,\text{in}}$ and $\dot{q}''_{r,\text{out}}$ are approximately equal. So $\dot{q}''_{\text{net,in}}$ is much smaller for the thin solid. For the thick solid, the larger $\dot{q}''_{\text{net,in}}$ at the flame base is due to the heat conduction into the solid interior, as illustrated in the lower plane in Fig. 4.

Another key difference between the thin and thick solids is the magnitude of $\dot{q}''_{\text{net,in}}$ in the preheating at the steady states. For the thick sample, it is zero since flame growth stops. For the thin sample, as shown in Fig. 7, $\dot{q}''_{\text{net,in}}$ at the pyrolysis front reaches a constant nonzero value compatible with the steady spread rate. This nonzero $\dot{q}''_{\text{net,in}}$ in the preheating can also be seen in the inset in Fig. 8(*d*).

To explain the nonmonotonic trend of the flame tip spread rate V_p with respect to time, we note that V_p is proportional to the total heat input to the preheat zone. In thin solids, almost all the heat input comes from the gas phase and is equal to the product of the average heat flux (per unit area) and the preheat length. Initially, the heat flux is high and the preheat length is small. Later, the preheat length becomes large but the heat flux diminishes (as shown in Figs. 6 and 7). The product of the two results in a peak during the flame growth process, and hence, the nonmonotonic trend of V_p shown in Fig. 7.

3.2.2 Flow Entrance Length Effect. In the previous thin-solid fuel case, the position where the forced plug-flow is imposed varies with time so that the flow entrance length (the distance from the plug-flow to the pyrolysis base) is kept fixed (6.3 cm in the example computed). As stated before, this seemingly artificial specification is necessary so that a true steady spreading flame can be realized. In this section, this condition is removed, and the forced plug-flow will be imposed at a fixed position, 6.3 cm upstream of the initial interface of the inert and fuel solids. As the pyrolysis base moves downstream during the flame growth process, the position of the imposed forced flow does not move. As a result, the flow entrance length seen by the flame base increases with time, and the flame sees an incoming flow with a smaller velocity. This affects the flame profile and the spreading characteristics. The computed effect of the flow entrance length is reported next.

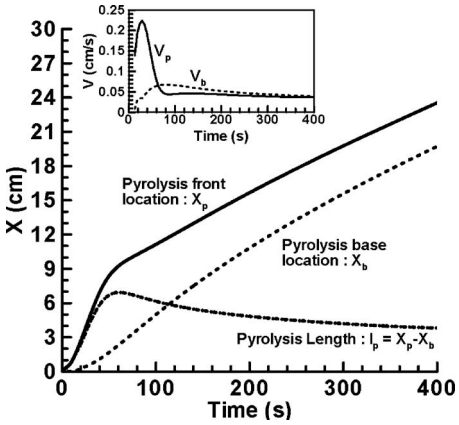

Fig. 9 Pyrolysis front, pyrolysis base locus and pyrolysis length versus time for the thin solid with $\rho_s\tau$=28.4 mg/cm^2. Inset: Velocities of pyrolysis front and pyrolysis base versus time. The flow entrance length is variable (from 6.3 cm to 27.6 cm). Flow condition: $X_{O_2,\infty}$=21%, V_∞=5 cm/s.

The positions of pyrolysis front and pyrolysis base of a flame with variable entrance length are shown in Fig. 9. Compared with Fig. 6, we have similar flame growth time histories but there are several differences. First, we see that with a varying flow entrance length, the pyrolysis length does not reach a constant for large time. After an initial quick increase, it monotonically decreases with time. The movements of the pyrolysis front and base do not approach true steady states at large times either. Both trajectories curve slightly at large times. The slow-down of these movements can be seen more clearly from the velocity plot in the inset in Fig. 9. The velocity-time history shows that, in addition, the pyrolysis base propagates faster than the pyrolysis front after $t>65$ s, resulting in a slowly shrinking pyrolysis length. This is in contrast to the previous case of a constant limiting pyrolysis length shown in Fig. 6. At the end of the simulation, the entrance length becomes 27.6 cm (the initial entrance length is 6.3 cm). The pyrolysis length (3.76 cm) and the spread rate (0.038 cm/s) are only 47.6% and 48.1%, respectively, of those in the constant entrance length case, reflecting the effect of a smaller flow velocity at the flame zone after it moves downstream.

Although the case with constant flow entrance length simplifies the interpretation of the results, this case with variable entrance length is easier to establish in an experiment.

4 Conclusion

A two-dimensional, nonsteady, laminar flame spread model over solids in low-speed concurrent forced flow has been formulated and numerically solved. The model consists of governing partial differential equations for the conservations of mass, momentum, energy, species, and gas-phase radiation heat transfer. The model has a quasi-steady gas phase and a transient solid phase. Computations were performed for two cases: a thick solid, where no local solid burnout occurs, and a thin solid, where there is solid burnout. The numerical solutions provide a time history of the flame growth process including detailed gas and solid profiles as well as the heat-flux distributions. The following are some of the key findings of this paper:

(1) For thick samples without solid burnout, the flame base is stationary and only the flame tip propagates downstream during the flame growth process. The growth rate decreases with time, however. A limiting flame length is asymptotically reached and flame growth finally stops. In this two-dimensional forced concurrent configuration, the mechanism of flame stop is the vanishing downstream heat flux as a result of the cancellation between convective heat input and radiative heat loss.

(2) For thin samples, the solid burnout at the flame base is essential in determining the fate of the flame. Solid burnout makes it possible to attain a steady propagating flame with a constant limiting length. This condition is reached when the flame tip propagation velocity equals the flame base velocity. It is the nonzero finite net heat input over the preheat region, which enables the pyrolysis front to advance downstream.

(3) There are qualitative differences on the time histories of the flame tip (or pyrolysis front) spreading characteristics between the thick and thin solids. In this low-speed forced concurrent flow, the flame tip motion decelerates after ignition all the way to practically zero velocity for the thick sample. In thin samples, flame tip first accelerates, then decelerates, and ends with a constant nonzero steady spread. The difference between the two cases lies on the different heat-flux distributions between the two cases and also whether solid burnout will occur or not.

(4) True steady spread and true constant limiting length can be realized only when the flame base sees the same incoming flow velocity with time, i.e., same flow entrance length. If the entrance length varies with time as a result of the flame base movement, the flame spread rate and flame length will slowly vary, i.e., instead of a steady state, a quasi-steady state is reached.

Acknowledgment

This research is supported by a grant from NASA Glenn Research Center monitored by Dr. Gary Ruff.

Nomenclature

A_s = solid-phase pre-exponential factor
C_p = gas-phase specific heat
C_s = solid-phase specific heat
D_i = diffusion coefficient of species i
E_s = solid-phase activation energy
k = thermal conductivity
l = length
L = latent heat
L_i = initial entrance length
L_s = external heat flux width
$\dot{m}''$ = mass burning rate or fuel vapor mass flux
$\dot{q}''_{c,\text{in}}$ = convective heat flux to the solid surface from the gas phase
$\dot{q}''_{r,\text{out}}$ = net radiative heat loss from the solid surface
$\dot{q}''_{\text{net,in}}$ = net heat flux entering the solid interior ($=\dot{q}''_{c,\text{in}} - \dot{q}''_{r,\text{out}} - \dot{m}''L$)
R_u = universal gas constant
Re = Reynolds number
t = time
T = temperature
$T_{s,w}$ = solid surface temperature
V = velocity
x = x-coordinate
$X_{O_2,\infty}$ = freestream oxygen molar fraction
y = y-coordinate
α = thermal diffusivity
δ = flame tip stand-off distance
ρ = density
μ = viscosity
τ = solid thickness
$\dot{\omega}_F$ = fuel vapor consumption rate

Superscripts

$'$ = per unit length
$''$ = per unit area
$\cdot$ = per unit time

Subscripts

b = burnout
f = flame
F = fuel
g = gas phase
p = pyrolysis
s = solid phase
∞ = ambience

Appendix: Condition for Quasi-Steady Gas-Phase Approximation

Quasi-steady gas-phase approximation is valid if the characteristic time of the gas phase is much smaller than that of the solid phase. In this model, the gas-phase characteristic time is represented by the gas residence time in the flame

$$t_g \sim l_f / V_\infty \tag{A1}$$

The solid-phase characteristic time is taken to be the heat-up time in the preheat region of the solid. For a thermally thick-solid fuel, the heat-up time is

$$t_s \sim \frac{\pi \rho_s C_s k_s (T_p - T_\infty)^2}{4(\dot{q}''_{\text{net,in}})^2} \tag{A2}$$

As we see in this paper, $\dot{q}''_{\text{net,in}} (= \dot{q}''_{c,\text{in}} - \dot{q}''_{r,\text{out}} - \dot{m}''L)$ denotes the net heat flux entering the solid in the preheat region. Normally, $\dot{q}''_{r,\text{out}}$ and $\dot{m}''L$ are negligible compared with $\dot{q}''_{c,\text{in}}$ in the preheat region and $\dot{q}''_{c,\text{in}}$ decays from its value at the pyrolysis front monotonically downstream over the preheat region. Hence, $\dot{q}''_{\text{net,in}}$ can be estimated as follows:

$$\dot{q}''_{\text{net,in}} = \dot{q}''_{c,\text{in}} - \dot{q}''_{r,\text{out}} - \dot{m}''L \sim \dot{q}''_{c,\text{in}} \leq \frac{k_g (T_f - T_p)}{\delta} \tag{A3}$$

In this paper, δ is defined as the vertical distance from the solid surface to the temperature peak. Hence, the right hand side of Eq. (A3) is of the order of the convective heat flux at the pyrolysis front, which is also the convective heat flux maximum over the preheat region. Using the boundary layer theory for a diffusion flame, δ can be estimated as

$$\delta \sim \frac{l_f}{\sqrt{\text{Re}}} \sim \sqrt{\frac{\mu l_f}{\rho_g V_\infty}} \tag{A4}$$

Using Eqs. (A1)–(A4), the ratio of the solid-phase characteristic time to the gas-phase characteristic time for a thermally thick-solid fuel is

$$\frac{t_s}{t_g} \sim \frac{\pi \rho_s C_s k_s (T_p - T_\infty)^2 V_\infty}{4(\dot{q}''_{\text{net,in}})^2 l_f} \geq \frac{\pi \rho_s C_s k_s \mu (T_p - T_\infty)^2}{4 \rho_g k_g^2 (T_f - T_p)^2} \tag{A5}$$

Inserting the properties used in this paper, $t_s / t_g \sim 50$, which is much greater than unity. Hence, the quasi-steady gas-phase approximation is appropriate for the thermally thick-solid fuel. Since the net heat flux in Eq. (A5) is evaluated at the maximum location in the preheat zone (i.e., at the pyrolysis front), this is a conservative estimate.

For a thermally thin-solid fuel, the heat-up time is

$$t_s \sim \frac{\rho_s \tau C_s (T_p - T_\infty)}{2 \dot{q}''_{\text{net,in}}} \tag{A6}$$

assuming there is flame on both sides of the solid. Using Eqs. (A1), (A3), (A4), and (A6), the ratio of t_s to t_g for a thermally thin-solid fuel is

$$\frac{t_s}{t_g} \sim \frac{\rho_s \tau C_s (T_p - T_\infty) V_\infty}{2 \dot{q}''_{\text{net,in}} l_f} \geq \frac{\rho_s \tau C_s (T_p - T_\infty)}{2 k_g (T_f - T_P)} \sqrt{\frac{\mu V_\infty}{\rho_g l_f}} \tag{A7}$$

One sees that for $t_s / t_g \gg 1$, $\rho_s \tau$ cannot be too small. In our computations for the thin solid, $\rho_s \tau$ is chosen to be 28.4 mg/cm^2, which gives $t_s / t_g > 10$. As with the thermally thick-solid estimate, this is also conservative. Since $t_s / t_g \gg 1$ for both thick- and thin-solid fuel cases, the quasi-steady gas-phase is a good approximation in this paper.

References

[1] Fernandez-Pello, A. C., 1978, "A Theoretical Model for the Upward Laminar Spread of Flames Over Vertical Fuel Surfaces," Combust. Flame, **31**, pp. 135–148.
[2] Orloff, L., DeRis, J., and Markstein, G. H., 1974, "Upwind Turbulent Fire Spread and Burning of Fuel Surface," Proc. Combust. Inst., **15**, pp. 183–192.
[3] Carrier, G. F., Fendell, F. E., and Feldman, P. S., 1980, "Wind-Aided Flame Spread Along a Horizontal Fuel Slab," Combust. Sci. Technol., **23**, pp. 41–78.
[4] Brehob, E. G., and Kulkarni, A. K., 1998, "Experimental Measurements of Upward Flame Spread on a Vertical Wall With External Radiation," Fire Saf. J., **31**, pp. 181–200.
[5] Tewarson, A., 2002, "Generation of Heat and Chemical Compounds in Fires," *The SFPE Handbook of Fire Protection Engineering*, 3rd ed., The National Fire Protection Association Press, Quincy, MA, pp. 3-82–3-161.
[6] Ivanov, A. V., Balashov, Ye. V., Andreeva, T. V., and Melikhov, A. S., 1999, "Experimental Verification of Material Flammability in Space," NASA Report No. CR 1999–209405.
[7] Honda, L. K., and Ronney, P. D., 2000, "Mechanisms of Concurrent-Flow Flame Spread Over Solid Fuel Beds," Proc. Combust. Inst., **28**, pp. 2793–2801.
[8] Chu, L., Chen, C.-H., and T'ien, J. S., 1981, "Upward Spreading Flames Over Paper Samples," ASME Paper No. 81-WA/HT-42.
[9] Jiang, C.-B., T'ien, J. S., and Shih, H.-Y., 1996, "Model Calculation of Steady Upward Flame Spread Over A Thin Solid in Reduced Gravity," Proc. Combust. Inst., **26**, pp. 1353–1360.
[10] Feier, I. I., Shih, H.-Y., Sacksteder, K. R., and T'ien, J. S., 2002, "Upward Flame Spread Over Thin Solids in Partial Gravity," Proc. Combust. Inst., **29**, pp. 2569–2577.
[11] Kleinhenz, J., Feier, I. I., Hsu, S.-Y., T'ien, J. S., Ferkul, P. V., and Sacksteder, K. R., 2008, "Pressure Modeling of Upward Flame Spread and Burning Rates Over Solids in Partial Gravity," Combust. Flame, **154**, pp. 637–643.
[12] Ferkul, P. V., and T'ien, J. S., 1994, "A Model of Low-Speed Concurrent Flow Flame Spread Over a Thin Fuel," Combust. Sci. Technol., **99**, pp. 345–370.
[13] Shih, H.-Y., and T'ien, J. S., 2003, "A Three-Dimensional Model of Steady Flame Spread Over a Thin Solid in Low-Speed Concurrent Flows," Combust. Theory Modell., **7**, pp. 677–704.
[14] Kumar, A., Shih, H.-Y., and T'ien, J. S., 2003, "A Comparison of Extinction Limits and Spreading Rates in Opposed and Current Spreading Flames Over Thin Solids," Combust. Flame, **132**, pp. 667–677.
[15] Tseng, Y.-T., 2007, "Ignition and Flame Growth in Concurrent Forced Flow Over Thick Solids," MS thesis, Case Western Reserve University, Cleveland, OH (available at http://filer.case.edu/yxt46/).
[16] Tseng, Y.-T., and T'ien, J. S., 2009, "The Effect of Different Pyrolysis Descriptions on Flame Spread Over Solids in Concurrent Flows," *Proceedings of the Sixth U.S. National Combustion Meeting*, Ann Arbor, MI (available at http://filer.case.edu/yxt46/).
[17] Brown, A. I., and Marco, S. M., 1958, *Introduction to Heat Transfer*, 3rd ed., McGraw-Hill, New York.
[18] Shih, H.-Y., and T'ien, J. S., 2000, "Modeling Concurrent Flame Spread Over a Thin Solid in a Low-Speed Flow Tunnel," Proc. Combust. Inst., **28**, pp. 2777–2784.
[19] T'ien, J. S., Shih, H.-Y., Jiang, C.-B., Ross, H. D., Miller, F. J., Fernandez-Pello, A. C., Torero, J. L., and Walther, D., 2001, *Microgravity Combustion: Fire in Free Fall*, H. Ross, ed., Academic, San Diego, CA, pp. 299–418.
[20] Jiang, C.-B., 1995, "A Model of Flame Spread Over a Thin Solid in Concurrent Flow With Flame Radiation," Ph.D. thesis, Case Western Reserve University, Cleveland, OH.
[21] Grayson, G. D., Sacksteder, K. R., Ferkul, P. V., and T'ien, J. S., 1994, "Flame Spreading Over a Thin Solid in Low-Speed Concurrent Flow—Drop Tower Experimental Results and Comparison With Theory," Microgravity Sci. Technol., **VII**(2), pp. 187–195.
[22] Rhatigan, J. L., Bedir, H., and T'ien, J. S., 1998, "Gas-Phase Radiative Effects on the Burning and Extinction of a Solid Fuel," Combust. Flame, **112**, pp. 231–241.
[23] Patankar, S. V., 1980, *Numerical Heat Transfer and Fluid Flow*, Hemisphere, New York.
[24] Loh, H.-T., and Fernandez-Pello, A. C., 1984, "A Study of the Controlling Mechanisms of Flow Assisted Flame Spread," Proc. Combust. Inst., **20**, pp. 1575–1582.
[25] Ferkul, P., Kleinhenz, J., Shih, H.-Y., Pettegrew, R., Sacksteader, K., and T'ien, J. S., 2004, "Solid Fuel Combustion Experiments in Microgravity Using a Continuous Fuel Dispenser and Related Numerical Simulations," Microgravity Sci. Technol., **15**(2), pp. 3–12.
[26] Loh, H.-T., and Fernandez-Pello, A. C., 1986, "Flow Assisted Flame Spread Over Thermally Thin Fuel," *Fire Safety Science—Proceedings of the First International Symposium*, pp. 65–74.
[27] Markstein, G. H., and DeRis, J., 1973, "Upward Fire Spread Over Textiles," Proc. Combust. Inst., **14**, pp. 1085–1097.

Effect of Selective Accommodation on Soot Aggregate Shielding in Time-Resolved Laser-Induced Incandescence Experiments

K. J. Daun
Department of Mechanical and Mechatronics Engineering,
University of Waterloo,
200 University Avenue West,
Waterloo, ON, N2L 3G1, Canada
e-mail: kjdaun@mme.uwaterloo.ca

Time-resolved laser-induced incandescence is an emerging diagnostic for characterizing primary particle size distributions within soot-laden aerosols. This measurement requires an accurate model of heat conduction between the laser-energized soot and the surrounding gas, which is complicated by the fractal-like structure of soot aggregates since primary particles on the aggregate exterior shield the interior from approaching gas molecules. Previous efforts to characterize aggregate shielding through direct simulation Monte Carlo analysis assume a Maxwell scattering kernel, which poorly represents actual gas/surface interactions. This paper shows how selective thermal accommodation into the translational and rotational modes of the gas molecule influences the aggregate shielding effect using the Cercignani–Lampis–Lord kernel and thermal accommodation coefficients derived from molecular dynamics simulations. [DOI: 10.1115/1.4001614]

Keywords: combustion, laser-induced incandescence, soot, free-molecular conduction, gas-surface scattering

1 Introduction

A growing understanding of how particle morphology influences the impact of soot on human health [1] and the environment [2] has motivated particle size-specific regulations for soot-producing combustion technologies [3] and a corresponding need for increasingly accurate nanoparticle diagnostics to assess compliance with these regulations. Diagnostics are also used to control synthesis of engineered nanoparticles such as carbon blacks [4] since the optical, mechanical, and chemical properties of these particles depend on their size and structure. Finally, soot diagnostics are important tools for designing the next generation of industrial combustion devices such as boilers and engines since soot formation within these devices influences their performance through combustion chemistry and radiative heat transfer [5].

Most types of nanoparticle diagnostics demand some understanding of momentum or heat transfer physics between the particles and the surrounding gas molecules. For example, particle sizing based on thermophoretic [6] and electrostatic [7] sampling requires an accurate model of momentum transfer between the particles and the surrounding gas since this influences the collection efficiency of different particle size classes. Time-resolved laser-induced incandescence (TiRe-LII) [8] is another type of nanoparticle sizing technique that uses a pulsed laser to energize refractory nanoparticles in the laser path to incandescent temperatures, typically 3000–3600 K in low fluence experiments. The energized particles cool back to the ambient gas temperature between the pulses, mainly by conduction with the surrounding gas molecules, and the spectral incandescence of particles contained in a sample volume is imaged onto a photodetector. The primary particle size distribution can be inferred from the observed incandescence decay by relating the drop in sensible energy to the particle cooling rate, as long as the latter quantity is modeled accurately.

Momentum [9] and heat [10] transfer between isolated nanospheres and surrounding gas molecules is generally well understood in both the free-molecular and transition regimes. Soot-laden aerosols consist not only of monomers, however, but groups of nanospheres (called primary particles) arranged in a fractal-like structure formed through repeated monomer-aggregate and aggregate-aggregate collisions within the aerosol. This complex structure complicates heat and momentum transfer calculations because primary particles on the aggregate exterior shield the aggregate interior from incident gas molecules, so simply multiplying heat or momentum transfer rates calculated for isolated spheroids by the number of primary particles in the aggregate overestimates the actual transfer between the aggregate and the surrounding gas.

Snelling et al. [11] developed a heuristic approach for calculating heat conduction from a soot aggregate in TiRe-LII experiments based on scaling rules normally used to infer the 3D fractal structure of soot particles from 2D electron microscopic images [12], reasoning that an approaching gas molecule "sees" the 2D projection of the soot aggregate, particularly when the mean free path in the gas is much larger than the aggregate. This treatment underestimates the true heat transfer rate, however, since it neglects gas molecules that partially accommodate with primary particles on the aggregate exterior and then scatter towards the aggregate interior, where they reach primary particles that are otherwise inaccessible through direct scattering.

More rigorous estimates of heat and momentum transfer between soot aggregates and a surrounding gas are found through direct simulation Monte Carlo (DSMC), which was first adapted by Filippov et al. [13] and Liu and co-workers [14,15] to calculate heat transfer from laser-energized soot particles in TiRe-LII experiments and Markowski [16] for modeling momentum transfer in thermophoretic soot particle sampling. This approach starts by generating simulated soot aggregates that obey fractal relations

Contributed by the Heat Transfer Division of ASME for publication in the JOURNAL OF HEAT TRANSFER. Manuscript received July 2, 2009; final manuscript received March 15, 2010; published online June 28, 2010. Editor: Yogesh Jaluria.

known to apply to real soot particles. Simulated gas molecules are then assigned initial random locations over a surface that envelopes the soot particle, and initial velocity components are randomly sampled from cumulative distribution functions (CDFs) that describe the velocity distribution within the gas. Gas molecule trajectories are traced until the molecules leave the computational domain through the enveloping surface; each time a molecule intercepts the soot particle, new velocity components are sampled from CDFs derived from a scattering kernel that describes the probability of a molecule scattering with a particular velocity conditional on its incident velocity. The net energy or momentum transfer between a gas molecule and the soot aggregate is calculated by comparing initial and final molecular states and the overall transfer rates between the gas and the particle are found by repeating this process for millions of simulated molecules.

Although the DSMC approach is an improvement in predicting the aggregate shielding effect over heuristic estimates, all simulations carried out to date use a Maxwell scattering kernel [17] that assumes gas molecules either equilibrate with the soot surface and scatter diffusely according to the Maxwell–Boltzmann distribution at the soot temperature or reflect in a purely adiabatic, specular manner. Moreover, all the heat conduction studies assume that surface energy transfers equally into the translational and internal modes of the gas molecule or neglect the internal mode altogether. On the contrary, however, recent TiRe-LII experiments carried out on soot entrained in different monatomic and polyatomic carrier gases [18] and molecular dynamics (MD) simulations carried out under corresponding conditions [19,20] show that surface energy enters the normal-translational mode over the internal energy modes of the gas molecule and, consequently, the Maxwell scattering kernel does not reproduce the lobular-shaped directional scattering observed in the MD simulations [19,20]. Instead, the scattering is better modeled by a Cercignani–Lampis kernel [21], which accounts for preferential accommodation of surface energy into different translational modes of the gas molecule and the extension by Lord [22,23] that accounts for accommodation into the internal modes.

This study evaluates how using the Cercignani–Lampis–Lord (CLL) kernel in place of the Maxwell kernel affects heat conduction calculations from soot aggregates in the free-molecular regime with a focus on how the scattering kernel impacts aggregate shielding. The paper first reviews the construction of simulated soot aggregates and then how the Monte Carlo integration is carried out over incident molecular trajectories and states. The results show that using the CLL kernel has a non-negligible influence over heat conduction from soot aggregates, and should be considered when inferring particle sizes from TiRe-LII data.

2 Generation of Simulated Soot Aggregates

As described above, the fractal-like structure of soot aggregates arises from the agglomeration of primary particles, which themselves are synthesized through polymerization of partially oxidized fuel fragments [24]. The fractal structure of soot aggregates is described by the scaling rule

$$N_p = k_f \left(\frac{R_g}{a} \right)^{D_f} \tag{1}$$

where N_p is the number of primary particles in the aggregate, a is the primary particle radius, and k_f and D_f are the fractal prefactor and exponent, respectively. The aggregate size is defined by the radius of gyration

$$R_g^2 = \frac{1}{N_p} \sum_{i=1}^{N_p} (\boldsymbol{r}_i - \boldsymbol{r}_0)^2 \tag{2}$$

where $\boldsymbol{r}_i$ points to the center of the ith primary particle and $\boldsymbol{r}_0$ is the aggregate centroid. The values of k_f and D_f relate the number of primary particles to the aggregate size with larger values corresponding to more densely packed aggregates for a given value of N_p. These parameters are usually found by applying quasi-heuristic scaling rules and image processing algorithms to two-dimensional images of soot particles in scanning electron microscope (SEM) and transmission electron microscope (TEM) images.

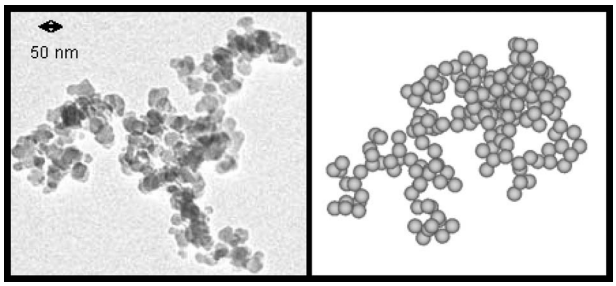

Fig. 1 Comparison of a TEM image of a soot aggregate with a randomly simulated aggregate generated using the same fractal parameters

The simulated aggregates consist of uniformly sized primary particles, a reasonable assumption in most soot-laden aerosols [25], which are further assumed to be in point-contact within the aggregate (i.e., no overlap caused by sintering.) Simulated soot aggregates are generated using the procedure formalized by Filippov et al. [13] that mimics agglomeration physics in soot-laden aerosols and produces simulated aggregates that correlate well with TEM images of thermophotetically sampled soot. This procedure starts by specifying the aggregate parameters N_p, a, D_f, and k_f. Next, the number of precursor aggregates, each containing between five to eight primary particles, is determined so that the total number of primary particles contained in these aggregates sums to N_p. The set of precursor aggregates are then generated by sequentially adding primary particles to the aggregate, starting from two randomly oriented primary particles in point-contact. Each new primary particle is randomly positioned at a distance Γ from the centroid of the existing aggregate with

$$\Gamma^2 = \frac{N_p{}^2 a^2}{N_p - 1} \left(\frac{N_p}{k_f} \right)^{2/D_f} - N_p a^2 \left(\frac{N_p - 1}{k_f} \right)^{2/D_f} \tag{3}$$

to satisfy Eq. (1). The new particle is then rotated about the existing centroid to place it in point-contact with the closest existing particle and then undergoes further rotation to eliminate any interference with other primary particles while preserving the distance between the centroids of the two aggregates.

Larger aggregates are then formed from cluster-cluster aggregation in a pairwise manner. First, one cluster is positioned randomly with its centroid at a distance Γ from the centroid of the second cluster to satisfy Eq. (1), where

$$\Gamma^2 = N_p^2 R_g^2 - N_p \frac{(N_{p,A} R_{g,A}^2 + N_{p,B} R_{g,B}^2)}{N_{p,A} N_{p,B}} \tag{4}$$

In Eq. (4) $R_{g,A}$, $R_{g,B}$, and $N_{p,A}$, $N_{p,B}$ are the radii of gyration and the number of primary particles of the two clusters, respectively, $N_p = N_{p,A} + N_{p,B}$ is the number of primary particles in the new cluster, and R_g is the corresponding radius of gyration calculated from Eq. (2). The closest pair of primary particles between the two clusters is identified and one cluster is rotated about its centroid to place them in point-contact. Further rotations are performed as needed to remove any interference between other primary particles while simultaneously preserving the distance between the cluster centroids. Cluster-cluster aggregation continues until only one cluster remains. Figure 1 compares a numerically simulated soot aggregate with a TEM image of an aggregate sampled from a laminar diffusion flame.

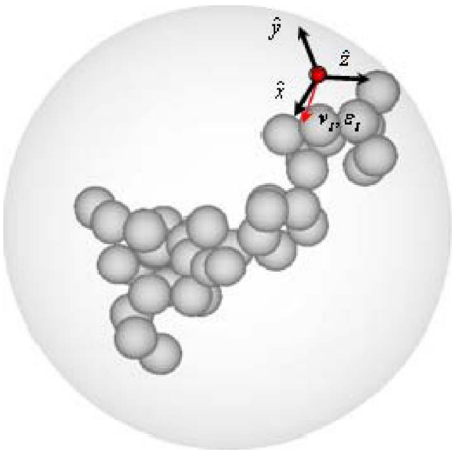

Fig. 2 Computational domain of the Markov chain Monte Carlo simulation

3 Calculation of the Aggregate Shielding Factor With DSMC

The simulated soot particle is then enveloped within a close-fitting surface, usually a sphere [13–15], as shown in Fig. 2, or a cube [16]. Simulated gas molecules are assigned random inception positions on the enveloping surface and initial velocities sampled from CDFs that correspond to the velocity distribution within the gas. A local coordinate system is defined at the molecular inception point on the enveloping surface with the x-direction aligned with the normal vector. If the surrounding gas is in equilibrium, the incident gas molecular velocities obey a Maxwell–Boltzmann (MB) distribution and the normal and tangential velocity components are sampled from [26]

$$u = \sqrt{-\ln(R_n)}/\beta_g \tag{5}$$

and

$$V_t = \sqrt{-\ln(R_t)}/\beta_g \tag{6}$$

where R_n and R_t are the uniform random deviates and $1/\beta_g = (2k_B T_g/m_g)^{1/2}$ is the most probable molecular speed at the gas temperature T_g. The y- and z-velocity components are then found by $v = V_t \cos(2\pi R_v)$ and $w = V_t \sin(2\pi R_w)$. Polyatomic gas molecules are also assigned an initial internal energy; linear molecules such as N_2, O_2, and CO_2 are modeled as having two rotational degrees of freedom since vibrational energy states are mostly inaccessible to the vibrating surface atoms in LII experiments in which the high surface energy of the laser-energized particle prevents adsorption of the incident gas molecule. In this case, the initial molecular internal energy is found by [25]

$$\varepsilon_i = -\ln(R_i) k_B T_g \tag{7}$$

The gas molecular trajectory is traced along a piecewise straight path until it again intercepts the enveloping surface at which point it leaves the computational domain. Whenever the gas molecule intercepts the soot particle, a new set of velocities (and a new internal energy for polyatomic molecules) is sampled using a scattering kernel that defines the probability of a molecule scattering with a given energy state per unit volume of phase space, conditional on the incident energy state. All simulations carried out to date [13–15] used the Maxwell scattering kernel [17]

$$R(\boldsymbol{v}_o|\boldsymbol{v}_i) = (1-\alpha)\delta[\boldsymbol{v}_i - \boldsymbol{v}_o + 2\boldsymbol{n}(\boldsymbol{n}\cdot\boldsymbol{v}_o)] + \alpha f_s(\boldsymbol{v}_o)|\boldsymbol{n}\cdot\boldsymbol{v}_o| \tag{8}$$

where $\boldsymbol{v}_i$ and $\boldsymbol{v}_o$ are the incident and scattered velocities, respectively, $\boldsymbol{n}$ is the outward unit normal vector at the intercept location, $f_s(\boldsymbol{v}_o)$ is the MB distribution at the surface temperature T_s, and α is the thermal accommodation coefficient. Maxwell's kernel assumes that gas molecules equilibrate with the surface temperature and re-emit diffusely with a probability of α and are otherwise reflected in a specular, adiabatic manner. Although it does not explicitly account for internal energy accommodation, Maxwell's kernel can be extended to treat polyatomic gas molecules by assuming that the internal energy modes equilibrate with the surface at T_s with a probability of α and otherwise remain unchanged [10].

If the incident gas molecular velocity obeys a MB distribution at T_g, Eq. (8) combined with Eqs. (5)–(7) can be integrated over all possible incident velocities to find the overall heat transfer rate between the particle and the surrounding gas. For an isolated sphere the integration can be carried out analytically to yield [10]

$$q_{pp} = \alpha q_{pp,max} = \alpha 4\pi a^2 N''[2k_B(T_s - T_g) + \overline{\varepsilon}(T_s) - \overline{\varepsilon}(T_g)] \tag{9}$$

where $q_{pp,max}$ is the heat transfer rate that would occur if every incident gas molecule equilibrated with the surface, N'' is the incident molecular number flux

$$N'' = \frac{1}{4} n_g \overline{c}(T_g) = \frac{1}{2\sqrt{\pi}} \frac{P_g}{k_B T_g} \frac{1}{\beta_g} \tag{10}$$

and $\overline{\varepsilon}(T)$ is the average internal energy per molecule within an equilibrium gas at a temperature T; for linear molecules having two rotational degrees of freedom and negligible accommodation into the vibrational modes, $\overline{\varepsilon}(T_s) - \overline{\varepsilon}(T_g) = k_B(T_s - T_g)$. Equation (9) shows that the probabilistic interpretation for α in the Maxwell kernel is consistent with its traditional definition (e.g., Ref. [25]),

$$\alpha \equiv \frac{\langle E_o - E_g \rangle}{\langle E_s - E_g \rangle} = \frac{\langle E_o - E_g \rangle}{2k_B(T_s - T_g) + \overline{\varepsilon}(T_s) - \overline{\varepsilon}(T_g)} \tag{11}$$

where $\langle E_o - E_g \rangle$ is the average increase in energy per molecule and $\langle E_s - E_g \rangle$ is the maximum increase in energy, which would occur if every incident molecule fully equilibrated with a thermal reservoir at T_s.

In the case of a soot aggregate, integration is carried out using a Markov chain Monte Carlo procedure. Whenever a molecule "hits" the soot surface, a random number R_α is sampled and compared to the accommodation coefficient. If $R_\alpha < \alpha$, the gas molecule is assigned a new velocity and internal energy sampled from a MB distribution using Eqs. (5)–(7) but with T_s substituted in place of T_g. Otherwise, the molecule is reflected in a specular, adiabatic manner by reversing the velocity component in the surface normal direction and preserving the tangential velocity and internal energy. After tracing millions of simulated molecules, an unbiased estimate of the aggregate heat transfer rate is given by

$$q_{agg} \approx \frac{1}{N} \sum_{k=1}^{N} \left[\left(\frac{m(\boldsymbol{v}_o^k \cdot \boldsymbol{v}_o^k - \boldsymbol{v}_i^k \cdot \boldsymbol{v}_i^k)}{2} \right) + \varepsilon_o - \varepsilon_i \right] \cdot N'' \cdot A \tag{12}$$

where subscript "o" denotes the energy state of the gas molecule leaving the computational domain and A is the area of the enveloping surface.

Following this procedure, Filippov et al. [13] calculated the aggregate shielding factor $\eta \equiv q_{agg}/N_p q_{pp}$ for various accommodation coefficients, aggregate sizes, and fractal parameters. They note that η depends only on aggregate structure and the accommodation coefficient, and in the case of complete accommodation ($\alpha = 1$) heat transfer can be modeled using an equivalent sphere, $A_{cond} = 4\pi R_{eff}^2$, where R_{eff} is found using the fractal relationship [13]

$$N_p = k_h \left(\frac{R_{eff}}{a} \right)^{D_h} \tag{13}$$

and k_h and D_h are tabulated in terms of k_f and D_f. Equation (13) can be rewritten in terms of the shielding factor

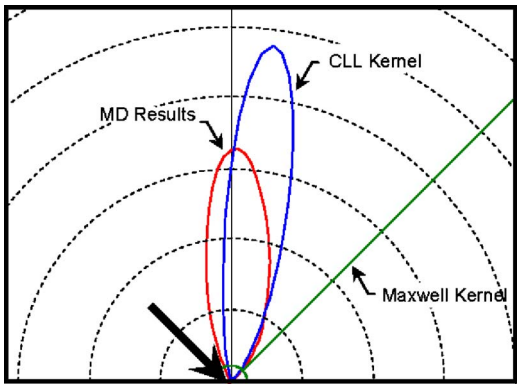

Fig. 3 Directional scattering probability in the incidence plane of a molecular beam [19]

$$\eta = N_p^{2/D_h - 1}/k_h \tag{14}$$

which shows that shielding is more pronounced for larger aggregates since D_h is always greater than one. Filippov et al. [13] also show that aggregate shielding diminishes (i.e., $\eta \to 1$) as α increases since molecules that hit primary particles on the aggregate exterior are more likely to undergo specular, adiabatic scattering into the aggregate interior, where they can accommodate with primary particles that are otherwise inaccessible to incident gas molecules following a ballistic trajectory from the equilibrium gas. They do not, however, provide a correlation for R_{eff} or η for incomplete accommodation.

Liu et al. [14] extended this result by showing that Eqs. (13) and (14) can be modified to account for $\alpha < 1$ using quadratic fits for k_h and D_h

$$k_h(\alpha) = 1.04476 + 0.22329\alpha + 7.14286 \times 10^{-3}\alpha^2 \tag{15}$$

and

$$D_h(\alpha) = 1.99345 + 0.30224\alpha - 0.11276\alpha^2. \tag{16}$$

4 Cercignani–Lampis–Lord Kernel

Although the Maxwell kernel is conceptually simple and easy to implement in a Monte Carlo simulation, recent MD studies [19,20] suggest that it does not represent the scattered velocity distribution. This is clear in Fig. 3, which shows how neon molecules from a monochromatic beam at 300 K scatter in the plane of incidence. Indeed, the Maxwell kernel is known to poorly approximate actual gas-surface scattering [17], particularly, in systems in which molecules scatter directly or undergo a brief "chattering" type interaction with the surface; these conditions prevail in LII experiments since the surface energy of laser-energized soot prevents gas molecular adsorption onto the soot surface.

In this type of interaction, surface energy accommodates preferentially into the normal-translational mode of the gas molecule, followed by the rotational mode (for polyatomic molecules) while comparatively little energy enters the tangential-translational mode. This gives rise to the lobular-shaped distribution in Fig. 3, in contrast to the hemispherical shape predicted by Maxwell kernel, which assumes that normal and tangential-translational modes accommodate surface energy with equal efficiency. To distinguish varying degrees of surface energy accommodation into the energy modes of the gas molecule, separate coefficients are defined for the normal-translational, tangential-translational, and rotational modes

$$\alpha_n = \frac{\langle E_{o,n} - E_{i,n} \rangle}{k_B(T_s - T_g)} = \frac{1/2 m_g \langle v_{o,n}^2 - v_{i,n}^2 \rangle}{k_B(T_s - T_g)} \tag{17}$$

Table 1 MD-simulated accommodation coefficients between soot and selected monatomic [19] and polyatomic [20] gases for $T_g = 300$ K and $T_s = 3000$ K

Species	α_n	α_t	α_r	α	α (exp.) [18]
He	0.22	0.22	-	0.22	0.21
Ne	0.65	0.06	-	0.36	0.37
Ar	0.76	0.06	-	0.41	0.46
N_2	0.66	0.07	0.23	0.32	0.33[a]
CO	0.67	0.07	0.34	0.36	0.32[a]
CO_2	0.68	0.09	0.48	0.42	0.38[a]
N_2O	0.68	0.08	0.48	0.41	0.40[a]

[a]Values are rescaled from those reported in Ref. [18] to be consisted with Eq. (11), by excluding vibrational accommodation when calculating the maximum possible energy transfer between the surface and the gas molecule.

$$\alpha_t = \frac{\langle E_{o,t} - E_{i,t} \rangle}{k_B(T_s - T_g)} = \frac{1/2 m_g \langle v_{o,t}^2 - v_{i,t}^2 \rangle}{k_B(T_s - T_g)} \tag{18}$$

and

$$\alpha_r = \frac{\langle E_{o,r} - E_{i,r} \rangle}{\zeta_r/2 k_B(T_s - T_g)} \tag{19}$$

where $\langle E_{o,n} - E_{i,n} \rangle$, $\langle E_{o,t} - E_{i,t} \rangle$, and $\langle E_{o,r} - E_{i,r} \rangle$ are the average increases in normal-translational, tangential-translational, and rotational energy, respectively, and ζ_r is the number of rotational degrees of freedom ($\zeta_r = 2$ for linear molecules.) These accommodation coefficients are related to the overall thermal accommodation coefficient through $\alpha = (\alpha_n + \alpha_t)/2$ for monatomic molecules, and $\alpha = (\alpha_n + \alpha_t + \alpha_r)/3$ for linear polyatomic molecules, assuming the denominator of Eq. (11) excludes vibrational modes. Table 1 shows parameters found by averaging the difference between incident and scattered energy states for hundreds of independent, MD-simulated molecular trajectories [19,20], which match independent, LII-derived accommodation coefficients for soot aggregates entrained in various gases [18].

Cercignani and Lampis [21] used α_n and α_t to define a scattering kernel that accounts for preferential accommodation into the normal-translational mode of monatomic molecules over the tangential-translational mode by assuming that these two modes accommodate energy according to independent probability distributions. Multiplying these distributions together results in

$$R(\boldsymbol{\xi}_o | \boldsymbol{\xi}_i) = \frac{2\xi_{o,n}^2}{\pi \alpha_n \alpha_t} I_0\left(\frac{2\sqrt{1-\alpha_n}}{\alpha_n} \xi_{o,n} \xi_{i,n} \right) \times \exp\left[-\frac{\xi_{o,n}^2 + (1-\alpha_n)\xi_{i,n}^2}{\alpha_n} - \frac{(\boldsymbol{\xi}_{o,t} + \sqrt{1-\alpha_t}\boldsymbol{\xi}_{i,t})^2}{\alpha_t} \right] \tag{20}$$

where $\boldsymbol{\xi}_i$ and $\boldsymbol{\xi}_o$, respectively, denote the incident and scattered velocities normalized by the most probable speed at T_s, $1/\beta_s$. (This kernel sometimes appears in a different form because the authors originally denoted tangential momentum accommodation by α_t [21] but Eq. (20) is more consistent when discussing thermal accommodation [22,23].) Lord [22,23] extended the Cercignani–Lampis kernel to include internal energy modes by again assuming that rotational accommodation is independent of translational accommodation; for linear polyatomic molecules having two rotational degrees of freedom, the probability of a gas molecule scattering with internal energy ε_o conditional on an incident internal energy ε_i is

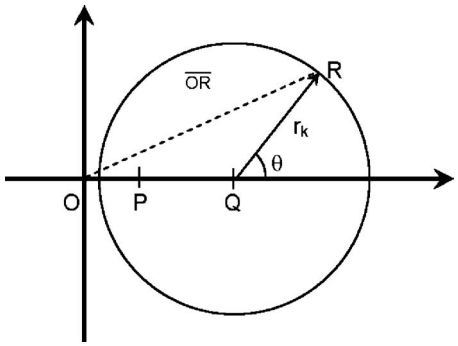

Fig. 4 Geometric representation of the CLL [21–23] kernel. Points P, Q, and R, respectively, denote the incident, expected, and actual energy contained in the normal-translational, tangential-translational, and rotational modes of the gas molecule.

$$f(\varepsilon_o|\varepsilon_i) = \frac{1}{\alpha_r} \mathrm{I}_0\left[\frac{2\sqrt{(1-\alpha_r)\varepsilon_i\varepsilon_o}}{\alpha_r}\right] \exp\left[-\frac{\varepsilon_o + (1-\alpha_r)\varepsilon_i}{\alpha_r}\right] \tag{21}$$

Combining Eqs. (20) and (21) forms the CLL kernel. Figure 3 shows that the distribution predicted by the CLL kernel agrees with the MD-simulated trajectories; similar agreement was observed in a follow-up study that examined thermal accommodation of polyatomic molecules in TiRe-LII experiments [20].

Lord [22,23] also presented an efficient way to incorporate the CLL kernel into DSMC simulations, based on the fact that the normal-translational, tangential-translational, and rotational energy of scattered molecules obey Gaussian distributions centered on the conditional-expected values defined by α_n, α_t, and α_r. The incident and scattered energy states are represented on a two-dimensional plot shown in Fig. 4; Q denotes the expected scattered energy state while R represents the actual energy state, located a distance r from Q and making an angle θ with the x-axis. (A local coordinate system is defined in the molecular reference frame so that the incident tangential-translational or rotational energy is contained in one coordinate.) The total amount of scattered energy in the normal-translational, tangential-translational, or rotational mode corresponds to the distance between the origin and R while projections of $\overline{OR}$ onto the axes represent individual tangential or rotational-velocity components. To calculate a scattered velocity component, then, r and θ are first sampled from their CDFs by

$$r_k = \sqrt{-\alpha_k \ln R_r}, \quad \theta_k = 2\pi R_\theta \tag{22}$$

where α_k is the corresponding accommodation coefficient of the kth mode and R_r and R_θ are random numbers between zero and one. The expected scattered state Q is located a distance

$$\xi_{m,k} = \sqrt{1-\alpha_k}|\xi_{i,k}| \tag{23}$$

from the origin, where $|\xi_{i,k}|$ is the incident normal-, tangential-, or rotational-velocity magnitude normalized by the corresponding most probable speed at T_s. The normal component of scattered velocity corresponds to $\overline{OR}$ and is given by

$$\xi_{o,n} = \sqrt{r_n^2 + {\xi_{m,n}}^2 + 2r_n\xi_{m,n}\cos\theta_n}. \tag{24}$$

The magnitude of the scattered tangential velocity $\|\boldsymbol{\xi}_{o,t}\|$ and the rotational-velocity $\|\boldsymbol{\xi}_{o,r}\|$ are also obtained by following these steps and their components are found by projecting $\overline{OR}$ onto the x- and y-axes. For example, the scattered tangential velocity is given by

$$\xi_{o,t,v} = \xi_{m,t} + r_t\cos(\theta_t), \quad \xi_{o,t,w} = r_t\sin(\theta_t) \tag{25}$$

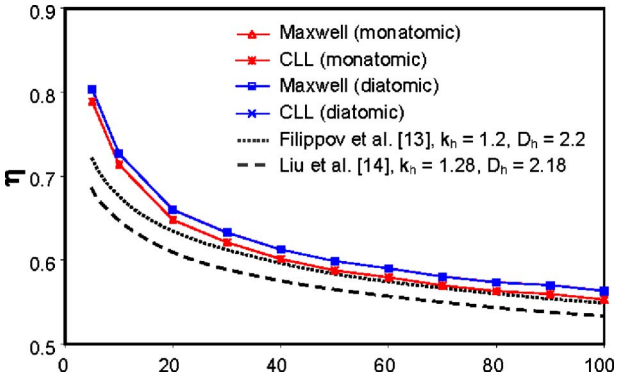

Fig. 5 Aggregate shielding factor η versus N_p for perfect thermal accommodation

5 Effect of Selective Thermal Accommodation on Aggregate Shielding

For an isolated sphere in the free-molecular regime, combining the CLL kernel with the probability distribution functions of incident gas molecular velocity and internal energy and then analytically integrating over all possible incident energy states produces Eq. (9) for any combination of α_n, α_t, and α_r. The same result is obtained through DSMC simulation, which is a good way to validate implementation of Eqs. (22)–(24).

For a soot aggregate with perfect accommodation, i.e., $\alpha_n=\alpha_t=\alpha_r=1$, the CLL and Maxwell kernels should also predict identical aggregate shielding factors since substituting these accommodation coefficients into the CLL kernel yields MB distributions for normal-translational, tangential-translational and rotational energy at T_s. The shielding factors calculated for a monatomic gas with $\alpha_n=\alpha_t=1$ and a diatomic gas with $\alpha_n=\alpha_t=\alpha_r=1$ are plotted in Fig. 5. Each point is found by averaging individual DSMC-derived η values for 30 simulated aggregates generated using $k_f=2.3$ and $D_f=1.8$, typical values for flame-synthesized aggregates. Molecules are repeatedly sampled and traced until the standard deviation of the mean of 20 independent subsamples of η drops below 0.1%.

Figure 5 shows the Maxwell and CLL kernels indeed provide identical results for both types of gas. The monatomic gas results from the present study agree with those of Filippov et al. [13] for $N_p>30$ and follow the same trend as predicted by Liu et al. [14], although their values are about 3% lower than those of the present study. (Poor agreement between the DSMC results and Eq. (14) at small N_p is expected since k_h and D_h values reported in Refs. [13,14] were derived using DSMC data over a much larger range of N_p and both trends fail to interpolate $\eta=1$ in the limiting case of $N_p=1$.) Also note that while the DSMC-derived η values for a monatomic gas agree well with the fit parameters reported in Ref. [13] (also derived assuming a monatomic gas), values obtained using a diatomic gas are slightly higher due to the internal energy modes.

Figures 6 and 7 show values of η calculated using the Maxwell and CLL kernels for soot aggregates immersed in neon and nitrogen found with MD-derived thermal accommodation coefficients, as well as trends predicted by Eqs. (14)–(16). These figures show that the shielding parameters obtained using the CLL kernel agree with the fractal-law results of Liu et al. [14] for $N_p \geq 40$, which is surprising since the results of the present study agree better with the correlation of Filippov et al. [13] for perfect accommodation and, furthermore, Liu et al. [14] derived Eqs. (15) and (16) from their own DSMC results carried out using Maxwell's kernel and a monatomic gas.

The relative magnitudes of η in Figs. 6 and 7 shows that aggregate shielding is slightly reduced by nitrogen's rotational degrees of freedom, consistent with the perfect thermal accommo-

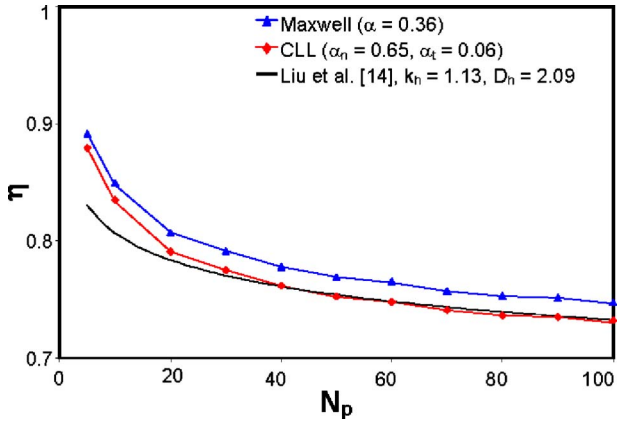

Fig. 6 Aggregate shielding factor η versus N_p for neon

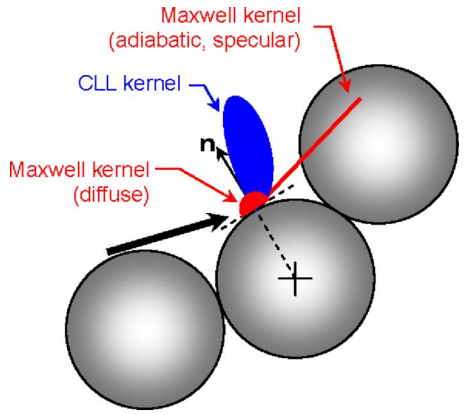

Fig. 9 Molecules following the adiabatic-specular scattering channel of the Maxwell kernel are more likely to accommodate with subsequent primary particles compared to those that scatter preferentially in the surface normal direction, as predicted by the CLL kernel

dation results in Fig. 5. In contrast to the perfect thermal accommodation case, however, the CLL kernel predicts increased aggregate shielding compared to the Maxwell kernel for both Ne and N_2. The Maxwell- and CLL-derived results diverge as aggregate size increases, an effect that is most pronounced in the case of nitrogen with a difference of approximately 4% at $N_p=100$.

Differences between the Maxwell and CLL kernels are further explored by visualizing the shielding per primary particle shown in Fig. 8 for a soot aggregate composed of 50 primary particles. (In this context shielding is the ratio of heat conduction from a primary particle in the aggregate to that of an isolated primary particle.) Figure 8 shows that both the Maxwell and CLL kernels predict substantial primary particle shielding within the aggregate by particles on the aggregate exterior, as expected but closer inspection shows that the CLL kernel predicts slightly more shielding of primary particles closer to the exterior. This is due to preferential accommodation of surface energy into the normal-translational mode of the gas molecules, as shown in Fig. 9, making them prone to scatter in the surface normal direction, where they are unlikely to encounter other primary particles. The Maxwell kernel, in contrast, assumes that incident molecules perfectly accommodate and re-emit diffusely (in which case they are unable to absorb surface energy from other primary particles), or scatter adiabatically, following a specular, "mirrorlike" path. This latter interaction permits a greater number of trajectories tangential to the surface that are more likely to intercept adjacent primary particles, compared to those biased in the surface normal direction as predicted by the CLL kernel.

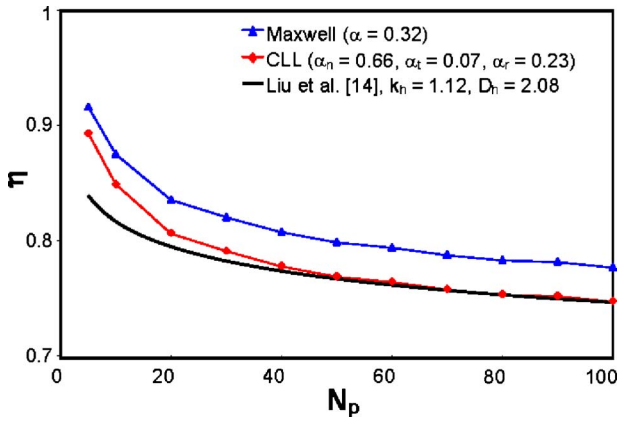

Fig. 7 Aggregate shielding factor η versus N_p for nitrogen

The above results show that selective accommodation has a non-negligible (~3–4%) effect on the aggregate shielding effect and, accordingly, about the same impact on particle sizes inferred from TiRe-LII data. Since the results are in good agreement with the shielding parameter predicted by Liu et al. [14], the best course of action is to use Eqs. (14)–(16) when carrying out TiRe-LII particle sizing on small soot aggregates in the free-molecular regime, which can be extended into the near-transition regime using the Fuchs boundary sphere method [14,27]. A recent 3D-DSMC simulation of heat conduction from soot aggregates [15] shows that this treatment is inappropriate for larger aggregates or in high-pressure gases, however, since it neglects intermolecular collisions occurring within the enveloping surface. The onset of these effects can probably be predicted from the Knudsen number defined using the radius of gyration rather than the primary par-

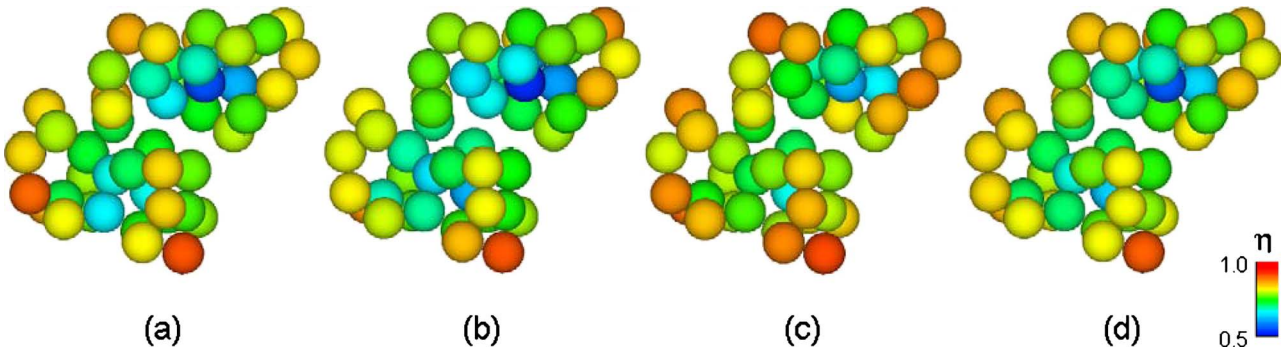

Fig. 8 Primary particle shielding parameters for an aggregate with $N_p=50$: (*a*) Maxwell kernel for neon, (*b*) CLL kernel for neon, (*c*) Maxwell kernel for nitrogen, and (*d*) CLL kernel for nitrogen

ticle diameter but further study is required to elucidate under what conditions transition-regime effects invalidate the shielding parameters presented in this study.

6 Conclusions

Reliable TiRe-LII particle sizing is predicated on accurately modeling heat conduction between laser-energized aggregates and the surrounding gas. There are, however, uncertainties in this model due to the aggregate shielding effect. Previous DSMC-based estimates of aggregate shielding exclusively used the Maxwell scattering kernel in which gas molecules either accommodate perfectly with the surface and re-emit diffusely or scatter in an adiabatic/specular manner. Although this treatment is conceptually simple and easily incorporated into a DSMC code, it is also physically unrealistic since the Maxwell kernel neglects different surface energy accommodation rates into the normal-translational, tangential-translational, and rotational modes of the gas molecule.

This study investigates the effect of selective accommodation on aggregate shielding using the CLL kernel, which more accurately represents gas-surface scattering physics in TiRe-LII experiments. DSMC simulations are carried out using accommodation coefficients derived from molecular dynamics simulations and validated by comparison with experimental results. The present study shows that the Maxwell kernel underpredicts aggregate shielding by neglecting preferential accommodation into the normal-tangential mode of the gas molecule, although a previously derived correlation based on fractal-scaling laws is in excellent agreement with shielding factors found with the CLL kernel.

While the CLL kernel more accurately represents gas-surface scattering in TiRe-LII experiments, the methodology used to calculate the aggregate scattering coefficient neglects intermolecular collisions immediately adjacent to the soot aggregate, which could significantly affect the overall heat conduction rates. Future work will address this question by adapting the CLL kernel to more rigorous 3D-DSMC simulations of heat conduction from soot aggregates.

Acknowledgment

This work was made possible by the facilities of the Shared Hierarchical Academic Research Computing Network (SHARCNET: www.sharcnet.ca). The author is grateful to Mr. Umakaran Nemallen for his assistance with the cluster-cluster aggregation code and to Dr. Fengshan Liu and Dr. Greg Smallwood of the National Research Council Canada for their mentorship and helpful discussions.

Nomenclature

a = primary particle radius
A = surface area
D_f = fractal exponent, Eq. (1)
E = average molecular energy
k_B = Boltzmann's constant, 1.380×10^{-23} J/K·molecule
k_f = fractal prefactor, Eq. (1)
m = gas molecular mass
$\boldsymbol{n}$ = surface normal vector
N'' = molecular number flux
N_p = number of primary particles in an aggregate
q = heat transfer rate
R_k = uniform random iterate for the kth variable
$R(|)$ = scattering kernel
R_{eff} = radius of equivalent sphere, Eq. (13)
R_g = radius of gyration of a soot aggregate
T = temperature
$\boldsymbol{v}$ = gas molecular velocity
u,v,w = gas molecular velocity components.
α = accommodation coefficient
β = inverse of the most probable molecular speed
ε_i = internal energy
Γ = distance between aggregate centroids, Eqs. (3) and (4)
η = aggregate shielding factor
λ_{MFP} = molecular mean free path
ζ_r = rotational degrees of freedom
$\boldsymbol{\xi}$ = normalized velocity

Subscripts and Superscripts

agg = aggregate
g = gas
i = incident
n = normal mode/direction
o = scattered
pp = primary particle
r = rotational mode
s = surface
t = tangential mode/direction
δ = boundary sphere

References

[1] Pope, C. A., and Dockery, D. W., 2006, "Health Effect of Fine Particulate Air Pollution: Lines That Connect," J. Air Waste Manage. Assoc., **56**, pp. 749–752.
[2] Bond, T. C., and Sun, H., 2005, "Can Reducing Black Carbon Emissions Counteract Global Warming?," Environ. Sci. Technol., **39**, pp. 5921–5926.
[3] 2004, "Air Quality Criteria for Particulate Matter," U.S. Environmental Protection Agency, Washington, DC, Paper No. EPA/600/P-99/002aF.
[4] Dankers, S., Leipertz, A., Will, S., Arndt, J., Vogel, K., Schraml, S., and Hemm, A., 2003, "In-Situ Measurement of Primary Particle Sizes During Carbon Black Production," Chem. Eng. Technol., **26**, pp. 966–969.
[5] Baukal, C. E., Jr., 2000, *Heat Transfer in Industrial Combustion*, CRC, Boca Raton, FL.
[6] Dobbins, R. A., and Megaridis, C. M., 1987, "Morphology of Flame-Generated Soot as Determined by Thermophoretic Sampling," Langmuir, **3**, pp. 254–259.
[7] Zhao, B., Yang, Z., Wang, J., Johnson, M. V., and Wang, H., 2003, "Analysis of Soot Nanoparticles in a Laminar Premixed Ethylene Flame by Scanning Mobility Particle Sizer," Aerosol Sci. Technol., **37**, pp. 611–620.
[8] Snelling, D. R., Smallwood, G. J., Liu, F., Gülder, Ö. L., and Bachalo, W. D., 2005, "A Calibration-Independent Laser-Induced Incandescence Technique for Soot Measurement by Detecting Absolute Light Intensity," Appl. Opt., **44**, pp. 6773–6785.
[9] Gallis, M. A., Rader, D. J., and Torczynski, J. R., 2004, "A Generalized Approximation for the Thermophoretic Force on a Free-Molecular Particle," Aerosol Sci. Technol., **38**, pp. 692–706.
[10] Liu, F., Daun, K. J., Snelling, D. R., and Smallwood, G. J., 2006, "Heat Conduction From a Spherical Nano-Particle: Status of Modeling Heat Conduction in LII," Appl. Phys. B: Lasers Opt., **83**, pp. 355–382.
[11] Snelling, D. R., Liu, F., Smallwood, G. J., and Gülder, Ö. L., 2004, "Determination of the Soot Absorption Function and Thermal Accommodation Coefficient Using Low-Fluence LII in a Laminar Coflow Ethylene Diffusion Flame," Combust. Flame, **136**, pp. 180–190.
[12] Brasil, A. M., Farias, T. L., and Carvalho, M. G., 1999, "A Recipe for Image Characterization of Fractal-Like Aggregates," J. Aerosol Sci., **30**, pp. 1379–1389.
[13] Filippov, A. V., Zurita, M., and Rosner, D. E., 2000, "Fractal-Like Aggregates: Relation Between Morphology and Physical Properties," J. Colloid Interface Sci., **229**, pp. 261–273.
[14] Liu, F., Yang, M., Hill, F. A., Snelling, D. R., and Smallwood, G. J., 2006, "Influence of Polydisperse Distributions of Both Primary Particle and Aggregate Size on Soot Temperature in Low-Fluence LII," Appl. Phys. B: Lasers Opt., **83**, pp. 383–395.
[15] Liu, F., and Smallwood, G. J., 2008, "Study of Heat Conduction Between Fractal Aggregates and the Surrounding Gas in the Transition Regime Using the DSMC Method," 40th Thermophysics Conference, Seattle, WA, Jun. 23–26, Paper No. AIAA-2008-3917.
[16] Mackowski, D. W., 2006, "Monte Carlo Simulation of Hydrodynamics Drag and Thermophoresis of Fractal Aggregates of Spheres in the Free-Molecule Flow Regime," J. Aerosol Sci., **37**, pp. 242–259.
[17] Cercignani, C., 1975, *Theory and Application of the Boltzmann Equation*, Scottish Academic, Edinburgh, UK, pp. 118–120.
[18] Daun, K. J., Smallwood, G. J., and Liu, F., 2008, "Investigation of Thermal Accommodation Coefficients Using Laser-Induced Incandescence," ASME J. Heat Transfer, **130**, p. 121201.
[19] Daun, K. J., Smallwood, G. J., and Liu, F., 2008, "Molecular Dynamics Simulations of Translational Thermal Accommodation Coefficients for Time-Resolved LII," Appl. Phys. B: Lasers Opt., **94**, pp. 39–49.
[20] Daun, K. J., 2009, "Thermal Accommodation Coefficients Between Polyatomic Gas Molecules and Soot in Laser-Induced Incandescence Experiments," Int. J. Heat Mass Transfer, **52**, pp. 5081–5089.

[21] Cercignani, C., and Lampis, M., 1971, "Kinetic Models for Gas-Surface Interactions," Transp. Theory Stat. Phys., **1**, pp. 101–114.
[22] Lord, R. G., 1990, "Application of the Cercignani-Lampis Scattering Kernel to Direct Simulation Monte Carlo Calculations," *Proceedings of the 17th International Symposium of Rarefied Gas Dynamics*, A. E. Beylich, ed., VCH Verlag, Aachen, Germany, Jul. 8–15.
[23] Lord, R. G., 1991, "Some Extensions to the Cercignani-Lampis Gas-Surface Scattering Kernel," Phys. Fluids A., **3**, pp. 706–710.
[24] Shaddix, C. R., and Williams, T. C., 2007, "Soot: Giver and Taker of Light," Am. Sci., **95**, pp. 232–239.
[25] Tian, K., Liu, F., Thomson, K. A., Snelling, D. R., Smallwood, G. J., and Wang, D., 2004, "Distribution of the Number of Primary Particles of Soot Aggregates in a Nonpremixed Laminar Flame," Combust. Flame, **138**, pp. 195–198.
[26] Bird, G. A., 1994, *Molecular Gas Dynamics and the Direct Simulation of Gas Flows*, Claredon, Oxford, UK, pp. 423–428.
[27] Fuchs, N. A., 1964, *The Mechanics of Aerosols*, Pergamon, Oxford, UK.

Reacting Turbulent Flow and Thermal Field in a Channel With Inclined Bluff Body Flame Holders

Cheng-Xian Lin[1]

Richard Jack Holder

Department of Mechanical, Aerospace, and Biomedical Engineering, University of Tennessee, Knoxville, TN 37996

In this paper, a numerical study has been carried out to investigate the effects of inlet turbulent intensity and angle of attack on the chemically reacting turbulent flow and thermal fields in a channel with an inclined bluff body V-gutter flame holder. With a basic geometry used in a previous experimental study, the inlet turbulent intensity was varied from 2% to 100%, while the angle of attack of the V-gutter was varied from 0 deg to 30 deg. The turbulent flow was modeled with a realizable k-ε two-equation turbulence model. The chemical reaction was premixed propane-air combustion with an equivalence ratio of 0.6. The chemistry-turbulence interaction was simulated with an eddy-dissipation model. Numerical results indicated that increasing the inlet turbulent intensity and V-gutter angle of attack resulted in an increase not only in the size, but also in the magnitude of the downstream high turbulence areas with shedding vortexes. The recirculation flow behind the flame holder tended to maintain the rear wall at constant temperature, except at the edges of the wall. The friction factor of the flow channel was more sensitive to the change in inlet turbulence intensity at smaller angle of attack of the V-gutter. [DOI: 10.1115/1.4001627]

Keywords: chemically reacting flow, combustion, turbulent heat transfer, flame holder, channel flow

1 Introduction

Bluff body flame holders such as V-gutters are widely used in many modern combustion devices, such as augmenters or afterburners in turbojet/turbofan engines and ramjet engines. A V-gutter bluff body creates a recirculation zone that acts as an ignition source for incoming fuel/air mixture by recycling hot products and radicals from the burned mixture. It was proven to be very effective in anchoring the flame created in the combustion environments [1,2]. A V-gutter can also be used as an effective mixing device because it generates many downstream turbulent eddies, which in turn creates a very strong mixing effect [3]. For some new combustor concepts, application of the V-gutter within a combustor such as a high-g inter-turbine burner might be able to improve both exit flow profile and flame holding [4]. Although the V-gutter flame holder has been investigated for many years, the underlined physical phenomena are still not well understood due to the nature of the complexity in the chemically reacting turbulent flows. In order to optimize the flame holder's performance for various applications, much research needs to be conducted under various flow conditions or configurations.

Experimental studies on this subject are essential, but a large scale systematic analysis via experimental measurements can be both expensive and time consuming. Fujii et al. [5] and Yue et al. [6] carried out experiments to study cold flow (without reaction) characteristics behind a flame stabilizer. Sanquer et al. [7] investigated the chemically reacting flow characteristics behind V-gutters. Kiel et al. [8], Bush and Gutmark [9], Sjunnesson et al. [10], and Fujii and Eguchi [11] performed comparisons of cold and reacting flows involving a V-gutter. A common observation among these studies was that the strong vortex shedding in nonreacting flow could become absent in the reacting flow. Fujji and Eguchi [11] determined that the turbulence was suppressed by the combustion. In the research by Sanquer et al. [7], the effects of the shape of the flame holder on the wake structure downstream was investigated. Recently, Cuppoletti et al. [12] measured the high frequency combustion instabilities with a radial V-gutter.

On the other hand, computational fluid dynamics (CFD) has been used extensively in the study of turbulent reacting flows over flame holders. Many numerical studies, based on either Reynolds-averaged Navier–Stokes (RANS) or large eddy simulation (LES) methodologies, are concerned with model validation [13–16]. The RANS-based approach has been broadly used in design and analysis primarily due to its lower requirement in computational resources and its capability to directly generate time-averaged flow properties. Among the many RANS-based studies, Bai and Fuchs [17] applied a two-equation k-ε turbulence model to investigate the influence of the reaction mechanisms on the reacting flow over a bluff body. Johansson and Davidson [18] applied the standard k-ε turbulence model to simulate the unsteady two-dimensional turbulent flow without combustion behind a flame holder. Although direct numerical simulation (DNS) is able to resolve all of the turbulence scales, its computational resource requirements are prohibited for practical applications. In recent year, LES and hybrid RANS/LES approaches received great attentions among researchers as it can capture much transient turbulence structures than RANS for flame holder studies [13,14,19–23]. For example, Kim et al. [13] and Smith et al. [20] performed LES simulation to predict the lean blow out (LBO) phenomena over a flame holder. Giacomazzi et al. [22] and Gokulakrishnan et al. [23] investigated the turbulence-chemistry interaction in the LES simulation of the bluff body. Although much progress has been made in LES, its higher computational cost than RANS, although lower than DNS, still remains as one of the biggest challenges for practical design or parametric studies.

[1]Corresponding author.

Contributed by the Heat Transfer Division of ASME for publication in the JOURNAL OF HEAT TRANSFER. Manuscript received August 16, 2009; final manuscript received February 2, 2010; published online June 30, 2010. Assoc. Editor: Walter W. Yuen.

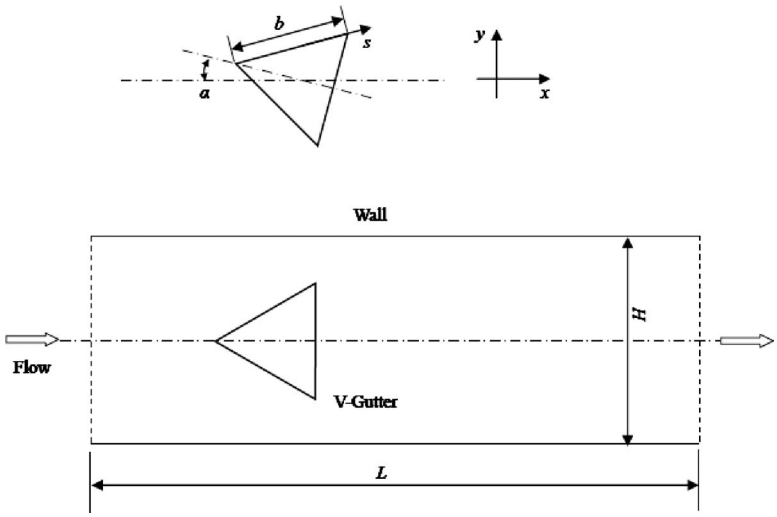

Fig. 1 Schematic of a symmetric V-gutter in a horizontal flow channel

A comprehensive literature survey have showed that in all of the previous research, emphases have been placed on the turbulent flow and chemical reactions downstream the flame holder itself with no angle of attack. Even though the flame holder is usually placed in a flow channel or duct, the flame holder's effects on the pressure drop and temperature distributions in the flow channel were generally not considered. To the authors' knowledge, little to none of the previous research have been carried out on the turbulent flow and thermal fields around a V-gutter flame holder in a flow channel at different levels of turbulence intensity at the inlet and angle of attack of the V-gutter. This background information formed the foundation that motivated the research reported in the present paper.

In this paper, the effects of inlet turbulence intensity and angle of attack on the chemically reacting turbulent flow and temperature distributions around a V-gutter in a flow channel were investigated in detail by a finite volume method. Emphasis was on the influence of the angled V-gutter on the reacting flow inside a flow channel, the walls of which could impact the flow around the V-gutter, at different turbulence levels at the inlet. As our primary interests in this paper are in the time-averaged thermal fluid behaviors of the flame holder in the flow channel at different conditions, a RANS-based simulation approach has been adopted. The obtained numerical results were analyzed to determine how inlet turbulence intensity and angle of attack of the flame holder would affect the size and location of the recirculation zones, the temperature profiles along the solid walls, and the friction factors of the flow channel.

2 Physical Problem

The basic computational setup for this analysis duplicated the V-gutter flame holder at zero angle of attack in a flow channel used in the experiments by Fujii and Eguchi [11]. A two-dimensional approximation was made by examining the experimental results. Figure 1 shows the full computational domain with a basic V-gutter and an angled V-gutter, which were investigated in this paper. The full dimensions of the test section [11] were 305×50 mm^2. The shape used for the V-gutter was an equilateral triangle with each side equal to 25 mm. This resulted in a blockage ratio of 0.5 (or 50%) within the flow channel. The gas flow into the channel was a premixed combination of propane-air with an equivalence ratio of 0.6. It was given a velocity of 10 m/s and initially had 2% turbulent intensity I at the inlet of the channel.

For the parametric study, the inlet turbulent intensity I was varied to determine its effects on downstream flow and heat transfer. After the initial I of 2%, additional cases of I at 25%, 50%, 75%, and 100% were simulated. The case of $I=100\%$ serves as the assumed maximum inlet turbulence intensity investigated in this paper. The angle of attack α, defined as the angle between the axial direction of the channel and the chord of the V-gutter, as shown in Fig. 1, was also varied. Initially, this angle of attack α was set to 0 deg as a baseline case, then the V-gutter was rotated to $\alpha=5$ deg, 10 deg, 20 deg, and 30 deg, respectively.

3 Mathematical Models

3.1 Governing Equations. The basic governing equations to be solved are the RANS equations, including the mass, momentum, and energy conservation equations. The conservation of mass is described by

$$\frac{\partial \rho}{\partial t}+\frac{\partial}{\partial x_i}(\rho u_i)=S_m \tag{1}$$

where the source term S_m includes any mass added to the continuous phase. The conservation of momentum is as follows:

$$\frac{\partial}{\partial t}(\rho u_i)+\frac{\partial}{\partial x_j}(\rho u_i u_j)=-\frac{\partial p}{\partial x_i}+\frac{\partial}{\partial x_j}\left[\mu\left(\frac{\partial u_i}{\partial x_j}+\frac{\partial u_j}{\partial x_i}-\delta_{ij}\frac{\partial u_l}{\partial x_l}\right)\right]+\frac{\partial}{\partial x_j}(-\overline{\rho u_i' u_j'})+\rho g_i \tag{2}$$

where ρg_i is the gravitational body force. The Reynolds stress $-\overline{\rho u_i' u_j'}$ will be modeled via a turbulence model to be described in Sec. 3.2. The standard Boussinesq hypothesis is used to relate the Reynolds stresses to the mean velocity gradients

$$-\overline{\rho u_i' u_j'}=\mu_t\left(\frac{\partial u_i}{\partial x_j}+\frac{\partial u_j}{\partial x_i}\right)-\frac{2}{3}\left(\rho k+\mu_t\frac{\partial u_k}{\partial x_k}\right)\delta_{ij} \tag{3}$$

where δ_{ij} is the Kronecker delta with i, j, and $k=1,2,3$. μ_t is the turbulent viscosity determined from the turbulence model.

Turbulent heat transport is modeled using the concept of Reynolds' analogy to turbulent momentum transfer. The conservation of energy is of the following form:

$$\frac{\partial}{\partial t}(\rho E)+\frac{\partial}{\partial x_i}[u_i(\rho E+p)]=\frac{\partial}{\partial x_j}\left[\left(c+\frac{C_p\mu_t}{\mathrm{Pr}_t}\right)\frac{\partial T}{\partial x_j}+u_i(\tau_{ij})_{\mathrm{eff}}\right]+S_h \tag{4}$$

where c is the thermal conductivity. The term $C_p\mu_t/\mathrm{Pr}_t$ is the turbulent thermal conductivity c_t. The effective conductivity is formed by $c+c_t$. E is the total energy. E includes enthalpy h, flow work $-p/\rho$, and kinetic energy $v^2/2$. $(\tau_{ij})_{\mathrm{eff}}$ is the effective devia-

toric stress tensor, the mathematical expression of which is similar to Eq. (3) with μ_t replaced with μ_{eff}. S_h is a source term, including the heat generated by the chemical reaction.

3.2 Turbulence Model. The reactive flow in the channel was considered to be within turbulent regime in the present paper. As the time-averaged flow properties at different parameters were of primary interests in this paper, the RANS-based two-equation realizable k-ε model [24] was used. The transport equations for turbulence kinetic energy (k) and its dissipation rate (ε) are

$$\frac{\partial}{\partial t}(\rho k) + \frac{\partial}{\partial x_j}(\rho k u_j) = \frac{\partial}{\partial x_j}\left[\left(\mu + \frac{\mu_t}{\sigma_k}\right)\frac{\partial k}{\partial x_j}\right] + G_k + G_b - \rho\varepsilon - Y_M + S_k \tag{5}$$

and

$$\frac{\partial}{\partial t}(\rho\varepsilon) + \frac{\partial}{\partial x_j}(\rho\varepsilon u_j) = \frac{\partial}{\partial x_j}\left[\left(\mu + \frac{\mu_t}{\sigma_c}\right)\frac{\partial \varepsilon}{\partial x_j}\right] + \rho C_1 S\varepsilon - \rho C_2 \frac{\varepsilon^2}{k + \sqrt{\nu\varepsilon}} + C_{1c}\frac{\varepsilon}{k}C_{3c}G_b + S_c \tag{6}$$

where

$$C_1 = \max\left[0.43\frac{\eta}{\eta+5}\right], \quad \eta = S\frac{k}{\varepsilon}, \quad S = \sqrt{2S_{ij}S_{ij}} \tag{7}$$

The main difference between the realizable k-ε and the standard k-ε model is the calculation of μ_t

$$\mu_t = \rho C_\mu \frac{k^2}{\varepsilon} \tag{8}$$

The C_μ term is variable in the realizable k-ε model, whereas it is a constant in the standard model. It is defined by

$$C_\mu = \frac{1}{A_0 + A_S\dfrac{kU^*}{\varepsilon}} \tag{9}$$

where $A_0 = 4.04$ and $A_S = \sqrt{6}\cos(\varphi)$.

3.3 Combustion Model. Evaluation of the most accurate combustion model was beyond the scope of this paper. For simplicity, the propane-air combustion was simulated using a one-step irreversible chemical reaction

$$C_3H_8 + 5O_2 \rightarrow 3CO_2 + 4H_2O \tag{10}$$

The species transport, which occurs as a result of this reaction, was modeled using the following equation:

$$\frac{\partial}{\partial t}(\rho Y_i) + \nabla\cdot(\rho \boldsymbol{v} Y_i) = -\nabla\cdot\boldsymbol{J}_i + R_i + S_i \tag{11}$$

where $\boldsymbol{v}$ is the resultant velocity vector. $\boldsymbol{J}_i$ is the diffusion flux of species i, due to concentration gradient. Y_i is the local mass fraction of the species being calculated, S_i is the rate of creation by addition from the dispersed phase if any, and R_i is the net rate of production by chemical reaction of the species being calculated.

The eddy-dissipation model [25] was used for the turbulence-reaction interaction. In this model, the reaction rates are assumed to be controlled by the turbulence, so expensive Arrhenius chemical kinetic calculations can be avoided. The net rate of production (R_i) value was calculated by taking the smaller value of these two equations

$$R_{i,r} = \nu'_{i,r}M_{w,i}A\rho\frac{\varepsilon}{k}\min_R\left(\frac{Y_R}{\nu'_{R,r}M_{w,R}}\right) \tag{12}$$

Table 1 Grid convergence study

Grid size	Exit temperature (K)	% difference	Exit axial velocity (m/s)	% difference
20,871	1731.41		57.67	
41,039	1704.89	1.53	56.18	2.60
82,301	1787.43	4.84	60.58	7.83
147,051	1812.12	1.38	61.64	1.76
278,701	1802.03	0.56	61.22	0.69
361,521	1805.10	0.17	61.45	0.38

$$R_{i,r} = \nu'_{i,r}M_{w,i}AB\rho\frac{\varepsilon}{k}\frac{\Sigma_P Y_P}{\Sigma_j^N \nu'_{j,p}M_{w,j}} \tag{13}$$

where Y_P is the mass fraction of the product being calculated, Y_R is the mass fraction of the reactant being calculated, A is an empirical constant ($A=4.0$), and B is an empirical constant ($B=0.5$) [25].

3.4 Boundary Conditions. As mentioned earlier, the initial boundary conditions, such as inlet velocity (10 m/s) and turbulence intensity (2%), were chosen to match those of the experimental setup to be used as a baseline. The inlet temperature was set to 300 K. The equivalence ratio of 0.6 resulted in a propane mass fraction of 0.037, an oxygen mass fraction of 0.2245, and a nitrogen mass fraction of 0.7385. The walls of both the V-gutter and the flow channel were assumed to be adiabatic. At the outlet of the flow channel, the pressure boundary condition was specified.

4 Numerical Computations

4.1 Numerical Methods. A finite volume method [26] was used to solve all the governing equations. The algebraic equations resulted from discretization were solved using an iterative under relaxation method to improve stability. Second-order upwind schemes were used for the solution of all the governing equations by the SIMPLE solver in FLUENT 6.3.26 [27].

The numerical solution was iterated at least 3000 times for each case in order to reach convergence. Residual convergence levels were set to 10^{-5} for continuity, momentum, k, and ε, 10^{-8} for energy, and 10^{-3} for all the other variables. For the first 1500 iterations, standard pressure discretization was used along with first order discretization schemes for all other variables. After this was completed, the pressure discretization scheme was changed to PRESTO!, and second order discretization for all other variables was implemented for the final 1500 plus iterations. Convergence was further verified by monitoring the overall energy and mass balances in the computational domain.

4.2 Computational Mesh. A grid independent study was performed to determine the optimal grid with a good balance of accuracy and speed. Structured mesh sizes ranged from approximately 21,000 cells to 361,000 cells were created by GRIDGEN V 15.10 [28]. For each case, the near wall spacing was held constant, which resulted in $y+$ values no larger than 4.0 (most in the order of 1.0) at any point along the wall and V-gutter. This was important due to that fact that enhanced wall functions were used in the turbulence model, which required the $y+$ values not to exceed 10 for results of the highest accuracy. The smaller near wall spacing was necessary to properly capture the interaction of the turbulent flow with the walls of the flame holder and the resulting viscous boundary layer.

The parameters examined to determine the grid convergence were the area-averaged exit temperature and the area-averaged axial velocity. Table 1 lists each mesh size tested and the results obtained from each mesh. After examining the results with different grid sizes, it was found that the optimal grid size was approximately 279,000 cells. This mesh provided converged results with-

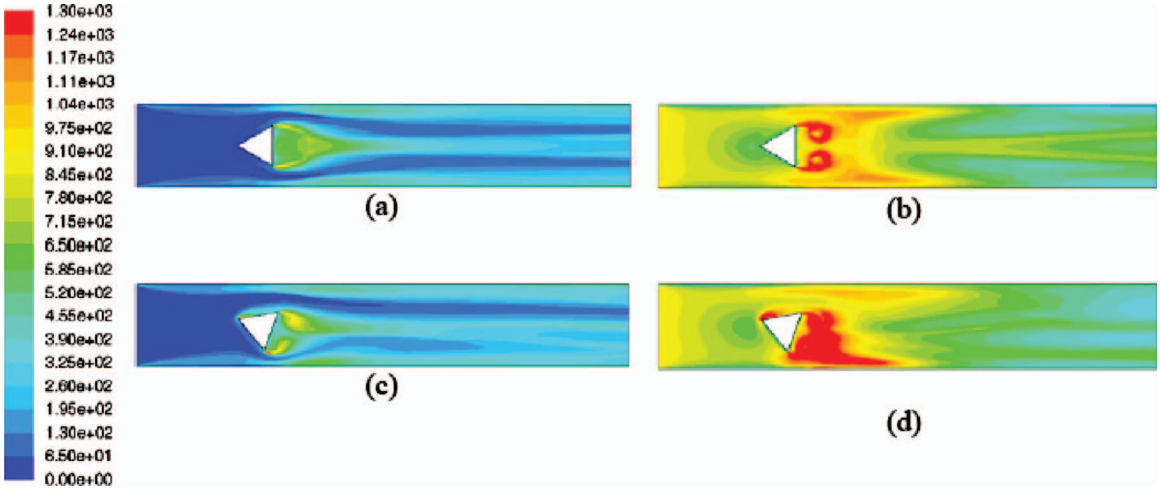

Fig. 2 Local turbulent intensity contours at different angle of attack and inlet turbulence intensity levels: (*a*) *I* =2%, α=0 deg; (*b*) *I*=100%, α=0 deg; (*c*) *I*=2%, α=20 deg; (*d*) *I*=100%, α=20 deg

out exceptionally high computational time. All calculations were carried out on a Linux cluster of 68 processors with 208 cores in the University of Tennessee.

5 Results and Discussion

A validation study performed by the authors against the experimental data has shown that the numerical model outlined in this paper had predicted the reacting turbulent flow fairly well [29]. This gives us confidence to perform a parametric study under different conditions. In the following, numerical results through the parametric study of the effects of inlet turbulence intensity (I) and angle of attack (α) of the V-gutter were presented and analyzed.

5.1 Reacting Turbulent Flow Fields. Figure 2 shows the contours of local turbulence intensity at two typical angles of attack, α=0 deg and 20 deg, and two typical inlet turbulence intensities, I=2% and 100%. At I=2%, two strips of low turbulence intensity above and below the V-gutter can be observed clearly in the flow channel, with the higher turbulence levels located in either the V-gutter wake or near-channel-wall regions. At the fixed value of α, the increase in I greatly increased the turbulent intensity downstream of the V-gutter. As the patterns of the turbulence intensity behind the V-gutter mimic the turbulent eddies, this implied that the turbulent eddies shedding off of the trailing edges become larger in both size and magnitude. At α =0 deg, the turbulence patterns are symmetric, while at α =20 deg, the turbulence patterns are not only asymmetric, but also elevated in intensity. Figures 2(d) and 2(b) show that there is much turbulence shedding near the lower wall of the channel when α is increased.

The angle of attack's effect to generate asymmetric flow patterns can be further confirmed by the velocity vector field behind an inclined V-gutter, as shown in Fig. 3. Our numerical results indicated that as the inlet turbulent intensity was increased, the velocities downstream of the V-gutter were increased. This included the recirculation velocity. When the angle of attack was varied, a different effect was observed—the velocities remained basically unchanged, but the size and location of the recirculation zones changed.

Table 2 provides the changes in the size of the recirculation zone behind the V-gutter at different levels of I and α. The recirculation zone's sizes were determined by plotting the velocity vectors and determining the points where recirculation ended. Since two separate recirculation subzones occurred behind the V-gutter, two separate top and bottom y spans of the recirculation was specified. The table shows that for an angle of attack of zero, there was basically no change in the recirculation zone size as inlet turbulent intensity was increased. Increasing the angle of attack resulted in a decrease in the x span and an increase in the total y span of the recirculation zone. Also, the lower recirculation zone became enlarged while the upper recirculation zone shrank. For the cases of nonzero angle of attack, when the inlet turbulent intensity was increased, there was a decrease in x span and a slight increase in the total y span, but there were significant differences in the y spans of the upper and lower recirculation subzones. In overall, the increases in the inlet turbulent intensity resulted in a larger lower recirculation zone and a smaller upper recirculation zone.

With these basic turbulent flow patterns revealed, it is of interest to determine what effect they would have on the combustion properties of the V-gutter. Figure 4 compares the temperature contours of the baseline setup with relatively extreme inlet turbulent intensity and the angle of attack. Figure 5 gives the same comparison as Fig. 4, except using carbon dioxide levels instead of temperature. It can be seen that both angle of attack and inlet turbulent intensity affect the combustion phenomena significantly. When the inlet turbulent intensity alone was increased, the CO_2 levels in Fig. 5 showed that complete combustion occurs directly downstream of the V-gutter, which was much different than the baseline case. This can also be seen in the temperature contours in

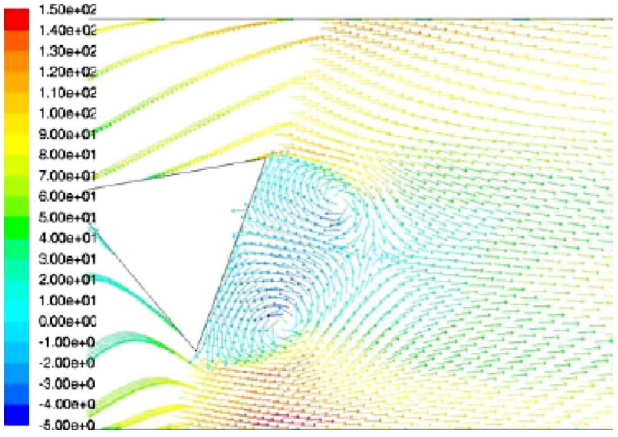

Fig. 3 Velocity vector plots colored by axial velocity at angle of attack α=20 deg, *I*=100%

Table 2 Recirculation zone size differences for varied angle of attack and inlet turbulence intensity

	α=0 deg, I=2%	α=0 deg, I=25%	α=0 deg, I=50%	α=0 deg, I=75%	α=0 deg, I=100%	α=20 deg, I=2%	α=20 deg, I=25%	α=20 deg, I=50%	α=20 deg, I=75%	α=20 deg, I=100%
x span (mm)	24.7	24.7	24.6	24.5	24.5	22.6	18.9	18.5	17.8	17.4
y span top (mm)	12.5	12.5	12.5	12.5	12.5	8.8	6.7	6.4	6.1	5.9
y span bottom (mm)	12.5	12.5	12.5	12.5	12.5	15.4	17.8	18.4	19	19.7
y span total (mm)	25	25	25	25	25	24.2	24.5	24.8	25.1	25.6

Fig. 4, where low temperature flow did not penetrate nearly as far downstream when compared with the baseline. When the angle of attack alone was increased, the amount of combusted reactants seemed to be increased below the V-gutter, but decreased above the V-gutter. The low temperature and CO_2 levels were greatly decreased below the V-gutter, but the opposite occurs above the V-gutter. As would be expected from the high angle of attack scenario, complete combustion occurs sooner below the V-gutter than above the V-gutter.

Table 3 gives a comparison of each of the four cases examined in the previous two figures about the maximum values of temperature, axial velocity, and turbulent intensity in the flow channel. For each of these three parameters, the baseline configuration produced the minimum of all the cases. Increasing only the inlet turbulent intensity caused a large increase in all three values. The maximum velocity and turbulence values approximately doubled, while the maximum temperature raised by approximately 65 K. When only the angle of attack was increased, all of the values were raised as well, but not to the same level as what was achieved by raising the inlet turbulent intensity. The combination of increasing both angle of attack and inlet turbulent intensity resulted in the highest values of both maximum turbulent intensity and axial velocity.

These maximum values were further plotted in Fig. 6, which depicts the clear trend with the variations of angle of attack and inlet turbulent intensity. These curves show that any increase in angle of attack or inlet turbulent intensity results in an increase in the maximum values being examined. There were some differences in how they were changed, though. Both maximum axial velocity and turbulent intensity increased fairly uniformly with the increase in inlet turbulent intensity at each angle of attack. However, the increasing speed for the maximum temperature at higher

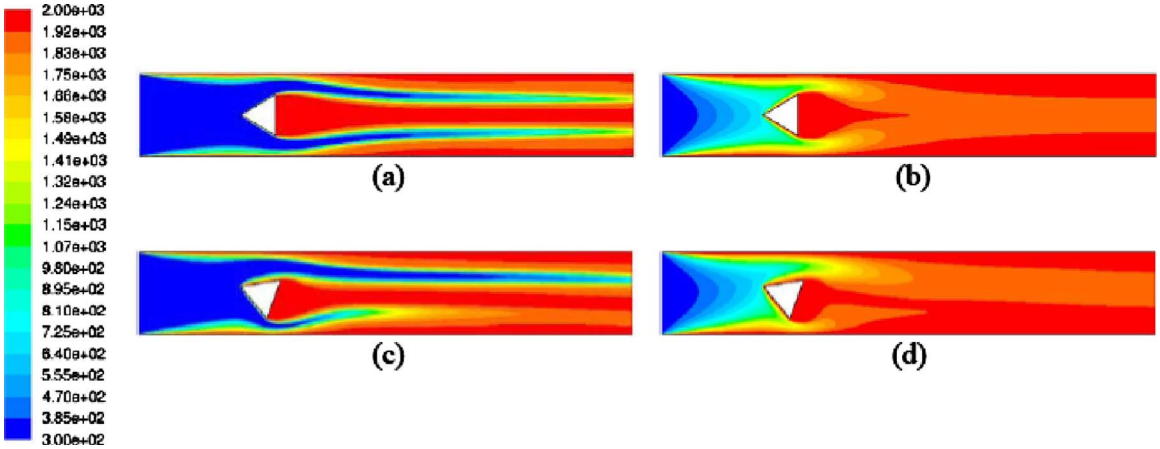

Fig. 4 Temperature contours at different angle of attack and inlet turbulence intensity levels: (*a*) I=2%, α=0 deg; (*b*) I=100%, α=0 deg; (*c*) I=2%, α=20 deg; (*d*) I=100%, α=20 deg

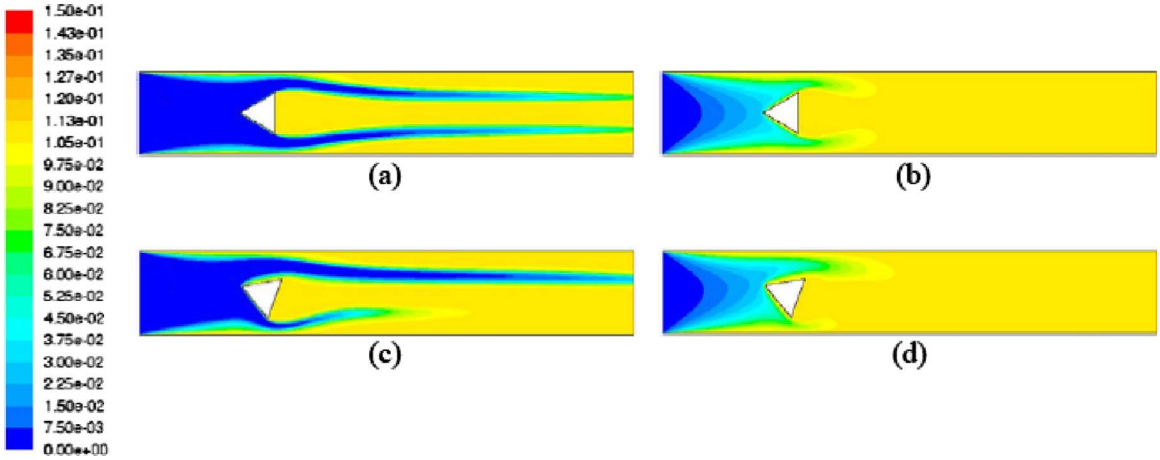

Fig. 5 CO_2 mass fraction contours at different angle of attack and inlet turbulence intensity levels: (*a*) I=2%, α=0 deg; (*b*) I=100%, α=0 deg; (*c*) I=2%, α=20 deg; (*d*) I=100%, α=20 deg

Table 3 Comparison of maximum values of temperature, axial velocity, and turbulence intensity

	$\alpha=0$ deg, $I=2\%$	$\alpha=0$ deg, $I=100\%$	$\alpha=20$ deg, $I=2\%$	$\alpha=20$ deg, $I=100\%$
Max temperature (K)	1978.97	2043.76	2001.28	2039.81
Max axial velocity (m/s)	72.11	141.24	76.90	152.67
Max turbulence intensity (%)	1235.03	2996.01	1500.22	3178.32

angle of attack α was found slower than the lower α, causing the crossing over of the two curves shown in Fig. 6(*a*).

5.2 Wall Temperature Profiles. Temperature distributions along the walls of both V-gutter and channel are important to the combustion system's lifetime. Therefore, it was of great interest to determine what effects the inlet turbulent intensity and angle of attack would have on these temperature profiles. Figure 7 shows the temperature profiles of the upper and lower walls of the flow channel at $\alpha=0$ deg and $\alpha=30$ deg. Due to the symmetry of the geometry at $\alpha=0$ deg, the temperature profiles on the upper and lower channel wall are identical (Fig. 7(*a*)). At the zero angle of attack, an increase in inlet turbulent intensity results in the wall reaching higher temperatures, particularly in the region closer to the inlet of the channel. This implies that combustion has occurred closer to the inlet along the walls due to the increased turbulence level. As expected, there was no substantial variation in the temperature profiles on the channel walls in the region far away from the flame holder. At an angle of attack of $\alpha=30$ deg, the main difference noticed was a dip in wall temperature on the lower wall just downstream of the V-gutter when the value of I is low (2%). This was caused by the V-gutter forcing the uncombusted mixture toward the lower wall at the increased angle of attack. This effect vanished at high inlet turbulent intensities because combustion of the reactants occurred closer to the inlet, releasing heat to eliminate the temperature dip on the wall.

Figure 8 shows the corresponding temperature profiles of the upper and lower V-gutter walls for both $\alpha=0$ deg and $\alpha=30$ deg. As can be seen from the figure, an increase in inlet turbulent intensity I resulted in high V-gutter wall temperatures moving closer to the leading edge of the V-gutter at $\alpha=0$ deg. When the angle of attack α was increased to 30 deg, the wall temperature reached high levels much closer to the leading edge on the upper V-gutter wall, although its sensitivity to inlet turbulence intensity I was relatively lower. At the same angle of attack, the opposite effect was observed along the lower V-gutter wall (Fig. 8(*c*)). In addition to the large temperature variations along the lower V-gutter wall, the level of temperature along the entire lower V-gutter wall was also much lower, particularly at low inlet turbulence intensity ($I=2\%$). Also observed was a drop in wall temperature near the trailing edge of the V-gutter. This wall temperature drop became less considerable at higher inlet turbulent intensity due to increased turbulent mixing around the V-gutter.

Figure 9 shows the temperature profiles of the rear wall of the V-gutter at $\alpha=0$ deg and $\alpha=30$ deg. At $\alpha=0$ deg, the temperature profiles were basically constant along the entire wall. This near-constant temperature value increased as the inlet turbulent intensity was increased. When the angle of attack α was increased to 30 deg, there was an initial high spike of temperature near the upper edge of the wall. Further along the wall, the temperature increased very slowly with a small drop-off at the lower edge.

Considering the results presented in Figs. 7–9 together, it was found that an increase in the inlet turbulent intensity I actually resulted in an increase in temperature level everywhere along the wall at different values of angle of attack α.

5.3 Fraction Factors. Another important consideration in V-gutter design is the pressure loss associated with its blockage

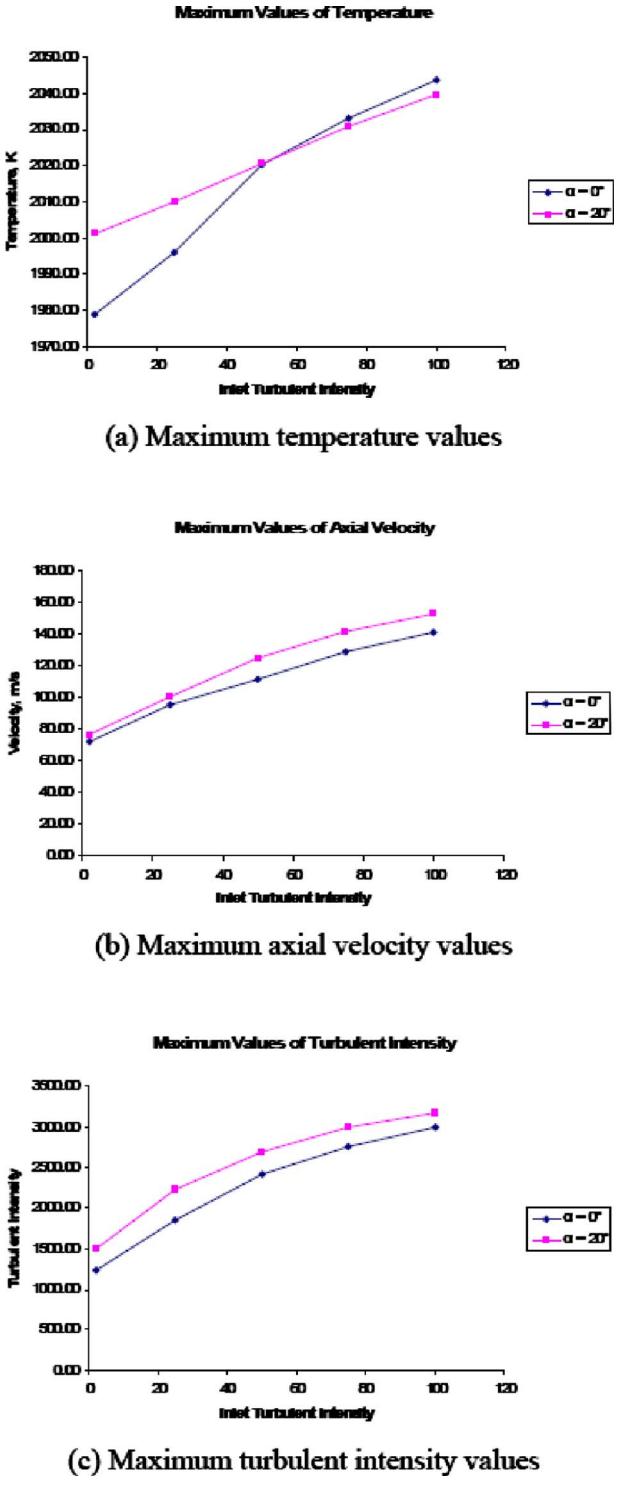

Fig. 6 Maximum values of temperature, axial velocity, and turbulent intensity at different *I*

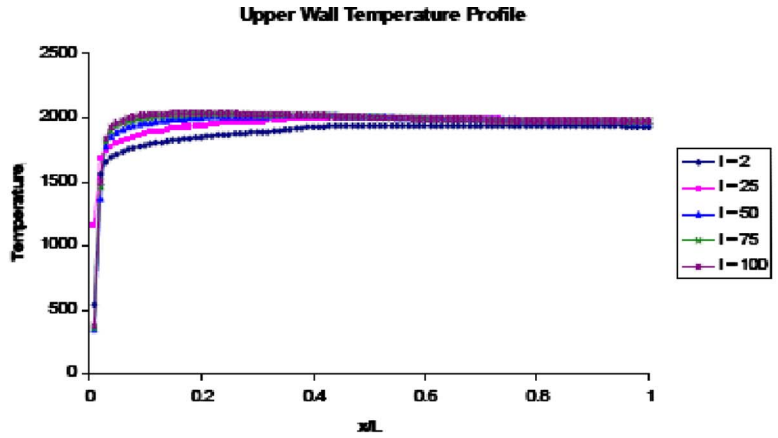

(a) $\alpha = 0°$

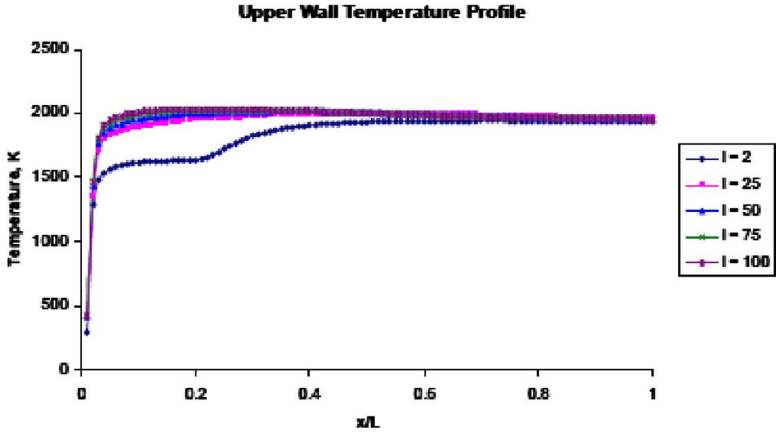

(b) $\alpha = 30°$

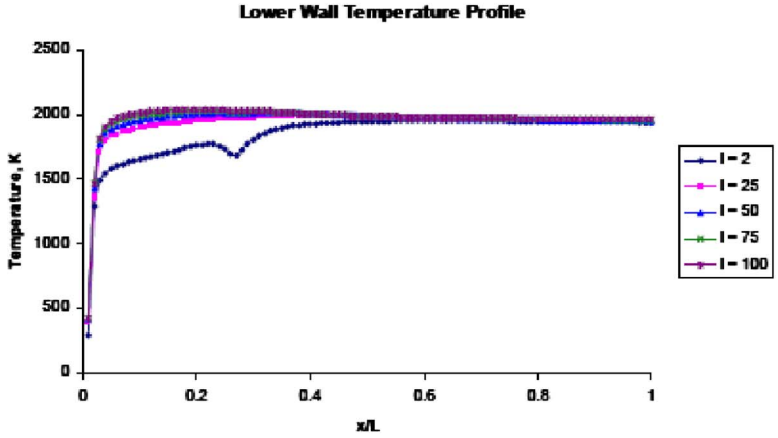

(c) $\alpha = 30°$

Fig. 7 Temperature profiles on the upper and lower channel walls at α =0 deg and α=30 deg: (*a*) upper wall and lower wall, α=0 deg; (*b*) upper wall, α=30 deg; (*c*) lower wall, α=30 deg

across the entire channel. Because the Mach number at the inlet is rather low and the hydraulic pressure loss due to the presence of the V-gutter could be significant as compared with stagnation pressure change due to heat addition, a single parameter to represent the pressure loss across the channel was used. For the channel flow problem, the friction factor had been used to represent the normalized pressure drop [30]. The formula used to calculate the friction factor in the channel was as follows:

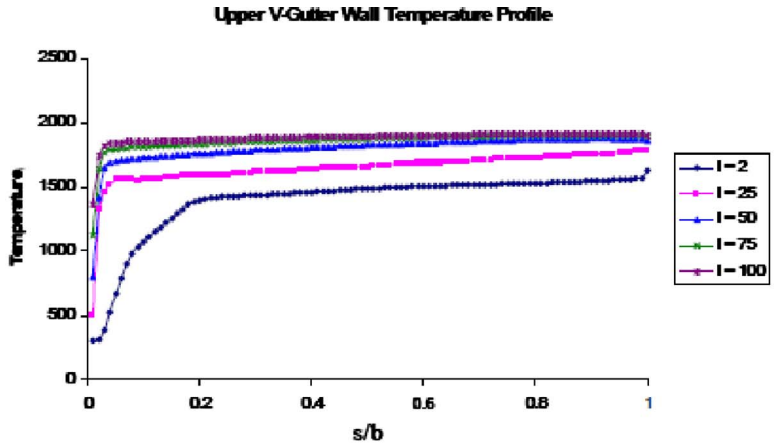

(a) $\alpha = 0°$

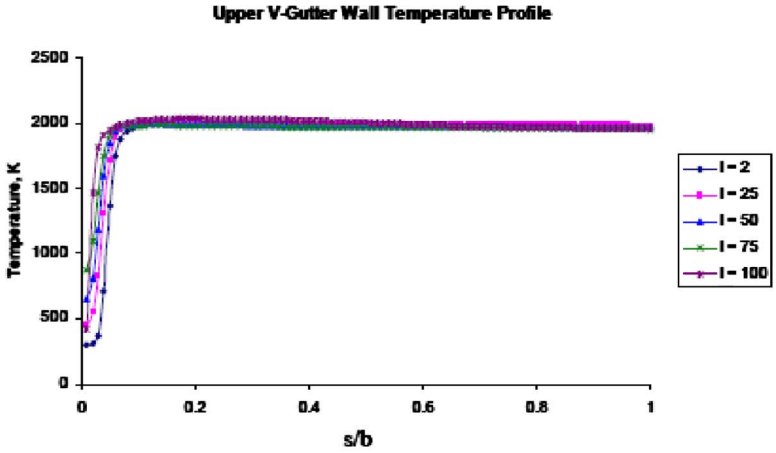

(b) $\alpha = 30°$

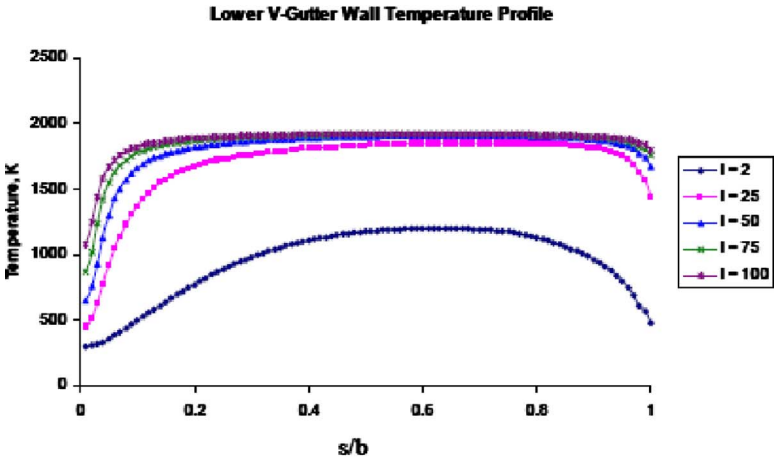

(c) $\alpha = 30°$

Fig. 8 Temperature profiles on the upper and lower V-gutter walls at α =0 deg and α=30 deg: (*a*) upper wall and lower wall, α=0 deg; (*b*) upper wall, α=30 deg; (*c*) lower wall, α=30 deg

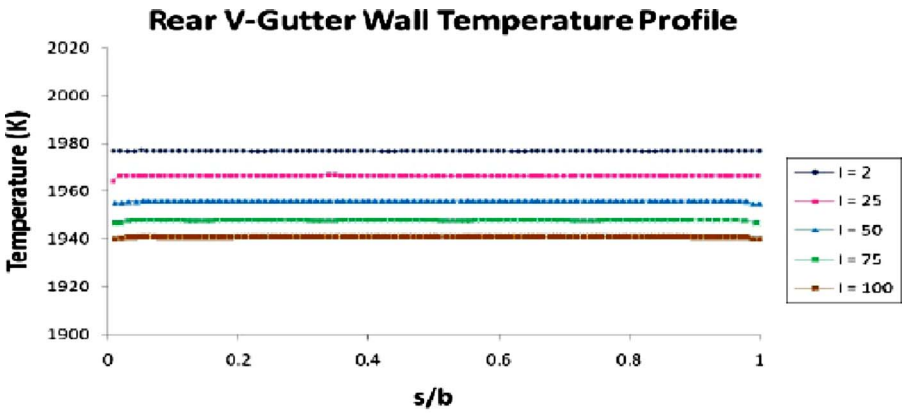

(a) $\alpha = 0°$

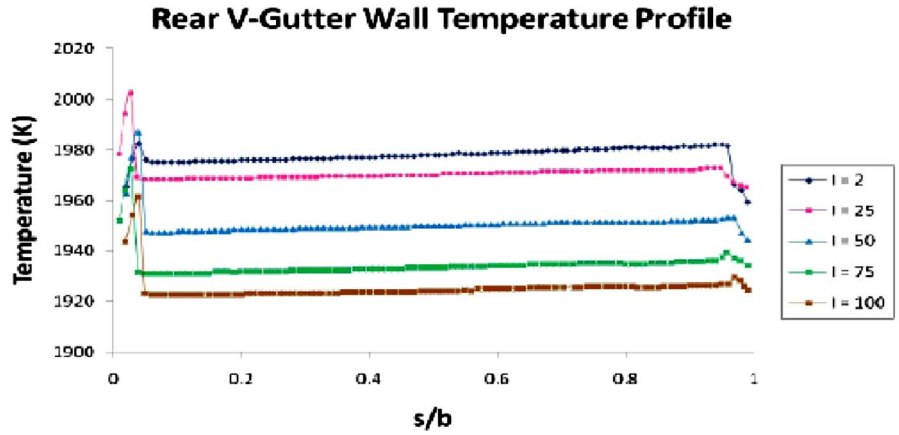

b) $\alpha = 30°$

Fig. 9 Temperature profile on the rear V-gutter wall: (*a*) α=0 deg; (*b*) α=30 deg

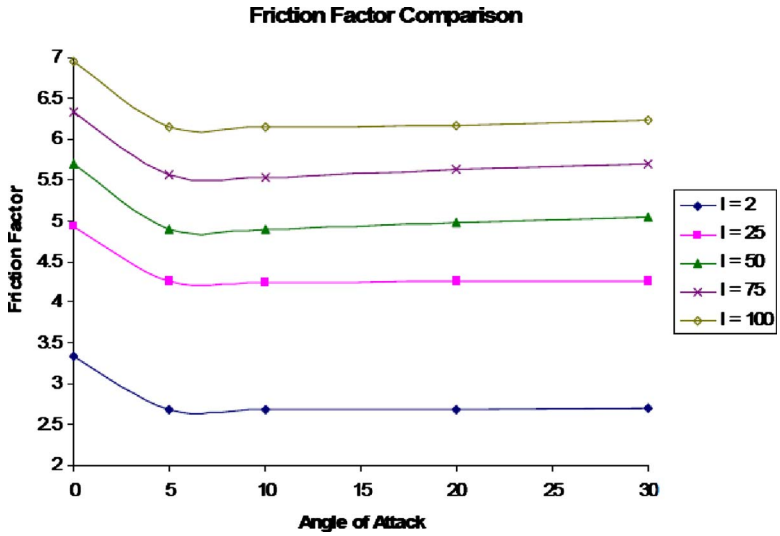

Fig. 10 Friction factor at different angle of attacks and inlet turbulence intensity

$$f = 2\rho D_h \left(\frac{\Delta p}{\Delta x}\right)\left(\frac{A_c}{\dot{m}}\right)^2 \tag{14}$$

Figure 10 shows the effects that varying both inlet turbulent intensity I and angle of attack α has on the friction factor of the flow channel. It can be seen from the figure that the friction factor decreased significantly as turbulent intensity was decreased. Within the small angle of attack range of 0 deg to 5 deg, the increase in the angle caused an apparent drop in friction factor. Beyond this range of angle of attack, any increase in the angle made little difference in the fraction factors. In order to further minimize the friction factor, and thus minimize the pressure drop, the interior leading edge angle of the V-Gutter could be decreased in order to create a smaller blockage ratio, which will be carried in our future research.

6 Concluding Remarks

Numerical simulations were carried out to investigate the effects of varying the angle of attack and inlet turbulent intensity on the chemically reacting turbulent flow and thermal fields in a channel containing a V-gutter flame holder. Within the investigated parameter ranges, the following were observed.

- An increase in inlet turbulent intensity resulted in a higher level of turbulence downstream of the V-gutter, which in turn caused an increase in both velocity and temperature in the reacting turbulent flow.
- With the increase in the angle of attack, the lower recirculation zone grew while the upper other shrunk behind the V-gutter. The turbulent recirculation flow was found to have contributed in keeping the rear V-gutter wall near-isothermal.
- Both inlet turbulent intensity and angle of attack caused considerable variations in wall temperature profiles, particularly in the regions near the leading and trailing edges of the V-gutter.
- The effect of the inlet turbulence intensity was to increase the value of the fraction factor of the flow channel. The influence of the angle of attack was limited to a range of small angle of attack, less than about 5 deg.

Nomenclature

A_c = flow cross-sectional area of test channel (m^2)
b = height of the V-gutter (m)
c = thermal conductivity (W/m K)
C_p = constant pressure specific heat (J/kg K)
C = constants
D_h = hydraulic diameter (m)
E = total energy (J)
f = friction factor
g = gravity (m/s^2)
G_b = generation of turbulence kinetic energy due to buoyancy ($kg/m\ s^3$)
G_k = generation of turbulence kinetic energy due to mean velocity gradients ($kg/m\ s^3$)
H = channel height (m)
I = unit tensor
k = turbulence kinetic energy (m^2/s^2)
L = channel length (m)
$M_{w,i}$ = molecular weight of species i
p = static pressure (Pa)
R_i = net rate of production by chemical reaction of species ($kg/s\ m^3$)
s = local coordinate along a wall (m)
S = source term
S_i = rate of creation by addition from the dispersed phase ($kg/s\ m^3$)
t = time (s)
T = temperature (K)
u_i = time-averaged velocity (m/s)
v = resultant velocity (m/s)
x,y = Cartesian coordinates (m)
Y_i = local mass fraction of chemical species
Y_p = mass fraction of any product species
Y_R = mass fraction of a particular reactant

Greek Symbols

α = angle of attack (deg)
ε = turbulence kinetic energy dissipation rate (m^2/s^3)
μ = viscosity (kg/m s)
ν_i' = stoichiometric coefficient for reactant i
ρ = density (kg/m^3)
$\overline{\tau}$ = stress tensor (Pa)

Subscript Description

b = denotes buoyancy
i,j,k = species or spacial index
r = reaction
t = turbulent

References

[1] Hill, P., and Peterson, C., 1992, *Mechanics of Thermodynamics of Propulsion*, Addison-Wesley, Reading, MA.
[2] Longwell, J. P., 1953, "Flame Stabilization by Bluff Bodies and Turbulent Flames in Ducts," Proc. Combust. Inst., **4**, pp. 90–97.
[3] White, F., 2006, *Viscous Fluid Flow*, McGraw-Hill, New York.
[4] Lin, C., Sekar, B., Holder, R., Zelina, J., and Thornburg, H., 2008, "Numerical Simulation of Inter-Turbine Burner (ITB) Flows With the Inclusion of V-Gutter Flame Holders," ASME Paper No. GT2008-50337.
[5] Fujii, S., Gomi, M., and Eguchi, K., 1978, "Cold Flow Tests of a Bluff-Body Flame Stabilizer," J. Fluids Eng., **100**, pp. 323–332.
[6] Yue, L., Liu, B., and Yang, M., 2003, "Study on the Near-Wake Flow Behind EBMC Flame Holder," Proc. SPIE, **5058**, pp. 188–198.
[7] Sanquer, S., Bruel, P., and Deshaies, B., 1998, "Some Specific Characteristics of Turbulence in the Reactive Wakes of Bluff Bodies," AIAA J., **36**(6), pp. 994–1001.
[8] Kiel, B., Garwick, K., Gord, J. R., Miller, J., Lynch, A., Hill, R., and Phillips, S., 2007, "A Detailed Investigation of Bluff Body Stabilized Flames," AIAA Paper No. AIAA 2007-168.
[9] Bush, S. M., and Gutmark, E. J., 2007, "Reacting and Nonreacting Flowfields of a V-Gutter Stabilized Flame," AIAA J., **45**(3), pp. 662–672.
[10] Sjunnesson, A., Olovsson, S., and Sjoblom, B., 1991, "Validation Rig: A Tool for Flame Studies," *Proceedings of the International Symposium on Air Breathing Engine*, Paper No. 91-7038.
[11] Fujii, S., and Eguchi, K., 1981, "A Comparison of Cold and Reacting Flows Around a Bluff-Body Flame Stabilizer," ASME J. Fluids Eng., **103**, pp. 328–334.
[12] Cuppoletti, D. R., Kastner, J., Reed, J., Jr., and Gutmark, E. J., 2009, "High Frequency Combustion Instabilities With Radial V-Gutter Flameholders," AIAA Paper No. AIAA-2009-1176.
[13] Kim, W., Lienau, J., Slooten, P., Colket, M., Malecki, R., and Syed, S., 2006, "Towards Modeling Lean Blow Out in Gas Turbine Flameholder Applications," ASME J. Eng. Gas Turbines Power, **128**, pp. 40–48.
[14] Hasse, C., and Sohm, V., 2009, "Hybrid URANS/LES Turbulence Simulation of Vortex Shedding Behind a Triangular Flameholder," Flow, Turbul. Combust., **83**, pp. 1–20.
[15] Fureby, C., 2000, "Large Eddy Simulation of Combustion Instabilities in a Jet Engine Afterburner Model," Combust. Sci. Technol., **161**, pp. 213–243.
[16] Porumbel, I., and Menon, S., 2006, "Large Eddy Simulation of Bluff Body Stabilized Premixed Flame," AIAA Paper No. AIAA 2006-152.
[17] Bai, X. S., and Fuchs, L., 1994, "Modeling of Turbulent Reacting Flows Past a Bluff Body: Assessment of Accuracy and Efficiency," Comput. Fluids, **23**(3), pp. 507–521.
[18] Johansson, S., and Davidson, L., 1991, "Calculation of the Unsteady Turbulent Flow Behind a Triangular Flameholder," Paper No. CERFACS TR/RF/91/53.
[19] Erickson, R. R., Soteriou, M. C., and Meha, P. G., 2006, "The Influence of Temperature Ratio on the Dynamics of Bluff Body Stabilized Flames," AIAA Paper No. AIAA 2006-753.
[20] Smith, C. E., Nickolaus, D., Leach, T., Kiel, B., and Garwick, K., 2007, "LES Blowout Analysis of Premixed Flow Past V-Gutter Flameholder," AIAA Paper No. AIAA 2007-170.
[21] Roach, J. M., Fisher, T. C., Frankel, S. H., Sekar, B., and Kiel, B. V., 2008, "CFD Predictions of Damkohler Number Fields for Reduced Order Modeling of V-Gutter Flame Stability," AIAA Paper No. AIAA 2008-509.
[22] Giacomazzi, E., Battaglia, V., and Bruno, C., 2004, "Coupling of Turbulence and Chemistry in a Premixed Bluff-Body Flame as Studied by LES," Combust. Flame, **138**(4), pp. 320–335.

[23] Gokulakrishnan, P., Bikkani, R., Klassen, M. S., Roby, R. J., and Kiel, B. V., 2009, "Influence of Turbulence-Chemistry Interaction in Blow-Out Predictions of Bluff-Body Stabilized Flames," AIAA Paper No. AIAA 2009-1179.
[24] Shih, T.-H., Liou, W. W., Shabbir, A., Yang, Z., and Zhu, J., 1995, "A New k-ε Eddy-Viscosity Model for High Reynolds Number Turbulent Flows—Model Development and Validation," Comput. Fluids, **24**(3), pp. 227–238.
[25] Magnussen, B. F., and Hjertager, B. H., 1976, "On Mathematical Models of Turbulent Combustion With Special Emphasis on Soot Formation and Combustion," *Proceedings of the 16th International Symposium on Combustion*, The Combustion Institute.
[26] Patankar, S. V., 1980, *Numerical Heat Transfer and Fluid Flow*, Taylor & Francis, London.
[27] Fluent Inc., 2007, FLUENT 6.3.26, www.fluent.com
[28] Pointwise, Inc., 2004, GRIDGEN V15.
[29] Holder, R., and Lin, C. X., 2008, "Numerical Simulation of Reactive Turbulent Flows Over Bluff Body Flame Holders: A Parametric Study," ASME Paper No. HT2008-56245.
[30] Ahn, H. S., 2007, "Heat Transfer Enhancement for Turbulent Flow Through Blockages With Round and Elongated Holes in a Rectangular Channel," J. Heat Transfer, **129**, pp. 1611–1615.

Theoretical Study on Transient Hot-Strip Method by Numerical Analysis

Gaosheng Wei
e-mail: gaoshengw@126.com

Xiaoze Du
e-mail: duxz@ncepu.edu.cn

School of Energy and Power Engineering,
Key Laboratory of Condition Monitoring and Control for Power Plant Equipment of Ministry of Education,
North China Electric Power University,
Beijing 102206, China

Xinxin Zhang

Fan Yu

Department of Thermal Engineering,
University of Science and Technology Beijing,
Beijing 100083, China

This paper presented the effects of finite dimensions of the sample and nonzero heat capacity of the strip on thermal conductivity determination with the transient hot-strip method. Through the numerical analysis of the temperature field within the system composed of the samples and the strip, the temperature transients at the strip surface were obtained to calculate the thermal conductivities of materials, which were compared with the exact values. The effect of heat losses out of the external surfaces of the sample and the heat capacity of the strip on thermal conductivity determination were then analyzed comprehensively. It is shown that the sample finite dimensions have a great effect on thermal conductivity determination, especially on the materials with relatively higher thermal diffusivities, and the measured thermal conductivity is always lower than the exact value due to the lower convective heat transfer coefficient out of the external surfaces of the sample. The measurement error is estimated to be less than 2.1% for the material with thermal diffusivity less than 4.0×10^{-6} m^2/s *with the sample dimensions of* 120×60 mm^2 *(width* $\times$ *thickness) and the fitting time interval of 20–300 s. The nonzero heat capacity of the strip has a great effect on thermal conductivity determinations of the materials with relatively lower thermal diffusivities. The measurement error is estimated to be less than 5% for the material with thermal diffusivity larger than 0.8* $\times10^{-7}$ m^2/s *with Cr20Ni80 alloy as the strip.* [DOI: 10.1115/1.4001611]

Keywords: numerical simulation, thermal conductivity, thermophysical properties, transient hot-strip method

1 Introduction

The theory of the transient hot-strip (THS) method [1,2] is similar to the transient hot-wire (THW) method, which was widely used for the experimental determination of thermal conductivities of insulation materials, construction materials, loose materials, and fluids in the past 3 decades [3–9]. This technique is based upon the experimental detection of the thermal transient in the material sample that appears due to the sudden electric heating of a strip sandwiched between the samples by a small thermocouple or only through the electric voltage variation between the two sides of the strip. The THS method is more adaptable to the solid material than the THW method for the ideal contact between the strip and the sample. The usual experimental arrangement of the THS method is schematically shown in Fig. 1. If the measured material is solid, the test samples are usually composed of two rectangular blocks with identical dimensions that joined together. If the temperature transient on the surface of the strip (the M point in Fig. 1) is obtained in the experimental measurement, the thermal conductivity of the measured material is then calculated with Eq. (1), based on the theory of the THS method [1,2]

$$k = \frac{P}{4\pi} \Big/ \frac{dT_m(t)}{d\ln(t)} \tag{1}$$

where k is the thermal conductivity of the sample, P is the output of power in the strip per length (W/m), t is the time (s), and $dT_m(t)/d\ln(t)$ is the slope of temperature transient $T_m(t)$ to $\ln(t)$ over a long time.

However, in applying the above equation in thermal conductivity determination by the THS method, it assumes that the strip has a zero heat capacity, and the measured sample can be considered as an infinite medium. This assumption implies that the temperature transient picked up during the experiment cannot be altered by the fact that the actual sample has finite dimensions, and the strip has a nonzero heat capacity. These considerations mean some restrictions in the applicability of the THS technique in terms of possible sample sizes and allowable thermal conductivity measurement ranges. Although the measurement uncertainty is discussed with the THS method and the THW method by many researches [10–12], the effect of the finite dimensions of the samples and the nonzero heat capacity of the strip on thermal conductivity determination with the THS method is not considered comprehensively.

Therefore, the main purpose of this paper is to investigate how and to what extent the finite dimensions of the actual samples and the nonzero heat capacity of the strip can affect the results of the thermal conductivity measurements by the THS method. In order to achieve these purposes, a numerical analysis of the temperature field within the system composed of the samples, and the strip is accomplished, assuming finite dimensions and the heat losses through the external surfaces of the test sample, also with nonzero heat capacity of the strip. With this procedure, the temperature transient at the surface of the strip is then obtained from a computer simulation. This numerically generated temperature transient on the surface of the strip is then regarded as the one that would be obtained in a THS experiment. By applying Eq. (1), a value for the experimental thermal conductivity (k_{exp}) is obtained and can be compared with the assumed value (k_{num}) that was set in the transient simulation. The distance between these two values ($k_{exp}-k_{num}$) for thermal conductivity will be a measure of the effects of the heat losses out of the external surfaces of the sample or the nonzero heat capacity of the strip.

Contributed by the Heat Transfer Division of ASME for publication in the JOURNAL OF HEAT TRANSFER. Manuscript received June 24, 2009, final manuscript received January 7, 2010; published online June 23, 2010. Assoc. Editor: Ofodike A. Ezekoye.

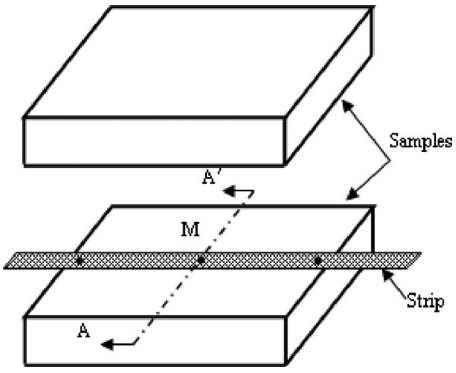

Fig. 1 Schematic show of THS technique

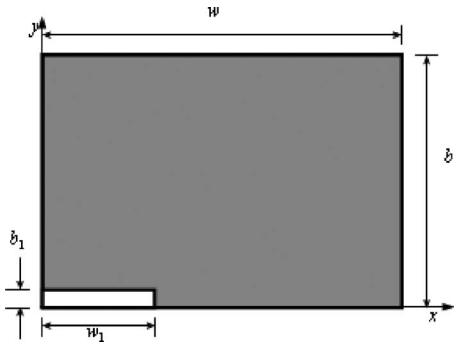

Fig. 3 A quarter of the transverse section for numerical calculation

2 Theory of Transient Hot-Strip Method

As indicated in Fig. 2, a long thin metal strip is embedded in an infinite medium. The THS method makes use of an extended metal strip, having its length at least 20 times as long as its width and its thickness as extremely small compared with the width. Initially, both the strip and the medium maintain the same temperature $T(x,y,t)=T_0$. When a constant direct current I is passed through the strip, it serves as a continuous heat source of power $\Phi=UI$. If the effect of the finite length of the strip, the finite dimension of medium, and the thermal contact resistance between the strip and the medium are neglected, the temperature field in the strip and medium can be expressed as [1,2]

$$T(x,y,t)-T_0=(4a\sqrt{\pi})^{-1}\int_0^{2\sqrt{at}}\frac{q}{\rho c_p}\cdot\exp(-x^2/\sigma^2)\left[\operatorname{erfc}\left(\frac{y-d}{\sigma}\right)-\operatorname{erfc}\left(\frac{y+d}{\sigma}\right)\right]d\sigma \tag{2}$$

where a is the thermal diffusivity of the measured medium, q is the heat flux per area on the strip, ρc_p is the heat capacity of the medium by volume, and d and v are the half width and half thickness of the strip, respectively. Since the thickness of the strip is very thin ($v \ll d$), the temperatures at the center and at the surface of the strip can be considered in the same value, and the average temperature $T_m(t)$ of the strip is expressed as

$$T_m(t)-T_0=\frac{1}{2d}\int_{-d}^{d}[T(0,y,t)-T_0]dy=\frac{P_0}{2\sqrt{\pi}k}\cdot f(\tau) \tag{3}$$

where

$$f(\tau)=\tau-\tau\operatorname{erfc}(1/\tau)-\tau^2(4\pi)^{-1/2}[1-\exp(-1/\tau^2)]+(4\pi)^{-1/2}[-\operatorname{Ei}(-1/\tau^2)]$$

$$\tau=(at)^{1/2}/d$$

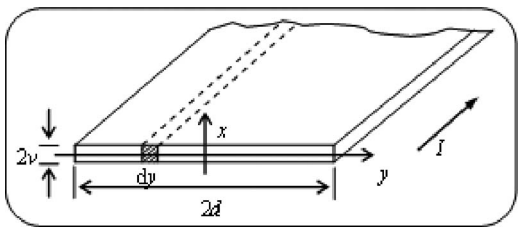

Fig. 2 The strip in infinite medium

$$\operatorname{erfc}(u)=2(\pi)^{-1/2}\int_u^{\infty}\exp(-v^2)dv$$

$$-\operatorname{Ei}(-u)=\int_u^{\infty}v^{-1}\exp(-v)dv$$

For a sufficiently long time ($\tau \gg 1$ or $t \gg d^2/a$), this then yields a variation in temperature as a function of time in simplified form as

$$T_m(t)-T_0=\frac{P_0}{4\pi k}\left[\ln\left(\frac{at}{d^2}\right)-\gamma\right] \tag{4}$$

where $\gamma=0.5772$ is the Euler constant. The thermal conductivity of the surrounding medium is then calculated as Eq. (1).

If a thermocouple is welded in a fixed point on the strip to record the variation in the temperature rise versus time evolution, the slope of $T_m(t)$ to $\ln(t)$ over a long time $dT_m(t)/d\ln(t)$ can be easily obtained, which allows identification of the thermal conductivity of the medium with Eq. (1). In the actual measurement process, considering that the width of the strip $2d=2$ mm, and the thermal diffusivity of the medium $a=10^{-6}$ m^2/s, it matches the condition of $\tau \gg 1$ by several seconds later.

3 Numerical Calculation Model

In order to carry out the proposed numerical analysis in appropriate time, a transverse section of the sample (section AA′ in Fig. 1) passing through the measuring point (M) is considered for there are almost no temperature variation along the strip length direction. Only one-forth of the sample can be considered for the symmetry characteristic of the system, and on the assumption that the strip is surrounded thoroughly by the sample, as shown in Fig. 3. The dimensions of this transverse section of the sample are b (sample thickness), w (one-half of the sample width), b_1 (one-half of the strip thickness), and w_1 (one-half of the strip width). The strip dimensions are also included here for it is convenient to consider the effect of the nonzero heat capacity of the strip on thermal conductivity measurement.

It can be considered that a constant heat source $\dot{\phi}$ exists in the strip for a constant direct current that is passed through the strip from the initial time according to the basis theory of the THS method, and the mathematical models are as follows:

$$\frac{\partial T}{\partial t}=a\left(\frac{\partial^2 T}{\partial x^2}+\frac{\partial^2 T}{\partial y^2}\right) \quad \text{(in the samples)} \tag{5}$$

$$\frac{\partial T}{\partial t}=a_1\left(\frac{\partial^2 T}{\partial x^2}+\frac{\partial^2 T}{\partial y^2}\right)+\frac{\dot{\phi}}{\rho_1 c_1} \quad \text{(in the strip)} \tag{6}$$

initial condition

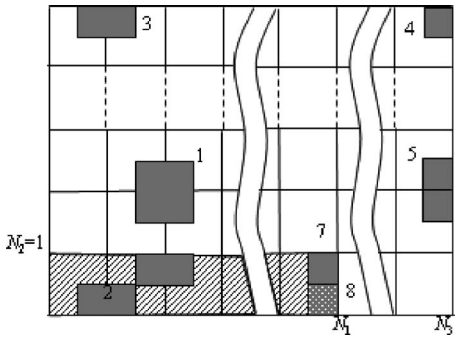

Fig. 4 The mesh distribution in transverse plane

$$T(x,y,t)|_{t=0} = T_0 \tag{7}$$

boundary conditions

$$\left.\frac{\partial T(x,y,t)}{\partial x}\right|_{x=0} = \left.\frac{\partial T(x,y,t)}{\partial y}\right|_{y=0} = 0$$

$$-k\left.\frac{\partial T(x,y,t)}{\partial y}\right|_{y=b} = h[T(x,y,t) - T_0]$$

$$-k\left.\frac{\partial T(x,y,t)}{\partial x}\right|_{x=w} = h[T(x,y,t) - T_0] \tag{8}$$

where a and a_1 are the thermal diffusivities of the sample and the strip, respectively (m^2/s), k is the thermal conductivity of the sample ($W/(m\,K)$), T is the temperature (K), and T_0 is the environmental temperature surrounding the sample (K). ρ_1 and c_{p1} are the density and specific heat of the strip, respectively. h is the convective heat transfer coefficient out of the external surfaces of the sample, and is considered as a constant value here ($W/(m\,K)$). The temperature rising curve of the system can be obtained by solving the above equations numerically.

4 Discretization

The spatial discretization of the transverse plane is done with a mesh of rectangular elements, as shown in Fig. 4. Considering that the strip is usually very thin in thickness direction, one mesh is assigned on the strip in the thickness direction, and the mesh number in the width direction is denoted as N_1. The total meshes on the whole plane are denoted as $N_3 \times N_4$ with nodes (i,j). The implicit differential equations are then established for all nodes, including the inside nodes and boundary nodes by using the general energy balance that takes into account the contributions of heat transfer by conduction and by convection, internal heat generation in the strip, and the time rate of change in the internal energy of both the strip and the measured material associated with the nodes. The discretized implicit differential equations are summarized in Table 1. The discretized differential equations for the adiabatic boundary nodes are not given in Table 1 for they have the same discretized equation form with the interior nodes 1 or 2 in Fig. 4, where

$$\mathrm{Fo}_{\Delta 1} = \frac{a\Delta t}{\Delta x^2}, \quad \mathrm{Fo}_{\Delta 2} = \frac{a\Delta t}{\Delta y^2}, \quad \mathrm{Bi}_{\Delta 1} = \frac{h\Delta x}{k}, \quad \mathrm{Bi}_{\Delta 2} = \frac{h\Delta y}{k},$$

$$\mathrm{Fo}_{\Delta 3} = \frac{a_1\Delta t}{\Delta x^2}, \quad \mathrm{Fo}_{\Delta 4} = \frac{a_1\Delta t}{\Delta y^2}$$

$$\mathrm{Bi}_{\Delta 3} = \frac{h\Delta x}{k_1}, \quad \mathrm{Bi}_{\Delta 4} = \frac{h\Delta y}{k_1}, \quad F_5 = \frac{\Delta t}{(\rho c_p + \rho_1 c_{p1})\Delta x^2},$$

$$F_6 = \frac{\Delta t}{(\rho c_p + \rho_1 c_{p1})\Delta y^2}, \quad F_7 = \frac{\Delta t}{(3\rho c_p + \rho_1 c_{p1})\Delta x^2},$$

$$F_8 = \frac{\Delta t}{(3\rho c_p + \rho_1 c_{p1})\Delta y^2}$$

Δx and Δy are the spatial steps in the coordinate x and y directions, respectively, Δt is the time step, and k_1 is the thermal conductivity of the strip. ρ and ρ_1 are the densities of the sample and the strip, respectively. c_p and c_{p1} are the specific heats of the sample and the strip, respectively.

5 Results and Discussion

The discretized differential equation system in Table 1 is then solved in uniform mesh of rectangular elements, as shown in Fig. 4. As a reference case, the values for w_1 and b_1 are set to 0.005 mm and 1 mm because these are typical values of the strip that appear in the THS technique. The dimensions of the sample vary from 30×30 mm^2 ($w \times b$) to 60×60 mm^2, and the heat capacity of the strip $\rho_1 c_{p1}$ varies from 0 $kg/(m^3\,K)$ to 3.87×10^3 $kg/(m^3\,K)$ in order to evaluate the effects of the finite dimensions of the sample and the nonzero heat capacity of the strip on thermal conductivity measurements. The thermal conductivity of the strip k_1 is set to 16.75 $W/(m\,K)$, which is the thermal conductivity of Cr20Ni80 alloy. The heat source produced by the electric current passing through the strip generates the temperature transient within the material and the strip. The amount of electric current passing through the strip is usually adjusted to create in the test sample a temperature rise not so small that it can hardly be detected or too big to invalidate the basic assumption that the material properties are not affected by the temperature changes during the measurement process. That means that in the experiments, properties of the specimen must be assumed as constant values. $5-10\,^{\circ}C$ is generally an accepted maximum temperature transient in the experiments. Therefore, the different values of heat source are adopted corresponding to the different thermal conductivities in numerical calculations here in order to realize the appropriate temperature transient, as shown in Table 2.

Considering that the measurement process is usually accomplished in still air, the natural convection heat transfer occurs

Table 1 A summary of the discretized implicit differential equations

The nodes	Discretized equations
Interior nodes in the sample (1)	$T_{i,j}^{p+1} = T_{i,j}^{p} - 2(\mathrm{Fo}_{\Delta 1} + \mathrm{Fo}_{\Delta 2})T_{i,j}^{p+1} + \mathrm{Fo}_{\Delta 1}(T_{i-1,j}^{p+1} + T_{i+1,j}^{p+1}) + \mathrm{Fo}_{\Delta 2}(T_{i,j-1}^{p+1} + T_{i,j+1}^{p+1})$
Interior nodes in the strip (2)	$T_{i,j}^{p+1} = T_{i,j}^{p} - 2(\mathrm{Fo}_{\Delta 3} + \mathrm{Fo}_{\Delta 4})T_{i,j}^{p+1} + \mathrm{Fo}_{\Delta 3}(T_{i-1,j}^{p+1} + T_{i+1,j}^{p+1}) + \mathrm{Fo}_{\Delta 4}(T_{i,j-1}^{p+1} + T_{i,j+1}^{p+1}) + \dot{\phi}\Delta t/\rho_1 c_{p1}$
Boundary nodes (3)	$T_{i,j}^{p+1} = T_{i,j}^{p} - 2[\mathrm{Fo}_{\Delta 1} + \mathrm{Fo}_{\Delta 2} + \mathrm{Fo}_{\Delta 2}\cdot\mathrm{Bi}_{\Delta 2}]T_{i,j}^{p+1} + \mathrm{Fo}_{\Delta 1}(T_{i-1,j}^{p+1} + T_{i+1,j}^{p+1}) + 2\mathrm{Fo}_{\Delta 2}T_{i,j-1}^{p+1} + 2\mathrm{Fo}_{\Delta 2}\cdot\mathrm{Bi}_{\Delta 2}T_0$
Boundary nodes (4)	$T_{i,j}^{p+1} = T_{i,j}^{p} - 2[\mathrm{Fo}_{\Delta 1}(1+\mathrm{Bi}_{\Delta 1}) + \mathrm{Fo}_{\Delta 2}(1+\mathrm{Bi}_{\Delta 2})]T_{i,j}^{p+1} + 2\mathrm{Fo}_{\Delta 1}T_{i-1,j}^{p+1} + 2\mathrm{Fo}_{\Delta 2}T_{i,j-1}^{p+1} + 2(\mathrm{Fo}_{\Delta 1}\cdot\mathrm{Bi}_{\Delta 1} + \mathrm{Fo}_{\Delta 2}\cdot\mathrm{Bi}_{\Delta 2})T_0$
Boundary nodes (5)	$T_{i,j}^{p+1} = T_{i,j}^{p} - 2[\mathrm{Fo}_{\Delta 1}(1+\mathrm{Bi}_{\Delta 1}) + \mathrm{Fo}_{\Delta 2}]T_{i,j}^{p+1} + 2\mathrm{Fo}_{\Delta 1}T_{i-1,j}^{p+1} + \mathrm{Fo}_{\Delta 2}(T_{i,j-1}^{p+1} + T_{i,j+1}^{p+1}) + 2\mathrm{Fo}_{\Delta 1}\cdot\mathrm{Bi}_{\Delta 1}T_0$
The contact nodes (6)	$T_{i,j}^{p+1} = T_{i,j}^{p} - 2(k+k_1)(F_5+F_6)T_{i,j}^{p+1} + (k+k_1)F_5(T_{i-1,j}^{p+1} + T_{i+1,j}^{p+1}) + 2F_6(k_1T_{i,j-1}^{p+1} + kT_{i,j+1}^{p+1}) + \dot{\phi}F_5\Delta x^2$
The contact nodes (7)	$T_{i,j}^{p+1} = T_{i,j}^{p} - 2(3k+k_1)(F_7+F_8)T_{i,j}^{p+1} + \dot{\phi}F_7\Delta x^2 + 2F_7[(k+k_1)T_{i-1,j}^{p+1} + 2kT_{i+1,j}^{p+1}] + 2F_8[(k+k_1)T_{i,j-1}^{p+1} + 2kT_{i,j+1}^{p+1}]$
The contact nodes (8)	$T_{i,j}^{p+1} = T_{i,j}^{p} - 2(k+k_1)(F_5+F_6)T_{i,j}^{p+1} + 2F_5(k_1T_{i-1,j}^{p+1} + kT_{i+1,j}^{p+1}) + \dot{\phi}F_5\Delta x^2 + (k+k_1)F_6(T_{i,j-1}^{p+1} + T_{i,j+1}^{p+1})$

Table 2 The thermal conductivities and the corresponding values of heat source in simulation

k/W/(m K)	0.04	0.1	0.5	1.0	1.5	2.0	5.0
$\dot{\phi}\times10^{-6}$/W/m^3	4.0	4.5	32	72	84.5	112.5	162

there; a value of 10 W/(m^2 K) was assumed for the convection heat transfer coefficient at all the external surface of the measured samples. The initial temperature of the test material (T_0) was set to be equal to the ambient temperature (T_a), and the value of 20°C was adopted. The heat capacity of the test material ρc_p was set as a fixed value of 5×10^5 J/(m^3 K) for all the numerical calculations with thermal conductivities varying from 0.04 W/(m K) up to 5 W/(m K).

Figure 5 shows the typical numerically calculated temperature transients at the surface of the strip that coincides with the measuring point (point M in Fig. 1) in the hypothetical experimental setup for different values of the material thermal conductivities and different sample dimensions. Actually, the temperature rise is shown as the dimensionless normalized excess temperature at the measuring point versus time

$$\theta_m = \frac{T_m - T_0}{T_a} \tag{9}$$

where T_m is the temperature at M point in Fig. 1, T_0 is the initial temperature of the system, and T_a is the ambient temperature.

A relative long time interval of about 0–800 s has been adopted to complete the calculation in order to emphasize the effect of the finite dimensions of the sample. It can be shown in Fig. 5 that at some time point, the convection heat transfer out of the external surfaces of the samples start affecting the assumption that the temperature rise on the surfaces of the strip follows the linear relationship of Eq. (4). Actually this time point can be valued by the thermal penetration depth definition [13,14]

$$\Delta p = 2\sqrt{at_{\max}} \tag{10}$$

represents the minimum distance from any part of the heating area of the sensor to the lateral boundary of the sample, i.e., the available probing depth. Therefore, $t_{\max}$ is considered as the maximum time that the temperature rise on the surface of the strip follows the linear relationship of Eq. (4). It can be shown that this convection heat transfer forces the temperature transient from this time point to rise more rapidly than before, which surely is not predicted by the theoretical THS model given by Eq. (4). This effect can be clearly seen for the results with the higher thermal conductivity (or thermal diffusivity) values and the smaller sample dimensions. It is because that the natural convection heat transfer value of 10 W/(m^2 K) out of the external surfaces of the test samples is a very low heat transfer value. The heat transfer intensity by natural convection is lower than the value by conduction in the sample. It makes the test sample have an insulation surrounding, and this insulation effect is more evident for the results with the relative big thermal conductivity values when the test samples have the same dimensions.

If the upper limit of the fitting time interval for thermal conductivity determination exceeds this $t_{\max}$ in real experimental measurement, it means that the thermal conductivity determination will be affected by the heat losses out of the external surfaces of the sample. This effect is valued through the numerical calculation in this paper, as summarized in Fig. 6 and Table 3. In Table 3, $k_{\exp}$ denote the thermal conductivities obtained by applying Eq. (1) and numerically generated temperature transients at the surface of the strip, and k_{num} denote the thermal conductivities that have been set in the computer simulations, and which can be regarded as the exact values. The results show (Fig. 6) that the

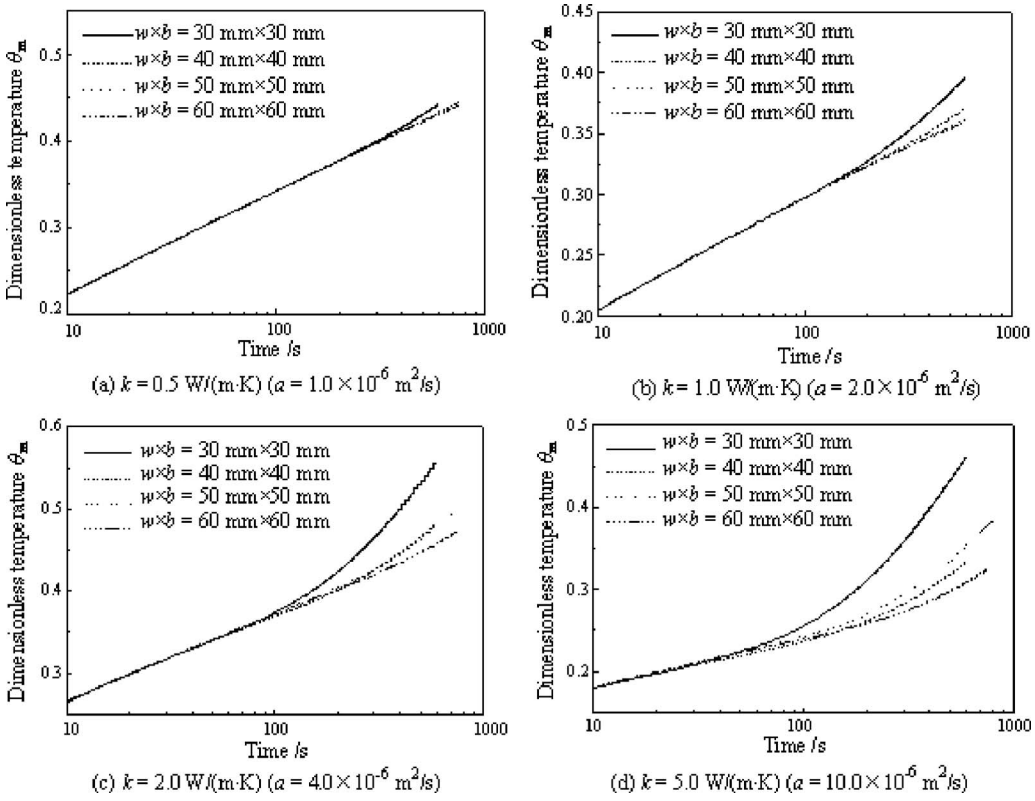

Fig. 5 Temperature transients at the surface of the strip with difference sample dimensions

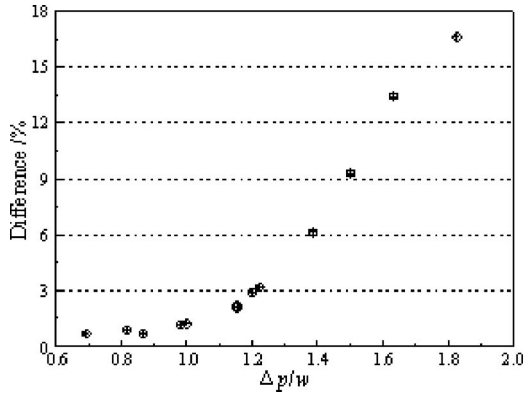

Fig. 6 Effect of finite dimensions of the samples on thermal conductivity determination

finite dimensions of the sample have a great effect on thermal conductivity determination if the penetration depth exceeds the width of the sample. The measurement error will rise rapidly with the penetration depth departing from the sample width. It must be sure that the ratio of Δp versus the minimum distance from the strip to the lateral boundary of the sample is less than 1.2 in order to guarantee that the measurement uncertainty is less than 3% due to the finite dimensions effect of the samples.

If a fixed time interval is used to determine the thermal conductivity of the sample, it should employ bigger sample dimensions in experimental arrangement for the samples with bigger thermal diffusivities in order to insure the measurement precision. As both the sample dimensions and the heating power to the strip cannot possibly augment unlimitedly, the THS method is more adapt to measure the samples with relatively low thermal diffusivities. An important information can also be seen (Table 3) that it always makes the estimated thermal conductivity lower than the exact value if the penetration depth exceed the sample width because the lower convection heat transfer out of the external surface of the sample forces the temperature transient at the strip surface to rise more rapidly from the given t_{max}. The fitting time intervals should be carefully selected in real experimental measurement with the THS method. The short time interval makes the range of linear relationship of the temperature transient versus logarithm of time that is small, which may cause any measurement error in the actual experiment, and a long time interval also causes great measurement error, for the penetration depth may exceed the minimum distance from strip to the lateral boundary of the sample.

In order to evaluate the effect of the nonzero heat capacity of the strip on thermal conductivity determination, the temperature transients at the strip surface with different strip heat capacity are also calculated, as shown in Fig. 7. It is shown that the strip heat capacity has a great effect on the temperature transients at the initial stage, especially on the materials with low thermal diffusivities. With the material thermal diffusivity increases, these effects are weakening. The detailed results of the nonzero heat capacity of the strip on thermal conductivity determinations are shown in Fig. 8. It is shown that the measurement error increases with the increases of the strip heat capacity, and this error can be lowered by adjusting the fitting time intervals for thermal conductivity estimation in some degree. The measurement error increases evidently with the decrease in the material thermal diffusivity. Therefore, the THS method is not recommended to determine the thermal conductivities of the materials with very low thermal diffusivities.

According to the theory of the THS method, the thickness of the strip must be thin enough to guarantee the temperatures at the center, and the surfaces of the strip are in the same value. The actual thickness of the strip may also affect the thermal conductivity determination just like the effect of the nonzero heat capacity of the strip. This is also examined through numerical calculations by employing different thicknesses of the strip, as shown in

Table 3 Effects of the heat losses out of the external surfaces of the samples on thermal conductivity determination with difference sample dimensions ($\rho_1 c_{p1}=0$, $t=20-300$ s)

		30×30 mm^2($w\times b$)		40×40 mm^2($w\times b$)		50×50 mm^2($w\times b$)		60×60 mm^2($w\times b$)	
k_{num} (W/(m K))	Δp (mm)	k_{exp} (W/(m K))	Difference (%)	k_{exp} (W/(m K))	Difference (%)	k_{exp} (W/(m K))	Difference (%)	k_{exp} (W/(m K))	Difference (%)
0.04	9.798	0.04011	0.267	0.03997	0.066	0.04018	0.452	0.04017	0.425
0.1	15.49	0.10109	1.090	0.09935	0.65	0.10097	0.9697	0.10042	0.421
0.5	34.64	0.48916	2.167	0.4974	0.52	0.49653	0.694	0.49732	0.536
1.0	48.99	0.86578	13.42	0.9682	3.179	0.98825	1.174	0.9913	0.871
1.5	60.00	1.0846	27.69	1.3607	9.28	1.4569	2.874	1.4817	1.216
2.0	69.28	1.2067	39.66	1.6523	17.38	1.87736	6.132	1.9583	2.083
5.0	109.54	1.4261	71.47	2.3725	52.55	3.392	32.15	4.2691	14.61

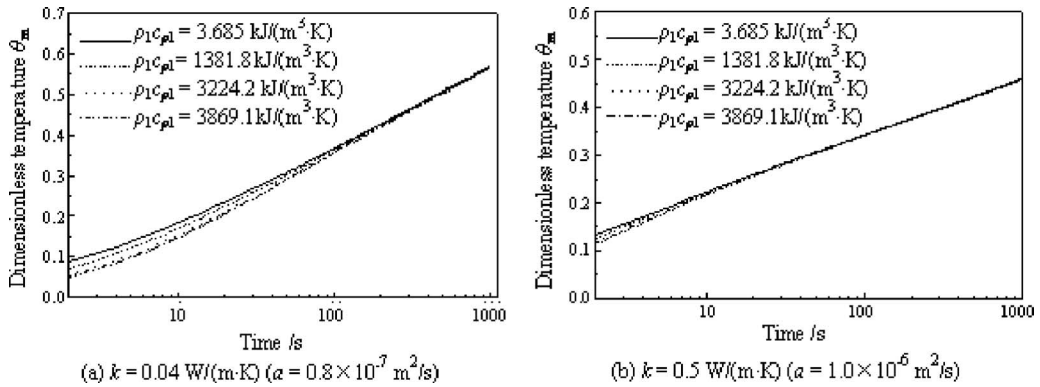

(a) $k = 0.04$ W/(m·K) ($a = 0.8\times10^{-7}$ m^2/s) (b) $k = 0.5$ W/(m·K) ($a = 1.0\times10^{-6}$ m^2/s)

Fig. 7 Temperature transients at the surface of the strip with difference heat capacities of the strip

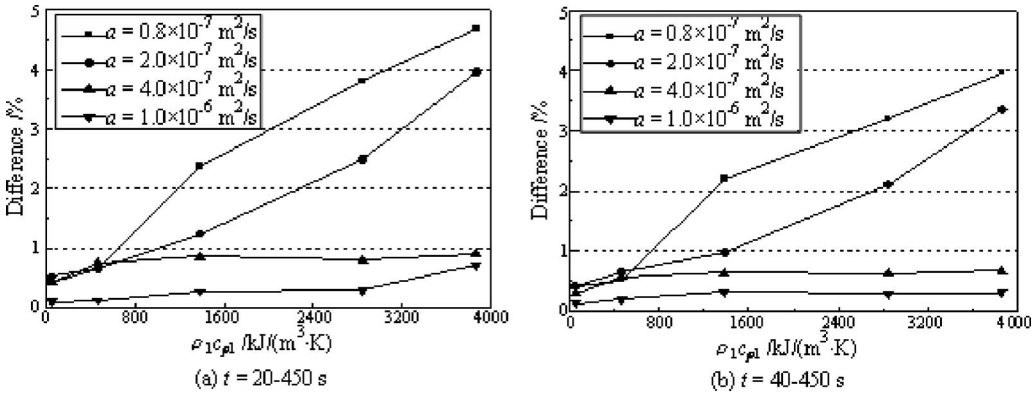

Fig. 8 Effect of the nonzero heat capacity of the strip on thermal conductivity determination

Fig. 9. It is shown that the measurement error decreases with the decrease in the strip thickness, and decreases with the increase in the thermal diffusivity of the material.

6 Conclusions

In this paper, temperature transients in a finite system composed of the samples and the strip is numerically simulated, and the temperature transients at the strip surface are used to calculate the material thermal conductivities with the same procedure that is used in the THS method. The theoretical model that is used in the THS method assumes that the strip has a zero heat capacity, and the sample behaves as an infinite medium. The finite dimensions and the nonzero heat capacity of the strip in the actual experiment are therefore a source of potential errors in thermal conductivity determinations, since both the heat losses out of the external surfaces and the nonzero heat capacity can alter the temperature profile within the system. Through simulation, the effects of the finite dimensions of the sample and the nonzero heat capacity of the strip on thermal conductivity determination are discussed comprehensively. It is shown that the sample dimensions have a great effect on thermal conductivity determination, especially on the materials with relatively higher thermal diffusivities, and the measured thermal conductivity is always lower than the real one due to the lower convective heat transfer coefficient out of the external surfaces of the sample. The measurement error is estimated to be less than 2.1% for the material with thermal diffusivity less than 4.0×10^{-6} m^2/s with the sample dimensions of 120×60 mm^2 (width $\times$ thickness) and the fitting time interval of 20–300 s. The nonzero heat capacity of the strip has a great effect on thermal conductivity determinations for the materials with relatively lower thermal diffusivities. The measurement error is estimated to be less than 5% for the materials with thermal diffusivities larger than 0.8×10^{-7} m^2/s with Cr20Ni80 alloy as the strip.

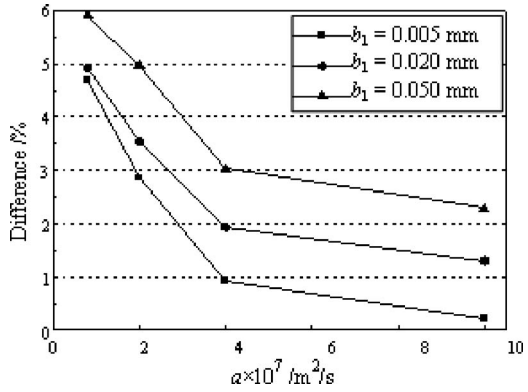

Fig. 9 Effect of the strip thickness on thermal conductivity determination with $\rho_1 c_{p1}=3.87\times10^3$ kJ/(m^3 K)

Acknowledgment

This research was financially supported by the National Natural Science Foundation of China (Grant No. 50806021), National Basic Research Program of China (Grant No. 2009CB219804), and the Program for Changjiang Scholars and Innovative Research Team in University (Grant No. PCSIRT0720).

Nomenclature

- a = thermal diffusivity (m^2/s)
- Bi = Biot number
- b = thickness (mm)
- c = specific heat (J/(kg K))
- d = width (mm)
- Fo = Fourier number
- h = convective heat transfer coefficient ($W/(m^2 K)$)
- I = current (A)
- k = thermal conductivity (W/(m K))
- P = power (W/m)
- q = heat flux (W/m^2)
- T = temperature (K)
- t = time (s)
- U = voltage (V)
- w = width (mm)
- ρ = density (kg/m^3)
- υ = thickness (mm)
- τ = dimensionless time
- γ = constant
- $\dot{\phi}$ = heat source (W/m^3)

Subscripts

- 0 = initial
- a = air
- exp = experimental
- num = numerical
- p = pressure

References

[1] Gustafsson, S. E., Karawacki, E., and Khan, M. N., 1979, "Transient-Hot-Stripe Method for Simultaneously Measuring Thermal Conductivity and Thermal Diffusivity of Solids and Fluids," J. Phys. D, **12**(9), pp. 1411–1421.

[2] Gustafsson, S. E., Karawacki, E., and Chohan, M. A., 1986, "Thermal Transport Studies of Electrically Conducting Materials Using the Transient Hot-Stripe Technique," J. Phys. D, **19**(5), pp. 727–735.

[3] Singh, R., Saxena, N. S., and Chaudhary, D. R., 1985, "Simultaneous Measurement of Thermal Conductivity and Thermal Diffusivity of Some Building Materials Using the Transient Hot Strip Method," J. Phys. D, **18**(1), pp. 1–8.

[4] Saxena, N. S., Gustafsson, S. E., Chohan, M. A., and Maqsood, A., 1989, "Temperature Dependence of Thermal Conductivities and Thermal Diffusivities of Composites Using Transient Hot-Strip Method," Int. J. Energy Res., **13**(4), pp. 411–417.
[5] Groß, U., Song, Y. W., and Hahne, E., 1992, "Measurements of Liquid Thermal Conductivity and Diffusivity by the Transient Hot-Strip Method," Fluid Phase Equilib., **76**(2), pp. 273–282.
[6] Log, T., 1993, "Transient Hot-Strip (THS) Method for Measuring Thermal Conductivity of Thermally Insulating Materials," Fire Mater., **17**(3), pp. 131–138.
[7] Jannot, Y., and Meukam, P., 2004, "Simplified Estimation Method for the Determination of the Thermal Effusivity and Thermal Conductivity Using a Low Cost Hot Strip," Meas. Sci. Technol., **15**, pp. 1932–1938.
[8] Yu, F., and Zhang, X. X., 2005, "Experimental Investigation on the Thermal Conductivity Measurement of Materials With Hot-Strip Method," Acta Metrologia Sinica, **26**(1), pp. 27–29 (in Chinese).
[9] Wei, G. S., Zhang, X. X., and Yu, F., 2008, "Thermal Conductivity Measurements on Xonotlite-Type Calcium Silicate by the Transient Hot-Strip Method," J. Chin. Univ. Sci. Technol., **15**(6), pp. 791–795.
[10] Hammerschmidt, U., and Sabuga, W., 2000, "Transient Hot Strip (THS) Method: Uncertainty Assessment," Int. J. Thermophys., **21**(1), pp. 217–248.
[11] Hammerschmidt, U., and Sabuga, W., 2000, "Transient Hot Wire (THW) Method: Uncertainty Assessment," Int. J. Thermophys., **21**(6), pp. 1255–1278.
[12] Labudová, G., and Vozárová, V., 2002, "Uncertainty of the Thermal Conductivity Measurement Using the Transient Hot Wire Method," J. Therm Anal. Calorim., **67**(1), pp. 257–265.
[13] Gustavsson, M., Wang, H., Trejo, R. M., Lara-Curzio, E., Dinwiddie, R. B., and Gustafsson, S. E., 2006, "On the Use of the Transient Hot-Strip Method for Measuring the Thermal Conductivity of High-Conducting Thin Bars," Int. J. Thermophys., **27**(6), pp. 1816–1825.
[14] Gustavsson, M., Nagai, H., and Okutani, T., 2007, "Characterization of Anisotropic and Irregularly-Shaped Materials by High-Sensitive Thermal Conductivity Measurements," Solid State Phenom., **124–126**(2), pp. 1641–1644.

Analytical Solutions for Anisotropic Heat Conduction Problems in a Trimaterial With Heat Sources

Ming-Ho Shen[1]
Department of Automation Engineering,
Nan Kai University of Technology,
568 Chung Cheng Road, Tsao Tun,
Nantou County 542, Taiwan
e-mail: mhshen@nkut.edu.tw

Fu-Mo Chen
Department of Mechanical Engineering,
Nan Kai University of Technology,
568 Chung Cheng Road, Tsao Tun,
Nantou County 542, Taiwan

Shih-Yu Hung
Department of Automation Engineering,
Nan Kai University of Technology,
568 Chung Cheng Road, Tsao Tun,
Nantou County 542, Taiwan

In this work, the analytical solution of a fundamental problem of heat conduction in anisotropic medium is derived. The steady-state temperature field in an anisotropic trimaterial subject to an arbitrary heat source is analyzed. "Trimaterial" denotes an infinite body composed of three dissimilar materials bonded along two parallel interfaces. The method of analytical continuation is applied across the two parallel interfaces in order to derive the trimaterial solution in a series form from the corresponding homogeneous solution. A variety of problems, e.g., bimaterial, a finite thin film on a semi-infinite substrate, and a finite strip, can be analyzed as special cases of the present study. The numerical results of the temperature distributions for some practical examples are provided in graphic form and discussed in details. [DOI: 10.1115/1.4001613]

Keywords: heat conduction, anisotropic trimaterial, analytical continuation

1 Introduction

The ever-growing application of composite materials in engineering practice has motivated the development of the science and engineering of heat conduction in anisotropic media since the middle of this century. This fact was manifested in that a number of standard monographs [1,2] devoted a considerable portion of their contents to the treatment of conduction of heat in anisotropic bodies. Due to the mathematical difficulties, investigations on heat conduction problems in anisotropic media still, indeed, remain extremely scarce in the open literature, to date.

In recent decades, many analytical works were presented to deal with relevant anisotropic heat conduction problems. Tauchert and Akoz [3] used complex conjugate quantities to solve the thermal field in a two-dimensional anisotropic slab. Mulholland and Gupta [4] investigated a three-dimensional anisotropic body by using coordinate transformations to principal axes. Chang [5] solved the heat conduction problem in a three-dimensional configuration by conventional Fourier transformation. By a transformation of anisotropic problems to orthotropic ones, Poon [6] first investigated the anisotropic temperature field in layered composites. Thereafter, Poon et al. [7] treated the anisotropic heat conduction problem by further extending the transformation, such that the mapped domain is governed by isotropic heat conduction. Zhang [8] developed a partition-matching technique to solve a two-dimensional anisotropic strip with prescribed temperature on the boundary.

In earlier papers, analytical solutions of anisotropic heat conduction problems have been limited to simple or special cases [9]. In conventional studies of a multidimensional anisotropic medium subjected to distribute temperature or heat flux in or on the media, the analytical solution was obtained by Fourier transformation. It is not possible to find in most cases the general solutions with respect to each of the spatial variables to satisfy partial differential equations of anisotropic heat conduction equations and boundary conditions. The work of Yan et al. [10] studied two layered isotropic bodies with homogeneous form of the conduction equation, and the Green's function solution was used to incorporate the effects of the internal heat source and nonhomogeneous boundary conditions. They obtained the series solutions for three-dimensional temperature distribution by Fourier transformation, Laplace transformation, and eigenvalue methods. Yang and Shi [11] established a new stability test for heat conduction in one-dimensional multilayer composite solids that have internal heat generation at a rate proportional to the interior temperature. Jain et al. [12] presented an analytical double-series solution for the time-dependent asymmetric heat conduction in a multilayer annulus. Shiah et al. [13] applied the direct domain-mapping technique in the boundary element method (BEM) to investigate the heat conduction in composites consisting of multiple anisotropic media with embedded point heat sources.

Consequently, it is more difficult to get general analytical solutions satisfying all the boundary conditions for a multilayered anisotropic heat conduction problem because of the continuity of temperature and heat flux on the interfaces. Due to the mathematical difficulties of the problem, only a few solutions for heat conduction in anisotropic media have appeared in the literature, and much more work remains to be done. By using a linear coordinate transformation method in conjunction with the Fourier transform and the series expansion technique, Hsieh and Ma [14] and Ma and Chang [15] respectively investigated the heat conduction problem of a thin-layer anisotropic media and a multilayered anisotropic media recently. They solved the steady-state temperature and heat flux fields for the case when point heat sources or prescribed temperature are located on the surface of the layered media. To the best of our knowledge, the heat conduction problem of a three-layered anisotropic medium with arbitrary point heat sources seems not to have been solved analytically. In this study, we employ the complex variables and the method of analytical continuation, instead of the complicated integral transform, to solve the conduction problem in a trimaterial anisotropic medium. Explicit analytical solutions for the temperature and heat flux are expressed in a series form. Numerical results of the full field temperature distribution for concentrated heat sources in the composite system are presented in graphic form and discussed in detail.

[1]Corresponding author.

Contributed by the Heat Transfer Division of ASME for publication in the JOURNAL OF HEAT TRANSFER. Manuscript received July 1, 2009; final manuscript received March 4, 2010; published online June 28, 2010. Editor: Yogesh Jaluria.

2 Basic Equations

In a fixed rectangular coordinates system (x_1,x_2,x_3), the governing equations for stationary heat conduction problems can be written as

$$q_i = -k_{ij}T_j \tag{1}$$

$$q_{i,i} = 0 \tag{2}$$

In the above equations, the repeated indices mean summation, and a comma stands for partial differentiation, q_i, T, and $k_{ij}=k_{ji}$ are the corresponding heat flux, temperature, and heat conduction coefficients, respectively.

When the temperature state of the body is independent of the x_3-coordinate, the governing equations (1) and (2) become

$$k_{11}\frac{\partial T^2}{\partial x_1^2} + 2k_{12}\frac{\partial T^2}{\partial x_1\,\partial x_2} + k_{22}\frac{\partial T^2}{\partial x_2^2} = 0 \tag{3}$$

For the temperature function, we assume

$$T(x_1,x_2) = \theta(x_1 + px_2)$$

This form will give a solution to Eq. (3) if p satisfies the equation

$$k_{22}p^2 + 2k_{12}p + k_{11} = 0 \tag{4}$$

Since the quadratic form k_{ij}, q_i, and q_j are positive-definite [1,16], the two roots of Eq. (4) are complex conjugate. The root with the positive imaginary part will be denoted by p_t with complex conjugate $\overline{p_t}$

$$p_t = -\frac{k_{12}}{k_{22}} + i\frac{k_t}{k_{22}}, \quad k_t = \sqrt{k_{11}k_{22} - k_{12}^2} > 0 \tag{5}$$

Hence, a general form for the temperature function may be written as

$$T(x_1,x_2) = \theta(z_t) + \overline{\theta}(\overline{z_t}) = 2\,\mathrm{Re}[\theta(z_t)], \quad z_t = x_1 + p_t x_2 \tag{6}$$

Substitution of Eq. (6) into Eq. (1) leads to

$$q_i = -2\,\mathrm{Re}[(k_{i1} + p_t k_{i2})\theta'(z_t)] \tag{7}$$

The resultant heat flow Q passing an open curve AB is given by

$$Q = \int_A^B q_n ds = \int_A^B q_1 dx_2 - q_2 dx_1 \tag{8}$$

where s is the arc length measured along AB, and q_n is referred to as the heat flux in the direction normal to s. By substituting Eq. (7) into Eq. (8), we have

$$Q = 2\,\mathrm{Re}[ik_t\theta(z_t)]_A^B \tag{9}$$

In Eq. (9), point A is assumed to be fixed at all times, point B is permitted to move, and its coordinate is denoted by z_t. Under these assumptions, Eq. (9) provides

$$Q = 2\,\mathrm{Re}[ik_t\theta(z_t)] \tag{10}$$

where an arbitrary constant in the right side of the above equation has been absorbed into $\theta(z_t)$, since this does not affect the heat flow.

3 A Singularity in a Homogeneous Medium

In this section, we describe the temperature function $\theta_0(z_t)$ for a homogeneous infinite medium subjected to a heat source q_0 and a temperature dislocation of discontinuity T_0 at an arbitrary point $z_0=x_{10}+ix_{20}$; in this case, the temperature function takes the form [17]

$$\theta_0(z_t) = q_t \log(z_t - z_{t0}) \tag{11}$$

where $z_{t0}=x_{10}+p_t x_{20}$, q_t is a constant to be determined from the single valued conditions of temperature and the equilibrium condition of energy when z moves a closed contour c around the point z_0. From Eqs. (6) and (10), these condition are written as

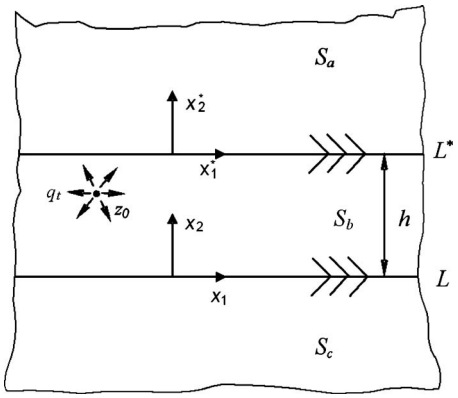

Fig. 1 A trimaterial with a singularity located in S_b

$$2\oint_c \mathrm{Re}[\theta_0'(z_t)]dz_t = T_0 \tag{12}$$

$$2\oint_c \mathrm{Re}[ik_t\theta_0'(z_t)]dz_t = q_0 \tag{13}$$

From the above conditions, it is found that

$$q_t = -\frac{q_0}{4\pi k_t} - i\frac{T_0}{4\pi} \tag{14}$$

4 A Singularity in a Trimaterial

4.1 A Singularity Located in S_b . Considering a trimaterial with a singularity located in S_b, as shown in Fig. 1, we assume the temperature function as

$$\begin{aligned}
\theta_a(z_t) &= \theta_{aa}(z_t); \quad z_t \in S_a \\
\theta_b(z_t) &= \theta_0(z_t) + \theta_{ba}(z_t) + \theta_{bc}(z_t); \quad z_t \in S_b \\
\theta_c(z_t) &= \theta_{cc}(z_t); \quad z_t \in S_c
\end{aligned} \tag{15}$$

where $\theta_{aa}(z_t)$ and $\theta_{ba}(z_t)$, $\theta_{bc}(z_t)$ are introduced to satisfy the continuity condition across L^*, $\theta_{cc}(z_t)$ and $\theta_{ba}(z_t)$, $\theta_{bc}(z_t)$ are introduced to satisfy the continuity condition across L. It should be noticed that $\theta_{aa}(z_t)$, $\theta_{ba}(z_t)$, $\theta_{bc}(z_t)$, and $\theta_{cc}(z_t)$ are holomorphic in the regions $z_t \in S_a$, $z_t \in S_a+S_b$, $z_t \in S_b+S_c$, and $z_t \in S_c$, respectively, and $\theta_0(z_t)$ is related to the homogeneous solution.

Along the bonded interface L, the temperature and the heat flow should be continuous that

$$\mathrm{Re}[\theta_0(\sigma) + \theta_{ba}(\sigma) + \theta_{bc}(\sigma)] = \mathrm{Re}[\theta_{cc}(\sigma)] \quad \sigma \in L \tag{16}$$

$$\mathrm{Re}[ik_{tb}\theta_0(\sigma) + ik_{tb}\theta_{ba}(\sigma) + ik_{tb}\theta_{bc}(\sigma)] = \mathrm{Re}[ik_{tc}\theta_{cc}(\sigma)] \quad \sigma \in L \tag{17}$$

By the analytical continuation method, we have

$$\theta_{bc}(z_t) + \overline{\theta_{ba}}(z_t) + \theta_0(z_t) - \theta_{cc}(z_t) = 0 \tag{18}$$

$$k_{tb}\theta_{bc}(z_t) - k_{tb}\overline{\theta_{ba}}(z_t) + k_{tb}\theta_0(z_t) - k_{tc}\theta_{cc}(z_t) = 0 \tag{19}$$

Solve the above equations to yield

$$\theta_{ba}(z_t) = \beta_{cb}\overline{\theta_0}(z_t) + \beta_{cb}\overline{\theta_{bc}}(z_t) \tag{20}$$

$$\theta_{cc}(z_t) = \alpha_{cb}\theta_0(z_t) + \alpha_{cb}\theta_{bc}(z_t) \tag{21}$$

where

$$\alpha_{cb} = \frac{2k_{tb}}{k_{tb} + k_{tc}}, \quad \beta_{cb} = \frac{k_{tb} - k_{tc}}{k_{tb} + k_{tc}} \tag{22}$$

The temperature and heat flow continuity across the interface L^* should be continuous that

$$\mathrm{Re}[\theta_a(\sigma)] = \mathrm{Re}[\theta_0(\sigma) + \theta_{ba}(\sigma) + \theta_{bc}(\sigma)] \quad \sigma \in L^* \tag{23}$$

$$\mathrm{Re}[ik_{ta}\theta_a(\sigma)] = \mathrm{Re}[ik_{tb}\theta_0(\sigma) + ik_{tb}\theta_{ba}(\sigma) + ik_{tb}\theta_{bc}(\sigma)] \quad \sigma \in L^* \tag{24}$$

Since the temperature function is independent on the coordinate system, with a coordinate translation $z_t^* = z_t - p_t h$ (see Fig. 1), it is easy to show that the function $\theta(z_t)$ in the z_t coordinate system is related to the function $\theta^*(z_t^*)$ in the z_t^* coordinate system by

$$\theta^*(z_t^*) = \theta(z_t) = \theta(z_t^* + p_t h)$$
$$\overline{\theta^*}(z_t^*) = \overline{\theta}(z_t - p_t h + \overline{p_t} h) \tag{25}$$

Let us solve the boundary conditions (23) and (24) in the z_t^* coordinate system. By the analytical continuation method, we have

$$\theta_a^*(z_t^*) - \theta_{ba}^*(z_t^*) - \overline{\theta_{bc}^*}(z_t^*) - \theta_0^*(z_t^*) = 0 \tag{26}$$

$$k_{ta}\theta_{aa}^*(z_t^*) - k_{tb}\theta_{ba}^*(z_t^*) + k_{tb}\overline{\theta_{bc}^*}(z_t^*) - k_{tb}\theta_0^*(z_t^*) = 0 \tag{27}$$

Solve the above equations to yield

$$\theta_{aa}^*(z_t^*) = \alpha_{ab}\theta_{ba}^*(z_t^*) + \alpha_{ab}\theta_0^*(z_t^*) \tag{28}$$

$$\theta_{bc}^*(z_t^*) = \beta_{ab}\overline{\theta_{ba}^*}(z_t^*) + \beta_{ab}\overline{\theta_0^*}(z_t^*) \tag{29}$$

where

$$\alpha_{ab} = \frac{2k_{tb}}{k_{ta} + k_{tb}}, \quad \beta_{ab} = \frac{k_{tb} - k_{ta}}{k_{ta} + k_{tb}} \tag{30}$$

With the coordinate translation (25), Eqs. (28) and (29) lead to

$$\theta_{aa}(z_t) = \alpha_{ab}\theta_0(z_t) + \alpha_{ab}\theta_{ba}(z_t) \tag{31}$$

$$\theta_{bc}(z_t) = \beta_{ab}\overline{\theta_{ba}}(z_t - p_{tb}h + \overline{p}_{ab}h) + \beta_{ab}\overline{\theta_0}(z_t - p_{tb}h + \overline{p}_{tb}h) \tag{32}$$

Decoupling of Eqs. (20), (21), (28), and (29) yields the full field temperature functions

$$\begin{aligned}
\theta_{aa}(z_t) &= \alpha_{ab}\sum_{n=0}^{\infty}(\beta_{cb}\beta_{ab})^n[\theta_0(z_t + (p_{tb} - \overline{p_{tb}})nh) \\
&\quad + \beta_{cb}\overline{\theta_0}(z_t + (p_{tb} - \overline{p_{tb}})nh)] \\
\theta_{ba}(z_t) &= \beta_{cb}\overline{\theta_0}(z_t) + \sum_{n=1}^{\infty}(\beta_{cb}\beta_{ab})^n[\theta_0(z_t + (p_{tb} - \overline{p_{tb}})nh) \\
&\quad + \beta_{cb}\overline{\theta_0}(z_t + (p_{tb} - \overline{p_{tb}})nh)] \\
\theta_{bc}(z_t) &= \beta_{ab}\sum_{n=1}^{\infty}(\beta_{cb}\beta_{ab})^{n-1}[\overline{\theta_0}(z_t - (p_{tb} - \overline{p_{tb}})nh) \\
&\quad + \beta_{cb}\theta_0(z_t - (p_{tb} - \overline{p_{tb}})nh)] \\
\theta_{cc}(z_t) &= \alpha_{cb}\theta_0(z_t) + \alpha_{cb}\beta_{ab}\sum_{n=1}^{\infty}(\beta_{cb}\beta_{ab})^{n-1}[\overline{\theta_0}(z_t - (p_{tb} - \overline{p_{tb}})nh) \\
&\quad + \beta_{cb}\theta_0(z_t - (p_{tb} - \overline{p_{tb}})nh)]
\end{aligned} \tag{33}$$

The convergence rate of the above equation depends on two nondimensional bimaterial constants β_{ab} and β_{cb}. The present series solution converges to the true solution since those bimaterial constants are always less than 1.

For a special case when material b and material c are the same, Eq. (33) reduces to a bimaterial solution

$$\theta_a(z_t) = \alpha_{ab}\theta_0(z_t)$$
$$\theta_b(z_t) = \theta_0(z_t) + \beta_{ba}\overline{\theta_0}(z_t)$$

which is in agreement with Ref. [17].

For another case when $k_{11} = k_{22} = k$, $k_{12} = 0$, in view of Eq. (6), we have $p_t = i$ and $z_t = z = x_1 + ix_2$. Hence, Eq. (33) can be reduced to an isotropic trimaterial solution

$$\begin{aligned}
\theta_a(z) &= \alpha_{ab}\sum_{n=0}^{\infty}(\beta_{cb}\beta_{ab})^n[\theta_0(z + 2inh) + \beta_{cb}\overline{\theta_0}(z + 2inh)] \\
\theta_b(z) &= \theta_0(z) + \beta_{cb}\overline{\theta_0}(z) + \sum_{n=1}^{\infty}(\beta_{cb}\beta_{ab})^n[\theta_0(z + 2inh) \\
&\quad + \beta_{cb}\overline{\theta_0}(z + 2inh)] + \beta_{ab}\sum_{n=1}^{\infty}(\beta_{cb}\beta_{ab})^{n-1}[\overline{\theta_0}(z - 2inh) \\
&\quad + \beta_{cb}\theta_0(z - 2inh)] \\
\theta_c(z) &= \alpha_{cb}\theta_0(z) + \alpha_{cb}\beta_{ab}\sum_{n=1}^{\infty}(\beta_{cb}\beta_{ab})^{n-1}[\overline{\theta_0}(z - 2inh) \\
&\quad + \beta_{cb}\theta_0(z - 2inh)]
\end{aligned}$$

where

$$\theta_0(z) = -\left(\frac{q_0}{4\pi k} + i\frac{T_0}{4\pi}\right)\log(z - z_0)$$

which is in agreement with Chao and Chen [18].

4.2 A Singularity Located in S_c . For singularity located in S_c, as in Eq. (15), the temperature function can be assumed as

$$\begin{aligned}
\theta_a(z_t) &= \theta_{aa}(z_t); \quad z_t \in S_a \\
\theta_b(z_t) &= \theta_{ba}(z_t) + \theta_{bc}(z_t); \quad z_t \in S_b \\
\theta_c(z_t) &= \theta_0(z_t) + \theta_{cc}(z_t); \quad z_t \in S_c
\end{aligned} \tag{34}$$

By the same procedure as in Sec. 4.1, one can find the full field temperature functions

$$\begin{aligned}
\theta_{aa}(z_t) &= \alpha_{ab}\sum_{n=0}^{\infty}(\beta_{cb}\beta_{ab})^n\alpha_{bc}\theta_0(z_t + (p_{tb} - \overline{p_{tb}})nh) \\
\theta_{ba}(z_t) &= \sum_{n=0}^{\infty}(\beta_{cb}\beta_{ab})^n\alpha_{bc}\theta_0(z_t + (p_{tb} - \overline{p_{tb}})nh) \\
\theta_{bc}(z_t) &= \beta_{ab}\sum_{n=1}^{\infty}(\beta_{cb}\beta_{ab})^{n-1}\alpha_{bc}\overline{\theta_0}(z_t - (p_{tb} - \overline{p_{tb}})nh) \\
\theta_{cc}(z_t) &= \beta_{bc}\overline{\theta_0}(z_t) + \alpha_{cb}\beta_{ab}\sum_{n=1}^{\infty}(\beta_{cb}\beta_{ab})^{n-1}\alpha_{bc}\overline{\theta_0}(z_t - (p_{tb} - \overline{p_{tb}})nh)
\end{aligned} \tag{35}$$

where

$$\alpha_{bc} = \frac{2k_{tc}}{k_{tb} + k_{tc}}, \quad \beta_{bc} = \frac{k_{tc} - k_{tb}}{k_{tb} + k_{tc}}$$

Similarly, for the special case when $k_{11} = k_{22} = k$, $k_{12} = 0$, Eq. (35) can be reduced to an isotropic trimaterial solution

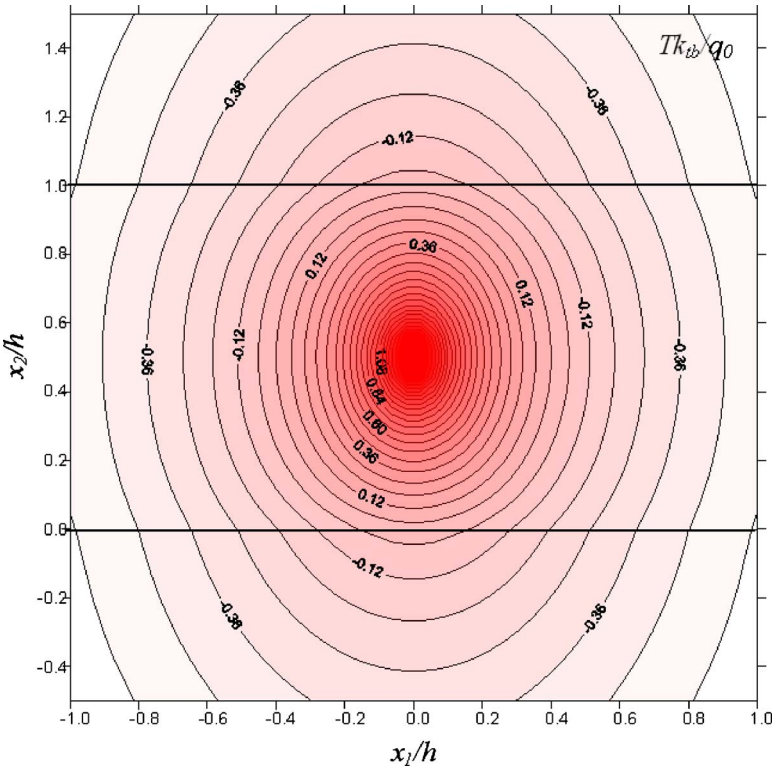

Fig. 2 Temperature distribution in an anisotropic trimaterial for a concentrated heat source applied within the middle layer ($k_{11a}=k_{11c}=2k_{11b}$, $k_{22a}=k_{22c}=4k_{11b}$, $k_{22b}=2k_{11b}$)

$$\theta_a(z) = \alpha_{ab}\sum_{n=0}^{\infty}(\beta_{cb}\beta_{ab})^n\alpha_{bc}\theta_0(z+2inh)$$

$$\theta_{ba}(z) = \sum_{n=0}^{\infty}(\beta_{cb}\beta_{ab})^n\alpha_{bc}\theta_0(z+2inh) + \beta_{ab}\sum_{n=1}^{\infty}(\beta_{cb}\beta_{ab})^{n-1}\alpha_{bc}\overline{\theta_0}(z-2inh)$$

$$\theta_c(z) = \theta_0(z) + \beta_{bc}\overline{\theta_0}(z) + \alpha_{cb}\beta_{ab}\sum_{n=1}^{\infty}(\beta_{cb}\beta_{ab})^{n-1}\alpha_{bc}\overline{\theta_0}(z-2inh)$$

which is in agreement with Chao and Chen [18].

5 Numerical Results and Discussions

By using the analytical solutions derived in the previous sections in conjunction with a personal computer, accurate numerical calculations of the temperature field are obtained.

5.1 A Singularity Located in S_b . Figure 2 shows the full field distributions of temperature in an anisotropic trimaterial for a concentrated heat source applied within the middle layer at $(0, h/2)$. In an anisotropic medium, the symmetry for the temperature field that is found in the isotropic material is distorted due to the material anisotropy. The temperature in the anisotropic medium occur primarily in the x_2-direction owning to the larger thermal conductivity in the direction $k_{22}>k_{11}$. One can also find in Fig. 2 that the distributions of the isothermal contours in the top layer (or bottom layer) are relatively sparse than those in the middle layer since its thermal conductivity is larger than that of the middle layer. In Fig. 3, the distributions of the isothermal contours in the top layer (or bottom layer) are relatively dense than those in the middle layer since its thermal conductivity is smaller than that of the middle layer. Besides, it is shown in the figures that the temperatures in the x_2-direction are continuous across the interface. This also indicates that the convergence and accuracy for the numerical calculation are satisfied.

In the following discussion, we will apply the derived trimaterial solution to investigate a finite strip problem. First, we consider a concentrated heat source applied in a strip under isothermal boundary conditions. One can assume $k_{11a}=k_{22a}=\infty$, $k_{11c}=k_{22c}=\infty$, and $k_{ta}=k_{tc}=\infty$ to simulate this case, and therefore, the temperature function can be obtained just by letting $\alpha_{ab}=0$, $\alpha_{cb}=0$, $\beta_{ab}=-1$, and $\beta_{cb}=-1$ in Eq. (33)

$$\theta_b(z_t) = \theta_0(z_t) - \overline{\theta_0}(z_t) + \sum_{n=1}^{\infty}[\theta_0(z_t+(p_{tb}-\overline{p_{tb}})nh) - \overline{\theta_0}(z_t+(p_{tb}-\overline{p_{tb}})nh)] - \sum_{n=1}^{\infty}[\overline{\theta_0}(z_t-(p_{tb}-\overline{p_{tb}})nh) - \theta_0(z_t-(p_{tb}-\overline{p_{tb}})nh)]$$

Figures 4 and 5 respectively show the distribution of temperature for a finite strip with a concentrated heat source located at $(0, h/2)$ and $(0, h/4)$. As expected, the temperature on the surfaces of the strip is vanished. One can find that the isothermal contours are symmetric about the x_2 axis, but they are not symmetric about the x_2 axis in Fig. 6 due to the existence of k_{12}.

Next, we consider a concentrated heat source applied in a strip under adiabatic boundary conditions. One can assume $k_{11a}=k_{22a}=0$, $k_{11c}=k_{22c}=0$, and $k_{ta}=k_{tc}=0$ to simulate this problem, and therefore the temperature function can be obtained just by letting $\alpha_{ab}=2$, $\alpha_{cb}=2$, $\beta_{ab}=1$, and $\beta_{cb}=1$ in Eq. (33)

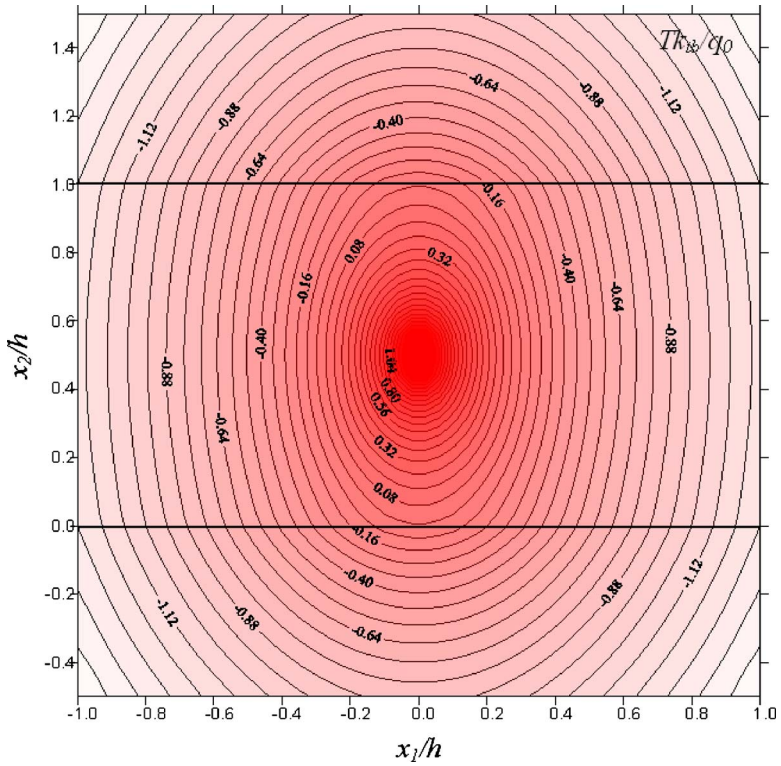

Fig. 3 Temperature distribution in an anisotropic trimaterial for a concentrated heat source applied within the middle layer ($k_{11a}=k_{11c}=0.5k_{11b}$, $k_{22a}=k_{22c}=k_{11b}$, $k_{22}=2k_{11}$)

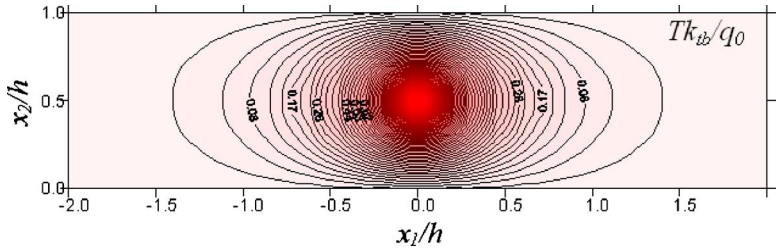

Fig. 4 Temperature distribution for a concentrated heat source applied at (0, $h/2$) of a strip under isothermal boundary conditions ($k_{22b}=k_{11b}$, $k_{12b}=0$)

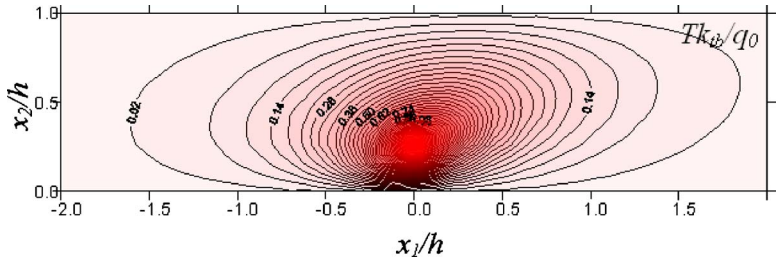

Fig. 5 Temperature distribution for a concentrated heat source applied at (0, $h/4$) of a strip under isothermal boundary conditions ($k_{22b}=0.5k_{11b}$, $k_{12b}=0.25k_{11b}$)

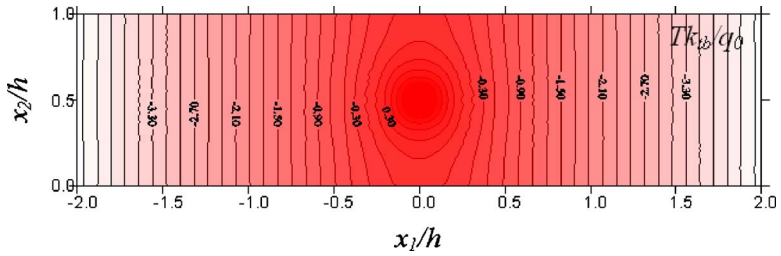

Fig. 6 Temperature distribution for a concentrated heat source applied at (0, $h/2$) of a strip under adiabatic boundary conditions ($k_{22b}=k_{11b}$, $k_{12b}=0$)

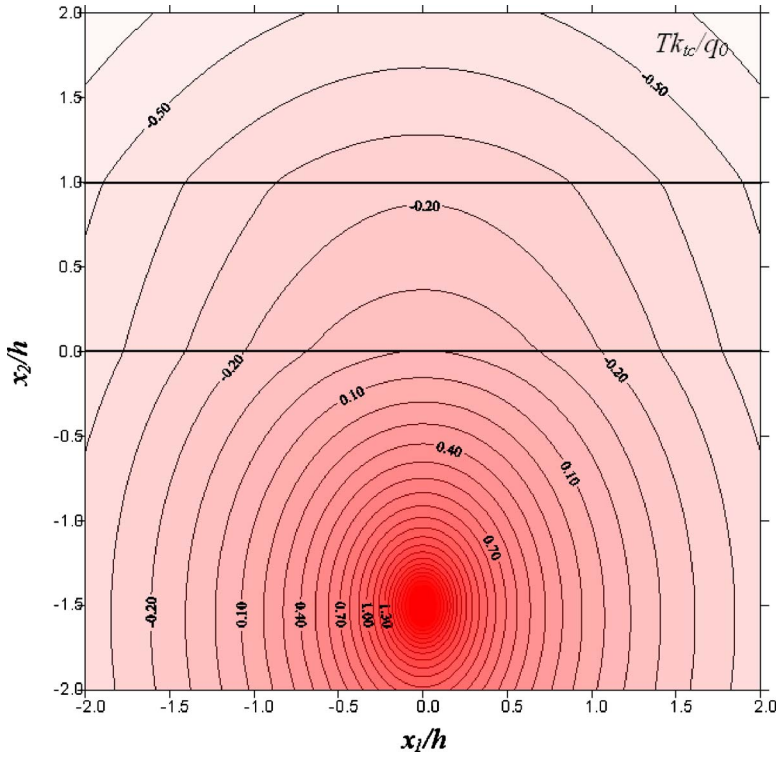

Fig. 7 Temperature distribution in an anisotropic trimaterial for a concentrated heat source applied within the bottom layer ($k_{11a}=k_{11c}$, $k_{11b}=2k_{11c}$, $k_{22a}=k_{22c}=2k_{11c}$, $k_{22b}=4k_{11c}$)

$$\theta_b(z_t) = \theta_0(z_t) + \overline{\theta_0}(z_t) + \sum_{n=1}^{\infty} [\theta_0(z_t + (p_{tb} - \overline{p_{tb}})nh) + \overline{\theta_0}(z_t + (p_{tb} - \overline{p_{tb}})nh)] + \sum_{n=1}^{\infty} [\overline{\theta_0}(z_t - (p_{tb} - \overline{p_{tb}})nh) + \theta_0(z_t - (p_{tb} - \overline{p_{tb}})nh)]$$

Figure 6 shows the distribution of temperature for a finite strip with a concentrated heat source located at $(0, h/2)$. One can find far away from the heat source that the temperature contours are uniform along the x_1 direction and perpendicular to the free surface, which means on the surfaces, the heat flow can just travel in the direction parallel to the surface due to the insulated condition.

5.2 A Singularity Located in S_c . Figures 7 and 8 show the full field distributions of temperature in an anisotropic trimaterial for a concentrated heat source applied within the bottom layer at $(0, -1.5h)$ for different material combinations. One can find in Fig. 7 that the distributions of the isothermal contours in the middle layer are relatively sparse than those in Fig. 8 since the thermal conductivity of the middle layer is larger than that of the neighbor layers. In the figures, the temperatures in the x_2-direction are continuous across the interface, which demonstrates again that the continuity conditions at the interface are indeed satisfied.

In the following discussion, we will apply the derived trimaterial solution to investigate a film-substrate structure problem. First we consider a concentrated heat source applied in a substrate and the surface of the film is isothermal. One can assume $k_{11a}=k_{22a}=\infty$ to simulate this case, and therefore, the temperature function can be obtained just by letting $\alpha_{ab}=0$, $\alpha_{cb}=0$, $\beta_{ab}=-1$, and $\beta_{cb}=-1$ in Eq. (35)

$$\theta_b(z_t) = \sum_{n=0}^{\infty} (-\beta_{cb})^n \alpha_{bc} \theta_0(z_t + (p_{tb} - \overline{p_{tb}})nh) - \sum_{n=1}^{\infty} (-\beta_{cb})^{n-1} \alpha_{bc} \overline{\theta_0}(z_t - (p_{tb} - \overline{p_{tb}})nh)$$

$$\theta_{cc}(z_t) = \theta_0(z_t) + \beta_{bc}\overline{\theta_0}(z_t) - \alpha_{cb}\sum_{n=1}^{\infty} (-\beta_{cb})^{n-1} \alpha_{bc} \overline{\theta_0}(z_t - (p_{tb} - \overline{p_{tb}})nh)$$

Figure 9 shows the full field distributions of temperature in a film-substrate structure with a concentrated heat source applied within the substrate at $(0, -h)$ under isothermal boundary conditions. The results are in agreement with those provided by Hsieh and Ma [14], except the positive direction of the x_2 axis is different.

Similarly, we can assume $k_{11a}=k_{22a}=0$ and $k_{ta}=0$ to simulate the problem of a film-substrate structure under adiabatic condition, of which the temperature function can be obtained just by letting $\alpha_{ab}=2$ and $\beta_{ab}=1$ in Eq. (35)

$$\theta_b(z_t) = \sum_{n=0}^{\infty} (\beta_{cb})^n \alpha_{bc} \theta_0(z_t + (p_{tb} - \overline{p_{tb}})nh) + \sum_{n=1}^{\infty} (\beta_{cb})^{n-1} \alpha_{bc} \overline{\theta_0}(z_t - (p_{tb} - \overline{p_{tb}})nh)$$

$$\theta_{cc}(z_t) = \theta_0(z_t) + \beta_{bc}\overline{\theta_0}(z_t) + \alpha_{cb}\sum_{n=1}^{\infty} (\beta_{cb})^{n-1} \alpha_{bc} \overline{\theta_0}(z_t - (p_{tb} - \overline{p_{tb}})nh)$$

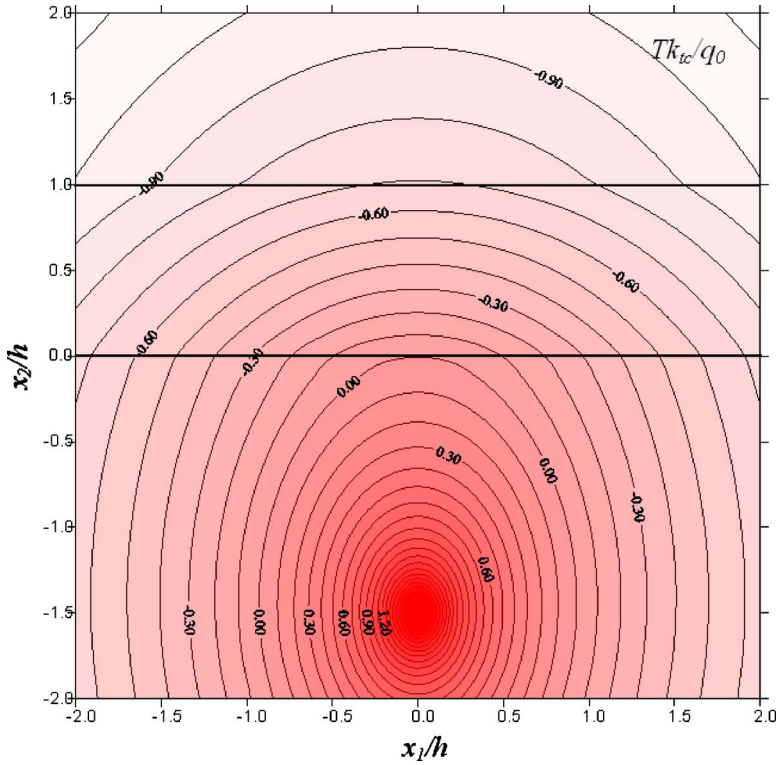

Fig. 8 Temperature distribution in an anisotropic trimaterial for a concentrated heat source applied within the bottom layer ($k_{11a}=k_{11c}$, $k_{11b}=0.5k_{11c}$, $k_{22a}=k_{22c}=2k_{11c}$, $k_{22b}=k_{11c}$)

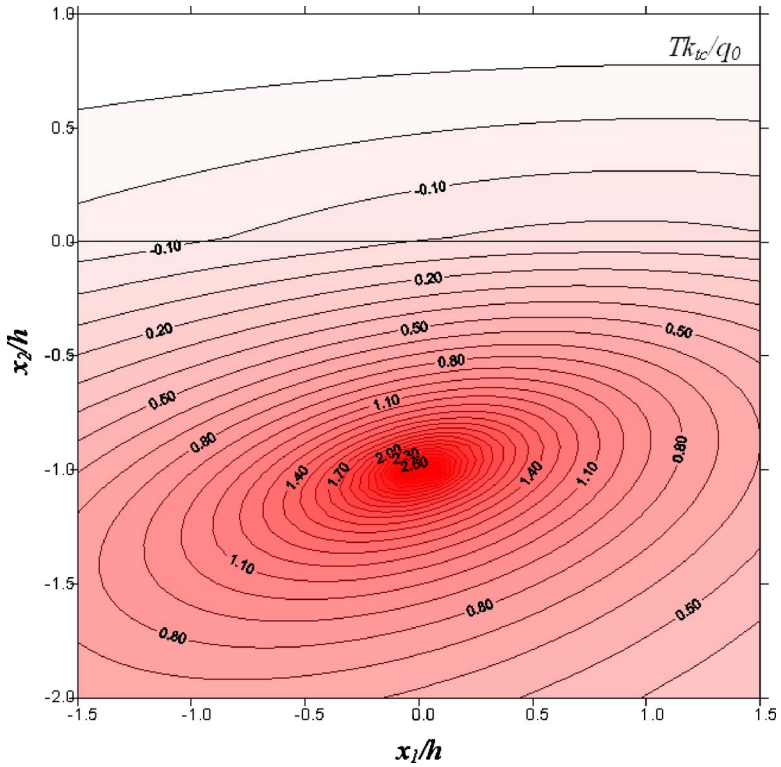

Fig. 9 Temperature distributions in a film-substrate with a concentrated heat source applied within the substrate under isothermal boundary conditions (k_{11c}, k_{12c}, $k_{22c}=83.6$, 18.1, 20.8, k_{11b}, k_{12b}, $k_{22b}=76.5$, 20.6, 52.7)

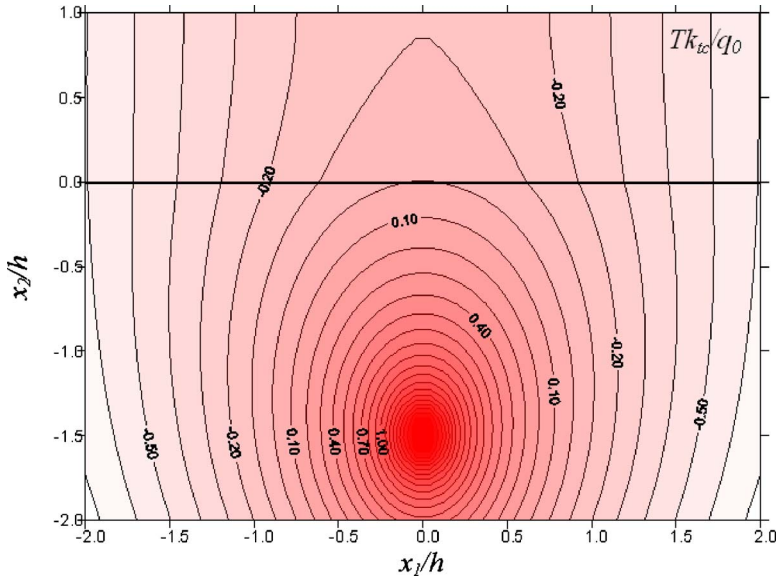

Fig. 10 Temperature distributions in a film-substrate with a concentrated heat source applied within the substrate under adiabatic boundary conditions ($k_{11b}=2k_{11c}$, $k_{22b}=4k_{11c}$, $k_{22c}=2k_{11c}$)

Figure 10 shows the full field distributions of temperature in a film-substrate structure with a concentrated heat source applied within the substrate at $(0, -1.5h)$. One can find far away from the heat source that the temperature contours are perpendicular to the free surface due to the insulated condition.

6 Conclusion

The method of analytic continuation is employed to solve the heat conduction problem of an anisotropic trimaterial subjected to an arbitrary heat source. A homogeneous solution for singularities serves as a base to derive the trimaterial solution for the same singularities in a series form. The trimaterial solution studied here can be applied to a variety of problems, e.g., a bimaterial (including a half-plane problem), a finite thin film on a semi-infinite substrate, and a finite strip. It is evident from numerical results that the material anisotropy has a marked influence on the distribution of temperature. In fact, this solution procedure can be extended to solve a more complicated system with any number of interphase layers.

Nomenclature

x_1, x_2, x_3 = coordinates (m)
T = temperature (K)
q_1, q_2 = heat fluxes (W/m^2)
k_{ij} = thermal conductivity coefficients (W/m K)
Q = resultant heat flow (W/m)
q_0, = line heat source (W/m)
x_{10}, x_{20} = location of the concentrated heat source (m)
h = thickness of the middle layer (m)
p_t = heat eigenvalue

Greek Symbols

$\theta(z_t)$ = temperature function
α_{ab}, $\beta_{ab}\alpha_{cb}$, $\beta_{cb}\alpha_{bc}$ = bimaterial constant

Subscripts

a, b, c = material a, material b, and material c

References

[1] Carslaw, H. S., and Jaeger, J. C., 1959, *Conduction of Heat in Solids*, Oxford University Press, London.
[2] Özisik, M. N., 1980, *Heat Conduction*, Wiley, New York.
[3] Tauchert, T. R., and Akoz, A. Y., 1975, "Stationary Temperature and Stress Fields in an Anisotropic Elastic Slab," ASME J. Appl. Mech., **42**, pp. 647–650.
[4] Mulholland, G. P., and Gupta, B. P., 1977, "Heat Transfer in a Three-Dimensional Anisotropic Solid of Arbitrary Shape," ASME J. Heat Transfer, **99**, pp. 135–137.
[5] Chang, Y. P., 1977, "Analytical Solution for Heat Conduction in Anisotropic Media in Infinite Semi-Infinite and Two-Place-Bounded Regions," Int. J. Heat Mass Transfer, **20**, pp. 1019–1028.
[6] Poon, K. C., 1979, "Transformation of Heat Conduction Problems in Layered Composites From Anisotropic to Orthotropic," Lett. Heat Mass Transfer, **6**, pp. 503–511.
[7] Poon, K. C., Tsou, R. C. H., and Chang, Y. P., 1979, "Solution of Anisotropic Problems of First Class by Coordinate-Transformation," ASME J. Heat Transfer, **101**, pp. 340–345.
[8] Zhang, X. Z., 1990, "Steady-State Temperatures in an Anisotropic Strip," ASME J. Heat Transfer, **112**, pp. 16–20.
[9] Sharma, B., 1958, "Thermal Stresses in Transversely Isotropic Semi-Infinite Elastic Solids," ASME J. Appl. Mech., **25**, pp. 86–88.
[10] Yan, L., Sheikh, A. H., and Beck, J. V., 1993, "Thermal Characteristics of Two-Layered Bodies With Embedded Thin-Film Heat Source," J. Electron. Packag., **115**, pp. 276–283.
[11] Yang, B., and Shi, H., 2009, "A Thermal Stability Criterion for Heat Conduction in Multilayer Composite Solids," ASME J. Heat Transfer, **131**, p. 111304.
[12] Jain, P. K., Singh, S., and Rizwan-uddin, 2009, "Analytical Solution to Transient Asymmetric Heat Conduction in a Multilayer Annulus," ASME J. Heat Transfer, **131**, p. 011304.
[13] Shiah, Y. C., Hwang, P. W., and Yang, R. B., 2006, "Heat Conduction in Multiply Adjoined Anisotropic Media With Embedded Point Heat Sources," ASME J. Heat Transfer, **128**, pp. 207–214.
[14] Hsieh, M. H., and Ma, C. C., 2002, "Analytical Investigations for Heat Conduction Problems in Anisotropic Thin-Layer Media With Embedded Heat Sources," Int. J. Heat Mass Transfer, **45**, pp. 4117–4132.
[15] Ma, C. C., and Chang, S. W., 2004, "Analytical Exact Solutions of Heat Conduction Problems for Anisotropic Multi-Layered Media," Int. J. Heat Mass Transfer, **47**, pp. 1643–1655.
[16] Wu, C. H., 1984, "Plane Anisotropic Thermoelasticity," ASME J. Appl. Mech., **51**, pp. 724–726.
[17] Kattis, M. A., Papanikos, P., and Providas, E., 2004, "Thermal Green's Functions in Plane Anisotropic Bimaterials," Acta Mech., **173**, pp. 65–76.
[18] Chao, C. K., and Chen, F. M., 2004, "Thermal Stresses in an Isotropic Trimaterial Interacted With a Pair of Point Heat Source and Heat Sink," Int. J. Solids Struct., **41**, pp. 6233–6247.

D. K. Kim
Postdoctoral Research Associate
e-mail: dkkim@tamu.edu

E. E. Marotta
Fellow ASME
e-mail: emarotta@tamu.edu

Department of Mechanical Engineering,
Conduction Heat Transfer Laboratory,
Texas A&M University,
TAMU 3123 ENPH 401,
College Station, TX 77843-3123

L. S. Fletcher
Honorary Member
Fellow ASME
Texas A&M University,
College Station, TX 77843-3123

Thermal Modeling of a Multilayer Insulation System

An analytical investigation of a novel multilayer insulation concept was conducted using an extended analytical model. This model was developed to accommodate a multilayer screen wire insulation system with interstitial shim layers. The goal of this study was to provide a simplified model for evaluating this insulation system, which included either a single or multilayer composite structure in order to predict optimal performance. With the present model, the feasibility and performance characteristics of the insulation concept were predicted. The thermal predictions have demonstrated a very good comparison with previously published experimental data. By adding a radiative resistance to the model, improved performance predictions of overall thermal resistance/conductance were possible, leading to the extension of single layer analytical model to multiple-layered cases. From the parametric study, the key thermophysical property of the screen wire was found to be the wire's thermal conductivity. The present model provided excellent performance prediction capability for other screen wire materials, and these results were also validated with a comparison to previously published experimental results.
[DOI: 10.1115/1.4001624]

1 Introduction

Conduction is the primary mode of heat transfer between two surfaces in contact experiencing a temperature difference. When a fluid is present at the contacting interface, and taking into consideration other heat transfer modes such as convection and/or radiation, the rate of heat transfer may increase. In contrast, the heat transfer rate can be reduced with the addition of a low thermal conductivity material acting as an interstitial insulation at the interface, thus affecting all heat transfer modes. Therefore, lower thermal conductance may be achieved with the use of an interstitial material with selected thermophysical, mechanical and geometrical properties, thus controlling the amount of heat transferred.

Under special environmental conditions, such as high hydrostatic pressure and low fluid temperature (e.g., deep water subsea applications), novel insulation techniques are necessary. Several insulation techniques use low conductivity materials and coatings on the external tubular or pipe surface, such as syntactic foam or urethane, to achieve desired thermal performance (e.g., lower thermal conductance). However, these techniques often have severe limitations such as water damage due to large hydrostatic pressure differentials and installation issues [1–3]. Therefore, more advanced insulation techniques must be developed to ensure greater insulation performance for tubulars and pipe lines in increasingly challenging environments.

Raymond et al. [3] developed a new insulation technique, named insulation liquid-solid (ILS), which uses a liquid-solid phase change material that acts as a thermal energy accumulator under normal (steady state) conditions. But during cool-down periods, it restores the stored thermal energy. It is claimed that ILS can enhance the cool-down period two to four times longer with respect to existing insulation technologies. Azzola et al. [4] developed an insulation technique, named vacuum insulated tubing (VIT), which contains a vacuum sealed annulus between the inner and outer pipe walls. This technique minimizes heat loss from the hot inner pipe walls, up to 90% of total heat loss. The compact space of the insulation layer, high load capacity (200,000–500,000 lbf tension, 889,644–2,224,110 N), and high thermal insulation values are known advantages. However, there continues to be concern about these new insulation techniques such as environmental pollution when leakage occurs, and the difficulty in maintaining a vacuum. Such concerns may cause additional maintenance cost; thus it is necessary to evaluate the trade-offs between performance and cost.

In the present investigation, an analytical investigation of a newly developed insulation technique, which contains one or more layers of a wire screen as an interstitial material (as shown in Fig. 1), was conducted.

A reduction in the heat transfer rate, and thus an increase in cool-down times, can be achieved without the concerns previously noted. Moreover, the manufacture and installation of this insulation system will be greatly simplified [5]. Within the interstitial screen wire material, the interstitial fluid considered was air, which remains stagnant. Other gases, however, may be employed to achieve greater insulation performance. Air spaces between the interfaces were small enough to limit natural convection, i.e., calculated Rayleigh numbers less than 1750, which leads to conduction heat transfer through the gap. Radiation heat transfer will be minimal at these temperatures. Therefore, the dominant heat transfer mechanism for this insulation technique will be conduction through nonconforming contacts between the tube surface and wire screen. In addition, conforming microcontacts within the screen wire and tube surface can provide an additional resistive path between contacting interfaces, hence a low thermal conductivity insulation can be achieved.

Sections 2 and 3 include the description of the analytical model developed to quantify each resistance for a unit cell of wire screen mesh, and the subsequent multilayer configuration, which has included the portion attributed to radiation exchange between layers. A comparison to experimentally obtained data by Marotta and Fletcher [5] was conducted to validate the analytical expressions. Furthermore, a parametric study was conducted to evaluate the sensitivity of each geometric and thermophysical property for its influence on the overall thermal conductance. In addition, the analysis provides an insight into opportunities to optimize the multilayer structure for enhanced performance as a thermal barrier. These analyses are presented in Sec. 3. This manuscript concludes with a set of findings and conclusions drawn from the analytical and experimental investigation.

Contributed by the Heat Transfer Division of ASME for publication in the JOURNAL OF HEAT TRANSFER. Manuscript received July 8, 2009; final manuscript received March 4, 2010; published online June 29, 2010. Assoc. Editor: Peter Vadasz.

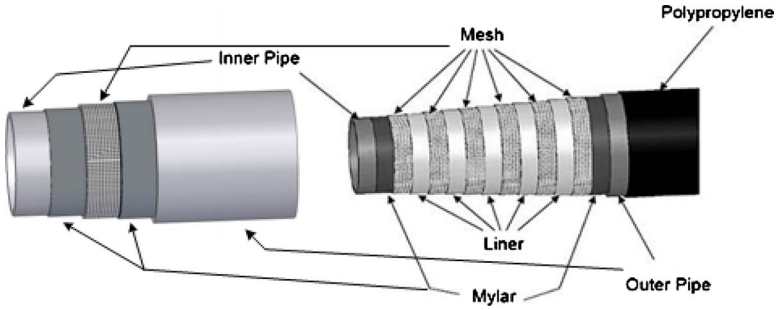

Fig. 1 Coaxial pipe with single layer (left) and six layers (right) of a wire screen mesh as an interstitial insulation material

2 Analytical Modeling

There have been a number of papers, which detail correlations and analytical models for contact resistance for rough, conforming surfaces and nonconforming contacting surfaces. Yovanovich et al. [6] and Cividino et al. [7] analyzed joint conductance for a woven wire screen utilizing only Hertzian theory [8] to predict the macrocontact area when a wire screen contacts a solid surface. For the microresistances present at each interface, Kim et al. [9] reviewed the available elastic and plastic models for microcontact deformation. It was determined that a plastic deformation model provided better predictability for these types of interface contacts. Furthermore, a gap conductance model was included to account for heat transfer across gaps filled with a fluid. However, to develop a more accurate model a radiative resistance between the screen wire and interfaces is also required. Therefore, the goal of this investigation was to develop an analytical model that combines macro-/microcontact conduction with radiation heat transfer to predict the overall joint resistance for contacting surfaces containing a wire screen. Furthermore, the new model was compared with thermal conductance values for several screen wire sizes, materials, and mesh number. To aid in the model development, a thermal network circuit is shown in Fig. 2 to help visualize the heat path between inner wall and outer wall.

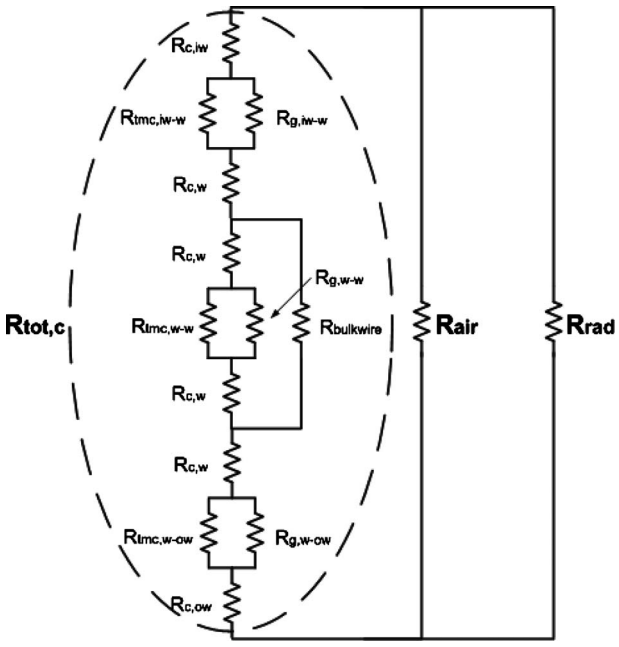

Fig. 2 Total thermal circuit for a screen wire node

2.1 Radiative Resistance in the Space Within Walls and Wire Screen. Radiation is one of the heat transport modes in the interstitial space between the surfaces and the wire screen, with assumptions that this complex process is simplified. The radiative thermal resistance between two separate surfaces can be expressed as [6]

$$R_{\text{rad}} = \frac{T_i - T_j}{\sigma A_a F_{ij}(T_i^4 - T_j^4)} = \frac{1}{4\sigma A_a F_{ij}\overline{T_{ij}^3}} \tag{1}$$

where $4\overline{T_{ij}}^3 \approx (T_i^4 - T_j^4)/(T_i - T_j)$ and $\overline{T_{ij}} = (T_i + T_j)/2$.

For the thermal resistance between two walls and screen wire, the view factor can be obtained from geometrical relationship between infinite flat plane and row of cylinders as shown in Fig. 3 and expressed by Eq. (2) [10],

$$F_{\text{iw-}w} = 1 - \left[1 - \left(\frac{D_w}{s}\right)^2\right]^{1/2} + \left(\frac{D_w}{s}\right)\tan^{-1}\left[\left(\frac{s^2 - {D_w}^2}{{D_w}^2}\right)^{1/2}\right] \tag{2}$$

where s is the distance between wires.

In the radiative thermal resistance circuit, it is assumed that the screen wire behaves as a reradiating surface (i.e., $\ddot{q}_w = 0$) as shown in Fig. 4, thus the radiative thermal resistance may be expressed by Eq. (3).

$$R_{\text{rad}} = \frac{\dfrac{1-\varepsilon_{\text{iw}}}{\varepsilon_{\text{iw}}A_{\text{iw}}} + \left(A_{\text{ow}}F_{\text{ow-iw}} + \dfrac{1}{\dfrac{1}{A_{\text{iw}}F_{\text{iw-}w}} + \dfrac{1}{A_{\text{ow}}F_{\text{ow-}w}}}\right)^{-1} + \dfrac{1-\varepsilon_{\text{ow}}}{\varepsilon_{\text{ow}}A_{\text{ow}}}}{4\sigma\overline{T_{\text{iw-ow}}^3}} \tag{3}$$

The radiative resistance was considered in parallel with the air gap and total thermal contact resistance within a node as shown in Fig. 2; thus the total thermal resistance at any node may be written as Eq. (4),

$$R_{\text{tot,node}} = \left(\frac{1}{R_{\text{tot},c}} + \frac{1}{R_{\text{air}}} + \frac{1}{R_{\text{rad}}}\right)^{-1} \tag{4}$$

where $R_{\text{tot},c}$ and R_{air} are [9],

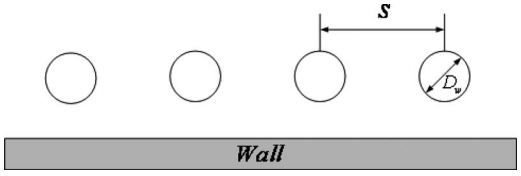

Fig. 3 View factor between wall and screen wire elements

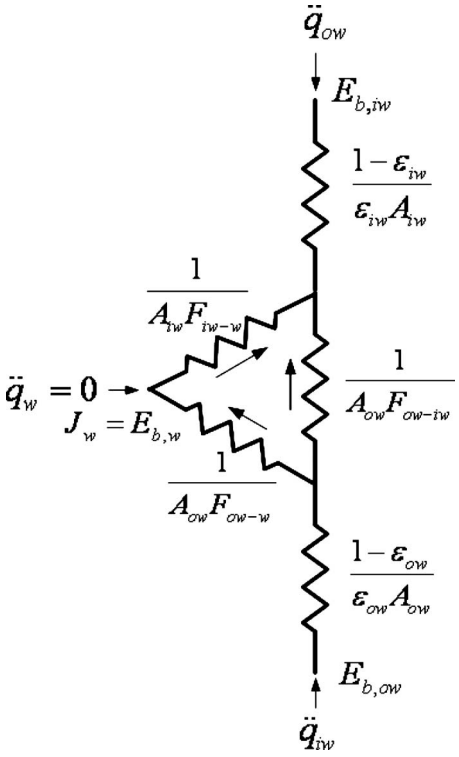

Fig. 4 Thermal circuit for radiation among walls and wire at a node

$$R_{\text{tot},c} = R_{c,\text{iw-}w} + R_{c,\text{w-w}} + R_{c,w\text{-ow}}$$
$$= \left[R_{c,\text{iw}} + \left(\frac{1}{R_{\text{tmc,iw-}w}} + \frac{1}{R_{g,\text{iw-}w}} \right)^{-1} + R_{c,w} \right]$$
$$+ \left[\left(\frac{1}{\left(R_{c,w} + \left(\frac{1}{R_{\text{tmc,w-w}}} + \frac{1}{R_{g,\text{w-w}}} \right)^{-1} + R_{c,w} \right)} + \frac{1}{R_{\text{bulk wire}}} \right)^{-1} \right]$$
$$+ \left[R_{c,w} + \left(\frac{1}{R_{\text{tmc,}w\text{-ow}}} + \frac{1}{R_{g,w\text{-ow}}} \right)^{-1} + R_{c,\text{ow}} \right]$$

$$R_{\text{air}} = \frac{2D_w - \delta_{\text{iw-}w} - \delta_{\text{w-w}} - \delta_{w\text{-ow}}}{k_{\text{air}} A_{\text{air}}}$$

With the total thermal resistance defined at a node, the total resistance for a unit cell, which contains four nodes, for the total joint thermal resistance, and subsequent thermal conductance for a given interface area can be defined, respectively, as shown by Eq. (5) and (6).

$$R_{\text{actual}} = \left(\frac{N_{\text{cell}}}{R_{\text{tot,cell}}} \right)^{-1} \tag{5}$$

where $R_{\text{tot,cell}} = (4/R_{\text{tot,node}})^{-1}$ and $N_{\text{cell}} = A_{\text{actual}}/A_{\text{cell}}$.

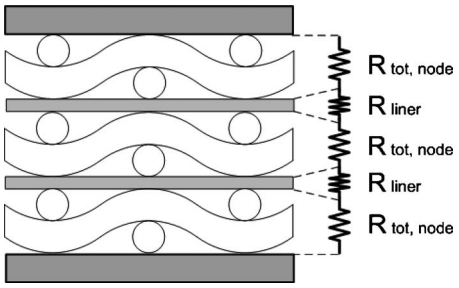

Fig. 5 Schematic of the multilayer (three layers) structure and thermal circuit between walls, wire, and liner in a node

$$h_{\text{actual}} = \frac{1}{R_{\text{actual}} A_{\text{actual}}} \tag{6}$$

2.2 Comparison With Several Mesh Numbers and Materials. The analytical model was developed such that the thermal resistive performance of the interstitial insulation technology with different mesh materials and numbers (i.e., number of wires per square inch) can be predicted. For validation purposes, with material and geometric properties shown in Table 1, a comparison between model predictions and experimental data was conducted for a single layer initially. The experimental investigation conducted by Marotta and Fletcher [5] had an uncertainty value, which ranged from 4.4% to 10.5% for the measured conductance values.

2.3 Multilayer Model. A multilayer model is required for the actual design and optimization of the interstitial insulation technology. The multilayer model should be able to predict the overall thermal conductance and deformation of each wire screen layer. In a multilayer design, the selection of a liner material, between each subsequent layer, is important since it functions as a radiation shield, as well as a separator for the individual layers. In the multilayer model, the properties of the outer and inner walls were used in conjunction with the liner material. In the midsection, the middle layers, liner mechanical, and thermophysical properties were used exclusively.

For the resistance calculations, the temperatures of each layer were required. The heat rate was first calculated with the use of Eq. (7). With the computed heat rate, the temperatures of each layer were obtained with Eq. (8).

As shown in Fig. 5, the overall thermal resistance of the multilayer structure may be calculated from the summation of the serial type resistances.

$$Q_{\text{node}} = \frac{T_H - T_L}{R_{\text{tot,node}}} = \frac{T_H - T_i}{R_{\text{node},i}} \tag{7}$$

$$T_{i+1} = T_i - Q_{\text{node}} \cdot R_{\text{node},i+1} \tag{8}$$

The modified model for the multilayer structure includes the macro- and microcontact resistances, as well as air-gap and radiation resistances.

Table 1 Properties of screen mesh material [5]

Material	Mesh No.	Thermal conductivity at 366 K (W/m K)	Young's modulus (GPa)	Wire diameter (mm)
SS 316	5	16.4	190	0.925
Inconel	5	9.8	207	0.819
Titanium	9	22.3	116	0.812
	14	22.3	116	0.406
	18	22.3	116	0.616

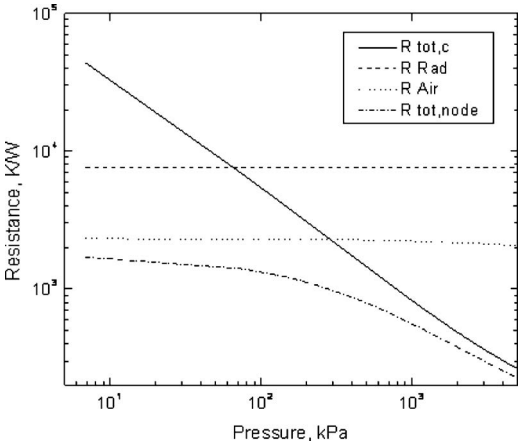

Fig. 6 Thermal resistance as a function of applied pressure in a single node

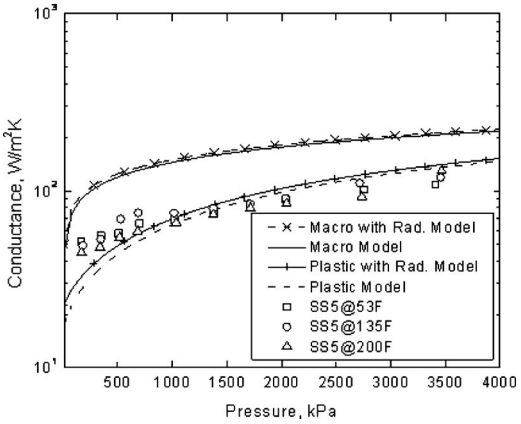

Fig. 7 Prediction of thermal conductance for each model with/without radiation model and compared with experimental data as a function of applied pressure

2.4 Parametric Study. One of the most important benefits that results from a validated model is that a parametric study can be performed to optimize the geometric and thermophysical properties. A parametric study was executed such that one parameter was varied with other parameters fixed (i.e., selected mechanical, geometrical, and thermophysical properties). A key objective of the study was to determine the most important parameter or property that most affects the thermal performance. With the present modeling, it was possible to find the dominant thermophysical property for metallic materials. However, for nonmetallic materials, a different modeling approach is needed.

3 Results

In this investigation, along with an improved model for macro- and microcontact resistances, the fluid gap resistances were developed simultaneously. Predictions from the enhanced model are compared with experimental data from a previous experimental study [5], which contained an interstitially wire screen material in the annulus of a simulated coaxial pipe.

From previously reported coupon testing [5], an insulation system incorporating a low thermal conductivity screen mesh was shown to be an effective passive thermal insulation solution. It has been established that a thermal resistance (due to the metrology of the contacting surfaces) was created at an interface between two materials. If the two contacting surfaces are further separated by a screen wire or mesh at the pipe and liner interface, then a higher thermal interface resistance will result, which will significantly increase the resistance to heat transfer. The screen wire reduces the heat transfer by restricting the path for conduction and forms a stagnant air gap to minimize convective heat transfer.

3.1 Radiative Resistance Model. As one of the heat transfer modes, within the interstitial space, thermal transport by radiation was included in the model. Radiation heat transfer was placed in the thermal circuit as a parallel resistance along with the total contact resistance and air resistance. To determine the contribution of each resistance to the overall resistance in a node, the total contact resistance, air resistance, radiative resistance, and the total resistance for a node were plotted as a function of applied pressure, as shown in Fig. 6. This figure indicates that the contact resistance dominates in the low pressure range ($\sim$25 kPa) and linearly decreases as applied pressure is increased; meanwhile, the radiative and air resistance decrease only slightly. Therefore, as noted the total resistance in a node was highly dependent on the change in contact resistance, which was similar to the predicted results without the radiative resistance included. After adding the radiative mode, the analysis showed a higher thermal conductance (lower thermal resistance) at the lower pressure range, as shown in Figs. 7 and 8. After the inclusion of the radiative model, the underprediction of thermal conductance at the light pressure range was decreased, while at the high pressure range the change was negligible. This is a positive effect to the prediction of the thermal performance.

3.2 Comparison With Other Mesh Numbers and Materials. The present model was applied to several materials such as Inconel screen wire with a mesh number of 5 and material properties, as shown in Table 1. A comparison of the experimental and theoretical thermal conductance values as a function of applied pressure was conducted, as shown in Fig. 9. The trend for the predicted values correlates well with the experimental data; however, an underprediction of the conductance occurred for the low pressure range as shown previously with stainless steel 316. At an interface pressure of 172 kPa, the difference in thermal conductance between the model prediction and experimental data was 15.2 $W/m^2 K$, while the difference was decreased to 0.91 $W/m^2 K$ at 2080 kPa.

Figure 10 shows a comparison between the model predictions and experimental data for stainless steel and Inconel screen wire with a mesh number of 5, and titanium screen wire with a mesh number of 9. The model predicted the thermal conductance well for the pressure range tested. As a quantitative comparison, between model prediction and experimental data, the rms error was calculated for each wire material, as shown in Table 2. For In-

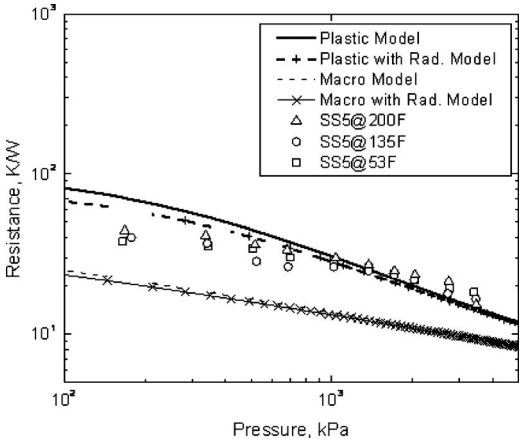

Fig. 8 Prediction of thermal resistance for each model with/without radiation and comparison with experimental data as a function of applied pressure

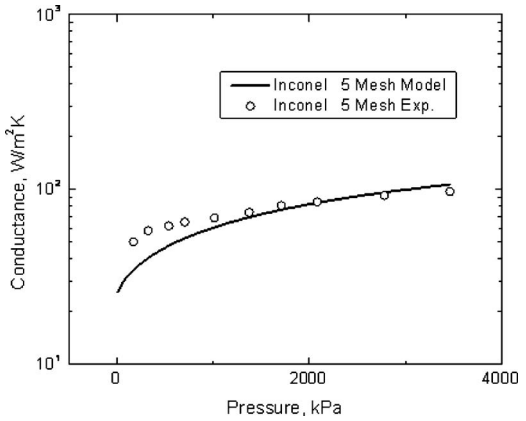

Fig. 9 Prediction of the thermal conductance of Inconel wire mesh for the present model compared with experimental data as a function of applied pressure

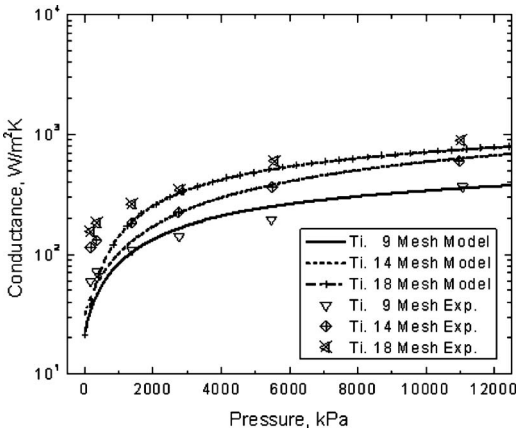

Fig. 11 Prediction of the thermal conductance of different mesh size of Titanium wire mesh for the present model compared with experimental data as a function of applied pressure

conel, the rms error was 10.5%, which was the lowest among the three materials investigated, while the titanium mesh material had a value of 21.9%, the highest error computed.

For the titanium screen wire at different mesh numbers (e.g., 9, 14, and 18), a comparison between the predicted and experimental data for thermal conductance as a function of applied pressure is shown in Fig. 11. As the mesh number increased, the difference between model predictions and experimental data increased noticeably at low interface pressures. Again, a possible explanation for this effect is the observed predeformation at the wire-to-wire interface as the number of nodes increased, causing the apparent contact area to increase.

3.3 Multilayer Model. In real applications, the performance of an interstitial insulation is paramount to its acceptance as a viable alternative. Geometrical factors play a pivotal role in the present design's performance; therefore, determination of the number of layers is an important parameter for identifying critical thickness. This helps achieve the optimum performance at the lowest cost. Figure 12 shows the thermal conductance as a function of pressure. Each line represents the number of layers from a single screen wire mesh to 50 layers. As the number of layers increased, the thermal conductance of the insulation structure decreased. In Fig. 12, the conductances of a single layer at an applied interface pressure of 145 kPa were calculated as 27.5 W/m^2 K and 3.3 W/m^2 K for 8 layers and 1.6 W/m^2 K for 16 layers. These multilayer conductance values showed a big decrease; however, the rate of decrease in conductance (i.e., $\Delta h_{i-i+1}=h_i-h_{i+1}$), by adding each additional layer, decreases as the number of layers increased. For instance, the decrease in conductance between a single and a double layer was 14.1 W/m^2 K (or 51.2%), between the 8th and 9th layers it was 0.36 W/m^2 K (or 11.2%), and between the 16th and 17thh layers it was 0.09 W/m^2 K (or 5.9%), while a linear increase in thermal resistance was observed as the applied pressure increased, as shown in Fig. 13. In this figure, the resistance for a single layer was 71 K/W, and it increased to 146 K/W by 75 K/W (or 104.9%) with the addition of one more layer, and the resistance was 75.7 K/W (or 6.3%) due to adding one more layer between 16th and 17th layers. The rate of increase in resistance (i.e., $\Delta R_{(i-1)-i}=R_{i+1}-R_i$) was observed as nearly constant and the thermal resistance was more sensitive to the applied pressure due to greater interface deformation, which resulted in a contact area increase.

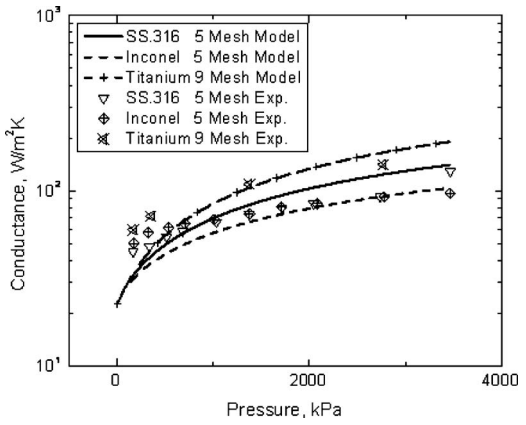

Fig. 10 Prediction of the thermal conductance of different mesh material for the present model compared with experimental data as a function of applied pressure

Table 2 rms error between the experimental data and the present model

Material	Mesh No.	rms
SS 316	5	13.6
Inconel	5	10.5
Titanium	9	21.9

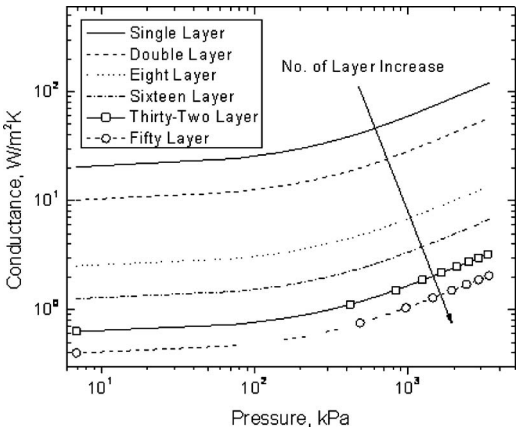

Fig. 12 Thermal conductance of multilayer insulation as a function of applied pressure

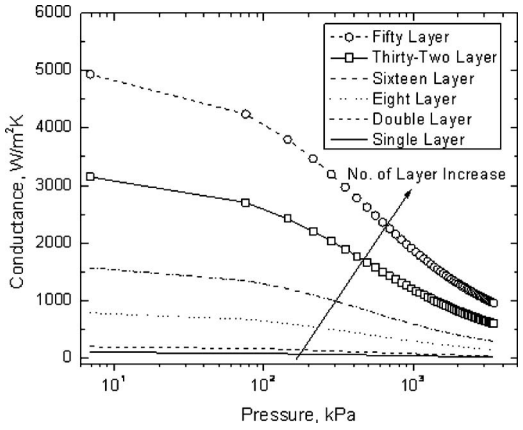

Fig. 13 Thermal resistance of multilayer insulation as a function of applied pressure

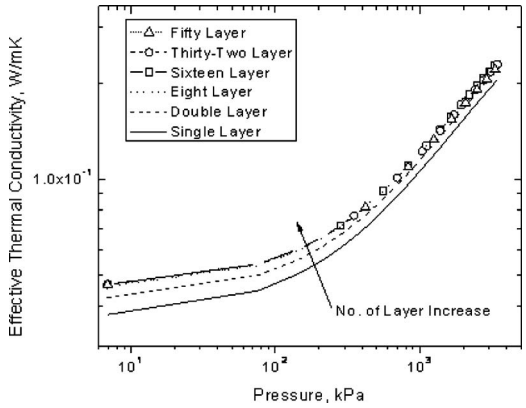

Fig. 15 Effective thermal conductivity of multilayer insulation as a function of applied pressure

Figure 14 shows the total thickness of each multilayer structure as a function of the applied interface pressure. It indicates that the amount of structural deformation can be attributed to greater compliance of the layered structure.

The effective thermal conductivity can be calculated by the following equation;

$$k_{\text{eff}} = h \cdot t \tag{9}$$

The effective thermal conductivity of a multilayer structure as a function of applied pressure is shown in Fig. 15. At 145 kPa interface pressure, the effective thermal conductivity of a single layer was 0.050 W/m K, while the value was 0.059 $\text{W/m}^2\,\text{K}$ for an 8 layer structure and 0.060 $\text{W/m}^2\,\text{K}$ for 16 layer configuration. The change in effective thermal conductivity value by adding one additional layer decreases as the number of layers increase. For instance, the change in thermal effective conductivity value ($\Delta k_{\text{eff},i+1-i} = k_{\text{eff},i+1} - k_{\text{eff},i}$) was 0.005 $\text{W/m}^2\,\text{K}$ for a single to double layer, 0.000126 $\text{W/m}^2\,\text{K}$ for an 8–9 layer structure, and 0.000019 $\text{W/m}^2\,\text{K}$ for 16–17 layer structure at 145 kPa interface pressure.

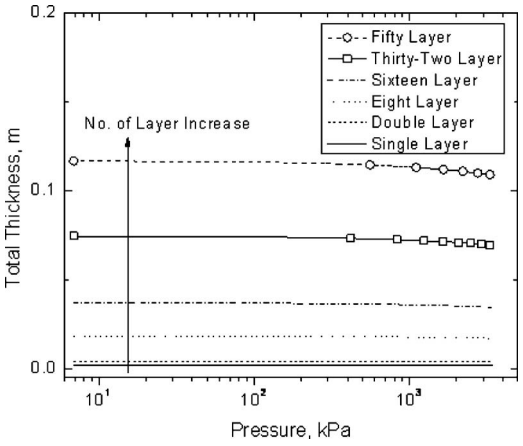

Fig. 14 Total thickness of multilayer insulation as a function of applied pressure

In summary, an optimal overall thickness may be found from the use of the multilayer model. As the number of layers increases, the overall thermal conductance decreases (resistance increases); however, the rate of reduction decreased after 16 layers; thus the effectiveness by adding more layers was decreased. This can be observed easily from the effective thermal conductivity comparison between 8 layers and 16 layers case as a function of interface pressure as shown in Fig. 15.

3.4 Parametric Study. A parametric study was conducted to determine the influence of the variation in geometrical, mechanical, and thermophysical properties of the overall thermal conductance of a single layer. The parametric study was conducted by choosing to vary one parameter while holding the remaining parameters constant. The geometrical property chosen was the surface roughness, σ, the mechanical property was Young's modulus, E, while the thermophysical properties selected were the thermal conductivity, k, and the surface emissivity, ε. All these properties are influential parameters in choosing the optimum material for the application design. To determine the most dominant parameter among the selected parameters, each was changed by 10%, 20%, and 30% from the nominal values shown in Table 3.

For variations that are 10% from nominal, a significant reduction in thermal conductance is observed; however, this reduction was mainly attributable to the thermal conductivity parameter while negligible effects were observed from the other parameters. This is shown in Fig. 16. When thermal conductivity value was varied, the thermal conductance reduction value was 2.66 $\text{W/m}^2\,\text{K}$ at 144 kPa, and this value increased as applied pressure was increased, which was 13.55 $\text{W/m}^2\,\text{K}$ at 3454 kPa. Figure 17 shows the thermal conductance percent differences between the nominal parameter value and a 10% change in its value. From Fig. 17, the percent reduction in thermal conduction as a function of pressure for each parameter can be identified easily.

The conductance reduction by varying the thermal conductivity increased up to 9.5% at 900 kPa, with negligible increases observed thereafter. Other parameters affected the conductance reduction by only 1.7%. For the emissivity case, the conductance

Table 3 Properties of selected materials for parametric study

Walls/wire	Nominal	10%	20%	30%
Thermal conductivity (W/m K)	46.7/16.5	42.03/14.85	37.36/13.2	32.69/11.55
Surface roughness (μm)	1.5/0.4	1.65/0.44	1.8/0.48	1.95/0.52
Young's modulus (GPa)	207/190	227.7/209	248.4/228	269.1/247
Surface emissivity	0.44/0.22	0.396/0.198	0.352/0.176	0.308/0.154

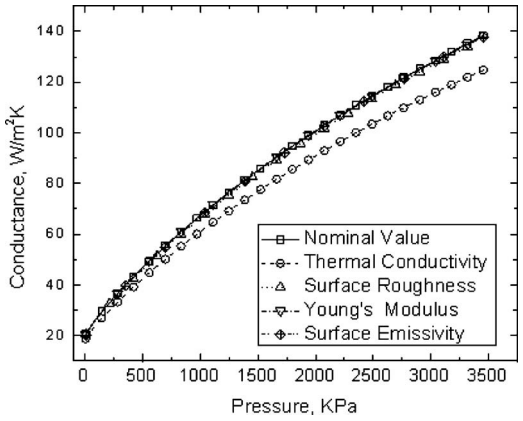

Fig. 16 Thermal conductance for each parameter varied by 10% as a function of applied pressure

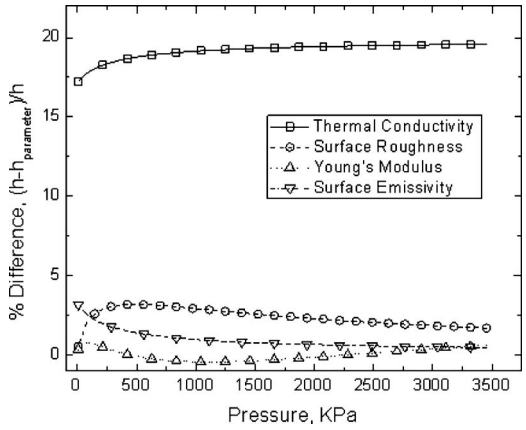

Fig. 19 Thermal conductance difference for a 20% variation in parameters as a function of applied pressure

reduction decreased as pressure increased, with a 1.6% reduction at the low-end pressure (6.8 kPa) and a 0.23% at the high-end pressure (3454 kPa), respectively. When each parameter was varied by 20%, the overall thermal conductance as a function of interface pressure is shown in Fig. 18.

Thermal conductivity was observed as the most important parameter affecting the overall conductance among the selected parameters, and in the 10% case, the conductance reduction was 27 W/m^2 K at 3454 kPa. Figure 19 shows the percent change in thermal conductance as a function of interface pressure with 20% variation in each parameter. When the thermal conductivity was changed, an upper limit of 19.5% reduction in thermal conductance can be expected and for the other parameters only 3.1% reduction can be expected. When roughness was varied, the reduction in thermal conductance increased up to 3.17% at 489 kPa, and then decreased as the interface pressure increased. For 30% parameter changes, Fig. 20 shows the thermal conductance as a function of pressure when the selected parameters were changed one after another. Similar to the 10% and 20% varying cases, the thermal conductivity was the most influential parameter on thermal conductance, with a 5.3 W/m^2 K reduction at 6.8 kPa and a 40.6 W/m^2 K reduction at 3454 kPa. When the reduction was plotted in percent difference from nominal conductance, as shown in Fig. 21, up to a 29.3% reduction can be expected by varying thermal conductivity. For Young's modulus, the reduction was increased up to 1.05% at 75.8 kPa interface pressure, and then it decreased with a negative reduction (increase in conductance) up to −0.75%. However, the reduction due to Young's modulus was small enough to neglect.

In summary, a parametric study was conducted using the present model, which showed that thermal conductivity, k, was definitely the most important parameter among the parameters that were varied. Surface roughness, σ, Young's modulus, E, and surface emissivity, ε showed negligible influence on thermal conductance values. Each parameter, however, showed a change as a function of interface pressure but not to the extent as that shown by thermal conductivity.

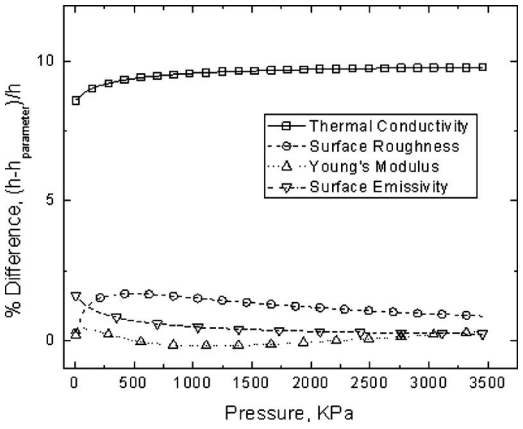

Fig. 17 Thermal conductance difference for 10% variation in parameters as a function of applied pressure

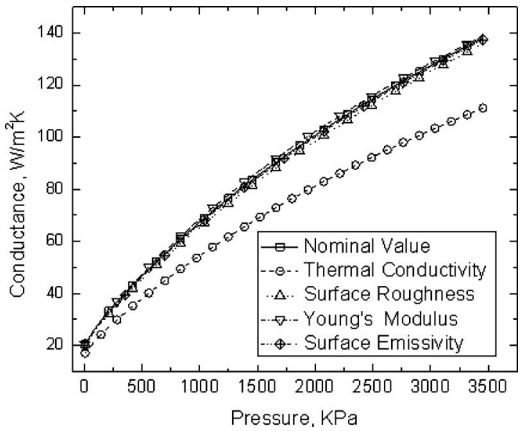

Fig. 18 Thermal conductance for each parameter varied by 20% as a function of applied pressure

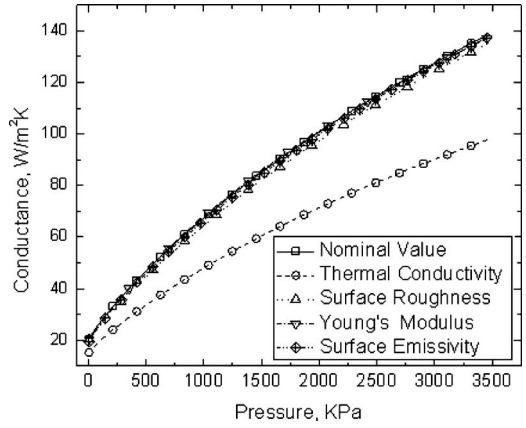

Fig. 20 Thermal conductance for each parameter varied by 30% as a function of applied pressure

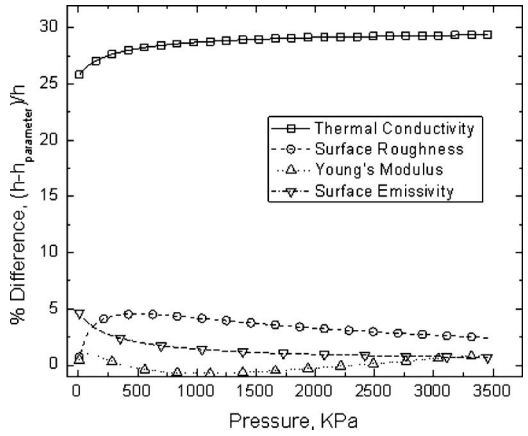

Fig. 21 Thermal conductance difference for a 30% variation in parameters as a function of applied pressure

4 Conclusions

In this investigation, an analytical model was developed for an interstitial insulation technology, including an analysis for performance predictions. By developing an analytical model for a multilayer screen wire composite structure, the thermal conductance (resistance) was predicted for a given contact pressure for a 1 in. (2.54 cm) diameter coupon.

Macro- and microcontact resistance models were used to predict the thermal performance of an interstitial insulation technology, which contained wire screen. The model developed showed very good agreement with the experimentally measured conductance, h, values over an appropriate pressure range.

A radiative resistance was added to the present model as a parallel thermal resistance to the thermal contact resistance and air resistance. With the modified model, the contribution of the radiative resistance was investigated. As a result, the underprediction of thermal conductance (overprediction of thermal resistance) at light pressures was reduced while at high pressures the change was negligible, which is a positive result in the prediction of thermal performance.

Thermal conductance predictions for different wire mesh materials and mesh number were also compared with experimental data. The model predicted the thermal conductance very well over the pressure range tested with results similar to stainless steel. It is felt that this model can be used for an entire array of wire screen mesh sizes.

For a multilayer structure, for an increase in the number of layers from a single layer to a number of layers, the performance characteristic was predicted with the new multilayer model. The predictions indicate that as the number of layers increased, the thermal conductance of the insulation structure decreased. However, the rate of decrease in conductance by adding each additional layer decreased as the number of layers increased. A linear increase in overall thermal resistance was observed with additional layers. The thermal resistance seemed to be more sensitive to applied pressure. The effective thermal conductivity of the multilayer structure increased as the number of layer increased; however, the rate of increase decreased as the layers increased.

By conducting a parametric study with surface roughness σ as a geometrical property, Young's modulus E as a mechanical property, and thermal conductivity k and emissivity ε as the thermophysical properties, it was observed that thermal conductivity was the dominant variable and each parameter's contribution to the thermal performance improvement (reduction in thermal conductance) was identified as a function of applied interface pressure. Therefore, by modifying the geometrical, mechanical, and thermophysical parameters of the wire screen, an optimum design can be achieved.

As a result of the modeling, the viability of using a wire mesh as an insulating material has been proven in this investigation. However, to ensure the best performance, optimization of the multilayer insulation is necessary and further study is needed to account for the overprediction at lighter pressures, as indicated by the analytical contact model. Predeformation of the contact area within the wire-to-wire interface was clearly observed in the previously conducted coupon size experiments [5]. This could be attributed to wire tension forces from the fabrication process.

In summary, the multilayer insulation technique is a strong candidate for the reduction in heat losses in many applications. The advantages are higher structural strength, ease of installation, relatively low product cost, and an environmentally satisfactory design due to nonchemical based material usage. Thus, the present technology shows promise for many industrial applications.

Nomenclature

A = area (m^2)
D = diameter (m)
E = emissivity power (W/m^2)
F = view factor
J = radiosity (W/m^2)
N = number of unit cell, dimensionless
P = pressure (N/m^2 Pa)
Q = heat rate (W)
R = thermal resistance (K/W)
T = temperature (K)
h = thermal conductance, heat transfer coefficient (W/m^2 K)
k = thermal conductivity (W/m K)
$\ddot{q}$ = heat flux (W/m^2)
s = length between nodes (m)
t = layer thickness (m)
δ = normal deformation of surface (m)
ε = emissivity, dimensionless
σ = Stefan–Boltzmann constant (5.67×10^{-8} W/m^2 K^4)

Subscripts

1, 2 = surfaces 1 and 2
H = higher temperature
L = lower temperature
actual = actual
air = air
b = black body
bulk wire = wire length
c = contact, constriction or spreading
cell = unit cell
eff = effective
g = gas
i = number of layer
iw = inner wall
node = node
ow = outer wall
rad = radiation
tmc = total microcontact
tot = total
w = wire of screen mesh

References

[1] Watkins, L., and Hershey, E., 2004 "Subsea Insulation," World Pipelines, pp. 49–54.
[2] Dominique, C., Angele, C., and Christian, B., 2002, "Insulation Materials for Ultra Deep Sea Flow Assurance: Evaluation of the Material Properties, OTC 14115, pp. 1–8.
[3] Raymond, H., Angele, C., and Stephane, C., 2002, "ILS—A Passive Insulation Solution to Answer Cool Down Time Challenges on Deep Water Flowlines," OTC 14117, pp. 1–10.
[4] Azzola, J. H., Pattillo, P. D., Richey, J. F., and Segreto, S. J., 2004, "The Heat

Transfer Characteristics of Vacuum Insulated Tubing," SPE 90151, pp. 1–8.
[5] Marotta, E. E., and Fletcher, L. S., 2005 "Interstitially Insulated Coaxial Pipe," MMS/OTRC MEEN CHTL-05-509-35663, pp. 2–3, and 24–25.
[6] Yovanovich, M. M., and Marotta, E. E., 2003, *Thermal Spreading and Contact Resistances, Heat Transfer Handbook*, Wiley, New York, Chap. 4.
[7] Cividino, S., Yovanovich, M. M., and Fletcher, L. S., 1974 "A Model for Predicting the Joint Conductance of a Woven Wire Screen Contacting Two Solids," ASME Paper No. 74-695.
[8] Johnson, K. L., 1985, *Contact Mechanics*, Cambridge University Press, Cambridge.
[9] Kim, D. K., Silva, C., Marotta, E. E., and Fletcher, L. S., 2007, "Characterization/Modeling of Wire Screen Insulation for Deep-Water Pipes," J. Thermophys. Heat Transfer, **21**(1), pp. 145–152.
[10] Incropera, F. P., DeWitt, D. P., Bergman, T. L., and Lavine, A. S., 2005, *Fundamentals of Heat and Mass Transfer*, 6th ed., Wiley, Hoboken, NJ.

Jason Stafford[1]
e-mail: jason.stafford@ul.ie

Ed Walsh

Vanessa Egan

Pat Walsh

Department of Mechanical and Aeronautical Engineering,
Stokes Institute,
University of Limerick,
Limerick, Ireland

Yuri S. Muzychka
Faculty of Engineering,
Memorial University of Newfoundland,
St. John's, NL, A1B 3X5, Canada

A Novel Approach to Low Profile Heat Sink Design

This paper discusses the importance of developing cooling solutions for low profile devices. This is addressed with an experimental and theoretical study on forced convection cooling solution designs that could be implemented into such devices. Conventional finned and corresponding finless designs of equal exterior dimensions are considered for three different heat sink profiles ranging from 1 mm to 4 mm in combination with a commercially available radial blower. The results show that forced convection heat transfer rates can be enhanced by up to 55% using finless designs at low profiles with relatively small footprint areas. Overall, this paper provides optimization and geometry selection criteria, which are relevant to designers of low profile cooling solutions.
[DOI: 10.1115/1.4001626]

Keywords: electronic cooling, heat exchangers, forced convection

1 Introduction

Cooling solutions within electronic packages have always been an important aspect in the overall design of electronic devices. It is an area that influences both performance and reliability of the device. Historically, space constraint issues for electronic device design were of much lower importance than in recent years. Consequently, volume constraints for proficient cooling solutions posed little problem. This resulted in poorly designed heat sinks with few goals other than dissipating adequate heat from the heat source. Increased heat flux densities due to advances in performance capabilities and reductions in device dimensions have meant cooling requirements are now more stringent than before. In addition, and in particular for portable devices, efficient power usage is on a similar level of importance in the cooling solution design. As these trends continue, design optimization and enhancements on current methods are required to meet these demands.

Optimization of fan-heat sink designs were completed [1–3], however, the majority of literature reflects larger scale cooling solutions for desktop and server applications [4]. At the low profile scale, there has been less attention to design optimization. One aforementioned study [3] does consider application in portable electronics for similar footprint areas considered in this work. Axial and radial fan types were used to compare thermal resistance performance for various channel width to channel length ratios in order to source an optimum operating point. The heat sink profile examined, however, was 20 mm, making it too cumbersome for implementation in many modern portable electronics that are typically less than 10 mm in width. Indeed, the absence of literature on forced convection cooling at ultra low profiles considered here is indicative of the portable electronics industry's reliance on passive cooling methods. Mobile phones, netbooks, mobile gaming and internet devices, and many other portable electronics are now required to perform simultaneous applications on a similar level to much larger form factor devices. As portable electronic devices increase in functionality, heat flux densities may reach the limits of passive cooling, rendering a choice between a compromise in performance or the development of the current cooling techniques to enhance cooling power; the latter being an objective of the current study. The cooling solution designs examined in the current study are aimed at the aforementioned electronic devices, and in general, portable devices of 10 mm or less in profile.

Although there is a general shortfall of literature addressing implementation of forced air cooling into portable electronic devices, some experimental studies were previously considered by the authors in this area [5–7], where cooling solutions are examined with profile heights under 10 mm. The first of these studies [5] highlighted the importance of combined fan and heat sink designs, as higher flow rates did not always yield higher performance. Instead, optimum performance was achieved for particular fan blade and heat sink fin arrangements. A similar study [6] on a radial finned heat sink centered around a radial blower in the absence of a volute compliments the previous findings. A number of blade designs were analyzed and the effect of aligned or impinging flow on fins were evaluated. Results showed that optimum performance was attained when blade and fin angles were set so that impinging flow was eliminated, i.e., flow leaving fan blades were aligned with heat sink fins. Also investigated in this study was the effect of the rotor diameter within a set cooling solution volume. It was found that heat sink performance remained largely unchanged while varying the rotor diameter, and inversely varying the heat sink surface area. As a result, the concept of an optimum coefficient of performance was introduced since smaller fans require considerably less pumping power. This suggests that an ideal solution can be achieved, which will adequately deal with the thermal loads in portable electronic devices and lead toward more energy efficient solutions.

Egan et al. [7] analyzed one of the smallest commercially available centrifugal fans having a footprint area of 256 mm^2 and 5 mm profile height, in conjunction with custom made finned and finless heat sinks. The results showed that heat transfer enhancements using the simple finless design at the miniature scale could be achieved over that of the conventional finned design at lower fan speeds. Particle image velocimetry was also used to obtain the velocity profile within the heat sink channels. A study, which followed on from this work [8], analyzed the possible enhancements that could be achieved through alignment of the fan exit flow and the heat sink channels using diffusers. This was addressed using particle image velocimetry, and an optimized diffuser design was selected so that flow was aligned with the heat sink fins and within

[1]Corresponding author.

Contributed by the Heat Transfer Division of ASME for publication in the JOURNAL OF HEAT TRANSFER. Manuscript received July 29, 2009, final manuscript received January 26, 2010; published online June 29, 2010. Assoc. Editor: Roger Schmidt.

the finless channel. The results showed that the finless heat sink outperformed the dimensionally similar finned heat sink design for the majority of fan speeds examined. Added benefits of lower manufacturing cost, reduced fouling issues, and lower weight were highlighted, making the finless design a preferable solution for the cost driven and energy conserving portable electronics market. The finless concept for low profile electronics cooling was first introduced by Walsh [9] as a possible alternative to conventional forced convection finned geometry designs.

The current study considers both finned and finless heat sink designs combined with a larger scale radial blower. The previous studies [7,8] experimentally examine a single profile design; however, the focus herein is on analyzing a number of different heat sink profiles ranging from 1 mm to 4 mm. The objective is to determine the impact of this profile scaling on the performance of both designs. Additionally, a theoretical approach is also implemented, which has not been considered in the previous works [7,8]. Specific emphasis is placed on highlighting the cross over criteria in design choice from the conventional finned design to a preferred finless design using both experimental and theoretical analyses. Subsequently, a design optimization tool that allows designers to predict heat transfer performance is introduced and validated through experimental measurements.

2 Theory

This section describes the theoretical approach for the prediction of heat sink performance. The thermal and overall system performance are defined and developed using a solution for laminar forced convection heat transfer and heat exchanger theories. The conventional heat exchanger theory has been adapted for use with single-fluid heat sink geometries.

2.1 Flow Configuration. The flow configuration within the majority of heat sinks reflects simultaneously developing hydrodynamic and thermal boundary layers, and is particularly evident in the current study where a radial fan or blower is positioned adjacent to the heat sink channels. Optimization relies on this consideration, as high heat transfer rates are achieved in the thermally developing flow region. Analytical and experimental solutions for such flow conditions in compact heat exchangers were considered in the literature [10]. This study utilizes a model developed for predicting heat transfer coefficients in noncircular ducts with simultaneously developing hydrodynamic and thermal boundary layers [11]. The individual channels of the finned and the finless heat sink geometries are representative of rectangular ducts. For a rectangular duct and an isothermal boundary condition, the dimensionless heat transfer is defined as [11]

$$\mathrm{Nu}_{\sqrt{A}} = \left[\left(\frac{2f(\mathrm{Pr})}{\sqrt{L^*_{\sqrt{A}}}} \right)^m + \left(\left\{ 0.6135 \left(\frac{f\,\mathrm{Re}_{\sqrt{A}}}{L^*_{\sqrt{A}}} \right)^{1/3} \right\}^5 + \left\{ 3.24 \left(\frac{f\,\mathrm{Re}_{\sqrt{A}}}{8\sqrt{\pi} \in^{1/10}} \right) \right\}^5 \right)^{m/5} \right]^{1/3} \tag{1}$$

where $f(\mathrm{Pr})$, $f\,\mathrm{Re}_{\sqrt{A}}$, $L^*_{\sqrt{A}}$, and m are defined in Ref. [11]. The duct aspect ratio $\in$ is b/a. The mean heat transfer coefficient can be resolved using its relationship with the Nusselt number

$$h = \frac{\mathrm{Nu}_{\sqrt{A}} k_f}{\sqrt{A}} \tag{2}$$

The system characteristics can also be predicted through the relationship between the pressure drop across the channel and the shear stress or frictional effects

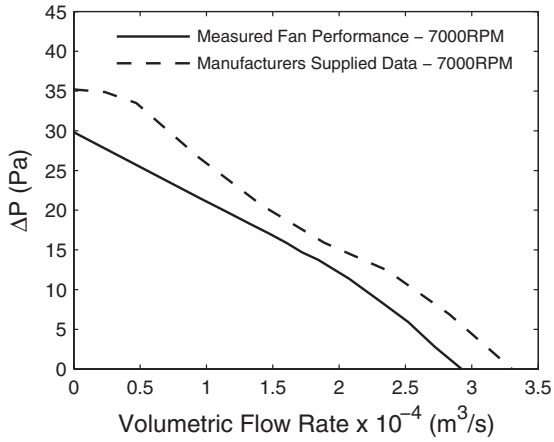

Fig. 1 Fan performance curve at fan speed of 7000 rpm

$$\Delta P = \frac{\dot{m}}{n} \left[\frac{1}{2} \frac{f_{\mathrm{app}}\,\mathrm{Re}_{\sqrt{A}} P L \mu}{\rho A^{5/2}} \right] \tag{3}$$

where $f_{\mathrm{app}}\,\mathrm{Re}_{\sqrt{A}}$ is the apparent friction factor Reynolds number also defined in Ref. [11]. Equation (3) is valid for both finned and finless geometries, where n denotes the number of channels in the heat sink. For the finless cases, this equates to 1.

2.2 Heat Exchanger Theory. Heat exchanger design primarily addresses both heat transfer and fluid pumping power required to overcome friction within the exchanger for multiple fluid applications. The heat transfer analysis here is addressed using the effectiveness-number of transfer units (ε-NTU) method. The heat transfer for a single-fluid forced convection heat sink is [12]

$$Q = \dot{m} Cp (T_w - T_i)[1 - e^{(-hA_{\mathrm{conv}}/\dot{m}Cp)}] \tag{4}$$

The experimental analysis provides the heat transfer performance using the inlet temperature difference method. Similarly, the heat transfer coefficient for the prediction model can be represented as

$$h_{\mathrm{ITD}} = \frac{Q}{A_{\mathrm{conv}}(T_w - T_i)} \tag{5}$$

Also, h_{ITD} can be used to determine the dimensionless heat transfer based on inlet temperature difference

$$\mathrm{Nu}_{\mathrm{ITD}} = \frac{h_{\mathrm{ITD}} D_h}{k_f} \tag{6}$$

where D_h is the hydraulic diameter ($4A/P$) of the heat sink channel and k_f is the thermal conductivity of air.

3 Experimental

The current section is structured to describe first the heat sink and fan design. The heat transfer experiments, pressure and flow rate characteristics, and finally, uncertainty in the results are then discussed.

The fan tested for the present study is the Sunon B0535ADB2-8 radial flow fan. This has a footprint area of 1225 mm^2 [35 $\times$ 35 mm^2] and a profile height of 7 mm. The pressure and flow rate data used to characterize the fan at the nominal operating speed of 7000 rpm is presented in Fig. 1. The manufacturer's supplied data [13] is shown along with an experimentally measured performance curve for the same rotational speed, acquired using a test facility designed in accordance with BS848 [14]. A calibration of this facility was previously performed determining the relationship between flow rate and pressure drop, and is detailed in Ref. [15].

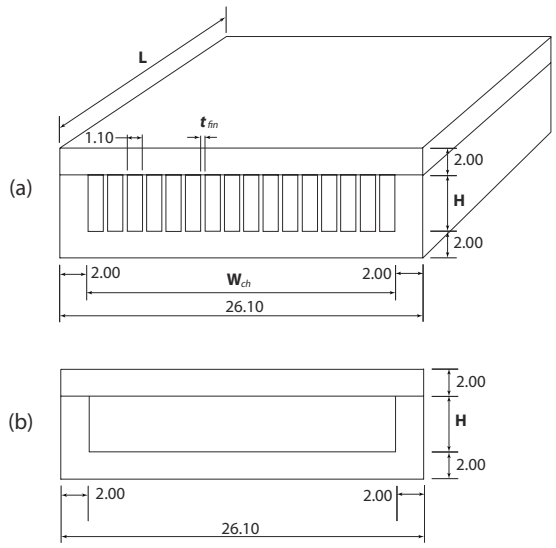

Fig. 2 Schematic of (*a*) finned and(*b*) finless heat sink designs showing the common dimensions along with the varied parameters *H* and *L*. Dimensions in millimeters.

Fan performance was measured across the range of speeds examined in this study from 3000 rpm to 11,000 rpm. The manufacturer's stated performance at 7000 rpm was scaled using conventional fan scaling laws [16] to acquire the performance directly available to the designer over this range also. These laws are defined as

$$\dot{Q} \propto \omega \tag{7}$$

$$\Delta P \propto \omega^2 \tag{8}$$

In Fig. 1, the supplied data predicts a fan performance of approximately 10–15% greater than that measured for the same fan speed. The current study utilizes both the experimentally measured and supplied data to predict heat transfer performance, highlighting any discrepancy when using the available data provided by the manufacturer.

In order to quantify the influence of profile height on the combined fan-heat sink cooling solutions, a range of finned heat sinks were designed based on dimensions shown in Fig. 2(*a*).

Three profiles were selected based on fin heights of 4 mm, 2 mm, and 1 mm. The largest profile dimension equates to the standard height of the fan outlet. Fin spacing was also set at 1.1 mm for each finned heat sink examined. Fin thickness was optimized to ensure fin efficiency greater than 99% [17].

Using copper as the heat sink material, this was achieved when the fin thickness was greater than 0.135 mm. The manufacturing technique, however, required this dimension to be at least 0.3 mm, resulting in a more than adequate fin thickness for all three designs. In addition to the finned heat sink designs, dimensionally alike finless geometries were comparatively examined with the conventional finned geometries. This design is presented in Fig. 2(*b*).

The heat sink length was chosen relative to the profile height to cover a wide range of flow conditions from thermally and hydrodynamically developing to a predominantly fully developed flow pattern within the heat sink channels. Hence, as the profile height decreases, the channel length is increased. Although not optimum for each case, these dimensions were chosen to allow a more complete theoretical validation of the problem by spanning three orders of magnitude of L^*_{Dh}, the dimensionless thermally developing coordinate. The 4 mm profile designs are shown in Fig. 3. The top covers that confine the flow, preventing any bypass during experiments have been removed for illustration purposes to distinguish the heat sink geometries. End views of each cooling solution are presented in Fig. 4, clearly showing the reductions in the channel height considered, and also defining the corresponding channel lengths.

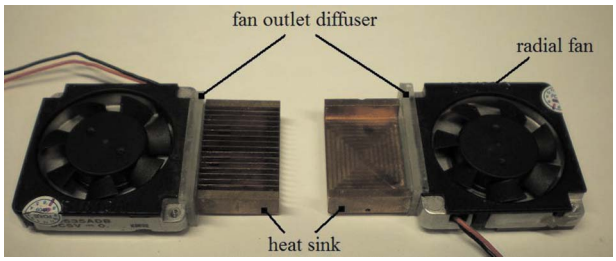

Fig. 3 Finned (left) and finless heat sink designs

As previously mentioned, the fan outlet has a height of 4 mm, equaling the largest profile heat sink inlet from Fig. 4. In order to direct all the flow from the fan into the smaller heat sinks of heights 2 mm and 1 mm, and prevent any bypass effects, diffusers were manufactured to downsize the blower outlet to the appropriate heat sink channel height. Although not required for the heat sinks with a 4 mm channel height, a diffuser was also used during experimentation so the developing length between the fan blade tip and heat sink entrance was equal for all cases. This diffuser, indicated in Fig. 3, was manufactured from polycarbonate and also prevented conduction from the heat sink to the die-cast aluminum frame of the fan housing.

3.1 Thermal Resistance. The 4 mm profile cooling solutions are shown in Fig. 3. The fan was powered using a DC power supply for a range of speeds between 3000 rpm and 11,000 rpm. Fan speed was measured and monitored during experiments using an optical tachometer. The heat sources used for each heat sink were thin-film polyimide heaters, attached to the base and sized to closely match the base footprint area. In doing so, heat spreading effects could be minimized. The heat sink temperature was monitored using K-type thermocouples, embedded in the base and side of the heat sink, and also attached to the top cover of the heat sink. Another K-type thermocouple was used to record the ambient air temperature. All thermocouples were connected to a National Instruments 9211 High Speed USB Carrier and temperatures were logged using LABVIEW 8. The experiments were undertaken for an almost isothermal boundary condition, as a maximum temperature difference between heat sink walls of approximately 3% was noted.

In electronics cooling, the most widely used thermal performance indicator is thermal resistance based on inlet temperature difference, defined in Eq. (9) as

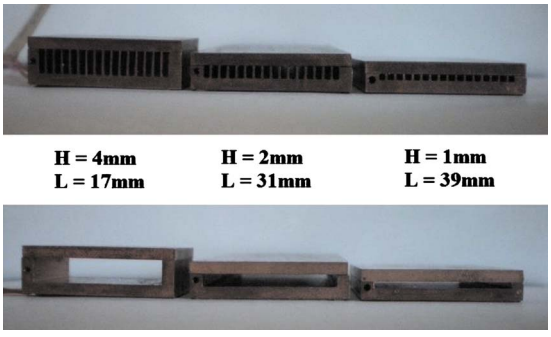

Fig. 4 Finned (top) and finless heat sinks showing reductions in profile height

$$R_T = \frac{(T_w - T_i)}{Q_{\text{input}}} \tag{9}$$

In the above expression, Q_{input} is the power supplied to the thin-film heater, T_w is the steady state wall temperature, and T_i is the ambient inlet air temperature. The wall temperature was calculated by averaging the temperature readings recorded over the entire heat sink.

Equation (9) considers the total thermal resistance of the heat sink. The power dissipated through forced convection is independent of the application. Consequently, it is of interest to account for losses due to secondary heat transfer mechanisms

$$R_{FC} = \frac{(R_T)(R_{\text{Losses}})}{(R_{\text{Losses}} - R_T)} \tag{10}$$

All experiments were conducted at a constant temperature difference of 45 K between heat sink and ambient air. Measuring the losses was achieved by setting the fan speed to 0 rpm, where $Q_{FC}=0$, and blocking both heat sink ends with insulation to prevent any flow due to natural convection from exiting the heat sink surfaces where forced convection is apparent during normal operation. The maximum contribution of secondary cooling mechanisms was evident for the 1 mm profile heat sinks, where $R_{\text{Losses}}=23$ K/W. These designs have the largest surface area where natural convection and radiation occur.

The forced convection heat transfer coefficient based on inlet temperature difference is calculated using Eq. (10), and presented below as

$$h_{\text{ITD}} = \frac{1}{R_{FC} A_{\text{conv}}} \tag{11}$$

The experimental Nusselt number can be calculated using Eq. (6).

3.2 System Characterization. Heat transfer measurements alone cannot describe the overall performance of a cooling solution. Knowing the pressure drop across a heat sink and pumping power required to dissipate adequate heat are essential for optimization and design selection. Flow rates and pressure drop were measured for each heat sink over the range of fan speeds examined using the same test facility designed to BS848 in Ref. [14] and discussed in this section previously. The theory of operation and schematics of this test facility are presented in Refs. [6,15] and are not discussed in this study.

3.3 Uncertainty. The influence of measurement uncertainties on the calculated results previously discussed has been accounted for using an uncertainty analysis [18]. This uncertainty analysis is based around a worst case combination approach, evaluated through the use of

$$\delta W = \begin{Bmatrix} (W_{X1+\delta X1} - W_{X1})^2 + \\ (W_{X2+\delta X2} - W_{X2})^2 + \dots \\ (W_{XN+\delta XN} - W_{XN})^2 \end{Bmatrix}^{1/2} \tag{12}$$

where each $W_{X+\delta X} - W_X$ term defines the result as a function of an independent variable. The uncertainty in the measured values of voltage, current, temperature, length, and pressure were estimated as 5 mV, 5 mA, 0.5 K, 50 μm, and 5% of the measured pressure. All measurements recorded were analyzed using this approach to determine the largest variance. This resulted in the examination of 36 samples. The relative uncertainty is calculated by

$$u_w = \frac{\delta W}{W} \tag{13}$$

Consequently, the maximum uncertainties in the forced convection thermal resistance, Nusselt number, volumetric flow rate, and L^*_{Dh} were found to be 5.3%, 5.31%, 2.3%, and 2.8%, respectively. The optical tachometer used for measuring the fan rotor speed has an accuracy related to the resolution limit of 1 rpm. For the entire speed range considered however, uncertainty in the fan rotational speed was noted as approximately 50 rpm, due to variations in the speed monitored over the test duration. As all maximum uncertainties in the results are below 5.5%, experimental error bands have been neglected when presenting the data.

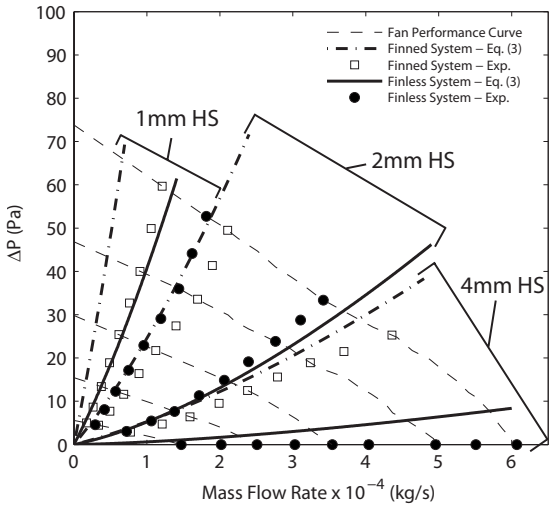

Fig. 5 Heat sink performance curves

4 Results and Discussion

The main objective of this study is to quantify the influence on heat transfer due to profile scaling of finned and finless forced convection heat sinks and define the parameters where a finless design can be a beneficial design choice. Optimization at the low profile scale has been considered experimentally using thermal resistance and flow rate measurements, and is presented in this section. Additionally, a useful design optimization tool, using a laminar duct flow heat transfer model [11] and heat exchanger theory, is used to compare with the experimental results and provide a predictive technique for the thermal engineer. Pressure and flow rate characteristics are presented first, followed by thermal resistance measurements of each heat sink design investigated. Finally, optimization and geometry choice are deciphered with the associated dimensionless parameters to allow a generalization of the finned versus finless approach.

The performance curves depicting mass flow rate through the heat sink, and pressure drop across the same, are presented in Fig. 5 for each profile examined. Measured fan characteristic curves for a range of speeds are also displayed, and expressed in terms of the mass flow rate. The pressure drop across each heat sink system at each operating point is predicted to within 10% over the entire speed range, except for the 4 mm profile finless heat sink, which does not register any significant pressure drop experimentally. This is due to the lack of resistance in the heat sink geometry as it attributes the same channel dimensions as the fan outlet dimensions and only 17 mm in length.

For the majority of heat sinks tested, pressure drop is overpredicted with the exception being for the 2 mm profile finless heat sink, which underpredicts for fan speeds above 5000 rpm to a maximum 6% deviation. This overprediction in pressure drop influences the expected mass flow rates considerably for high system resistance heat sinks such as the 1 mm finned heat sink, where a 10% deviation in pressure drop between the prediction and experimental data leads to a reduction in the predicted mass flow rate of almost 50%.

Due to the contracting effects of reduction in the fan outlet from 4 mm down to 1 mm in height, it was initially expected that the experimental performance curves would show a higher pressure

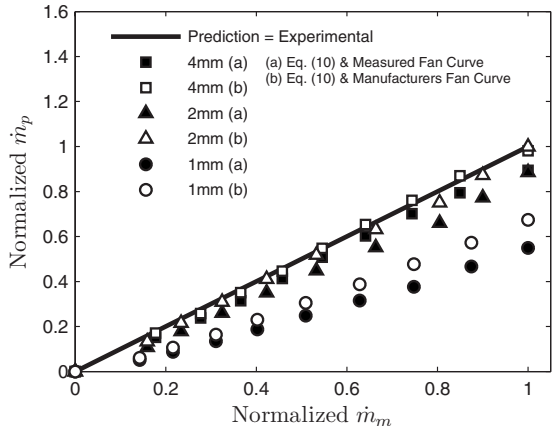

Fig. 6 Normalized finned heat sink mass flow rates showing predictions based on measured and manufacturers fan performance data

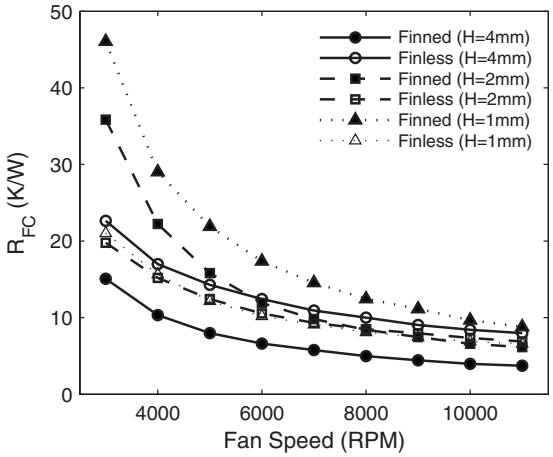

Fig. 7 Finned and finless heat sink thermal resistances

drop than the predicted model as the additional drop in pressure due to this contraction is not included in Eq. (3). As previously discussed, the difference in the pressure drop between predicted and experimental is almost the same for all examples, including the 4 mm profile finned heat sink, which does not contract the fan outlet. Consequently, the influence of this contraction appears to be negligible relative to the overall pressure drop across the heat sink.

The difference in predicted and measured flow rate for the finned heat sinks is displayed in Fig. 6. The data for each profile considered has been normalized with the respective maximum measured flow rates at 11,000 rpm. Two predictions have been compared with the actual mass flow rate measured through each heat sink. One prediction defines the operating points when using Eq. (3) and the measured fan performance curves. The other defines the predicted operating points using Eq. (3) and the manufacturer supplied fan performance data, which is directly available to the thermal designer.

As previously mentioned with reference to Fig. 5, as system resistance increases, the deviation between the expected flow rate and the measured data also increases. This is clearly distinguished in Fig. 6 as both predictions for the 4 mm profile fit the measured data with relatively minor differences. As the profile height decreases and channel length increases however, the underprediction of the mass flow rate increases, a pattern that is also noted for the finless cases but at a lower magnitude due to the low system resistance of the finless design. The deviation between both prediction models is never above 13% of the maximum flow rate for each profile, and is closer to 5% for the majority of fan speeds. This difference is caused from the overprediction of fan performance by the manufacturer, described previously through Fig. 1.

The effect of the fan rotational speed on the forced convection thermal resistance is presented in Fig. 7 for heat sink profile heights of 4 mm, 2 mm, and 1 mm, respectively. For the 4 mm profile, the finned heat sink clearly outperforms the finless alternative over the entire speed range. However, Fig. 9 also shows that as the fan speed decreases, the performance trend of the finless heat sink is increasing, relative to the finned design. At 11,000 rpm, the finless heat sink has a 53% higher thermal resistance but decreases to approximately 33% at the minimum speed of 3000 rpm considered.

The thermal performance of the 2 mm profile height finned and finless heat sinks are also presented in Fig. 7. Through the change in profile height and heat sink length, a different trend has emerged. At the lower speeds between 3000 rpm and 7000 rpm, the finless heat sink outperforms the finned comparison by up to 45%. At approximately 7600 rpm however, this increase diminishes and there is a cross over in geometry selection. The use of the finned heat sink produces lower thermal resistance for the remainder of speeds considered. This indicates the importance of the relevant design parameters on heat sink choice such as fan performance over the intended operating range and dimensional constraints. The benefits of using the finless design is shown when operating in the 3000–7000 rpm range. In order to achieve the same finless thermal resistance, at a given speed, using the conventional finned geometry, an increase of approximately 1000 rpm is required. This increases both the pumping power requirement and noise, while also decreasing the fan or blower reliability.

The influence of a further decrease to a 1 mm profile height provides a similar conclusion. The lowest thermal resistance achieved at 11,000 rpm using the finned design can be equaled at approximately 7000 rpm using the finless design. An important design consideration particularly in portable electronic devices is power usage. The fan required 0.31 W to operate at 7000 rpm, and 0.86 W at 11,000 rpm. Therefore, the combined finless cooling solution can achieve 9 K/W at 35% of the power input required to achieve the same, using the combined finned cooling solution at this scale.

Figure 8 presents the Nusselt number based on the inlet temperature difference, Eq. (6), which provides the heat transfer data of Fig. 7 in a concise form. The hydraulic diameter is chosen as the characteristic length scale as it results in each heat sink aspect ratio to collapse to one line predominantly, with a small spread as the flow transitions from the developing to fully developed condition. This can be described simply using two asymptotes to denote these flow conditions. Heat transfer in the developing flow region can be described using a model presented by Sparrow [19] for laminar forced convection in the entrance region of flat rectangular ducts. This was selected as it best fits the experimental data over the transitional region. The fully developed asymptote is formed from an energy balance in the limit of very long ducts, where the fluid outlet temperature asymptotically approaches the wall temperature for an isothermal wall condition. Combining both asymptotes using the Churchill and Usagi [20] asymptotic correlation method gives

$$\mathrm{Nu}_{\mathrm{ITD}} \approx \left[(4L_{Dh}^{*})^3 + \left(\frac{1}{\frac{0.664}{\sqrt{L_{Dh}^{*}}\,\mathrm{Pr}^{1/6}}\left[(1 + 7.3(L_{Dh}^{*}\,\mathrm{Pr})^{1/2})^{1/2}\right]} \right)^3 \right]^{-1/3} \tag{14}$$

The asymptotic correlation of Eq. (14) indicates a transition to the fully developed flow condition at $L_{Dh}^{*} \sim 0.1$. The experimental data show good agreement over the range of L_{Dh}^{*} considered. However, for the 4 mm and 2 mm profile finless heat sinks as L_{Dh}^{*} decreases the deviation in the experimental Nusselt number in-

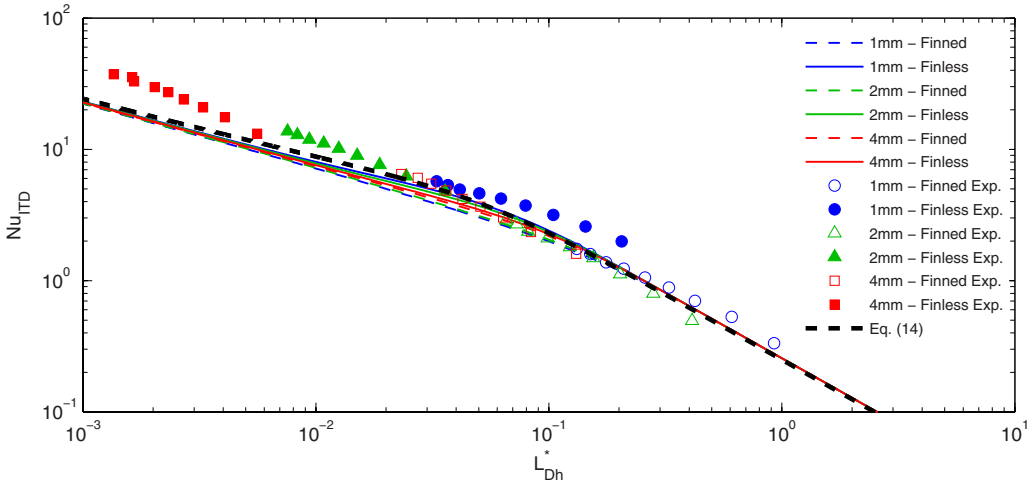

Fig. 8 Forced convection Nusselt number, based on the inlet temperature difference, in both the entrance and fully developed region of an isothermal heat sink

creases over the expected result. Conversely, as L^*_{Dh} increases for the 1 mm finless profile, higher Nusselt numbers were measured compared with those predicted. This is indicative of a delayed onset to fully developed flow, which results in higher heat transfer. This suggests that flow patterns created due to the combination of this fan and a larger flow area in the finless design are enhancing heat transfer. The larger flow area of the finless design does not confine the flow to the longitudinal direction as rapidly as the finned channels. This has been shown previously by Egan et al. [7], where the fan exit flow was redirected longitudinally much sooner for a finned geometry than in a finless geometry. Consequently, the flow pattern in the finned channels achieves a structured flow similar to a laminar parabolic profile before the heat sink exit. This provides reason for the agreement in Fig. 8 between the finned heat sinks and theory. It is therefore difficult to accurately predict the finless performance as it is highly dependent on fan exit flow characteristics, reinforcing the need to develop both fan and heat sink as a combined cooling solution rather than separately as is largely the case.

The ratio of heat transfer between dimensionally alike finned and finless geometries can be used to determine a suitable design and is represented in Eq. (15) below. The heat dissipated Q is based on the experimental conditions of a constant temperature difference of 45 K between heat sink and inlet air temperatures

$$Q^* = \frac{Q_{\text{finned}}}{Q_{\text{finless}}} \tag{15}$$

For example, when $Q^* < 1$, the finless heat sink provides a higher heat transfer rate than the finned heat sink design, and should be the preferred choice for the designer. Q^* can therefore quantify the relative enhancements and reductions in heat transfer performance for both designs. In Fig. 6, the deviation between two mass flow rate predictions, one using Eq. (3) and the measured fan performance, and the other using Eq. (3) and the scaled manufacturer stated fan performance, is presented. The resultant information using the latter of these two predictions for both finned and finless geometries is used to calculate one of the heat transfer predictions labeled in Figs. 9–11. The other heat transfer prediction in Figs. 9–11 is calculated using the measured flow rate through the heat sink, described by the experimental data points in Fig. 5.

Also included is Q^*_{max}, the maximum theoretical Q^* for each fan speed, or flow rate, using the manufacturer's fan performance data. This was achieved by determining the optimum finned heat sink design, which maximized heat transfer performance for an unrestricted fin thickness and fin spacing, where $n \approx HW_{\text{ch}}/ab$. The data is presented against fan rotational speed to deduce the dependency of heat transfer enhancements on rotor speed as opposed to fluid pumping power. Although system performance, Eq. (3), is described in terms of pumping power, fan performance is

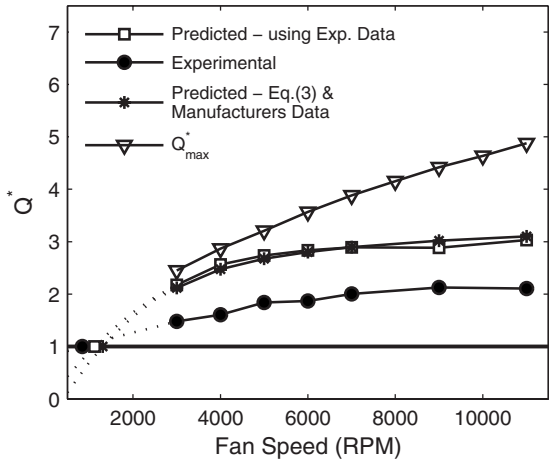

Fig. 9 Ratio of heat transfer rates—*H*=4 mm

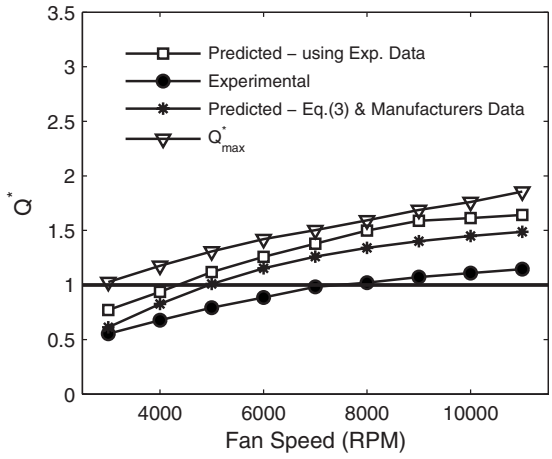

Fig. 10 Ratio of heat transfer rates—*H*=2 mm

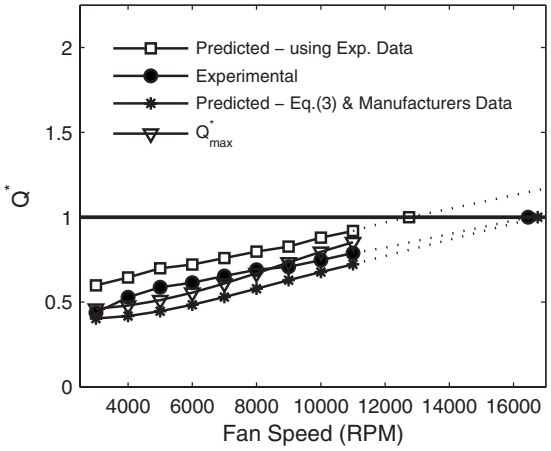

Fig. 11 Ratio of heat transfer rates—*H*=1 mm

relative to fan rotational speed, as shown in Eqs. (7) and (8), and a more suitable choice to compare the attributes of the finned and finless heat transfer ratio.

Previous literature shows that optimization of parallel plate spacing occurs when the plate length is the same order of magnitude as the thermal entrance length [21]. This occurs at $L^*_{Dh} \sim 0.1$. The experimental transition from finless geometry to finned geometry, where $Q^*=1$ in Fig. 10, occurs at this point. Extrapolating the 1 mm profile data in Fig. 11, this transition also occurs at a similar L^*_{Dh} position. The 4 mm profile case cannot be considered in the same manner, as the finless heat sink Nusselt number is at much lower L^*_{Dh} values than the transitional region, and subsequently, is not optimized for any fan speed considered. The 4 mm finned and 1 mm finless heat sinks have been shown to outperform their alternate geometries for the range of fan speeds examined. The range of L^*_{Dh} for both is similar and is spread across the transitional region, $0.02 \leq L^*_{Dh} \leq 0.2$, from developing to fully developed thermal boundary layers. This region also contains the 2 mm profile results, where the finned heat sink is beneficial, and where the finless heat sink is the preferred design choice. Consequently, increased thermal performance can be achieved over a large range of fan speeds by operating in the transitional region stated.

For all profiles examined, the experimental ratio indicates that a cross over at $Q^*=1$ from finless to finned design will be incorrectly predicted using the measured flow rates. The premature cross over prediction shown in Figs. 10 and 11, and based on the actual mass flow rates, reinforces the conclusions from Fig. 8 that flow patterns promoted within the larger flow area finless heat sink, due to the air delivery from the blower, are in fact enhancing the heat transfer rates of the finless design. The extended data in Fig. 9 for the 4 mm profile design prediction displays a cross over that is almost the same when compared with the experimental heat transfer measurements. However, the remainder of fan speeds considered confirms that the ratio of heat transfer is overestimated with both predictions based on measured flow rates and the supplied fan data. The predicted and experimental cross over is clearly shown in Fig. 10 for the 2 mm profile case. Measured heat transfer rates show that below 7600 rpm, the finless design will start to outperform the finned heat sink. The value predicted using the experimental flow rate data, however, is much lower at 4400 rpm, suggesting that in the design of forced convection cooling solutions at this scale, the performance attributes of the finless design can be underestimated. The same is apparent when comparing the prediction model using the manufacturer's data available to the designer. In this case, a cross over fan speed of $\sim$5000 rpm is anticipated. The nominal operating speed stated by the fan manufacturer is 7000 rpm. The predicted heat transfer ratio using the manufacturer's data in Fig. 10 suggests that by operating at this speed, the finned design outperforms the finless design by 25%, a margin, which could clearly distinguish the choice of geometry to the designer. In reality, however, the finless design is at a similar level of heat dissipation.

The heat sink length also varies according to profile height to provide a wide range of flow conditions. This influences the difference in experimental and predicted ratios in heat transfer. In Fig. 9, over the range of speeds examined for the 4 mm profile heat sinks, there is a mean difference of 47% between the predicted ratio using experimental flow data and experimental ratio. However, for the 2 mm profile height presented in Fig. 10, a pattern begins to emerge that relates the fan rotational speed with the deviation in predicted and experimental data. As fan speed increases, this deviation begins to increase from 38% at 3000 rpm up to 45% at 11,000 rpm. Considering the 1 mm profile height, the information based on experimentation presented in Fig. 11 produces almost parallel offset curves, and as a result, the deviation between the predicted ratio and experimental ratio varies as a percentage relative to fan speed. At 3000 rpm, the enhancement produced in the finless design is much greater than predicted, resulting in a deviation of 36%. This difference begins to reduce almost linearly above 5000 rpm to approximately 15% at the highest speed. The decrease in flow area for both geometries, combined with an increase in length over the previous profile examples, allows the flow to reach a more stable developed form before exiting the heat sink. Hence, a closer representation of the flow profile used in the development of the prediction model. The prediction using the theoretical model with the manufacturer's data is much lower than that predicted using the measured flow rates. This is related to the system performance of the 1 mm profile designs in Fig. 5. The relatively small discrepancy in pressure difference between theory and measured, results in a large discrepancy in flow rate. Consequently, the lower capacitance rate envisaged theoretically produces a lower heat transfer rate. A similar discrepancy between theoretical and measured pressure difference for the 4 mm profile in Fig. 5 have a lesser influence on the capacitance rate. Hence, both predicted heat transfer rates are similar, as shown in Fig. 9.

The geometry selection can also be decided based on the above information. As previously mentioned, the theoretical model underpredicts the heat transfer for the finless heat sink, however, the dimensionless thermal entry length will be predicted close to the actual values based on the lower system resistance curves of the finless designs in Fig. 5. The designer can therefore create a suitable finless geometry to fall in the transitional L^*_{Dh}, knowing that it will outperform an alternate finned design of like dimensions. A useful design tool given the dimensional constraints in many portable devices combined with the simplicity of the finless design. The adverse of course applies if a finned design is optimized, as seen for the 4 mm profile in this study; however, for low profile portable devices, the simple finless concept can prove effective in removing adequate heat with a lower manufacturing cost, reduced weight, and reduced fouling issues.

5 Conclusion

The influence of profile height on low profile forced convection cooling solutions has been examined. The experimental findings showed that as the heat sink profile decreases, benefits in heat transfer performance can be achieved by implementing a finless design as opposed to the conventional finned designs. The flow configuration within the heat sink was represented by a model for predicting heat transfer in the combined entry region of a rectangular duct. The experimental data showed that higher heat transfer rates were evident over those predicted due to the flow patterns created with the radial flow fan and the larger flow area finless designs. Deviations resulting from the use of the manufacturer's fan performance data with the prediction methods outlined have been highlighted. A performance enhancement criterion has been

presented for a forced convection heat sink that also adheres to low profile designs. Finally, the criterion for optimization observed agreed with that found in the literature, and the flow rates at which finless methodology is advantageous can be approximated using the theory presented.

Nomenclature

A = channel cross sectional area (m^2)
A_{conv} = forced convective surface area (m^2)
a = major channel dimension (m)
b = minor channel dimension, m
Cp = specific heat (J/kg K)
D_h = hydraulic diameter (m)
f = friction factor
$f(\mathrm{Pr})$ = function dependant on fluid Prandtl number
H = fin height, channel height (m)
h = average heat transfer coefficient (W/m^2 K)
k = thermal conductivity (W/m K)
L = heat sink length (m)
L^+ = hydrodynamically developing entrance coordinate
L^* = thermally developing entrance coordinate ($L^*_{\sqrt{A}} = \mu L/(\dot{m}/n)\mathrm{Pr}$)
m = correlation parameter
$\dot{m}$ = mass flow rate through heat sink (kg/s)
n = number of heat sink channels
Nu = Nusselt number
NTU = number of transfer units
P = perimeter (m)
Pr = fluid Prandtl number
ΔP = static pressure difference (Pa)
Q = heat transfer rate (W)
$\dot{Q}$ = volumetric flow rate (m^3/s)
Q^* = ratio of finned to finless heat transfer rate
Re = Reynolds number
R = thermal resistance (K/W)
T = temperature (K)
t_{fin} = fin thickness (m)
u_w = relative uncertainty (%)
W = result disregarding uncertainty in measured variables
W_{ch} = heat sink channel width (m)
δW = variance in the result

Greek Symbols

$\in$ = aspect ratio
ε = heat exchanger effectiveness
μ = dynamic viscosity (kg/m s)
ρ = density (kg/m^3)
ω = fan rotational speed (rpm)

Subscripts

app = apparent
finned = based on finned geometry
finless = based on finless geometry
FC = forced convection
i = inlet
input = input power
ITD = inlet temperature difference
Losses = secondary losses
max = maximum
T = total
w = wall
X = independent measured variable

References

[1] Copeland, D., 2000, "Optimization of Parallel Plate Heatsinks for Forced Convection," *Proceedings of the 16th IEEE Semi-Therm Symposium*.
[2] Xu, G., Guenin, B., and Vogel, M., 2004, "Extension of Air Cooling for High Power Processors," *Proceedings of the Ninth Intersociety Conference on Thermal and Thermomechanical Phenomena in Electronic Systems (ITherm)*, pp. 186–193.
[3] Loh, C. K., Nelson, D., and Chou, D. J., 2001, "Thermal Characterization of Fan-Heat Sink Systems in Miniature Axial Fan and Micro Blower Airflow," *Proceedings of the 17th IEEE Semi-Therm Symposium*.
[4] Copeland, D., 2005, "Review of Low Profile Cold Plate Technology for High Density Servers," Electronics Cooling, **11**(2), pp. 14–18.
[5] Walsh, E. J., and Grimes, R., 2007, "Low Profile Fan and Heat Sink Thermal Management Solution for Portable Applications," Int. J. Therm. Sci., **46**, pp. 1182–1190.
[6] Walsh, E., Walsh, P., Grimes, R., and Egan, V., 2008, "Thermal Management of Low Profile Electronic Equipment Using Radial Fans and Heat Sinks," J. Heat Transfer, **130**(12), pp. 125001.
[7] Egan, V., Walsh, P. A., Walsh, E., and Grimes, R., 2009, "Thermal Analysis of Miniature Low Profile Heat Sinks With and Without Fins," J. Electron. Packag., **131**(3), pp. 031004.
[8] Egan, V., Stafford, J., Walsh, P. A., and Walsh, E., 2009, "An Experimental Study on the Design of Miniature Heat Sinks for Forced Convection Air Cooling," J. Heat Transfer, **131**(7), pp. 071402.
[9] Walsh, E. J., 2006, "High Temperature Electronics and Thermal Management—Low profile Thermal Management," *Proceedings of the EPEC European Center for Power Electronics*, Sud-West Park Conference Center, Nuremburg, Germany, Nov. 9–10.
[10] Kays, W. M., and London, A. L., 1984, *Compact Heat Exchangers*, 3rd ed., McGraw-Hill, New York.
[11] Muzychka, Y. S., and Yovanovich, M. M., 2004, "Laminar Forced Convection Heat Transfer in the Combined Entry Region of Non-Circular Ducts," ASME J. Heat Transfer, **126**, pp. 54–61.
[12] Stafford, J., Walsh, E., Egan, V., Walsh, P., and Muzychka, Y. S., 2009, "An Experimental and Theoretical Study of Finned and Finless Heat Sinks for Low Profile Applications," *Proceedings of the ASME Summer Heat Transfer Conference*, San Francisco, CA.
[13] 1998, Sunon B0535ADB2-8 DC Brushless Blower Specification, Issue Date 08/28/1998.
[14] 1980, BS848: Fans for General Purposes, Part 1: Methods for Testing Performance.
[15] Grimes, R., Walsh, E., Kunz, S., Davies, M., and Quin, D., 2003, "Scaling the Performance of Micro-Fans," *Proceedings of the First International Conference on Mini-Microchannels*, Rochester, New York.
[16] Blieir, F. P., 1997, *Fan Handbook: Selection, Application and Design*, McGraw-Hill, New York.
[17] Ellison, G. N., 1989, *Thermal Computations for Electronic Equipment*, Krieger Publishing Company, Malabar, FL.
[18] Moffat, J. R., 1997, *Uncertainty Analysis in Thermal Measurements in Electronics Cooling*, K. Azar, ed., CRC, Boca Raton, FL, pp. 45–80.
[19] Sparrow, E.M., 1955, "Analysis of Laminar Forced-Convection Heat Transfer in Entrance Region of Flat Rectangular Ducts," NACA Technical Paper No. 3331.
[20] Churchill, S. W., and Usagi, R., 1972, "A General Expression for the Correlation of Rates of Transfer and Other Phenomena," AIChE J., **18**, pp. 1121–1128.
[21] Bejan, A., and Sciubba, E., 1992, "The Optimal Spacing of Parallel Plates Cooled by Forced Convection," Int. J. Heat Mass Transfer, **35**, pp. 3259–3264.

Momentum Conservation and Condensing Vapor Bubbles

I. Eames
University College London,
Torrington Place,
London WC1E 7JE, UK

Boiling is a common feature of many daily processes, such as making tea, cooking, and heating. The growth, rise, collapse, and final disappearance of vapor bubbles are ubiquitous features of nucleate boiling. New experimental observations show that a vortex is generated as a consequence of the bubble disappearing. We categorize the possible mechanisms that lead to the generation of a vortex by bubbles. When the bubble collapses but does not change topology, the vortex is created by viscous effects, where the attached wake behind the vapor bubble persists after the bubble has disappeared. But when the bubbles collapse so rapidly that they change topology, the vortex is created by an inviscid mechanism. The total momentum communicated to the flow by the collapse processes is calculated and compared with the measurements of the vortex impulse.
[DOI: 10.1115/1.4001604]

Keywords: boiling, heat exchange, momentum, vapor bubbles

1 Introduction

Boiling is a ubiquitous feature of many daily processes—making tea, cooking, and heating. The mode of boiling depends on the wall temperature and heat flux from the heating element. As the wall temperature increases, the mode of heat transfer changes from convection through to vapor bubbles, vapor columns, film boiling, and finally burn out. For wall temperatures above the saturation temperature, bubbles grow at nucleation sites. The life cycle of a vapor bubble starts with its growth at nucleation sites on a heating element, detaches (when the buoyancy and shear forces exceeds the surface tension anchoring it), decreases in size, and ultimately disappears as it rises into cooler ambient surroundings [1]. Through the extensive use of high speed photography and laser interferometery [2,3], the characteristics of such bubbles are well-documented, and good agreement has been obtained between various analytical models that describe the bubble size during growth and collapse. Most attention has been paid to the bubble detachment size, velocity, and thermal signature on the wall and in the fluid. A large number of researchers have techniques for generating single or streams of bubbles issuing from localized heating elements [4] or direct injection of vapor [3]. More recent works [5,6] have been successful in applying particle image velocimetry (PIV) to measure the flow around sliding bubbles or bubbles rising from a single nucleation site. Numerical techniques (using level-set, meshless models, and boundary fitted meshes) have been applied, leading to significant progress in understanding bubble dynamics [7].

The consequence of a vapor bubble disappearing due to condensation is profound. As the bubble accelerates due to buoyancy and added-mass forces, it communicates the momentum to the ambient fluid. After the bubble disappears it must necessarily leave behind a vortex in order for the momentum to be globally conserved, as argued conclusively by Benjamin and Ellis [8] for collapsing cavitating bubbles. The generation of this ghost vortex has largely been overlooked by the heat transfer community. How this vortex is generated depends on whether the vortex changes topology during its collapse process. Delmas and Angelino [9] reported one of the few studies of the effect of subcooling on the collapse shape, presenting a phase diagram to distinguish between stable rising and nonlinear rupture of bubbles, which is similar to the distinction of nontopological and topological collapses applied in this paper. Kalman [10] recently studied the thermal signature and wake structure of freon bubbles condensing in water and observed a vortex created during the collapse process. But the properties of the vortex, the explanation of its occurrence (when topological change does not occur), and its correlation to the action of the vapor bubble in a viscous fluid has not been studied in any detail. Part of the difficulty of understanding these processes is to quantify rigorously the momentum associated with the translation and disappearance of a moving deforming bubble in a viscous fluid. This difficulty arises because the heuristic definition of the momentum, as the integral of density weighted velocity over an infinite domain, is not absolutely convergence [11]. Some of the general features of the generation of a vortex by bodies moving and disappearing, applicable to fuel droplets evaporating, has been recently reviewed by Eames [12].

In the context of cavitation (see review of Plesset and Prosperetti [13]), the generation of a vortex as a consequence of a bubble collapse is well-known [14]. As the main interest tends to be cavitation damage, in most studies, bubbles are considered close to boundaries, which, due to the action of the Bjerknes force, leads to bubbles accelerating toward the wall with the direction of the penetrating tip directed toward the wall. Most theoretical studies involve an inviscid (boundary-integral) treatment, which, while globally conserving the momentum, use a mathematical cut in the computational domain (between the toroidal bubble lobes) that precludes their application to calculating the characteristics of the vortex following collapse [15]. More recent detailed numerical calculations permit the penetrating bubble tip characteristics to be analyzed fully [16].

The purpose of this paper is to analyze what happens after a vapor bubble has disappeared and (a) explain why a vortex must be generated and (b) identify the possible mechanisms that lead to its generation, and (c) the characteristics of the vortex (radius and speed of propagation) and impulse. In Sec. 2, the experimental methodology and observations are described. In Sec. 3, a series of mathematical models are introduced to explain these questions, before the experimental results are then linked. The conclusions are made in Sec. 5.

2 Experimental Observations

The experimental literature pertaining to the collapse of vapor bubbles in subcooled liquids is vast. The aim of the experiments the author described is to demonstrate the generation of a vortex following the collapse of a vapor bubble in water and to provide a

Contributed by the Heat Transfer Division of ASME for publication in the JOURNAL OF HEAT TRANSFER. Manuscript received March 25, 2008; final manuscript received February 11, 2010; published online June 23, 2010. Assoc. Editor: Milind A. Jog.

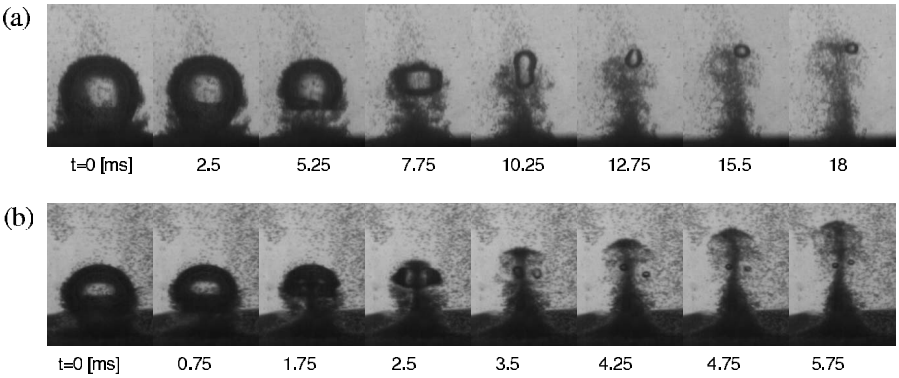

Fig. 1 Experimental observations of the collapse of a vapor bubble for collapse times (*a*) $t_c=0.014$ s and (*b*) $t_c=0.003$ s when $\Delta T=30$ deg

technique to measure the characteristics. The bubbles were generated by heating a metal plug of 0.4 cm in diameter, encased by a ceramic tube, made flush at one end. A tubular heater was attached to the metal plug. To visualize the wake and vortex, we performed our experiments using a 5 mm layer of unconsolidated glass ballotini particles with diameters of 30–80 μm, which were stirred and then sedimentated onto the bottom of a heating element. Fines were removed by decanting the water many times, and the water was boiled for a period of 20 min to remove most of the dissolved air. The sediment provided a means of visualizing the flow following the collapse process. The heating chamber was illuminated by a diffuse back light. The flow was recorded using a high speed camera (set at 4000 fps). The temperature of the ambient fluid was measured using a thermocouple. We analyzed the data from over a hundred bubble sequences determined.

2.1 Characteristics of the Bubble Collapse. The vapor bubble radius was measured from digitial images by determining the cross-sectional area A_b and the equivalent area radius $a_0=(A_b/\pi)^{1/2}$. The vapor bubbles are typically 0.2 cm in radius, slightly larger than those generated on a flat heater due to the effect of the sediment layer. Figure 1(*a*) shows a sequence following the emergence of a vapor bubble from the sediment layer for subcooling $\Delta T=30$ deg (defined as the difference between the water temperation and saturation temperature). The bubble is initially oblate and deforms during its collapse but does not change topology. This is typical of many reported experiments [3]. As the bubble moved forward, sediment is displaced forward in a manner reminiscent of the drift profiles observed for air bubbles rising through dye layers [17]. The bubble collapses in a time $t_c=0.014$ s and initially has a radius $a_0=0.19$ cm. Following the collapse of the bubble, a vortex is clearly observed, which initially grows to a constant size and moves vertically at a constant speed. The presence of the vortex was further highlighted by the dense sediment being thrown out of the vortex core. An air bubble is formed after the vapor bubble has condensed because the water was not completely degassed. At a later time, the sediment becomes detrained from the vortex as it settles.

For higher degrees of subcooling (or more rapid collapse), vapor bubbles are observed to undergo a topological change. Figure 1(*b*) shows a time sequence of a vapor bubble collapsing in a much shorter time $t_c=0.003$ s. The rear of the bubble accelerates through the front of the bubble, generating an intense jet. The bubble becomes toroidal and finally, because of the presence of dissolved air, two air bubbles are finally produced. We analyzed a large number of bubble collapse sequences and discriminated between when a topological change occurred or did not occur, and when the collapse was unclear.

2.2 Characteristics of the Vortex. From the sequence of the images, the size and position of the vortex were identified by interrogating a sequence of images using MATLAB's image processing toolbox. The cross-sectional area and centroid of the vortex were estimated by drawing a closed loop around the approximate edge of the vortex; the cross-sectional area (A_v) was calculated from the number of pixels within the closed loop (which was determined within an error of 10%) and the height from the average vertical position of the pixels within the loop. The vortex motion is very clearly seen in a movie sequence of the experiments, but more difficult to be visualized from individual images. An alternative approach to highlight the vortex was to use a PIV algorithm (MATPIV) applied to the image pairs, which examines the cross-correlation of intensity fields (caused by the sediment and bubble). Since the entire region near the bubble was illuminated, the results are more of a method to visualize the vortex, but no quantitative information can be drawn since the sediment is not passive. Figure 2 shows results from the PIV, where the vortex is clearly identified.

The height of the vortex above the center of bubble at the point of detachment h_v is plotted in Fig. 3(*a*) for the time after the bubble has condensed ($t-t_c$), for a number of bubble collapse. In all cases, the height of the vortex increases (approximately) linearly with time, indicating that the vortex is moving approximately with a constant velocity. The vortex translation velocity U_v was estimated using a linear least-squares fit to h_v, i.e., $h_v=U_v(t-t_c)+\text{const}$. The initial shape of the vortex appeared to depend on how it is created—when the bubble undergoes a topological change the vortex is created by the shear of the piercing jet passing through the top of the bubble. In this case, the vortex initially appears as a localized jet, whose width is much smaller than the bubble radius. When the bubble does not change topology, the vortex is created at the rear of the bubble and tends to be oblate. The vortex radius $R_v=(A_v/\pi)^{1/2}$ is plotted in Fig. 3(*b*), and is rendered dimensionless using the equivalent bubble radius a_0. After the vortex is created, it goes through an inviscid process of adjustment over at time scale $\sim R_v/U_v$. In the absence of external body forces (an assumption we discuss in more details in Sec. 3), the momentum or impulse of the vortex is conserved even when viscous effects are important. The impulse of a steady vortex moving in a straight line is

$$M_v=\rho_f(1+C_m)U_vV_v \tag{1}$$

where C_m is the added-mass coefficient of the vortex, V_v is the vortex volume ($=4\pi R_v^3/3$), and ρ_f is the fluid density. The vortex is assumed to be spherical so that $C_m=1/2$ and its impulse is

$$M_v=2\pi\rho_f R_v^3U_v \tag{2}$$

Both R_v and U_v can be measured, enabling M_v to be estimated.

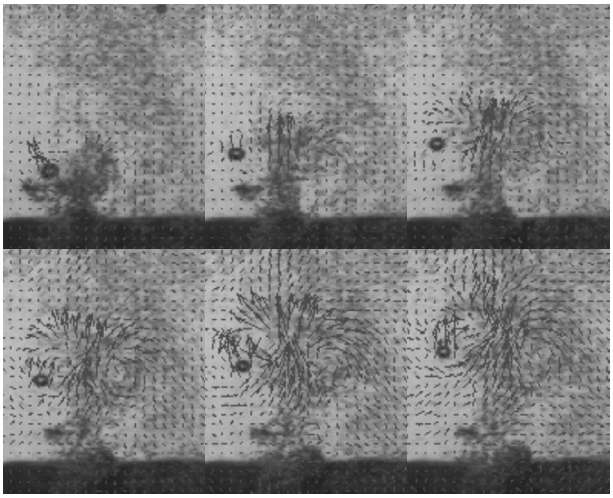

(*a*)

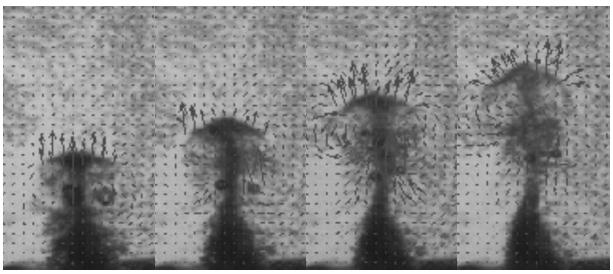

(*b*)

Fig. 2 Qualitative visualization of the vortex generated using PIV. The two examples are (*a*) a bubble of radius a_0 =0.136 cm, collapsing without a topological change in t_c =0.0055 s and (*b*) a bubble of initial radius a_0=0.167 cm collapsing in t_c=0.0058 s through a topological change.

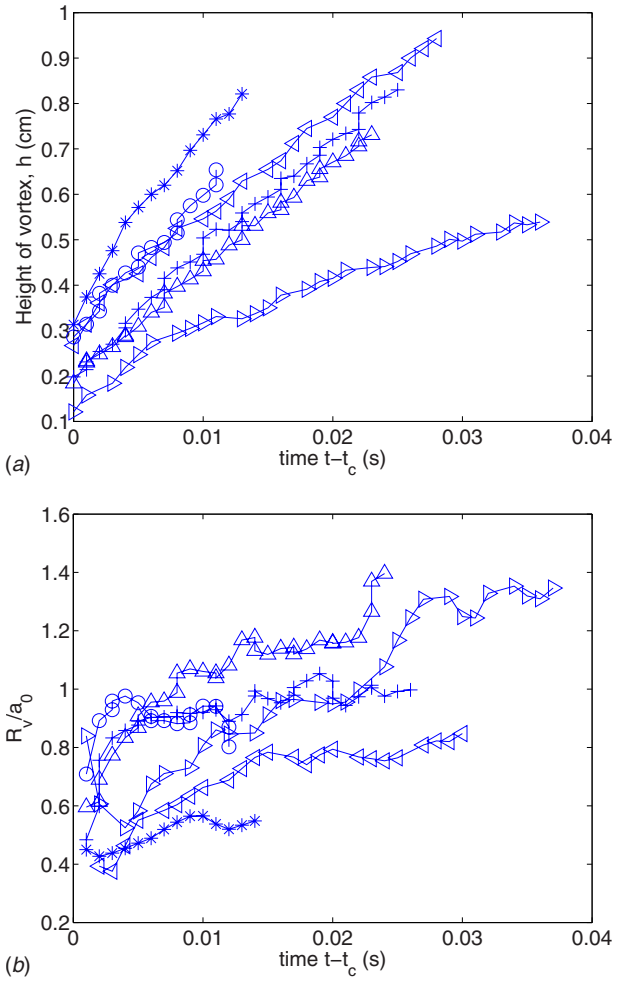

Fig. 3 Characteristics of the vortex generated: (*a*) height as a function of time and (*b*) radius as a function of time. The symbols corresponds to ○ (a_0=0.147 cm, t_c=0.011 s), + (a_0 =0.129 cm, t_c=0.050 s), ▷ (a_0=0.110 cm, t_c=0.048 s), ◁ (a_0 =0.163 cm, t_c=0.011 s), △ (a_0=0.0989 cm, t_c=0.0018 s), and ∗ (a_0=0.193, t_c=0.0073 s).

3 Mathematical Model

The purpose of the mathematical model is to explain why a vortex is created by a single bubble condensing and how the vortex is created, and then to provide a link between the models and experiments. Certainly the major results (why and how) are *independent* of the type of closure expressions used to describe the force on the bubble. The model used to describe the dynamics of a bubble depends on the semi-empirical closures for the drag coefficient and rate of bubble collapse, but is of a type which has been used many times before [16,18,10]. Implicit in our discussion in Secs. 3.2 and 3.3 is that the Reynolds number characterizing the bubble motion is high, so that the flow is inertially dominated.

3.1 Global Conservation of the Momentum: Why is the Vortex Generated? To build up a physical picture of the processes associated with bubble collapse, we first consider the simpler problem of a vapor bubble introduced into an unbounded fluid, and then rises and condenses. The bubble is assumed to be introduced, by injection or heating, and starts with an initial velocity $\boldsymbol{U}_0$. The bubble volume V decreases from its initially value V_0 and disappears in a time t_c after release, so that $V(t_c)=0$. The effect of vapor condensation introduces two additional contributions to the momentum equation—first, the condensation process introduces a weak momentum flux into the ambient fluid, but this can be ignored (and we justify this later). The second contribution arises because the ambient fluid is heated and changes density. This creates a buoyant parcel of fluid which is a source of the momentum, which is negligible over the timescale of the bubble collapse, but is ultimately important.

The dynamics of an isolated vapor bubble with zero mass are described by

$$\mathbf{0} = \boldsymbol{F} + \boldsymbol{F}_B \tag{3}$$

where the force on the bubble is defined by

$$\boldsymbol{F} = \int_{S_b} (p\boldsymbol{I} - \boldsymbol{\tau}) \cdot \hat{\boldsymbol{n}} dS \tag{4}$$

and the buoyancy force is $\boldsymbol{F}_B=\rho_f \boldsymbol{g} V_b$, where $\boldsymbol{g}$ is the gravitational acceleration. The integration is taken over the surface of the bubble S_b, and p is the pressure (above the hydrostatic component), and $\boldsymbol{\tau}$ is the stress tensor. Here $\hat{\boldsymbol{n}}$ is the unit normal vector directed out of the flow domain (into the bubble; see Fig. 4). The force on the bubble will consist of contributions from added-mass, drag, and history forces [19,20], although it is not necessary to deal with explicit forms for $\boldsymbol{F}$ at this stage.

The force may be rewritten as an integral over a larger (fictious) bounding surface S_∞ and volume V_∞, expressed as

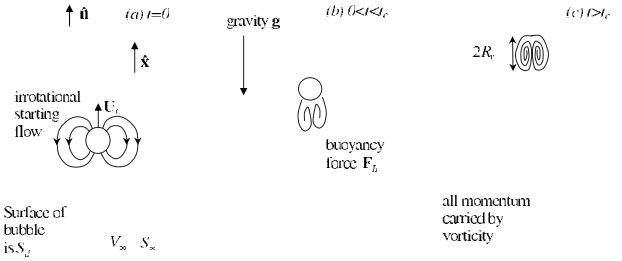

Fig. 4 Schematic of the control volume used in Sec. 3.1 to analyze the conservation of momentum in an unbounded flow

$$\boldsymbol{F} = -\int_{S_\infty} (p\boldsymbol{I} - \boldsymbol{\tau}) \cdot \hat{\boldsymbol{n}} dS - \int_{V_\infty - V} \rho_f \frac{D\boldsymbol{u}}{Dt} dV \tag{5}$$

V_∞ is taken to be sufficiently large that the flow is irrotational on S_∞. Here we assume ρ_f is constant. Thus, in the far field, the fluid stress is negligible, but there is an unsteady pressure contribution from $p = -\rho_f \partial\phi/\partial t$, where the velocity potential ϕ can be defined in terms of a line integral of velocity from infinity. Equation (5) can be arranged to give

$$\boldsymbol{F} = -\rho_f \frac{d}{dt}\left(\int_{V_\infty - V} \boldsymbol{u} dV - \int_{S_\infty} \phi \hat{\boldsymbol{n}} dS \right) \tag{6}$$

The right-hand side of Eq. (6) is essentially the rate of decrease in the fluid momentum, which is defined by

$$\boldsymbol{M} = \rho_f \left(\int_{V_\infty - V} \boldsymbol{u} dV - \int_{S_\infty} \phi \hat{\boldsymbol{n}} dS \right) \tag{7}$$

(A crucial caveat is that the flow is unbounded). This provides an entirely new definition of the momentum valid for viscous flows and circumvents the traditional discussion (of Batchelor [11] and Saffman [21]) in terms of impulsively applied forces. Combined together

$$\boldsymbol{F} = -\frac{d\boldsymbol{M}}{dt} \tag{8}$$

Physically, the momentum of the flow is increased by the force on the bubble

$$\boldsymbol{M}(t) - \boldsymbol{M}_0 = -\int_0^t \boldsymbol{F} dt = \int_0^t \boldsymbol{F}_B dt \tag{9}$$

where $\boldsymbol{M}_0$ is the initial momentum of the flow. Since the bubble initially moves with a velocity $\boldsymbol{U}_0$ and the boundary layers on the bubble are likely to be thin due to the vapor bubble growing in size, the initial momentum of the fluid is mostly due to the inviscid character of the flow and

$$\boldsymbol{M}_0 = \rho_f C_{m0} \boldsymbol{U}_0 V_0 \tag{10}$$

where C_{m0} is the added-mass of the bubble. The momentum associated with the fluid immediately after the bubble has collapsed is

$$\boldsymbol{M}_c = \rho_f C_{m0} \boldsymbol{U}_0 V_0 + \int_0^{t_c} \boldsymbol{F}_B dt \tag{11}$$

or

$$\boldsymbol{M}_c = \rho_f C_{m0} \boldsymbol{U}_0 V_0 + \lambda \rho_f V_0 t_c \boldsymbol{g} \tag{12}$$

is finite and $\lambda = \int_0^{t_c} V dt / V_0 t_c$ depends on the rate of collapse of the bubble. Since $|\boldsymbol{M}_c| > 0$, there must be vorticity in the flow, i.e., a vortex, since this is the only way a fluid can carry momentum (in the absence of moving boundaries).

After the vapor bubble has disappeared and the vortex is moving steadily, Eq. (12) can be used to estimate the properties of the vortex. The integral of the fluid velocity over the whole domain can be calculated by considering separately the contributions from inside and outside the vortex. The contribution from outside the vortex is $\rho_f C_m U_v V_v$, while the contribution from inside the vortex is $\rho_f U_v V_v$, so in total

$$\boldsymbol{M}_v = \rho_f (1 + C_m) U_v V_v \hat{\boldsymbol{x}} \tag{13}$$

where $\hat{\boldsymbol{x}}$ is directed upwards, returning to the caveat concerning the changes in the density of the ambient fluid. After the vortex has been created, the heat from the condensation process creates a buoyant packet of fluid or vortex. The maximum relative density difference between the hot fluid in the vortex and cooler ambient fluid is $\Delta\rho/\rho_\infty \sim \gamma$, where $\gamma \sim 0.02$ (for a temperature contrast of 30 deg) and is small. Buoyancy forces acting on the vortex will increase its momentum, so that

$$\boldsymbol{M}_v \approx \boldsymbol{M}_c + V_v(t) \Delta\rho \boldsymbol{g} (t - t_c) \tag{14}$$

From Eq. (14) and a slow collapse, we estimate that the momentum of the vortex essentially doubles over a period of $\sim \rho_\infty t_c / \Delta\rho \sim 50 t_c$. Therefore over a period of $\sim 10 t_c$ after the bubble has disappeared, the momentum of the vortex created will have increased by less than 20% and $\boldsymbol{M}_v \approx \boldsymbol{M}_c$.

3.2 How is the Vortex Generated? As we have described previously, the condensation of a vapor bubble moving under gravity must always lead to the creation of a vortex. The movement of a bubble will certainly lead to the baroclinic generation of vorticity (or circulation) on the surface of the bubble. The key question then is how vorticity is communicated to the ambient fluid. In the following discussion, the author described three mechanisms and developed dimensionless measures of their strength. The author generalized our analysis by considering a bubble having a density ρ_v, radius $a(t)$ (where $a_0 = a(0)$ is the initial bubble radius), and acceleration dU/dt. A characteristic velocity scale is U_{T0} is the terminal rise speed based on a bubble with radius a_0.

3.2.1 Inviscid Mechanism: Topological Change. A collapsing vapor bubble which deforms sufficiently for its topology to change, from a spherical to a toroidal shape, creates circulation at the point where reconnection occurs because the integral of the velocity potential around the internal surface becomes nonzero [22] (see Fig. 5(*a*)). In reality, vapor is trapped between the two vapor/water interfaces, allowing the penetrating jet to be observed; otherwise, in a strictly inviscid framework, the jet will consist of a cylindrical vortex sheet. Some previous models, which identify the circulation only within the toroidal bubble, are clearly therefore in error, since while the momentum is conserved, they do not explain how the momentum is permanently communicated to the exterior fluid. The generation of circulation in an inviscid fluid does not contravene Kelvin's circulation theorem, which is associated with material surfaces. Benjamin and Ellis [8] argued that cavitating bubbles must go through a topological change to conserve impulse. The production of circulation through a topology change occurs widely in fluid mechanics such as the topology change accompanied by surface waves breaking in the ocean, which create a descending jet and a subsurface vortex [23].

When bubble acceleration is large, it can overcome the pressure from the surface tension, which stabilizes the bubble shape, resulting in a sufficiently large bubble deformation that the bubble changes topology. The potential for deformation is characterized by the ratio of the pressure difference across the height of the bubble due to acceleration (which causes the bubble to deform) to the pressure change across the bubble surface due to the surface tension (which stabilizes the bubble shape), expressed as

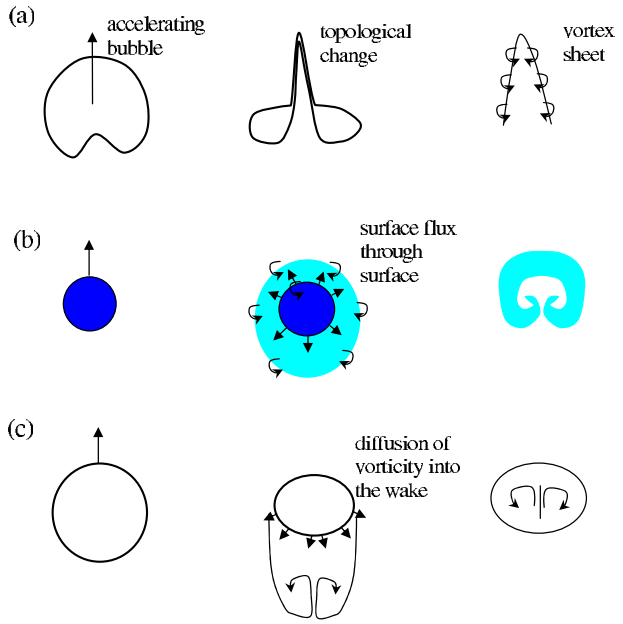

Fig. 5 Summary of the three mechanisms of communicating bound vorticity into the fluid interior (*a*) inviscid topological mechanism, (*b*) inviscid through-surface flow, and (*c*) viscous mechanism

$$\mathcal{I} \sim \frac{\rho_f a^2 |dU/dt|}{\sigma} \tag{15}$$

where σ is the surface tension (which is 7.28×10^{-2} N/m for a clean air-water interface at 20 deg). Measure $\mathcal{I}$ varies with time as the bubble rises and condenses, but it is sensible to suggest that a criterion for its applicability is a threshold.

3.2.2 Inviscid Mechanism: Surface Flux. The flow past a moving body may be interpreted as bound vorticity (moving with the flow), with the external flow described as free vorticity. Image vorticity is required to ensure that the kinematic boundary condition on the bubble surface is satisfied in the presence of free vorticity [21] (see Fig. 5(*b*)). When the body "dissolves," as in the case of Taylor's [24] disappearing disk "thought-experiment," bound vorticity is converted to free vorticity. This method is sometimes employed to generate dipolar vortices, where an open ended cylinder is translated forward in a fluid and then removed [25]. While a portion of the final vortex created is due to the vorticity in the wake, for short translation distances, the primary contribution is from the conversion of bound vorticity to free vorticity.

In the context of condensing bubbles, a flow through the bubble surface is generated by a phase change. The radial blow speed scales as $u_r \sim \rho_v a_0/\rho_f t_c$, which convects bound vorticity into the ambient fluid. This mechanism is determined by the ratio of the through-surface velocity to a characteristic translation velocity of the bubble, estimated as

$$\mathcal{II} \approx \frac{u_r}{U_{T0}} \sim \frac{\rho_v}{\rho_f}\frac{a_0}{U_{T0}t_c} \tag{16}$$

3.2.3 Viscous Mechanism. Vorticity is generated on the bubble surface either through surface contamination, rendering part of the surface immobile, or through the shear free condition, leading to vorticity production. The most obvious mechanism of generating vorticity in the exterior flow is through the diffusion of boundary layer vorticity into the flow interior and advection downstream (see Fig. 5(*c*)). For high Reynolds number $\mathrm{Re}_0 = 2U_{T0}a_0/\nu \gg 1$, vorticity accumulates in the rear of the bubble and is deposited in the ambient fluid behind the bubble. A measure of this mechanism is the ratio of the collapse time to the advective time scale

$$\mathcal{III}_{\mathrm{Re}\gg1} \sim \frac{U_{T0}t_c}{a_0} \tag{17}$$

3.3 Bubble Dynamics. In this section, we attempt to understand more about discriminating between mechanisms $\mathcal{I}$ and $\mathcal{III}$ described above, using semi-empirical closures for the force expression. We assume that the bubble is spherical with radius $a(t)$ (where $a_0 = a(t)$) and remains spherical during its lifetime. We focus on how the measure $\mathcal{I}$ varies in time, and the conditions when it is sufficiently large that the bubble is expected to depart from a spherical shape. When $\mathcal{I}$ is sufficiently large, the spherical bubble deforms and the model is expected to break down.

The dynamics of a massless bubble of volume $V = 4\pi a^3(t)/3$ rising under gravity are generally expressed by Eq. (3). To solve Eq. (3) it is necessary to specify the contributions to the total force acting on the bubble. Limiting our discussion to a bubble rising in a straight line (with velocity U), the force on the bubble largely consists of the added-mass and drag forces, and the dynamics are described by

$$0 = -\frac{d(\rho_f C_m V U)}{dt} - \frac{1}{2}\rho_f C_D \pi a^2 U^2 + \rho_f g V \tag{18}$$

The form of Eq. (18) is one which has widely applied to study vapor bubble dynamics (see Refs. [26,10,18]). The first term on the right-hand side is the added-mass force, where the added-mass coefficient C_m is a geometrical measure of the bubble' oblateness; for a spherical shaped bubble, $C_m = 1/2$. For a steadily translating spherical bubble, the drag coefficient C_D is to leading order 48/Re. Since the potential for large accelerations, beyond the limit in which this is valid, we assume that the bubble drag tends to a constant, and so

$$C_D = \frac{48}{\mathrm{Re}} + 0.44 \tag{19}$$

for $\mathrm{Re} = 2aU/\nu > 100$. The bubble center rises a distance h in time t after detachment, where

$$U = \frac{dh}{dt} \tag{20}$$

and disappears in a finite distance $h_c = h(t_c)$. The effect of the wall can be included through corrections to C_D and C_m.

As a vapor bubble rises into a cooler ambient fluid, it decreases in size due to condensation caused by the heat flux through the bubble surface. A large number of studies have examined the condensation of vapor bubbles. Table 1 shows a compilation of various forms of the collapse times, their relation to the degree of subcooling, and the form of the shrinkage. The majority of the empirical closures take the algebraic form

$$a = a_0\left(1 - \frac{t}{t_c}\right)^n \tag{21}$$

where n is taken to have a range of 0.8–1. For $n < 1$, the final stage of the bubble collapse consists of an unphysical infinite bubble velocity. For this reason, we assign $n = 1$.

The bubble is characterized by a response time $t_r = U_{T0}/g$, where U_{T0} is the terminal rise velocity based on the initial radius a_0, expressed implicitly by $U_{T0} = (8a_0 g/3C_D(\mathrm{Re}))^{1/2}$. U_{T0} was calculated numerically by solving Eq. (18) when $dU/dt = 0$. The solutions to the coupled equations (Eqs. (18), (19), and (21)) were calculated numerically. The acceleration of the vapor bubble was weakly dependent on its initial vertical velocity, which was set to zero.

For $t_c/t_r > 1$, the bubble is accelerated by buoyancy, so that $dU/dt = +g/C_m$ and $U \sim gt/C_m$, and the drag force increases. The balance between the drag and buoyancy forces is achieved in a

Table 1 Summary of the different forms for the bubble radius after it has left a wall. Peclet number $Pe=2a_0U_{T0}/\nu$, Prandtl number $Pr=\nu/D_L$, Archimedes number, $Ar=g(2a_0)^3/\nu^2$, $Re=2a_0U_{T0}/\nu$, and U_{T0} is the rise speed of the bubble. Here D_L is the thermal diffusivity and $Ja=\rho_L c_p\Delta T/\rho_g h$ is the Jacob number. Modified from Ref. [3].

Author	Equation (a/a_0)	Collapse time t_c
Floschuetz and Chao [27]	$1-\sqrt{t/t_c}$	$\pi a_0^2/16\mathrm{Ja}^2D_L$
Voloshko and Vurgaft [28]	$1-t/t_c$	$40<\mathrm{Ja}<75,\ a_0^2/6.8\times10^4D_L$
Voloshko and Vurgaft) [29]	$1-(t/t_c)^{2/3}$	$\sqrt{2\pi}a_0^2/11.4D_L\mathrm{JaPe}^{1/2}$
Moalem and Sideman [30]	$(1-t/t_c)^{5/7}$	$2<a_0<4$ mm, $2\sqrt{2a_0^2}/5\mathrm{JaPe}^{1/2}D_L$
	$(1-t/t_c)^{4/5}$	$a_0<1$ mm, $2\sqrt{2}a_0^2/5\mathrm{Ja}D_L\mathrm{Pe}^{1/2}$
Akiyama [31]	$(1-t/t_c)^{5/7}$	$a_0^2\mathrm{Pr}^{0.27}/0.8D_L\mathrm{JaPe}^{0.6}$
Dimic [32]	$(1-t/t_c)^{4/5}$	$\sqrt{2a_0^2}/\mathrm{Ar}^{1/4}\mathrm{Pr}^{1/2}\mathrm{Ja}D_L$,
Chen and Mayinger [3]	$(1-t/t_c)^{0.9}$	$a_0^2/0.56\mathrm{Re}^{0.7}D_L\mathrm{Pr}^{0.5}\mathrm{Ja}$

time $\sim t_r$, and the continuing dynamics are determined by this balance. For a quadratic drag law, $U\sim U_{T0}(a/a)^{1/2}$ and $h_c\sim U_{T0}t_c/(n+1/2)$. During this phase, the bubble is decelerating at a rate $dU/dt=-2U_{T0}(a/t_ca_0)$. The numerical results follow closely the curve $U=U_{T0}(a/a_0)^{1/2}$. In the second order, the added-mass force must be included, increasing the rise speed by a fractional amount, so that $U\sim U_{T0}(a/a_0)^{1/2}+8C_ma_0/C_Dt_c$, resulting in a nonzero bubble speed at $t=t_c$. As the bubble rises, it is initially accelerated, leading to the flattening of the rear side of the bubble, and during the deceleration phase, the front of the bubble flattens, leading, for large bubbles and rapid collapse, to penny-shaped bubbles.

For $t_c/t_r<1$, over a large portion of the trajectory, $U\sim 2gt$ and $h_c\sim gt_c^2$. After the initial acceleration of the bubble, all three forces come into play. In this limit, the decrease in the bubble volume accelerates the bubble. The drag force is insufficient to cause the bubble velocity to decrease, and the velocity becomes unbounded. For $t_c/t_r\ll 1$, the acceleration is $dU/dt\sim U_{T0}/t_c$.

From the numerical solution to Eq. (18), we calculate

$$\mathcal{I}_{\max}=\max_{0<t<t_c}\frac{\rho_f a^2 dU/dt}{\sigma} \tag{22}$$

Since both the bubble acceleration and radius change with time, it is difficult to estimate the maximum value of $\mathcal{I}$ a priori. However, a suitable bulk measure of the destabilizing influence of acceleration, which can be estimated from the experimental data, is

$$\mathcal{I}_E=\frac{\rho_f a_0^2 U_{T0}}{\sigma t_c} \tag{23}$$

Figure 6 shows a comparison between $\mathcal{I}_{\max}$ and $\mathcal{I}_E$ for two bubble radii ($a_0=0.1$ cm and 0.2 cm) and for a variety of collapse times $t_c/t_r=0.2$ to 1 (which spans the range of our experimental study). The numerical results indicate that $\mathcal{I}_E$ correlates quite well with the maximum bubble acceleration ($\mathcal{I}_E/\mathcal{I}_{\max}\sim 0.43$) and provides a useful proxy measure of when the bubble changes topology.

4 Interpretation of the Experimental Results

4.1 Bubble Dynamics. For each bubble sequence, we discriminated between the conditions when the bubble underwent a topological change, when it did not, and when the collapse process was unclear. Figure 7 shows the experimental points when the topological and nontopological collapses were observed. The numerical calculations in Fig. 6 indicates that $\mathcal{I}_E$ is correlated with $\mathcal{I}_{\max}$ and provides a useful measure of the destabilizing influence of bubble acceleration and whether the bubble undergoes a topological change. The experimental measurements indicate that when the measure $\mathcal{I}_E$ is above a critical value $\mathcal{I}_c\sim 2$, the bubble undergoes a topological change. This can be more usefully expressed as

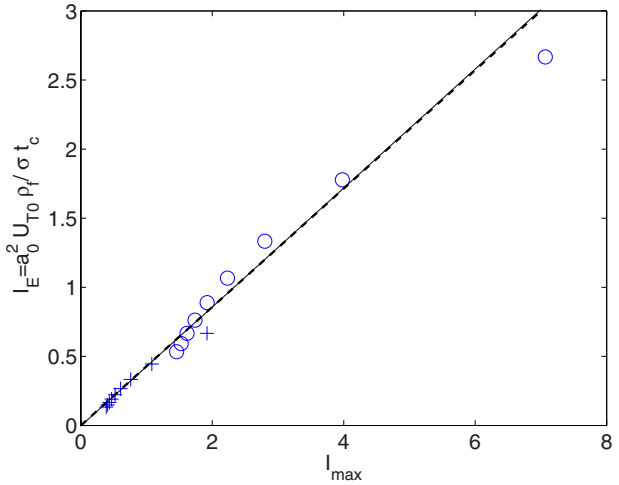

Fig. 6 The bulk measure of the destabilizing effect of gravity $\mathcal{I}_E$ is plotted versus the maximum value of measure $\mathcal{I}_{\max}$ calculated numerically over the bubble lifetime. The symbols + and ○ corresponds to bubbles of initial radius $a_0=0.1$ and 0.2, respectively. The symbols correspond to the varying collapse times $t_c/t_r=0.2,0.3,\ldots,1$.

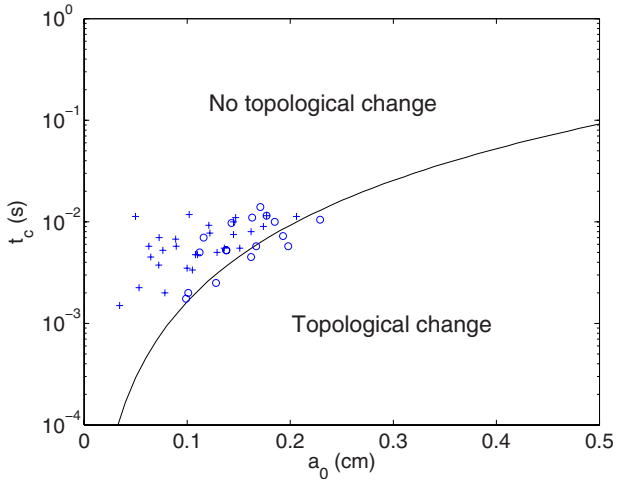

Fig. 7 Phase diagram showing when the topological mechanism of collapse occurs (○) and when it does not (+). Equation (24) is plotted as a full line.

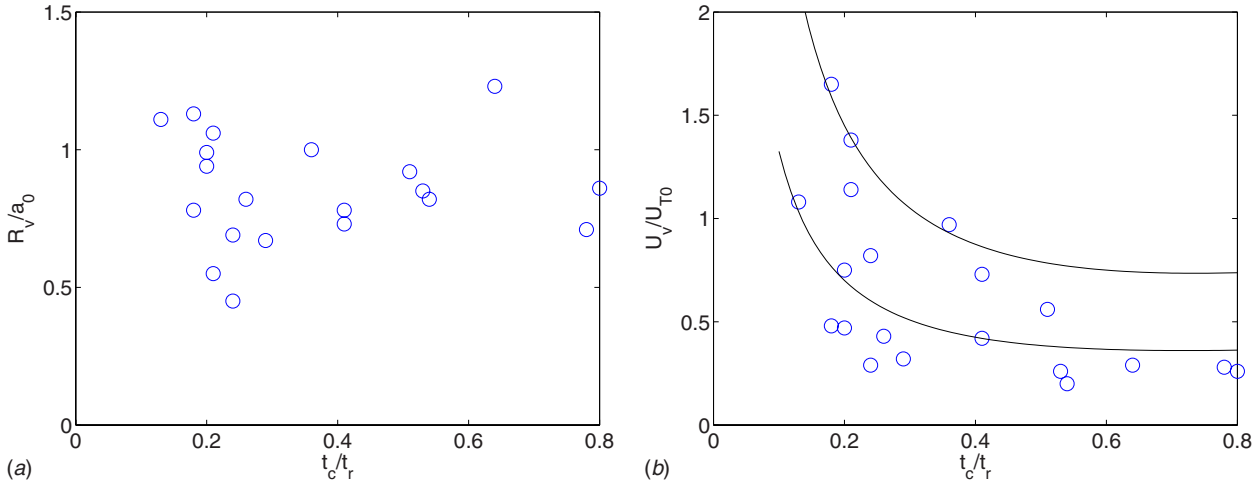

Fig. 8 Properties of the vortex: the variation in the vortex radius R_v and velocity U_v are shown in (*a*) and (*b*), respectively, as functions of t_c/t_r

$$t_c < \frac{\rho_f a_0^2 U_{T0}}{\mathcal{I}_c \sigma} \tag{24}$$

which is plotted in Fig. 7. While there is a great deal of scatter in the experimental results, the criterion broadly discriminates between the two modes of bubble collapse.

The measure for the inviscid surface flux mechanism is $\mathcal{II} \sim 10^{-3} a_0/U_{T0}t_c \sim 10^{-4} t_r/t_c$. Since $t_c/t_r > 0.1$ in our experiments, the effect of the through-surface flow can effectively be ignored. The fraction of the final vortex momentum, which arises from this mechanism $\rho_v/\rho_f \sim 10^{-3}$, further underlines its lack of importance.

4.2 Vortex Dynamics. During the condensation of a vapor bubble, a vortex is created and remains after the bubble has disappeared. When the bubble does not undergo a topological change, the vortex is created through a viscous mechanism. When the bubbles collapse after translating a short distance ($h_c/a_0 < 5$), the starting vortex created by the bubble moving essentially forms the ghost vortex, as observed in the experiments. However, if the bubble translates a significant distance compared with its initial radius, we would expect that there is an increasing contribution from the vorticity deposited behind the bubble, especially when the flow is viscously dominated.

The model we have developed shows that the momentum of the vortex increases slowly due to the action of a buoyancy force on the buoyant vortex, but this occurs approximately over a time period of $\sim 50t_c$, so that up to $10t_c$ after the bubble has disappeared, the momentum of the vortex is approximately constant. Our analysis of the vortex motion shows that it moves at a constant speed, but initially undergoes an inviscid adjustment (or roll-up) over a timescale of R_v/U_v.

Figure 8(*a*) shows a comparison between the vortex radius and the bubble size on detachment.[1] The majority of the data falls with the range of $R_v/a_0 \sim 0.5-1.0$, suggesting that the final vortex size scales with the initial bubble size, which could be anticipated because it is the characteristic geometrical length scale of the problem, though we provide a stronger physical justification below. Figure 8(*b*) shows a comparison between the vortex translation velocity and the characteristics velocity U_{T0}. Although there is scatter in the results, the general trend is that the vortex moves much slower that U_{T0} for slowly collapsing bubbles ($t_c/t_r \sim 1$), and the speed tends to increase as the collapse time decreases.

When the vortex is initially generated, it then goes through an initial inviscid adjustment, before viscous effects become important. During the inviscid adjustment phase, impulse and circulation are conserved. We can estimate the properties of the vortex signature by using these conservation conditions, assuming that the final state, after the inviscid adjustment, is a Hill's spherical vortex, which is consistent with the experimental observations. This technique has been used, for instance, by Taylor [24] to estimate the size and speed of a vortex created by disk dissolving. Defining the circulation $\Gamma = \int_A \omega dA$ (where A is the half plane through the axis of symmetry; see p. 526 of Ref. [11]) the conservation of the momentum requires

$$\frac{2}{5}\rho_f \pi R_v^2 \Gamma = M_c \tag{25}$$

The vortex radius and speed of propagation of a Hill's spherical vortex can be expressed in terms of the vortex momentum and circulation through

$$R_v = \left(\frac{5M_c}{2\pi\Gamma\rho_f}\right)^{1/2}, \quad U_v = \frac{\Gamma}{2R_v} \tag{26}$$

To close the argument, we need to estimate the total circulation of the vorticity in the wake.

For rapid collapse ($t_c/t_r \ll 1$), most of the momentum is generated by the bubble rising away from the wall and $M_c \sim \rho_f V_0 U_0$. The circulation in this case will scale as $\Gamma \sim U_0 a_0$, giving $R_v \sim a_0$ and $U_v/U_{T0} \sim U_0/U_{T0}$. Our measurements indicate that the bubble grows over a time $t_g \sim 0.2t_c$, so that $U_0 \sim 5a_0/t_c$ and $U_v/U_{T0} \sim 0.2t_r/t_c$ For slow bubble collapse ($t_c/t_r \sim 1$), most of the momentum is generated during the buoyancy driven rise and collapse, and $M_c \sim V_0 t_c g$. The total circulation in the wake depends on the distance the bubble moves before it collapses and which scales as $U_{T0}t_c$ so that $\Gamma \sim t_c U_{T0}^2$. Thus the vortex size is $R_v \sim (a_0 V_0 g/U_{T0}^2)^{1/2} \sim a_0$ and $U_v/U_{T0} \sim 0.2(t_c/t_r)$, which tends to be much smaller than the characteristic rise speed of the bubble.

An alternative, but equivalent argument, is from the conservation of the momentum, where

$$\rho_f C_{m0} V_0 U_0 + \rho_f \lambda t_c V_0 g = \rho_f (1 + C_m) V_v U_v \tag{27}$$

Rearranging

[1]There were three anomalous data points, where $R_v/a_0 \sim 3$. On further examination, we found that the bubbles were shrinking while in contact with the wall, so that they were much smaller on detachment from the sediment layer ($a_0 \sim 0.03$ cm) than the rest of the data set, where $a_0 = 0.1-0.2$ cm, and were omitted.

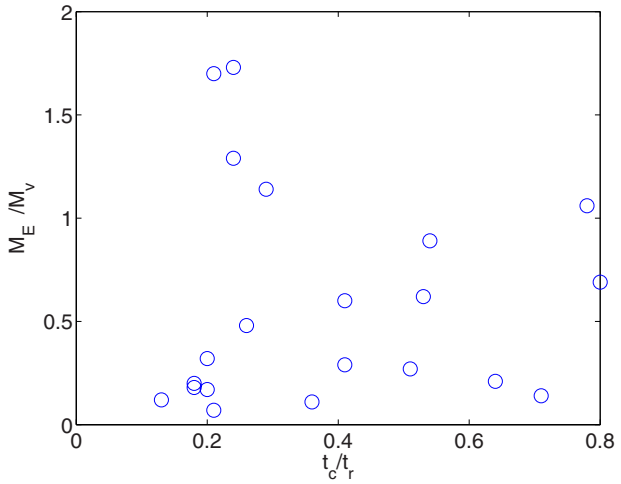

Fig. 9 Ratio of the estimated momentum of the vortex (M_E) to the measured vortex momentum (M_v)

$$\frac{U_v}{U_{T0}} = \frac{C_{m0}}{1 + C_m}\frac{V_0}{V_v}\frac{U_0}{U_{T0}} + \lambda\frac{t_c}{t_r}\frac{V_0}{V_v} \tag{28}$$

The coefficients are estimated to be $C_{m0} \sim 0.5-1.0$ (which is estimated to be larger than 0.5 as the bubbles are initially oblate), $V_0/V_v \sim 1-2.0$, and $\lambda = 1/(3n+1) \sim 1/4$ (from Eq. (21)). We estimate the initial bubble velocity as $U_0 \sim 0.2a_0/t_c$. Combined together

$$\frac{U_v}{U_{T0}} \sim [0.13-0.27]\frac{t_r}{t_c} + [0.25-0.5]\frac{t_c}{t_r} \tag{29}$$

The numbers in the brackets represents the uncertainty in estimating the premultiplying coefficients in Eq. (28). The scaling analysis suggests that the vortex scales with the size of the bubble, which is largely confirmed by Fig. 8(*a*), a result that could be anticipated from dimensionless analysis. While there is a scatter in the vortex rise velocity shown in Fig. 8(*b*), the experimental data suggest that the vortex speed tends to increase as the collapse time decreases, and this is largely explained by the above scaling analysis. The two curves shown in Fig. 8(*b*) show the bounds for the estimated vortex rise speed calculated in Eq. (29). For slow collapse times, the vortex tends to move quite slowly while for rapid bubble collapse, the vortex moves much faster.

From the measurements of R_v and U_v, we can accurately estimate the momentum of the vortex M_v created immediately after the bubble has disappeared. The model we have presented enables the momentum communicated to the ambient flow to be estimated from the initial bubble size a_0 and collapse time t_r, from Eq. (27), i.e., $M_E = \rho_f C_{m0} V_0 U_0 + \rho_f \lambda t_c V_0 g$. As argued above, we take $\lambda = 1/4$, $U_0 = 0.2a_0/t_c$, and $C_{m0} \sim 0.5-1$. Figure 9 shows the ratio M_E/M_v plotted as a function of t_c/t_r. The largest errors are associated with our measurements of t_c and a_0, since discriminating the point of detachment is slightly ambiguous. The equivalent initial bubble volume is based on the equivalent areal radius, $V_0 = 4\pi a_0^3/3$, which magnifies the errors (to about 40%). Despite the scatter in the data, the analysis provides reasonable order-of-magnitude estimates of the vortex momentum.

5 Concluding Remarks

The disappearance of a condensing vapor bubble must necessarily lead to the generation of a vortex to conserve the momentum. New experimental observations confirm the presence of the vortex. Of the three principal mechanisms, which may contribute to bound vorticity being transported from the bubble surface into the interior, the main mechanisms are either through a topological change in the bubble shape, when the bubble collapses rapidly, or through a viscous mechanism where the starting wake vortex is essentially left behind after the bubble has disappeared. We introduced a new approach to examine the global momentum of the system. The general properties of the bubble collapse can be summarized as follows:

5.1 ***Topological Change:*** $t_c < (\rho_f a_0^2 U_{T0}/\mathcal{I}_c\sigma)$ **.** When a vapor bubble collapses rapidly, it goes through a topological change. The penetration of the front of the bubble by the rear creates interfacial shear and circulation. For this type of collapse, viscous effects are negligible and the momentum of the vortex is largely determined by the initial motion of the bubble. The resulting vortex has a size comparable to the bubble and moves at a speed comparable to the initial bubble rise velocity.

5.2 ***Nontopological Change:*** $t_c > (\rho_f a_0^2 U_{T0}/\mathcal{I}_c\sigma)$ **.** When a vapor bubble collapses slowly, it does not change topology. Vorticity diffuses from the bubble surface into the near wake region, creating a starting vortex. Once the bubble disappears, the wake vortex remains behind. When bubbles translate a significant distance compared with their radius, before they collapse, vorticity will also be deposited in the fluid downstream behind the bubble. The resulting vortex is comparable in size to the bubble, but tends to move much more slowly than the characteristic rise velocity.

In a practical context, bubble streams are created at nucleation sites. The collective effect of many bubbles collapsing would be to create a buoyant jet above the nucleation site. Close to the nucleation site, the jet will be the momentum dominated with a flux approximately equal to NM_c (where N is the number of bubbles created per second), but the effect of heating caused by the condensation process will eventually lead to a buoyant plume far above the region of bubble collapse. Therefore a stream of condensing vapor bubbles will essentially create an intense nonlocal flow field. The absence of this effect in computational models of boiling is perhaps one explanation of the difficulty of developing appropriate closures for boiling. Our future aim is to examine the characteristics of buoyant jets.

Acknowledgment

Dr. Mark Landeryou helped with the image processing of the experiments. Support from a Phillip Leverhulme Prize is gratefully acknowledged.

Nomenclature

- a = bubble radius; the subscript 0 corresponds to the initial bubble radius
- A_b = cross-sectional area; the subscripts b and v correspond to the bubble and vortex, both of which are measured experimentally
- C = coefficient; the subscripts m and D correspond to added mass and drag (the subscript $m0$ corresponds to the added-mass coefficient when the bubble has detached from the wall)
- $\boldsymbol{F}$ = force on the bubble; the subscript B corresponds to the buoyancy force
- h = height; the subscripts v and c correspond to vortex height (as a function of time) and collapse height of bubble from the wall
- $\mathcal{I}$, $\mathcal{II}$, and $\mathcal{III}$ = metrics for the three mechanisms of vortex generation
- $\boldsymbol{M}$ = fluid momentum; the subscripts 0 and v correspond to the initial momentum of the ambient fluid and the vortex momentum
- n = constant that indicates how quickly the bubble radius decreases with time
- p = pressure

t = time; the subscripts c and b correspond to the collapse and characteristic response times

ΔT = degree of subcooling

R = radius; the subscript v corresponds to the vortex radius

Re = Reynolds number; the subscript 0 corresponds to the Reynolds number of the vapor bubble as it detaches from the wall

U = velocity; the subscripts v and $T0$ correspond to the vortex and characteristic terminal rise speed based on the radius a_0

V = volume; the subscript v corresponds to vortex volume.

σ = surface tension of the vapor-water interface

ρ = density; the subscripts f, v, and ∞ correspond to the fluid, vapor, and fluid (far from the bubble); $\Delta\rho$ is the change in water density due to heating

$\boldsymbol{\tau}$ = fluid stress tensor

References

[1] Roshenow, W. M., Hartnett, J. P., and Cho, Y. I., 1998, *Handbook of Heat Transfer*, McGraw-Hill, New York.

[2] Chen, Y. M., and Mayinger, F., 1985, "Holographic Interferometry Studies of the Temperature Field Near a Condensing Bubble," *Optical Methods in Dynamics of Fluids and Solids, Proceedings of an International Symposium, IUTAM*, M. Pichal, ed., Springer Verlag, Berlin, Germany.

[3] Chen, Y. M., and Mayinger, F., 1992, "Measurement of Heat Transfer at the Phase Interface of Condensing Bubbles," Int. J. Multiphase Flow, **18**, pp. 877–890.

[4] Cieslinski, J. T., and Szymczyk, J. A., 1999, "Measurements of Gas and Vapor Bubbles Motion by Means of Visualization Techniques," *Proceedings of the Second International Symposium on Two-Phase Flow Modelling and Experimentation*, G. P. Celata, P. Di Marco, and R. K. Shah, eds., Edizioni ETS, Pisa, Italy, Vol. 3, pp. 1441–1448.

[5] Yan, Y., Kenning, D. B. R., Pan, X., and Grant, I., 1997, "A PIV Investigation of Flows Around Sliding Air Bubbles in Water Under a Heated Inclined Plate," *Proceedings of the Third International Conference on Fluid Dynamic Measurement and Its Applications*, Beijing, China.

[6] Stickland, M. T., Dempster, W. M., Oldroyd, A. B., and Lothian, L., 1996, "PIV Studies of Bubble Growth and Detachment by High Speed Photography," *Proceedings of the 22nd International Symposium on High Speed Photography and Photonics*, Santa Fe, NM.

[7] Li, D., and Dhir, V. K., 2007, "Numerical Study of Single Bubble Dynamics During Flow Boiling," ASME J. Heat Transfer, **129**, pp. 864–876.

[8] Benjamin, T. B., and Ellis, A. T., 1966, "The Collapse of Cavitation Bubbles and the Pressures Thereby Produced Against Solid Boundaries," Philos. Trans. R. Soc. London, Ser. A, **260**, pp. 221–240.

[9] Delmas, H., and Angelino, H., 1975, "Instabilities au cour de la contraction de bulles de vapeur non spheriques," Int. J. Heat Transfer, **19**, pp. 218–221.

[10] Kalman, H., 2003, "Condensation of Bubbles in Miscible Liquids," Int. J. Heat Mass Transfer, **46**, pp. 3451–3463.

[11] Batchelor, G. K., 1967, *An Introduction to Fluid Mechanics*, Cambridge University Press, Cambridge, England.

[12] Eames, I., 2008, "Disappearing Bodies and Ghost Vortices," Philos. Trans. R. Soc. London, Ser. A, **366**, pp. 2219–2232.

[13] Plesset, M. S., and Prosperetti, A., 1977, "Bubble Dynamics and Cavitation," Annu. Rev. Fluid Mech., **9**, pp. 145–185.

[14] Blake, J. R., and Gibson, D. C., 1987, "Cavitation Bubbles Near Boundaries," Annu. Rev. Fluid Mech., **19**, pp. 99–123.

[15] Blake, J. R., Hooton, M. C., Robinson, R. B., and Tong, R. P., 1997, "Collapsing Cavities, Toroidal Bubbles and Jet Impact," Proc. Roy. Soc., **355**, pp. 537–550.

[16] Zhang, S., Duncan, J. H., and Chahine, G. L., 1993, "Collapse of a Cavitation Bubble Near a Rigid Wall," J. Fluid Mech., **257**, pp. 147–181.

[17] Bush, J. W. M., and Eames, I., 1998, "Fluid Displacement by Bubbles Rising in a Thin Gap," Int. J. Multiphase Flow, **24**, pp. 411–430.

[18] Keshock, E. G., and Siegel, R., 1964, "Forces Acting on Bubbles in Nucleate Boiling Under Normal and Reduced Gravity Conditions," Lewis Research Centre, NASA Technical Note No. NASA TN D-2299.

[19] Legendre, D., Boree, J., and Magnaudet, J., 1998, "Thermal and Dynamic Evolution of a Spherical Bubble Moving Steadily in a Superheated or Subcooled Liquid," Phys. Fluids, **10**, pp. 1256–1272.

[20] Magnaudet, J., and Eames, I., 2000, "The Motion of High-Reynolds-Number Bubbles in Inhomogeneous Flows," Annu. Rev. Fluid Mech., **32**, pp. 659–708.

[21] Saffman, P. G., 1992, *Vortex Dynamics*, Cambridge University Press, Cambridge, England.

[22] Lamb, H., 1932, *Hydrodynamics*, Dover, New York.

[23] Melville, W. K., Veron, F., and White, C. J., 2002, "The Velocity Field Under Breaking Waves: Coherent Structures and Turbulence," J. Fluid Mech., **454**, pp. 203–233.

[24] Taylor, G. I., 1953, "Formation of a Vortex Ring by Giving an Impulse to a Circular Disk and Then Dissolving It Away," J. Appl. Phys., **24**, p. 104.

[25] Eames, I., and Flor, J. B., 1988, "Fluid Transport by Dipolar Vortices," Dyn. Atmos. Oceans, **28**, pp. 93–105.

[26] Hamburger, L. G., 1965, "On the Growth and Rise of Individual Bubbles," Int. J. Heat Mass Transfer, **8**, pp. 1369–1386.

[27] Floschuetz, L. W., and Chao, B. T., 1965, "On the Mechanics of Vapour Bubble Collapse," J. Heat Transfer, **87**, pp. 209–220.

[28] Voloshko, A. A., and Vurgaft, A. V., 1971, "Study of Condensation of Single vapour Bubbles in a Layer of Subcooled Liquid," Heat Transfer-Sov. Res., **3**, pp. 2–7.

[29] Voloshko, A. A., and Vurgaft, A. V., and Aksel'rod, L. S., 1973, "Condensation of Vapour Bubbles in a Liquid," Theor. Osnovy Khim. Tekhnologii, **7**, p. 269–272.

[30] Moalem, D., and Sideman, S., 1973, "The Effect of Motion on Bubble Collapse," Int. J. Heat Mass Transfer, **16**, pp. 2321–2329.

[31] Akiyama, M., 1973, "Bubble Collapse in Subcooled Boiling," Bull. JSME, **16**(93), pp. 530–575.

[32] Dimic, M., 1977, "Collapse of One-Component Vapour Bubbles With Translatory Motion," Int. J. Heat Mass Transfer, **20**, pp. 1325–1332.

Rishi Raj
e-mail: rraj@umd.edu

Jungho Kim[1]
e-mail: kimjh@umd.edu

Department of Mechanical Engineering,
University of Maryland,
College Park, MD 20742

John McQuillen
NASA Glenn Research Center,
21000 Brookpark Road,
Cleveland, OH 44135
e-mail: john.b.mcquillen@nasa.gov

Gravity Scaling Parameter for Pool Boiling Heat Transfer

Although the effects of microgravity, earth gravity, and hypergravity (>1.5 g) on pool boiling heat flux have been studied previously, pool boiling heat flux data over a continuous range of gravity levels (0–1.7 g) was unavailable until recently. The current work uses the results of a variable gravity, subcooled pool boiling experiment to develop a gravity scaling parameter for n-perfluorohexane/FC-72 in the buoyancy-dominated boiling regime ($L_h/L_c>2.1$). The heat flux prediction was then validated using heat flux data at different subcoolings and dissolved gas concentrations. The scaling parameter can be used as a tool to predict boiling heat flux at any gravity level in the buoyancy dominated regime if the data under similar experimental conditions are available at any other gravity level. [DOI: 10.1115/1.4001632]

Keywords: scaling parameter, variable gravity, pool boiling, microgravity

1 Introduction

An understanding of boiling is of importance to the reliable design of phase change based electronic cooling systems, heat exchangers, cryogenic fuel storage, propulsion, and transportation units. The ability to remove large amounts of heat with relatively small temperature differences makes boiling an attractive technology for these applications. Over the years, significant research effort has been directed toward studying pool boiling. The presence of more than one phase, little understanding of the nucleation process, and a strong dependence on the fluid properties complicate investigations of the boiling process. The mechanisms by which heat is removed from the surface and the effect of parameters such as gravity, subcooling, wall superheat, fluid properties, heater surface geometry, and structure are still unclear.

Numerous boiling heat transfer models and correlations have been developed. However, due to the complexities discussed above, these models are restricted to the conditions they have been developed for. Space-based technologies for the prospective transit to and exploration of the moon and Mars require the development of phase change based systems for various gravity levels. In order to implement the existing boiling based technologies at gravity levels other than earth gravity, it is necessary to validate existing correlations under these conditions. Moreover, in a general sense, a better understanding of the effect of gravity on boiling heat transfer would substantiate the fundamental knowledge of physics behind boiling.

It has been assumed in the literature that the heat transfer dependence on gravity over all gravity levels can be captured through the use of a power law of the form $q'' \alpha\ a^m$, where m = constant. For example, the widely used semitheoretical model proposed by Rohsenow [1] is based on the assumption that the local agitation of the liquid flowing behind the wake of a departing bubble was responsible for the enhanced single phase convection heat transfer. He suggested using the vapor bubble departure velocity and the bubble departure diameter as velocity and length scales, respectively. Based on these assumptions, the Rohsenow [1] correlation suggests that $m=1/2$ in the nucleate boiling regime. Foster and Zuber [2] used bubble growth rate as the appropriate velocity scale; however, their model is independent of gravity level ($m=0$). Stephan and Abdelsalam [3] applied dimensional analysis along with statistical regression of the available data to develop a correlation for nucleate pool boiling heat transfer. Based on optimal fits to the experimental data, they proposed separate correlations for water, hydrocarbons, cryogenic fluids, and refrigerants. The effect of gravity was accommodated by including the bubble departure diameter in the dimensionless terms. Making use of the Fritz correlation [4], where departure diameter varies as $a^{-1/2}$, the power law coefficient for gravity varied from $m=-0.083$ for hydrocarbons to $m=0.48$ for water. A general correlation that was independent of fluid properties yielded a power law coefficient of $m=-0.033$, but with some sacrifice in accuracy. Siegel and Keshock [5] reported that the bubble departure diameter varied approximately as $m=-1/3$ for 0.1 g$<a<$1 g and $m=-1/2$ for $a<0.1$ g. Application of these coefficients to the Stephan–Abdelsalam correlation leads to an even wider distribution in the value of m for boiling heat flux.

Semitheoretical approaches have also been adopted to predict the critical heat flux (CHF). Kutateladze [6] observed a similarity between flooding phenomena in distillation columns and CHF in pool boiling. In a distillation column, vapor rich in the more volatile component flows upward while liquid containing a higher concentration of the less volatile component flows downward. If the relative velocity difference between the two streams becomes too large, the flow becomes Helmholtz unstable, impeding the flow of liquid to the heated surface. Chang [7] linked the Taylor interface stability analysis and pool boiling phenomena. These studies influenced Zuber [8] to develop a more detailed hydrodynamic model with Taylor wave motion and Helmholtz instability as the key elements. The power law coefficient for CHF was found to be $m=0.25$.

Substantial research on pool boiling under reduced gravity conditions has been performed over the years [9–11]. Under microgravity conditions, the buoyancy force is not sufficient to remove bubbles from the surface, resulting in a large bubble that coalesces with the smaller surrounding bubbles. If the liquid is subcooled, surface tension gradients can give rise to thermocapillary convection around the bubble that can significantly enhance the heat transfer in the absence of gravity. Lee et al. [12] reported pool boiling curves for microgravity environments using R-113. A large bubble formed during the initial nucleation that, depending on its growth rate, either hovered over or remained attached to the heater. This large bubble served as a vapor sink by coalescing with smaller nucleating bubbles generated on the heater, thereby allowing liquid to rewet the heater resulting in high heat transfer. The size of this bubble remained fairly constant, indicating a balance between condensation at the bubble cap and vapor addition

[1]Corresponding author.

Contributed by the Heat Transfer Division of ASME for publication in the JOURNAL OF HEAT TRANSFER. Manuscript received October 16, 2009; final manuscript received March 9, 2010; published online July 6, 2010. Assoc. Editor: S. A. Sherif.

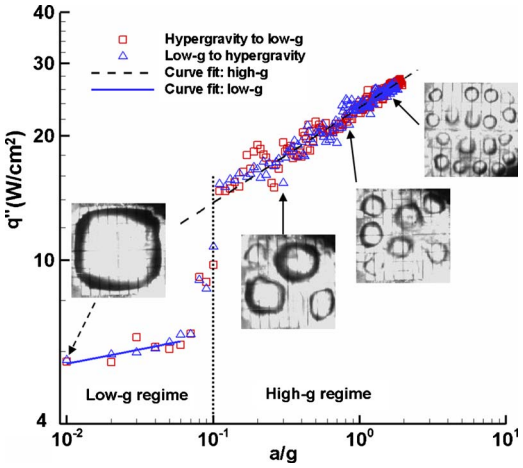

Fig. 1 Plot of the heat flux versus acceleration for the high dissolved gas concentration case ($c_g \sim 1216$ ppm) at $\Delta T_w = 44°C$, with superimposed bottom view images at 0.01 g, 0.3 g, 0.85 g, and 1.68 g [15]

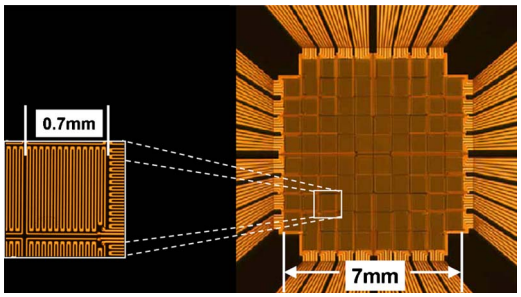

Fig. 2 Constant temperature microheater array

from the smaller nucleating bubbles at the base. As evident, the structure of boiling in microgravity is significantly different from that in earth gravity. Nevertheless, there have been efforts to correlate both microgravity and earth gravity data using a single equation. Based on the heat transfer in microgravity and earth gravity, Straub [13] reported a power law coefficient of $m=0.13$, while Kannengieser et al. [14] reported a power law coefficient of $m=0.17$. A general consensus on the value of the power law coefficient and an explanation for the wide range of predictions in the literature is needed.

Raj et al. [15] proposed a possible explanation for the observed discrepancy in the literature. Their variable gravity (0–1.7 g) experiment produced heat transfer data over a continuous range of gravity levels. An example is shown on Fig. 1. A sudden, distinct change in the heat flux was observed at a gravity level between ~0.1 g and 0.2 g. The data above and below this gravity level were referred to as being in the *high-g regime* and *low-g regime*, respectively. Any acceleration level higher than 1.5 g was referred to as *hypergravity*. The value of m was reported to be dependent on the wall superheat, increasing from a value of $m=0$ close to the onset of nucleate boiling (ONB) to approximately $m=0.25$ near CHF. Building on these observations and the existing discrepancy in the literature, they reasoned that the inability of a single power law to correlate the data across gravity levels was due to differences in the boiling structure between these regimes. It was proposed that in the high-g regime (e.g., earth gravity), boiling is dominated by buoyancy, and the heat transfer is independent of heater size. As the acceleration levels are decreased, the ratio of the heater length to the capillary length L_h/L_c also decreases, and the surface tension forces become increasingly important. The sudden drop in heat transfer below the threshold gravity level was due to the formation of a nondeparting, coalesced bubble. Based on further experiments with varying heater sizes [16], it was found that the transition from buoyancy to surface tension dominated boiling occurred when the heater size and bubble departure diameter were of the same order. The threshold value of L_h/L_c, at which this transition was observed and above which pool boiling was independent of the heater size, was found to be about 2.1 [16].

The objective of the current work is to use the study by Raj et al. [15] to develop a scaling parameter that accounts for gravity effects in the high-g, heater size independent regime for n-perfluorohexane/FC-72. Validation of the scaling parameter is performed by comparing with additional data taken under various dissolved gas concentrations, bulk fluid subcoolings, heater sizes, and heater surface morphologies.

2 Experimental Apparatus

The current work uses data obtained from two parabolic flight campaigns. Variable gravity pool boiling data were collected during the 48th ESA Parabolic Flight Campaign conducted during March 2008 [17]. Additional data at two lower liquid subcoolings were collected during the NASA Facilitated Access to the Space Environment for Technology Development and Training (FAST) reduced gravity flight campaign in August 2009. Although the same experimental setup was used for the two parabolic flight campaigns, the heater surface, test conditions, and fluids (isomer concentrations) were different. The next few sections describe the test apparatus, fluid conditions, data acquisition, and test procedure for the ESA campaign. The changes in the test conditions for the NASA flight are discussed as appropriate.

2.1 Test Package Description. A microheater array consisting of 96 platinum resistance heaters deposited in a 10×10 configuration onto a quartz substrate was used to measure the heat transfer distribution (Fig. 2). Each heater in the array was nominally 0.7×0.7 mm^2 in size. Power was transferred via gold power leads 1 μm thick. Individual heaters had a nominal resistance of 250 Ω and temperature coefficient of resistance of $0.0022°C^{-1}$. The heater temperature was kept constant using a bank of feedback circuits similar to those used in constant temperature hot-wire anemometry. The power, and thus the heat flux, required to maintain these heaters at the desired temperature were obtained by sampling the voltages across the heaters. The frequency response for the heaters and feedback circuits was very high (15 kHz). The reader is referred to Ref. [18] for the details regarding the heater construction.

The test package (Fig. 3) contained a sealed boiling chamber with about 3 l of test fluid, the microheater array, the electronic feedback circuits, two video cameras, LED arrays to illuminate the boiling chamber, a computer, a pressure sensor (Druck PDCR 130/W), and thermocouples and RTDs to measure the bulk liquid and backside air-jet temperature. Backside cooling of the heater array was required to minimize the lateral conduction and to prevent individual heaters from shutting off at low heat transfer levels. Air was forced through a 1.6 mm diameter nozzle placed 10 mm from the backside of the heater array. The cooling air flow was supplied by a compressed air bottle with pressure regulation nominally set at 150 kPa, and the air-jet temperature varied between 22°C and 24°C throughout the experiment. A separate rack (not shown) contained video recorders, displays, and power supplies.

N-perfluorohexane (98.9%), a straight chain isomer of FC-72 (C_6F_{14}, $T_{sat}=56°C$ at 1 atm), was used as the test fluid for the ESA campaign. The bulk liquid was maintained at 30°C ($\Delta T_{sub}=26°C$). Two dissolved gas (air) concentrations, low gas (~220 ppm) and high gas (~1216 ppm), were used to study the

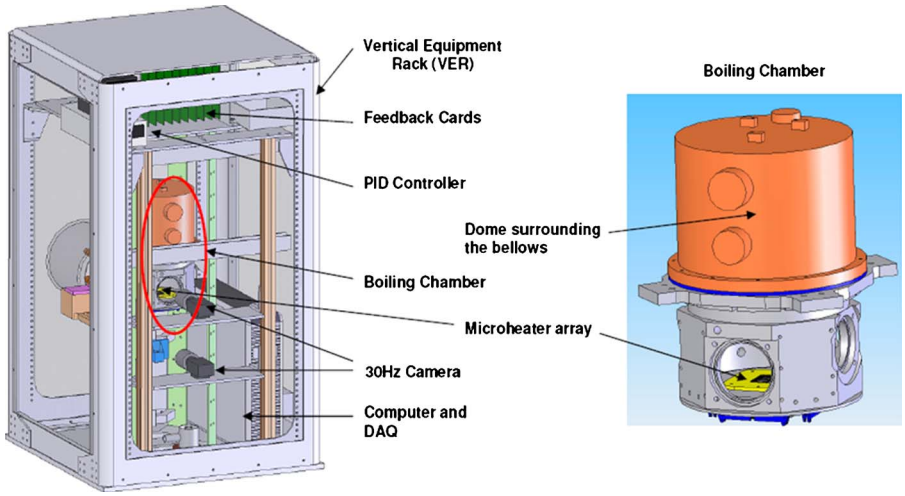

Fig. 3 CAD model of the experimental package

effect of gas concentration. The microheater temperature was varied between 65°C (ΔT_w=9°C) and 100°C (ΔT_w=44°C), and the liquid pressure was maintained at nominally 1 atm throughout the experiment.

2.2 Variable Gravity Environment. An Airbus A300 aircraft flew parabolic maneuvers providing ~20 s periods of low-g preceded and followed by ~20 s periods of ~1.8 g. The transition between the 1.8 g and low-g periods took about 5 s. A normal gravity (1 g) period lasting a few minutes was provided between successive parabolas and was used to set the test parameters. A typical parabola along with the acceleration levels is shown on Fig. 4. Thirty parabolas were flown per flight, and three flights were made.

2.3 Data Acquisition and Test Procedure. Individual microheaters were set to the desired temperature before the start of each test. The two cameras and the air-jet were activated prior to commencing data acquisition. The voltage drop across the LED array used to illuminate the boiling chamber was recorded by the data acquisition system and used to synchronize the video and the data acquisition system. The data acquisition system was programmed to cease acquisition after 30 s. Heater voltage, LED voltage, pressure, and bulk liquid temperature data were acquired at 100 Hz, while the bottom and side view images were recorded at 29.97 Hz. The reader is referred to Ref. [15] for the detailed data reduction procedure and uncertainty analysis. The uncertainties in the parameters for the experimental results are summarized in Table 1.

3 Results and Discussion

The pool boiling curves at representative gravity levels reported by Raj et al. [15] for the high levels of dissolved gas concentration are shown on Fig. 5. The heat transfer increased with the wall superheat in the high-g regime for a given acceleration level. With the onset of nucleate boiling, a significant increase in the slope of

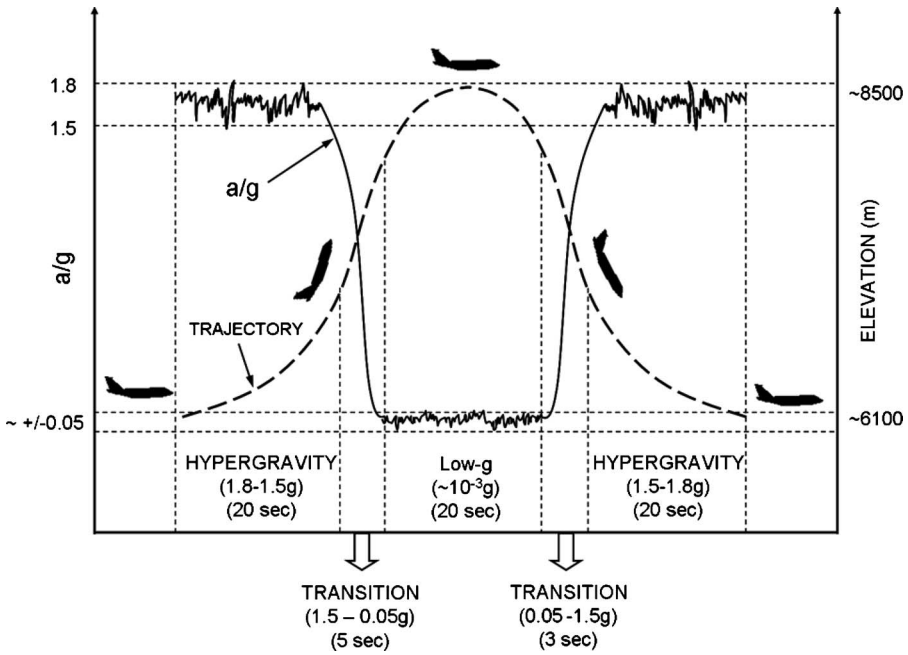

Fig. 4 Schematic of the parabolic flight trajectory and the corresponding acceleration levels [15]

Table 1 Summary of uncertainty estimates in the value of measured parameters

Quantity	Uncertainty
q''	1.2 (W/cm^2)
T_{bulk}	2 (°C)
T_{wall}	0.5 (°C)
T_{sat}	1.5 (°C)
ΔT_w	1.6 (°C)
a	0.01 (g)
c_g	6 (ppm)

the boiling curve was observed. Further increases in the wall superheat resulted in additional nucleation sites being activated.

To determine the effect of gravity and calculate the value of m, the boiling heat flux data at each wall superheat were plotted against the gravity level using logarithmic coordinates—an example is shown in Fig. 1. The squares correspond to the data for transition from hypergravity to low-g, while the triangles correspond to the data during transition from low-g to hypergravity. As can be seen in the figure, the two data sets lie atop each other, indicating quasi-steady behavior. Analysis of the acquired videos revealed that a nondeparting, coalesced bubble governed the heat transfer for acceleration levels less than 0.1 g; consequently, the effect of gravity was small, as indicated by a small m value. Above this threshold acceleration, bubble growth and departure dominated the heat transfer resulting in a larger value of m. Similar jumps in heat flux and discontinuities in m were observed at the other wall superheats, ruling out the possibility of using a constant m to account for gravity dependence over all gravity levels.

The variation in m with wall superheat for the high-g regime is shown on Fig. 6. The square symbols represent m for the high dissolved gas concentration case (~1216 ppm), while the diamond symbols represent the low dissolved gas concentration case (~220 ppm). Again, it is clear that a single constant cannot describe the effect of gravity on pool boiling heat transfer as reported in much of the existing literature since the heat transfer is a function of the wall superheat and is also dependent on the dissolved gas concentration.

3.1 Development of the Gravity Scaling Parameter. Referring to Fig. 5, the pool boiling curve near the ONB is independent of the acceleration level (i.e., m approaches zero) since the single

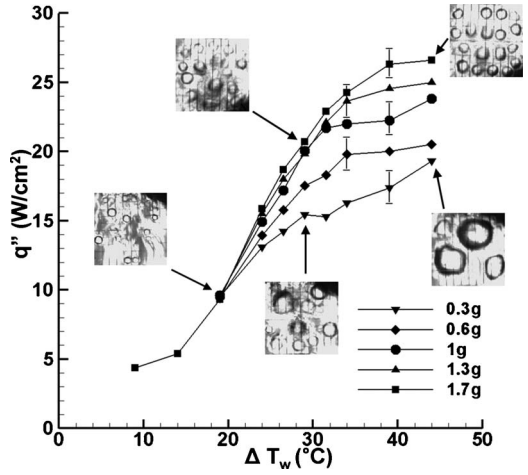

Fig. 5 Pool boiling curve at various acceleration levels for the high dissolved gas concentration case (~1216 ppm) with superimposed bottom view images at 0.3 g and 1.7 g

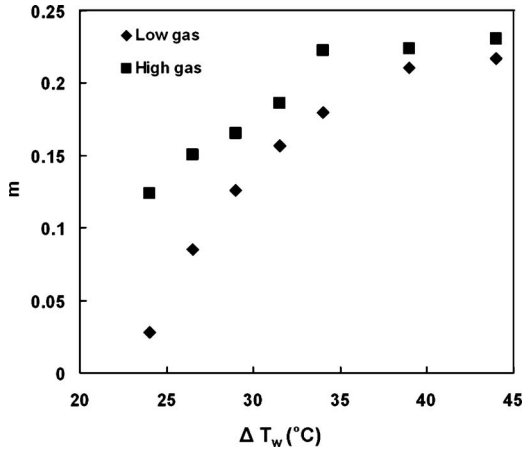

Fig. 6 Plot of the power law coefficient m versus superheat for the two dissolved gas concentrations

phase, natural convection heat transfer is small compared with that due to boiling. The typical heat flux values encountered in the single phase regime (0.7–1.4 W/cm^2) are comparable to the experimental uncertainty (1.2 W/cm^2), making it impossible to observe any differences between different gravity levels. However, the absolute value of heat flux (~4 W/cm^2) reported for the regime (ΔT_w=9°C and ΔT_w=14°C) is higher than the expected range (0.7–1.4 W/cm^2) since a few nucleation sites were active within the heater, even at these relatively small superheats. At higher superheats, the power law coefficient approaches a value of 0.25 (Fig. 6), similar to what is predicted by the correlation of Kutateladze [6] and Zuber [8] for gravity effects on CHF. It is well known that as CHF is approached, there is very little change in the wall superheat with incremental increases in heat flux, and for the purposes of scaling analysis, it is assumed that CHF for all gravity levels occurs at the same wall superheat. Based on this assumption, a nondimensional wall temperature can be defined as follows:

$$T^* = \frac{T_w - T_{ONB}}{T_{CHF} - T_{ONB}} \tag{1}$$

For the high dissolved gas concentration case, the natural convection regime was observed for wall superheats lower than 14°C, while boiling was first observed at a superheat of 19°C. The temperature resolution of 5°C near ONB did not allow exact identification of superheat at ONB. Hence, the average superheat of 16.5°C (T_{ONB}=72.5°C) was selected as ONB for the high dissolved gas concentration. For the low dissolved gas concentration case, single phase heat transfer was observed until the wall superheat of 19°C, while boiling was first observed at a wall superheat of 24°C. As a result, ONB was assumed to occur at a superheat of 21.5°C (T_{ONB}=77.5°C).

The wall superheats investigated in the current experiment were not high enough (Fig. 5) for distinct identification of CHF. As a result, two analyses were conducted to understand the sensitivity of superheat at CHF on the scaling parameter. The trend of the boiling curve suggests that the CHF should occur close to a superheat of 44°C. For the first analysis (Analysis 1), CHF was assumed to occur at a wall superheat of 44°C (T_{CHF}=90°C) for both dissolved gas concentrations. For the second analysis (Analysis 2), an interpolation of the boiling curve at 1.7 g (steady conditions) was performed to estimate the superheat at CHF. This resulted in a superheat of 46.5°C (T_{CHF}=92.5°C) for the high dissolved gas concentration and 49°C (T_{CHF}=95°C) for the low dissolved gas concentration. A lower value of superheat at CHF for the high dissolved gas concentration is expected.

Table 2 Sensitivity analysis of ONB and CHF on the gravity scaling parameter

	High dissolved gas concentration (~1216 ppm)				Low dissolved gas concentration (~220 ppm)			
	Analysis 1	Analysis 2	Analysis 3	Analysis 4	Analysis 1	Analysis 2	Analysis 3	Analysis 4
T_{ONB} (°C)	72.5	72.5	70	75	77.5	77.5	75	80
T_{CHF} (°C)	90	92.5	92.5	92.5	90	95	95	95
a/g	q''_{rms} (W/cm^2)							
0.3	0.35	0.35	0.36	0.37	0.24	0.28	0.25	0.29
0.6	0.19	0.21	0.20	0.23	0.19	0.18	0.19	0.18
1.3	0.23	0.22	0.23	0.21	0.16	0.15	0.15	0.16
1.7	0.30	0.29	0.31	0.27	0.20	0.20	0.22	0.21

As mentioned earlier, there existed an uncertainty of 5°C in the estimation of ONB. Moreover, repeated use of the heaters could possibly result in slight changes in surface properties leading to a few degree changes in temperature at ONB. Hence, two additional analyses (Analyses 3 and 4) were performed to understand the sensitivity of ONB on the scaling parameter. Table 2 summarizes the results of the sensitivity analysis. The results presented in the next few sections are based on the assumption of Analysis 2. However, an examination of the root mean squared (rms) errors in the heat flux prediction due to the lack of knowledge of exact ONB and CHF temperatures showed that the difference between the four analyses are insignificant (Table 2).

The variation in m for the two dissolved gas concentrations as a function of T^* is shown on Fig. 7. The curves for the two gas concentrations overlap, indicating that the shapes of the two curves are similar if the appropriate scaling parameter for temperature is used. A curve fit was performed on the data assuming m approaches a value of 0 for $T^*=0$ and a value of 0.25 for $T^*=1$. An empirical curve satisfying these conditions that fits the data well is given by

$$m = \frac{0.9T^*}{1 + 2.6T^*} \tag{2}$$

Based on this variation in m, the heat flux at any two gravity levels can be related as follows:

$$\frac{q''_2}{q''_1} = \left(\frac{a_2}{a_1}\right)^m \tag{3}$$

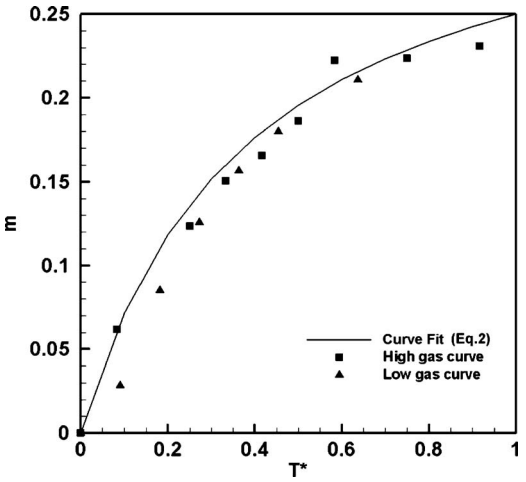

Fig. 7 Plot of the power law coefficient m versus nondimensional wall temperature for the two dissolved gas concentrations

This scaling parameter can be used to predict the heat transfer at any gravity level in the heater size independent, buoyancy-dominated boiling regime ($L_h/L_c > 2.1$) if the heat transfer under similar conditions at any other gravity level in this regime is known. A convenient choice for q_1'' would be the experimentally determined boiling curve in earth gravity ($a_1=g$). Moreover, since correlations available in the literature are based on earth gravity observations, they could also be used for q_1''. Section 3.2 validates the applicability of this scaling parameter at four gravity levels and two gas concentrations.

3.2 Validation of Results. The pool boiling curves for various gravity levels shown in Fig. 5 (high dissolved gas concentration case) were used to validate the applicability of the scaling parameter. The boiling curve at 1 g was chosen to be q_1'' and used to predict the boiling curves at 0.3 g, 0.6 g, 1.3 g, and 1.7 g. The results of the prediction and the actual data along with the earth gravity results and error bars are shown on Fig. 8. The prediction and the experimental data are in very good agreement, indicating the suitability of the scaling parameter.

Boiling curves similar to those in Fig. 5 were also obtained for the low dissolved gas concentration case [15]. ONB was delayed at the low dissolved gas concentration. This is also clear from Fig. 6, where the value of m approaches a value of zero (ONB) at higher wall superheat. Prediction and experimental results (Fig. 9) are also in very good agreement, further demonstrating the effectiveness of the proposed scaling parameter to account for dissolved gas content. The root mean square errors between the predicted and experimental results using the four analysis approaches are shown in Table 2. The four analyses seem to be insensitive to the superheat at ONB and CHF. The errors for both the high gas and low gas case are small and of the same magnitude. The maximum error was 0.37 W/cm^2, considerably smaller than the typical heat flux values at these acceleration levels and within the experimental uncertainty of 1.2 W/cm^2.

3.3 Effect of Subcooling. Additional parabolic flight experiments were performed in August 2009 to verify the validity of the scaling parameter at different subcoolings ΔT_{sub}, namely, 16.6°C ($T_{bulk}=40$°C) and 6.6°C ($T_{bulk}=50$°C). The test fluid was FC-72 (an isomeric blend of C_6F_{14}, $T_{sat}=56$°C at 1 atm) and the gas concentration was maintained at $c_g=174$ ppm. The experimental procedure and data reduction techniques were similar to the previous campaign. However, the transition from high-g to low-g and vice versa was not smooth during the NASA flights and occurred over a much shorter time duration (~1–2 s). There was also no 1-g period between two successive parabolas. As a result, the time interval between two parabolas was not sufficient for data storage, and hence, the second transition (low-g to high-g) was also used for data storage purposes. The absence of data during the second transition made it impossible to validate the quasi-steady state assumption during transition and extract variable gravity boiling

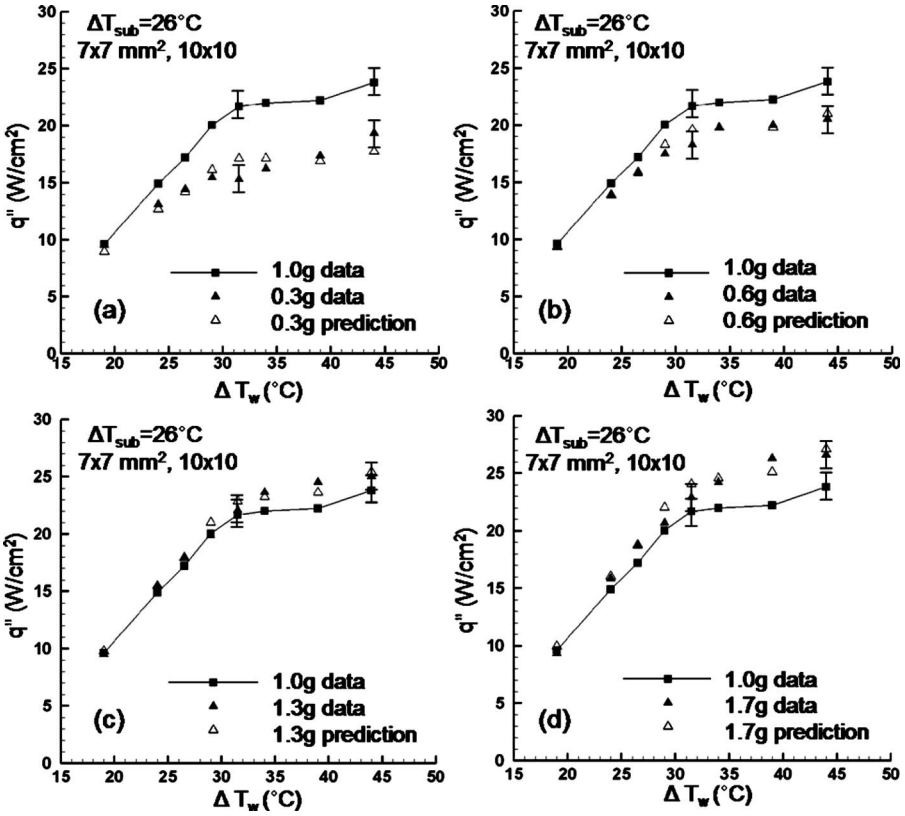

Fig. 8 Comparison of the measured and predicted heat flux for the high dissolved gas concentration case (~1216 ppm) and full heater (7.0×7.0 mm²) at (*a*) 0.3 g, (*b*) 0.6 g, (*c*) 1.3 g, and (*d*) 1.7 g

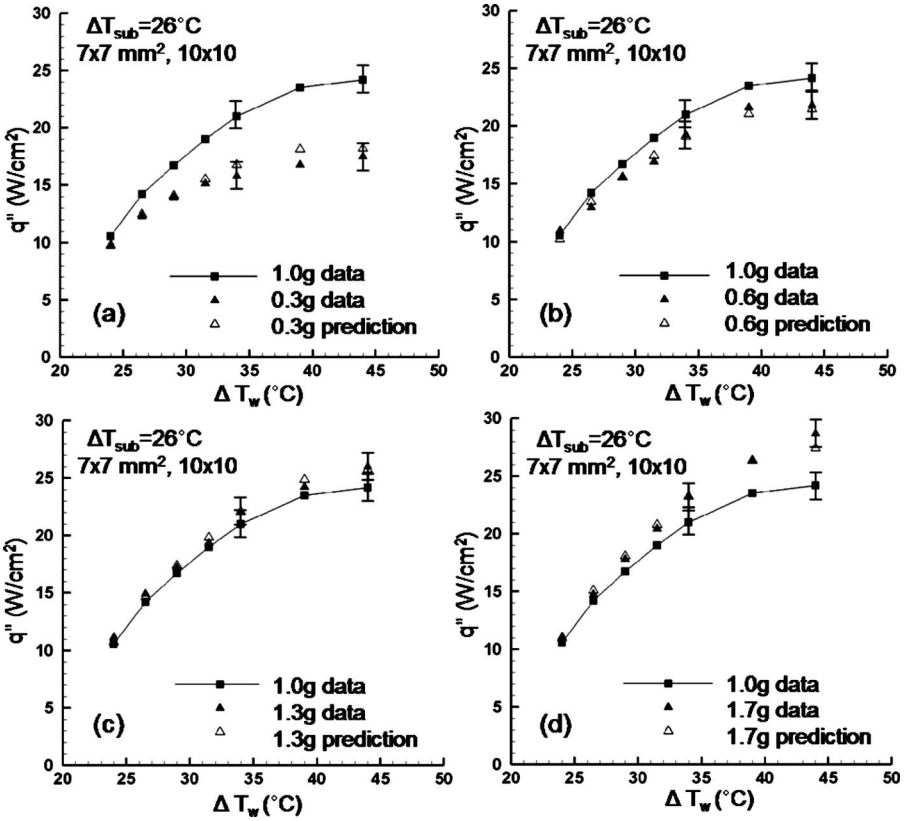

Fig. 9 Comparison of the measured and predicted heat flux for the low dissolved gas concentration case (~220 ppm) and full heater (7.0×7.0 mm²) at (*a*) 0.3 g, (*b*) 0.6 g, (*c*) 1.3 g, and (*d*) 1.7 g

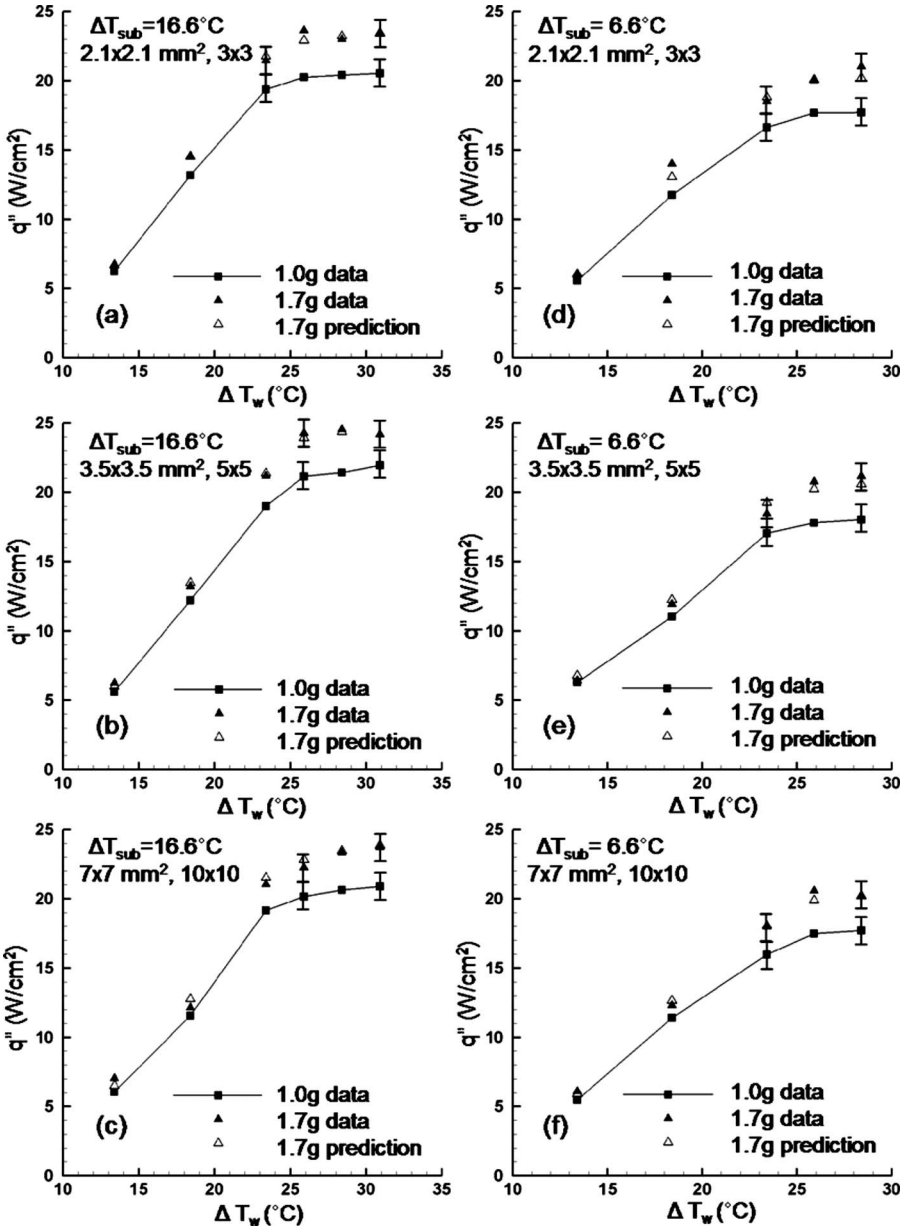

Fig. 10 Comparison of the measured and predicted heat flux for various heaters sizes and subcoolings: (*a*) 2.1×2.1 mm² and 16.6°C, (*b*) 3.5×3.5 mm² and 16.6°C, (*c*) 7.0×7.0 mm² and 16.6°C, (*d*) 2.1×2.1 mm² and 6.6°C, (*e*) 3.5×3.5 mm² and 16.6°C, (*f*) 7.0×7.0 mm² and 6.6°C (heater 2)

curves from the NASA campaign. As a result, only the high gravity (1.7 g) and earth gravity results were used to validate the scaling parameter under different subcoolings.

A different microheater array was also used to verify the dependence of heater surface properties (e.g., nucleation site density) on the scaling parameter. The microheater used for the ESA campaign will hereafter be referred to as Heater 1 (all the results in Sec. 3.2), while that used for the NASA flights will be referred to as Heater 2. The microheater temperature during the NASA flights was varied between 65°C (ΔT_w=8.4°C) and 100°C (ΔT_w =43.4°C), and the pressure was maintained at 1 atm throughout the experiment.

The experimental heat flux values along with the prediction results are shown in Fig. 10. The curves represented by solid line and closed square symbols are the 1 g boiling curves. The earth gravity heat flux value was multiplied by the scaling parameter to predict the heat flux at hypergravity (1.7 g) conditions (open triangles). Closed triangles represent the experimental data at high-g (1.7 g). Three heated areas were used to study the heater size effect: 2.1×2.1 mm² (3×3 elements), 3.5×3.5 mm² (5×5 elements), and 7.0×7.0 mm² (10×10 elements). The ratio of heater size to capillary length L_h/L_c was larger than 2.1 for this data, hence the boiling curves were in the heater size independent regime.

Good agreement was found between the experimental results and prediction at both subcoolings and three heater sizes. The root mean square errors between the predicted and experimental results at two subcoolings are shown in Table 3. Although the root mean square error is slightly larger than that observed in the previous set of experiments (ESA campaign), the maximum error was again considerably smaller (0.57 W/cm²) than the typical heat flux magnitude and uncertainty (1.2 W/cm²) at these acceleration levels.

Table 3 Root mean square error between the predicted and experimental results

Size	q''_{rms} (W/cm^2) $\Delta T_{sub}=16.6°C$	$\Delta T_{sub}=6.6°C$
2.1×2.1 mm^2 (3×3 elements)	0.34	0.57
3.5×3.5 mm^2 (5×5 elements)	0.43	0.55
7.0×7.0 mm^2 (10×10 elements)	0.47	0.36

A summary of the experimental data versus predicted results for all the test conditions discussed above is shown on Fig. 11. The data in this plot include the effects of wall temperature, heater size, bulk liquid subcooling, gas concentration, heater surface morphology, and gravity level (0.3g, 0.6g, 1.3g, and 1.7g). The error in the prediction is considerably smaller ($<10\%$) than that for the boiling correlations based on a constant power law coefficient.

3.4 Guidelines for Using Scaling Parameter. The scaling parameter can be used as a tool to predict boiling heat flux at any gravity level if the data under similar experimental conditions are available at another gravity level. Figure 12 shows the comparison of the results at two subcoolings using the same heater. A large compilation of pool boiling data in the literature (including the current work) suggests that nucleate pool boiling heat transfer is relatively insensitive to the liquid subcooling. However, heat flux at CHF increases with subcooling. Moreover, the temperature/superheat at which CHF is observed increases with subcooling. The change in CHF or the corresponding wall superheat is accounted for in the scaling parameter and prediction is accurate if experimental data at the same subcooling and any gravity level is available (1 g in the current case).

A comparison of the results obtained from the two heaters with different surface morphologies as evidenced by different boiling curves is shown on Fig. 13. The closed symbols represent the boiling curves for Heater 1 ($\Delta T_{sub}=26.6°C$), while the open symbols represent the boiling curves for Heater 2 ($\Delta T_{sub}=16.6°C$). The superheat at ONB was observed to be different for the two heaters. However, for each case, the scaling parameter is valid and the corresponding earth gravity data can be used to predict the heat flux at 1.7 g. The nondimensional temperature T^* accounts for the change in superheat at ONB and the corresponding shift in the boiling curve.

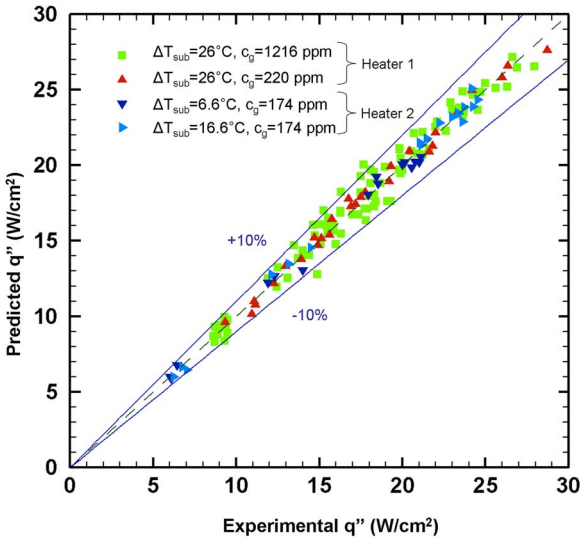

Fig. 11 Comparison of the experimental data and predicted heat flux values using the gravity scaling parameter

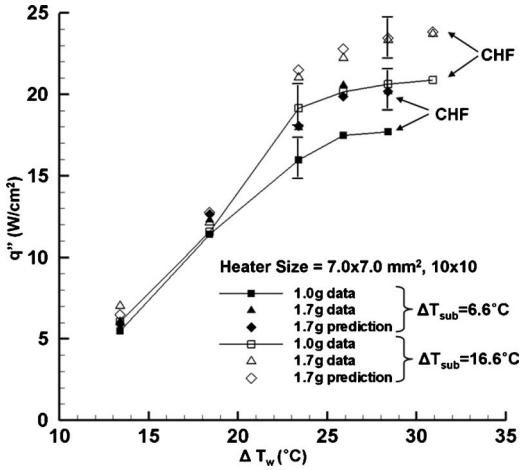

Fig. 12 Comparison of the measured and predicted heat flux at two subcoolings (heater 2)

4 Conclusions

Variable gravity pool boiling data in the heater size independent, buoyancy-dominated boiling regime ($L_h/L_c>2.1$) was used to develop a gravity scaling parameter for pool boiling heat transfer. A possible explanation for the observed discrepancies in the value of the power law coefficient was provided. The power law coefficient for the gravity effect was observed to be a function of wall superheat. A nondimensional wall temperature was used to obtain a gravity scaling parameter for upward facing heaters. The predicted results were found to be in good agreement with the heat transfer data over a wide range of gravity levels, two dissolved gas concentrations, three subcoolings, and two surface morphologies. Although the scaling parameter was obtained using subcooled pool boiling experimental data for n-perfluorohexane/FC-72, it is expected to be valid for refrigerants with similar properties. The use of this scaling parameter to obtain heat transfer at varying gravity levels can save considerable experimental resources required to validate the performance of phase change based systems under different gravity conditions.

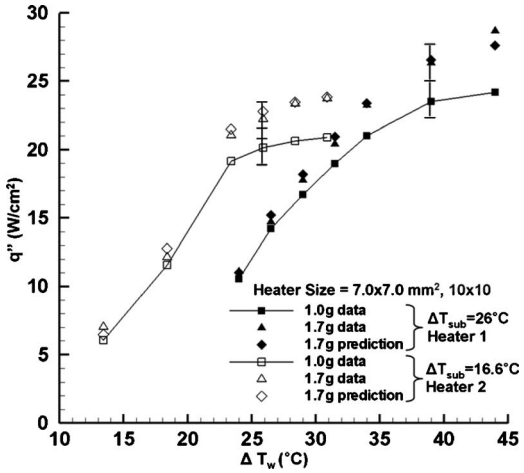

Fig. 13 Comparison of the measured and predicted heat flux for two microheater arrays

Acknowledgment

This work was supported by NASA under Grant No. NNX08AI60A through the Advanced Capabilities Division in the Exploration Systems Mission Directorate at NASA Headquarters. The authors would like to thank the European Space Agency for accommodating our experiment on the 48th ESA Parabolic Flight Campaign in March, 2008.

Nomenclature

a = acceleration (m/s^2)
c = concentration (ppm)
g = acceleration at earth gravity (m/s^2)
L_h = heater length (m)
L_c = capillary length (m), $\sqrt{\sigma/(\rho_l-\rho_v)g}$
q'' = heat flux (W/cm^2)
T = temperature (°C)
T^* = nondimensional temperature

Subscripts

bulk = bulk liquid
g = gas
sat = saturation
sub = subcooling
w = superheat
Wall = heater wall

References

[1] Rohsenow, W. M., 1962, "A Method of Correlating Heat Transfer Data for Surface Boiling of Liquids," Trans. ASME, **84**, pp. 969–976.
[2] Forster, H. K., and Zuber, N., 1955, "Dynamics of Vapor Bubbles and Boiling Heat Transfer," AIChE J., **1**, pp. 531–535.
[3] Stephan, K., and Abdelsalam, M., 1980, "Heat Transfer Correlations for Natural Convection Boiling," Int. J. Heat Mass Transfer, **23**, pp. 73–87.
[4] Fritz, W., 1935, "Berechnung des Maximalvolume von Dampfblasen," Phys. Z., **36**, pp. 379–388.
[5] Siegel, R., and Keshock, F. G., 1964, "Effects of Reduced Gravity on Nucleate Boiling Bubble Dynamics in Saturated Water," AIChE J., **10**(4), pp. 509–517.
[6] Kutateladze, S. S., 1948, "On the Transition Film Boiling Under Natural Convection," *Kotloturbostroenie*, Vol. 3, pp. 10–12.
[7] Chang, Y. P., 1957, "A Theoretical Analysis of Heat Transfer in Natural Convection and in Boiling," Trans. ASME, **79**, pp. 1501–1513.
[8] Zuber, N., 1959, "Hydrodynamic Aspects of Boiling Heat Transfer," AEC Report No. AECU-4439.
[9] Di Marco, P., 2003, "Review of Reduced Gravity Boiling Heat Transfer: European Research," J. Jpn. Soc. Microgravity Appl., **20**(4), pp. 252–263.
[10] Kim, J., 2003, "Review of Reduced Gravity Boiling Heat Transfer: U.S. Research," J. Jpn. Soc. Microgravity Appl., **20**(4), pp. 264–271.
[11] Ohta, H., 2003, "Review of Reduced Gravity Boiling Heat Transfer: Japanese Research," J. Jpn. Soc. Microgravity Appl., **20**(4), pp. 272–285.
[12] Lee, H. S., Merte, H., and Chiaramonte, F., 1997, "Pool Boiling Curve in Microgravity," J. Thermophys. Heat Transfer, **11**(2), pp. 216–222.
[13] Straub, J., 2001, "Boiling Heat Transfer and Bubble Dynamics in Microgravity," Adv. Heat Transfer, **35**, pp. 57–172.
[14] Kannengieser, O., Colin, C., Bergez, W., and Lacapere, J., 2009, "Nucleate Pool Boiling on a Flat Plate Heater Under Microgravity Conditions: Results of Parabolic Flight, and Development of a Correlation Predicting Heat Flux Variation Due to Gravity," *Proceedings of the Seventh ECI International Conference on Boiling Heat Transfer*, Florianopolis, Brazil, May 3–7.
[15] Raj, R., Kim, J., and McQuillen, J., 2009, "Subcooled Pool Boiling Under Variable Gravity Environments," J. Heat Transfer, **131**, pp. 091502.
[16] Raj, R., and Kim, J., 2010, "Heater Size and Gravity Based Pool Boiling Regime Map: Transition Criteria Between Buoyancy and Surface Tension Dominated Boiling," ASME J. Heat Transfer, **132**(9), p. 091503.
[17] DeLombard, R., McQuillen, J., and Chao, D., 2008, "Boiling Experiment Facility for Heat Transfer Studies in Microgravity," *Proceedings of the 46th AIAA Aerospace Sciences Meeting and Exhibit*, Reno, NV, Jan. 7–10.
[18] Rule, T. D., and Kim, J., 1999, "Heat Transfer Behavior on Small Heaters During Pool Boiling of FC-72," ASME J. Heat Transfer, **121**(2), pp. 386–393.

Heater Size and Gravity Based Pool Boiling Regime Map: Transition Criteria Between Buoyancy and Surface Tension Dominated Boiling

Rishi Raj
e-mail: rraj@umd.edu

Jungho Kim[1]
e-mail: kimjh@umd.edu

Department of Mechanical Engineering,
University of Maryland,
College Park, MD 20742

A pool boiling regime map demarcating the boundary between the surface tension and buoyancy dominated boiling regimes is developed based on heater size and gravity. For large heaters and/or high gravity conditions, boiling is dominated by buoyancy, and the ebullition cycle dominates the contribution to heat transfer. As the gravity level and/or heater size is decreased, surface tension forces become increasingly dominant, and a decrease in heat transfer is observed. The ratio of the heater size L_h (length of a side for a square heater) to the capillary length L_c is found to be a suitable parameter to define the transition criterion between these regimes. Based on the data obtained using FC-72 and pentane, the threshold value of L_h/L_c above which pool boiling is buoyancy dominated was found to be about 2.1. This transition criterion was found to be the same for gravity levels between ~0g–1.7g and liquid subcoolings between 6.6°C and 26.6°C.
[DOI: 10.1115/1.4001635]

Keywords: pool boiling, capillary length, heater size, gravity, surface tension, buoyancy, regime map

1 Introduction

The ability to dissipate large heat flux with relatively small temperature differences have attracted engineers toward boiling as an efficient alternative solution to cooling problems. Some of the major applications include cooling of electronic products and design of space based hardware. With the advancement in device technology, the electronic industry is moving toward high-speed devices with constantly increasing thermal loads. The crisis of real estate in electronic packages combined with the state-of-the-art manufacturing technology has led to the miniaturization of these devices. Moreover, the space based technologies require these products to operate efficiently under a wide range of gravity levels. Understanding of boiling under different gravity conditions and at these smaller length scales is hence of paramount importance to the design of these products and their successful operation.

Boiling on large heaters under earth gravity conditions is buoyancy dominated and is a combination of natural convection, liquid-vapor phase change, and transient conduction. The ebullition cycle associated with nucleation, bubble growth, departure, and rewetting dominates the contribution to heat transfer. Many semitheoretical models have been developed that predict boiling behavior in earth gravity [1–5]. However, most of these models assume that the heater is sufficiently large and boiling is independent of the heater size. It is generally understood that classical boiling is observed if the heater size is considerably larger than the departure diameter D_d. Hence, the most suitable length scale to study heater size independence should be the departure diameter. However, estimation of the departure diameter D_d under actual boiling conditions is not straightforward. Experimental measurement of D_d is difficult due to increased turbulence when multiple bubbles nucleate. Although there are correlations for D_d, most of them are only valid for single bubbles and rely on other parameters (e.g., contact angle, departure frequency), which are not easily estimated or measured. Use of the various correlations in the literature can result in values for D_d that vary by an order of magnitude or more. For example, Yaddanapuddi and Kim [6] compared the bubble departure diameter and frequency obtained from numerous correlations in the literature, and found that they gave widely varying results, with errors between −26% and 1400%.

On the other hand, capillary length L_c (the ratio of the surface tension and buoyancy forces) defined as

$$L_c = \left(\frac{\sigma}{g(\rho_l - \rho_v)} \right)^{1/2} \tag{1}$$

mimics the variation in the departure diameter, depends only on fluid properties and gravity level, and hence, is easy to estimate. As a result, the ratio of the heater size L_h and capillary length L_c has widely been used in boiling literature [7]. The quantity $(L_h/L_c)^2$ can also be interpreted as a heater size-based Bond number. Most of the available boiling correlations have been stated to be valid only if the heater size is considerably larger than the capillary length scale

$$\frac{L_h}{L_c} \gg 1 \tag{2}$$

Boiling on small heaters under earth gravity conditions has also been studied extensively [8–14]. Most studies on small heaters [8–10] have generally focused on issues such as nucleation, bubble growth rate, and single bubble dynamics. Bakhru and Lienhard [15] studied boiling on small diameter wires. They observed that boiling curves for small wires deviate from the classical boiling behavior. No typical boiling behavior from nucleate to

[1]Corresponding author.

Contributed by the Heat Transfer Division of ASME for publication in the JOURNAL OF HEAT TRANSFER. Manuscript received December 3, 2009; final manuscript received March 19, 2010; published online July 6, 2010. Assoc. Editor: Satish G. Kandlikar.

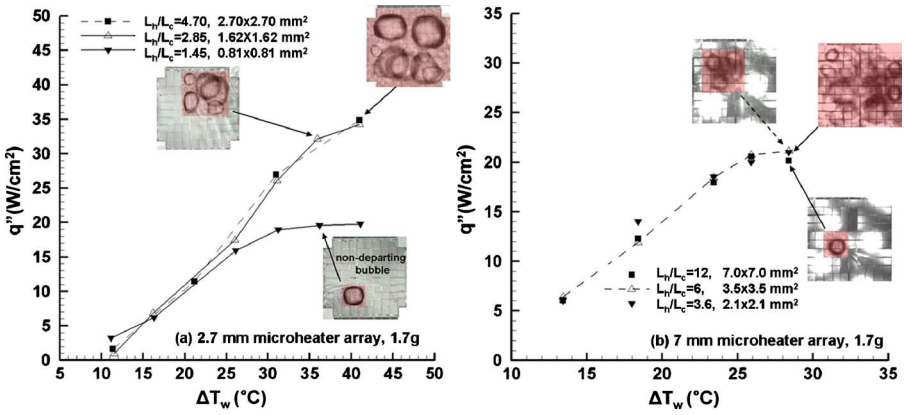

Fig. 1 Boiling curves using FC-72 at 1.7*g* for selected heaters on (*a*) 2.7 mm microheater array [12], ΔT_{sub}=31°C, and (*b*) 7 mm microheater array [13], ΔT_{sub}=6.6°C, and *P*=1 atm

film boiling was observed for $L_h/L_c<0.15$. The Leidenfrost point and critical heat flux (CHF) were also not observed in their study. The heat transfer increased monotonically between the first nucleation and full film boiling. It was concluded that the classical boiling curve is only observed if the heater diameter is of the order of $L_h/L_c>0.15$. They also proposed that similar behavior could be observed for large cylinders at small gravity levels, thus, proposing a similarity between the heater size and gravity effects.

Henry and Kim [12] obtained boiling curves with three heater sizes (0.81×0.81 mm^2, 1.62×1.62 mm^2, and 2.7×2.7 mm^2) in high gravity environments ($\sim1.7g$) (Fig. 1(*a*)). At the same superheat, heat fluxes for the two larger sizes were comparable, while a smaller heat flux was observed for the smallest size. It was reported that boiling on 0.81×0.81 mm^2 heated area at $1.7g$ ($L_h/L_c\sim1.5$) was surface tension dominated, and a stable, nondeparting primary bubble similar to boiling in microgravity was formed. The results of a recent experiment [13] with three heater sizes (7×7 mm^2, 3.5×3.5 mm^2, and 2.1×2.1 mm^2) at $1.7g$ and a smaller subcooling were also consistent with this observation (Fig. 1(*b*)). The boiling behavior was buoyancy dominated for all three heater sizes because the area for all heaters was larger than 1.62×1.62 mm^2 (Henry and Kim). The value of heat flux near CHF and lower subcooling (Fig. 1(*b*)) was smaller than that observed near CHF for higher subcooling (Fig. 1(*a*)). The differences in the value of heat flux may also be due to the different nucleation behaviors of the heaters used in these experiments.

An effect of the heater size on heat flux is evident from these results. Below a particular heater size (heater width for flat heaters and heater diameter for wires), boiling is surface tension dominated. In this regime, the maximum bubble size becomes comparable to the heater size, and a nondeparting primary bubble forms on the heater surface (e.g., 0.81×0.81 mm^2, Fig. 1(*a*)). The heat flux is *heater size dependent*, and the boiling curve is specific to that particular heater size. On the other hand, if the heater size is considerably larger than the capillary length, buoyancy dominates boiling. The bubble size, percentage dryout area, and departure frequency are not influenced by the size of the heater. For any heater size large enough such that boiling is buoyancy dominated, the boiling curve is *heater size independent*, and hence, can be generalized. As an example, for heater sizes of 1.62×1.62 mm^2 and 2.7×2.7 mm^2 in Fig. 1(*a*), the boiling curves are similar and are thus heater size independent. Similarly, all sizes in Fig. 1(*b*) are in the buoyancy dominated regime, and similar boiling curves are observed.

Raj et al. [14] observed that the heat flux for three heater sizes ranging from 7×7 mm^2 to 3.5×3.5 mm^2 (96–24 heaters) were similar if the acceleration was larger than $0.3g$ (Fig. 2). However, for experiments with acceleration values smaller than $0.3g$, the heat transfer varied significantly with the heater size. It was proposed that in the boiling regime, where normal bubble departure was observed (e.g., $0.3g$, $1.0g$, and $1.7g$), boiling was dominated by buoyancy, and the heat transfer was heater size independent. As the ratio L_h/L_c decreased due to a decrease in gravity, surface tension forces became increasingly important ($0.05g$). The sudden drop in heat transfer observed below a particular threshold gravity level was due to the formation of a nondeparting, coalesced bubble. Due to the limited number of heated areas used, no conclusion about the exact threshold value of L_h/L_c for heater size independence could be made.

It is clear that a threshold value of L_h/L_c exists above which boiling is dominated by buoyancy. The presence of the capillary length in this ratio along with the variable gravity study [14] suggests a similarity between the gravity and heater size effect on the pool boiling curve. Hence, a study of pool boiling with varying heater sizes and gravity levels is needed. It would be interesting to study the dependence of the transition criteria between the boiling regimes on the gravity level. If the transition between the surface tension and the buoyancy dominated boiling regimes is found to occur at a constant L_h/L_c over a wide range of gravity levels and heater sizes, it would be highly desirable to verify if the heat flux values for boiling in low gravity is also similar to the heat flux values with small heaters in earth gravity, provided that the value of L_h/L_c is the same under the two conditions. If true, this would possibly allow the simulation of many of the partial and low gravity experiments (surface tension regime) in an earth gravity environment using small heaters.

This paper identifies the threshold value of L_h/L_c above which pool boiling is dominated by buoyancy and is heater size independent. Pool boiling experiments with varying heater sizes and two fluids (FC-72 and pentane) were performed under earth gravity conditions. The effect of gravity is explained by correlating the current results with those performed at other gravity levels. A pool boiling regime map is developed by combining the current results and those published in the literature.

2 Experimental Setup and Test Procedure

2.1 Test Package Description. Two microheater arrays, i.e., 7 mm and 2.7 mm, consisting of 96 platinum resistance heaters deposited in a 10×10 configuration (four corners missing, 96 heaters) onto a quartz substrate were used to measure the heat transfer distribution (Fig. 3). Each heater in the 7 mm and 2.7 mm microheater arrays was nominally 0.7×0.7 mm^2 and 0.27×0.27 mm^2 in area, respectively. Power was transferred via gold power leads 1 μm thick. Individual heaters in the 7 mm microheater array had a nominal resistance of 250 Ω and a temperature

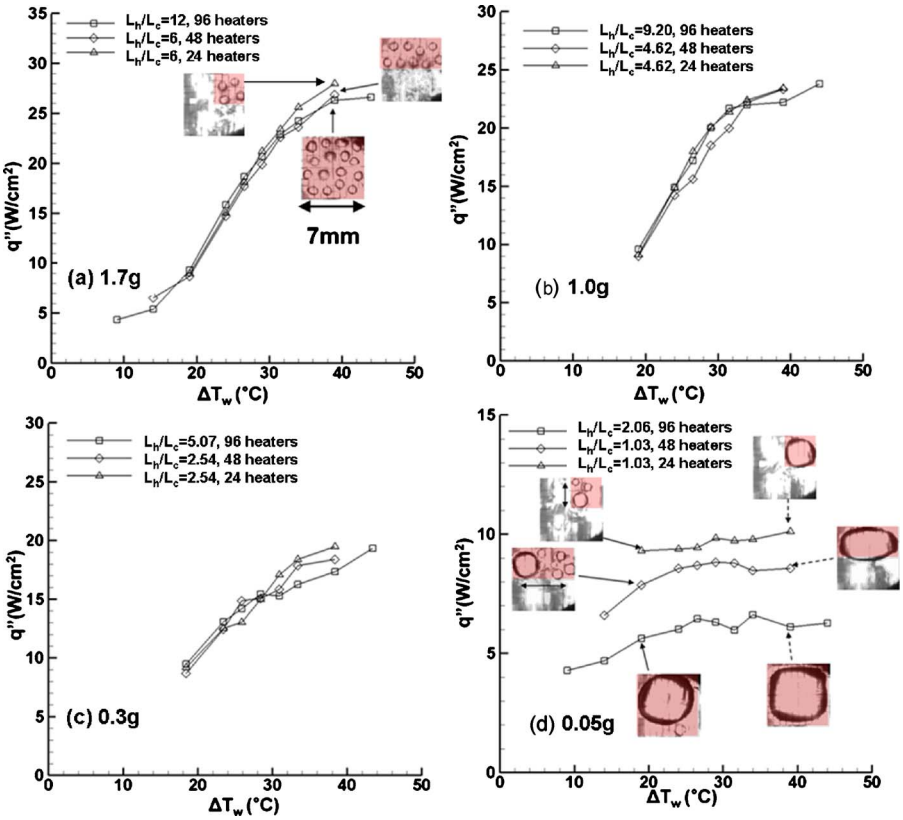

Fig. 2 Boiling curve using n-perfluorohexane at three heater sizes and (*a*) 1.7*g*, (*b*) 1.0*g*, (*c*) 0.3*g*, and (*d*) 0.05*g* [14], ΔT_{sub}=26°C, and *P*=1 atm (7 mm microheater array)

coefficient of resistance (TCR) of 0.0023°C^{-1}. The properties of the two microheater arrays are summarized in Table 1. The heated area was maintained at a constant temperature using a bank of feedback circuits similar to those used in constant temperature hot-wire anemometry. The power, and thus the heat flux, required to maintain these heaters at the desired temperature were obtained by sampling the voltages across the heaters. The frequency response for the heaters and feedback circuits was very high (15 kHz). The reader is referred to Ref. [16] for details about the heater construction and operation.

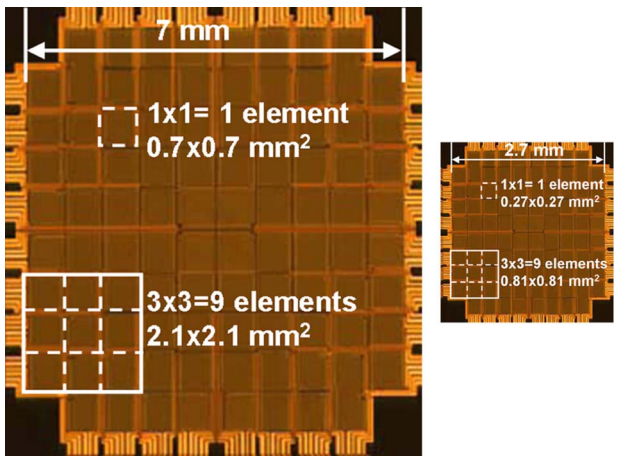

Fig. 3 7 mm (left) and 2.7 mm (right) microheater arrays

Table 1 Comparison of 7 mm and 2.7 mm microheater arrays

Microheater array (mm)	Area of each element (mm^2)	Heater resistance (Ω)	TCR (°C^{-1})
7	0.7×0.7	~250	~0.0023
2.7	0.27×0.27	~975	~0.0021

The main advantage of the microheater array is that it simultaneously provides time and space resolved temperature and heat flux measurements under nucleating bubbles. Images captured through the bottom surface were correlated with the temperature and heat flux distribution over the array for better visualization of the phenomena. The ability to selectively power a subset of the heater elements (1, 4, 9, 16, 25, 36, 64, and 96) in a square pattern out of the 10×10 configuration made the microheater array ideal for use in a variable heater size study. For example (Fig. 3), powering a 3×3 configuration, i.e., nine elements resulted in heated areas of 2.1×2.1 mm^2 and 0.81×0.81 mm^2 on the 7 mm and 2.7 mm heaters, respectively.

Figure 4 shows a CAD model of the test package. The test rack contained a sealed boiling chamber with approximately 3 l of test fluid, a microheater array (7 mm/2.7 mm), the electronic feedback circuits, two video cameras, a computer with a data acquisition unit, a pressure sensor (PDCR 130/W), and thermocouples and RTDs for the bulk liquid and backside air-jet temperature measurements. A PID temperature controller (OMEGA CNi 16) in conjunction with two thermocouples and Kapton thin film heaters was used to hold the fluid within the chamber at a desired bulk liquid temperature. Backside cooling of the heater array was required to minimize the fraction of heat dissipated by lateral conduction and to prevent individual heaters from shutting off at low heat transfer levels. Air was forced through a 1.6 mm diameter nozzle placed 10 mm from the backside of the heater. The cooling air flow was maintained by a compressed air bottle with pressure regulation nominally set at 340 kPa. The air-jet temperature varied between 17°C and 19°C throughout the experiment.

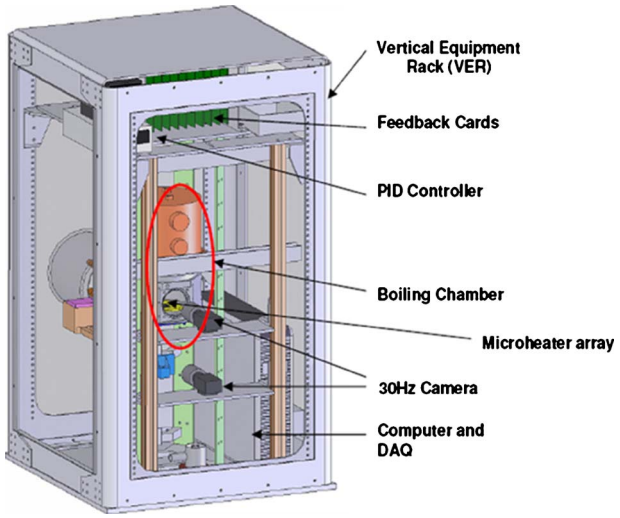

Fig. 4 CAD model of the experimental package

2.2 Test Conditions. At first glance, a complete investigation of the heater size effect would require around 800 experiments (ten sizes each for the 7 mm and 2.7 mm microheater arrays, two subcoolings, about ten wall superheats for the full nucleate boiling curve, and at least two fluids). However, observations from the analysis of the data acquired in the early stages of the experiment revealed that many of these parameters have a negligible effect on heater size independence, and hence, do not require a detailed investigation of all the possible conditions. As a result, fewer tests (~300) were sufficient to understand and explain the effect of these parameters and arrive at a threshold value of L_h/L_c.

Earth gravity subcooled pool boiling experiments were performed at a pressure of 1 atm. The heater temperature was varied to acquire data in the nucleate boiling regime. Different heater sizes L_h were obtained by operating a subset of heaters in the array, as explained in Sec. 2.1. Table 2 provides a complete list of experimental conditions used in this study.

2.3 Data Acquisition and Test Procedure. The selected heater elements for any given configuration were set to the desired temperature before the start of each data acquisition run. The two cameras and the air-jet were activated after which the data acquisition commenced. The LED array illuminating the boiling chamber then turned on—the step change in the voltage across the LED recorded by the data acquisition system and the change in illumination observed in the video were used to synchronize the video and the data. The data acquisition system was programmed to stop acquisition after 30 s. Heat flux, LED voltage, pressure, and bulk liquid temperature data were acquired at 300 Hz, while the bottom and side view images were acquired at 29.97 Hz.

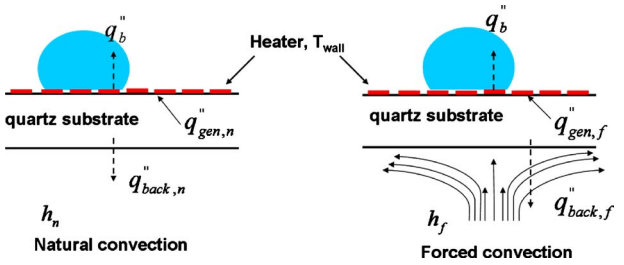

Fig. 5 The schematic of the dominant heat transfer paths for the (*a*) natural convection and (*b*) forced convection cases

2.4 Data Reduction. The raw voltage data obtained from the individual heaters for the 96 heater case were first converted to the total heat flux, and a spatial average was computed for each time step (q''_{gen}). Various heat transfer paths within the chip are illustrated in Fig. 5. Thermal resistance within the chip in the lateral direction is one to two orders of magnitude higher than that in the backside of the chip. As a result, the component of heat transfer in the lateral direction is neglected in the analysis. Only a portion of the total heat generated (q''_{gen}) in the heater was removed by the liquid (q''_b) with the remainder lost to the ambient either through natural convection or forced convection (q''_{back}). Figure 5(*a*) represents the case without the backside air-jet—a small amount of heat ($q''_{back,n}$) was lost through the back of the chip by natural convection to the ambient air, while Fig. 5(*b*) represents the situation with the air-jet during which considerably more heat ($q''_{gen,f}$) was lost by forced convection to the ambient.

The energy balance for these cases are given by

$$q''_b = q''_{gen,n} - q''_{back,n} \quad \text{(natural convection)} \tag{3}$$

$$q''_b = q''_{gen,f} - q''_{back,f} \quad \text{(forced convection)} \tag{4}$$

If the heater surface is at the same temperature for both the cases, the heat supplied to the liquid q''_b for boiling remains unchanged, and

$$q''_{gen,f} - q''_{gen,n} = q''_{back,f} - q''_{back,n} \tag{5}$$

Spatially averaged heat flux data were calculated with the air-jet on ($q''_{gen,f}$) and the air-jet off ($q''_{gen,n}$) for all wall superheats and the 96 heater configuration. A natural convection heat transfer coefficient h_n of 10 W/m^2 K was assumed at the back of the chip for the case without the air-jet. A COMSOL™ finite element model with appropriate boundary conditions and h_n of 10 W/m^2 K was used to calculate $q''_{back,n}$. With all three quantities known, Eq. (5) was solved for $q''_{back,f}$. With the forced convection substrate conduction loss known, the COMSOL model was used to back-calculate the spatial averaged forced convection heat transfer coefficient (h_f). The average of the heat transfer coefficient over all superheats with other appropriate boundary conditions was then used to cal-

Table 2 Test matrix

	FC-72		Pentane
Microheater array (mm)	7	2.7	7
T_{sat} (°C), P (atm)	56.6, 1	56.6, 1	36, 1
ΔT_{sub} (°C)	8.6 and 26.6	16.6	8
T_w (°C)	65, 70, 75, 80, 82.5, 85, 87.5, 90, 95, 100	75, 77, 78, 79, 80, 82.5, 85	60, 65, 70, 75, 77.5, 80, 82.5, 85, 87.5, 90
L_h (mm)	0.7, 1.4, 2.1, 2.8, 3.5, 4.2, 5.6, 7.0	0.81, 1.08, 1.35, 1.62, 2.16, 2.7	0.7, 1.4, 2.1, 2.8, 3.5, 4.2, 5.6, 7.0
L_c (mm)	0.75	0.75	1.51
Range of L_h/L_c	$0.93 \le L_h/L_c \le 9.3$	$1.08 \le L_h/L_c \le 3.6$	$0.47 \le L_h/L_c \le 4.7$

Table 3 Summary of the uncertainty estimates (absolute) in the value of the measured parameters

Quantity	Uncertainty
q'' (W/cm^2)	0.65
T_{bulk} (°C)	0.45
T_{wall} (°C)	0.35
T_{sat} (°C)	1.5
ΔT_w (°C)	1.5

culate the substrate conduction losses for other sizes.

The constant temperature boundary condition assumption for the microheater array gets worse with decreasing heater size. However, the heat transfer coefficient at the back of the chip is the same, irrespective of the heater size. For cases where the constant temperature boundary condition cannot be applied (heated areas smaller than 2.8×2.8 mm^2, 16 elements), a constant heat flux boundary condition was applied at the heaters in the COMSOL simulations. This heat flux was iteratively varied until the area averaged temperature of the heated area equaled the set temperature of the heater. This value of heat flux ($q''_{back,f}$) was subtracted from the raw heat transfer to obtain the heat flux utilized for boiling. The uncertainty associated with the calculation of temperature and heat flux is discussed in Sec. 2.5.

2.5 Uncertainty. Substrate conduction was the major source of uncertainty in the heat flux. The uncertainty in q''_{gen} was negligible since the voltage and heater resistance were accurately measured. Higher uncertainties in substrate conduction were associated with the partitioning of q''_{gen} into q''_b and q''_{back}. Natural convection heat transfer coefficients for gases can vary from 2 W/m^2 K to 25 W/m^2 K [17]. The uncertainty in $q''_{back,n}$ due to the selection of h_n of 10 W/m^2 K in Sec. 2.4 was computed to be 0.21 W/cm^2. According to Eq. (5), this uncertainty in $q''_{back,n}$ results in the same uncertainty in $q''_{back,f}$. The maximum deviation in the averaged heat transfer coefficient from the individual value at each superheat was 40 W/m^2 K. This error in the heat transfer coefficient resulted in an uncertainty of 0.6 W/cm^2 in $q''_{back,f}$, and hence, in q''_b.

The thermistor used to measure the fluid temperature and the RTD used to control the chamber sidewall temperature were calibrated in a constant temperature bath using a NIST traceable thermometer to within 0.2°C. For the given set of experiments, the bulk liquid temperature never varied by more than 0.4°C. Hence, the uncertainty in the bulk liquid temperature is estimated to be less than 0.45°C. The uncertainty of 0.2°C associated with the calibration temperature and a temperature resolution of 0.29°C due to the least count of the digital potentiometer used in the feedback circuit could at most introduce an uncertainty of 0.35°C in the measurement of the wall temperature. A summary of the uncertainty estimates is given in Table 3.

3 Results and Discussion

In Secs. 3.1–3.4, results from subcooled pool boiling experiments under earth gravity using numerous heater sizes and varying experimental conditions (Table 2) are presented. For ease of understanding, this section has been divided into the following subsections: heater size effect, effect of nucleation site density, effect of subcooling, and effect of fluid properties. The test matrix was optimized to minimize the number of experiments and efficiently arrive at threshold value of L_h/L_c. As a result, some overlap between the sections was unavoidable. However, the reader will have a clear understanding of the effect of parameters on heater size independence toward the end of the paper.

3.1 Heater Size Effect. Boiling curves for numerous heater sizes using a 7 mm microheater array and FC-72 were obtained in normal earth gravity with the heater facing upward. Subcooling was maintained at 26.6°C. Figure 6 presents the boiling curve for the various heater sizes tested. Most of the heated area experienced natural convection at lower superheats, resulting in low heat transfer. Nucleation was observed to occur between $\Delta T_w = 13.4$°C and $\Delta T_w = 18.4$°C. With the ONB, a significant increase in the slope of the boiling curve was observed. Further increase in the wall superheat resulted in additional nucleation sites being activated. The boiling curves for nine heater elements (2.1×2.1 mm^2) or larger were similar and followed the same trend, i.e., the boiling curves were heater size independent (buoyancy dominated regime). For heated areas with one and four elements, nucleation was also observed to occur between $\Delta T_w = 13.4$°C and $\Delta T_w = 18.4$°C, but the slope of the boiling curve was smaller, and lower heat transfer was observed in the nucleate boiling regime (surface tension dominated regime).

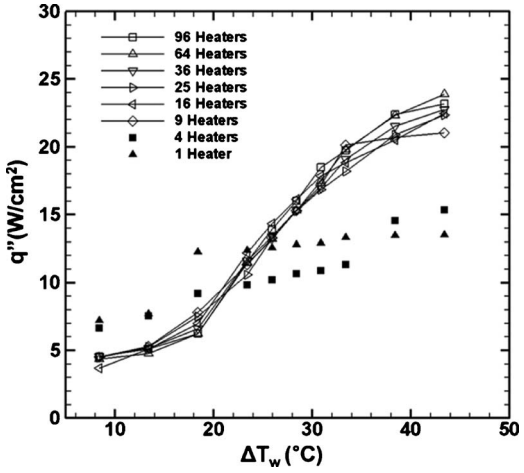

Fig. 6 Boiling curve for different heater sizes using FC-72 at $\Delta T_{sub}=26.6$°C, $P=1$ atm, and 7 mm microheater array

The bottom view images and the departure frequencies provide more insight into the mechanism responsible for this behavior. Figure 7 shows bottom view images for 36, 9, and 4 heaters at three superheats. At the lower superheat ($\Delta T_w = 23.4$°C), the bubble departure diameter was similar for all three cases (Fig. 7). Departure diameter increased with wall superheat ($\Delta T_w = 30.9$°C and 38.4°C). The difference in the bubble departure diameter is more pronounced at higher superheat close to CHF ($\Delta T_w = 38.4$°C), where the smaller bubbles coalesce to form larger

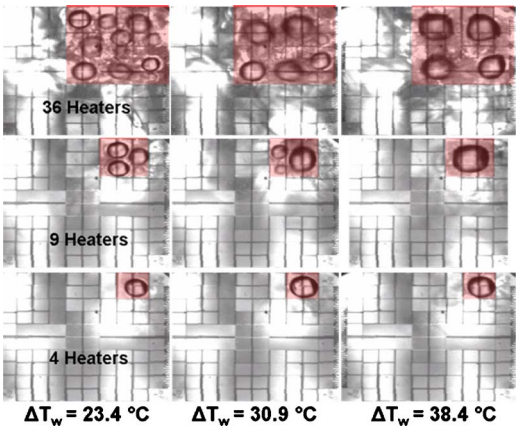

Fig. 7 Bottom view images for 36, 9, and 4 heaters at three superheats, FC-72, $\Delta T_{sub}=26.6$°C, $P=1$ atm, and 7 mm microheater array

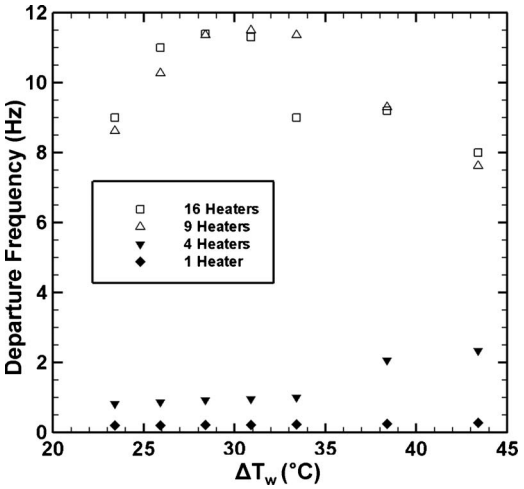

Fig. 8 Departure frequency versus superheat for FC-72, $\Delta T_{sub}=26.6°C$, $P=1$ atm, and 7 mm microheater array

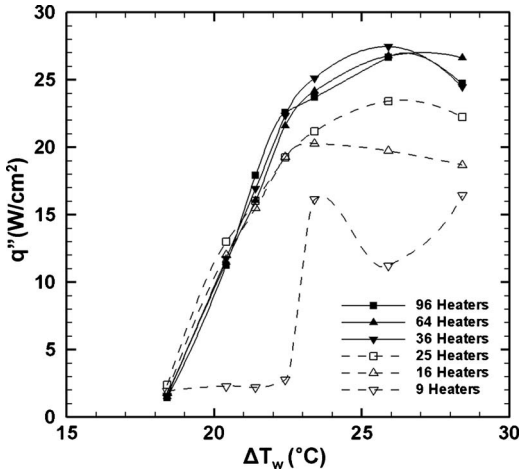

Fig. 9 Boiling curve for different heater sizes using FC-72, $\Delta T_{sub}=16.6°C$, $P=1$ atm, and 2.7 mm microheater array

bubbles (nine and 36 heaters). For the 36 heater case, four relatively large bubbles formed, while just one primary bubble formed for the nine heater case. The 36 heater configuration can be visualized as a combination of four cases with nine heaters. Hence, although the total heat dissipated by 36 heaters was four times that of nine heater case, the heat flux, and as a result, the boiling curves were similar for both sizes. However, for the four heater case, bubble growth was limited by the heater size, and single bubble was observed at all superheats.

The boiling behavior for the nine and 36 heaters are representative of the buoyancy dominated regime, while the behavior for the four heater configuration illustrated boiling behavior in the surface tension dominated regime. Figure 8 presents the departure frequency for 1, 4, 9, and 16 heater cases. The departure frequency was calculated by correlating the bottom view images, side view images, and the heat transfer data. The low video capture frequency of 29.97 Hz and increased turbulence due to larger number of bubbles made it difficult to distinguish between the bubble cycles for the larger heated areas (>16 heaters). The departure frequency of the coalesced bubble (Fig. 7) in the surface tension dominated regime (≤ 4 heaters) was significantly smaller than the bubble departure frequency in the buoyancy dominated regime (≥ 9 heaters). The departure frequency varied from 0.20 Hz to 0.27 Hz for the one heater case, while it varied from 0.8 to 2.33 for the four heater case. For larger heaters (nine and 16 elements), the shape, the size, and hence, the departure frequency were not limited by the heated area, and the departure frequency was observed to be as high as 11 Hz. For the smaller heaters (one and four heaters), bubble growth was limited by the heater size and surface tension dominated over buoyancy. Bubble growth was not spherical once the diameter was comparable to the heater size. Further evaporation resulted in bubble elongation toward the top, allowing contact with relatively cooler liquid. Contact with cold liquid increased condensation, decreasing the bubble growth rate, and hence, the departure frequency. The decrease in the departure frequency was primarily responsible for the overall decrease in heat transfer for smaller heaters (one and four heaters).

The use of a 7 mm microheater array limited the length scale resolution to 0.7 mm. The capillary length/departure diameter of FC-72 is of the same order as the minimum length scale (0.7 mm) under earth gravity conditions. Additional experiments were performed with FC-72 and the 2.7 mm microheater array, where each element was 0.27×0.27 mm^2. The use of a different microheater array implied different nucleation characteristics. Even though the nucleation characteristics changed the value of heat flux at a given superheat and the slope of the boiling curve, the minimum heater length above which heater size independence was observed was not affected. Subcooling was set at 16.6°C and was different from the subcooling for the previous set of experiments using the 7 mm microheater array (26.6°C). As will be explained in Sec. 3.3, subcooling does not affect the transition between regimes, and the minimum heater length for heater size independence remains unchanged for the range of subcoolings investigated in this study ($6.6°C\leq\Delta T_{sub}\leq 26.6°C$).

The boiling curves obtained at earth gravity using the 2.7 mm microheater array are shown on Fig. 9. ONB was observed between wall superheats of $\Delta T_w=18.4°C$ and $\Delta T_w=20.4°C$. The boiling curves were found to be heater size independent for cases where the heater size was larger than 1.62×1.62 mm^2 (6×6 heaters). The value of heat flux at CHF was significantly lower for square heaters smaller than 1.62 mm a side, suggesting surface tension dominated boiling. This is consistent with the results obtained using the 7 mm microheater array where the transition occurred between 1.4×1.4 mm^2 (four heaters) and 2.1×2.1 mm^2 (nine heaters). A nondeparting, stable coalesced bubble similar to microgravity conditions was observed for the smallest size (nine heaters), similar to the observations of Henry and Kim [12] under 1.7g conditions.

The shape of the boiling curves for the smaller heated area cases, which are in the surface tension dominated boiling regime, does not follow any specific trend (one and four heaters in Figs. 6 and 9, and 16 and 25 heaters in Fig. 9). This situation is very similar to those under microgravity conditions [12,18], where the shape of the boiling curves differ significantly even under a slight variation in the experimental conditions. Although no concrete explanations are available in the literature, it is speculated that many other parameters that have inconsequential effect under earth gravity become dominant under microgravity conditions. The abovementioned smaller heated area cases are also in the surface tension dominated boiling regime such as microgravity boiling, and hence, no definite trend of the boiling curve. Further investigations are required to identify the root cause behind such variation.

3.2 Effect of Nucleation Site Density. ONB and the slope of the boiling curve depend on the surface properties (microstructures) of the heater used. For the 2.7 mm microheater array, ONB was observed to occur at a higher wall superheat (18.4°C–20.4°C) compared with that for 7 mm microheater array (13.4°C–18.4°C). The slope of the boiling curve for the 2.7 mm microheater array (Fig. 9) in the nucleate boiling regime was also significantly larger compared with what was observed for the 7 mm microheater array (Fig. 6). The large slope in the nucleate

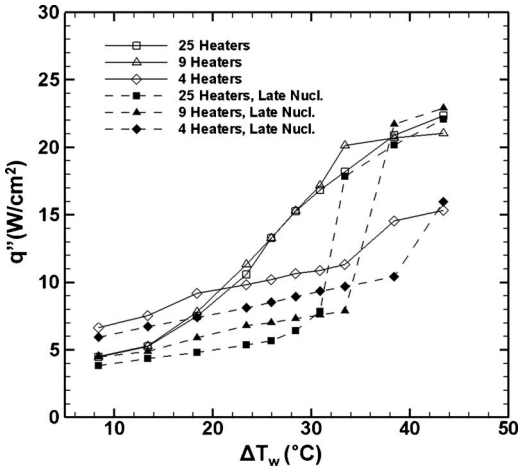

Fig. 10 Boiling curve using FC-72 for different heater sizes for normal and delayed nucleations, $\Delta T_{sub}=26.6°C$, $P=1$ atm, and 7 mm microheater array

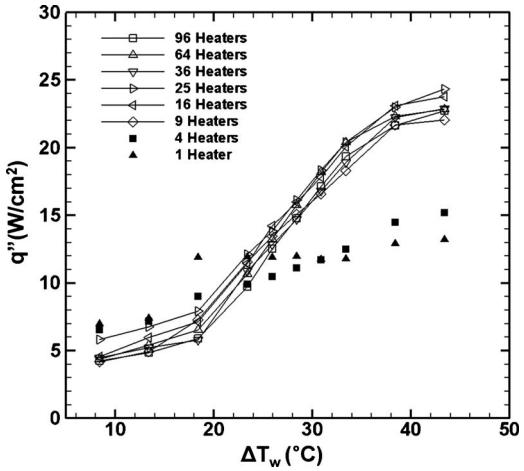

Fig. 11 Boiling curve for different heater sizes using FC-72, $\Delta T_{sub}=8.6°C$, $P=1$ atm, and 7 mm microheater array

boiling regime for the 2.7 mm microheater array can be attributed to a very uniform nucleation site density on the heater surface. The uniformity in the microstructures allows all nucleation sites to activate over a narrow range of temperature, causing a sudden increase in heat flux at ONB. Large slope in the boiling curve resulted in CHF at a significantly lower wall superheat of 25.9°C for the 2.7 mm microheater array. Even though the nucleation characteristics (ONB and CHF) and heat transfer behavior change with heaters (Figs. 1, 2, 6, and 9), the heater size independence effect was observed for all these cases.

Even within a heater, the nucleation characteristics might vary. This section highlights the nonuniformity in the nucleation site density within a heater by discussing the heat transfer results obtained for various sizes using different subsets of heaters within a single microheater array. The thermal boundary layer of the superheated liquid above the heated surface might also play an important role in ONB. The model of Hsu [19] for the criteria of ONB postulates that the embryo bubble would grow and that the cavity would activate if the equilibrium superheat was equaled or exceeded all around the perimeter of the embryo bubble. This occurs if the temperature at $y=b$ (height of the embryo bubble) is greater than the equilibrium superheat temperature. The thickness of the superheated boundary layer is affected by the area of the heated surface. As the heater size decreases, the thermal boundary layer thickness decreases due to increased edge effects. Cavities that might have nucleated on a large heater may not nucleate as the heater size is decreased as a result. Also, fewer candidate nucleation sites in a smaller heated area might also be responsible for delayed nucleation.

Nucleation was observed to be dependent on the size and location of the heated areas. For a large heated area, the distribution of the nucleation site density is mostly uniform, and the average superheat required for nucleation is also uniformly distributed. However, if we concentrate on a smaller area, the nonuniformity in the nucleation site density and superheat for nucleation becomes prevalent. There are patches on the array where the nucleation site density is less and/or the required superheat for ONB is higher and nucleation can be delayed (e.g., dashed lines, Fig. 10). On the other hand, solid curves represent cases on the microheater array where the required superheat was either lower or the number of nucleation sites were higher. As a result, ONB occurred at lower temperature. Even for the cases where nucleation was delayed, the rest of the nucleate boiling curve was unaffected, and heat flux values were similar to what was observed for the early nucleation (solid lines).

3.3 Effect of Subcooling. The effect of subcooling was studied by performing experiments at different subcoolings with the 7 mm microheater array. Boiling curves for numerous sizes at a lower subcooling ($\Delta T_{sub}=8.6°C$) are shown in Fig. 11. Boiling was heater size independent for nine or more heaters, similar to what was observed for the $\Delta T_{sub}=26.6°C$ case (Fig. 6). This is also consistent with the observations of Henry and Kim [12], where the transition between regimes at $1.7g$ was observed at same heater size at all four subcoolings investigated ($\Delta T_{sub}=8°C$, 16°C, 25°C, and 31°C).

The departure frequency in the buoyancy dominated regime was higher for lower subcooling (Fig. 12(*a*)) since the condensation at the bubble top was reduced, allowing the bubble to grow more rapidly. The effect of subcooling on the departure frequency in the surface tension dominated regime is shown in Fig. 12(*b*). For high superheats ($\Delta T_w \geq 34°C$), the departure frequency was higher for the lower subcooling case. However, the departure frequency at low superheats was higher for higher subcooling. Moreover, no departure was observed for the one heater case and lower subcooling ($\Delta T_{sub}=8.6°C$). Once nucleated, the bubble was observed to oscillate in size. Irrespective of the nondeparting bubble, heat transfer was similar to the case with higher subcooling ($\Delta T_{sub}=26.6°C$). A strong convective current observed near the bubble top for $\Delta T_{sub}=8.6°C$ is thought to be responsible for the high heat transfer even without departure. The actual mechanism behind this convective current is in dispute [20–23] and requires further investigation.

3.4 Effect of Fluid Properties. All the above studies and those presented in the literature review section showed two boiling regimes for FC-72: a heater size independent regime, where buoyancy dominates, and a heaters size dependent regime, where surface tension forces dominate. These observations encouraged further experiments with a different fluid to understand the effect of fluid properties on the transition. The capillary length L_c of pentane (1.51 mm) is twice that of FC-72 (0.75 mm) at earth gravity. Hence, pentane ($T_{sat}=36°C$ at 1 atm), was used to verify the heater size dependence results observed in the previous section. Subcooling was maintained at 8°C. The heater temperature varied between 60°C ($\Delta T_w=24°C$) and 90°C ($\Delta T_w=54°C$), and the pressure was maintained at 1 atm throughout the experiment.

The boiling curves under earth gravity conditions for various heater sizes using the 7 mm microheater array are shown in Fig. 13. Two boiling regimes were observed, and heater size independent results were observed only for heaters larger than 3.5×3.5 mm^2 (25 heaters). It was not possible to measure D_d without significant uncertainty due to increased turbulence and complex merger processes. However, careful observation of the bot-

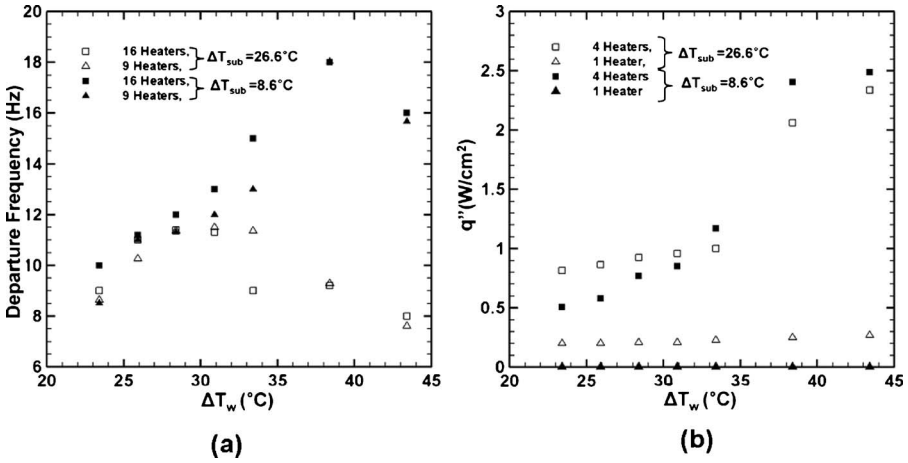

Fig. 12 Departure frequency versus superheat for the (*a*) buoyancy dominated regime and (*b*) the surface tension dominated regime at two subcoolings using 7 mm microheater array and FC-72

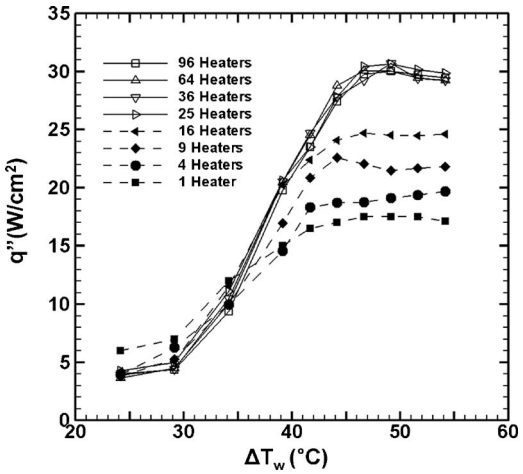

Fig. 13 Boiling curves at different heater sizes for pentane, $\Delta T_{sub}=8°C$, $P=1$ atm, and 7 mm microheater array

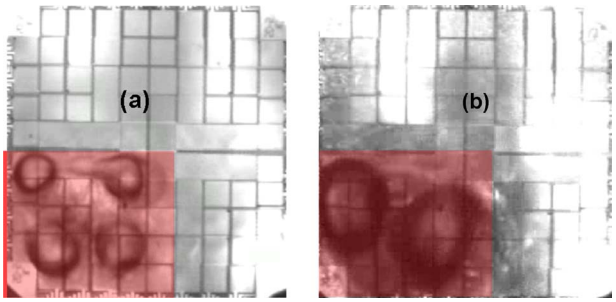

Fig. 14 Bottom view image for 25 heaters: (*a*) FC-72, $\Delta T_{sub}=8.6°C$; (*b*) pentane, $\Delta T_{sub}=8°C$, $P=1$ atm, $\Delta T_w \sim 40°C$, and 7 mm microheater array

tom view videos showed that D_d for pentane (Fig. 14(*b*)) was approximately two times that for FC-72 (Fig. 14(*a*)). As a result, the heater size independent behavior was observed at larger size (25 heaters) compared with that for FC-72 (nine heaters). Decreased departure frequency with decreasing heater size was attributed for the decrease in heat transfer in the surface tension dominated regime. Again, vigorous boiling and increased turbulence did not allow accurate measurements.

4 Pool Boiling Regime Map

The results from the current work using two fluids, and those from Refs. [12,14] are compiled in Tables 4 and 5. Under earth gravity conditions for FC-72 ($L_c=0.75$ mm), the minimum heater size L_h above which boiling was buoyancy dominated was 1.62 mm (36 heaters, 2.7 mm heater, Fig. 9), resulting in a value of $L_h/L_c=2.1$. Similarly, the minimum value of L_h/L_c from the $1.7g$ experiments of Henry and Kim [12] was 2.8, while a value of 2.5 was obtained from the variable gravity experiment. The capillary length L_c of pentane at normal earth gravity is 1.51 mm. Based on an element width of 0.7 mm and 5×5 heater configuration (25 heaters, Fig. 13), the minimum value of L_h/L_c above which boiling was heaters size independent was found to be 2.3. Table 4 presents the minimum value of L_h/L_c at which heat transfer results were heater size independent.

Table 5 shows the maximum value of L_h/L_c at which the heat transfer results were observed to be in the heater size dependent regime. The value was found to range between 1.4 and 2.1 for different experimental conditions. Comparison of the two tables reveals that the transition between regimes occurs at a threshold value of $L_h/L_c=2.1$.

Based on the above observations, a pool boiling regime map was developed for flat heated surfaces (Fig. 15). The test conditions corresponding to the data points presented in Fig. 15 are summarized in Table 6. The nondimensionalized acceleration a/g

Table 4 Minimum value of L_h/L_c for heater size independence

	Henry and Kim [12] (FC-72, 2.7 mm)	Raj et al. [14] (FC-72, 7 mm)	Current work (FC-72, 2.7 mm)	Current work (Pentane, 7 mm)
g (m/s^2)	1.7	0.3	1	1
L_h (mm)	1.62	3.5	1.62	3.5
L_c (mm)	0.58	1.38	0.75	1.51
L_h/L_c	2.8	2.5	2.1	2.3

Table 5 Maximum value of L_h/L_c for heater size dependent boiling

	Henry and Kim [12] (FC-72, 2.7 mm)	Raj et al. [14] (FC-72, 7 mm)	Current work (FC-72, 7 mm)	Current work (Pentane, 7 mm)
g (m/s^2)	1.7	0.05	1	1
L_h (mm)	0.81	7	1.4	2.8
L_c (mm)	0.58	3.34	0.75	1.51
L_h/L_c	1.39	2.1	1.9	1.9

and the ratio of the heater size to capillary length L_h/L_c were used as the two axes. A line of constant L_h/L_c divides the pool boiling into two regimes: *heater size independent/buoyancy dominated boiling regime* and *heater size dependent/surface tension dominated boiling regime*. Data in the heater size dependent/surface tension dominated boiling regime (solid symbols) lie below the line $L_h/L_c=2.1$, while all the data in the heater size independent/buoyancy dominated regime (open symbols) lie above the line $L_h/L_c=2.1$. This transition criterion also seems to be independent of the gravity level and holds for the two fluids investigated.

To summarize, subcooled pool boiling of FC-72 at earth gravity was found to be buoyancy dominated for heated areas equal to or larger than 1.62×1.62 mm^2 (36 elements, 2.7×2.7 mm^2 heater, Fig. 9). The heat flux was heater size independent when $L_h/L_c>2.1$. When L_h/L_c was smaller than this, surface tension dominated boiling and heat flux decreased. Similar behavior was observed for pentane and the threshold value of L_h/L_c was found to be 2.3, indicating the current results for FC-72 may also be applicable to other fluids. Experiments with other fluids and at various gravity levels are required for further verification of this hypothesis.

5 Summary and Conclusions

This paper summarizes our efforts to quantify when heaters can be called "small heaters" during boiling heat transfer. Conventionally, boiling has been associated with normal ebullition cycle, as observed under earth gravity conditions, where nucleation, bubble growth, departure, and rewetting are observed in a repetitive pattern. However, the bubble departure frequency begins to decrease as the gravity level and/or heater size are reduced. At very low values, a stable, nondeparting coalesced bubble forms, similar to what is observed under microgravity conditions. The findings of this paper show that the term "small heater" is not completely descriptive of the boiling conditions. The term "small heaters" and/or "low gravity" conditions are better expressed as "surface tension dominated boiling." Heat transfer results are heater size dependent in this regime.

Similarly, the "buoyancy dominated boiling/classical boiling" is a better expression for boiling under "high gravity" conditions and/or for "large heaters." Heat transfer results are heater size independent in this regime. The nondimensional ratio L_h/L_c, which incorporates the effect of gravity and heater size, was found

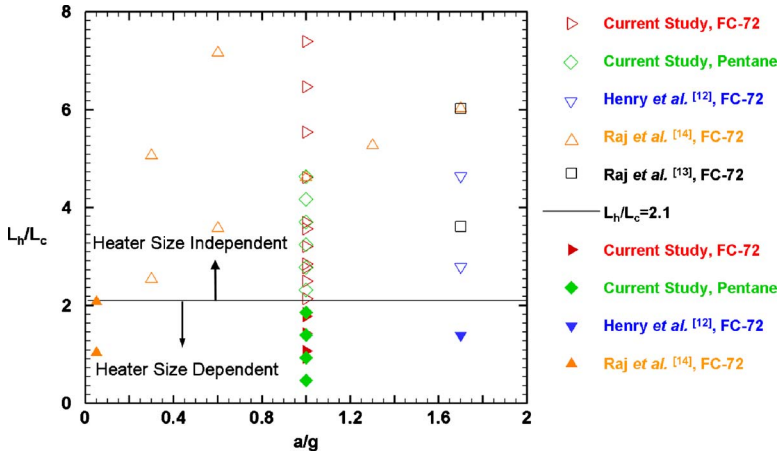

Fig. 15 Pool boiling regime map for flat surfaces

Table 6 The test conditions corresponding to the data presented in Fig. 15

	Henry and Kim [12] (FC-72)	Raj et al. [13] (FC-72)	Raj et al. [14] (FC-72)	Current work (FC-72)	Current work (Pentane)
g (m/s^2)	1.7	1.7	0.05, 0.3, 0.6, 1, 1.3, 1.7	1	1
L_h (mm)	0.81, 1.62, 2.7	2.1, 3.5, 7.0	3.5, 7.0	0.27, 0.54, 0.7, 0.81, 1.08, 1.35, 1.4, 1.62, 2.1, 2.16, 2.7, 2.8, 3.5, 4.2, 5.6, 7.0	0.7, 1.4, 2.1, 2.8, 3.5, 4.2, 5.6, 7.0
L_c (mm)	0.58	0.58	3.34, 1.38, 0.98, 0.75, 0.67, 0.58	0.75	1.51
ΔT_{sub} (°C)	31	6.6	26	8.6, 16.6, 26.6	8

suitable to differentiate between the boiling regimes. Transition between the regimes was observed to occur at $L_h/L_c \sim 2.1$.

Acknowledgment

This work was supported by NASA (Grant No. NNX08AI60A). Mr. John McQuillen was the grant monitor. The authors would also like to thank ZIN Technologies for providing opportunities to perform additional experiments with the microheater array boiling experiment (MABE) in the boiling experiment facility (BXF).

Nomenclature

b = height of the embryo bubble (mm)
D = diameter (mm)
g = normal earth gravity (m/s^2)
h = heat transfer coefficient (W/m^2 K)
L = length scale (mm)
P = pressure (atm)
q'' = heat flux (W/cm^2)
T = temperature (°C)
y = coordinate perpendicular to the heater

Greek

ρ = density (kg/m^3)
σ = surface tension (N/m)

Subscripts

b = boiling
back = back of the chip
bulk = bulk liquid
c = capillary
d = departure
f = forced convection, air-jet on
gen = generated
h = diameter/width of a side of the heated area
l = liquid
n = natural convection, air-jet off
sat = saturation
sub = subcooling
v = vapor
w = superheat
wall = heater wall

References

[1] Rohsenow, W. M., 1962, "A Method of Correlating Heat Transfer Data for Surface Boiling of Liquids," Trans. ASME, **84**, pp. 969–976.
[2] Forster, H. K., and Zuber, N., 1955, "Dynamics of Vapor Bubbles and Boiling Heat Transfer," AIChE J., **1**, pp. 531–535.
[3] Stephan, K., and Abdelsalam, M., 1980, "Heat Transfer Correlations for Natural Convection Boiling," Int. J. Heat Mass Transfer, **23**, pp. 73–87.
[4] Kutateladze, S. S., 1948, "On the Transition Film Boiling Under Natural Convection," *Kotloturbostroenie*, Vol. 3, pp. 10–12.
[5] Zuber, N., 1959, "Hydrodynamic Aspects of Boiling Heat Transfer," AEC Report No. AECU-4439.
[6] Yaddanapuddi, N., and Kim, J., 2000, "Single Bubble Heat Transfer in Saturated Pool Boiling of FC-72," Multiphase Sci. Technol., **12**(3–4), pp. 47–63.
[7] Di Marco, P., and Grassi, W., 2000, "Pool Boiling in Microgravity: Assessed Results and Open Issues," *Proceedings of the Third European Thermal-Sciences Conference*, Pisa, Italy, ETS, Sept. 10–13.
[8] Lin, L., and Pisano, A., 1991, "Bubble Forming on a Microline Heater," *Proceedings of the ASME Winter Annual Meeting, Dynamic Systems and Control Division*, Vol. 32, pp. 147–163.
[9] Iida, Y., Okuyama, K., and Sakurai, K., 1994, "Boiling Nucleation on a Very Small Film Heater Subjected to Extremely Rapid Heating," Int. J. Heat Mass Transfer, **37**, pp. 2771–2780.
[10] Yin, Z., Prosperetti, A., and Kim, J., 2004, "Bubble Growth on an Impulsively Powered Microheater," Int. J. Heat Mass Transfer, **47**, pp. 1053–1067.
[11] Kim, J., Benton, J. F., and Wisniewski, D., 2002, "Pool Boiling Heat Transfer on Small Heaters: Effect of Gravity and Subcooling," Int. J. Heat Mass Transfer, **45**(19), pp. 3919–3932.
[12] Henry, C. D., and Kim, J., 2004, "A Study of the Effects of Heater Size, Subcooling, and Gravity Level on Pool Boiling Heat Transfer," Int. J. Heat Fluid Flow, **25**, pp. 262–273.
[13] Raj, R., Kim, J., and McQuillen, J., 2010, "Gravity Scaling Parameter for Pool Boiling Heat Transfer," ASME J. Heat Transfer, **132**(9), p. 091502.
[14] Raj, R., Kim, J., and McQuillen, J., 2009, "Subcooled Pool Boiling Under Variable Gravity Environments," ASME J. Heat Transfer, **131**, p. 091502.
[15] Bakhru, N., and Lienhard, J. H., 1972, "Boiling From Small Cylinders," Int. J. Heat Mass Transfer, **15**, pp. 2011–2025.
[16] Rule, T. D., and Kim, J., 1999, "Heat Transfer Behavior on Small Horizontal Heaters During Pool Boiling of FC-72," ASME J. Heat Transfer, **121**(2), pp. 386–393.
[17] Incropera, F. P., Dewitt, D. P., Bergman, T. T., and Lavine, A. S., 2007, *Fundamental of Heat and Mass Transfer*, 6th ed., Wiley, New York, p. 8.
[18] Kim, J., 2003, "Review of Reduced Gravity Boiling Heat Transfer: US Research," J. Jpn. Soc. Microgravity Appl., **20**(4), pp. 264–271.
[19] Hsu, Y., 1962, "An Analytical and Experimental Study of the Thermal Boundary Layer and the Ebullition Cycle in Nucleate Boiling," NASA Report No. TN-D-594.
[20] Straub, J., 2002, "Origin and Effect of Thermocapillary Convection in Subcooled Boiling: Observations and Conclusions From Experiments Performed at Microgravity," Ann. N.Y. Acad. Sci., **974**, pp. 348–363.
[21] Marek, R., and Straub, J., 2001, "The Origin of Thermocapillary Convection in Subcooled Nucleate Pool Boiling," Int. J. Heat Mass Transfer, **44**, pp. 619–632.
[22] Barthes, M., Reynard, C., Santini, R., and Tadrist, L., 2007, "Non-Condensable Gas Influence on the Marangoni Convection During a Single Vapor Bubble Growth in a Subcooled Liquid," EPL, **77**, pp. 14001-p1–14001-p5.
[23] Henry, C. D., Kim, J., and McQuillen, J., 2006, "Dissolved Gas Effects on Thermocapillary Convection During Subcooled Boiling in Reduced Gravity Environments," Heat Mass Transfer, **42**, pp. 919–928.

Mohammad Shanbghazani
Mem. ASME
Department of Mechanical Engineering,
Islamic Azad University,
Ilkhchi Branch,
Emam Street,
Ilkhchi 51839-87173, Iran
e-mail: shanbghazani@iauil.ac.ir

Vahid Heidarpoor
Mem. ASME
Department of Mechanical Engineering,
Urmia University,
Sero Road,
Urmia 165-57153, Iran
e-mail: vahid.heidarpoor@gmail.com

Marc A. Rosen
Faculty of Engineering and Applied Science,
University of Ontario Institute of Technology,
Oshawa, ON, L1H 7K4, Canada

Iraj Mirzaee
Department of Mechanical Engineering,
Urmia University,
Urmia 165-57153, Iran

Numerical Investigation of Local Entropy Generation for Laminar Flow in Rotating-Disk Systems

The entropy generation is investigated numerically in axisymmetric, steady-state, and incompressible laminar flow in a rotating single free disk. The finite-volume method is used for solving the momentum and energy equations needed for the determination of the entropy generation due to heat transfer and fluid friction. The numerical model is validated by comparing it to previously reported analytical and experimental data for momentum and energy. Results are presented in terms of velocity distribution, temperature, local entropy generation rate, Bejan number, and irreversibility ratio distribution for various rotational Reynolds number and physical cases, using dimensionless parameters. It is demonstrated that increasing rotational Reynolds number increases the local entropy generation rate and irreversibility rate, and that the irreversibility is mainly due to heat transfer while the irreversibility associated with fluid friction is minor.
[DOI: 10.1115/1.4001612]

Keywords: numerical study, rotating disk, entropy generation, irreversibility, Bejan number, rotational Reynolds number

1 Introduction

In the past several decades, increasing awareness of the limits of world energy resources and their implications on the environment has caused countries to re-examine their energy policies. Many governments have taken measures to reduce or eliminate energy losses. The scientific and engineering communities have begun to examine more closely energy conversion devices and to develop new techniques and methods for improving the utilization of existing resources. Systems for producing, converting, and utilizing energy resources are being carefully re-examined to reduce as much as reasonably possible factors that reduce thermodynamic efficiency, such as processes that lead to exergy (available-work) destruction and entropy generation. From a fundamental perspective, such increases in efficiency can only be attained by applying the second law of thermodynamics, which relates to entropy, exergy, and other concept generation [1,2].

Many technologies utilize rotating-disk systems. Such systems can be used to model the flow that occurs in the internal cooling air-systems of gas turbines or other rotating bodies, centrifugal pumps, viscometers, and other devices [3]. Much work has been done to investigate fluid flow and heat transfer on a plate disk rotating with constant angular velocity. For such rotary systems thermal efficiencies may not be functions of only temperature. The reason for this phenomenon is the complexity of the flow and thermal fields and the lack of implicit analytical expressions for each field. It is important to know how the flow and the thermal fields behave at every stage to permit safe and effective operation of rotary-type machines. To accurately determine the temperature distribution, the flow field parameters must be solved as precisely as possible [3]. Since the governing equations, namely, the momentum equations, are highly nonlinear and coupled, it is difficult to obtain an exact analytical solution [4].

A schematic of the flow for a free rotating disk is shown in Fig. 1. A free disk is defined as a plane disk rotating with constant angular velocity Ω about its polar axis in a quiescent environment. A boundary layer is formed on the surface of the disk in which fluid is entrained axially and pumped radially outward under the action of the centrifugal force. The flow in the boundary layer may be laminar or turbulent, the transition occurring when the local Reynolds number Re_φ exceeds a critical value. Here, $\mathrm{Re}_\varphi = \Omega r^2/\nu$, where r denotes the radius and ν the kinematic viscosity of the fluid. This type of flow was first investigated theoretically with an approximate method by von Karman [5]. Experimental work of Theodorsen and Regier [6] and the later work of Gregory et al. [7] measured velocity profiles in the boundary layer. Rogers and Lance [8] also calculated accurate solutions by means of a numerical integration of the governing equations. Cobb and Saunders [9] conducted experiments for a disk with uniform temperature, while McComas and Hartnett [10] measured the heat transfer on a free disk.

Most of the previous investigations have been done by solving the pertinent conservation equations (e.g., momentum and energy) and studying experimentally the flow field and heat transfer. However, second law analysis, especially entropy and exergy analyses [2], can provide enhanced insights into the problem. With such an approach, the second law of thermodynamics is applied to investigate irreversibilities in terms of the entropy generation rate. Since the entropy generation of the system is proportional to its destruction of exergy (or available energy), it becomes important in efforts to improve system performance to determine the system sites responsible for the greatest entropy generation. Using the second law of thermodynamics, which is related to entropy generation, is more meaningful than using first law-based calculations because the latter do not relate to the best possible performance and thus may be misleading. For improved efficiency, the irreversibilities present in a physical process must be reduced. This method has been used by Bejan [11–14]. Other studies on the second law of thermodynamics, entropy generation rates, and irreversibilities for basic arrangements have been published [15,16,2,17–21].

The effect of slip on entropy generation was investigated for

Contributed by the Heat Transfer Division of ASME for publication in the JOURNAL OF HEAT TRANSFER. Manuscript received June 30, 2009; final manuscript received March 4, 2010; published online June 28, 2010. Assoc. Editor: Giulio Lorenzini.

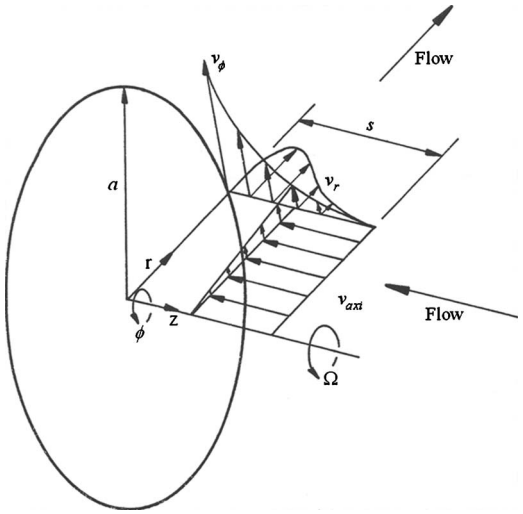

Fig. 1 Schematic of the flow for a rotating disk

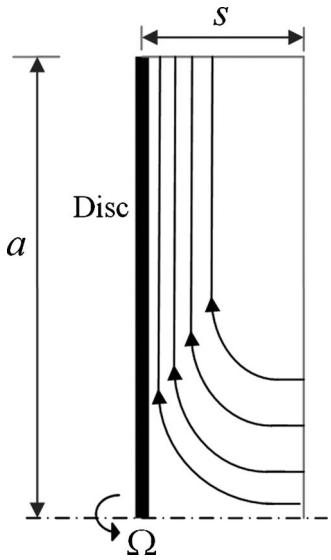

Fig. 2 Physical model of a single disk

flow over a rotating free disk by Arikoglu et al. [4]. In a similar study, they investigated the effect of entropy generation for a single rotating disk in magnetohydrodynamics flow [1]. Erbay et al. [22] studied the effect of the motion of the bottom plate, in the case of two parallel plates, on entropy generation. In a similar investigation [23], the mechanism of entropy generation, as well as its distribution through the flow field for basic channel geometries, including one fixed plate and one moving plate, is examined considering approximate analytical expressions. Yilbas [24] determined the heat transfer characteristics and the resulting entropy generation across annuli with a rotating outer cylinder for the case of a linear velocity distribution. Entropy generation due to laminar mixed convection from an isothermal rotating cylinder was calculated numerically by Abu-Hijleh et al. [25].

In this paper, consequently, the entropy generation due to fluid flow and heat transfer for rotating single-disk systems is modeled and numerically assessed. The main objective is to understand where the exergy destruction occurs in a rotating-disk system and which parameters (friction, heat transfer, etc.) are the main causes of entropy generation. The loss of some of the mechanical energy via conversion to thermal energy, i.e., entropy generation, results in a higher portion of the available energy being used. A secondary objective of this work is to relate entropy generation to the flow and heat field solutions so as to provide information that can help analysts and designers in the proper evaluation of efficiencies and in the geometrical optimization of such rotating systems or systems having rotating parts.

2 Modeling

For the computational aspect of this research, a rotating single disk is modeled (see Fig. 2). The disk is taken to have a radius a, to be in the plane $z=0$ and to be rotating with an angular velocity Ω about the z-axis. If the boundary-layer thickness δ is defined as the axial distance from the disk at which the tangential velocity falls to 1% of the disk speed, then δ is given by $\delta=5.5(\nu/\Omega)^{1/2}$ [3]. Thus the integration domain is truncated at a distance s in the axial direction, with the axial distance s taken as $20(\nu/\Omega)^{1/2}$, where ν is the kinematic viscosity of the working fluid [3]. The rotating-disk system is assumed to operate at steady state, be axisymmetric, and involve incompressible flow.

The relevant governing equations for continuity, momentum, and energy, assuming constant thermophysical properties, are as follows.

For continuity,

$$\frac{\partial v_r}{\partial r}+\frac{v_r}{r}+\frac{\partial v_z}{\partial z}=0 \tag{1}$$

For momentum,

$$v_r\frac{\partial v_r}{\partial r}+v_z\frac{\partial v_r}{\partial z}-\frac{v_\phi^2}{r}=-\frac{1}{\rho}\frac{\partial p}{\partial r}+\frac{\mu}{\rho}\left(\nabla^2 v_r-\frac{v_r}{r^2}\right) \tag{2}$$

$$v_r\frac{\partial v_\phi}{\partial r}+v_z\frac{\partial v_\phi}{\partial z}+\frac{v_\phi v_r}{r}=\frac{\mu}{\rho}\left(\nabla^2 v_\phi-\frac{v_\phi}{r^2}\right) \tag{3}$$

$$v_r\frac{\partial v_z}{\partial r}+v_z\frac{\partial v_z}{\partial z}=-\frac{1}{\rho}\frac{\partial p}{\partial z}+\frac{\mu}{\rho}\nabla^2 v_z \tag{4}$$

where

$$\nabla^2=\frac{\partial^2}{\partial r^2}+\frac{1}{r}\frac{\partial}{\partial r}+\frac{\partial^2}{\partial z^2}$$

For energy,

$$v_r\frac{\partial T}{\partial r}+v_z\frac{\partial T}{\partial z}=\frac{k}{\rho C_p}\nabla^2 T+\frac{1}{\rho C_p}\mu\Phi \tag{5}$$

$$\Phi=2\left(\frac{\partial v_r}{\partial r}\right)^2+2\left(\frac{v_r}{r}\right)^2+2\left(\frac{\partial v_z}{\partial z}\right)^2+\left(\frac{\partial v_\phi}{\partial r}-\frac{v_\phi}{r}\right)^2+\left(\frac{\partial v_\phi}{\partial z}\right)^2+\left(\frac{\partial v_z}{\partial r}+\frac{\partial v_r}{\partial z}\right)^2$$

The boundary conditions for the problem are defined as follows.

At the disk wall, i.e., $z=0$, $0\le r\le a$: $v_r=0$, $v_\phi=\Omega r$, $v_z=0$, and T_w is constant (i.e., $T=T_w$).

At the end of integration domain, i.e., $z=s$, $0\le r\le a$: $v_r=0$, $v_\phi=0$, $\partial v_z/\partial z=0$, and $T=T_\infty$.

At the center of the disk, i.e., $r=0$, $0\le z\le s$: $v_r=0$, $v_\phi=0$, $\partial v_z/\partial r=0$, and $\partial T/\partial r=0$.

At the circumference of the disk, i.e., $r=a$, $0\le z\le s$: $\partial/\partial r(v_r/r)=0$, $\partial/\partial r(v_\phi/r)=0$, $\partial v_z/\partial r=0$, and $\partial T/\partial r=0$.

3 Numerical Analysis

A computational fluid dynamics (CFD) code developed by the authors is used for solving the relevant mathematical expressions for the rotating-disk system. This computer code is a finite-volume, steady, axisymmetric, elliptic, and multigrid solver. The system of governing equations (1)–(5) is solved using a control-

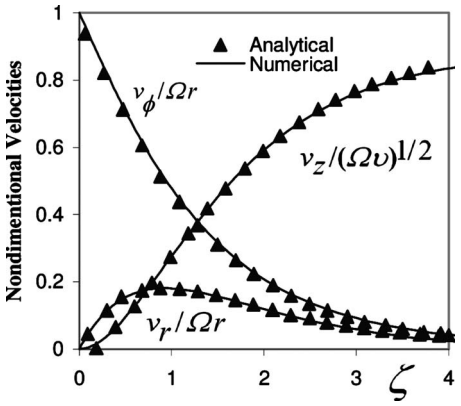

Fig. 3 Axial variation of velocity components near a disk for $Re_\phi = 4\times10^4$

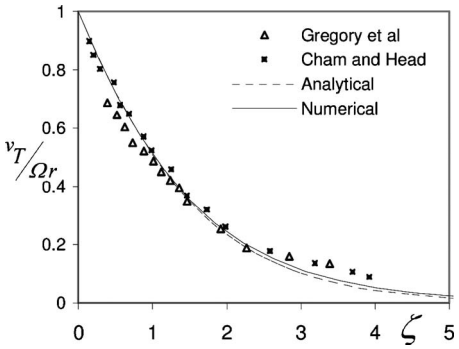

Fig. 4 Axial variation of nondimensional total velocity for $Re_\phi = 4\times10^4$

volume approach. The control-volume technique converts the governing equations to a set of algebraic equations that can be solved numerically. The control-volume approach employs the conservation principles and physical relations represented by the overall governing equations on each finite control volume. A first-order upwind scheme is employed to discretize the convection terms, diffusion terms, and other quantities in the governing equations. The use of a first-order upwind scheme appears justified here because a first-order numerical scheme, either upwind or hybrid, is usually considered to yield reasonably accurate results when the Peclet number exceeds than unity, as is the case here. Note that a first-order upwind scheme has been employed in investigations by various other researchers to solve the momentum and energy equations, with good agreement obtained with experimental data. The grid schemes used are staggered, and velocity components are evaluated at the center of the control-volume interfaces, while all scalar quantities are evaluated at the center of the control volume. Pressure and velocity are coupled using the semi-implicit method for pressure linked equations (SIMPLE) of Patankar [26].

The CFD code solves the linear systems resulting from the discretization schemes using a point implicit (Gauss–Seidel) linear equation solver in conjunction with an algebraic multigrid method. During the iterative process, the residuals are carefully monitored. For all simulations performed in the present study, convergence is deemed to be achieved when the residuals resulting from the iterative process for all governing equations, i.e., Eqs. (1)–(5), are smaller than 10^{-6}.

The grid used in the present analysis is 40×20, with 40 volumes in the r-direction and 20 in the z-direction. Grids having 60×40 and 80×60 configurations are also tested. As all grid configurations yield similar values of velocity and temperature, the 40×20 grid is accepted as sufficiently fine. This grid size is also validated using experimental data in Sec. 4.

4 Numerical Model Validation

The aim of this work is to investigate numerically entropy generation for a rotating-disk system. First, it is necessary to validate the numerical model by comparing it to previously available data for momentum and energy.

Figures 3–5 show the axial variation with nondimensional axial distance ζ, where $\zeta = z\sqrt{\Omega/\nu}$, of velocity components ($v_\phi/\Omega r$, $v_r/\Omega r$, and $v_z/(\Omega\nu)^{1/2}$), the magnitude of the nondimensional total velocity ($v_T/\Omega r$, where $v_T=(v_r^2+v_\phi^2)^{1/2}$), and the nondimensional temperature distribution at $Re_\phi = 4\times10^4$. In Figs. 3 and 4, the computational results for the velocity components are compared with the analytical solution of von Karman [5] and the experimental results of Gregory et al. [7] and Cham and Head [27]. The comparison shows the agreement between the results obtained with CFD and those obtained via analytical and experimental methods.

Figure 5 shows the computed distributions of dimensionless temperature $\Theta(\zeta)=(T-T_\infty)/(T_w-T_\infty)$ as a function of $\zeta = z(\Omega/\nu)^{1/2}$. A good agreement is observed between the computed results and experimental data of McComas and Hartnett [10].

5 Entropy Generation

In fluid flow, irreversibility arises due to heat transfer and viscous frictional effects in the fluid. The entropy generation rate can be expressed as the sum of contributions due to viscous and thermal effects, and depends functionally on local velocities and temperatures in the domain of interest. When both temperature and velocity fields are known, the volumetric entropy generation rate S'''_{gen} at a point in a system can be evaluated as follows [14]:

$$S'''_{gen} = (S'''_{gen})_{heat} + (S'''_{gen})_{fric} \tag{6}$$

Here, $(S'''_{gen})_{heat}$ and $(S'''_{gen})_{fric}$ denote the entropy generation rates due to heat transfer and fluid friction, respectively, and can be expressed as

$$(S'''_{gen})_{heat} = \frac{k}{T^2}\left[\left(\frac{\partial T}{\partial r}\right)^2 + \left(\frac{\partial T}{\partial z}\right)^2\right] \tag{7}$$

$$(S'''_{gen})_{fric} = \frac{\mu}{T}\Phi \tag{8}$$

The Bejan number Be, which compares the entropy generation due to heat transfer to the total entropy generation, is defined by

$$\mathrm{Be} = \frac{(S'''_{gen})_{heat}}{S'''_{gen}} \tag{9}$$

The Bejan number varies between 0 and 1. When $\mathrm{Be}\gg0.5$, the irreversibility due to heat transfer dominates, while for $\mathrm{Be}\ll0.5$

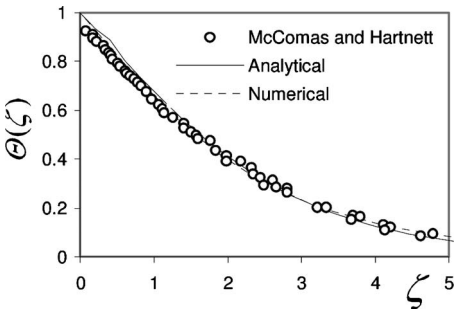

Fig. 5 Axial variation of temperature near an isothermal disk for $Re_\phi = 4\times10^4$

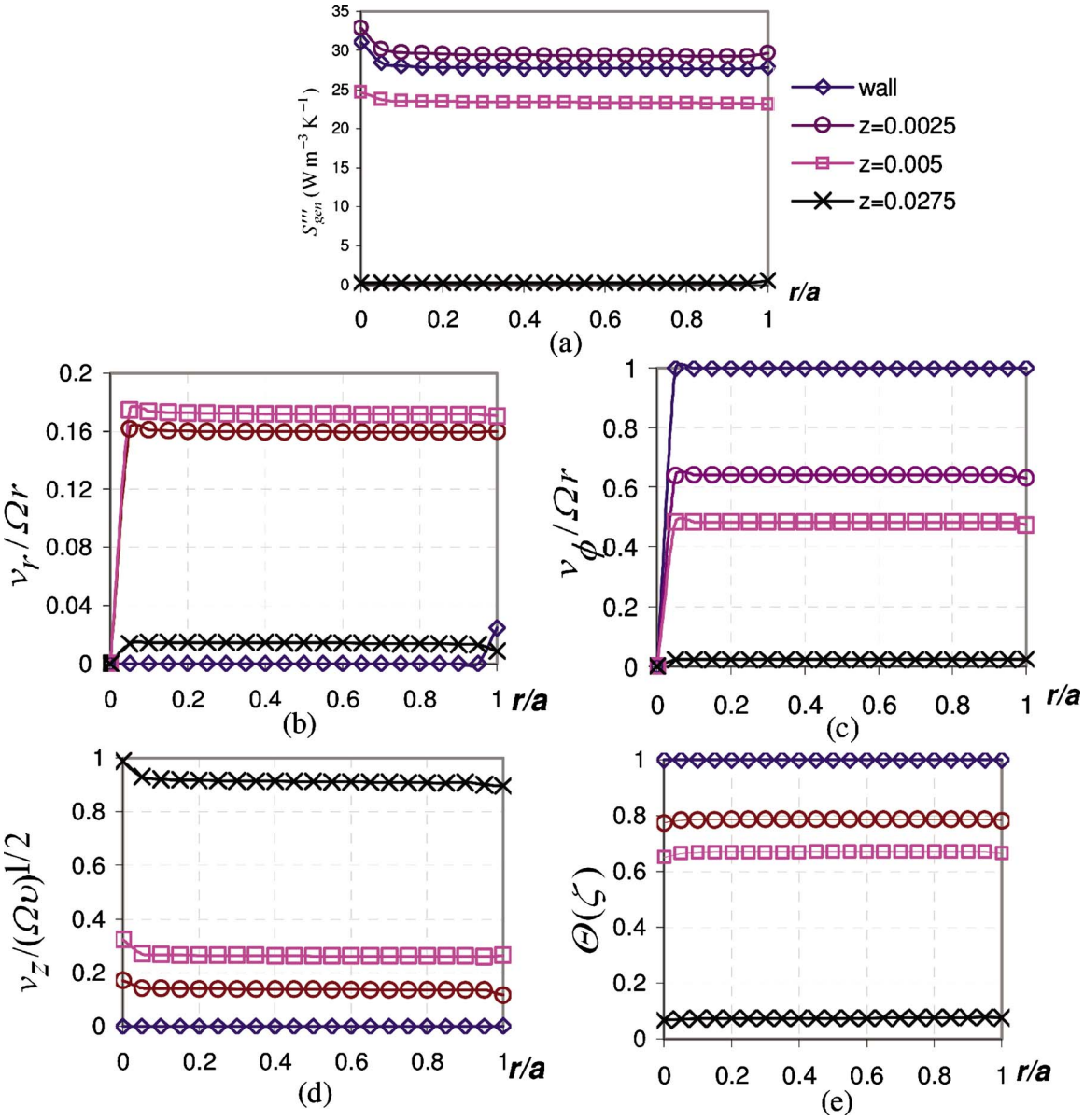

Fig. 6 Radial variation of (*a*) entropy generation rate, (*b*) radial velocity, (*c*) tangential velocity, (*d*) axial velocity, and (*e*) dimensionless temperature, for several values of *z* at $Re_\phi = 4 \times 10^4$

the irreversibility due to viscous effects dominates. For $Be \cong 0.5$, entropy generation due to heat transfer is of approximately the same magnitude as that due to fluid friction.

In situations where convection is present, both fluid friction and heat transfer contribute to the entropy generation. To better appreciate whether fluid friction or heat transfer entropy generation dominates, it is useful to consider a criterion known as the irreversibility ratio ψ defined as

$$\psi = \frac{(S'''_{gen})_{fric}}{(S'''_{gen})_{heat}} \tag{10}$$

The irreversibility ratio can be expressed in terms of the Bejan number using Eqs. (6) and (9) as follows:

$$\psi = \frac{1 - Be}{Be} \tag{11}$$

Heat transfer irreversibility dominates for $0 < \psi < 1$ and fluid friction dominates for $\psi > 1$. The situation where heat transfer and fluid friction have similar contributions to entropy generation is characterized by $\psi = 1$. Note that the irreversibility ratio is introduced because it is a commonly used parameter for comparing fluid friction and heat transfer contributions to the total entropy generation. The Bejan number is similar, and is somewhat more informative when comparing the ratio of heat transfer irreversibility to the total irreversibility.

6 Results and Discussion

Figures 6(*a*)–6(*e*) show the radial variation for several values of axial distance *z* of entropy generation rate, radial velocity, tangential velocity, axial velocity, and dimensionless temperature, respectively. The rotational Reynolds number for these figures is $Re_\varphi = 4 \times 10^4$.

It can be seen for all values of *z* that the maximum entropy generation rate occurs near the axis of rotation and that there is almost no variation with *z* far from the axis. It is also observed in Fig. 6(*a*) that the entropy generation rate variation inside the boundary layer is nonuniform, which is consistent with the behavior of the velocity components. The results confirm the fact that,

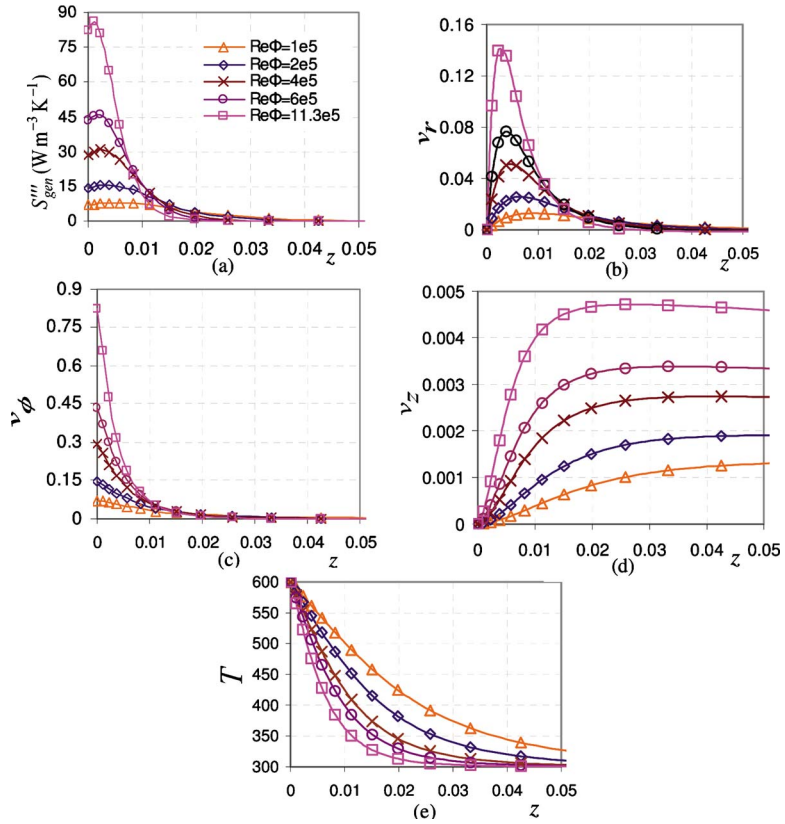

Fig. 7 Axial variation of (*a*) entropy generation rate, (*b*) radial velocity, (*c*) tangential velocity, (*d*) axial velocity, and (*e*) temperature

as indicated in Eq. (6), entropy generation in fluid and heat transfer problems is attributable to friction and heat transfer.

The axial variation of entropy generation rate, radial velocity, tangential velocity, axial velocity, and dimensionless temperature are shown in Figs. 7(*a*)–7(*e*), respectively. In Fig. 7(*a*), the variation is shown of the axial distribution of the total entropy generation rate for different values of rotational Reynolds number. Increasing the rotational Reynolds number is seen in this figure to increase the value of entropy generation rate inside the boundary layer. However, the effect of Re_φ is almost negligible outside the boundary layer.

It is noted in Figs. 7(*a*)–7(*e*) that the entropy generation rate and radial component of the velocities exhibit similar trends. This observation suggests that, although the temperature boundary condition affects significantly the initial values of the entropy generation rate on the disk (at $z=0$), the entropy generation rate profile is influenced more by the radial component of velocity rather than temperature.

The radial variation of entropy generation rate for several values of the rotational Reynolds number at $z=0$ is shown in Fig. 8. The maximum value of entropy generation rate at constant Re_φ can be seen to occur at the centerline and there is little variation far from the centerline. As Re_φ increases, the entropy generation rate increases.

The axial variation of entropy generation rate is shown in Fig. 9 for several values of Re_φ at $r/a=0.5$. It is observed that, although increasing Re_φ increases the entropy generation rate, this effect becomes negligible outside the boundary layer.

The axial distribution of entropy generation rate at different radial locations for $\mathrm{Re}_\varphi=4\times10^4$ is shown in Fig. 10. Except for the region of small r/a, similar behavior can be seen of the entropy generation rate for all values of r/a. This observation is consistent with the discussion of all curves identical for Fig. 8. The maximum entropy generation rate occurs inside the boundary layer next to the disk. This finding implies that the entropy generation rate is influenced by the radial velocity of the domain. At higher values of z, the entropy generation rate decreases with increasing z.

Figure 11 shows the radial variation of Bejan number for several values of Re_φ at $z=0$. It is observed in this figure that at large values of r (e.g., $r/a>0$), the Bejan number decreases as Re_φ increases. For small values of r (e.g., $r/a<0$), the Bejan number is independent of Re_φ and approaches unity as r/a approaches zero.

The radial variation of Bejan number for different values of z at $\mathrm{Re}_\varphi=9.9\times10^5$ is shown in Fig. 12. It is observed in this figure that the maximum Bejan number ($\mathrm{Be}=1$) occurs at the axis of rotation for all values of z and that the Bejan number decreases as r/a increases.

The radial variation of irreversibility ratio on the free disk system is presented in Fig. 13 for several rotational Reynolds numbers. It can be seen that the irreversibility ratio is zero at $r/a=0$

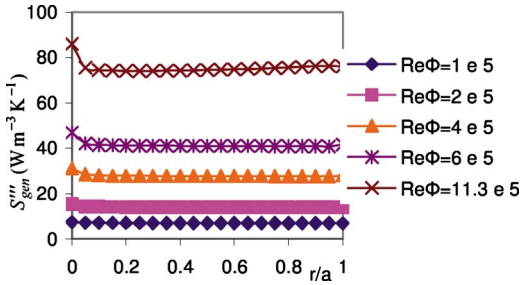

Fig. 8 Variation of radial entropy generation rate for several values of Re_ϕ at wall (disk)

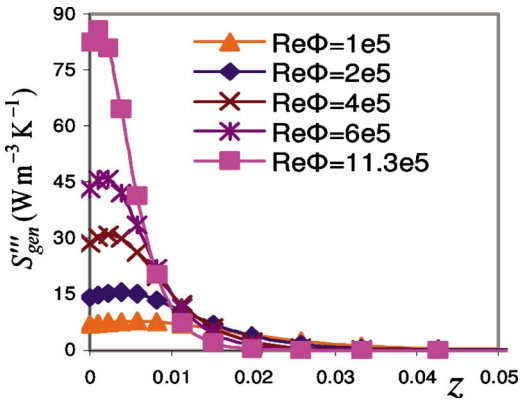

Fig. 9 Variation of axial entropy generation rate for several values of Re_ϕ at $r/a=0.5$

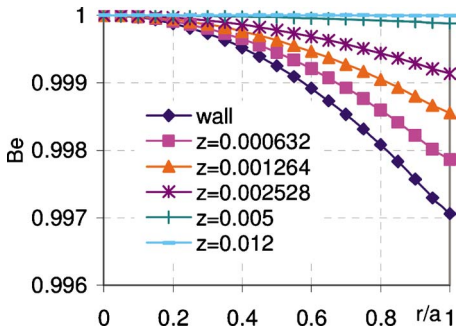

Fig. 12 Radial Bejan number profiles at $Re_\phi=9.9\times10^5$ for several values of z

and increases with increasing radial position. It can also be seen that increasing the rotational Reynolds number increases the irreversibility ratio. From the irreversibility expression, it is evident for the case of $\psi=0.01$ that the irreversibility due to the viscous effects is 100 times higher than the irreversibility due to heat transfer (i.e., $Be \ll 0.5$) and that this effect increases as rotational Reynolds number increases.

The radial variation of irreversibility ratio at $Re_\phi=9.9\times10^5$ for several values of z is shown in Fig. 14. The irreversibility ratio exhibits a maximum at the wall (i.e., at $z=0$) and decreases with increasing z.

7 Conclusions

The influence of rotational Reynolds number and distances on the entropy generation is investigated in a free disk system for axisymmetric, steady-state, and incompressible laminar flow at constant wall temperature. Representations for volumetric values of entropy generation rate, Bejan number, and irreversibility ratio are obtained for various values of characterizing parameters. The common feature observed is that increasing the rotational Reynolds number causes the magnitude to increase the local entropy generation and irreversibility ratio. The temperature and flow fields are computed numerically using the finite-volume method. At all values of z, the entropy generation exhibits a maximum near the axis of rotation and is almost fixed far from the axis. The local entropy generation, the irreversibility ratio variation, and the Bejan number are computed and their behaviors discussed. The results demonstrate that the irreversibility is mainly due to heat transfer and fluid friction irreversibility is minor, as expected for a rotating free disk system. In particular, the entropy generation rate and radial component of the velocities are observed to exhibit similar trends, with the large gradient for radial velocity affecting the local entropy generation, while the Bejan and irreversibility numbers show the main cause of entropy generation to be heat transfer. It is also found that as disk radial velocity increases the

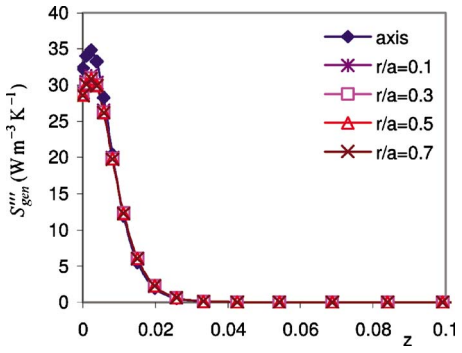

Fig. 10 Axial distribution of entropy generation rate at various radial locations for $Re_\phi=4\times10^4$

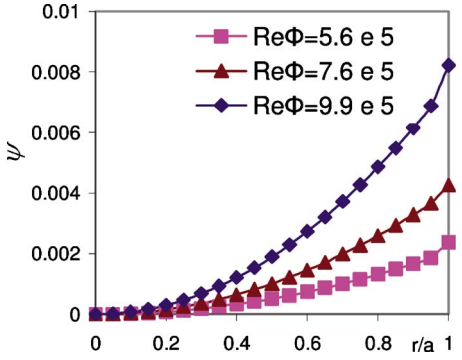

Fig. 13 Radial irreversibility ratio profiles on the disk for different Re_ϕ

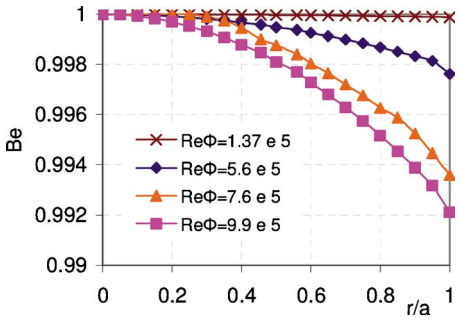

Fig. 11 Radial Bejan number profiles at disk (wall) for several values of Re_ϕ

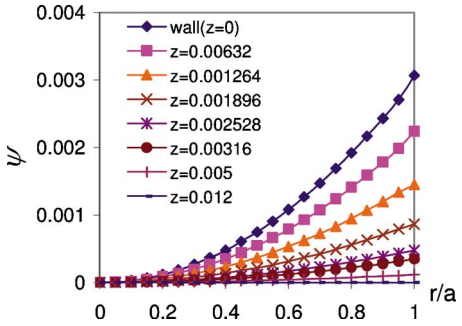

Fig. 14 Axial variation of radial irreversibility ratio profiles at $Re_\phi=9.9\times10^5$

entropy generation increases, leading to an increase in the irreversibility ratio and a decrease in the Bejan number. Furthermore as distance from the disk wall increases the irreversibility ratio decreases while the Bejan number increases. As expected, the Bejan number varies from 0 to 1 (at the outside boundary layer) while the irreversibility ratio varies in the opposite manner. The results demonstrate the significance of second law considerations in rotating fluidic systems and the need to utilize second law analysis in assessments. In particular, the results help understand where exergy destruction occurs in a rotating-disk system and the main causes, facilitating efforts to develop means to reduce these losses. The results are expected to be useful to those involved in the design of engineering systems including, for example, turbine and compressor disks of gas-turbine engines and rotating systems incorporating rotating disks. For such systems, the results can help understand where the exergy destruction occurs in a rotating-disk system and the main causes of the destruction of the potential to produce work during the process.

Nomenclature

a = disk radius, m
Be = Bejan number, $(S'''_{\text{gen}})_{\text{heat}}/S'''_{\text{gen}}$
c_p = specific heat, kJ kg^{-1} K^{-1}
k = thermal conductivity, W m^{-1} K^{-1}
p = pressure, N m^{-2}
r = radial distance, m
Re_ϕ = rotational Reynolds number, $\rho\Omega a^2/\mu$
S'''_{gen} = entropy generation rate, W m^{-3} K^{-1}
T = temperature, K
T_w = wall temperature, K
T_∞ = temperature at infinity, K
v_r = radial velocity component, m s^{-1}
v_z = axial velocity component, m s^{-1}
v_ϕ = tangential velocity component, m s^{-1}
v_T = total velocity, m s^{-1}
z = axial distance, m

Greek Letters

ζ = nondimensional axial distance
μ = dynamic viscosity, N s m^{-2}
ν = kinematic viscosity, m^2 s^{-1}
ρ = density, kg m^{-3}
ϕ = tangential direction
Φ = viscous dissipation function, s^{-1}
ψ = irreversibility ratio, (1–Be)/Be
Ω = angular velocity, rad s^{-1}

References

[1] Arikoglu, A., Ozkol, I., and Komurgoz, G., 2008, "Effect of Slip on Entropy Generation in a Single Rotating Disk in MHD Flow," Appl. Energy, **85**, pp. 1225–1236.
[2] Dincer, I., and Rosen, M. A., 2007, *Exergy: Energy, Environment and Sustainable Development*, Elsevier, Oxford, UK.
[3] Owen, J. M., and Rogers, R. H., 1989, *Flow and Heat Transfer in Rotating Systems*, Vol. 1, Wiley, New York.
[4] Arikoglu, A., Komurgoz, G., and Ozkol, I., 2008, "Effect of Slip on the Entropy Generation From a Single Rotating Disk," ASME J. Fluids Eng., **130**, p. 101202.
[5] von Karman, T., 1921, "Über laminare und turbulente reibung," Z. Angew. Math. Mech., **1**, pp. 233–252.
[6] Theodorsen, T., and Regier, A., 1944, "Experiments on Drag of Revolving Disks, Cylinders, and Streamline Rods at High Speed," NACA, Report No. 793.
[7] Gregory, N., Stuart, J. T., and Walker, W. S., 1955, "On the Stability of Three-Dimensional Boundary Layer With Application to the Flow Due to a Rotating Disc," Mathematical and Physical Sciences, **248**(943), pp. 155–199.
[8] Rogers, M. H., and Lance, G. N., 1960, "The Rotationally Symmetric Flow of a Viscous Fluid in the Presence of an Infinite Rotating Disc," J. Fluid Mech., **7**(4), pp. 617–631.
[9] Cobb, E. C., and Saunders, O. A., 1956, "Heat Transfer From a Rotating Disc," Mathematical and Physical Sciences, **236**(1206), pp. 343–351.
[10] McComas, S. T., and Hartnett, J. P., 1970, "Heat Transfer From a Rotating Disc," Proc. R. Soc. London, Ser. A, **236**, pp. 343–351.
[11] Bejan, A., 1979, "A Study of Entropy Generation in Fundamental Convective Heat Transfer," ASME J. Heat Transfer, **101**, pp. 718–725.
[12] Bejan, A., 1980, "Second Law Analysis in Heat Transfer," Energy, **5**, pp. 720–732.
[13] Bejan, A., 1994, *Entropy Generation Through Heat and Fluid Flow*, Wiley, New York.
[14] Bejan, A., 1996, *Entropy Generation Minimization*, CRC Press, New York.
[15] Carrington, C. G., and Sun, Z. F., 1992, "Second Law Analysis of Combined Heat and Mass Transfer in Internal and External Flows," Int. J. Heat Fluid Flow, **13**, pp. 65–70.
[16] Dincer, I., and Cengel, Y. A., 2001, "Energy, Entropy and Exergy Concepts and Their Roles in Thermal Engineering," Entropy, **3**(3), pp. 116–149.
[17] Rosen, M. A., and Scott, D. S., 2003, "Entropy Production and Exergy Destruction—Part I: Hierarchy of Earth's Major Constituencies," Int. J. Hydrogen Energy, **28**(12), pp. 1307–1313.
[18] Naterer, G. F., and Camberos, J. A., 2003, "Entropy and the Second Law in Fluid Flow and Heat Transfer Simulation," J. Thermophys. Heat Transfer, **17**(3), pp. 360–371.
[19] Rosen, M. A., Dincer, I., and Kanoglu, M., 2008, "Role of Exergy in Increasing Efficiency and Sustainability and Reducing Environmental Impact," Energy Policy, **36**(1), pp. 128–137.
[20] Shanbghazani, M., Khalilarya, Sh., and Mirzaee, I., 2008, "Exergy Analysis of a Gas Turbine System With Evaporative Cooling at Compressor Inlet," Int. J. Exergy, **5**, pp. 309–325.
[21] Haseli, Y., Dincer, I., and Naterer, G. F., 2008, "Entropy Generation of Vapor Condensation in the Presence of a Non-Condensable Gas in a Shell and Tube Condenser," Int. J. Heat Mass Transfer, **51**, pp. 1596–1602.
[22] Erbay, L. B., Ercan, M. S., Sulus, B., and Yalcin, M. M., 2003, "Entropy Generation During Fluid Flow Between Two Parallel Plates With Moving Bottom Plate," Entropy, **5**(5), pp. 506–518.
[23] Mahmud, S., and Fraser, R. A., 2003, "The Second Law Analysis in Fundamental Convective Heat Transfer Problems," Int. J. Therm. Sci., **42**(2), pp. 177–186.
[24] Yilbas, B. S., 2001, "Entropy Analysis of Concentric Annuli With Rotating Outer Cylinder," Int J. Exergy, **1**, pp. 60–66.
[25] Abu-Hijleh, B. A. K., and Heilen, W. N., 1999, "Entropy Generation Due to Laminar Natural Convection Over a Heated Rotating Cylinder," Int. J. Heat Mass Transfer, **42**(22), pp. 4225–4233.
[26] Patankar, S., 1980, *Numerical Heat Transfer and Fluid Flow*, Hemisphere, Washington, DC.
[27] Cham, T. S., and Head, M. R., 1969, "Turbulent Boundary-Layer Flow on a Rotating Disc," J. Fluid Mech., **37**(1), pp. 129–147.

Manish Mishra[1]
Department of Mechanical and Industrial Engineering,
Indian Institute of Technology,
Roorkee 247667, India
e-mail: mishra_md@yahoo.com
mmishfme@iitr.ernet.in

P. K. Das
Department of Mechanical Engineering,
Indian Institute of Technology,
Kharagpur 721302, India
e-mail: pkd@mech.iitkgp.ernet.in

Sunil Sarangi
National Institute of Technology,
Rourkela 769008, India
e-mail: sarangiskr@nitrkl.ac.in
director@nitrkl.ac.in

Transient Behavior of Crossflow Heat Exchangers Due To Sinusoidal Excitation

Transient temperature response of crossflow heat exchangers with both fluids unmixed and finite wall capacitance is investigated numerically for sinusoidal excitation provided in hot fluid inlet temperature. The effect of two-dimensional longitudinal conduction in separating sheet and the axial dispersion in fluids has also been considered on the thermal performance of the heat exchanger. The present method has good accuracy and simplicity. An attempt has also been made to study the performance of the sinusoidal excitation in the graphical form. [DOI: 10.1115/1.4001605]

Keywords: axial dispersion, crossflow, heat exchanger, longitudinal conduction, sinusoidal, transient

1 Introduction

Heat exchangers are generally designed to meet certain performance requirements under steady operating conditions. However, transient behavior of heat exchangers is often needed for designing the control strategy of different heating, ventilation and air-conditioning (HVAC) systems, cryogenic, and chemical process plants. Apart from routine functioning like start-up and shutdown, the problems such as failure and accidents have motivated investigations of transient thermal response in crossflow heat exchangers. It also elps the designer to rely upon a solution for the time dependent temperature problems, essential for thermal stress analysis. Besides, transient testing techniques are often adopted for determining the thermal characteristics of heat exchangers using a suitably developed mathematical model.

In the past few decades, numerous attempts have been made for modeling the dynamic behavior of heat exchangers. The researchers not only considered the heat exchangers of different types but also proposed various methodologies. A pioneering effort [1] for modeling the dynamic behavior of an air-to-gas plate-fin type crossflow heat exchanger has been carried out using finite difference technique based on a number of simplified assumptions, such as negligible local heat storage in the gas and air stream. The three governing equations were proposed [2] for the simulation of transient heat exchange in a crossflow heat exchanger and five independent nondimensional parameters have been identified. Next they assumed one of the fluids to be mixed, which renders the temperature variation in that stream one dimensional and greatly simplifies the problem. Further simplifications were sought assuming a large wall capacitance and finally an approximate analytical solution was obtained using integral heat balance technique.

Based on the basic model [2], different researchers have analyzed the transient response of crossflow heat exchangers relaxing one or more number of approximations. Solutions [3,4] were obtained for a step change of inlet temperature by finite difference technique using transformation of variables. While infinite capacitance of one of the fluids was assumed in the former work, large wall capacitance was considered in the latter. Similarly, an analysis [5] has been given for the fluid streams of negligible capacitance subjected to step, ramp, and exponential inputs. Additionally, the effect of longitudinal conduction in the separator sheet has been shown on the deterioration of thermal performance of the heat exchanger. Later, the combined effect of longitudinal conduction in wall and axial dispersion in fluids was investigated numerically [6]. Furthermore, the effect of axial dispersion in fluid has also been studied on the performance of cryogenic regenerator [7].

Parallel efforts were also made to find out the dynamic response of heat exchangers analytically using the Laplace transform technique. Transient response has been obtained for gas-to-gas heat exchanger with large core capacitance in case of step input [8,9]. Two-dimensional temperature response [10] as integrals of modified Bessel's function in space and time has been obtained with step, ramp, and exponential inputs. Later, the assumption of large wall capacitance was relaxed and temperature response for a deltalike perturbation in temperature as well as for step input has been given [11,12]. The solution was further simplified for the limiting case of small capacitance of the fluid streams compared with the core [13]. Later, the dynamic behavior of crossflow heat exchanger has been worked out analytically with axial dispersion in one of the fluids [14]. Apart from the axial dispersion model used earlier, the hyperbolic axial dispersion model [15] has also been tried for getting the solution of such problems.

In all the above works, transient response has been obtained by two- or threefold Laplace transform. Next the temperature fields have been obtained by inversion of resulting Laplace equations. The task of inverting the transformed temperatures in the physical domain becomes progressively difficult with the increase in the number of simultaneous equations as well as with the increase in independent variables. This has motivated the investigators to use single Laplace transform along with numerical inversion. A single Laplace transform in conjunction with the power series technique has been carried out [16,17] for determining the response of crossflow heat exchangers with large and finite core capacitance.

The effect of sinusoidal excitation in transient behavior has been seen earlier for plate heat exchangers [18] and shell and tube heat exchangers [19]. To the best of author's knowledge, the detailed study of sinusoidal response of crossflow heat exchangers has not been done so far. In the periodic method [20] of testing compact heat exchangers, the temperature of the inlet air is continuously and periodically changed by a periodic (sinusoidal) power input to the electric heater. The phase shift and/or the amplitude change between the inlet and outlet or temperature is used to determine h and hence Colburn-j factors. Periodic temperature

[1]Corresponding author.

Contributed by the Heat Transfer Division of ASME for publication in the JOURNAL OF HEAT TRANSFER. Manuscript received September 19, 2008; final manuscript received January 23, 2010; published online June 23, 2010. Assoc. Editor: Ben Q. Li.

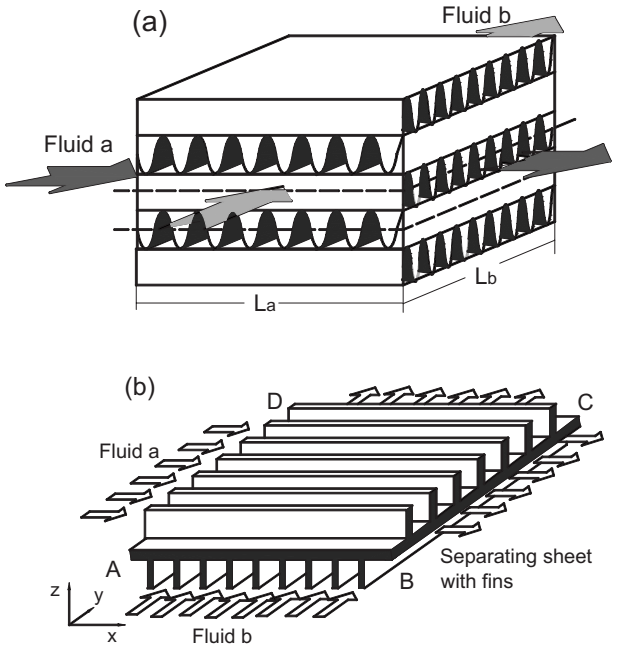

Fig. 1 (*a*) Crossflow heat exchanger and (*b*) schematic representation

waves are easier to generate experimentally than step function. Thus it needs to find out the temperature responses for the sinusoidal perturbation in inlet temperature of hot fluid apart from the standard step, ramp, and exponential responses.

The present work analyzes the direct-transfer, single pass crossflow heat exchanger with both fluids unmixed having finite capacitance wall separating the two-fluid streams. The combined effect of two-dimensional longitudinal conduction in wall and fluid axial dispersion has been carried out numerically using finite difference method to get the transient response for sinusoidal input given to the hot fluid. Two-dimensional temperature fields have been obtained to study the temperature profile. A graphical representation of the behavior of mean exit temperatures, after reaching to the steady state, with hot fluid inlet temperature, has also been presented in a convenient form.

2 Mathematical Formulation

A direct-transfer, two-fluid, crossflow, multilayer plate-fin heat exchanger is shown schematically in Fig. 1(*a*). The following assumptions are made for the mathematical analysis.

1. Both fluids are single phase, unmixed, and do not contain any volumetric source of heat generation.
2. The exchanger shell or shroud is adiabatic and the effects of the asymmetry in the top and bottom layers are neglected. Therefore, the heat exchanger may be assumed to comprise of a number of symmetric sections, as shown by dotted lines in Fig. 1(*a*) and in detail in Fig. 1(*b*).
3. The thermophysical properties of both fluids and walls are constant and uniform.
4. The primary and secondary areas of the separating plate have been lumped together so that the variation of wall temperature is also two dimensional.
5. The thermal resistance on both sides, including film heat transfer coefficient of primary and secondary surface and fouling resistance, are constant and uniform.
6. Heat transfer area per unit base area and surface configurations are constant.
7. Variation of temperature in the fluid streams in a direction normal to the separating plate (*z*-direction) is neglected.

Conservation of energy for wall and fluids considering longitudinal conduction in separating sheet and the axial dispersion in fluids can be expressed in nondimensional form [21] as given below:

$$\frac{\partial T_w}{\partial \theta} = T_a + RT_b - (1+R)T_w + \lambda_a N_a \frac{\partial^2 T_w}{\partial X^2} + \lambda_b N_b R \frac{\partial^2 T_w}{\partial Y^2} \quad (1)$$

$$V_a \frac{\partial T_a}{\partial \theta} = T_w - T_a - \frac{\partial T_a}{\partial X} + \frac{N_a}{\mathrm{Pe}_a} \frac{\partial^2 T_a}{\partial X^2} \quad (2)$$

$$\frac{V_b}{R} \frac{\partial T_b}{\partial \theta} = T_w - T_b - \frac{\partial T_b}{\partial Y} + \frac{N_b}{\mathrm{Pe}_b} \frac{\partial^2 T_b}{\partial Y^2} \quad (3)$$

where the nondimensional terms are defined as

$$X = \left[\frac{hA}{mc}\right]_a \frac{x}{L_a} = N_a \frac{x}{L_a}, \quad Y = \left[\frac{hA}{mc}\right]_b \frac{y}{L_b} = N_b \frac{y}{L_b}$$

where

$$N = \frac{hA}{mc}, \quad \theta = \frac{(hA)_a \tau}{MC_w}, \quad T = \frac{t - t_{b,\mathrm{in}}}{t_{\mathrm{ref}} - t_{b,\mathrm{in}}}$$

Capacity rate ratio,

$$E = \frac{(mc)_b}{(mc)_a}$$

Conductance ratio,

$$R = \frac{(hA)_b}{(hA)_a}$$

Heat capacity ratio,

$$V = \frac{LA_c \rho c}{MC_w}$$

Longitudinal heat conduction parameter,

$$\lambda_a = \frac{k\delta L_b}{L_a (mc)_a}, \quad \lambda_b = \frac{k\delta L_a}{L_b (mc)_b}$$

Axial dispersive Peclet number,

$$\mathrm{Pe} = \frac{WL}{A_c D} = \frac{(mc)L}{A_c D}$$

NTU is defined as

$$\frac{1}{NTU} = C_{\min}\left(\frac{1}{(hA)_a} + \frac{1}{(hA)_b}\right) \quad (4)$$

From the definitions of N_a and N_b, for $(mc)_a = (mc)_{\min}$,

$$N_a = NTU\left(1 + \frac{1}{R}\right), \quad N_b = \frac{NTU}{E}(R+1) \quad (5)$$

For $(mc)_b = (mc)_{\min}$,

$$N_a = NTU \cdot E\left(1 + \frac{1}{R}\right), \quad N_b = NTU(1+R) \quad (6)$$

The initial and boundary conditions are

$$T_a(X,Y,0) = T_b(X,Y,0) = T_w(X,Y,0) = 0, \quad (7)$$

$$T_a(0,Y,\theta) = \phi(\theta), \quad \left.\frac{\partial T_a(X,Y,\theta)}{\partial X}\right|_{X=N_a} = 0 \quad (8)$$

$$T_b(X,0,\theta) = 0, \quad \left.\frac{\partial T_b(X,Y,\theta)}{\partial Y}\right|_{Y=N_b} = 0 \quad (9)$$

$$\left.\frac{\partial T_w(X,Y,\theta)}{\partial X}\right|_{X=0} = \left.\frac{\partial T_w(X,Y,\theta)}{\partial X}\right|_{X=N_a} = \left.\frac{\partial T_w(X,Y,\theta)}{\partial Y}\right|_{Y=0} = \left.\frac{\partial T_w(X,Y,\theta)}{\partial Y}\right|_{Y=N_b} = 0 \quad (10)$$

$\phi(\theta) = \sin\theta$ is the perturbation in inlet temperature of the hot fluid.

3 Method of Solution

The conservation equations are discretized using the implicit finite difference technique [22]. Forward difference scheme is used for time derivatives, while upwind scheme and central difference scheme are used for the first and second order space derivatives, respectively. The difference equations along with the boundary conditions are solved using the Gauss–Seidel iterative technique. The convergence of the solution has been checked by varying the number of space grids and the size of time steps. The solution gives the two-dimensional temperature distribution for both the fluids and the separator plate. Additionally, one may calculate the bulk exit temperatures as follows:

$$\overline{T}_{a,\mathrm{ex}} = \frac{\int_0^{N_a} T_{a,\mathrm{ex}} u dy}{\int_0^{N_a} u dy} \quad \text{and} \quad \overline{T}_{b,\mathrm{ex}} = \frac{\int_0^{N_b} T_{b,\mathrm{ex}} v dx}{\int_0^{N_b} v dx} \quad (11)$$

To check the validity of the numerical scheme, the results of the present investigation have been compared with the available analytical results [10] using Laplace transform for balanced gas-to-gas crossflow heat exchangers in the absence of core longitudinal conduction and fluid axial dispersion for a conductance ratio of 1. Figure 2 depicts excellent agreements between the results of present investigation and those obtained analytically [10] for step, ramp, and exponential inputs.

4 Results and Discussions

The response of a crossflow heat exchanger under sinusoidal excitation in inlet temperature of the hot fluid ($T_{a,\mathrm{in}} = \phi(\theta) = \sin\theta$, θ being instantaneous time) is markedly different from its response for other modes of excitation such as step, ramp, and exponential [21]. The bulk exit temperature of the fluid streams will have oscillatory behavior throughout the entire period of operation. The frequency and amplitude of the oscillation will keep on varying until they reach a constant value indicating the attainment of steady state. At steady state, the mean exit temperatures will have steady periodic response. The responses can be represented by a sine function having the same frequency and different amplitudes from those of the inlet excitation. Performance of the heat exchanger was studied over a wide range of parameters as well as for a sufficient time duration so that steady state conditions are obtained for each individual excitation. Some of the salient results are discussed below.

4.1 Temperature Response of the Separating Sheet and the Two Fluids. The temperature of the fluid streams and the separator plate will continuously change in *x-y* plane until the heat exchanger attains steady state. The temperature profiles at any intermediate time step can be computed with the help of the present scheme. The variation of plate temperature is of particular interest for mechanical design. For the sinusoidal excitation, the amplitude of temperature of a point in the separating sheet, as well as that of fluids, keeps changing with time even after reaching to steady state. The separating sheet and five selected points (*p*, *q*, *r*, *s*, and *t*) and their corresponding temperature oscillations are shown in Figs. 3 and 4, respectively. The coordinate of any point shows the position of that point assuming the maximum dimension of the heat exchanger to be (50, 50). It can be observed that at different points the magnitude and the time lag of oscillations are different.

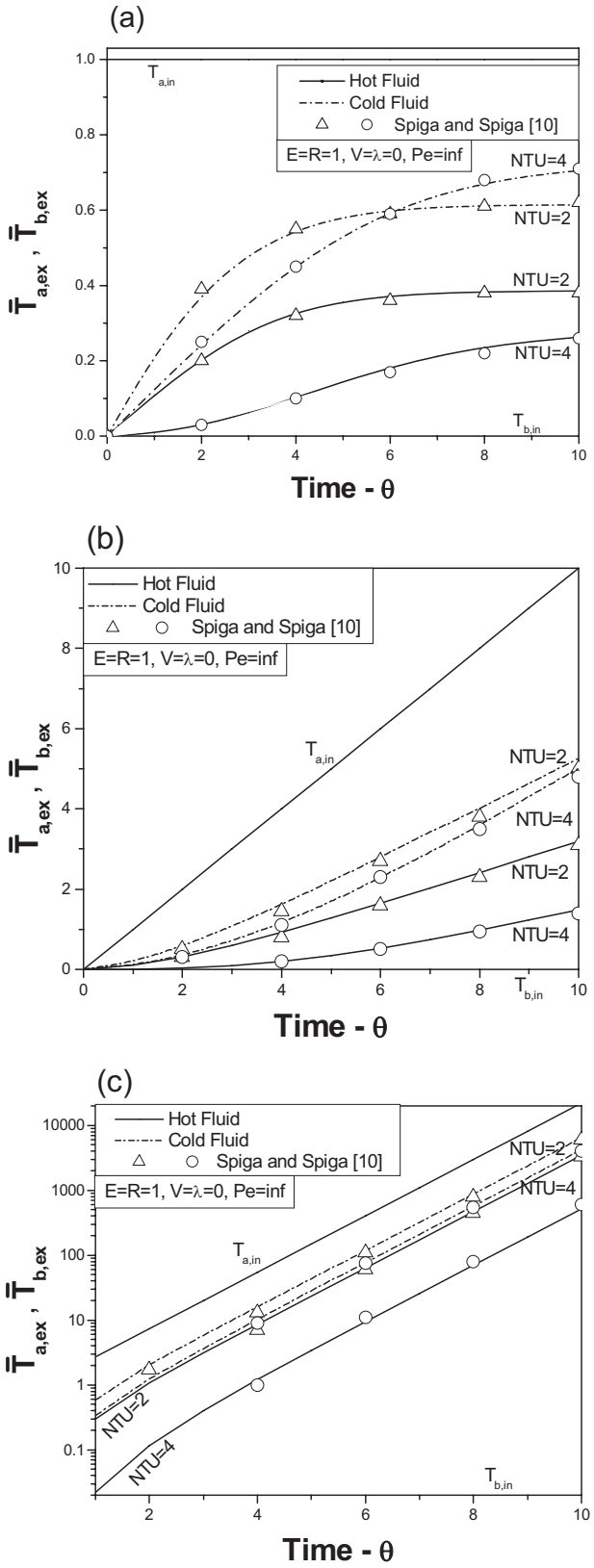

Fig. 2 Comparison of the solutions with the analytical results [10] for (*a*) step, (*b*) ramp, and (*c*) exponential inputs

Representing two-dimensional temperature profile at any instant will not give the actual picture of the temperature variation. Alternatively, Fig. 5 depicts the exit temperature behavior of the

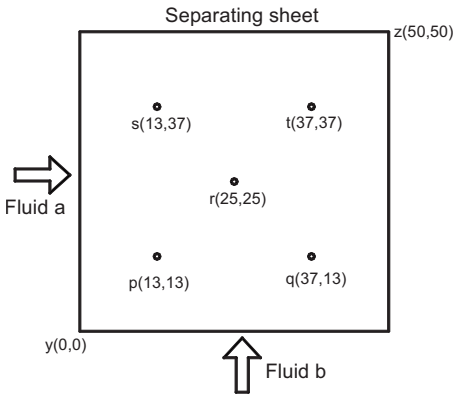

Fig. 3 Heat exchanger area and the points selected for the study of temperature oscillations

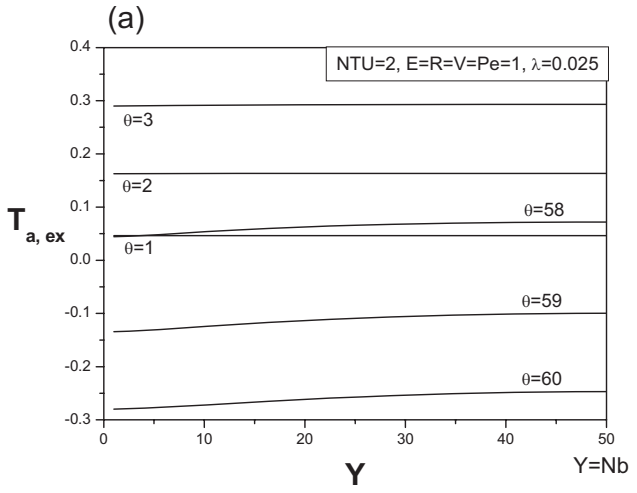

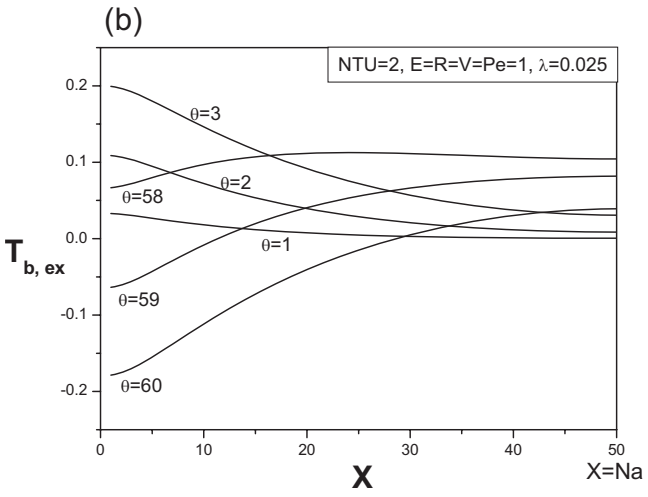

Fig. 5 Exit temperature behavior of (*a*) fluid a and (*b*) fluid b at different time levels

hot and the cold fluid streams at different time levels. The behavior of the exit temperature of the hot fluid is comparatively flat than that of cold fluid. Due to cyclic variation in the magnitude with time, the exit temperature history does not give any significant information. It suggests that the representation of bulk exit temperature would still be a better alternative for comparison and for understanding the results.

4.2 Effect of *NTU*. Variation of bulk exit temperatures of hot and cold fluids with *NTU* are shown in Fig. 6, where $E=R=1$, $V=\lambda=0$, and $\mathrm{Pe}\rightarrow\infty$, i.e., for large core capacity, in the absence of longitudinal conduction in wall and axial dispersion in fluids. The variation shows that with an increase in *NTU*, the amplitude of bulk exit temperatures of hot and cold fluids reduces. For the same surface configurations, high *NTU* means small thermal capacity, which leads to higher temperature difference between the inlet and exit of the fluid. The curves show that the damping function of the curves for both fluids not only depends on the values of heat capacities but also on the value of *NTU*. The damping increases with the increase in *NTU*, and the amplitude of the exit temperature curves reduces. The frequency of the oscillations goes on decreasing and the phase lag with respect to hot fluid inlet temperature increases. The increase in delay period of oscillations with the increase in *NTU* is predominant in the case of hot fluid bulk exit temperature, while that in the case of cold fluid is not significant.

4.3 Effect of Frequency. Variation of mean exit temperature of hot and cold fluids with frequency of input excitations (n and $5n$) is depicted in Fig. 7. As shown earlier also, frequencies of exit temperature responses are the same as that of corresponding input

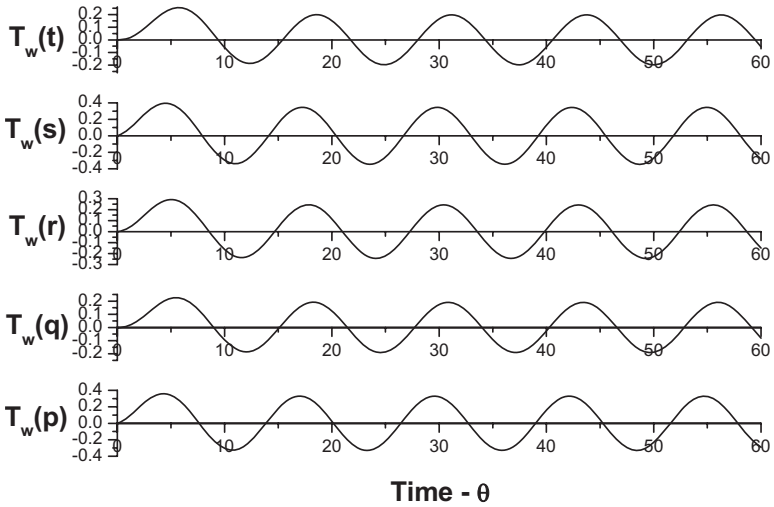

Fig. 4 Temperature oscillations with time for the five points shown in Fig. 3

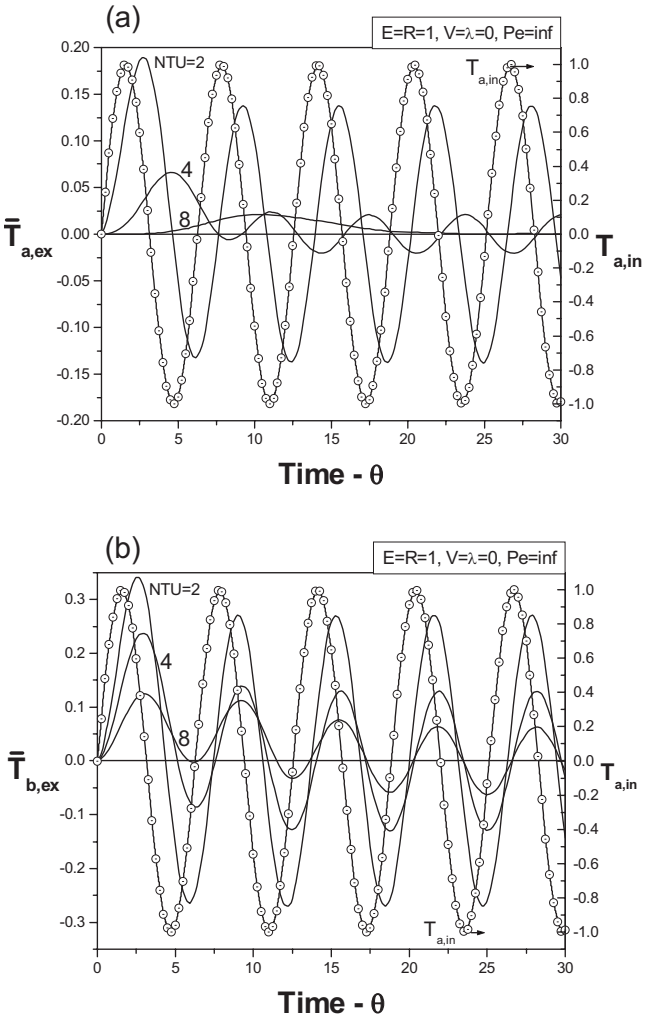

Fig. 6 Variation of mean exit temperatures with time for different *NTU*s. (*a*) Hot and (*b*) cold fluids.

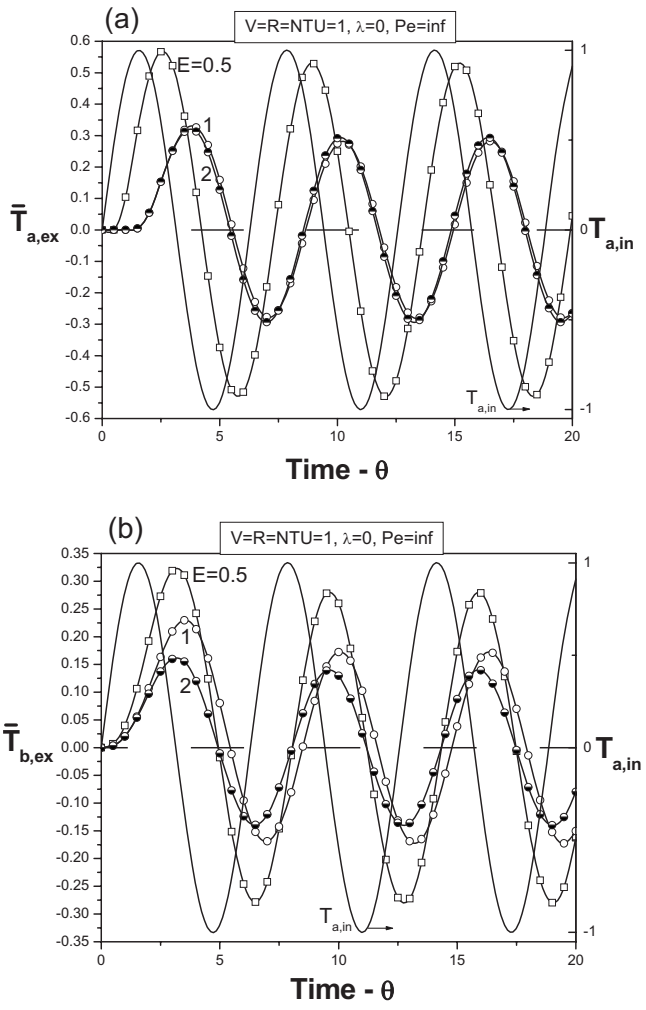

Fig. 8 Effect of heat capacity rate ratio on mean exit temperature of (*a*) hot and (*b*) cold fluids in the absence of longitudinal conduction in wall and fluid axial dispersion

excitations. Smaller frequencies take more time to stabilize the oscillations. As the frequency increases, the magnitude and phase lag of the mean exit temperatures of hot and cold fluids become close to each other. On the other hand, phase lag between the inlet and the exit responses increases with the increase in frequency.

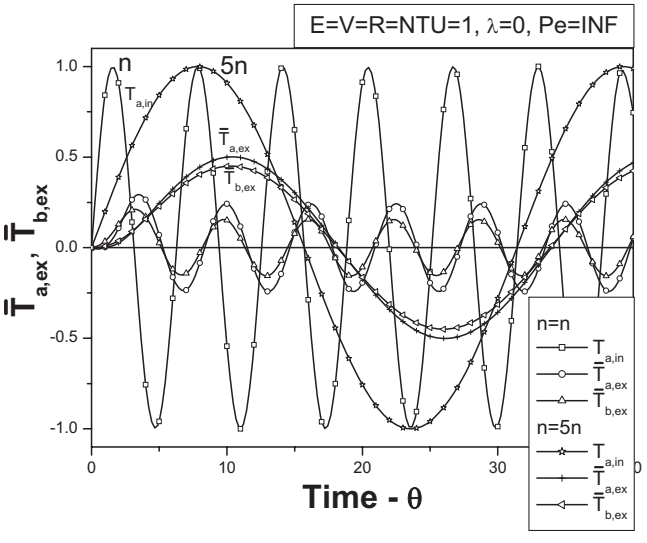

Fig. 7 Variation of mean exit temperature of hot and cold fluids with the change in frequency of input excitations

4.4 Effect of Heat Capacity Rate Ratio. Figure 8 shows the effect of capacity rate ratio E on bulk exit temperature of hot and cold fluids with sinusoidal excitation for $E=0.5$, 1, and 2. With the increase in E, the amplitude of the exit temperatures of both hot and cold fluids decreases. A significant reduction in amplitude and increase in time lag are observed for the oscillations of the hot fluid exit temperature when E changes from 0.5 to 1.0, while the difference in the two are only marginal when E changes from 1.0 to 2.0. However, in the case of cold fluid exit temperature, the amplitude decreases evenly with the increase in E. The time lag in the case of cold fluid increases with the change in E from 0.5 to 1.0. It again returns to its original value when E increases from 1.0 to 2.0. Thus the responses fully depend on the relative magnitude of the heat capacity rates of the two fluids.

4.5 Effect of Heat Capacity Ratio. When the heat capacity ratio V is smaller, the effect of fluid thermal capacity is less pronounced compared with that of separating sheet, and the time taken to transfer the heat from one fluid to the other is less. Soon the bulk exit temperatures reach the steady values. With the increase in heat capacity ratio, the phase lag and the time taken to reach its steady state value increase, while the amplitude of the oscillations decreases (Fig. 9). The delay period of oscillations is comparatively longer for hot fluid bulk exit temperature than that for cold fluid bulk exit temperature.

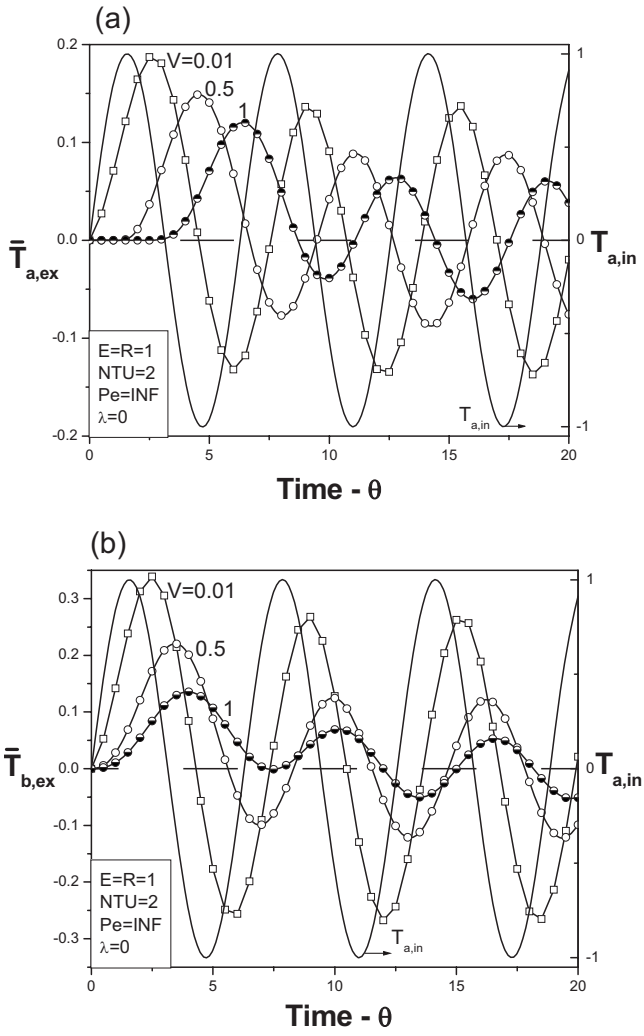

Fig. 9 Effect of heat capacity ratio on mean exit temperature of both the fluids on sinusoidal response without longitudinal conduction in wall and fluid axial dispersion

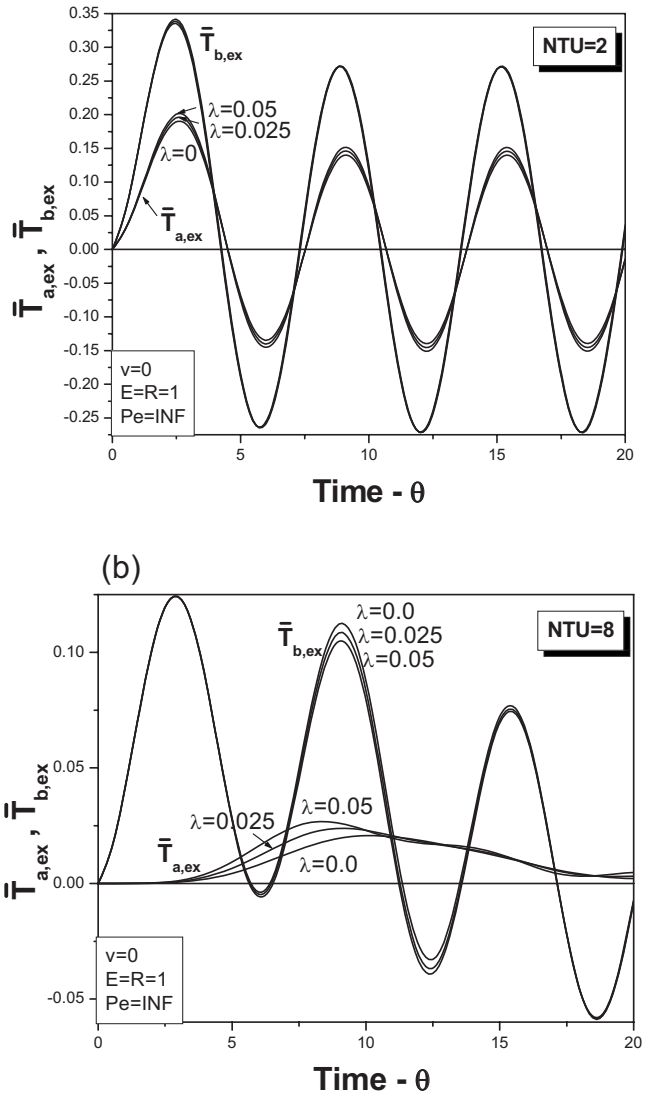

Fig. 10 Effect of longitudinal conduction on exit temperature response of hot and cold fluids at *NTU*s (*a*) 2 and (*b*) 8

4.6 Longitudinal Conduction in Wall. The effect of longitudinal conduction is significant only at higher *NTU*s. The effect of longitudinal conduction is more pronounced for exchangers with high *NTU*s and short conduction lengths where there is a reduction in local temperature difference, thereby reducing the effectiveness and the heat transfer rate. Similar to the other excitations there is significant increase in the amplitude of hot fluid mean exit temperature and decrease in that of cold fluid bulk exit temperature, resulting in deterioration in performance. This can be observed from Fig. 10. The deterioration observed is comparatively more significant in the case of cold fluid than that in hot fluid. It may also be noted that the deterioration is significant mainly in the amplitude, while not much change in the delay period can be seen.

The temperature responses due to the effect of axial dispersion in fluids are similar to those obtained without considering axial dispersion but the amount of deterioration is much less. Due to this fact the difference in the responses cannot be visualized easily. Figures 11 and 12 depict the percentage change in bulk exit temperature of the hot and the cold fluids, respectively, due to longitudinal conduction than the case when it is absent. The magnitude of the percentage change and the amount of irregular fluctuations increase with *NTU*. The percentage change due to longitudinal conduction in cold fluid mean exit temperature (Fig. 12) is smaller than that in hot fluid mean exit temperature (Fig. 11).

4.7 Effect of Axial Dispersion. The effects of variation of axial dispersion on dynamic behavior of hot and cold fluids are studied and presented in Fig. 13. As we decrease the Peclet number Pe (i.e., increasing the axial dispersion effect), the amplitudes of bulk exit temperatures of the hot and the cold fluids increase. For the cold fluid the change is gradual while for the hot fluid a large change is observed when Pe changes from 1 to 10. With further increase in Pe, the change in amplitude of hot fluid bulk exit temperature is not significant. However, the delay period in both hot and cold fluids increases evenly with the increase in Pe.

4.8 Relationship Between the Outlet Temperature of Hot and Cold Fluids With Hot Fluid Inlet Temperature: A Graphical Representation. There are some disturbances in the hot and the cold fluid responses before reaching to steady state values. These disturbances are for short duration if *NTU* is small and are longer for the higher values of *NTU*. Correspondingly the amplitude also goes on decreasing. It can be observed from the Fig. 6 for a gas-to-gas heat exchanger.

After reaching to steady state, when the hot and cold fluid exit temperatures are plotted with respect to hot fluid inlet temperature, an interesting representation similar to Lissajous figures, having its axis inclined to the *x*-*y* axes, is found. The minor axis

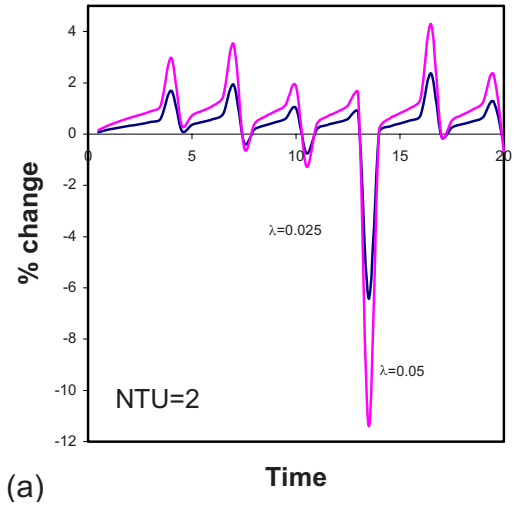

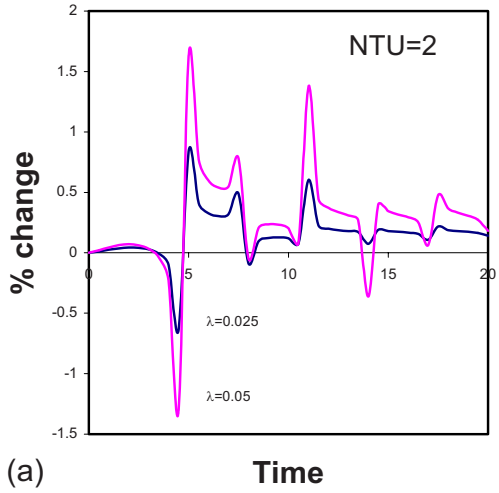

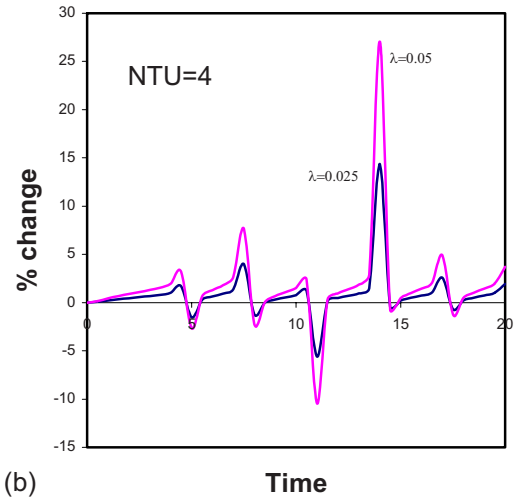

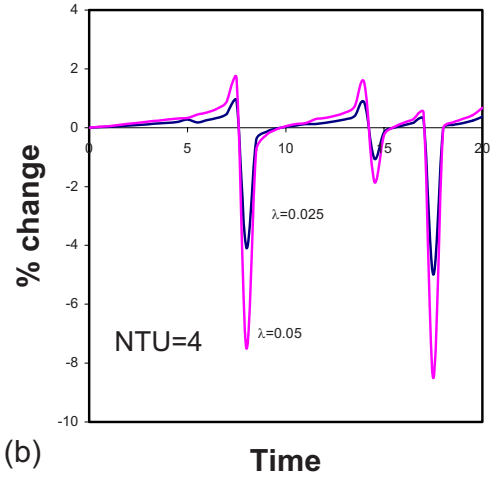

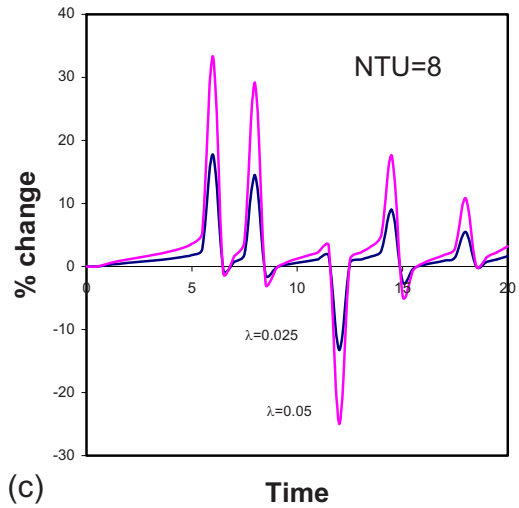

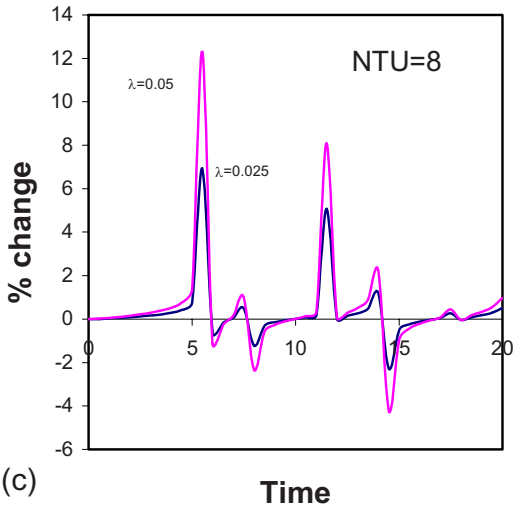

Fig. 11 % change in hot fluid mean exit temperature with time due to longitudinal conduction at *NTU* (*a*) 2, (*b*) 4, and (*c*) 8 for *E*=*R*=*V*=1 and Pe=∞

Fig. 12 % change in cold fluid mean exit temperature with time due to longitudinal conduction at *NTU* (*a*) 2, (*b*) 4, and (*c*) 8 for *E*=*R*=*V*=1 and Pe=∞

goes on decreasing with *NTU* and the angle between major axis with *x*-axis also reduces simultaneously (Fig. 14).

Similarly for the fluids other than gases ($E=R=V=1$, $\lambda=0$, and $\mathrm{Pe}=\infty$), the representations may be given, as depicted in Fig. 15. From these graphical representations, one can directly find out the hot and the cold fluid responses for any value of hot fluid inlet temperature with sinusoidal excitation. Though the figure gives an easy and direct relationship between the amplitudes of the mean

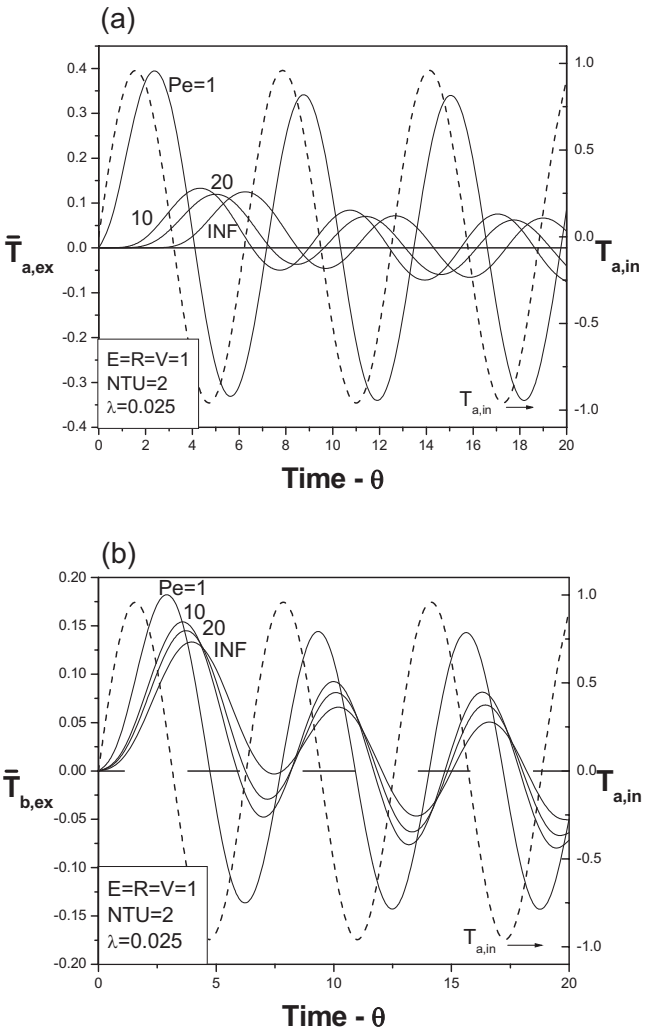

Fig. 13 Effect of axial dispersive Peclet number, Pe, on mean exit temperature of (*a*) hot and (*b*) cold fluids

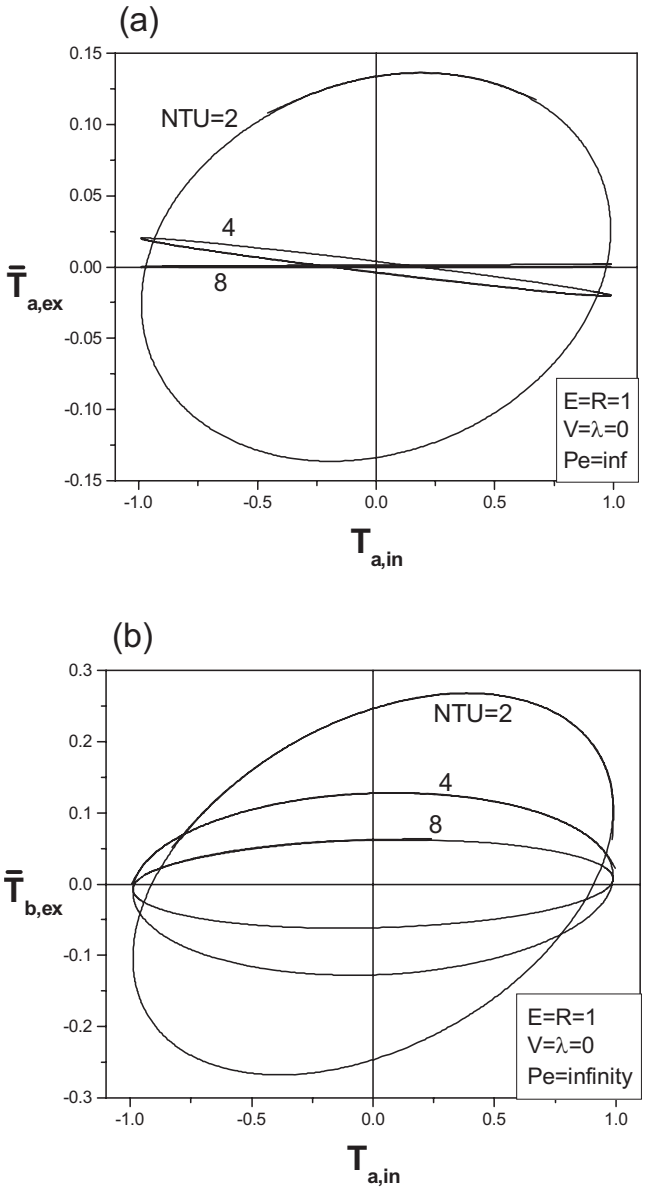

Fig. 14 Graphical representations of (*a*) hot and (*b*) cold fluid mean exit temperatures with hot fluid inlet temperature for infinite wall capacity

exit temperatures and the hot fluid inlet temperature, nothing can be said regarding the delay period.

5 Conclusion

A numerical solution is established showing the variation of the transient temperature fields due to the combined effect of two-dimensional core longitudinal conduction and axial dispersion. Transient responses of different points of the separating sheet have been obtained for sinusoidal excitation in inlet temperature of the hot fluid. It gives an exact idea about the two-dimensional temperature variation with time. It has been shown that the longitudinal conduction plays an important role at higher *NTU*s especially in hot fluid responses. Similarly fluid axial dispersion is important at smaller Pe. Both the conditions are very common in the case of compact crossflow heat exchangers working at high *NTU*s and low values of Reynolds number. An interesting behavior is observed for the variation of hot and cold fluid exit temperatures with respect to hot fluid inlet temperature for the sinusoidal excitation. The graphical representation gives an easy understanding of steady state behavior of the mean exit temperatures due to sinusoidal excitation. Thus an elaborated study of the dynamic behavior with sinusoidal excitation is very useful for the detailed thermal and mechanical design and control of compact heat exchangers at different practical situations.

Nomenclature

A = area of heat transfer (m^2)
A_c = area of cross section (m^2)
c = specific heat of fluid (J/kg K)
C_w = specific heat of the wall material (J/kg K)
D = diffusion coefficient (W/m K)
E = capacity rate ratio $=(mc)_b/(mc)_a$
h = heat transfer coefficient (W/m^2 K)
k = thermal conductivity of the separating sheet (W/m K)
L = heat exchanger length (m)
m = mass flow rate of fluid (kg/s)
M = mass of the separating sheet (kg)
NTU = number of transfer units (dimensionless)
Pe = axial dispersive Peclet number $=(mc)L/A_c \cdot D$ (dimensionless)
R = conductance ratio $=(hA)_b/(hA)_a$ (dimensionless)

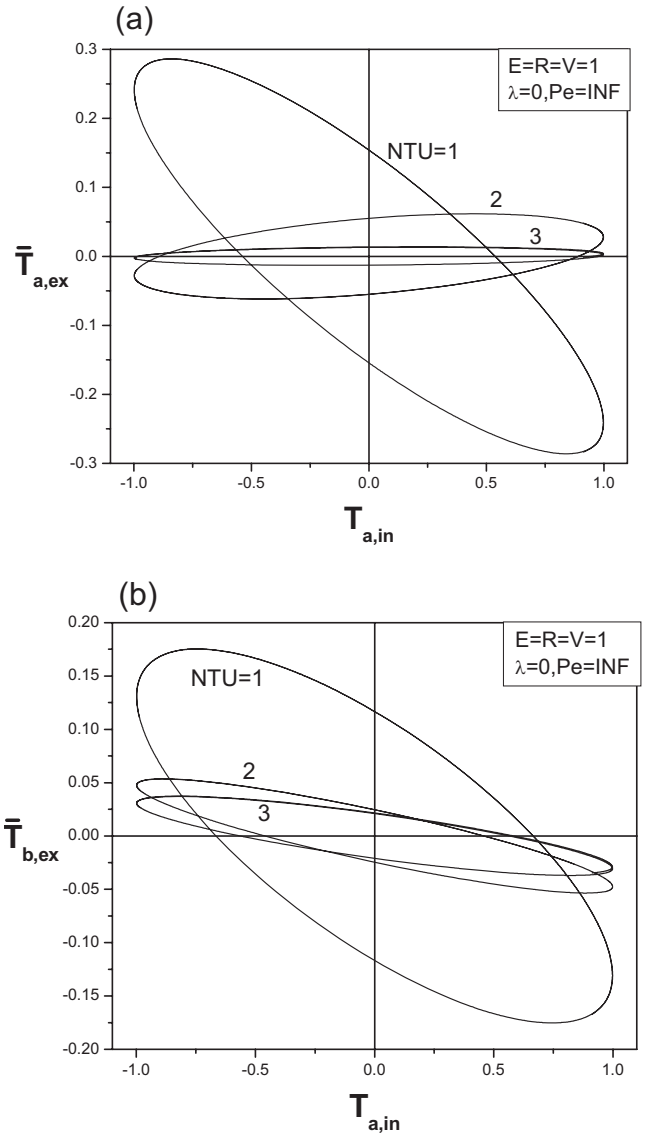

Fig. 15 Graphical representations of (*a*) hot and (*b*) cold fluid mean exit temperatures with hot fluid inlet temperature for finite wall capacity

Re = Reynolds number (dimensionless)
t = temperature (°C)
$T = t - t_{b,\text{in}} / t_{\text{ref}} - t_{b,\text{in}}$ (dimensionless)
$\overline{T}$ = dimensionless bulk mean temperature
u, v = uniform velocity in x and y directions (slug flow) (m/s)
U = overall heat transfer coefficient ($\text{W/m}^2\,\text{K}$)
V = capacitance ratio $= LA_c\rho c / MC_w$ (dimensionless)
x, y = direction, lengths from the entry (m)
X = $[hA/mc]_a x/L_a$, dimensionless length
Y = $[hA/mc]_b y/L_b$, dimensionless length

Greek Letters

δ = thickness of the separating sheet (m)
$\in$ = effectiveness (dimensionless)
η_o = efficiency (dimensionless)
θ = $(hA)_a \tau / MC_w$, dimensionless time
λ = longitudinal heat conduction parameter, $\lambda_a = k\delta L_b / L_a (mc)_a$, $\lambda_b = k\delta L_a / L_b (mc)_b$ (dimensionless)
μ = dynamic viscosity (N s/m^2)
ρ = density (kg/m^3)
τ = time (s)
$\phi(.)$ = perturbation in hot fluid inlet temperature

Subscripts

a, b = sides a and b
c = cold side
h = hot side
w = wall
in = inlet
ex = exit
min = minimum

References

[1] Dusinberre, G. M., 1959, "Calculation of Transients in a Crossflow Heat Exchanger," ASME J. Heat Transfer, **81**, pp. 61–67.
[2] Myers, G. E., Mitchell, J. W., and Norman, R. F., 1967, "The Transient Response of Crossflow Heat Exchangers, Evaporators, and Condensers," ASME J. Heat Transfer, **89**, pp. 75–80.
[3] Myers, G. E., Mitchell, J. W., and Lindeman, C. P., Jr., 1970, "The Transient Response of Heat Exchangers Having an Infinite Capacitance Rate Fluid," ASME J. Heat Transfer, **92**, pp. 269–275.
[4] Yamashita, H., Izumi, R., and Yamaguchi, S., 1978, "Analysis of the Dynamic Characteristics of Crossflow Heat Exchanger With Both Fluids Unmixed," Bull. JSME, **21**, pp. 479–485.
[5] Kou, H. S., and Yuan, P., 1994, ""Effect of Longitudinal Separator Sheet Conduction on the Transient Thermal Response of Crossflow Heat Exchangers With Neither Gas Mixed," Numer. Heat Transfer, Part A, **25**, pp. 223–236.
[6] Roetzel, W., 1996, "Transient Analysis in Heat Exchangers," *New Developments in Heat Exchangers*, N. Afgan, A. Bar-Cohen, D. Butterworth, W. Roetzal, M. da Graca Carvalho, eds., Gordon and Breach, Amsterdam, pp. 547–575.
[7] Sarangi, S., and Baral, H. S., 1987, "Effect of Axial Conduction in the Fluid on Cryogenic Regenerator Performance," Cryogenics, **27**, pp. 505–509.
[8] Romie, F. E., 1983, "Transient Response of Gas-to-Gas Crossflow Heat Exchangers With Neither Gas Mixed," ASME J. Heat Transfer, **105**, pp. 563–570.
[9] Gvozdenac, D. D., 1986, "Analytical Solution of the Transient Response of Gas-to-Gas Crossflow Heat Exchanger With Both Fluids Unmixed," ASME J. Heat Transfer, **108**, pp. 722–727.
[10] Spiga, G., and Spiga, M., 1987, "Two-Dimensional Transient Solutions for Crossflow Heat Exchangers With Neither Gas Mixed," ASME J. Heat Transfer, **109**, pp. 281–286.
[11] Spiga, G., and Spiga, M., 1988, "Transient Temperature Fields in Crossflow Heat Exchangers With Finite Wall Capacitance," ASME J. Heat Transfer, **110**, pp. 49–53.
[12] Spiga, G., and Spiga, M., 1992, "Step Response of the Crossflow Heat Exchanger With Finite Wall Capacitance," Int. J. Heat Mass Transfer, **35**(2), pp. 559–565.
[13] Romie, F. E., 1994, "Transient Response of Crossflow Heat Exchangers With Zero Core Thermal Capacitance," ASME J. Heat Transfer, **116**, pp. 775–777.
[14] Luo, X., 1998, "Das axiale Dispersionsmodell fur Kreuzstromwarmeubertrager," *Fortschritt-Berichte VDI*, VDI, Dusseldoef, Reihe 19, No. 109.
[15] Sahoo, R. K., and Roetzel, W., 2002, "Hyperbolic Axial Dispersion Model for Heat Exchangers," Int. J. Heat Mass Transfer, **45**(6), pp. 1261–1270.
[16] Chen, H. T., and Chen, K. C., 1991, "Simple Method for Transient Response of Gas-to-Gas Cross-Flow Heat Exchangers With Neither Gas Mixed," Int. J. Heat Mass Transfer, **34**(11), pp. 2891–2898.
[17] Chen, H. T., and Chen, K. C., 1992, "Transient Response of Crossflow Heat Exchangers With Finite Wall Capacitance," ASME J. Heat Transfer, **114**, pp. 752–755.
[18] Das, S. K., and Roetzel, W., 1995, "Dynamic Analysis of Plate Heat Exchangers With Dispersion in Both Fluids," Int. J. Heat Mass Transfer, **38**(6), pp. 1127–1140.
[19] Xuan, Y., and Roetzel, W., 1993, "Stationary and Dynamic Simulation of Multipass Shell and Tube Heat Exchangers With the Dispersion Model for Both Fluids," Int. J. Heat Mass Transfer, **36**(17), pp. 4221–4231.
[20] Stang, J. H., and Bush, J. E., 1974, "The Periodic Method for Testing Compact Heat Exchanger Surfaces," ASME J. Eng. Power, **96A**, pp. 87–94.
[21] Mishra, M., Das, P. K., and Sarangi, S., 2004, "Transient Behaviour of Crossflow Heat Exchangers With Longitudinal Conduction and Axial Dispersion," ASME J. Heat Transfer, **126**(3), pp. 425–433.
[22] Ozisic, M. N., 1994, *Computational Methods in Heat Transfer*, CRC, London.

Transient Thermal Analyses of Midwall Cooling and External Cooling Methods for a Gun Barrel

Avanish Mishra
Department of Mechanical Engineering and Mining Machinery Engineering,
Indian School of Mines Dhanbad,
Jharkhand 826004, India
e-mail: avanish.ism@gmail.com

Amer Hameed
e-mail: ahameed.cu@defenceacademy.mod.uk

Bryan Lawton

Weapon Systems and Engineering Dynamics Group,
DA-CMT,
Cranfield University,
Shrivenham, Swindon, Wilts, SN6 8LA, UK

Liquid cooling methods are often used for thermal management of a large caliber gun barrel. In this work, transient thermal analyses of midwall-cooled and externally cooled gun barrels were performed. At first, a novel simulation scheme was developed for the computation of the gun barrel temperature history (temperature variation over time), and its experimental validation was performed. In the computational scheme an internal ballistics code, GUNTEMP8.EXE, was developed to simulate the total heat transfer per cycle for the given ammunition parameters. Subsequently, a finite element (FE) model of the barrel was developed in ANSYS 11.0. Heat transfer to the barrel was approximated by an exponentially decaying heat flux. The FE model was solved to compute for barrel temperature history. Simulations were performed for a burst of 9 cycles, and the results were found to agree with the experimental measurements. Subsequently, the simulation scheme was extended to analyze a burst of 40 cycles at 10 shots per minute (spm). Three cases were investigated as follows: (1) a naturally cooled gun barrel, (2) a gun barrel with midwall cooling channels, and (3) an externally cooled gun barrel. Natural cooling was found insufficient to prevent cook-off, whereas midwall and external cooling methods were found to eliminate any possibility of it. In the context of a self-propelled howitzer, a midwall-cooled gun barrel connected to an engine cooling system was also analyzed. [DOI: 10.1115/1.4001607]

Keywords: cook-off, external cooling, gun barrel, howitzer, midwall cooling, temperature history

1 Introduction

During shot fire, a great amount of heat is transferred to the gun bore surface from hot gases. At the same instant, the gun barrel is naturally cooled by external environment at its outer surface, but combined convection heat transfer coefficient associated with natural cooling is very small. During operation, a gun may need to fire at a very high rate, leading to insufficient time between cycles to transfer all the heat input to the external environment by natural cooling. In such a scenario, the temperature of the gun bore surface keeps on increasing to ultimately attain the cook-off temperature. At cook-off temperature, the loaded charge of the next cycle will self-ignite given sufficient contact time between the ammunition and the hot gun bore surface. This premature self-ignition of charge may result in serious damage to the gun and injury to the crew members. Until the cook-off temperature is attained, the gun can be fired at any rate according to the operational requirement; however, once it is reached, the firing rate must be drastically reduced in order to maintain the initial temperature of subsequent cycles below the cook-off temperature [1]. Hence, thermal management of the large caliber gun barrel is necessary for maintaining a high rate of firing.

The thermal management of gun barrels has been classified into passive and active cooling methods [2]. Chromium plating and wear-reducing additives are examples of passive cooling methods. Wear-reducing additives such as talc powder or Swedish additive reduce heat transfer to the gun bore surface. Reduced heat transfer decreases the barrel wear and increases the number of shots that can be fired before cook-off occurs. Active cooling methods increase the heat dissipation rate by either utilizing fins or forced liquid cooling methods. Large caliber gun barrels are very thick; therefore, the outer barrel surface temperature does not rise to a very high level, and hence, the use of fins cannot be justified. So, liquid cooling methods are preferred for thermal management of large caliber gun barrels. In-bore liquid injection, midwall cooling, and external cooling methods are important examples of barrel liquid cooling technology [3]. In the midwall-cooling method, a gun barrel is manufactured in such a way that cooling channels are incorporated in the barrel structure itself, as shown in Fig. 1. Coolant is pumped through these cooling channels to cool the gun barrel. However, in the external cooling method, a jacket is provided around the gun barrel. The gun barrel is cooled by the pumping liquid into the annular space between the outer barrel surface and the jacket, as shown in Fig. 2. Midwall and external cooling has an advantage over the passive cooling that the possibility of cook-off can be entirely eliminated, and hence, the capability of continuous fire can be facilitated.

Hurn et al. [4] developed a high velocity midwall water cooling system and used it in an electromagnetic gun barrel to remove the maximum heat flux of 5 MJ m^{-2} per cycle [4]. Recently, Bass and De Swardt [5] proved the superiority of the midwall cooling method over natural cooling through thermal experiments on a 155 mm compound gun tube with full length integral midwall cooling channels. De Swardt and Andrews [6] conducted a finite element stress analysis of autofrettaged, midwall-cooled gun tubes and demonstrated that several configurations of midwall-cooled gun barrels are possible, in which working stresses can be maintained at an acceptable level. However, they also proved that the cooling channels significantly lower the internal pressure that a compound gun tube can tolerate in comparison to a monobloc gun barrel.

In this work, a novel computational scheme was developed for the simulation of the gun barrel temperature history, and its experimental validation was performed. Subsequently, this scheme was applied to analyze the performance of midwall and external cooling for a 155 mm gun barrel. Several inferences regarding the

Contributed by the Heat Transfer Division of ASME for publication in the JOURNAL OF HEAT TRANSFER. Manuscript received March 13, 2009; final manuscript received March 16, 2010; published online June 23, 2010. Assoc. Editor: Wei Tong.

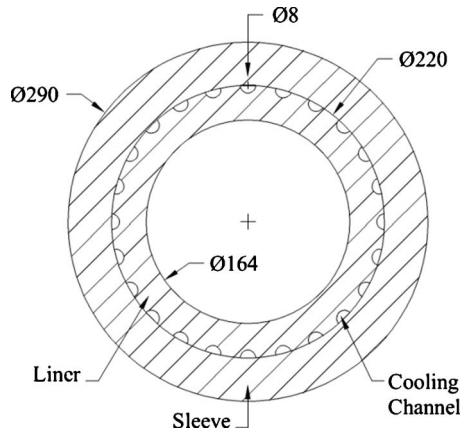

Fig. 1 Cross section of the gun barrel with midwall cooling channels

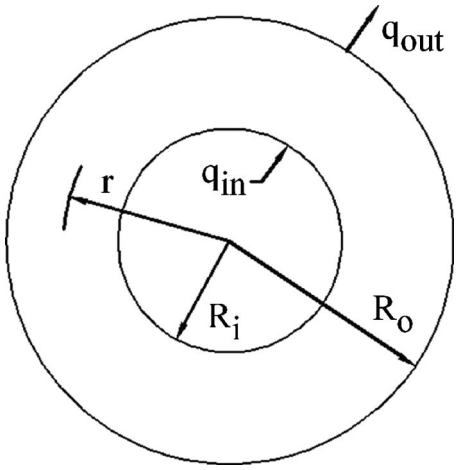

Fig. 3 Schematic of heat transfer to the gun barrel

performance of cooling methods were made on the basis of the computed results. Advantages and disadvantages of these active cooling methods for a self-propelled howitzer (SPH) were also analyzed.

2 Scheme for the Simulation of the Gun Barrel Temperature History and Its Experimental Validation

Accurate modeling of the gun barrel temperature variation over time is important to assess wear and the number of cycles needed to reach cook-off. The barrel heating problem was divided into two main parts, as follows: (1) determination of the total heat transfer from hot gases to the bore surface during a shot fire and (2) determination of the barrel temperature distribution, resulting from this heat transfer. An internal ballistics code, GUNTEMP8.EXE, was developed to simulate the total heat transfer per cycle for the given ammunition parameters. Subsequently, a finite element (FE) model of the barrel was developed in ANSYS 11.0. In FE model, heat transfer to the barrel was approximated by an exponentially decaying heat flux, which was applied as a boundary condition at the bore surface. The FE model was solved to compute for barrel temperature history. Simulations were performed for a burst of 9 cycles, and the results were found to match satisfactorily the corresponding experimental measurements. The advantage of this novel scheme is that it easily couples internal ballistics simulations with finite element methods. Wu et al. [3] conducted analytical and finite element analysis of heat transfer in a 155 mm midwall-cooled gun barrel. They also used exponentially decaying heat flux as a boundary condition in the finite element model. However, their scheme of simulation is different as it does not incorporate computation of the total heat transfer from the ammunition for particular ammunition properties; instead a preknown value of the total heat transfer for a 155 mm gun was utilized. In contrast, the current simulation scheme facilitates the generation of temperature histories using ammunition properties and other operational parameters. Moreover, the reduction in the convective heat input to the bore surface due to increasing bore temperature was also incorporated to improve accuracy.

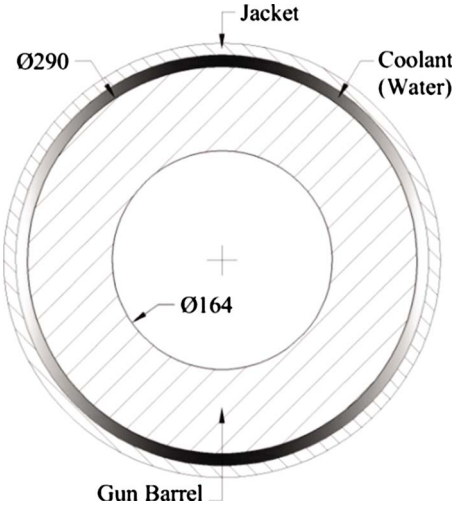

Fig. 2 Cross section of an externally cooled gun barrel

2.1 Formulation of the Gun Barrel Heating Problem. A schematic for the heat transfer in a gun barrel is shown in Fig. 3. Heat conduction in the axial direction can be assumed to be negligible in comparison to the radial direction [7]. Frictional heating between the projectile driving band and the bore surface can also be neglected [8]. Any effect of gravity on convection heat transfer was also neglected. The barrel was assumed to be uniformly thick at any transverse cross section along its length.

The mathematical formulation is presented in the cylindrical coordinate system. Based on the above assumptions, any possibility of azimuthal variation in the temperature was removed, and the problem was reduced to one-dimensional axisymmetric case. The governing equation (Eq. (1)) is the diffusion equation, which is the Fourier's conduction equation combined with the energy equation in cylindrical coordinates

$$\frac{1}{r}\frac{\partial}{\partial r}\left(kr\frac{\partial T}{\partial r}\right) = \rho c_p \frac{\partial T}{\partial t} \tag{1}$$

where r is the radius, varying from R_i to R_o, and k, ρ, and c_p are the thermal conductivity, density, and specific heat of the gun steel, respectively. The boundary condition at the bore and outside barrel surfaces are given by Eqs. (3) and (4), respectively

$$T = T_{\text{first}}, \quad t = 0, \quad R_i \le r \le R_o \tag{2}$$

$$-k\frac{\partial T}{\partial r} = h_g(T_g - T) = q_{\text{in}}, \quad t > 0, \quad r = R_i \tag{3}$$

$$-k\frac{\partial T}{\partial r} = h_\infty(T - T_\infty) = q_{\text{out}}, \quad t > 0, \quad r = R_o \tag{4}$$

where h_g is the combined convection heat transfer coefficient between the bore surface and hot propellant gases, and h_∞ is heat transfer coefficient between the outer barrel surface and the surrounding atmosphere.

2.2 Introduction to GUNTEMP8.EXE. GUNTEMP8.EXE models

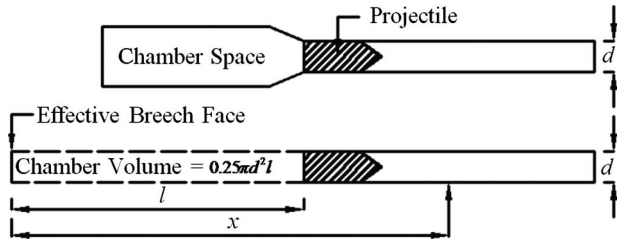

Fig. 4 Description of the effective breech face

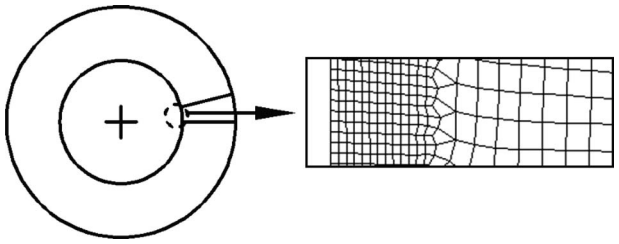

Fig. 5 Gun barrel cross section and meshed model

the temperature fluctuation of the bore surface ($T_{\max}-T_i$) and instantaneous heat transfer (H) at any specified position along the length of the barrel during the first cycle. An explicit finite difference scheme is followed for the computation of the bore temperature fluctuation. For thermal calculations, Eqs. (1) and (2) are utilized as such, and Eq. (3) is replaced by Eq. (5).

$$-k\frac{\partial T}{\partial r}=q_x, \quad t>0, \quad r=R_i \tag{5}$$

where q_x is the instantaneous heat flux between the propellant gases and gun bore surface at a distance x from the effective breech face. The definition of effective breech face can be understood from Fig. 4. q_x is usually determined from a semi empirical equation, in which the surface heat transfer coefficient is determined from the Nusselt number (Nu), which is correlated with the Reynolds (Re) and Prandtl (Pr) numbers. This is good for steady problems, but does not work for unsteady expanding flows, existing in a gun barrel, because the expansion of the gases distorts the temperature distribution in the thermal boundary layer [1]. In gun barrels an expanding flow exists as hot propellant gases expand when the shot moves down the barrel. Lawton and Klingenberg [1] demonstrated that q_x can be computed by Eq. (6)

$$q_x=\frac{k_g}{x}[a\ \mathrm{Re}_x^b(T_g-T_w)-cET_w] \tag{6}$$

where

$$\mathrm{Re}_x=\frac{\rho_g C_x x}{\mu_g} \tag{7}$$

$$E=\frac{(\gamma-1)}{V}\frac{\partial V}{\partial t}t'_0 \tag{8}$$

$$t'_0=\sqrt{\frac{m_c c_{vg} d^3}{V_c k_g C_m}} \tag{9}$$

E is a dimensionless number called the expansion number. The effect of the expansion number E when the gas volume is increasing is to reduce the heat flux. E is positive for diverging gas flow existing in gun systems. a, b, and c are constants, suitable values being $a=0.85$, $b=0.7$, and $c=2000$ [1].

2.3 Finite Element Model. The second part of the scheme of the simulation is the determination of the barrel temperature distribution. Total heat transfer and temperature fluctuation for the first cycle are known from the output of GUNTEMP8.EXE. Subsequently, one-dimensional, transient, thermal analysis was performed with commercial finite element analysis (FEA) package ANSYS 11.0. The solid, quad eight-node, thermal element was used throughout this work. The annulus segment, as shown in Fig. 5, was modeled to represent the barrel cross section. When a shot is fired, almost all of the heat transfer takes place within a few milliseconds. This induces very acute temperature gradients near the bore surface; hence, a very fine mesh was used in that zone. Figure 5 shows a small segment of the meshed model from near the bore surface.

Heat transfer to the gun bore surface can be modeled as an exponentially decaying heat flux [9] (Eq. (10)). In the FE model this was applied as a boundary condition at the bore surface. Equation (10) was integrated from zero to t, with respect to time, which resulted in the equation of heat transfer to the bore surface (Eq. (11)). In Eq. (11) $q_{\max}\times t_0$ can be denoted as H_∞, which is the total heat transfer per unit area per cycle. Often, H_∞ is also referred as the heat transfer per cycle. Total heat transfer ($H_\infty^{\mathrm{first}}$) and temperature fluctuation ($T_{\max}-T_i$) for first cycle are known from the output of Guntemp8.exe. $q_{\max}$ can be determined from Eq. (12), but before that, t_0 (time constant) should be known. According to Lawton and Klingenberg, t_0 can be determined from Eq. (13) [9]. So, the boundary conditions in the FE model of the gun barrel for simulation of the first cycle were same as for Eqs. (2) and (4), but Eq. (3) was interpreted differently as Eq. (14)

$$q_x=q_{\max}\exp\left(-\frac{t}{t_0}\right) \tag{10}$$

$$H=q_{\max}t_0\left[1-\exp\left(-\frac{t}{t_0}\right)\right] \tag{11}$$

$$q_{\max}\times t_0=H_\infty \tag{12}$$

$$T_{\max}-T_i=1.082\frac{H_\infty}{k}\sqrt{\frac{\alpha}{\pi t_0}} \tag{13}$$

$$-k\frac{\partial T}{\partial r}=q_{\max}\exp\left(-\frac{t}{t_0}\right), \quad t>0, \quad r=R_i \tag{14}$$

After application of all the boundary conditions, the FE model was solved to compute for the gun barrel temperature variation over time. For analysis of a burst, it is necessary to determine the total heat transfer for every cycle of the burst. Lawton and Klingenberg proposed Eq. (15) [1] to compute for the heat transfer for a particular cycle from the data of the total heat transfer of the first cycle ($H_\infty^{\mathrm{first}}$). It incorporates the reduction in the heat transfer with an increase in the bore temperature.

$$H_\infty^n=H_\infty^{\mathrm{first}}\left(\frac{T_r-T_i}{T_r-T_{\mathrm{first}}}\right) \tag{15}$$

where T_r is the radiation temperature, which is a characteristic property of the ammunition and T_i is the initial bore surface temperature of a cycle. H_∞^n is the total heat transfer for the nth cycle in the burst. Therefore, after the completion of each cycle, a new equation of exponentially decaying heat flux was used in the FE model, commensurate with the calculated value of the total heat transfer.

2.4 Experimental Validation of the Simulation Scheme. Experiments were performed on a 155 mm, 52 caliber gun barrel with charge A. The radiation temperature (T_r) for charge A was 1189.15 K. Temperature fluctuation and heat transfer were measured during the experiments at 5 cm from the commencement of rifling. Fast response, eroding type, thermocouples, available from

Table 1 155 mm gun barrel, experimental measurements at 0.05 m from the commencement of rifling

Shot number n	Initial bore surface temperature T_i (K)	Maximum bore surface temperature T_{max} (K)	Total heat transfer H_∞^n (K J m^{-2})	Time of firing (min)
1	307.6	1237	963.2	0
2	311.4	1246	957.3	5
3	316.9	1248	951.8	11
4	320.7	1250	959.1	16
5	322.4	1225	949.7	22
6	332.9	1254	977.4	26
7	331.1	1298	947.0	32
8	334.7	1269	948.9	37
9	338.8	1258	946.8	43

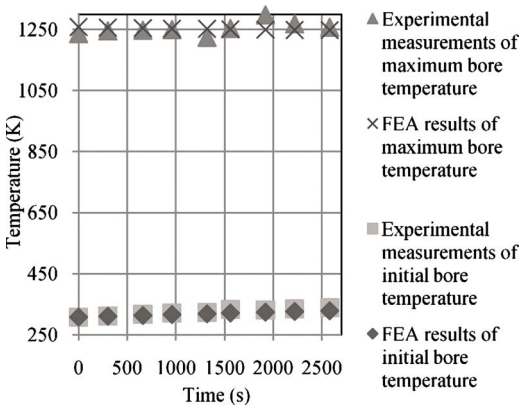

Fig. 7 Experimental and FEA results of 9 cycles

Swedish firm ASEA (The ABB Group, Västerås, Sweden) were used. A detailed description of the experimental procedure and instrumentation is available in Ref. [10]. Measurements were made for 9 cycles, and their details are given in Table 1. Each cycle was fired at an interval of 5–6 min; however the sixth shot was fired 4 min after shot number five. The bore surface temperature was measured before every shot fire and presented as the initial bore surface temperature in Table 1. The thermal diffusivity of the thermocouple was 7.3×10^{-6} m^2 s^{-1} compared with 9.0×10^{-6} m^2 s^{-1} for the typical gun steel, as mentioned in Table 2. Therefore, the thermocouple recorded temperatures that were approximately 11% greater than those in the typical gun steel subjected to the same heat input. Thermocouple properties were input into GUNTEMP8.EXE and FE model to compare simulated results directly with the thermocouple measurements. The initial temperature of the barrel for the first cycle (T_{first}) was 307.6 K, and the atmospheric temperature (T_∞) was 293 K. For charge A, the simulated results of GUNTEMP8.EXE are shown in Table 3.

Table 2 Thermal properties of the gun steel and thermocouple

	k (W m^{-1} K^{-1})	α (m^2 s^{-1})
Thermocouple	24	7.3×10^{-6}
Gun steel	35	9.0×10^{-6}

Table 3 Comparison of the measured and simulated results

	Experimental results	Simulated results of GUNTEMP8.EXE
Total heat transfer for the first cycle H_∞^{first} (K J m^{-2})	963.2	947
Maximum temperature T_{max} (K)	1237	1259.78

Using Eqs. (12) and (13), q_{max} and t_0 were estimated to be 202.78 MW m^{-2} and 4.67 ms, respectively. During a gun fire, typically in 60–80 ms, the total heat is transferred. Hence, an exponentially decaying heat flux was applied for 80 ms at the bore surface. For the rest of the cycle, a condition of zero heat flux was imposed. Equation (15) was utilized to calculate the total heat transfer for other cycles, and a new equation of exponentially decaying heat flux was computed for each cycle. A natural cooling boundary condition, given by Eq. (4), was applied at the outer surface of the barrel. For all 9 cycles, 27 loadstep files were written and solved in ANSYS to produce a temperature history of the 9 cycles, as shown in Fig. 6. Experimental data of the maximum and initial bore surface temperatures are in close agreement with the corresponding simulated results computed by finite element analysis (see Fig. 7 and Table 4). The maximum error in the results was found to be 3.69%, which is acceptable for complex guntube heat-

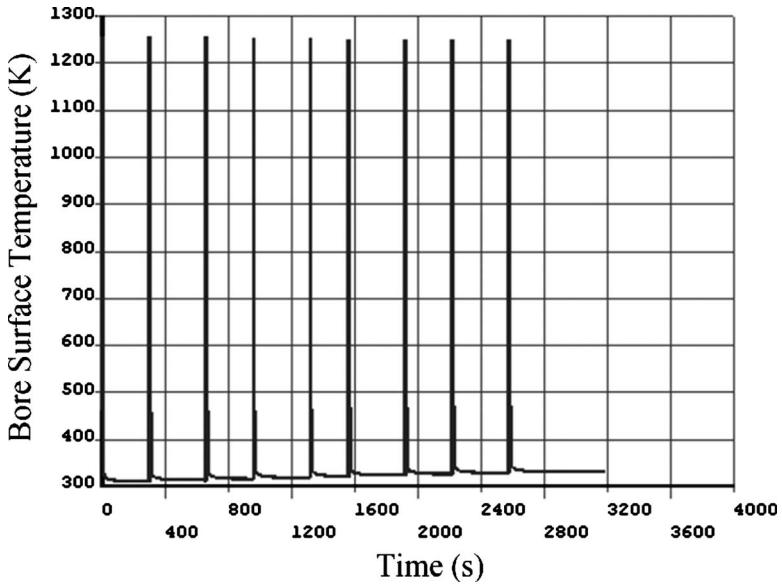

Fig. 6 Simulated temperature history of 9 cycles

Table 4 Experimental and FEA results of the bore surface temperature during 9 cycles

Shot number	Experimental measurements of the initial bore temperature (K)	FEA results of the initial bore temperature (K)	Experimental measurements of the maximum bore temperature (K)	FEA results of the maximum bore temperature (K)
1	307.6	307.6	1237	1258.57
2	311.4	310.522	1246	1256.64
3	316.9	313.209	1248	1254.9
4	320.7	315.969	1250	1253.24
5	322.4	318.553	1225	1252.84
6	332.9	321.391	1254	1251.01
7	331.1	323.779	1298	1250.1
8	334.7	326.371	1269	1248.91
9	338.8	328.769	1258	1247.96

ing problem. It clearly validates the methodology of the simulation. Moreover, it proves that exponentially decaying heat flux can be used as a boundary condition to very accurately model the temperature fluctuations. Error in the results is expected to be reduced by incorporating variation in the gun metal thermal properties (c_p and k) with the temperature.

The scheme of GUNTEMP8.EXE has been validated and widely used by Lawton and Klingenberg [1]. In this work, measured results were also found to satisfactorily match the computed results of GUNTEMP8.EXE (see Table 3). It is important to notice that in current simulation scheme, GUNTEMP8.EXE can be used to validate the FE model because the maximum bore surface temperature computed by GUNTEMP8.EXE should closely match the corresponding simulated result from the finite element analysis of the first cycle.

3 Investigation of Natural Cooling

Using the abovementioned scheme of simulation, three cases were investigated for a charge B: (1) a naturally cooled gun barrel, (2) a midwall-cooled gun barrel, and (3) an externally cooled gun barrel. A cross section located at 898 mm from the breech face of the tube was selected. Inner and outer diameters of the barrel at this cross section were 164 mm and 290 mm, respectively. During cook-off, the ignition of the ammunition starts from this cross section and propagates toward the rear face of the tube. Hence, this position can also be referred to as the "initiation of cook-off" position. Using GUNTEMP8.EXE, the total heat transfer and the maximum temperature at this cross section were computed to be 771.9 KJ m^{-2} and 893.65 K, respectively. The initial temperature of the gun barrel was assumed to be the same as the atmospheric temperature, i.e., 293 K. From Eqs. (12) and (13), q_{max} and t_0 were estimated to be 170.77 MW m^{-2} and 4.52 ms, respectively. Following the simulation scheme, finite element analysis was performed using the material properties of the gun steel, as given in Table 2. Exponentially decaying heat flux, $170.77\times10^6 \exp(-t/0.00452)$ was applied as a boundary condition at the bore surface. Convection load, as given by Eq. (4), was applied at the outer barrel surface. The heat transfer coefficient between the outer surface and atmosphere was assumed to be 20 W m^{-2} K^{-1}.

A maximum bore surface temperature of 892.59 K was obtained from the solution of the finite element model. Here, it is important to compare this result with the corresponding result of GUNTEMP8.EXE, which is 893.65 K. Both results are in close agreement with each other.

3.1 Simulation of the Burst. The FE model was extended to simulate a firing scenario of 10 spm. Each cycle of 6 s was divided into two parts. For the first 80 ms, an exponentially decaying heat flux was applied as a boundary condition at the bore surface, and for the remaining 5.92 s, a condition of zero heat transfer was imposed. To improve the accuracy, the variation in the gun steel thermal properties (k and c_p) with temperature was included in the finite element model. Using Eqs. (15) and (12), for each cycle, a new equation of exponentially decaying heat flux was developed. Simulation was performed for 40 cycles. The computed temperature history is shown in Fig. 8. During 40 cycles, the bore surface temperature increased from 293 K to 423.09 K. It is inferred that the bore surface temperature will steadily increase to the cook-off temperature, which is 453 K, if more shots are fired at the same rate. Hence, natural cooling is

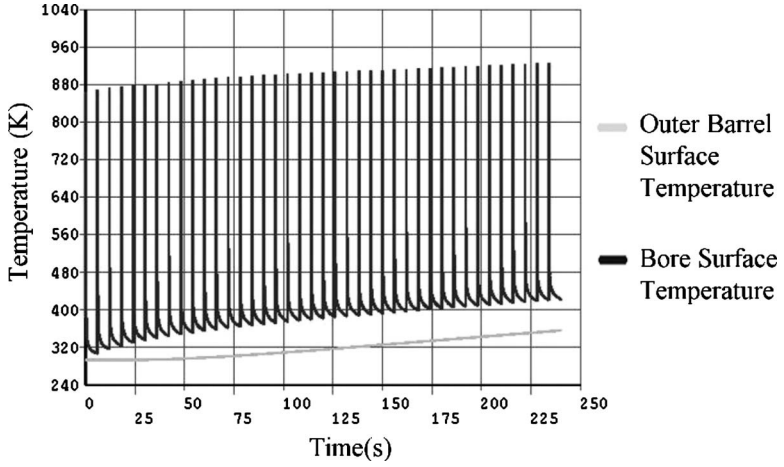

Fig. 8 Temperature history of the naturally cooled gun barrel

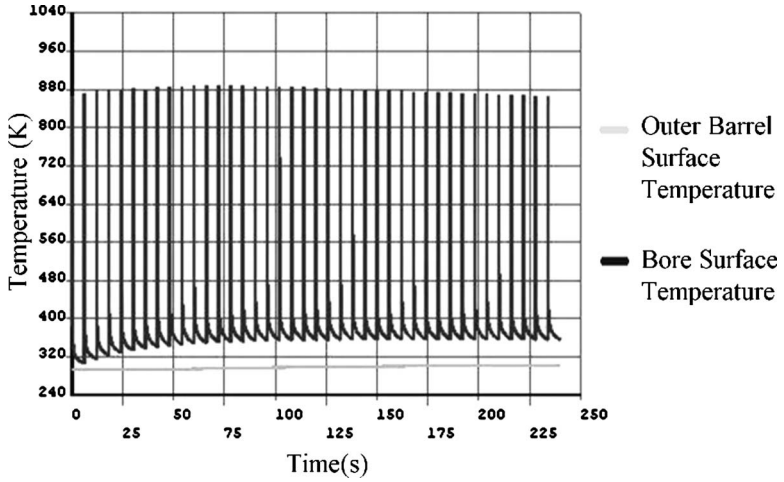

Fig. 9 Temperature history of the midwall-cooled gun barrel

insufficient for adequate thermal management of the gun barrel. Heat takes some time to reach the outer barrel surface; therefore, an initial lag was observed in the outer barrel surface temperature history.

4 Investigation of the Midwall Cooling Method

A 2D transient thermal analysis of the gun barrel was performed with midwall cooling channels. Cooling channels were assumed to be semicircular. The interface radius and the radius of the cooling channels were taken to be 110 mm and 4 mm, respectively, as shown in Fig. 1. Taking advantage of the symmetry, the computation time was reduced by modeling 1/48th part of the gun barrel. The performance of the cooling channels was investigated with a firing scenario of 10 spm. Water was used as a coolant, and the heat transfer coefficient between the channel surface and the coolant (h_c) was assumed to be 20 KW m^{-2} K^{-1}. The temperature of the coolant was taken to be 293 K. The outer surface of the gun barrel was naturally cooled by convection and radiation. Properties of the natural cooling were the same as those in the earlier cases. The temperature histories of the bore and outer barrel surfaces for 40 cycles are shown in Fig. 9.

For the naturally cooled gun barrel, the initial temperature of each cycle steadily increased from 293 K to 423.09 K (Fig. 8). However, with midwall cooling channels, an increase in the initial cycle temperature was observed during the first few cycles, but after 84 s, the temperature attained a steady magnitude of 356.23 K. This indicates that the gun can continue to fire at a sustained rate of 10 spm without any danger of cook-off.

5 Investigation of the External Cooling Method

The thermal performance of an externally cooled system was also assessed. The temperature of the coolant (water), and the heat transfer coefficient between the outer barrel surface and the coolant (water), were assumed to be 293 K and 20 KW m^{-2} K^{-1}, respectively. A firing scenario of 10 spm was investigated. The temperature histories of the bore and outer barrel surfaces for 40 cycles are shown in Fig. 10. After 40 cycles, the temperature of the gun bore surface was found to be 405.23 K. In the last 7–8 cycles, the bore temperature increment was found to be very small and gradually decreasing. It is expected to be approximately reduced to zero in the next 25–27 cycles. Hence, the external cooling method can also prevent cook-off and allow continuous fire, but for the external cooling method, equilibrium conditions were achieved at a higher temperature than for the midwall-cooled barrel.

It should be noted that in the external cooling method, a thin jacket is used around the gun barrel. For the same coolant temperature, the outer surface of the jacket will be at a lower tem-

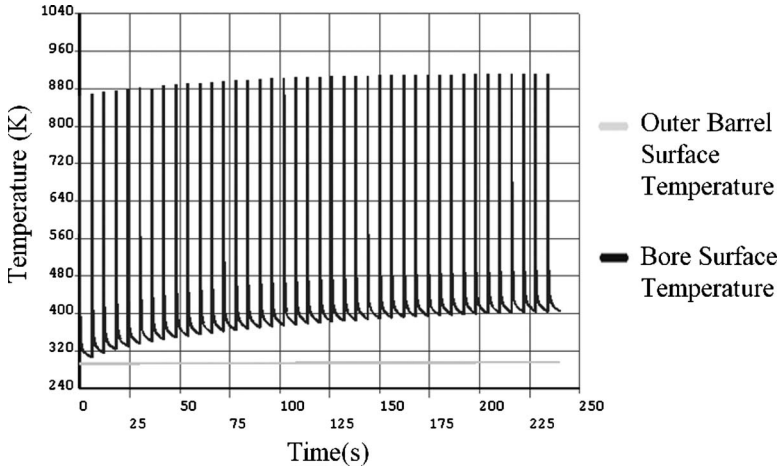

Fig. 10 Temperature history of the externally cooled gun barrel

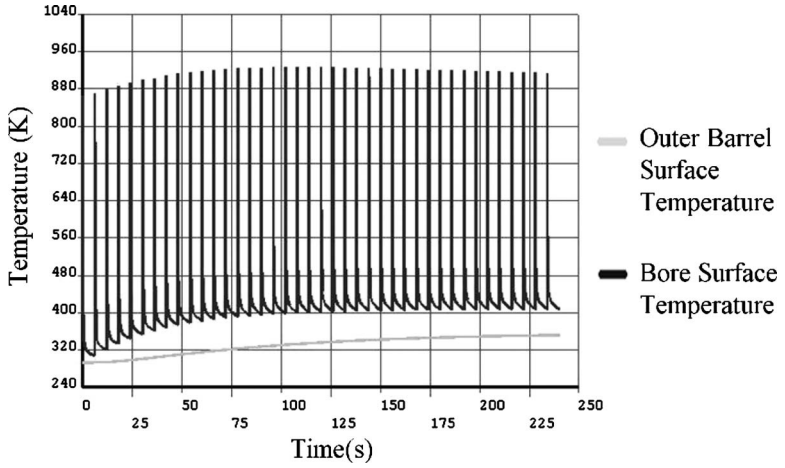

Fig. 11 Temperature history of the gun barrel utilizing midwall cooling with the engine cooling system

perature than the outer surface of a midwall-cooled barrel; hence, the externally cooled barrel will produce a lower thermal signature than the midwall-cooled gun.

6 Active Cooling Methods in the Context of the Self-Propelled Howitzer (SPH)

A gun tube utilizing midwall cooling connected to an engine cooling system was analyzed. The average temperature of the coolant, and the heat transfer coefficient between the channel surface and the coolant, were assumed to be 348 K and 20 KW m^{-2} K^{-1}. The temperature histories of the bore surface and outer barrel surfaces are shown in Fig. 11. The initial bore temperature was found to stabilize at 408 K. Hence, cook-off can be prevented. The outer barrel surface temperature after 240 s was found to be 351.84 K. High temperature of the engine coolant results in a high outer barrel surface temperature.

A self-propelled howitzer need not fire continuously at a very high rate. Generally, it fires 6–7 cycles at a time, moves to another location, and again fires 6–7 cycles, and so on. In such a scenario using a midwall or external cooling method, utilizing hot engine coolant may be disadvantageous. A separate cooling system can be used, but it will further reduce the available space and increase the capital and maintenance cost.

7 Conclusion

In this work, the performance of a midwall and an external cooling method for a 155 mm gun barrel were analyzed. Based on the results, the following conclusions are derived:

1. Natural cooling of the gun barrel is insufficient to prevent cook-off at 10 spm. For a burst of 40 cycles at 10 spm, the bore surface temperature was found to increase from 293 K to 423.09 K.
2. Midwall and external cooling methods can eliminate the possibility of cook-off at 10 spm. For $h_c = 20$ KW m^{-2} K^{-1}, with midwall cooling channels, the bore surface temperature was found to stabilize at 356.23 K. For the external cooling method, the temperature of the bore surface after 240 s was found to be 405.23 K, and it is expected to stabilize in the next 25–27 cycles.
3. For the same coolant temperature, the outer surface of the jacket of an externally cooled gun barrel is expected to have a lower temperature than the outer barrel surface of a midwall-cooled gun barrel. Therefore, under similar conditions, an externally cooled gun barrel is expected to have lower thermal signature than the midwall-cooled barrel.
4. In comparison to the midwall cooling method, external cooling provides the same advantages, besides being very cost effective. The midwall cooling method requires complex manufacturing processes, leading to higher costs. Provision of longitudinal midwall channels inside the gun barrel structure also reduces the maximum pressure that the gun can withstand.
5. For a SPH, the gun barrel utilizing midwall cooling channels with engine cooling system can prevent cook-off. But it does not offer great potential as a SPH need not fire continuously at a high rate. For a typical firing scenario, an active cooling method utilizing hot engine coolant will make the gun barrel hotter than a naturally cooled gun barrel.

Acknowledgment

The authors are grateful to the Department of Engineering Systems and Management at Cranfield University for funding this work and acknowledge the support of Mr. S. Thomson and Mr. A.E.G. Peare.

Nomenclature

C_m = muzzle velocity (m s^{-1})
c_p = specific heat of the gun steel (J kg^{-1} K^{-1})
c_{vg} = specific heat of the gas at constant volume (J kg^{-1} K^{-1})
C_x = gas velocity at position x (m s^{-1})
d = gun bore diameter (m)
E = expansion number
h_c = convection heat transfer coefficient between the coolant and cooling channel surface (W m^{-2} K^{-1})
h_g = combined convection heat transfer coefficient between the bore surface and hot propellant gases (W m^{-2} K^{-1})
h_∞ = heat transfer coefficient between the outer barrel surface and surrounding atmosphere (W m^{-2} K^{-1})
H = instantaneous total heat transfer per unit area during a cycle (J m^{-2})
H_∞ = total heat transfer per unit area per cycle (J m^{-2})
H_∞^{first} = total heat transfer per unit area for first cycle (J m^{-2})
H_∞^n = total heat transfer per unit area for the nth cycle in a burst (J m^{-2})

k = thermal conductivity of the gun steel ($W\ m^{-1}\ K^{-1}$)
k_g = thermal conductivity of the propellant gas ($W\ m^{-1}\ K^{-1}$)
m_c = charge mass (kg)
q_{in} = input heat flux at the bore surface ($W\ m^{-2}$)
q_{max} = maximum heat flux at the bore surface ($W\ m^{-2}$)
q_{out} = heat flux at the outer barrel surface ($W\ m^{-2}$)
q_x = instantaneous heat flux at the bore surface $W\ m^{-2}$
Re_x = Reynolds number of the propellant gas
R_i = inner radius of barrel (m)
R_o = outer radius of barrel (m)
T_{first} = initial temperature of the first cycle or uniform barrel temperature before the start of firing (K)
T_g = average cross sectional temperature of the gas (K)
T_i = initial bore surface temperature of a cycle (K)
T_{max} = maximum temperature during a cycle (K)
T_r = radiation temperature (K)
T_w = bore surface temperature at any time t (K)
T_∞ = temperature of the external environment (K)
t_0 = time constant (s)
t'_0 = characteristic time (s)
V = gas volume (m^3)
V_c = initial charge volume (m^3)
x = distance from the effective breech face (m)
α = thermal diffusivity of the gun steel ($m^2\ s^{-1}$)
γ = coefficient of the adiabatic expansion
μ_g = viscosity of the gas ($N\ s\ m^{-2}$)
ρ = density of the gun steel ($kg\ m^{-3}$)
ρ_g = density of the gas ($kg\ m^{-3}$)

References

[1] Lawton, B., and Klingenberg, G., 1995, *Transient Temperature in Engineering and Science*, Oxford University Press, Oxford, UK, pp. 444–467.
[2] Wu, B., 2005, "Barrel Cooling: A Key Technology for Improving Gun Performance," Journal of Battlefield Technology, **8**(3), pp. 1–4; see http://www.argospress.com/jbt/index.html.
[3] Wu, B., Chen, G., and Xia, W., 2008, "Heat Transfer in a 155 mm Compound Gun Barrel With Full Length Integral Midwall Cooling Channels," Appl. Therm. Eng., **28**(8–9), pp. 881–888.
[4] Hurn, T. W., D'Aoust, J., Sevier, L., Johnson, R., and Wesley, J., 1993, "Development of an Advanced Electromagnetic Gun Barrel," IEEE Trans. Magn., **29**(1), pp. 837–842.
[5] Bass, M., and De Swardt, R. R., 2006, "Laboratory Heat Transfer Experiments on a 155 mm Compound Gun Tube With Full Length Integral Mid-Wall Cooling Channels," ASME J. Pressure Vessel Technol., **128**(2), pp. 279–284.
[6] De Swardt, R. R., and Andrews, T. D., 2006, "Stress Analysis of Autofrettaged Midwall Cooled Compound Gun Tubes," ASME J. Pressure Vessel Technol., **128**(2), pp. 201–207.
[7] Gerber, N., and Bundy, M. L., 1991, "Heating of a Tank Gun Barrel: Numerical Study," Army Ballistic Research Laboratory, Aberdeen Proving Ground, MD, Report No. BRL-MR-3932.
[8] Gerber, N., and Bundy, M., 1992, "Effect of Variable Thermal Properties on Gun Tube Heating," Army Ballistic Research Laboratory, Aberdeen Proving Ground, MD, Report No. BRL-MR-3984.
[9] Lawton, B., and Klingenberg, G., 1995, *Transient Temperature in Engineering and Science*, Oxford University Press, Oxford, UK, pp. 61–63.
[10] Lawton, B., 2003, "The Influence of Additives on the Temperature, Heat transfer, Wear, Fatigue Life and Self Ignition Characteristics of a 155 mm Gun," ASME J. Pressure Vessel Technol., **125**(3), pp. 315–320.

Experimental Study on Heat Transfer and Pressure Drop of Recuperative Heat Exchangers Using Carbon Foam

Y. R. Lin

J. H. Du

W. Wu

L. C. Chow[1]
e-mail: lchow@mail.ucf.edu

Department of Mechanical, Materials and Aerospace Engineering,
University of Central Florida,
Orlando, FL 32816-2450

W. Notardonato
Cryogenic Test Laboratory,
Kennedy Space Center,
Titusville, FL 32899

This work focuses on the development of high-effectiveness recuperative heat exchangers using solid and corrugated carbon foam blocks. Characterization tests were conducted on heat transfer and pressure drop for a single carbon foam block with different sizes. Results show that carbon foam can be an effective medium for heat transfer enhancement, and a short length in the flow direction yields a high heat transfer coefficient. The corrugation can enhance heat transfer and reduce pressure drop at the same time. A recuperative heat exchanger with carbon foam, which consists of separate blocks of carbon foams packed between thin sheets of stainless steel, was designed. The hot and cold flow paths were arranged in counterflow in the recuperator. The heat exchanger was designed in a modular manner so that it can be scaled up for a larger heat transfer requirement or a higher overall effectiveness. The anisotropic property of carbon foam was exploited to achieve higher effectiveness for one pair of foam blocks. Experiments with four pairs of carbon foams were conducted to evaluate the performance of carbon foam used in the recuperative heat exchanger. Measurements were made for both solid and corrugated foams for comparison. With four pairs of carbon foam blocks, an overall effectiveness ε_{total} greater than 80% was achieved. This paper demonstrates an approach to reach an effectiveness ε_{total} of 98% by placing many pairs of carbon foams in series.
[DOI: 10.1115/1.4001625]

Keywords: heat transfer, recuperators, cryogenics

1 Introduction

NASA Kennedy Space Center (KSC) [1] has proposed a cryogenic system that incorporates integrated refrigeration using a reverse Brayton cycle with liquid oxygen storage to enable advanced operations on the lunar surface. Efficient liquefaction, storage, and transfer of oxygen are essential for a sustainable consumable transfer station for use on the lunar surface. The recuperative heat exchanger is one of the critical components of a cryocooler system. New heat exchanger designs that are modular, easily scalable, highly effective, compact, and lightweight must be developed. In order to remove 48 W of thermal energy at 90 K required for liquefaction and a zero loss storage of oxygen, the heat exchanger must have a 2000 W capacity for heat transfer. The heat exchanger must be designed to be modular to scale up for a high capacity. A high-effectiveness ($>$98%) recuperative heat exchanger is required to maintain the cryocooler at a high operational coefficient of performance (COP). Zhou et al. [2] investigated the effectiveness of the recuperator on the COP for a reverse Brayton cryocooler used for liquefaction of oxygen. A pressure ratio of 1.8 was used, and the isentropic efficiencies of the compressor and turbine were assumed to be 65% and 75%, respectively. The result indicated that the COP increases from 0.07 to 0.11 when the heat exchanger effectiveness increases from 0.96 to 0.98. Therefore, it is very critical to develop a high-effectiveness recuperative heat exchanger.

Some developmental efforts for recuperative heat exchangers for cryocoolers have been made. The microtube strip heat exchanger was developed for applications in reverse Brayton cycle systems, but this design is difficult to form a counterflow type heat exchanger, resulting in a reduction in effectiveness [3]. McCormick et al. [4] developed a radial flow heat exchanger (RFHX) for their turbo-Brayton cryocoolers, and their RFHX has an effectiveness of 0.89. Hill et al. [5] described the slotted-plate heat exchanger (SPHX), which is the current state-of-the-art recuperator for space systems. It is comprised of a stack of copper plates containing concentric rings of slotted flow passages separated by low-conductivity stainless steel spacers brazed between the concentric rings of slots. The effectiveness could reach 0.997 at a 1 g/s mass flow rate of neon in the system. They also developed a lighter and smaller recuperator by replacing the copper–stainless steel (Cu-SS) SPHX with a silicon micromachined recuperator (SMR). Hoch et al. [6] reported a modular design of a high-effectiveness recuperative heat exchanger for a pulse tube/reverse Brayton hybrid cryocooler. The design utilized etched cooper plates interleaved with a stainless steel axial conduction barrier. The measured effectiveness reached 0.93 at a 1 g/s mass flow rate of helium. Another design was suggested for a counterflow microheat exchanger with low pressure loss [7]. The square grooves were etched in polymer wafers, and the wafers were stacked one by one to form a rectangular heat exchanger. Special consideration was made to reduce the axial conduction in order to achieve high effectiveness.

In a recent study [8], we proposed a design for a compact, lightweight, recuperative heat exchanger with an effectiveness of 98% using 50 pairs of carbon foam blocks. It was shown that while the carbon foam blocks did provide superior heat transfer performance, the pressure drop across the recuperator could be excessively high. One attractive suggestion to reduce the pressure drop while improving heat transfer performance by a corrugated cutting of the carbon foam was made by Gallego and Klett [9].

[1]Corresponding author.

Contributed by the Heat Transfer Division of ASME for publication in the JOURNAL OF HEAT TRANSFER. Manuscript received July 23, 2009; final manuscript received April 2, 2010; published online June 29, 2010. Assoc. Editor: W. Q. Tao.

However, an explanation for the surprising heat transfer improvement with a lesser amount of carbon foam due to corrugated cutting was not provided.

In this study, we measured the heat transfer between a heated substrate and a gas passing through a solid carbon foam block and a corrugated carbon foam block. The goal was to provide an explanation for the physical mechanism for the large reduction in pressure drop and an increase in heat transfer performance due to corrugation. Also in this paper, we confirmed that the use of corrugated foams could lead to a highly effective recuperator with better heat transfer performance but a very large reduction in the overall pressure drop compared with a recuperator where solid carbon foams are used [8].

The carbon foams used in this study have an anisotropic thermal conductivity. The bulk thermal conductivity is 135 W/m K in the out-of-plane direction and is 45 W/m K in the other two in-plane directions [10]. To increase heat transfer between the hot and cold fluids, the out-of-plane direction (with higher thermal conductivity) is in the transverse direction of the recuperator. This study experimentally investigated the performance in heat transfer and pressure drop of a single carbon foam block. Tests were conducted on different-sized blocks with different lengths in the flow direction. The effects of corrugation on heat transfer and pressure drop were investigated for two different samples of carbon foam. Based on single carbon foam block results, a recuperative heat exchanger, which consists of separate blocks of carbon foam packed between thin sheets of stainless steel, was designed. Instead of using a continuous piece of carbon foam, multiple pairs of carbon foam blocks were used in the design. Spaces between the blocks were used to reduce heat transfer down the length of the heat exchanger. The anisotropic feature of carbon foam was exploited in the design for each pair of foam blocks. The relation between the overall effectiveness of the recuperative heat exchanger and the effectiveness of one pair and the number of pairs of carbon foams was given. Experiments were also conducted on four pairs of stacked carbon foams to verify the feasibility of the approach. Air was used to test the performance of the heat exchanger in this study. The corrugation effects on heat transfer and pressure drop were also investigated to show that corrugation can enhance heat transfer and reduce pressure drop at the same time. This design of recuperative heat exchanger can have an effectiveness of more than 98% with multiple pairs of foam blocks.

2 Heat Transfer and Pressure Drop of One Foam Block

Heat transfer between the hot and cold gases must be significantly improved in order to increase the effectiveness of the heat exchanger and reduce the size of the heat exchanger. Carbon foam was used for this purpose in this study. Carbon foam has an effective thermal conductivity of 100–230 W/m K in the out-of-plane direction [10], which is much higher than the effective thermal conductivity of aluminum foam (5–9 W/m K) [11]. The compressive strength of the carbon foam is 1–3 MPa [12]. In addition, it has been shown [13] that the thermal conductivity of carbon foam increases as its temperature changes from room temperature to 80 K. We have also submerged carbon foams in liquid nitrogen for a long period of time and have also found no noticeable physical changes. Yu et al. [14] reported an application of carbon foam in a compact recuperator for gas turbine systems. Their investigation was focused on heat transfer enhancement using carbon foam. Based on their thermal analysis using a full length foam block, they reported that a heat exchanger effectiveness of 100% can be achieved. No consideration was given on the effect of axial conduction along the carbon foam on the effectiveness.

Figure 1 shows a scanning electron microscopy (SEM) picture we took from a carbon foam, which was originally developed by Oak Ridge National Laboratory (ORNL) and licensed to Poco Graphite, Inc. [10]. Carbon foam has the feature of a porous medium with 350 μm pores connected with 110 μm holes between pores. The distance between two connecting holes represents the characteristic length of the pore structure in the carbon foam. The Poco carbon foams used in this work have a density of 0.6 g/cm^3 and a porosity of 0.75. The open-cell structure of the foams provides a large surface area to volume ratio ($>$40,000 m^2/m^3). Table 1 lists some typical properties of carbon foams and aluminum foams. In comparison with aluminum foams, carbon foams have a smaller pore size and a larger surface area per unit volume. Carbon foams have thick ligaments and high thermal conductivities. The high thermal conductivity of carbon foams with the open interconnected cellular structure provides a potential for effective heat transfer enhancement. Carbon foam has been identified as a potential replacement for metal fins for heat transfer enhancement in heat transfer equipment such as heat exchangers, radiators, and thermal protection systems.

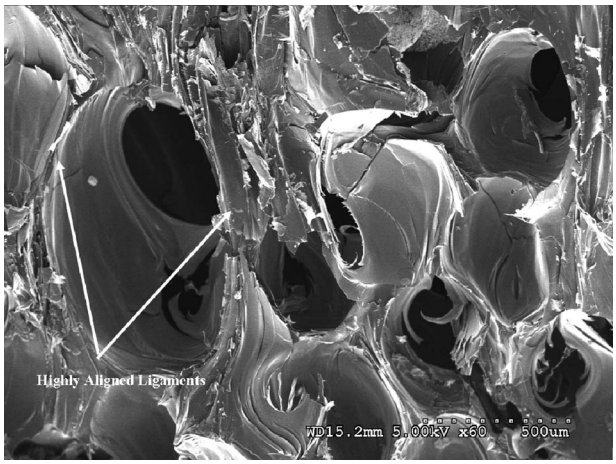

Fig. 1 SEM picture of carbon foam

There is a limited amount of information on heat transfer and pressure loss for gases in carbon foams. Klett et al. [15] and Gallego and Klett [9] reported the performance tests for air passing through a channel filled with carbon foams and aluminum foams with several different configurations at the front velocity from 1.5 m/s to 4.4 m/s. They reported that the heat transfer between a heated substrate and a moving air stream when carbon foam was used could be ten times higher compared with the heat transfer when aluminum foam was used. At an air velocity of 4.37 m/s, their study showed that carbon foam in the bulk solid form has a heat transfer coefficient of 2600 W/m^2 K, while for the aluminum foam, the heat transfer coefficient is 250 W/m^2 K. Mahjoob and Vafai [16] also investigated extensively on the performance metal foam heat exchangers and reported a heat transfer coefficient of 363 W/m^2 K at a gas (90% air, 10% CO_2) flow velocity of 5 m/s.

While carbon foams yield much higher heat transfer coefficients compared with metal foams at a flow velocity of 4.37 m/s, the pressure drop across carbon foams is more than 40 times higher compared with aluminum foams [9]. Gallego and Klett [9] also found that the pressure drop for solid foam could be signifi-

Table 1 Properties of carbon foam and aluminum foam [10,11]

Property	Al foams	Carbon foams
Ligament thickness (μm)	100–420	~500
Pore size (μm)	1–2	0.350
Porosity	$>$0.9	0.7–0.8
Effective k (W/m K)	5–9	100–230
Specific area (m^2/m^3)	800–2800	$>$40,000

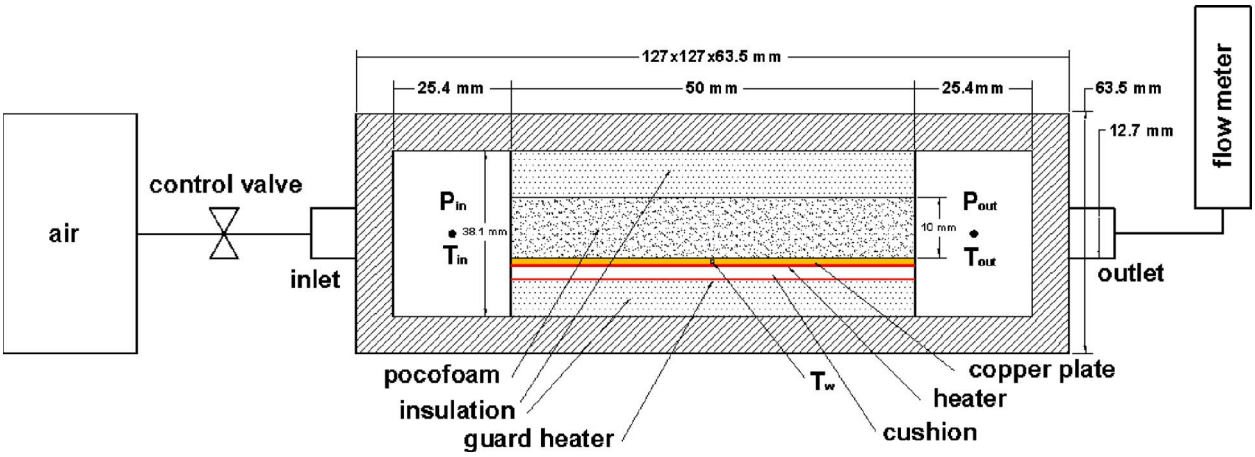

Fig. 2 Experimental setup of heat transfer and pressure drop of one foam block

cantly reduced by modifying the geometry of solid carbon foam as finned, pin-finned, and corrugated while keeping the heat transfer coefficient very high. With the corrugated geometry, compared with solid carbon foam, the heat transfer coefficient increases, while the pressure drop decreases. Though the reason for this unusual characteristic of carbon foam was not explained, it offers a very promising potential to use corrugated foam for heat exchanger applications.

In this work, we explore heat transfer and pressure drop of air passing through a single carbon foam block to evaluate the heat transfer performance of open-cell carbon foams when used as a gaseous heat exchanger at a low velocity (<1 m/s). A low velocity is needed to ensure a low pressure drop to avoid a significant reduction in COP for a reverse Brayton cryocooler. A low velocity was also chosen because this would lead to higher overall heat transfer effectiveness. Experiments were conducted at much lower velocities than those conducted by Gallego and Klett [9]. There are no available data in this range of velocity in the literature. Performance tests were evaluated on two different sizes of foam samples. The effects of corrugated configuration on heat transfer and pressure drop were investigated. Data for each foam configuration were correlated at different volumetric flow rates. Physical mechanisms underlying the phenomena were analyzed. The results of this study can serve as a reference for further optimization of the configuration to enhance the heat transfer coefficient and reduce the pressure drop at the same time.

The test setup shown in Fig. 2 consists of an air tank at a constant pressure and a channel for tests with an inlet and an outlet. Cooling air was forced through the test section. A control valve was used to regulate the flow rate, which was measured by a flow meter at the outlet. The foam samples were glued to a 5 cm $\times$ 5 cm $\times$ 1.2 mm thick copper plate with a silver loaded epoxy (Pyro-Duct) from Aremco [17]. This epoxy has a thermal conductivity of 9 W/m K. Heat was provided from the bottom with a foil heater purchased from Minco. The heater has the same footprint and area as the copper plate. A cushion was used to press the heater up against the plate in order to make good thermal contact. A guard heater was used to prevent heat loss through the bottom of the experimental apparatus. There were two thermocouples, one on each side of the cushion. The voltage for the guard heater was regulated to keep the two thermocouples at the same temperature in order to reduce heat loss. The foam was placed and secured in a Plexiglas chamber. The test chamber was insulated and sealed.

The variables measured in this experiment included power supplied to the heaters, the substrate temperatures, the temperatures at the inlet and outlet, the pressure difference across the sample, and the volumetric air flow rate. The power output of the heaters was calculated from the voltage across the heater and the current passing through it, which were measured by a multimeter (Keithley 2001). The substrate temperatures were measured by three 0.6 mm Omega type E thermocouples, which were inserted through three 0.88 mm holes. The inlet and outlet temperatures were measured with the same kind of thermocouples. The pressure difference across the foam samples was measured by an Omega RX139 series pressure differential gauge. The flow rate was measured by a float flow meter, which was calibrated with a high-precision mass flow meter. The velocity of air entering the foam was calculated from the flow meter readings, with adjustments made based on the inlet and outlet pressures and temperatures. The error in power calculation from the voltage and current measurements can be ignored in the experiments. The error in the flow rate and velocity was estimated to be less than 3%. The error in pressure difference was less than 3%. The error in temperature measurement was within 0.2°C. The error in h was less than 6%.

Performance tests were conducted on Poco foam samples with two different flow lengths. One foam sample was 5 cm (length) $\times$ 5 cm (width) $\times$ 1 cm (height), while the second was 1 cm (length) $\times$ 5 cm (width) $\times$ 1 cm (height). In one experiment with the first foam sample, the temperature distribution on one side of the foam was monitored with an infrared (IR) camera. In order to do this, the channel wall on this side was replaced by a thin (0.1 mm) sheet of stainless steel foil, which is bonded to the side of the foam block with the Pyro-Duct epoxy [17]. Since the heat loss from this side wall was very small, the temperature distribution of the foam should be approximately one-dimensional (in the direction normal to the heater). Figure 3 shows the IR image obtained with an air velocity of 0.5 m/s. The substrate temperature was measured to have an average temperature of 53°C with a 1°C variation. The IR image showed that the entire foam has a very uniform temperature throughout, with an

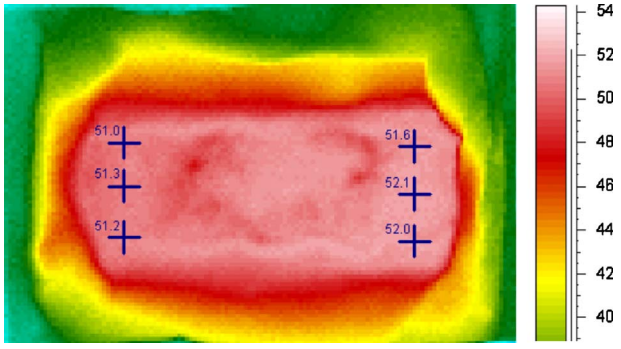

Fig. 3 IR image indicating carbon foam temperature

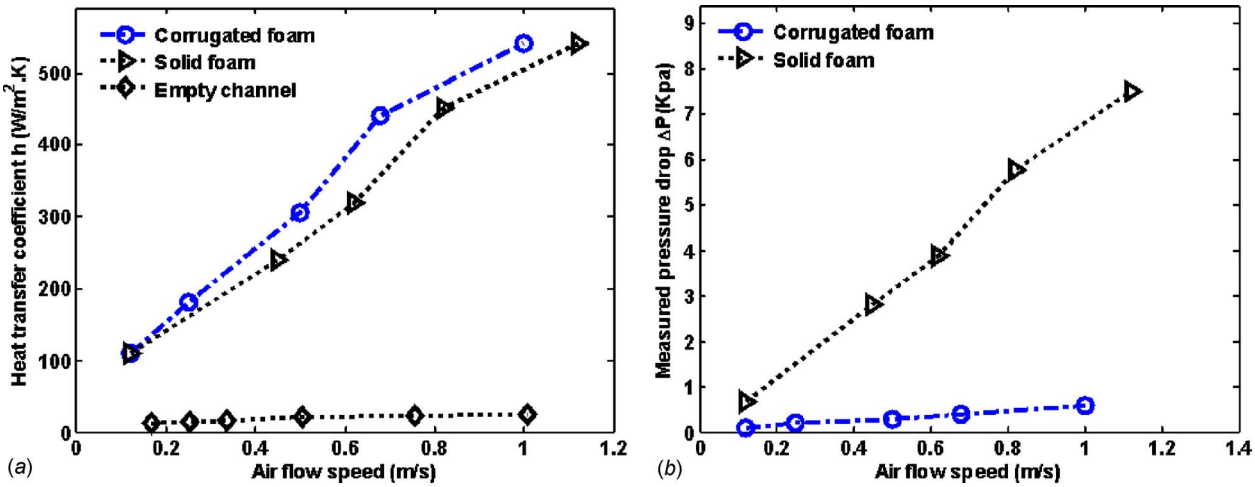

Fig. 4 (*a*) Heat transfer and (*b*) pressure drop versus velocity for 5×5×1 cm^3 solid and corrugated foams

average temperature of 51.5°C. This image demonstrated that carbon foam is a good medium for heat transfer enhancement because of its high thermal conductivity. The carbon foam acts essentially as a fin with a very large surface area and a fin efficiency of near unity.

The heat transfer of foam is characterized by the heat transfer coefficient, which is defined as

$$h = \frac{Q}{A\Delta T_{\mathrm{LMTD}}} \tag{1}$$

where Q is the heat absorbed by the air as it passes through the carbon foam. It is given by

$$Q = \dot{m} c_p \Delta T \tag{2}$$

where ΔT is the temperature increase of air $(T_o - T_i)$, A is the footprint area of the foam sample, and ΔT_{LMTD} is the log mean temperature difference given by

$$\Delta T_{\mathrm{LMTD}} = \frac{(T_w - T_i) - (T_w - T_o)}{\ln\left(\frac{T_w - T_i}{T_w - T_o}\right)} \tag{3}$$

Figure 4(*a*) shows the heat transfer coefficient for carbon foams (5×5 cm^2 with a 1 cm height) at different air velocities. The variation in heat transfer coefficient with velocities for corrugated foam was also shown in this figure. These results indicate that the heat transfer coefficient varies with velocity. These results follow the same trend as those reported in Klett et al. [15] though the air velocity reported in Ref. [13] is much higher. It should also be noted that the height of the carbon foam used in Ref. [13] is 31.75 mm, while the height of the samples in our experiments is 10 mm.

While the foam structure provides an excellent thermal path to reduce the temperature difference between the heater surface and the flowing fluid, the pressure drop is too high for many applications, as shown in Fig. 4(*b*). To reduce the flow resistance, Gallego and Klett [9] reported heat transfer and pressure drop results for a corrugated configuration of carbon foam. Figure 5 shows a picture of a piece of 5×5×1 cm^3 corrugated foam used in our experiments. There is a 2 mm layer of foam that is not cut at the bottom in order to keep good contact between the foam and the substrate. As shown in Fig. 4(*b*), the pressure drop is reduced by a factor of about 30 for a corrugated cutting, while the heat transfer coefficient increases by a small amount at a velocity of 1 m/s (see Fig. 4(*a*)). Figure 5 also illustrates the flow paths when air enters the corrugated foam. The flow path of air in the foam material is shorter in the corrugated carbon foam. Due to the larger frontal area where the frontal entrance length is increased from 5 cm to 19 cm, the air speed entering the corrugated foam is also lower than that in the solid foam. Since the pressure loss across foams is dependent on the flow length and air velocity, the pressure drop is significantly lower in the corrugated carbon foam configuration than it is in the solid foam configuration.

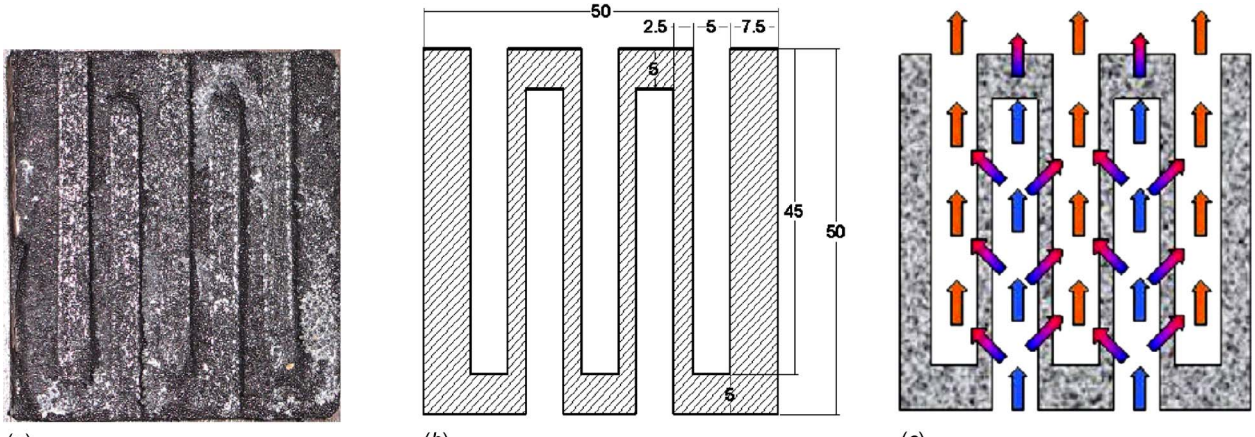

Fig. 5 Illustration of air flow in the 5×5 cm^2 corrugated foam

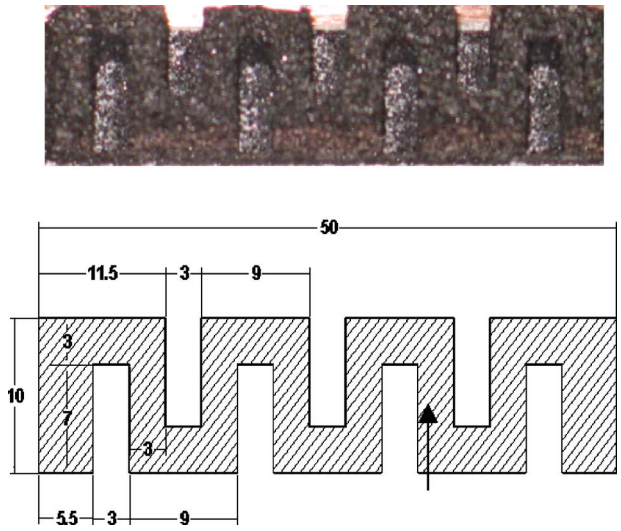

Fig. 6 1×5 cm² corrugated foam

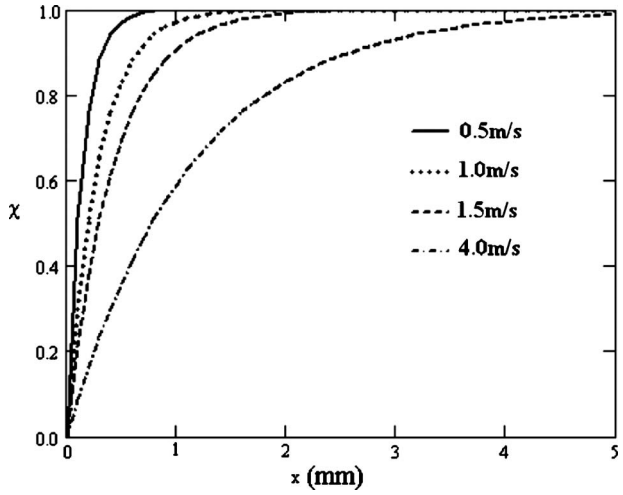

Fig. 7 The temperature variation in an assumed straight tube

Experiments were also conducted on a solid foam sample with the size of 1 cm (length)×5 cm (width) with 1 cm (height). The length in the flow direction was reduced from 5 cm to 1 cm. Figure 6 shows a picture of the $1\times5\times1$ cm^3 (tall) corrugated foam. Like the $5\times5\times1$ cm^3 corrugated foam, there is also a 2 mm layer of foam at the bottom near the substrate. Corrugation has effects on both heat transfer and pressure drop for carbon foam. Obviously, corrugation cutting has reduced the penetration length of air flow within the foam. This results in a reduction in the pressure drop with a corrugated configuration. The cutting also reduces the penetration velocity (defined as the air speed as it enters the foam), which is dependent on the original dimensions of the solid foam. In the $5\times5\times1$ cm^3 case, corrugated cutting reduced the penetration velocity by a factor of 4. Both shorter flow length and reduction in air penetration velocity result in a very significant reduction in pressure drop.

The effects of corrugated cutting on heat transfer are more complex. Corrugation changes the distribution of cold air in the foam significantly, as shown in Fig. 5(*c*). This results in a more effective and uniform cooling of the heater. In addition, corrugation reduces the thermal path from the heater surface to the cold air, leading to an overall smaller thermal resistance. The underlying mechanics is related to variations in temperature difference between the fluid (air in this study) and the solid matrix of the carbon foam. The open-cell structure of foam was modeled as many parallel tubes along the flow direction in the solid material with a uniform temperature. The diameter of the tubes was assumed to be the pore size of the foam (0.35 mm). The temperature difference between the axial surface and the mean temperature decreases exponentially with distance along the tube axis. It can be expressed as [18]

$$\chi = \frac{T_m(x) - T_m(0)}{T_w - T_m(0)} = 1 - \exp\left(-\frac{Px}{\dot{m}c_p}\overline{h}\right) \tag{4}$$

where $T_m(x)$ is the mean air temperature at position x, $T_m(0)$ is the mean air inlet temperature, T_w is the wall temperature of tube (i.e., the solid foam temperature), P is the tube perimeter ($P=\pi d$), $\overline{h}$ is the mean value of the heat transfer coefficient in the tubes, and $\dot{m}$ is the mass flow rate, where

$$\dot{m} = \frac{\rho v_m \pi d^2}{4} \tag{5}$$

and v_m is the mean air velocity in the tubes. To get a rough estimate of the distance x at which the air acquires a temperature close to that of the foam, one can assume a heat transfer coefficient corresponding to that of the fully developed laminar flow. Figure 7 shows the variations in the temperature difference at velocities of 0.5 m/s, 1.0 m/s, 1.5 m/s, and 4 m/s. It can be seen that the air temperature rises to near the wall temperature in a distance of less than 1 mm if the velocity in the tubes is 0.5 m/s. This corresponds to a frontal velocity of approximately 0.38 m/s in the experiments because the porosity of carbon foam ε is about 0.75. This length increases to 4 mm if the velocity is 4 m/s. In experiments on the $5\times5\times1$ cm^3 foam sample, when the frontal velocity was 1 m/s, the air acquired the foam temperature in a distance of 1 mm. After that flow length, the foam did little in heat transfer but caused more pressure loss. This explains why heat transfer from the foam to the air was not reduced when corrugation reduces the air flow length in the foam from 5 cm to 2.5 mm (see Fig. 5). In fact, as shown in Fig. 4(*a*), because of better air distribution over the heated surface (illustrated in Fig. 5(*c*)), the overall heat transfer coefficient is actually higher for corrugated foams.

For the shorter 1-cm-long foams, Fig. 8(*a*) shows results for the heat transfer while Fig. 8(*b*) shows results for the pressure drop. It can be seen that the heat transfer coefficient increases by about 10% with corrugated foam compared with the solid foam at a 1 m/s velocity, while the pressure drop reduces by 3.8 times compared with the solid foam at the same velocity. The pressure drop reduction is not as large compared with the previous case of the $5\times5\times1$ cm^3 sample (30 times for the $5\times5\times1$ cm^3 foam) partly because the frontal entrance length only increases from 5 cm to 10.6 cm.

It is interesting to note that the heat transfer coefficient for the $5\times5\times1$ cm^3 sample (Fig. 4(*a*)) is lower than that for the $1\times5\times1$ cm^3 sample (Fig. 8(*a*)). A decrease in the flow length by a factor of 5 leads to an increase in the heat transfer coefficient by a factor of about 3. This is because the heat transfer coefficient as defined by Eq. (1) is footprint area dependent (the area of the $1\times5\times1$ cm^3 sample is five times smaller). Since carbon foams have a small pore size and a very large surface area to volume ratio, air can pick up its temperature rapidly while moving through the foam. As the air temperature increases, the local temperature difference between the foam and air decreases along the flow direction. When carbon foam was cut shorter in the flow direction, the reduction in the amount of heat transferred from the solid substrate to air is not much, while the footprint area drops by a factor of 5. Therefore, shorter carbon foam in the flow direction yields higher heat transfer coefficients.

It can be concluded from these experiments that carbon foams are good media for heat transfer enhancement due to their high thermal conductivity of the material and the high specific heat transfer area. The results indicated that short-length samples in the

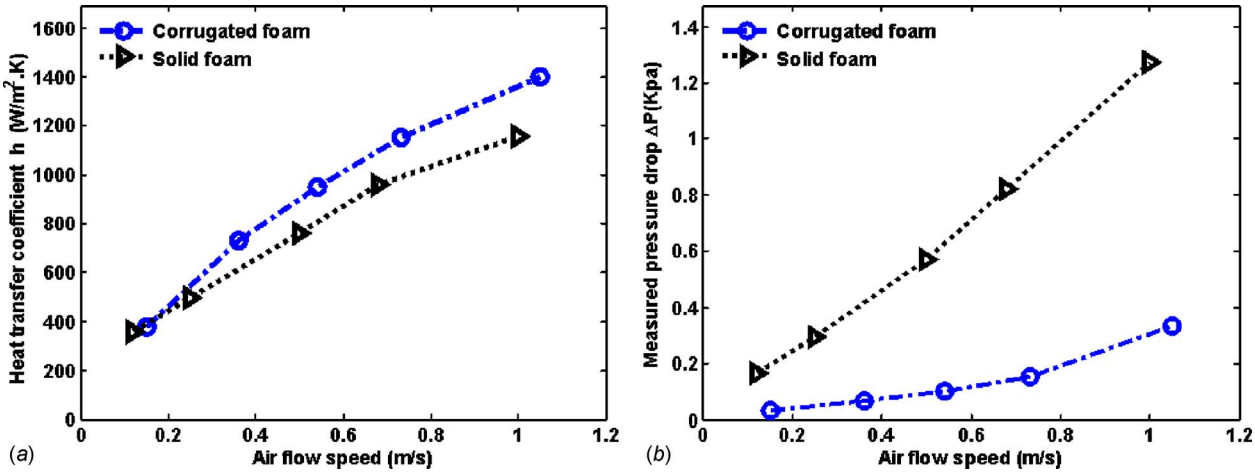

Fig. 8 Heat transfer and pressure drop versus velocity for 1×5×1 cm³ solid and corrugated foams

flow direction have a high heat transfer coefficient because air acquires heat in carbon foam within a short flow length. Corrugation increases heat transfer and reduces pressure drop at the same time. An optimal design that includes corrugation can enhance heat transfer and reduce pressure drop at the same time.

3 An Approach to High Effectiveness From One Pair to Multiple Pairs of Foam Blocks

As indicated from the experiments for one foam block, a short-length foam in the flow direction has a higher heat transfer coefficient with less pressure drop. Therefore, short-length foam blocks should be used instead of a long piece of foam in the recuperative heat exchanger. While it is important to reduce the thermal resistance in the transverse direction between the hot and cold fluids as much as possible, the axial conduction in the recuperative heat exchanger can degrade its performance considerably [19]. The high effectiveness of the heat exchanger needs to be achieved through a series of discrete carbon foam blocks instead of a continuous piece. Figure 9 shows a schematic of the concept of a recuperative heat exchanger. The basic unit was comprised of separate blocks of carbon foams packed between thin sheets of a solid material. The flow paths were piled alternately, and the hot and cold gas paths were arranged in counterflow. The stacked parallel plate arrangement allows symmetrical counterflow passages that balance flow across each heat transfer interface. This design is modular and can easily be scaled up for large capacity by using more stacks.

It is important to minimize axial conduction between the hot and cold ends of the heat exchanger to achieve high effectiveness. In order to reduce this axial heat conduction, several measures were taken in the design. First, the separation plates were made thin to reduce the cross-sectional area in the axial direction. Second, the material used should have a low thermal conductivity k. Commercially available 100-μm-thick stainless steel sheets were chosen ($k=11$ W/m K). It should be noted that the carbon foam blocks also act as a support for the thin stainless steel sheet and could allow a large pressure differential between the hot and cold fluids if needed. Huang and Vafai [20] numerically investigated convection heat transfer in a partially blocked channel using porous blocks on one side of the channel. Yucel and Guven [21] reported an investigation on forced convection in a partially blocked channel using porous blocks on both sides of a channel. Both papers reported results of cross flow over the porous blocks in the channels. In the configuration of the current study, the channel was fully blocked by carbon foam blocks. Air is forced to penetrate the carbon foam blocks uniformly to take advantage of the highly conducting carbon foam to achieve maximum heat exchange effectiveness. Flow and heat transfer in the partially and fully blocked configurations have different applications and performance.

The basic unit of the heat exchanger is a pair of foam blocks packed with a thin sheet of solid materials in between, as shown in Fig. 10. Since the flow rates are the same for both the hot and the cold sides, the effectiveness of the one-pair carbon foam heat exchanger is defined as

$$\varepsilon = \frac{T_{H,i} - T_{H,o}}{T_{H,i} - T_{C,i}} \quad \text{or} \quad \varepsilon = \frac{T_{C,o} - T_{C,i}}{T_{H,i} - T_{C,i}} \tag{6}$$

Transverse heat transfer from hot to cold is enhanced through the carbon foam blocks. Heat transfer in carbon foam involves the combined process of heat conduction within the carbon ligaments and convective heat transfer between the ligaments and air in the open-cell carbon foam. The foam is an open interconnected spherical structure. The orientation distribution of the carbon liga-

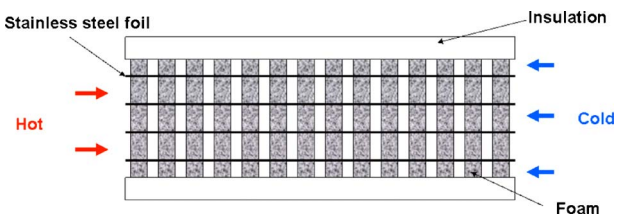

Fig. 9 Schematic of heat exchanger

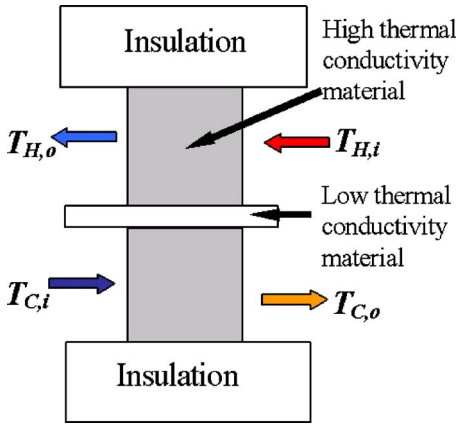

Fig. 10 Heat transfer between one carbon foam pair

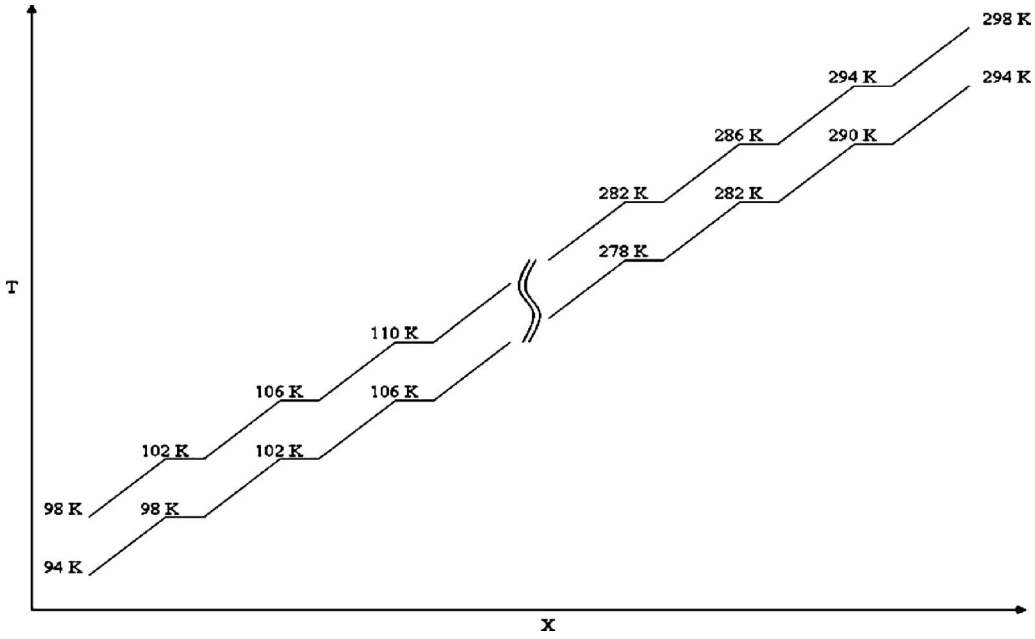

Fig. 11 Axial temperature distributions of hot and cold streams within recuperator

ment in the foam is randomly arranged. Dispersion generally has effects on the interfacial heat transfer between the solid structure and the fluid in porous media, which is highly dependent upon the specific structure of each kind of porous media. Heat transfer between solid and fluid in porous media due to temperature difference is dependent upon the properties of the fluids and solid. As carbon foams have a small pore size and a very large surface area to volume ratio and high solid-to-fluid thermal conductivity ratio (k_s/k_f) for gas flow in carbon foams, the equilibrium model with effective properties is applicable to heat transfer in carbon foam [22]. The major factor for the enhancement of heat transfer in this case is the extended surface effect. The axial conduction in the flow direction will reduce the effectiveness when only one pair of carbon foams is used in a recuperative heat exchanger.

In an earlier study, Yu et al. treated the carbon foam as a straight fin structure rather than a porous medium to simulate heat transfer enhancement [14]. They used Taylor's formulas to determine the thickness of the fins and space between them from the properties of the carbon foam. However, they did not consider axial conduction in their simulation and concluded that a heat exchanger effectiveness of 1.0 can be achieved.

Since heat is transferred from hot fluid to cold fluid, the carbon foams should be oriented with their out-of-plane direction with higher thermal conductivity in the transverse direction. The in-plane direction with lower thermal conductivity should be in the flow direction to lower the axial conduction effect [23]. Taking into account the anisotropic properties of the carbon foam and axial conduction effects, a fin model similar to that of Yu et al. [14] was developed, which showed that the effectiveness of one pair of foam blocks is 0.58 with a carbon foam pair of 1 cm length in the flow direction at an air speed of 0.67 m/s [8].

The effectiveness of one pair is limited because of axial heat conduction due to heat transfer from the hot end to the cold end for each pair of carbon foam blocks. An overall high effectiveness of the heat exchanger can be achieved through a series of carbon foam pairs. Figure 11 shows the predicted stepwise change of the hot and cold fluid temperatures in the heat exchanger. The present requirement for the recuperative heat exchanger is for the temperature of the hot stream to decrease from 298 K to 98 K (a 200 K difference), while the temperature of the cold stream has to increase from 94 K to 294 K (also a 200 K difference). This can be accomplished with a sufficient number of pairs of carbon foam blocks, with each pair responsible for a limited temperature change. The number of pairs required in the design of the heat exchanger depends on the performance of each pair. The relation between the overall effectiveness, $\varepsilon_{\text{total}}$, and the effectiveness of one pair, ε, can be expressed as follows:

$$\varepsilon_{\text{total}} = \frac{N \cdot \varepsilon}{1 + (N-1)\varepsilon} \tag{7}$$

where N is the number of carbon foam pairs.

Even if the effectiveness of each pair of carbon foam blocks is only 50%, the overall effectiveness can be as high as 98% through 50 pairs of them placed in series. From the above analysis, it appears that the design concept of using discrete 1 cm carbon foam blocks with a 0.2 cm air gap between them can provide an overall effectiveness of 98%.

4 Experiments on a Recuperative Heat Exchanger With Four Pairs of Foam Blocks

In the development of recuperative heat exchangers with carbon foam, experiments were conducted to validate the design with a heat exchanger with four pairs of foam blocks. Both solid foam and corrugated foam were used in experiments. Figure 12 shows the configuration of a recuperator where the hot and cold flow channels have four carbon foam blocks each. A schematic of the experimental setup is provided in Fig. 13. The dimensions of the flow channels are $10 \times 1.7 \times 1$ cm^3 (length $\times$ width $\times$ height). The cross sections of the air inlet and outlet are both 1.7×1 cm^2

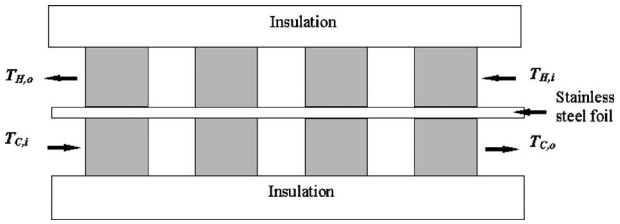

Fig. 12 Configuration of a recuperator with four pairs of carbon foams

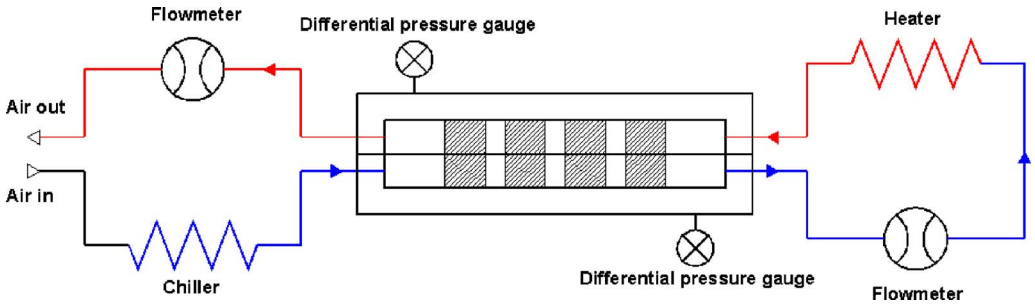

Fig. 13 Schematic of experimental setup for evaluating recuperator performance

(width × height). Carbon foam blocks of dimensions $1 \times 1.7 \times 1$ cm^3 (length × width × height) are glued to a 0.1-mm-thick stainless steel plate using a silver loaded epoxy (Pyro-Duct™).[17] Using the recommended procedure to apply the epoxy as described in the manufacturer data sheet, the contact resistance between the foam block and the stainless steel sheet can be estimated to be around 10^{-5} K/W and can be ignored due to the low heat flux in the present experiments. The thickness of epoxy is 250 μm, and the epoxy has a thermal conductivity of 9 W/m K. It was calculated that if the total length of the air gaps is equal to 20% of the total length of foam blocks, axial conduction would be less than 0.1% of the amount of heat transfer between the hot and cold streams. The total length of the air gaps is not expected to have much effect on the overall effectiveness of the heat exchanger. The carbon foam blocks were mounted and sealed inside a Plexiglas chamber. The carbon foam occupied the entire cross section of the flow channel. The entire test chamber was insulated and sealed to prevent air leaks. The cold air stream inlet was provided by passing room temperature air from the laboratory supply system through a cold thermal bath. The air from the cold outlet $T_{C,o}$ was then heated by another hot thermal bath to become the hot air stream at the inlet temperature $T_{H,i}$. In this way, both the cold and hot air streams have the same mass flow rate.

The performance of carbon foam blocks when used in a recuperative air heat exchanger was evaluated by the effectiveness and pressure drop. The overall heat transfer coefficient was obtained by measuring the inlet and outlet temperatures and flow rate. The air temperatures between the foam blocks were measured by 0.3 mm diameter thermocouples, which were placed in the space between the carbon foam blocks. The temperatures at the inlet and outlet ($T_{H,i}$, $T_{H,o}$, $T_{C,i}$, and $T_{C,o}$, i.e., hot/cold air inlet/outlet temperature) were also measured. The flow rate was measured with a flow meter that was calibrated with a high-precision mass flow meter. All data collection was automated using a Keithley 2700 data acquisition system and a personal computer. The thermocouples used in experiments were carefully calibrated, and the error in temperature measurement was within ± 0.1°C. The errors for pressure drop and flow rate were estimated to be less than ± 10 Pa and 1.2%, respectively.

The heat transfer performance of the heat exchanger with carbon foam blocks was evaluated by the overall heat transfer coefficient U, which is defined as

$$U = \frac{Q_{\text{air}}}{A_b \Delta T_m} \tag{8}$$

where Q_{air} is the heat given up by the hot air that passes through the carbon foam. It was calculated by

$$Q_{\text{air}} = \dot{m} c_p (T_{H,i} - T_{H,o}) \tag{9}$$

A_b is the heat transfer area between the hot and cold fluids; it coincides with the surface area of the dividing stainless steel sheet. ΔT_m is the log mean temperature difference and is defined as

$$\Delta T_m = \frac{(T_{H,i} - T_{C,o}) - (T_{H,o} - T_{C,i})}{\ln\left[\dfrac{T_{H,i} - T_{C,o}}{T_{H,o} - T_{C,i}}\right]} \tag{10}$$

where $T_{H,i}$, $T_{H,o}$, $T_{C,i}$, and $T_{C,o}$ are the hot and cold, inlet and outlet air temperatures.

The effectiveness of the heat exchanger can be calculated based on the temperature drop of the hot air or the temperature rise of the cold air,

$$\varepsilon_{\text{total } H} = \frac{(T_{H,i} - T_{H,o})}{(T_{H,i} - T_{C,i})} \tag{11}$$

$$\varepsilon_{\text{total } C} = \frac{(T_{C,o} - T_{C,i})}{(T_{H,i} - T_{C,i})} \tag{12}$$

Since the flow rates were the same for both the hot and the cold sides, and the specific heat could be assumed to be constant in the temperature range of the experiment, the hot and cold side effectiveness should be the same in theory. The small difference (error) in the effectiveness calculated from the hot and cold streams is due to measurement errors and the very small heat transfer between the flow channels with the surrounding air,

$$\text{error} = \frac{|\varepsilon_{\text{total } H} - \varepsilon_{\text{total } C}|}{\varepsilon_{\text{total } H}} \tag{13}$$

The average effectiveness of the heat exchanger is calculated as

$$\varepsilon_{\text{total}} = \frac{|\varepsilon_{\text{total } H} + \varepsilon_{\text{total } C}|}{2} \tag{14}$$

The air flow speed V and the inlet and outlet air temperatures were measured in the experiment. The measured data were processed using Eqs. (6)–(12). The uncertainty for U at $V = 0.25$ m/s is 25% due to a small temperature difference, but those at high velocities are small. The average uncertainties for Q_{air}, ΔT_m, and U are 4.2%, 3.1%, and 5.9%, respectively. The uncertainty for $\varepsilon_{\text{total}}$ was estimated to be 4.7% for the worst case with $V = 0.25$ m/s, and the average uncertainty for $\varepsilon_{\text{total}}$ was 3.2%.

The heat transfer and the total pressure drop across the four 1 cm carbon foam blocks were measured at air flow speeds of 0.25–1 m/s. Figure 14 shows the measured overall heat transfer coefficient and pressure drop of the recuperative heat exchanger with four pairs of solid and corrugated carbon foam blocks. The measured overall heat transfer coefficient U for the solid foam was about 568 W/m^2 K at the speed of 1 m/s. Without the four carbon foam pairs, the overall heat transfer coefficient was only 10.2 W/m^2 K for the empty flow channels at $V = 1$ m/s. Heat transfer enhancement by the carbon foam is significant. Corrugation foam increases the heat transfer coefficient further to 770 W/m^2 K at $V = 1$ m/s. The pressure drop for the solid foam compares well with the pressure drop across a 5-cm-long solid carbon foam measured by Klett et al. [15] when their pressure

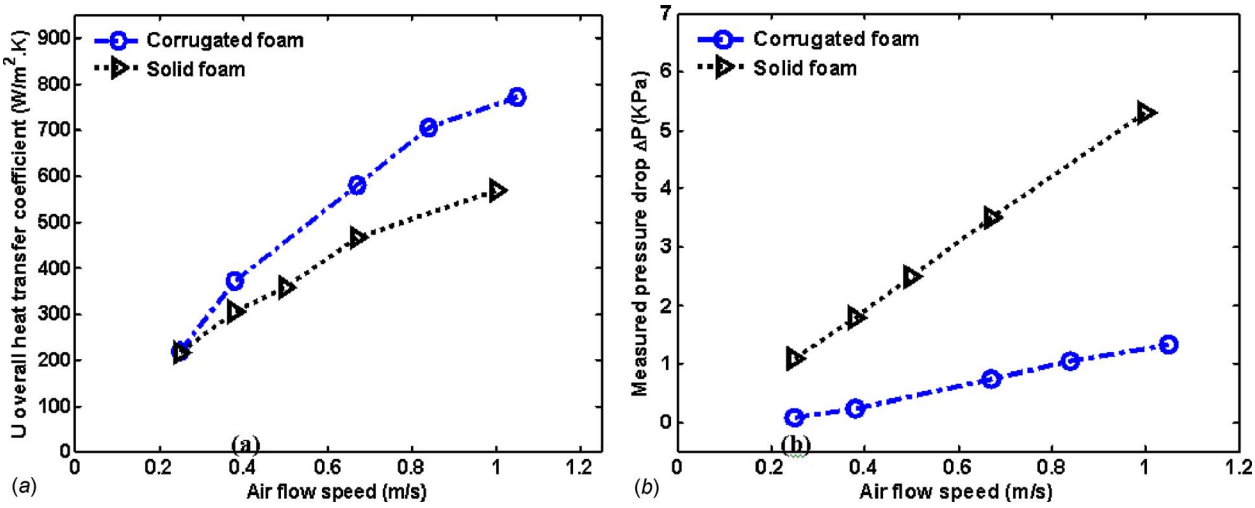

Fig. 14 Overall heat transfer coefficient versus air flow speed for heat exchanger (solid and corrugated foams)

drop was scaled down linearly from 5 cm to 4 cm so that the total lengths of the foam in the flow direction are the same. With a corrugated configuration, the pressure drop across the four pairs of foam blocks reduces more than five times at 1 m/s. These results demonstrate that corrugated carbon foam is better both for heat transfer enhancement and pressure drop reduction, as demonstrated in the experiments for the performance of one single carbon foam.

Figure 15 shows the overall effectiveness with four pairs of carbon foams for both the solid and the corrugated foam. The average measured effectiveness values of one-pair solid foam are about $\varepsilon=0.50$ and 0.57 when the flow velocities are $V=1$ m/s and 0.25 m/s, respectively. In a similar fashion, by using the air temperatures across two and three pairs of carbon foams, one could measure the average effectiveness for two and three pairs of carbon foams. The average measured effectiveness for one, two, three, and four pairs of carbon foams is plotted in Fig. 15. The measured effectiveness for four pairs of solid foams decreases slightly from 85% to 80% when the air speed V increases from 0.25 m/s to 1 m/s, while for the corrugated foam, the effectiveness drops from 86% to 81%.

It is noted that the average measured effectiveness values of one corrugated carbon foam pair at $V=1$ m/s and 0.25 m/s velocities are about $\varepsilon=0.51$ and 0.57, which are about the same as that of solid foam. Figure 15 also shows that though the average measured effectiveness for a one-pair foam at $V=0.25$ m/s is around 0.57, by using four pairs of them in series, one can increase the overall effectiveness to about 86% (for both solid and corrugated foams).

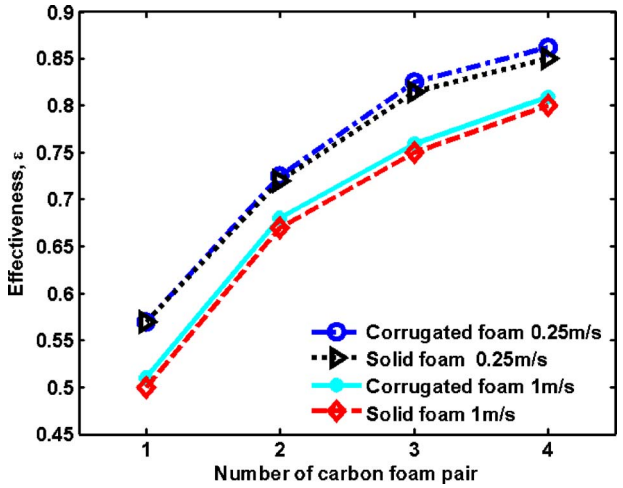

Fig. 15 Comparison of the average measured effectiveness (solid and corrugated foams)

5 Conclusion

Experiments using solid and corrugated carbon foams of different sizes show that carbon foam can enhance heat transfer, and the heat transfer coefficient increases as the foam length decreases. Corrugation can reduce the pressure drop while maintaining a high heat transfer coefficient. The effectiveness for one pair of carbon foam blocks is limited due to the axial conduction effect of the foam. The anisotropic property of carbon foam can be used to obtain a higher effectiveness for one pair of foam blocks. High effectiveness of the heat exchanger can be achieved by placing many pairs of carbon foam blocks in series. Experiments with four pairs of carbon foam blocks demonstrated that an effectiveness $\varepsilon_{\text{total}}$ greater than 80% could be achieved. Corrugation can enhance the overall heat transfer coefficient and reduce pressure drop at the same time in recuperative heat exchangers Corrugation does not have much effect on effectiveness though pressure drop is significantly reduced. Based on these test data, it is predicted that an overall heat exchanger effectiveness $\varepsilon_{\text{total}}$ of 98% can be reached by using 50 pairs of carbon foam blocks.

Acknowledgment

This research was sponsored by Florida Space Grant Consortium and NASA Kennedy Space Center.

Nomenclature

A = single block foam heat transfer area (m^2)
A_b = base heat transfer area of the foam exchanger (m^2)
h = heat transfer coefficient of a single foam block (W/m^2 K)
k = thermal conductivity (W/m K)
L = length of the carbon foam block (m)
$\dot{m}$ = mass flow rate of air (kg/s)
P = tube perimeter (m)
Q = heat transfer of a single block foam (W)
Q_{air} = heat transfer from the hot to cold fluids (W)
$T_{C,i}$ = cold air inlet temperature (K)
$T_{H,i}$ = hot air inlet temperature (K)
$T_{C,o}$ = cold air outlet temperature (K)

$T_{H,o}$ = hot air outlet temperature (K)
$T_m(x)$ = the mean temperature at the x position (K)
T_w = the wall temperature of tube (K)
ΔT_m = log mean temperature difference (K)
U = overall heat transfer coefficient based on the log mean temperature difference (W/m^2 K)
v_m = averaged small tube air flow speed (m/s)
c_p = heat capacity of the air (J/kg K)
ε = effectiveness of one-pair heat exchanger
$\varepsilon_{\text{total}}$ = total effectiveness of the heat exchanger
χ = nondimensional temperature

References

[1] Notardonato, W. U., 2007, "Development of Consumable Transfer Systems for Sustainable Lunar Exploration," 45th AIAA Aerospace Sciences Meeting and Exhibit, Reno, NV, AIAA Paper No. 2007-0957, January.
[2] Zhou, L., Kapat, J. S., Chow, L. C., and Li, X., 2000, "Design of a High Effectiveness Micro Heat Exchanger for Mars Application," SAE, Int. Journal of Aerospace, **109**(1), pp. 875–882.
[3] Doty, F. D., Hosford, G., Spitzmesser, J. B., and Jones, J. D., 1991, "The Microtube Strip Heat Exchanger," Heat Transfer Eng., **12**, pp. 31–41.
[4] McCormick, J. A., Nellis, G. F., Sixsmith, H., Zagarola, M. V., Gibbon, J. A., Izenson, M. G., and Swift, W. L., 2001, "Advanced Developments for Low Temperature Turbo-Brayton Cryocoolers," Cryocoolers, **11**, pp. 481–488.
[5] Hill, R. W., Izenson, M. G., Chen, W. B., and Zagarola, M. V., 2007, "A Recuperative Heat Exchanger for Space-Borne Turbo-Brayton Cryocoolers," Cryocoolers, **14**, pp. 525–533.
[6] Hoch, D. W., Nellis, G. F., Meagher, N. L., Maddocks, J. R., and Stephens, S., 2007, "Development and Testing of a Multi-Plate Recuperative Heat Exchanger for Use in a Hybrid Cryocooler," Cryocoolers, **14**, pp. 515–524.
[7] Zhou, L., Kapat, J., Chow, L., and Lei, S., 2000, "Design of a High Performance Cryocooler for Propellant Liquefaction and Storage on Mars," *Proceedings of the 2000 International Mechanical Engineering Congress and Exposition*, Orlando.
[8] Wu, W., Du, J. H., Lin, Y. R., Chow, L. C., and Notardonato, W., 2009, "Design and Experiment of Compact and Effective Carbon Foam Recuperative Heat Exchangers," J. Thermophys. Heat Transfer, **23**, pp. 339–345.
[9] Gallego, N., and Klett, J. W., 2003, "Carbon Foams for Thermal Management," Carbon, **41**, pp. 1461–1466.
[10] Poco Graphite Inc., 2000, PocoFoam Product Information.
[11] Leong, K. C., and Jin, L. W., 2006, "Effect of Oscillatory Frequency on Heat Transfer in Metal Foam Heat Sinks of Various Pore Densities," Int. J. Heat Mass Transfer, **49**, pp. 671–681.
[12] Klett, J. W., 1999, "High Thermal Conductivity, Mesophase Pitch-Derived Graphitic Foams," Composites in Manufacturing, **14**(4), pp. 1–5.
[13] Klett, J. W., Mcmillan, A. D., Gallego, N. C., and Walls, C. A., 2004, "The Role of Structure on the Thermal Properties of Graphitic Foams," J. Mater. Sci., **39**, pp. 3659–3676.
[14] Yu, Q., Thompson, B. E., and Straatman, A. G., 2005, "Carbon Foam—New Generation of Enhanced Surface Compact Recuperators for Gas Turbines," ASME Paper No. GT2005-69007.
[15] Klett, J. W., Tee, C. C., Stinton, D. P., and Yu, N. A., 2000, "Heat Exchangers Based on High Thermal Conductivity Graphite Foam," *Proceedings of the First World Conference on Carbon*, EuroCarbon, pp. 244–245.
[16] Mahjoob, S., and Vafai, K., 2008, "A Synthesis of Fluid and Thermal Transport Models for Metal Foam Heat Exchangers," Int. J. Heat Mass Transfer, **51**, pp. 3701–3711.
[17] Technical Bulletin A8, Aremco Company, www.aremco.com
[18] Incropera, F. P., Dewitt, D. P., Bergman, T. L., and Lavine, A. S., 2007, *Fundamentals of Heat and Mass Transfer*, 6th ed., Wiley, New York.
[19] Demko, J. A., and Chow, L. C., 1984, "Heat Transfer Between Counter Flowing Fluids Separated by a Heat-Conducting Plate," AIAA J., **22**(5), pp. 705–712.
[20] Huang, P. C., and Vafai, K., 1994, "Analysis of Forced Convection Enhancement in a Channel Using Porous Blocks," J. Thermophys. Heat Transfer, **8**, pp. 563–573.
[21] Yucel, N., and Guven, R. T., 2007, "Forced-Convection Cooling Enhancement of Heated Elements in a Parallel Plate Channel Using Porous Inserts," Numer. Heat Transfer, Part A, **51**(3), pp. 293–312.
[22] Lee, D. Y., and Vafai, K., 1999, "Analytical Characterization and Conceptual Assessment of Solid and Fluid Temperature Differentials in Porous Media," Int. J. Heat Mass Transfer, **42**, pp. 423–435.
[23] Jones, G. F., 1995, "Axial Conduction in a Thick-Wall Matrix Heat Exchanger," Cryogenics, **35**, pp. 581–588.

Experimental and Numerical Investigation of Heat Transfer Characteristics of Inline and Staggered Arrays of Impinging Jets

Yunfei Xing[1]
e-mail: yunfei.xing@itlr.uni-stuttgart.de

Sebastian Spring

Bernhard Weigand

Institut für Thermodynamik der Luft- und Raumfahrt (ITLR),
Universität Stuttgart,
Pfaffenwaldring 31,
70569 Stuttgart, Germany

A combined experimental and numerical investigation of the heat transfer characteristics within an array of impinging jets has been conducted. The experiments were carried out in a perspex model using a transient liquid crystal method. Local jet temperatures were measured at several positions on the impingement plate to account for an exact evaluation of the heat transfer coefficient. The effects of the variation in different impingement patterns, jet-to-plate spacing, crossflow schemes, and jet Reynolds number on the distribution of the local Nusselt number and the related pressure loss were investigated experimentally. In addition to the measurements, a numerical investigation was conducted. The motivation was to evaluate whether computational fluid dynamics (CFD) can be used as an engineering design tool in the optimization of multijet impingement configurations. This required, as a first step, a validation of the numerical results. For the present configuration, this was achieved assessing the degree of accuracy to which the measured heat transfer rates could be computed. The overall agreement was very good and even local heat transfer coefficients were predicted at high accuracy. The numerical investigation showed that state-of-the-art CFD codes can be used as suitable means in the thermal design process of such configurations. [DOI: 10.1115/1.4001633]

Keywords: impingement cooling, heat transfer, inline, staggered, CFD

1 Introduction

The last 20 years have seen a large improvement in gas turbine technology, mainly due to an increase in turbine pressure ratios and turbine inlet temperature. The effect of firing temperature is very important, as for approximately every 55 K increase in temperature, the work output increases by approximately 10% and results in 1–1.5% increase in overall efficiency [1]. In practice, high turbine inlet temperatures have been achieved because of the growth of material technology, new coatings, and new cooling schemes. Film cooling method has become an established technology for the conventional cooling of turbine vanes and blades or combustor liners. In particular for combustors, emission restrictions in recent years have accelerated the development of modern concepts such as dry low emission combustor with low production of NO_x emissions. However, control of the NO_x problem requires a minimization of film cooling and dilution air. Consequently, these combustors are typically cooled by enhanced backside convective heat transfer. Combustion liners typically have a double-wall structure and impingement cooling is often used to keep the cooling effectiveness high. Therefore, the impingement hole shape, size, and locations have to be tailored to attain both sufficiently high average heat transfer coefficient and uniformity in the surface heat transfer distribution to avoid local hot or cold spots.

Impingement cooling configurations have been investigated in numerous studies in the past. Several reviews have been published on the subject, respectively, aimed at summarizing the latest developments in impingement technology, measurement technique, and numerical computations. Among these are, for example, the works of Martin [2], Han and Goldstein [3], Jambunathan et al. [4], Viskanta [5], and Weigand and Spring [6].

Extensive studies have reported on impingement heat transfer characterizes with the jet-induced crossflow in one direction. Kercher and Tabakoff [7] made experimental investigations on the average surface heat transfer coefficient under a square array of round air jets. They found that the heat transfer is dominated by the jet Reynolds number and jet-to-jet spacing. Hollworth and Berry [8] measured local and average convective heat transfer coefficients for arrays with jet-to-jet spacings from 10 to 25 jet diameters. The results showed that local heat transfer coefficients are influenced by interference from neighboring jets only when the separation distance H/d was less than 5. Metzger et al. [9] compared heat transfer characteristics for corresponding inline and staggered hole pattern. They showed that the mean heat transfer coefficients for the inline pattern are in every case equal to or larger than those for the corresponding staggered pattern. Florschuetz and co-workers [10,11] showed the effect of channel height, hole spacing, hole diameter, and hole pattern on the heat transfer coefficient of circular jets. They presented correlations for both inline and staggered hole patterns. Van Treuren et al. [12] measured the local heat transfer coefficients and the adiabatic wall temperatures under an array of impinging jets using the double crystal analysis. The results showed that the thermal boundary condition can significantly affect the average cooling performance of an impingement array. Van Treuren et al. [13] made a detailed comparison of local and average heat transfer coefficients between inline and staggered impinging jets. They found that the average Nusselt number is slightly higher for the staggered case at low average Reynolds numbers. However, the difference increases for a higher average Reynolds number. Son et al. [14] measured the heat transfer and flow characteristics under a staggered array of

[1]Corresponding author.

Contributed by the Heat Transfer Division of ASME for publication in the JOURNAL OF HEAT TRANSFER. Manuscript received October 21, 2009; final manuscript received February 25, 2010; published online June 30, 2010. Assoc. Editor: Wei Tong.

uniform and nonuniform impingement holes. The particular impingement geometries were in the range of $X/d=3.0-4.8$, $Y/d=3.75-6.0$, and $H/d=1.875-3.0$. They found that the total averaged Nusselt number for both arrays turns out to be the same. Bailey and Bunker [15] investigated the heat transfer distributions for a series of square and inline arrays of impingement jets. Axial and lateral jet spacing values (X/d, Y/d) of 3, 6, and 9, jet-to-plate spacing (H/d) varying from 1.25 to 5.5, and Reynolds numbers ranging from 14,000 to 65,000 have been investigated. They extended the streamwise row averaged heat transfer coefficient correlation for design use. Bailey et al. [16] tested the heat transfer characteristics of a stationary gas turbine combustor liner cooled by impingement jets experimentally and numerically. They measured high jet Reynolds numbers ranging from 170,000 to 280,000. Park and co-workers [17,18] considered that it is not enough to evaluate the heat transfer coefficient only based on the Reynolds number. They found that the heat transfer shows a strong dependence on Mach number for Mach numbers larger than 0.2 (Reynolds number held constant). They presented a new correlation for spatially averaged Nusselt number for Mach numbers in the range of 0.2–0.6. Geers et al. [19] measured the heat transfer coefficients with the jets impinging on a flat plate with unrestricted flow of spent air for Reynolds number ranging from 5000 to 20,000 and presented a new correlation for the averaged Nusselt number for hexagonal and inline arrays of impinging jets. They mentioned that the multiple jet heat transfer is strongly influenced by jet interactions. Attalla [20] investigated the heat transfer characteristics from arrays of free impinging circular jets and hole channels for Reynolds numbers in the range of 1400–41,400, jet-to-jet spacing from 2 to 10, and jet-to-plate spacing from 1 to 10. The results showed that the multiple jet system enhances the heat transfer over the entire test range compared with those of the hole channel and single nozzle. The jet-to-plate spacing H/d has nearly no effect on the heat transfer in the range of $2 \leq H/d \leq 5$ for multiple jets.

In recent years, the numerical simulation of arrays of multiple impinging jets has begun to evolve a complement to costly experimental investigations. However, the numerical prediction of multijet systems remains a challenging task due to the large spectra of jet-to-jet and jet-to-crossflow interference. Requirements to spatial resolution and the numerical methods are accordingly high, in particular, when heat transfer is to be accounted for. Spring et al. [21] showed that impingement configurations at high jet Reynolds numbers with complex jet-crossflow interaction can numerically be predicted at reasonable cost by standard commercial computational fluid dynamics (CFD) tools by a proper definition of the domain boundaries. Another important matter associated with numerical predictions is the appropriate assessment of mesh sensitivity, as its effect on the result is of essential importance [6]. The predictive character of different turbulence models has been investigated by several authors and, for single impinging jets, was reviewed by Polat et al. [22] or Zuckerman and Lior [23]. Evidently, the regions most difficult to predict are typically the stagnation zones, where two-equation models tend to significantly overpredict heat transfer rates [16]. Regarding the systems of multiple impinging jets, more recent studies, e.g., Rao et al. [24], Zu et al. [25], or Spring et al. [26], reported on the shear stress transport (SST) turbulence model to be most suitable due to the good agreement between experimental and numerical data achieved at reasonable computational costs.

From literature survey, it can be concluded that jet interactions are quite important for jet array impingement heat transfer. Apart from other geometric conditions, it is, in particular, the direction of spent air that can influence the jet interaction strongly. A detailed knowledge on the effect of the direction of spent air is therefore essential for an accurate thermal design of multijet impingement systems. However, from the review of related literature, it appears that there is only little information available on the effect of jet-induced crossflow direction. Obot and Trabold [27] made a comparison of the effects of three jet-induced crossflow schemes on impingement heat transfer. The study covered jet Reynolds number of 1000 to 21,000. The results showed that the best heat transfer performance is obtained with minimum crossflow scheme. In their study, only area averaged heat transfer data were presented and no local Nusselt number distributions were given. Kanokjaruvijit and Martinez-Botas [28] measured the heat transfer coefficients from an inline array impinging onto a flat plate for three different crossflow schemes. The investigated parameters were Reynolds numbers ranging from 5000 to 15,000 and jet-to-plate spacings, which varied from 1 to 12. They confirmed that the minimum crossflow scheme leads to the highest average heat transfer, followed by the intermediate and maximum crossflow schemes, respectively. They compared the averaged data to literature correlations and the comparisons show the agreement. Since they primarily concentrated on a dimpled target plate, they missed to show detailed local heat transfer data for the flat target plate.

In the present study, a large scale impingement model was used to accurately investigate the heat transfer of different impingement cooling configurations. Particular attention was paid to the influence of the different crossflow schemes and the effect of impingement plate pattern. Results were evaluated in the form of local heat transfer coefficients, which provide significantly more detailed information than average values. The primary objective of this study was to explore the possibility to affect local heat transfer characteristics on the target plate by a variation in the crossflow schemes, the impingement pattern, and the jet-to-plate spacing. The present investigation has two main characteristics that are unique in this combination. These are the detailed investigation of all crossflow schemes including locally resolved heat transfer data on the one hand and the relatively high Reynolds number range for this type of investigation on the other hand. For a detailed assessment as to how the present investigation extends the available body of literature, the reader is referred to the review of Weigand and Spring [6], where numerical ranges of the investigated parameters can be found for a large number of previous studies. The results obtained from the present investigation are meant to serve as basic data for further investigations of multijet systems in combination with rib turbulators and dimples. The experimental part was complemented by numerical investigations. Due to the complex nature of the system of multiple impinging jets and the correspondingly high costs of an experimental investigation, our motivation was to evaluate whether CFD can be used as an engineering tool in the design and optimization of such configurations. For this, a validation of the numerical results was required as a first step. Thus, the secondary objective of this investigation was to determine the degree of accuracy to which a commercial CFD code is capable of predicting the experimentally obtained heat transfer rates. No problem-specific modifications or adoptions were made to the code so that the results computed represent the current state-of-the-art in predictive accuracy. In order to ensure that the capabilities of the CFD code were exploited to the maximum extent, the effort was spent on the generation of a three-dimensional mesh suited for a realistic reproduction of the experiments and the compliance of quality parameters affecting the numerical solution.

Details on the experimental setup along with information on the measurement technique and measurement uncertainties are provided in Sec. 2. The numerical setup is introduced in Sec. 3. There, information on the flow solver, the computational domain, and the numerical grid are summarized. The results of a detailed grid independency study are presented. The experimental results are compared with available data from literature in Sec. 4. The influence of the Reynolds number and the jet-to-plate spacing are discussed. The results from experiments and predictions are compared with each other for the case of a jet-to-plate spacing ratio of 3 and a Reynolds number of 35,000. This section concludes with

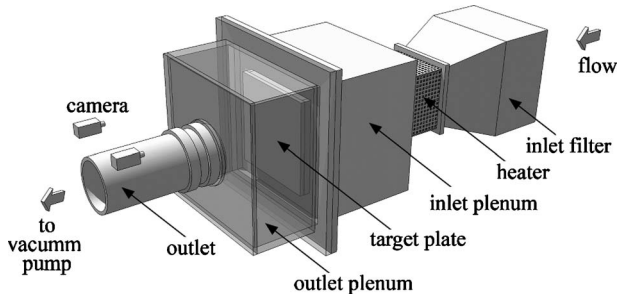

Fig. 1 Sketch of the experimental setup

a statement on the pressure loss for the investigated configurations. The main conclusions of this investigation are summarized in Sec. 5.

2 Experimental Setup

2.1 Test Section. Figure 1 shows a sketch of the experimental setup. A vacuum pump system was used to generate the desired air flow in the test channel. The air entered the channel under atmospheric conditions via filter and heater. The heater consisted of several meshes made out of stainless steel and was able to heat the air within less than 0.3 s from ambient temperature up to 100°C. Downstream of the heater, the air entered the inlet plenum and from there entered the impingement model. This model was equipped with thermocouples and pressure taps for the measurement of the reference temperature and pressure loss. The model itself consisted of an impingement plate, a target plate, and side rims with effusion outlet holes, as shown in Fig. 2. The spent air was routed through the outlet holes in the exit rims into an outlet plenum. The target plate was made out of perspex material, which was due to its low thermal conductivity and the optical access that was needed for the heat transfer measurements. The target plate was observed from the outside with two charge coupled device (CCD) video cameras. The model was symmetrical, therefore only half of the target plate was observed.

There was a total of 81 impingement jet holes for the inline pattern and of 77 impingement jet holes for the staggered pattern. The ratios of jet-to-jet spacing of the impingement plates were identical for both pattern, i.e., $X/d=Y/d=5$. Figure 3 shows the two impingement patterns used in the present work and the positions of the thermocouples used for the data evaluation. Note that due to symmetry, only half of the plate is presented. The thermocouples were placed directly at the jet exits. Grooves were milled into the wall of the impingement plate and the thermocouples along with their wires were glued into these grooves, as shown in Fig. 4. Three ratios of the jet-to-plate spacing ($H/d=3$, 4, and 5) as well as the three crossflow schemes (realized by changing the exit rims) were investigated, as shown in Fig. 5. The Reynolds numbers investigated in the experiments were 15,000, 25,000, and 35,000. Here, Reynolds number refers to the jet Reynolds number based on the jet diameter.

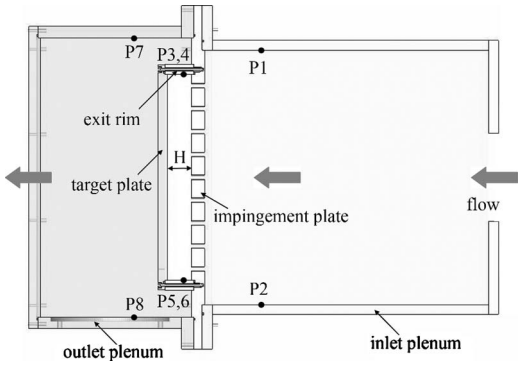

Fig. 2 The impingement model and positions of static pressure taps

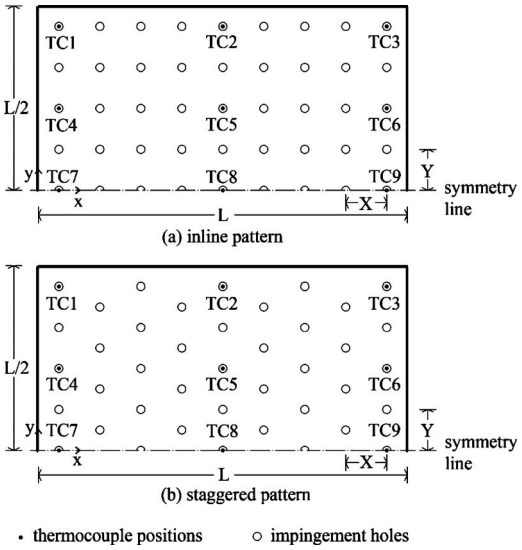

Fig. 3 Impingement patterns and the positions of thermocouples

2.2 Measurement Technique. A transient method using thermochromic liquid crystals (TLC) was applied for the measurement of heat transfer [29]. Narrow bandwidth liquid crystals (with an indication temperature of 31°C) were used in the present work. The TLC indication temperature was measured with a 1D calibration unit consisted of a block of copper, electric heater, and accommodate water cooling. The crystals were sprayed directly onto the target plate and covered with a coating of black paint in order to provide a uniform background for the image acquisition.

The local heat transfer coefficients were determined using the measured wall temperature and the solution of the one-

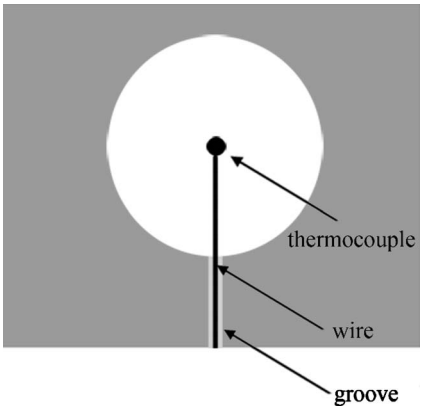

Fig. 4 View of the detailed position of thermocouple

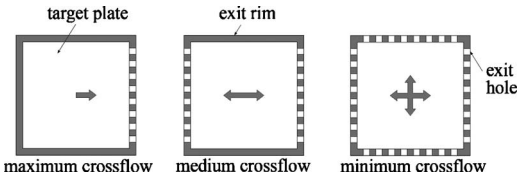

Fig. 5 Crossflow schemes

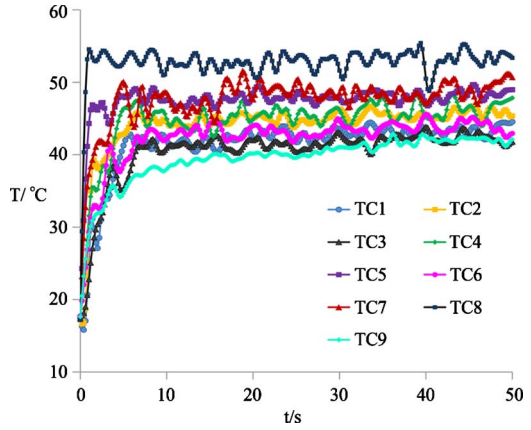

Fig. 6 Measured temperature evolution of thermocouples

dimensional transient heat conduction in a semi-infinite solid. In order to apply the analytical model, the assumption of the semi-infinite wall has to be assured. As shown by Wagner et al. [30], this assumption can be considered valid as long as the condition at $(\alpha t/d^2) < (1/4)$ is fulfilled. Here, α is the thermal diffusivity of the material. With typical material properties of Plexiglas, a wall thickness of 20 mm, and a maximum testing time of t=90 s the semi-infinite wall assumption was fulfilled. So in the present study, all the measurements were conducted in less than 90 s.

For a flat surface, the wall surface temperature and the heat transfer coefficient were related by the expression

$$\Theta = \frac{T_w - T_0}{T_B - T_0} = 1 - \exp(\tilde{h}^2)\mathrm{erfc}(\tilde{h}) \tag{1}$$

where $\tilde{h} = h\sqrt{t/k\rho c}$.

This equation has been solved numerically to obtain the heat transfer coefficient for a measured wall temperature T_W and the time t by which this temperature is reached (indicated by the color change in the liquid crystals). Equation (1) is only valid for an ideal temperature step within the flow but in reality the thermocouple records a time-dependant temperature evolution. To overcome this problem, the temperature data were divided into a series of small discrete intervals (N). Within these intervals the temperature evolution could be considered to be an ideal temperature step. Thus Eq. (1) can be extended for a temperature evolution according to the Duhamel principle [31]

$$T_w - T_0 = \sum_{i=1}^{N} \Theta(t - t_i)(T_{B,i} - T_{B,i-1}) \tag{2}$$

where $T_{B,i}$ is the bulk-temperature at one specific time t_i.

In a detailed impingement array, there is a variation in the local temperature distribution. In the present experimental configuration, the channel widened up considerably after the heater. This caused a noticeable temperature gradient from the center of the impingement plate toward the side rims. Typical temperature evolutions during an experiment are shown in Fig. 6 (for the positions of the thermocouples refer to Fig. 3). This figure is referred to the case with H/d=3, Re=35,000, and the inline pattern. For the other cases including the staggered pattern, we also did this analysis and obtained very similar results.

Due to the presence of a temperature gradient for the inlet flow, it was necessary to install a large number of thermocouples on the impingement plate to certain the local reference temperature. This in turn was needed for the precise calculation of the heat transfer coefficients. A heat transfer evaluation requires the temporal fluid temperature distribution for every position on the target plate until the indication time. The temporal evolution of all thermocouples was interpolated both spatially and temporally by the evaluation software program PROTEIN [32], which has been developed at the Institut für Thermodynamik der Luft- und Raumfahrt. Afterwards the film data and the bulk-temperature field were evaluated also by PROTEIN.

The pressure drop was measured by static pressure taps along the wall of the test section. The axial positions are sketched in Fig. 2.

The discharge coefficient C_d is generally used to evaluate the pressure loss of flow systems. It is defined as

$$C_d = \frac{\dot{m}}{\dot{m}_{ideal}} \tag{3}$$

In the present work, the discharge coefficients of the impingement plate and of the exit rims were defined for an incompressible flow as

$$C_{d,I} = \frac{\dot{m}}{\rho\frac{\pi n d^2}{4}}\sqrt{\frac{\rho}{2\Delta P_I}} \tag{4}$$

$$C_{d,O} = \frac{\dot{m}}{\rho A}\sqrt{\frac{\rho}{2\Delta P_o}} \tag{5}$$

where $\Delta P_I = 1/2(P_1+P_2) - 1/4(P_3+P_4+P_5+P_6)$ and $\Delta P_O = 1/4(P_3+P_4+P_5+P_6) - 1/2(P_7+P_8)$

2.3 Measurement Uncertainties. The approach used for the measurement error analysis here is based on the description by Kline and McClintock [33]. The accuracy of the measured heat transfer coefficient depended mainly on the accuracy of the thermocouples, the calibration of the liquid crystals, and the time detection.

The accuracy of the Reynolds number depended on the accuracy of the volume flow measured by the vortex meter and on the range of the static pressure sensors. The resulting uncertainty for the jet Reynolds number was below 2.5%. For narrow band TLC, the transitional temperature range is 1°C and the typical uncertainty in measuring this temperature is approximately 0.1°C [34]. T_B and T_0 were measured with thermocouples. A thermocouple calibration procedure showed that the error on temperature measurement was below 0.2°C.

It should be noted that the measurement uncertainties vary with the adiabatic wall temperature and therefore are different at every position at the target plate. In particular, in the stagnation point under the impinging jets, lateral heat conduction will have an effect. According to the method by Kingsley-Rowe et al. [35], the maximum error of the heat transfer coefficient due to lateral heat conduction has been calculated to be below 2%, when the dimensionless temperature ratio Θ is in the range of $0.3 \leq \Theta \leq 0.7$.

The total measurement uncertainty for the heat transfer coefficient was below 9% for all experiments that have been carried out in this study. The accuracy of the pressure measurements depends on the range of the pressure sensors. The maximum error of the pressure measurements was below 2.5%.

3 Numerical Setup

3.1 Flow Solver. For the numerical investigation of the impingement configurations, the commercial CFD software package ANSYS CFX version 11 was used. Spatial discretization was based on the second-order accurate upwind scheme.

Due to its good performance in previously investigated jet impingement configurations and the comparatively low computational costs, the SST turbulence model was used in all computations [36,37].

For the description of the flow in the region near the wall, a low-Reynolds number approach was used, which allows the resolving of details in the viscous sublayer by applying very fine

mesh length scales near the walls. This approach requires the dimensionless wall distance of the first node in the flow to be $y_1^+ < 2$, where

$$y_1^+ = \frac{u_\tau y_1}{\nu} \tag{6}$$

with u_τ representing the shear velocity, y_1 representing the absolute distance from the wall, and ν standing for the kinematic viscosity of the fluid.

3.2 Computational Domain and Boundary Conditions. The computational domain was generated following the geometric specifications of the experimental facility as accurately as possible in order to assure a realistic representation of the measurements. However, some simplifications were incorporated, which helped to increase mesh resolution on the available computing resources. Outlet holes from the side rims and the outlet plenum were not included in the domain model as both were assumed to influence upstream flow conditions only to a minor extent. The outlet boundary conditions were moved away from the impingement zones by extending the domain models at the respective domain exits. By this, it was ensured that outlet boundary condition had no effect on the flow field. The upstream jet plenum was also omitted in the computational domain. Consequently, jet inlets were modeled as circular planes. By these steps, the computational effort was significantly reduced. Furthermore, the negligence of the plenums had a substantial beneficial effect on overall convergence and stability of the simulations, as initial tests had indicated. Symmetry boundary conditions were applied, where possible, helping to reduce the computational model even further. For the minimum crossflow cases, the size of the computational domain was 25% of the experimental model, whereas for the intermediate and maximum crossflow cases the domain volume was 11% of the original size (see Fig. 5 for illustration).

Boundary conditions were applied to the computational model according to the data collected during the experiments. Measured jet Reynolds numbers were applied as inlet conditions to the individual jets. In the numerical investigation, all jets had uniform velocity profiles and a temperature approximately 30 K lower than the heated target plate. The target plate was considered as no-slip wall with a constant wall temperature boundary condition, whereas the impingement plate was modeled as an adiabatic no-slip wall. At the domain outlets, pressure type boundary conditions were defined.

From the computed results, Nusselt numbers were obtained from the known wall temperature, the local wall heat flux, and the jet total temperature as a fixed reference temperature.

3.3 Numerical Grid. Meshes for the CFD analysis were generated with ANSYS ICEMCFD version 11. Spatial discretization of the domain models was realized by block-structured grids with hexahedral elements. Reduced complexity due to the steps described above resulted in moderate cell sizes of the order of approximately 1.5×10^6 elements. Cell orthogonality was assured by the introduction of multiple O-grid type blocks for all jets. Requirements of the SST turbulence model regarding the near-wall resolution ($y_1^+ < 2$) were fulfilled for the target plate, where local maximum values of y_1^+ were typically around 1.5 for all configurations. At the impingement plate, the near-wall resolution was coarser. Thus, the low-Reynolds approach was used for the target plate while for the impingement plate wall-functions were used to describe the viscous sublayer. Figure 7 shows an exemplary three-dimensional view of the mesh used for the representation of the maximum crossflow cases. The corresponding volume in the original experimental setup is indicated as well.

3.4 Quantification of Numerical Accuracy. For an assessment of numerical stability, local heat transfer coefficients in the stagnation regions were monitored during the simulations. When fluctuations in the latter were in the order of 1–2%, the simulation

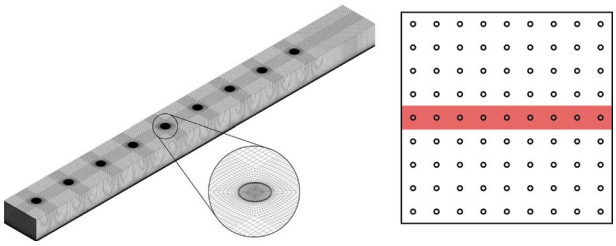

Fig. 7 Three-dimensional view on the hexahedral mesh used for the maximum crossflow cases (left) compared with the original volume of the experimental facility (right)

was considered stable. Iterative convergence was considered sufficient, when the normalized root mean square residuals had decreased by at least four orders of magnitude. For the present cases, this typically required between 500 and 1000 iterations. For all of the presented cases, no stability or convergence problems were encountered. All simulations were of steady state.

For an estimate on the numerical accuracy of the computed results, a mesh sensitivity analysis was performed. This was done before comparing the numerical results to the experimental data. The error that can be quantified by mesh refinement is known as the discretization error. For the quantification of the latter one, we selected an established method recommended by the Fluids Engineering Division of ASME [38]. The method is based, in principle, on the generalized Richardson extrapolation theory [39] but has been developed into a more generalized formulation applicable to a wider range of practical CFD cases by Roache [40,41]. The suggested grid convergence index (GCI) method can be regarded as a procedure for uniform reporting on grid refinement studies. The method yields discretization error bands for the investigated variable and thus represents a sophisticated quantification of mesh dependency. However, it is important to note that the GCI method, by definition, does not account for general modeling errors, such as the choice of boundary conditions or turbulence model; only the error due to an insufficient spatial resolution can be quantified by this method.

In the present investigation, the GCI method complied with its following requirements: The grid refinement was done systematically, which means that all grids were refined uniformly in every direction of space and only geometrically similar cells were used. Distances between the target plate and the first nodes off the wall were also scaled to account for changes in y_1^+. As the error was expected to increase with the jet Reynolds number, the mesh sensitivity analysis was carried out for the highest value of Re (Re = 35,000) at the maximum crossflow scheme. The parameters of the different meshes used in the sensitivity analysis are summarized in Table 1, where the mesh cell number N is given along with the local maximum dimensionless wall distance on the target plate.

The local discretization error distribution on the fine grid, which was calculated by application of the GCI method to target plate centerline Nusselt numbers distributions from the three different grids, is shown in Fig. 8.

Aside from some moderate peaks that occurred primarily in the stagnation zones, overall GCI values were quite low. From these observations, we concluded that the meshing parameters from the

Table 1 Parameters of the grids used in the sensitivity analysis with average results for the target plate

	N	Max. y_1^+
Coarse	303,912	2.04
Intermediate	703,010	1.63
Fine	1,535,310	1.25

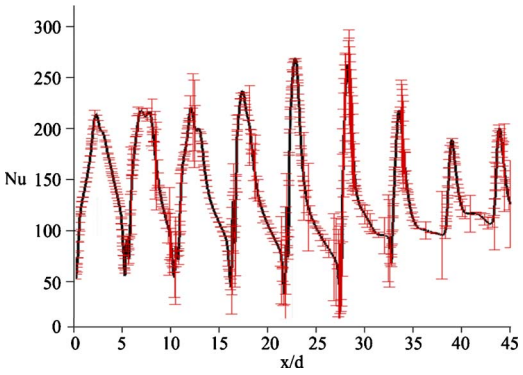

Fig. 8 Local GCI distribution for target plate centerline results on the fine grid

fine grid constituted a good compromise between numerical accuracy and computational effort. The overall discretization uncertainty was estimated to be below 5%. Consequently, the meshing parameters were applied to all grids used in the study.

4 Results and Discussion

4.1 Effect of Jet Reynolds Number. The effect of jet Reynolds number on heat transfer was similar for all investigated configurations. An increase in the jet Reynolds number increased the local heat transfer coefficient throughout the target plate. The form of the correlation developed in Ref. [7] is

$$\mathrm{Nu} = \phi_1 \phi_2 \, \mathrm{Re}^{\mathrm{m}} \, \mathrm{Pr}^{1/3} (\mathrm{H/d})^{0.091} \tag{7}$$

For the present geometry, m=0.8. In order to normalize the heat transfer value, the Nusselt number distribution in Fig. 9 has been referred to $\mathrm{Re}^{0.8}\,\mathrm{Pr}^{1/3}$. We can see that the spanwise averaged Nusselt number ratios were nearly identical for the different Reynolds numbers. This means that the heat transfer characteristics of the flow can be scaled with $\mathrm{Re}^{0.8}$, which is a typical value for a turbulent boundary layer. In the following we will therefore discuss results only for the highest jet Reynolds number of 35,000.

4.2 Effect of Jet-to-Plate Spacing. For a quantification of the effect of jet-to-plate spacing, spanwise averaged Nusselt numbers on the target plate were compared for different arrangements. The results are shown in Fig. 10.

For the maximum crossflow case, as shown in Fig. 10(*a*), the peak in heat transfer was located directly on the jet centerline at the upstream end of the array, where the crossflow was still small. No differences were apparent in the first three jet rows between the arrangements, except for the lower value reached by the inline pattern with H/d=5. As the crossflow developed, the peak position was observed to shift slightly downstream as the increased crossflow displaced the jets. The shapes of the Nusselt number spread were also changed. For jet rows 4–7, the inline pattern was better than the staggered one, the highest value being reached by the jet-to-plate spacings 3 and 4. For the last three jet rows, jet-to-plate spacing 3 was better than spacing 4.

Figure 10(*b*) shows the spanwise averaged Nusselt number distribution in x direction for the medium crossflow. In the middle of the target plate, the peak was nearly directly on the jet centerline. The peak shifted slightly as a result of the increasing jet-induced crossflow. The inline pattern with H/d=3 apparently reached the best heat transfer performance compared with the other arrangements.

Figure 10(*c*) shows the spanwise averaged Nusselt number distribution in x direction for minimum crossflow. There was less variation with different jet-to-plate spacing for the inline pattern unlike the other crossflow schemes. For the staggered pattern, the difference occurs in the zone near the exit.

The above comparison reveals that the largest difference between the inline and staggered pattern occurred in the case of maximum crossflow. The impingement pattern effect increased in significance in the downstream direction. The jets in the staggered pattern were arranged more distributed across the impingement plate compared with those of inline pattern. This in turn caused the distance between the adjacent jets to be larger and the interaction between the jets to be smaller compared with the inline pattern.

There are two main contributions to the heat transfer here: the impingement cooling and the convective heat transfer by the crossflow. We can see from Fig. 9 that the difference between different jet-to-plate spacing occurred mainly in the stagnation zone and the zone near the exit because of different spacing and different crossflow velocity. The local minima between the adjacent jets stayed nearly the same. The narrow jet-to-plate spacing H/d=3 in each case reached the higher value.

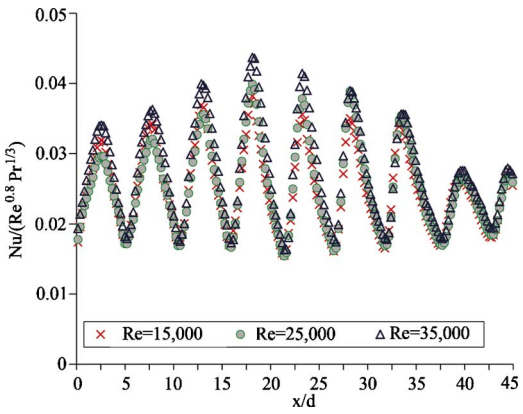

Fig. 9 Spanwise averaged Nusselt number ratios on the target plate (inline pattern, different Reynolds number, H/d=4, and maximum crossflow scheme)

4.3 Effect of Impingement Pattern. Table 2 shows the total area averaged Nusselt number on the target plate for the different arrangements. As already shown in Fig. 8, the normalized Nusselt numbers for all Reynolds numbers investigated were very similar. Therefore, only the results only for the highest Reynolds number are shown. The area used to calculate the area averaged Nusselt number is half of the target plate. For the different crossflow schemes, we obtained the same results that the inline pattern could always reach higher heat transfer coefficients than the staggered one for each jet-to-plate spacing, except for the case of jet-to-plate spacing H/d=5 at maximum crossflow. The inline pattern always performs better than to the staggered pattern. These trends were also found by Florschuetz and co-workers [10,11]. For the inline pattern, the jets are protected from the oncoming crossflow by the upstream jets. For the staggered pattern, the crossflow influences the jets more directly, which causes stronger diffusion and leads to a reduced overall heat transfer performance. The lowest jet-to-plate spacing (H/d=3) was better than the other spacing for both inline and staggered pattern. In the following, we shall therefore discuss local Nusselt numbers only for the jet-to-plate spacing (H/d=3) with inline pattern.

4.4 Effect of Crossflow. Figure 11 shows the spanwise averaged Nusselt number distributions on the target plate for Reynolds number 35,000, jet-to-plate spacing H/d=3, and different crossflow schemes. The flow field for multiple jet systems is very complex and is characterized by two types of interaction, which are jet-to-jet and jet-to-crossflow interferences. The different crossflow schemes consequently affect the interference. The heat transfer rates for maximum crossflow case were clearly much lower than the others. The heat transfer performance in the impinging zone increased first with increasing in the jet-induced crossflow

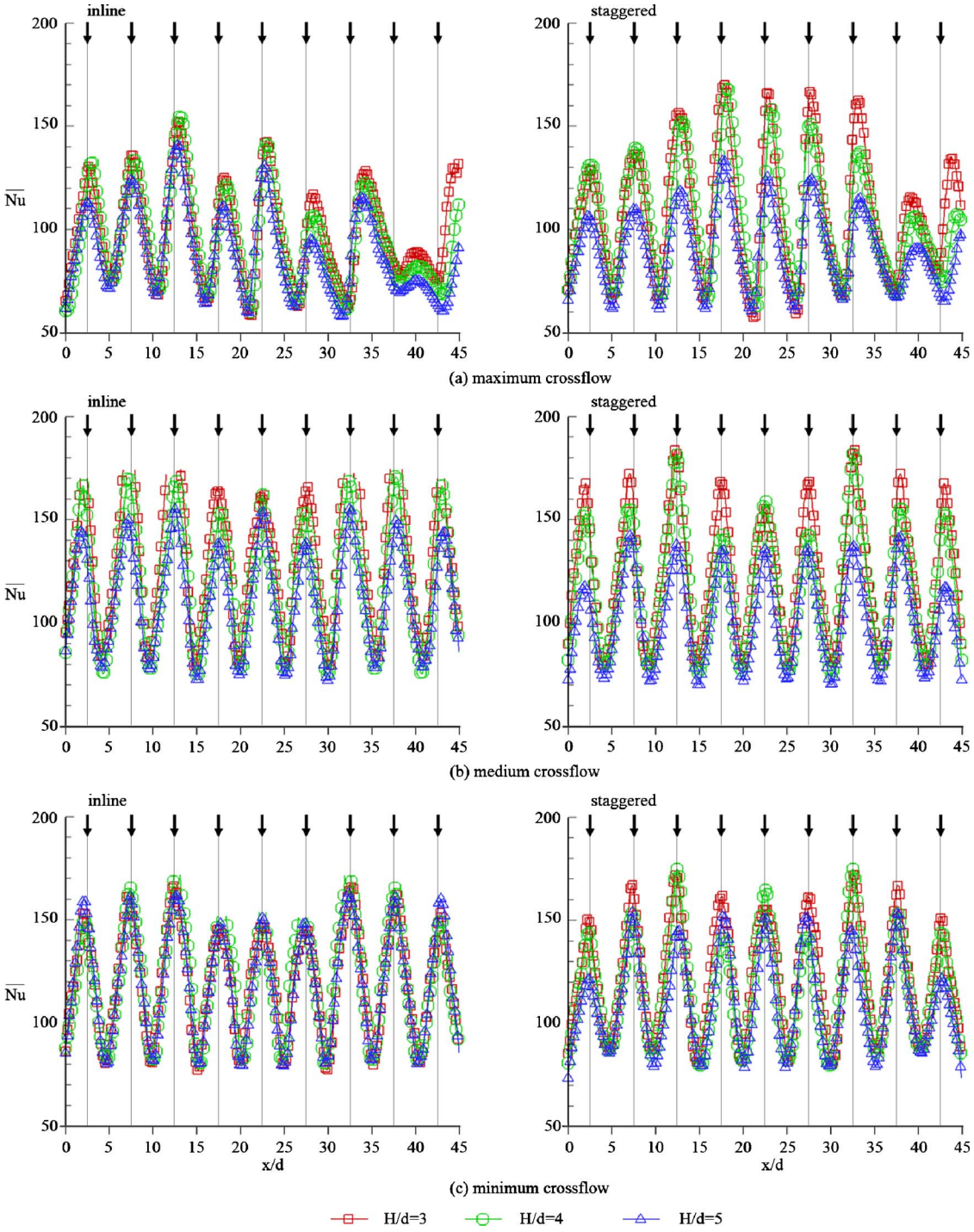

Fig. 10 Spanwise averaged Nusselt number distributions (inline and staggered patterns, Re=35,000, H/d=3, 4, and 5, and different crossflow schemes)

and it suddenly decreased in the last two jets due to the influence of crossflow confining the jet and reducing its coverage. Only the peak values of jet rows 4–6 achieved similar values as those of the other schemes. The upstream regions of target plate achieved lower values, which might be the reason of nonuniform distribution of mass flow caused by the direction of crossflow. The heat transfer in the downstream of the target plate was also lower because the strong crossflow decreased the heat transfer of the jets. The local minima value for the maximum crossflow scheme in the downstream region was lower than the others because the crossflow reduced the jet-to-jet interferences. The differences between the minimum and medium crossflow occurred in the stagnation points and in the local minima between the jets.

4.5 Comparison of Experimental and Numerical Data. In this section, results from the CFD simulations were compared with the experimental data. The objective was to determine the degree of accuracy to which the experimentally obtained heat transfer rates can be predicted and whether the characteristic flow and heat transfer features are represented. For the comparison,

Table 2 Area averaged Nusselt numbers and the relative differences to the inline Nusselt number (inline and staggered patterns, Re=35,000, H/d=3, 4, and 5, and different crossflow schemes)

	Maximum crossflow			Medium crossflow			Minimum crossflow		
	H/d=3	H/d=4	H/d=5	H/d=3	H/d=4	H/d=5	H/d=3	H/d=4	H/d=5
Inline pattern	108.1	96.7	85.1	121.2	112.3	104.8	120.9	115.2	108.4
Staggered pattern	95.8	89.8	87.3	108.2	106.1	97.9	116.3	106.9	99.5
Rel. diff. (%)	11.4	7.1	2.6	10.7	5.5	6.6	3.8	6.2	8.2

only the results for inline pattern with a jet-to-plate spacing of H/d=3 and a Reynolds number of Re=35,000 were considered.

One can see that the averaged Nusselt numbers for the medium and minimum crossflow are nearly identical. This explains by thinking of jet impingement on the target plate as a coupled effect of the actual impingement and the channel flow formed by the jet-induced crossflow. For the maximum crossflow case, jet-induced crossflow is accumulated over the array length and increases toward the exit. This growing mass of crossflow has a significant impact on the heat transfer in the downstream part of the target plate. For the medium and minimum crossflow schemes, the influence of the crossflow is relatively small compared with that of the actual jet impingement. This is due to the jets being able to impinge on the target plate more easily before the crossflow influences them. Consequently, the variation in the crossflow schemes cannot influence the heat transfer performance much and the heat transfer rates on the target plate are more based on the impingement itself.

Table 3 shows a comparison of area averaged Nusselt numbers, which were averaged over the entire target plate. As can be seen, the results from CFD and experiments agree remarkably well for all different crossflow schemes. A qualitative comparison of local heat transfer coefficients is shown next.

In Fig. 12, local Nusselt number distributions on the target plate are shown in the form of contour plots. It should be noted that due to symmetry conditions for the medium and maximum crossflow cases, one row of jets is shown while for the minimum crossflow case, a quarter of the target plate is shown. These areas correspond to the respective sizes of the computational domains used for the representation of the different crossflow cases (refer to Sec. 3.2). Comparing the measured Nusselt number distributions with the CFD results, the overall agreement was quite good. The contours of the heat transfer coefficients were reproduced correctly and the absolute values also agreed very well. Obviously, the complex phenomena of jet-to-jet and jet-crossflow interaction were also represented correctly in the numerical predictions. The spreading behavior of the jets, which can be visually derived from the shape of the Nusselt number contours, was also predicted fairly accurate. This is particularly remarkable, as the numerical prediction of jet spreading is known to be very problematic for two-equation turbulence models [42]. Some deviations could be observed in the zones in-between the individual jets. Here, experimentally determined Nusselt numbers were generally higher than their CFD counterparts. The reason for this could not be fully explored from the available data. One possible reason is test surface heat conduction. The local heat transfer coefficients were determined using the measured wall temperature and the solution of the one-dimensional transient heat conduction in a semi-infinite solid. But

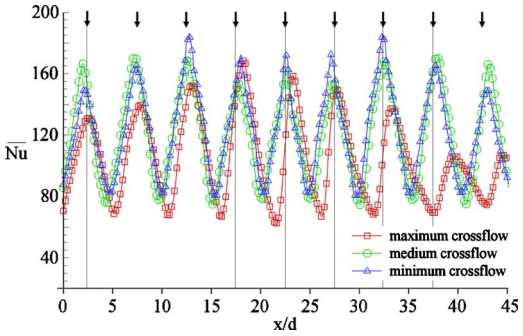

Fig. 11 Spanwise averaged Nusselt number distributions on the target plate (inline pattern, Re=35,000, H/d=3, and different crossflow schemes)

Table 3 Area averaged Nusselt numbers between experiment and CFD and the relative differences to the experiment data (inline pattern, Re=35,000, H/d=3, different crossflow schemes)

	Maximum crossflow	Medium crossflow	Minimum crossflow
Experiment	108.1	121.2	120.9
CFD	101.9	119.6	117.7
Rel. diff. (%)	5.7	1.3	2.6

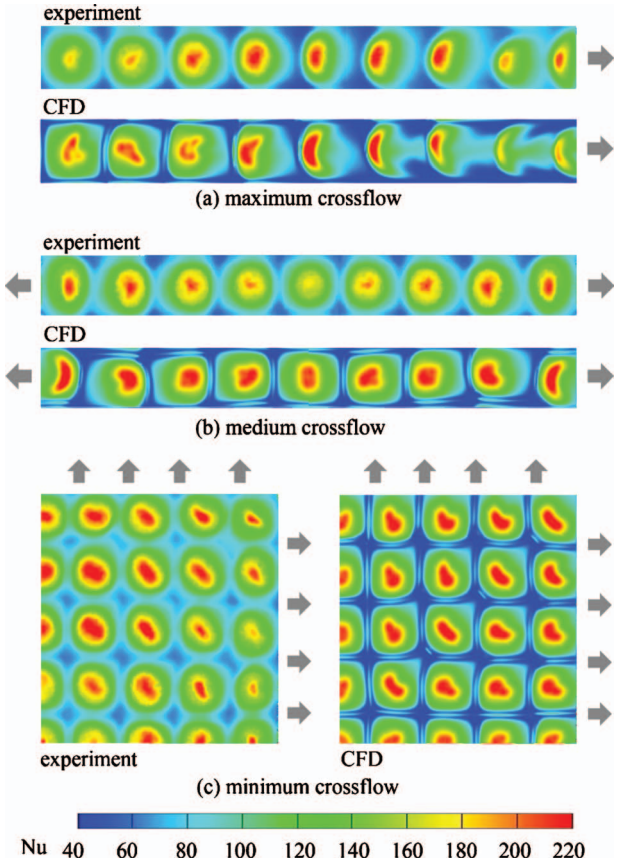

Fig. 12 Comparison of target plate Nusselt number distributions from experiments and CFD (inline pattern, Re=35,000, H/d=3, and different crossflow schemes)

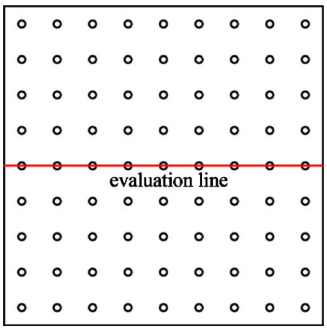

Fig. 13 Position of the line used for the evaluation of local heat transfer coefficients

in reality, the temperature gradients between the stagnation points and the zones in-between the individual jets might result in lateral heat conduction on the target surface. The well-known inadequacy of the two-equation turbulence model in predicting stagnation flows is also one possible reason, as the locations coincided with the secondary impingement zones where the head-on collisions of the wall jets occurred. However, a detailed analysis would require additional flow field studies, e.g., particle image velocimetry (PIV) measurements. Another explanation, at least in part, could be an insufficient spatial resolution in the experiments to fully capture the heat transfer minima. It is also possible that the deviations were related to the relatively high values of discretization errors in the CFD study at these specific regions (refer to Fig. 8). From the visual comparison of the contours in general, it seemed as if in the CFD simulations, the mass flow rate was more homogeneously distributed across the jets. We attributed this to the geometrical shape of the air supply and the inlet temperature gradient across the inlet plenum, so that the jet Reynolds number in the experiments was not as uniform as assumed in the numerical analysis. For the medium and maximum crossflow cases, the jets in the CFD results obviously had a lateral movement perpendicular to the direction of the mainstream flow, which was expressed in the contour plots by a shift in the jet footprint. Naturally, this was associated with a break of symmetry. We attributed these features to the unsteady nature of the flow within the impingement array that were captured to some extent by the CFD simulation. The fact that the unsteadiness was not observed in the experimental results was most likely due to the high frequency of these oscillations. A qualitative comparison of experimental and numerical results is presented in the following.

Regarding numerical predictions, most difficulties lie in the prediction of local heat transfer coefficients (average coefficients do not allow a meaningful conclusion). So in the next step we compare the local values from experimental and CFD along the centerline on the target plate as illustrated in Fig. 13. This allows for a more detailed analysis of the predictive quality of the CFD results.

The comparison of the results from both experiments and CFD is shown in Fig. 14. The overall agreement between the local Nusselt numbers from experiments and from CFD was very good. The key characteristics of multijet impingement heat transfer such as stagnation point values, jet spreading behavior, and jet-crossflow interactions were all reproduced accurately. Particularly remarkable was the good agreement that was achieved for the maximum crossflow case, as we considered this case the most complex one due to the manifold interactions between jet flow and mainstream flow and the associated streamline curvature of the jets. The largest deviations again occurred between pairs of adjacent jets, as already observed in the analysis of the Nusselt number contours (refer to Fig. 11). The inhomogeneous mass flow distribution and the temperature gradient for the incoming flow

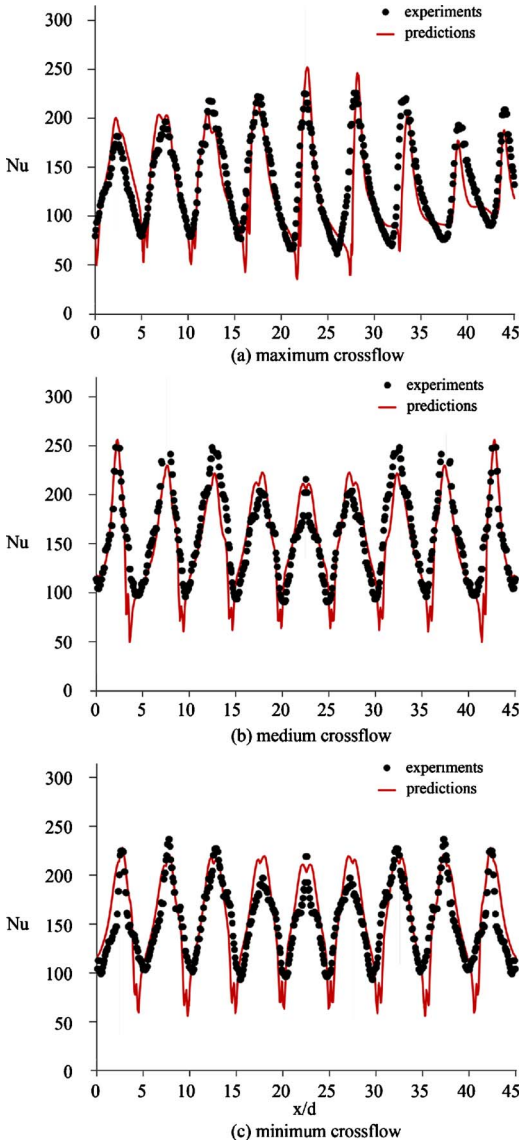

Fig. 14 Comparison of local Nusselt number distributions from experiments and CFD (centerline results, inline pattern, Re=35,000, H/d=3, and different crossflow schemes)

addressed earlier were visible in particular toward the sides of the impingement rig, where the deviations between experimental and numerical results were largest.

4.6 Comparison to Literature Data. A case of the inline pattern was compared with literature data from Son et al. [14], Park et al. [17] and El-Gabry and Kaninski [43]. Figure 15 shows the comparison of the present data and the published results. All experiments were conducted for the case of maximum crossflow, where the flow exits in only one direction. A good overall agreement is found. Although the geometric parameters for the different cases differently, the dependence of the area averaged Nusselt number on the jet Reynolds number in general shows the same trend.

4.7 Pressure Loss. Figure 16 shows the discharge coefficients of the impingement plate and outlet rims for different arrangements. It can be seen that the discharge coefficients of the impingement plate were generally lower than those of the exit rims. One can see that the discharge coefficients of the impingement plate were nearly the same for different Reynolds numbers, different jet-to-plate spacing, and different impingement pattern.

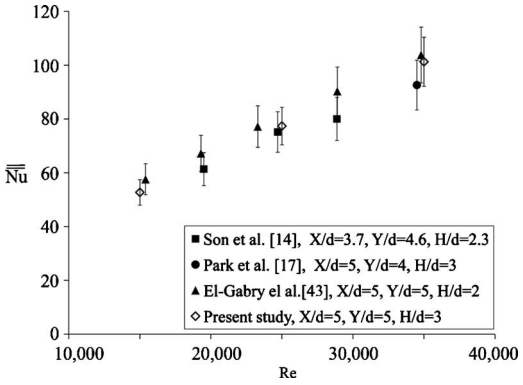

Fig. 15 Comparison to literature for the maximum crossflow scheme

Higher values were reached for the case of maximum crossflow.

The discharge coefficients of the exit rims were nearly independent of Reynolds numbers. The value of exit rims decreased with an increasing jet-to-plate spacing. The discharge coefficients were similar for the case of minimum and medium crossflows but the case of maximum crossflow reached the lower value of exit rim. Note that the staggered pattern reached the higher discharge coefficient of exit rims in general.

5 Conclusions

The present work investigated heat transfer characteristics within an impingement model of inline and staggered jets at different Reynolds numbers. The Nusselt number distributions were measured on the impingement target plate using a transient liquid crystal technique. Jet exit temperatures were interpolated both spatially and temporally to determine the reference temperature for the calculation of the heat transfer coefficient accurately. An increase in the jet Reynolds number increased the local heat transfer coefficients throughout the target plate. The heat transfer characteristics of the flow for the inline and staggered impingement plates could be scaled with $Re^{0.8}$. Independent of the crossflow scheme, the inline pattern always outperformed the staggered configuration in terms of achievable heat transfer rates for all jet-to-plate spacings. Heat transfer rates for the maximum crossflow case were clearly much lower than the medium and minimum crossflow cases. The differences between the minimum and medium crossflows occurred in the stagnation points and in the local minima between the jets. The jet-to-plate spacing ($H/d=3$) achieved the highest overall heat transfer coefficients with both inline and staggered patterns. The discharge coefficients of the impingement plate are similar for different arrangements. Some differences occur for the discharge coefficients of the exit rims for different Reynolds numbers and jet-to-plate spacings.

In addition to the experimental measurements, a numerical investigation was conducted. Simulations were carried out with a state-of-the-art commercial CFD code using a two-equation turbulence model that, to our knowledge, is well suitable for the prediction of multijet impingement configurations. The motivation was to evaluate whether CFD can be used as a design tool in the future optimization of such impingement configurations. The inline configuration at the highest Reynolds number and the lowest separation distance was selected for the CFD study. High numerical quality was assured by a detailed mesh sensitivity analysis. The accuracy of the predicted heat transfer results was assessed by a comparison of area averaged values, Nusselt number contours, and local heat transfer values. The overall agreement was very good and even local heat transfer coefficients were predicted at high accuracy. Some deviations occurred in the area between pairs of adjacent jets. From the comparison of experiments and CFD we concluded that for such a type of generic multijet impingement configuration, present CFD codes can be a suitable means in the design process. Based on this evaluation, future optimization of the impingement pattern could be done numerically at reliable predictive accuracy and low costs.

Nomenclature

A = open area of the exit rims (m^2)
c = specific heat (J/kg K)
C_d = discharge coefficient
d = impingement jet diameter (m)
h = heat transfer coefficient (W/m^2 K)
H = jet-to-plate spacing (m)
k = thermal conductivity (W/m K)
L = target plate length (m)
$\dot{m}$ = mass flow (kg/s)
N = discrete interval
$\underline{Nu}$ = Nusselt number, based on jet diameter
$\overline{Nu}$ = spanwise averaged Nusselt number
$\overline{\overline{Nu}}$ = area averaged Nusselt number
ΔP = pressure loss (Pa)
Pr = Prandtl number
Re = Reynolds number, based on jet diameter
T = temperature (°C)
t = time (s)
u = velocity (m/s)
x,y = coordinates (m)
X = spanwise jet-to-jet spacing (m)
Y = streamwise jet-to-jet spacing (m)

Greek Symbols

ρ = density (kg/m^3)
τ = shear (N/m^2)
Θ = temperature ratio
ν = thermal conductivity (W/m K)

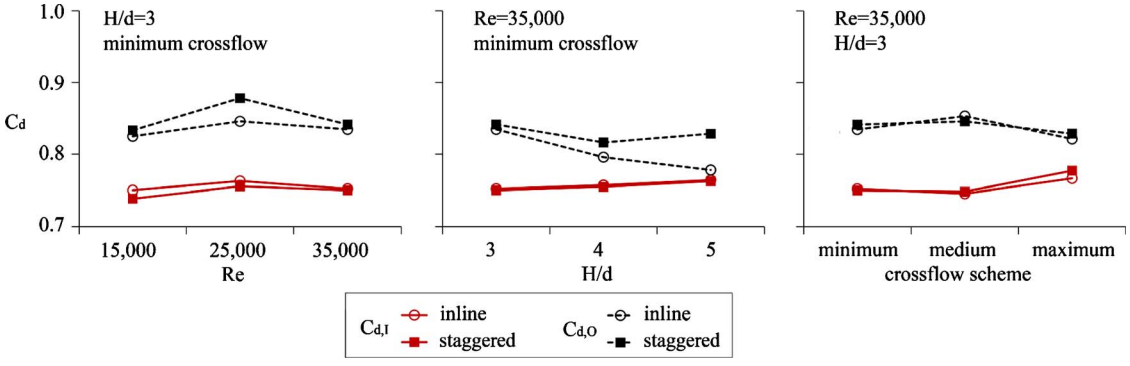

Fig. 16 Discharge coefficients of the impingement plate and exit rims for different arrangements

Superscript

+ = dimensionless distance

Subscripts

0 = initial condition
1 = index for first cell off the wall
B = bulk
i = index
I = impingement plate
ideal = ideal air condition
O = exit rim
W = wall

References

[1] Boyce, M. P., 2001, *Gas Turbine Engineering Handbook*, 2nd ed., Gulf, USA.
[2] Martin, H., 1977, "Heat and Mass Transfer Between Impinging Gas Jets and Solid Surfaces," Adv. Heat Transfer, **13**, pp. 1–60.
[3] Han, B., and Goldstein, R. J., 2001, "Jet-Impingement Heat Transfer in Gas Turbine Systems," Ann. N. Y. Acad. Sci., **934**(1), pp. 147–161.
[4] Jambunathan, K., Lai, E., Moss, M., and Button, B., 1992, "A Review of Heat Transfer Data for Single Circular Jet Impingement," Int. J. Heat Fluid Flow, **13**, pp. 106–115.
[5] Viskanta, R., 1993, "Heat Transfer to Impinging Isothermal Gas and Flame Jets," Exp. Therm. Fluid Sci., **6**, pp. 111–134.
[6] Weigand, B., and Spring, S., 2009, "Multiple Jet Impingement—A Review," International Symposium on Heat Transfer in Gas Turbine Systems, Antalya, Turkey.
[7] Kercher, D. M., and Tabakoff, W., 1970, "Heat Transfer by a Square Array of Round Air Jets Impinging Perpendicular to a Flat Surface Including the Effect of Spent Air," ASME J. Eng. Power, **92**, pp. 73–82.
[8] Hollworth, B. R., and Berry, R. D., 1978, "Heat Transfer From Arrays of Impinging Jets With Large Jet-to-Jet Spacing," ASME J. Heat Transfer, **100**, pp. 352–357.
[9] Metzger, D. E., Florschuetz, L. W., Takeuchi, D. I., Behee, R. D., and Berry, R. A., 1979, "Heat Transfer Characteristics for Inline and Staggered Arrays of Circular Jets With Crossflow of Spent Air," ASME J. Heat Transfer, **101**, pp. 526–531.
[10] Florschuetz, L. W., Berry, R. A., and Metzger, D. E., 1980, "Periodic Streamwise Variations of Heat Transfer Coefficients for Inline and Staggered Arrays of Circular Jets With Crossflow of Spent Air," ASME J. Heat Transfer, **102**, pp. 132–137.
[11] Florschuetz, L. W., Truman, C. R., and Metzger, D. E., 1981, "Streamwise Flow and Heat Transfer Distributions for Jet Array Impingement With Crossflow," ASME J. Heat Transfer, **103**, pp. 337–342.
[12] Van Treuren, K. W., Wang, Z., Ireland, P. T., and Jones, T. V., 1994, "Detailed Measurements of Local Heat Transfer Coefficient and Adiabatic Wall Temperature Beneath an Array of Impinging Jets," ASME J. Turbomach., **116**, pp. 369–374.
[13] Van Treuren, K. W., Wang, Z., Ireland, P. T., Jones, T. V., and Kohler, S. T., 1996, "Comparison and Prediction of Local and Average Heat Transfer Coefficients Under an Array of Inline and Staggered Impinging Jet," ASME Paper No. 96-GT-163.
[14] Son, C., Gillespie, D., and Ireland, P. T., 2000, "Heat Transfer and Flow Characteristics of an Engine Representative Impingement Cooling System," ASME Paper No. 2000-GT-219.
[15] Bailey, J. C., and Bunker, R. S., 2002, "Local Heat Transfer and Flow Distributions for Impinging Jet Arrays of Dense and Sparse Extent," ASME Paper No. GT-2002-30473.
[16] Bailey, J. C., Intile, J., Fric, T. F., Tolpadi, A. K., Nirmalan, N. V., and Bunker, R. S., 2003, "Experimental and Numerical Study of Heat Transfer in a Gas Turbine Combustor Liner," ASME J. Eng. Gas Turbines Power, **125**, pp. 994–1002.
[17] Park, J., Goodro, M., Ligrani, P., For, M., and Moon, H. K., 2007, "Separate Effects of Mach Number and Reynolds Number on Jet Array Impingement Heat Transfer," ASME J. Turbomach., **129**, pp. 269–280.
[18] Goodro, M., Park, J., Ligrani, P., Fox, M., and Moon, H. K., 2008, "Effects of Hole Spacing on Spatially-Resolved Jet Array Impingement Heat Transfer," Int. J. Heat Mass Transfer, **51**, pp. 6243–6253.
[19] Geers, L. F. G., Tummers, M. J., Bueninck, T. J., and Hanjalic, K., 2008, "Heat Transfer Correlation for Hexagonal an In-Line Arrays of Impinging Jets," Int. J. Heat Mass Transfer, **51**, pp. 5389–5399.
[20] Attalla, M. A. M., 2005, "Experimental Investigation of Heat Transfer Characteristics Form Arrays of Free Impinging Circular Jets and Hole Channels," Ph.D. thesis, Uni-Magdeburg, Germany.
[21] Spring, S., Weigand, B., Krebs, W., and Hase, M., 2008, "CFD Heat Transfer Predictions for a Gas Turbine Combustor Impingement Cooling Configuration," Proceedings of the 12th International Symposium on Transport Phenomena and Dynamics of Rotating Machinery, Honolulu, HI, Paper No. ISROMAC12-2008-20222.
[22] Polat, S., Huang, B., Mujumdar, A. S., and Douglas, W. J. M., 1989, "Numerical Flow and Heat Transfer Under Impinging Jets: A Review," Annu. Rev. Heat Transfer, **2**, pp. 157–197.
[23] Zuckerman, N., and Lior, N., 2005, "Impingement Heat Transfer: Correlations and Numerical Modeling," ASME J. Heat Transfer, **127**, pp. 544–552.
[24] Rao, G. A., Kitron-Belinkov, M., and Levy, Y., 2009, "Numerical Analysis of a Multiple Jet Impingement System," ASME Paper No. GT-2009-59719.
[25] Zu, Y. Q., Yan, Y. Y., and Maltson, J. D., 2009, "CFD Prediction for Multi-Jet Impingement Heat Transfer," ASME Paper No. GT-2009-59488.
[26] Spring, S., Lauffer, D., Weigand, B., and Hase, M., 2010, "Experimental and Numerical Investigation of Impingement Cooling in a Combustor Liner Heat Shield," ASME J. Turbomach., **132**, p. 011003.
[27] Obot, N. T., and Trabold, T. A., 1987, "Impingement Heat Transfer Within Arrays of Circular Jets: Part 1—Effects of Minimum, Intermediate, and Complete Crossflow for Small and Large Spacing," ASME J. Heat Transfer, **109**, pp. 872–879.
[28] Kanokjaruvijit, K., and Martinez-Botas, R. F., 2008, "Heat Transfer and Pressure Investigation of Dimple Impingement," ASME J. Turbomach., **130**, p. 011003.
[29] Ireland, P. T., and Jones, T. V., 2000, "Liquid Crystal Measurements of Heat Transfer and Surface Shear Stress," Meas. Sci. Technol., **11**, pp. 969–986.
[30] Wagner, G., Kotulla, M., Ott, P., Weigand, B., and von Wolfersdorf, J., 2004, "The Transient Liquid Crystal Technique: Influence of Surface Curvature and Finite Wall Thickness," ASME Paper No. GT2004-53553.
[31] Kays, W. M., Crawford, M. E., and Weigand, B., 2004, *Convective Heat and Mass Transfer*, McGraw-Hill, New York.
[32] Poser, R., von Wolfersdorf, J., and Lutum, E., 2007, "Advanced Evaluation of Transient Heat Transfer Experiments Using Thermochromic Liquid Crystals," Proc. Inst. Mech. Eng., Part A, **221**(6), pp. 793–801.
[33] Kline, S. J., and McClintock, F. A., 1953, "Describing Uncertainties in Single-Sample Experiments," Mech. Eng., **75**, pp. 3–8.
[34] Yan, Y., and Owen, J. M., 2002, "Uncertainties in Transient Heat Transfer Measurements With Liquid Crystal," Int. J. Heat Fluid Flow, **23**, pp. 29–35.
[35] Kingsley-Rowe, J. R., Lock, G. D., and Owen, J. M., 2005, "Transient Heat Transfer Measurements Using Thermochromic Liquid Crystal: Lateral-Conduction Error," Int. J. Heat Fluid Flow, **26**, pp. 256–263.
[36] Spring, S., Weigand, B., Krebs, W., and Hase, M., 2006, "CFD Heat Transfer Predictions of a Single Circular Jet Impinging With Crossflow," AIAA Paper No. 2006-3589.
[37] Menter, F., 1994, "Two-Equation Eddy-Viscosity Turbulence Models for Engineering Applications," AIAA J., **32**(8), pp. 1598–1605.
[38] Celik, I. B., Ghia, U., Roache, P. J., Freitas, C. J., Coleman, H., and Raad, P. E., 2008, "Procedure for Estimation and Reporting of Uncertainty Due to Discretization in CFD Applications," ASME J. Fluids Eng., **130**, p. 078001.
[39] Richardson, L., and Gaunt, A., 1927, "The Deferred Approach to the Limit. Part I. Single Lattice. Part II. Interpenetrating Lattices," Philos. Trans. R. Soc. London, Ser. A, **226**, pp. 299–361
[40] Roache, P. J., 1994, "A Method for Uniform Reporting of Grid Refinement Studies," ASME J. Fluids Eng., **116**, pp. 405–413.
[41] Roache, P. J., 2003, "Conservatism of the Grid Convergence Index in Finite Volume Computations on Steady-State Fluid Flow and Heat Transfer," ASME J. Fluids Eng., **125**, pp. 731–735.
[42] Pope, S. B., 1978, "An Explanation of the Turbulent Round-Jet/Plane-Jet Anomaly," AIAA J., **16**(3), pp. 279–281.
[43] El-Gabry, L. A., and Kaminski, D. A., 2005, "Experimental Investigation of Local Heat Transfer Distribution on Smooth and Roughened Surfaces Under an Array of Angled Impinging Jets," ASME J. Turbomach., **127**, pp. 532–544.

Nanofluid Convection in Microtubes

Joohyun Lee
e-mail: jhyunl@stanford.edu

Patricia E. Gharagozloo
e-mail: perahm@stanford.edu

Babajide Kolade

John K. Eaton

Kenneth E. Goodson

Department of Mechanical Engineering,
Stanford University,
Stanford, CA 94305

While there has been much previous research on the thermal conductivity and convection performance of nanofluids, these data are rarely reported together with effective viscosity data that govern the relevance for heat exchanger applications. We report here the effective convection coefficient and viscosity in microtubes ($D=0.5$ mm) along with stationary thermal conductivity measurements for nanofluids based on spherical particles (Al_2O_3, ZnO, and CuO) and carbon nanotubes. Sample data include an effective convection coefficient increase of 5% for 3 vol % Al_2O_3/DI water nanofluid, 13.3% for 4 vol % CuO/DI water nanofluid, and 11.6% for 0.2 vol % Carbon nanotube(CNT)/DI water nanofluid. When considered together with our viscosity measurement on the same fluids, we find that the only the CNT-based nanofluids are promising for microfluidic heat exchangers. [DOI: 10.1115/1.4001637]

Keywords: nanofluid, convection, heat transfer, carbon nanotubes, heat exchanger

1 Introduction

Fluid design considering thermal and viscous properties is a critical aspect of cooling system optimization for a variety of applications. This is particularly important for single-phase microfluidic heat exchangers for which the fluid thermal conductivity governs the thermal resistance and the viscosity governs the required pumping power at a given flowrate [1]. There is considerable interest in determining whether conventional heat transfer fluids, such as water, oils, and ethylene glycol, can be improved through nanoscale impurities. Recent data have suggested dramatic increases in the effective thermal conductivity of nanofluids with volume concentrations near or below 1% although the data have been inconsistent and incomplete from the perspective of fluid design. To make a rigorous determination of the potential relevance of nanofluids for heat exchangers, any increase in effective thermal conductivity must be weighed against the increase in effective viscosity.

Stationary nanofluid thermal conductivity data can be compared using an augmentation factor α_{cond}, which is defined using $k_{nano}/k_{bf}=1+\alpha_{cond}\phi$. In this equation, k_{nano} indicates the thermal conductivity of the nanofluid, k_{bf} is the conductivity of the base fluid, and ϕ is the nanoparticle volume concentration. Eastman et al. [2] reported a 60% thermal conductivity increase with 5 vol % of CuO/water nanofluid, yielding $\alpha_{cond}=12$. In a recent review, Kabelac and Kuhnke [3] reported that α_{cond} ranges from 2.5 to 6 for Al_2O_3/water and from 2.5 to 12 for CuO/water nanofluids. A significantly higher thermal conductivity increase was reported for Carbon nanotube(CNT)/water nanofluids. For example, Wen and Ding [4] measured $\alpha_{cond}=37$ and Zhang et al. [5] reported $\alpha_{cond}=50$ with CNT/water nanofluid. Regarding temperature dependence of nanofluid thermal conductivity, Chon et al. [6] reported that α_{cond} of Al_2O_3/water nanofluid varies from 2 to 7 at 20°C and at 70°C, respectively. Wen and Ding [4] observed α_{cond} of CNT/water nanofluid varies from 50 to 100 at 10°C and at 60°C, respectively. Most thermal conductivity data were obtained using the transient hot wire method, which measures the transient thermal response of a fine wire immersed in stationary fluids. In most cases, nanofluids were prepared by sonication of commercially available nanoparticles in a base fluid mixture. Frequently used particles included Al_2O_3, CuO, and CNT. The inconsistency of the past data indicates that many parameters can affect the thermal conductivity of nanofluids, such as particle size and shape, as well as the nanofluid preparation method and the fluid temperature.

Although there has been some research on nanofluid convection in macroscale tubes, these are rarely combined with measurements of pressure drop and effective viscosity. For consideration of convection applications, we define the convection heat transfer and viscosity augmentation factors α_{conv} and α_{visc} in an analogous manner to the thermal conductivity augmentation factor, as $h_{nano}/h_{bf}=1+\alpha_{conv}\phi$ and $\mu_{nano}/\mu_{bf}=1+\alpha_{visc}\phi$, respectively. Xuan and Li [7] measured 60% heat transfer coefficient increase with 2 vol % Cu/water nanofluid, which corresponds to $\alpha_{conv}=30$ under turbulent flow condition in a 10 mm diameter tube. They reported no change in the pressure drop with the addition of nanoparticles ($\alpha_{visc}=0$). Ding and co-workers [8,9] measured a substantial heat transfer improvement with Al_2O_3/water($\alpha_{conv}=30$) and CNT/water($\alpha_{conv}=350$) nanofluids under laminar flow conditions in a 4.5 mm diameter tube. Pressure drop data were not reported for their experiments. Lee and Mudawar [10] did not observe a large heat transfer increase ($\alpha_{conv}=3$) in a 341 μm hydraulic diameter microchannel with Al_2O_3/water nanofluid. They found that the pressure drop increased much more than expected from effective medium models. Rea et al. [11] and Williams et al. [12] investigated the convective heat transfer of Al_2O_3/water and Zirconia/water nanofluids in laminar and turbulent conditions, respectively. The results showed that the heat transfer coefficients and pressure drop of nanofluids can be accurately predicted by the traditional models. Because there are so few data available for the convective heat transfer and pressure drop of nanofluids, their usefulness as a heat transfer liquid in microchannels is still open to debate.

The present work measures the effective thermal conductivities in a laminar convection situation and viscosities of nanofluids containing CNTs as well as spherical oxide nanoparticles in a 500 μm microtube in laminar flow. The data are compared with stationary thermal conductivity data, also measured here for the same fluids. Nanofluids are prepared by using intensive sonication of the nanoparticles and base fluid mixture. To characterize nanofluids, we measured the nanoparticle size in nanofluids using a dynamic light scattering (DLS) system. Furthermore, SEM images were taken to investigate the morphology of nanoparticles.

Contributed by the Heat Transfer Division of ASME for publication in the JOURNAL OF HEAT TRANSFER. Manuscript received December 12, 2009; final manuscript received March 16, 2010; published online July 7, 2010. Assoc. Editor: Robert D. Tzou.

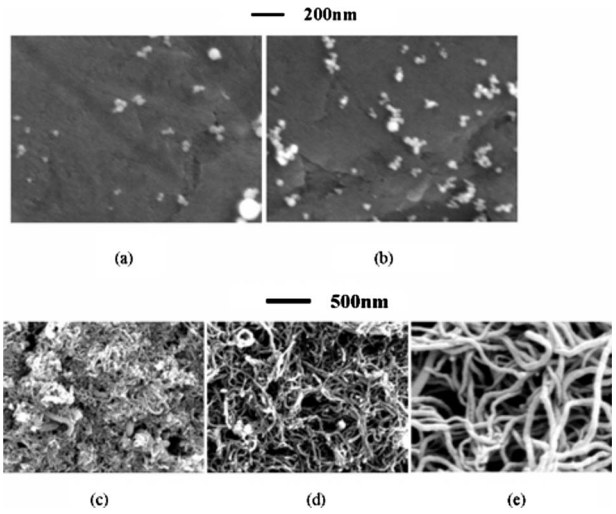

Fig. 1 Scanning electron microscopy images of (*a*) Al_2O_3 nanoparticles(40–50 nm), (*b*) CuO nanoparticles(13–37 nm), (*c*) multiwall CNT(A) (10–30 nm and 1–10 μm), (*d*) multiwall CNT(B) (10–30 nm and 0.5–50 μm), and (*e*) multiwall CNT(C) (40–60 nm and 5–15 μm) after evaporation of deionized water in nanofluids

2 Nanofluid Preparation and Preliminary Characterization

Nanofluids were prepared by applying a strong 1 h sonication using an ultrasonic probe (Hielscher Ultrasonics, Teltow, Germany) of commercially available nanoparticles and deionized water mixture. The Al_2O_3, CuO, and ZnO nanoparticles were purchased from Alfa Aesar Corp., Ward Hill, MA, and multiwall Carbon nanotubes (A), (B), and premade Al_2O_3 nanofluids were purchased from Sigma–Aldrich, St. Louis, MO. Multiwall CNT(C) was purchased from SES Research, Houston, TX. In the case of CNT/DI water nanofluids, gum arabic was added as a surfactant to produce a stable suspension. The prepared oxide nanofluids were stable for approximately 6 h and some sedimentation was observed after that period. The average particle size of spherical nanoparticles was measured by a particle size analyzer (90Plus, BIC Corp., Holtsville, NY). This equipment is based on the principle of DLS. The measured particle size was 155 nm for Al_2O_3/DI water nanofluids, 326 nm for CuO/DI water nanofluids, 371 nm for ZnO/DI water nanofluid, and 90 nm for premade Al_2O_3/DI water nanofluids. The measured particle size was at least four times larger than the nominal particle size claimed by the vendor. This finding implies that there are numerous agglomerated nanoparticles in the prepared nanofluids. Several efforts such as pH variation and a longer sonication time were attempted to separate the agglomerated nanoparticles in hopes of obtaining higher thermal conductivity increase. However, an effective particle size reduction method was not found. Figure 1 shows SEM images of the Al_2O_3, CuO nanoparticles, and three different kinds of multiwall CNT. For the sample preparation, several droplets of nanofluids were placed on the sample holder by pipette and dried in air. After the nanofluids were completely dried, a thin gold layer was applied using a sputter coater.

The SEM images showed that numerous particles were agglomerated for Al_2O_3 and CuO nanoparticles as expected. The agglomerated size was approximately equal to the DLS result. The SEM images of the three CNT samples show very different CNT shapes. The CNT(A) was composed of some short, irregular carbon tubes and many amorphous carbon pieces. On the other hand, the CNT(B) and CNT(C) had relatively long, uniform tube shape.

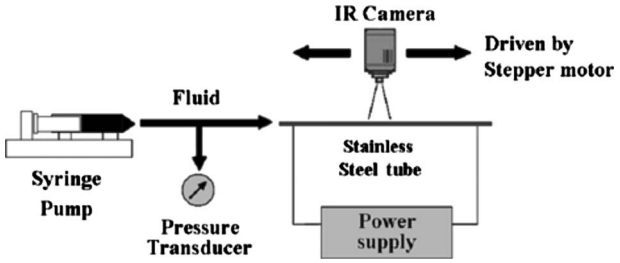

Fig. 2 Experimental apparatus of convection and pressure drop measurement. infrared camera measures the outside wall temperature of stainless steel tube heated by power supply; pressure transducer measures the pressure drop in the microtube

3 Thermal Convection Experiments in Microtubes

A simple microtube experiment was developed to measure the convection performance of nanofluids. Figure 2 illustrates the experimental apparatus. A 10 cm long stainless steel tube (Goodfellow Corp., Oakdale, PA) with an inside diameter of 500 μm was used as the test section. A syringe pump delivered fluid into the microtube at a constant flowrate. The test section was heated by passing dc power along the tube length. A constant heat flux condition was achieved along the tube due to the low thermal conductivity (16.3 W/m K) of stainless steel. A midwavelength (3–5 μm) infrared (IR) camera (Indigo Systems Corp., Goleta, CA) was mounted on a stepper motor driven traverse, which allowed the IR camera to move along the whole test section. A pressure transducer was connected near the inlet of the microtube to measure the pressure drop.

The calibration of the IR camera was conducted by using an electrically heated copper block heat exchanger. The microtube was connected to the outlet of the heat exchanger. Water was pumped into the heat exchanger through the microtube at a high flowrate. The calibration curves were obtained by measuring the copper block temperature with a K-type thermocouple and correlating the temperature with the intensity of the tube image taken by the IR camera.

Figure 3 shows the wall temperature data for DI water, 0.1 vol % and 0.2 vol % concentration CNT(B)/DI water nanofluids. The flowrate was 7 ml/min, the corresponding Reynolds number was 330, and 10 W power was applied to the test section. At the downstream region, the wall temperature decreased mono-

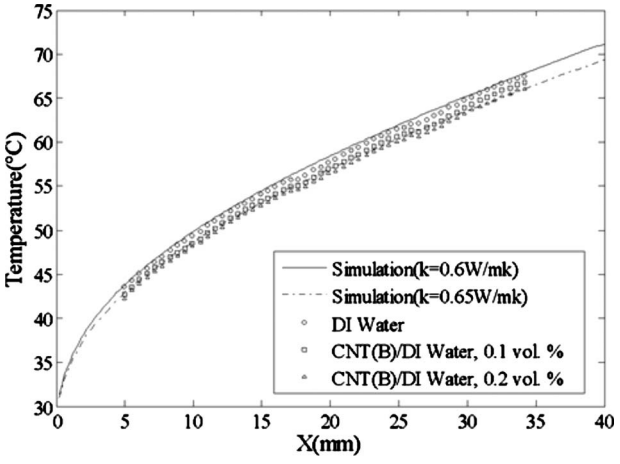

Fig. 3 Wall temperature distributions of DI water, 0.1 vol % and 0.2 vol % CNT(B)/DI water nanofluid data; effective thermal conductivity is extracted by performing conjugate simulation

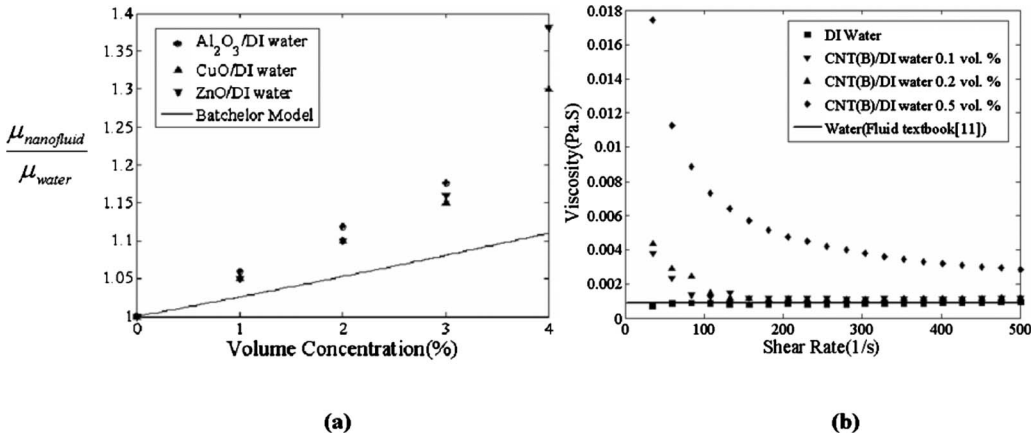

Fig. 4 (*a*) **Effective viscosity data of Al_2O_3/DI water, CuO/DI water, and ZnO/DI water nanofluids. Viscosity data were obtained by measuring the pressure drop in the microtube. Batchelor model of particle laden flow fail to predict the nanofluid viscosity.** (*b*) **Viscosity variation in CNT(B)/DI water nanofluids as a function of shear rate showing non-Newtonian shear-thinning behavior. Viscosity was measured using a rheometer.**

tonically with the increasing particle volume concentration, which indicates the effective thermal conductivity increase in the nanofluids. In order to estimate the thermal conductivity increase, a conjugate simulation was conducted. In the simulation, a constant thermal conductivity was used so the simulation did not consider the temperature-dependent thermal conductivity. A heat loss from the tube surface to the ambient air due to the natural convection was considered in the simulation based on the correlation provided by Churchill and Chu [13]. The calculated value of the nanofluid thermal conductivity was relatively insensitive to the natural convection heat transfer coefficient used in the analysis. For example, a doubling of the heat transfer coefficient resulted in only a 3% change in the calculated thermal conductivity. Validation of this experiment was achieved by confirming that results for plain water matched the simulation result within 1°C. After the simulation was matched with the water data, the thermal conductivity of the fluid in the simulation was increased until the tube wall temperature in the simulation matched the nanofluid temperature data. The value of the conductivity, which produced the best fit to the temperature data, was taken as the effective thermal conductivity of the nanofluid. The possible sources of measurement uncertainty were IR camera noise and calibration uncertainty, electrical power measurements of the applied heat flux, estimates of the convective losses, and thermocouple uncertainty. The biggest contribution to the uncertainty in the effective thermal conductivity was the IR camera, which contributed 2.1% uncertainty. The total uncertainty in the effective thermal conductivity measurements was less than 5.2%. This estimate was confirmed by repeated measurements of plain water, which always fell within 4% of the known value. One concern was that a given nanofluid could leave a residue on the tube surface, which would affect subsequent measurements. The tube was thoroughly rinsed with DI water between nanofluid measurements and the water measurements were repeated to confirm that there was no remaining effect of the nanofluid.

The effective thermal conductivity was increased by 8.3% for 0.2% volume concentration CNT(B)/DI water nanofluids. The corresponding α_{conv} value was 41.5. CNT nanofluids with higher concentration could not be measured due to the tube clogging problem. The CNT nanofluid at 0.3 vol % could not be pumped through the microtube by the syringe pump. The same procedures were carried out for the oxide nanofluids with concentrations ranging from 1 vol % to 4 vol %.

It is important to note that our analysis relating the tube wall temperature distribution to fluid conductivity assumes that the conductivity of the nanofluid is uniform. It is possible that the nanofluid particles could produce a nonuniform conductivity in the tube. In any case, the present measurements yield an effective conductivity value, which is what would be needed for the analysis of a convective heat transfer system.

The viscosity data for nanofluids were obtained by measuring the pressure drop in the microtube. The hydrodynamic entrance length was 7.5 mm when the Re number was 300. When fully developed, the laminar flow is assumed along the entire tube, a circular Poiseuille flow is achieved and the viscosity of fluid is directly proportional to the pressure drop in the tube. The circular Poiseuille flow is given in the following equation:

$$Q = -\frac{\pi d^4}{128\mu}\frac{dp}{dx} \tag{1}$$

In this equation, Q is a flowrate and d is an inner diameter of the tube. Therefore, the effective viscosity of the fluid could be determined by measuring the pressure drop through the microtube.

The uncertainty of the effective viscosity measurement was estimated to be less than 5% considering the uncertainty of the flowrate from the syringe pump and the pressure measurement uncertainty [14]. The experiment was validated by confirming that the measured viscosity of DI water matched tabulated values. The pressure drop with pure water was measured after each nanofluid measurement to ensure that the tube had not been partially clogged by nanoparticles. Figure 4(*a*) shows viscosities of the oxide nanofluids compared with water viscosity as a function of the particle volume concentration. The viscosity of nanofluids was increased significantly as a strong function of the particle volume concentration. The traditional Batchelor model of particle laden fluid [15] underpredicts the increase in the viscosity of nanofluids. The agglomerated nanoparticles appeared to increase the viscosity more rapidly than predicted by the Batchelor model. The Batchelor model explains the effective viscosity of a spherical particle laden fluid by considering the effect of hydrodynamic interaction of pairs of spheres and Brownian motion. The equation is shown below.

$$\mu^* = \mu(1 + 2.5\phi + 6.2\phi^2) \tag{2}$$

Here, μ^* is the effective viscosity, μ is the base fluid viscosity, and ϕ is the volume concentration of particles.

The viscosity of CNT(B)/DI water nanofluid was also measured by a rheometer (AR2000, TA Instruments, New Castle, DE). Figure 4(*b*) presents the viscosity variation in the CNT(B)/DI water nanofluid as a function of shear rate. The viscosity decreased ex-

Table 1 Measured thermal conductivities and viscosities of various nanofluids: all data are taken from microtube experiment

	Volume concentration (%)	k_{eff} (W/m K)	μ_{eff} ((Pa s)$\times 10^{-3}$)
Al_2O_3/DI water	3	0.63	7.13
Premade Al_2O_3/DI water	8	0.7	1.05
CuO/DI water	4	0.68	1.23
ZnO/DI water	4	0	1.16
CNT(A)/DI water	0.2	0	1.16
CNT(B)/DI water	0.2	0.65	1.09
CNT(C)/DI water	0.2	0.67	1.16

ponentially as the shear rate was increased over the entire shear rate of 0–500 (1/s). Thus the CNT(B)/DI water nanofluid has non-Newtonian shear-thinning behavior.

All the thermal conductivity and viscosity data obtained from microtube experiment are summarized in Table 1 at the maximum volume concentration.

4 Stationary Thermal Conductivity Measurements

The thermal conductivity of stationary nanofluids was also measured by the apparatus shown in Fig. 5 [16]. One inch square, copper plates spaced 500 μm apart hold the nanofluid. This spacing yields an average Rayleigh number of less than 10^3 and scaling analysis confirms that bulk fluidic motion due to buoyancy forces is negligible. A 250 μm thick Kapton heater (Omega/KHLV-101) generates Joule heat, which conducts across the nanofluid, and dissipates into a Peltier cooler and heat sink. A heat flux sensor (Omega/HFS-3) monitors the heat flux. The temperature distribution is measured with a high-resolution infrared microscope (QFI/Infrascope). The IR focal plane array is 256×256 InSb with 2–5.5 μm wavelength detection and 0.1 K temperature sensitivity. A 15×, 1.0 numerical aperture, Si/Ge objective obtains a 2.8 μm resolution. The 256 temperature lines are ensemble averaged. An encasing humidification chamber reduces evaporation.

A 20 μm thick polyester film covers the fluidic opening, serves as a uniform emissivity emitter, counteracts averaging effects from the IR penetration in water, and reduces fluid evaporation. The heat flux traveling through the film is calculated using a thermal resistor network as less than 0.06% of the applied heat flux. A COMSOL finite element thermal model predicts the difference in the calculated thermal conductivity from the temperature of the film compared with the fluid temperature of less than 1%. The emissivity is calibrated for each measurement with a two temperature surface emissivity correction at characteristic temperatures. The calibration is applied to the measurement images and corrects for reflected signal components and emissivity spatial and temperature dependencies.

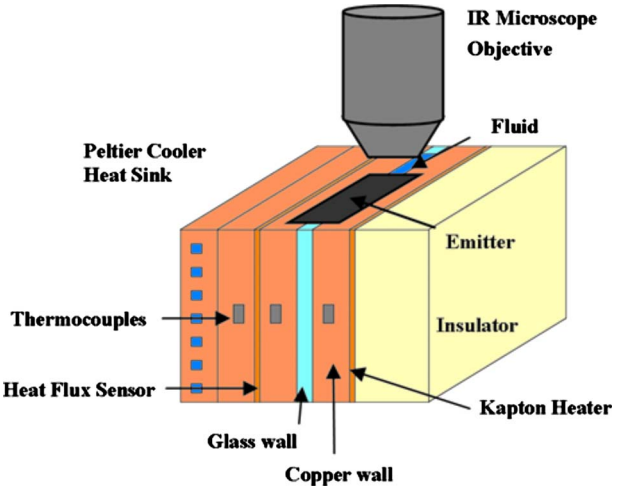

Fig. 5 Schematic of experimental apparatus measuring thermal conductivity of stationary nanofluids

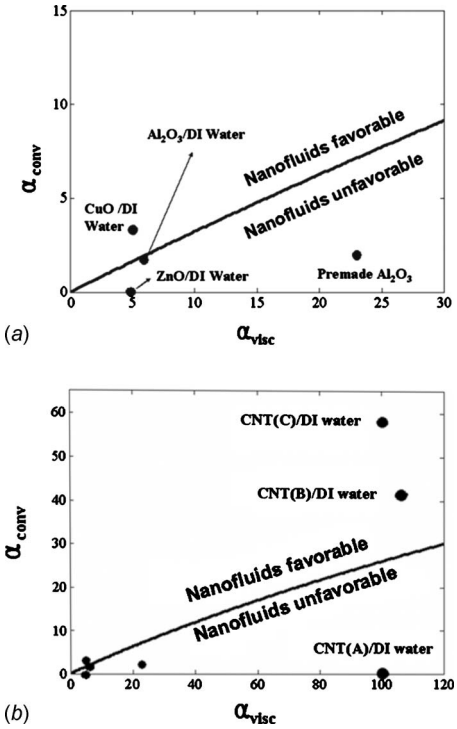

Fig. 6 Effective viscosity and heat transfer augmentation data of seven different nanofluids: CNT(A)/DI water, CNT(B)/DI water, CNT(C)/DI water, CuO/DI water, Al_2O_3/DI water, ZnO/DI water, and premade Al_2O_3/DI water; all data are obtained from microtube experiment

Heat loss from the apparatus to the environment is due to natural convection from the outer surfaces, conduction through the back insulator, and fluid evaporation. These losses are found to be less than 5% of the applied heating power and are systematically eliminated as part of the data extraction procedure. The ability to precisely determine the temperature-dependent conductivity of pure water is verified before each measurement. The thermal conductivities have repeatability to within 5% of the average value.

5 Results and Discussion

Figure 6 shows the α_{conv} and α_{visc} data of seven different nanofluids. These data are obtained from only the microtube experiment. A boundary line, which determines the effectiveness of nanofluids, is drawn in the same figure. This boundary line was

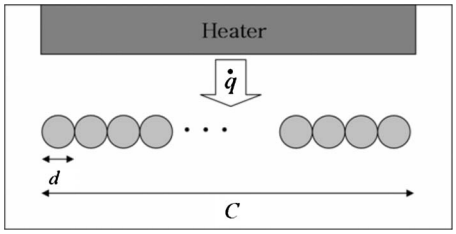

Fig. 7 Multiple parallel channels with each diameter of *d*; the total channel width is constant as *C*

Table 2 Effective heat transfer augmentation data of four nanofluids: CNT(B)/DI water, CNT(B)/silicone oil, Al_2O_3/DI water, and premade Al_2O_3/DI water: data are obtained from microtube experiment, stationary experiment, and macrotube experiment

	α_{conv} from microtube	α_{cond} from stationary [16,17]	α_{conv} from macrotube [18]
CNT(B)/DI water	41.5	40	Not measured
CNT(B)/silicone oil	Not measured	42	43
Al_2O_3/DI water	1.7	8	4
Premade Al_2O_3/DI water	2	3	Not measured

calculated by analyzing the flow and heat transfer of a coolant passing through parallel channels in a heated chip.

A schematic of a multiple parallel channel cooling system is shown in Fig. 7. A total heat transfer rate of $\dot{q}$ is uniformly distributed into each channel with a diameter d. The total width of the channels is fixed as a constant C. The total number of channels and the channel diameter can vary. We also assume hydrodynamically and thermally fully developed flow and all the fluid properties other than thermal conductivity and the viscosity stay the same. The constraints are the fixed total flowrate and the fixed pumping power. Other constraints could be chosen but the present choice would be typical for a designer deciding on the use of a nanofluid in a given cooling system.

Under these conditions, we find the minimum thermal conductivity increase needed to offset the decrease in flowrate caused by the viscosity increase in nanofluids. The result shows that nanofluid is effective as long as the thermal conductivity increase in the nanofluid is higher than the one third power of the viscosity increase.

From the results of Fig. 6, all the oxide nanofluids are not useful except CuO/DI water nanofluid. On the other hand, the CNT(B) and CNT(C)/DI water nanofluids are more effective than DI water despite the high α_{visc} value. CNT(A)/DI water should not be used. The remarkable point is the high α_{conv} values of CNT nanofluids. The CNT shape from the SEM images in Fig. 1 appears to affect the increase in the thermal conductivity. The CNT(B) and CNT(C) samples had long uniform tube shape and gave the result of extremely high α_{conv} of 41.5 and 58, respectively. The CNT(A) had short irregular tube shape and showed zero α_{conv} value. Although it is important to note that despite the large α_{conv} value for CNT nanofluids, the maximum increase in thermal conductivity was only 11.6%.

The effective thermal conductivity data obtained from the stationary experiment [16,17] and a 5 mm diameter macrotube convection experiment [18] are tabulated in Table 2 along with the results of the microtube experiment. The stationary measurement confirms the increase in the high thermal conductivity of CNT(B)/DI water nanofluids.

6 Summary and Concluding Remarks

In this work, several nanofluids are prepared and characterized by measuring the particle size using DLS system and by taking SEM images. The effective thermal conductivity of nanofluids is measured by microtube convection experiments and stationary thermal conductivity measurement. Viscosity data were acquired by measuring the pressure drop for laminar tube flow and using a rheometer. The effectiveness of a nanofluid for electronic cooling application is calculated by its thermal conductivity and viscosity.

When we compared the experimental data and the nanofluid effectiveness line, the results show oxide nanofluids are not effective so they should not be used in applications. Certain CNT nanofluids are effective despite the high viscosity increase.

The thermal conductivity of the CNT nanofluids is closely related to the shape of the nanotubes because only the long and uniform tubes increase nanofluid thermal conductivity significantly. However, CNT nanofluids can cause a clogging problem as well as an abrasion problem in the microchannel heat exchanger because numerous CNTs in the nanofluids are entangled and adhere to each other forming large clusters.

Acknowledgment

The authors gratefully acknowledge the financial support of the Office of Naval Research overseen by Dr. Mark S. Spector under Grant No. N00014-05-1-0374-P00001.

References

[1] Prasher, R. P., Song, D., Wang, J., and Phelan, P., 2006, "Measurements of Nanofluid Viscosity and Its Implications for Thermal Applications," Appl. Phys. Lett., **89**, p. 133108.
[2] Eastman, J. A., Choi, U. S., Li, S., Thompson, L. J., and Lee, S., 1996, "Enhanced Thermal Conductivity Through the Development of Nanofluids," *Proceedings of Materials Research Society Symposium*, Boston, MA, Dec. 2–5, Vol. 457, pp. 3–11.
[3] Kabelac, S., and Kuhnke, J. F., 2006, "Heat Transfer Mechanisms in Nanofluids—Experiments and Theory," Annals of the Assembly for International Heat Transfer Conference 13.
[4] Wen, D., and Ding, Y., 2004, "Effective Thermal Conductivity of Aqueous Suspensions of Carbon Nanotubes(Carbon Nanotube Nanofluids)," J. Thermophys. Heat Transfer, **18**(4), pp. 481–485.
[5] Zhang, X., Gu, H., and Fujii, M., 2006, "Effective Thermal Conductivity and Thermal Diffusivity of Nanofluids Containing Spherical and Cylindrical Nanoparticles," J. Appl. Phys., **100**, p. 044325.
[6] Chon, C., Kihm, K., Lee, S., and Choi, S., 2005, "Empirical Correlation Finding the Role of Temperature and Particle Size for Nanofluid (Al_2O_3) Thermal Conductivity Enhancement," Appl. Phys. Lett., **87**, p. 153107.
[7] Xuan, Y., and Li, Q., 2003, "Investigation on Convective Heat Transfer and Flow Features of Nanofluids," ASME J. Heat Transfer, **125**, pp. 151–155.
[8] Wen, D., and Ding, Y., 2004, "Experimental Investigation Into Convective Heat Transfer of Nanofluids at the Entrance Region Under Laminar Flow Conditions," Int. J. Heat Mass Transfer, **47**, pp. 5181–5188.
[9] Ding, Y., Alias, H., Wen, D., and Williams, R. A., 2006, "Heat Transfer of Aqueous Suspensions of Carbon Nanotubes," Int. J. Heat Mass Transfer, **49**, pp. 240–250.
[10] Lee, J., and Mudawar, I., 2007, "Assessment of the Effectiveness of Nanofluids for Single-Phase and Two-Phase Heat Transfer in Micro-Channels," Int. J. Heat Mass Transfer, **50**, pp. 452–463.
[11] Rea, U., McKrell, T., Hu, L., and Buongiorno, J., 2009, "Laminar Convective Heat Transfer and Viscous Pressure Loss of Alumina-Water and Zirconia-Water Nanofluids," Int. J. Heat Mass Transfer, **52**, pp. 2042–2048.
[12] Williams, W., Buongiorno, J., and Hu, L., 2008, "Experimental Investigation of Turbulent Convective Heat Transfer and Pressure Loss of Alumina/Water and Zirconia/Water Nanoparticle Colloids (Nanofluids) in Horizontal Tubes," ASME J. Heat Transfer, **130**, p. 042412.
[13] Churchill, S. W., and Chu, H. H. S., 1975, "Correlating Equations for Laminar and Turbulent Free Convection From a Horizontal Cylinder," Int. J. Heat Mass Transfer, **18**, pp. 1049–1053.
[14] White, F. M., 1991, *Viscous Fluid Flow*, 2nd ed., McGraw-Hill, New York.
[15] Batchelor, G. K., 1977, "The Effect of Brownian Motion on the Bulk Stress in a Suspension of Spherical Particles," J. Fluid Mech., **83**, pp. 97–117.
[16] Gharagozloo, P. E., Eaton, J. K., and Goodson, K. E., 2008, "Diffusion, Aggregation, and the Thermal Conductivity of Nanofluids," Appl. Phys. Lett., **93**, p. 103110.
[17] Gharagozloo, P. E., Eaton, J. K., and Goodson, K. E., 2007, "Impact of Thermodiffusion on Temperature Fields in Stationary Nanofluids," *Proceedings of ASME Interpack*, Vancouver, BC, Canada, Jul. 8–12.
[18] Kolade, B., Goodson, K. E., and Eaton, J. K., 2009, "Convective Performance of Nanofluids in a Laminar Thermally Developing Tube Flow," ASME J. Heat Transfer, **131**(5), p. 052402.

Harvesting Nanoscale Thermal Radiation Using Pyroelectric Materials

Jin Fang

Hugo Frederich

Laurent Pilon[1]
e-mail: pilon@seas.ucla.edu

Department of Mechanical and Aerospace Engineering,
Henri Samueli School of Engineering and Applied Science,
University of California, Los Angeles,
Los Angeles, CA 90095-1597

Pyroelectric energy conversion offers a way to convert waste heat directly into electricity. It makes use of the pyroelectric effect to create a flow of charge to or from the surface of a material as a result of heating or cooling. However, an existing pyroelectric energy converter can only operate at low frequencies due to a relatively small convective heat transfer rate between the pyroelectric materials and the working fluid. On the other hand, energy transfer by thermal radiation between two semi-infinite solids is nearly instantaneous and can be enhanced by several orders of magnitude from the conventional Stefan–Boltzmann law as the gap separating them becomes smaller than Wien's displacement wavelength. This paper explores a novel way to harvest waste heat by combining pyroelectric energy conversion and nanoscale thermal radiation. A new device was investigated numerically by accurately modeling nanoscale radiative heat transfer between a pyroelectric element and hot and cold plates. Silica absorbing layers on top of every surface were used to further increase the net radiative heat fluxes. Temperature oscillations with time and performances of the pyroelectric converter were predicted at various frequencies. The device using 60/40 porous poly(vinylidene fluoride–trifluoroethylene) achieved a 0.2% efficiency and a 0.84 mW/cm^2 electrical power output for the cold and hot sources at 273 K and 388 K, respectively. Better performances could be achieved with $0.9Pb(Mg_{1/3}Nb_{2/3})-0.1PbTiO_3$ (0.9PMN-PT), namely, an efficiency of 1.3% and a power output of 6.5 mW/cm^2 between the cold and hot sources at 283 K and 383 K, respectively. These results are compared with alternative technologies, and suggestions are made to further improve the device. [DOI: 10.1115/1.4001634]

Keywords: pyroelectric effect, ferroelectric, direct energy conversion, nanoscale thermal radiation, waste heat harvesting

1 Introduction

Industrial and developing nations are facing the challenge of meeting the rapidly expanding energy needs without further impacting the climate and the environment. Large amounts of energy are lost in the form of waste heat released as a by-product of power, refrigeration, or heat pump cycles, for example. In fact, in 2002 more than 50% of the net primary energy resource consumption in the U.S. was lost mainly in the form of waste heat [1]. Pyroelectric (PE) energy converter offers a novel direct energy conversion technology by directly transforming waste heat into electricity [2–12]. It makes use of the pyroelectric effect to create a flow of charge to or from the surface of a material as a result of successive heating or cooling cycles [13]. However, the operating frequency of the device is usually small ($\sim$0.1 Hz) and limited by convective heat transfer between the pyroelectric material and the working fluid subjected to oscillatory laminar flow between a hot and a cold source. This restricts the performance of the device. On the contrary, thermal radiative heat transfer takes place at the speed of light. In addition, the net radiation flux in vacuum between two surfaces at different temperatures can be increased by several orders of magnitude if they are separated by a distance comparable to or smaller than the characteristic wavelength given by Wien's displacement law [14,15]. Thus, nanoscale radiative heat transfer has the potential to increase the operating frequency of pyroelectric energy converters, resulting in a larger power density and efficiency. This paper explores a novel way to combine nanoscale radiative heat transfer and pyroelectric energy conversion in a device harvesting waste heat.

2 Background

2.1 Pyroelectric Materials. Pyroelectric materials feature a spontaneous polarization with strong temperature dependence. The displacement of the atoms from their equilibrium positions gives rise to the spontaneous polarization resulting in the pyroelectric effect. At steady state ($dT/dt=0$), the polarization is constant, and no current is generated. However, a rise in temperature ($dT/dt>0$) reduces the overall polarization through reduction in the dipole moment. The number of bound charges decreases, and the subsequent redistribution of charges results in current flowing in the circuit. If the sample is cooled, the direction of the current is reversed. In an open circuit, the free charges would remain on the electrodes, and a voltage would be established between them. The direction of polarization is usually constant throughout a pyroelectric material, but in some materials this direction can be changed by applying a coercive "poling" electric field [4]. In addition, the relationship between the charge and the open-circuit voltage at a constant temperature features a hysteresis loop [16].

Finally, all ferroelectric materials are pyroelectric, and all pyroelectric materials are piezoelectric. However, the converse is not true. The polarization of ferroelectric materials vanishes beyond the Curie temperature denoted by T_{Curie} when the material undergoes a phase transition from ferroelectric to paraelectric and the spontaneous polarization disappears. This phase transition process results in a large charge release [17]. Differential scanning calorimetry (DSC) measurements for the commercial pyroelectric material 60/40 porous poly(vinylidene fluoride–trifluoroethylene)

[1]Corresponding author.

Contributed by the Heat Transfer Division of ASME for publication in the JOURNAL OF HEAT TRANSFER. Manuscript received October 31, 2009; final manuscript received March 24, 2010; published online June 30, 2010. Assoc. Editor: Robert D. Tzou.

(P(VDF-TrFE)) were reported by Navid et al. [18]. The phase transition from ferroelectric to paraelectric takes place between $T_{p1}=42\,^{\circ}\mathrm{C}$ and $T_{p2}=90\,^{\circ}\mathrm{C}$ with a peak at temperature $T_{\mathrm{Curie}}=65.7\,^{\circ}\mathrm{C}$.

2.2 Direct Pyroelectric Energy Converter. Pyroelectric energy conversion is possible by alternatively placing the pyroelectric material sandwiched between two electrodes in contact with a hot and a cold reservoir. Unfortunately, this process is highly irreversible, and theoretical analysis predicts a low efficiency and a small power density [19–21]. This intrinsic limitation can be attributed to the fact that "the energy required to increase the temperature of the lattice is nearly always much larger than the energy required to destroy part of the polarization thus releasing electric charges" [20].

More recently, Itskovsky [22] noted that the above mentioned analysis [19–21] assumed very small temperature amplitudes of a few milli-Kelvin or Kelvin. Then, the pyroelectric current i is proportional to the time rate of change in temperature $\mathrm{d}T/\mathrm{d}t$, and the pyroelectric effect is linear, i.e., $i=p_c\mathrm{d}T/\mathrm{d}t$, where p_c is the pyroelectric coefficient. However, for energy conversion applications, the amplitude of the temperature oscillation is typically large and the pyroelectric effect is nonlinear. Accounting for these nonlinear effects, Itskovsky [22] studied $LiNbO_3$ featuring $T_{\mathrm{Curie}}=1140\,^{\circ}\mathrm{C}$ [23] and operating with tens of kelvin amplitude within the phase transition region. The author theoretically established that "the instantaneous energy conversion efficiency for ferroelectrics with parameters similar to those of $LiNbO_3$ type can reach over 20% in the relaxation process on cooling."

Moreover, the performance of pyroelectric energy converter can be significantly improved by using heat regeneration and multistages along with the Olsen cycle [2–5]. To date, only five prototypes of pyroelectric converters have been built. First, Olsen and co-workers [2,4,5] experimentally demonstrated 1 mW and 40 mW devices with an efficiency around 0.4% [4] but 16 times greater than the maximum efficiency predicted by van der Ziel [21]. They used lead zirconate titanate (PZT) as pyroelectric materials and silicone oil as the working fluid while they operated between $145\,^{\circ}\mathrm{C}$ and $178\,^{\circ}\mathrm{C}$ [4]. Later, Olsen et al. [3] assembled the only multistage device built to date using different grades of lead zirconate stannate titanate (PZST), in which Ti^{4+} was substituted by Sn^{4+} for a maximum output of 33 W/l of pyroelectric materials at 0.26 Hz and featuring a maximum thermodynamic efficiency of 1.05% at 0.14 Hz or 12% of the Carnot efficiency. Moreover, due to the cost of PZT ($10,000/W), Olsen et al. [6] proposed to use inexpensive single stage 73/27 P(VDF-TrFE) films 30–70 μm thick sandwiched between electrodes and rolled in a spiral stack placed into a cylindrical chamber containing silicone oil. The energy density between $20\,^{\circ}\mathrm{C}$ and $90\,^{\circ}\mathrm{C}$ achieved 30 mJ cm^3/cycle. Recently, Nguyen et al. [12] built and tested a pyroelectric converter using 60/40 P(VDF-TrFE) and achieved a maximum energy density of 130 J/l at a 0.061 Hz frequency with a temperature oscillating between 69.3 and $87.6\,^{\circ}\mathrm{C}$. Furthermore, a maximum power density of 10.7 W/l was obtained at 0.12 Hz between $70.5\,^{\circ}\mathrm{C}$ and $85.3\,^{\circ}\mathrm{C}$. In all these prototypes, the pumping was performed by a step motor with a piston amplitude of 2–10 cm. Ceramic stacks were used to reduce axial heat conduction and ensure laminar flow of the working fluid over the pyroelectric elements as turbulence would result in the mixing of the cold and hot fluids and would disrupt the oscillating temperature gradient. Theoretically, pyroelectric conversion based on heat regeneration and the Olsen cycle can reach the Carnot efficiency between a hot and a cold thermal reservoir [3,24]. Limitations in reaching the Carnot efficiency include (i) hysteretic and resistive losses, (ii) heat losses to the surrounding, and (iii) sensible (thermal) energy.

Furthermore, the electrocaloric effect corresponds to a change in material temperature upon application or withdrawal of an electric field under adiabatic condition. Consequently, a material having a very large electrocaloric activity also features a large pyroelectric energy harvesting capability [25]. The ratio of pyroelectric conversion efficiency to the Carnot efficiency increases as the temperature difference decreases. For a very small temperature difference, it is possible to harvest energy with Carnot efficiency [25]. In particular, a giant electrocaloric effect in a $0.9Pb(Mg_{1/3}Nb_{2/3})-0.1PbTiO_3$ composite thin film, also called 0.9PMN-PT, around 348 K was reported upon the application or withdrawal of an electric field of 895 kV/cm [26]. More recently, Sebald et al. [25] estimated an associated energy density of 432 J/l for pyroelectric conversion between 338 K and 348 K by using 0.9PMN-PT thin films about 260 nm in thickness.

2.3 Nanoscale Radiation. Based on the theory of electrical fluctuation and thermal radiation [27], it was shown that energy transfer by thermal radiation between two semi-infinite solids can be enhanced by several orders of magnitude if the vacuum gap size is smaller than the radiation peak wavelength given by Wien's displacement law ($\lambda_{\max}T=2898$ μm K) [14,15]. This can be attributed to (i) propagating wave interferences and (ii) tunneling of the evanescent waves across the gap [15]. Wave interferences take place in the vacuum gap due to multiple reflections at the gap/solid interfaces. Radiation tunneling relies on evanescent surface waves that decay exponentially with distance as it travels through the gap. These surface waves appear when total reflection occurs on the interface between two materials. They are due to coupling between the material resonant polarization oscillation and the electromagnetic field, also called polaritons. In the case of metals, these surface waves are supported by charged carriers and are called surface plasmon polaritons. In the case of dielectrics materials, the surface waves are supported by phonons and are called surface phonon polaritons. Surface phonon polaritons are excited by infrared radiation, while surface plasmon polaritons are excited in the visible or near-UV domain [28]. If the gap is small compared with $\lambda_{\max}$, the time-averaged Poynting vector associated with the evanescent wave incident on the surface is different from zero and energy tunnels across the gap. Nanoscale radiation has found applications in thermophotovoltaic devices [29,30] and in scanning thermal microscopy [31], for example.

Most studies on nanoscale radiative transfer have been theoretical in nature, and only a few experimental studies have been reported. One of the first experimental studies was performed by Hargreaves [32], who studied the effect of gap size on the net radiation heat transfer between two parallel glass plates coated with 0.1 μm thick chromium films at temperatures of $T_1=323$ K and $T_2=306$ K, respectively. The plate separation and parallelism were adjusted by means of piezoelectric ceramic pillars. The apparatus was placed in a vacuum chamber evacuated to 10^{-5} torr. The author observed that the net heat transfer rate between the plates deviated from the classical surface radiation theory for a distance less than 3 μm. He attributed this to the "proximity effect," but no quantitative comparison with theory was performed. Polder and Van Hove [15] theoretically found a qualitative agreement with experimental results by Hargreaves [32] but not in terms of absolute magnitudes. Similarly, Domoto et al. [33] studied radiative heat transfer between two parallel copper plates at a cryogenic temperature, but discrepancies between experimental and theoretical predictions were very large and were attributed to poor parallelism between the plates and to poor knowledge of optical properties. DiMatteo et al. [29] measured the photocurrent in an actively cooled thermophotovoltaic cell placed close to a heated surface. The authors found that their measurements were qualitatively consistent with theoretical predictions. However, Kittel et al. [34] found the contrary by measuring the power absorbed or emitted by the tip of a thermal profiler and a planar surface under high vacuum conditions. At distances below 10 nm, their experimental results deviated significantly from the predictions from fluctuating electrodynamics. They attributed this to scale effects in which the macroscopic description of dielectric properties fails below a certain size. Other

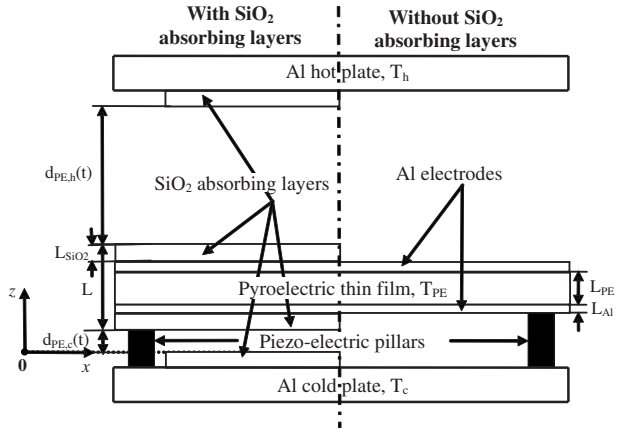

Fig. 1 Schematic of the PE plate as it oscillates between the hot and cold plates, with or without SiO_2 absorbing layers (not to scale)

possible reasons for discrepancies included poor parallelism between the plates, and the assumption of a semi-infinite plate might not be satisfied experimentally. Similarly, Pan [35] and Pan et al. [36] questioned the approach used in other theoretical studies computing the heat transfer between metal and dielectric plates [37,38]. More recently, Hu et al. [39] showed that the temperature dependence for the heat flux between two parallel glass surfaces at temperatures of 23°C and 50°C placed in vacuum and separated by a gap of 1.6 μm agreed with the theory. The authors used small polystyrene particles as spacers to maintain a micron-sized gap. Narayanaswamy et al. [40] measured radiative transfer between a silica sphere and a flat silica surface. The presence of strong near-field effects enhanced radiative heat transfer over the predictions of the Planck blackbody radiation theory [40,41]. Shen et al. [42] measured radiation heat transfer between a glass microsphere hotter by 16.5 K than flat surfaces at ambient temperature and made of glass, doped silicon, and Au down to 30 nm separation. The net energy transfer was the largest when the two surfaces were made of glass when it was three orders of magnitude larger than that of the blackbody radiation limit.

In addition, the effect of metallic or dielectric thin film coatings on the near-field radiative heat transfer between two plane surfaces is important from a fundamental as well as from an application point of view. Recent studies showed that the surface plasmon polariton excited in a metallic coating a few nanometers thick deposited on a metallic or dielectric substrate can significantly increase the radiative heat flux [43,44]. On the other hand, surface phonon polaritons are easier to excite thermally at low temperatures ($\sim$300 K) than surface plasmon polaritons since the resonant frequency of surface phonon polaritons is in the infrared region [45,46]. For example, the total radiative flux between a SiC slab set at 0 K and a metallic substrate [46] or a dielectric substrate [45] set at 300 K was shown to increase by coating the latter with a few nanometer thick SiC film. In addition, when the coating thickness exceeds 1 μm, Fu and Tan [46] showed that the contribution to the near-field radiative flux from the substrate was negligible and the heat flux was entirely contributed by the coating.

3 Analysis

3.1 Device Principle. Figure 1 illustrates a conceptual device combining nanoscale radiation and pyroelectric energy conversion consisting of a hot and cold plane-parallel plates and an oscillating PE plate. The PE plate is composed of a pyroelectric material film of thickness L_{PE} sandwiched between aluminum electrodes of thickness L_{Al} used to collect the electric charges and to apply an electric field. The hot and cold plates are made of aluminum. SiO_2 thin films of thickness L_{SiO_2} can be coated on both sides of the PE plate and on the hot and cold surfaces as absorbing layers, which emit and absorb nanoscale radiation to enhance radiative heat transfer. The total thickness of the PE plate is denoted by L_t. The hot plate is at temperature T_h, and the cold plate is at temperature T_c. The distances between the hot/cold plates and the PE plate are denoted by $d_{PE,h}$ and $d_{PE,c}$, respectively. The PE plate is mounted on piezoelectric pillars, which make it oscillate between the hot and cold plates. The entire device is operated under vacuum to minimize both friction on the oscillating PE plate and heat losses to the surroundings. In addition, the presence of air in the gap would hinder the temperature oscillations in the PE plate caused by nanoscale thermal radiation as heat conduction may dominate.

3.2 Assumptions. To make the problem mathematically trackable, the following assumptions have been made:

1. Hot and cold plates are assumed to be semi-infinite; i.e., end effects are neglected.
2. The absorbing SiO_2 layers and the electrodes are considered to be opaque and can be treated as semi-infinite. Indeed, a dielectric material such as SiO_2 exhibits a large absorption index at the peak wavelength λ_{max} around 8–10 μm at the temperatures of interest (300–400 K).
3. The absorbing layers deposited on the hot and cold plates are assumed to be at the same temperatures as the plates, namely, T_h and T_c, respectively.
4. Complex dielectric constants of metals and dielectric materials considered are modeled by the Drude and Lorentz models, respectively.
5. All properties are assumed to be independent of temperature.
6. The temperature is assumed to be uniform across the PE plate.
7. The location of the PE plate over time is assumed to be a step function. This is justified by the fact that the displacement of the PE plate is much faster than the temperature changes in the PE plate.
8. The pyroelectric material, which is also ferroelectric exhibits a very large charge redistribution across the phase transition from ferroelectric to paraelectric. A large part of the energy density denoted by N_D produced at every cycle is contributed from this phase transition. Thus, N_D is assumed to be constant and equal to the energy density generated by operating the Olsen cycle across the phase transition, as long as the operating temperature span is wider than the phase transition interval between $T_{p,1}$ and $T_{p,2}$.

3.3 Governing Equation. For an elementary element of the composite PE plate with a unit surface area and thickness L_t, the energy conservation equation can be written as

$$(\rho c_p)_{\text{eff}} L_t \frac{\mathrm{d}T_{\text{PE}}}{\mathrm{d}t} = q''_{h\to\text{PE}}(T_h, T_{\text{PE}}, d_{\text{PE},h}) - q''_{\text{PE}\to c}(T_{\text{PE}}, T_c, d_{\text{PE},c}) \tag{1}$$

where $(\rho c_p)_{\text{eff}}$ is the effective volumetric heat capacity of the composite PE plate. The heat flux $q''_{h\to\text{PE}}$ and $q''_{\text{PE}\to c}$ are the net radiative heat fluxes from the hot plate to the PE plate and from the PE plate to the cold plate, respectively. The generic radiative heat flux $q''_{1\to 2}(T_1, T_2, d)$ appearing in Eq. (1) accounts for the far-field (propagative) and the near-field (evanescent) contributions to the total radiative heat flux between two semi-infinite media 1 and 2 separated by a distance d and at temperatures T_1 and T_2, respectively. It can be estimated from the fluctuating electrodynamic theory [27] and is written in the general form as [28,47]

$$q''_{1\to 2}(T_1,T_2,d)=\int_0^\infty [I^0_{b\omega}(T_1)-I^0_{b\omega}(T_2)]\times\Phi_{12}(\omega,d)\mathrm{d}\omega \quad (2)$$

where $I^0_{b\omega}(T)$ is the spectral blackbody radiation intensity at frequency ω and temperature T, given by Planck's law as [48]

$$I^0_{b\omega}(T)=\frac{\omega^2}{4\pi^3c^2}\frac{\hbar\omega}{(e^{\hbar\omega/k_BT}-1)} \quad (3)$$

where $\hbar$ is the reduced Planck constant, c is the speed of light in vacuum, and k_B is the Boltzmann constant. The function $\Phi_{12}(\omega,d)$ corresponds to the spectral efficiency in radiative heat transfer between media 1 and 2 separated by a distance d and is expressed as [49]

$$\Phi_{12}(\omega,d)=\sum_{j=\mathrm{s,p}}\left(\int_{q=0}^{\omega/c}\frac{qc^2}{\omega^2}\frac{(1-|r^j_{31}|^2)(1-|r^j_{32}|^2)}{|1-r^j_{31}r^j_{32}e^{2ipd}|^2}\mathrm{d}q\right)+\sum_{j=\mathrm{s,p}}\left(\int_{q=\omega/c}^{\infty}\frac{qc^2}{\omega^2}\frac{4e^{-2|p|d}\,\mathrm{Im}(r^j_{31})\mathrm{Im}(r^j_{32})}{|1-r^j_{31}r^j_{32}e^{-2|p|d}|^2}\mathrm{d}q\right) \quad (4)$$

where p and q are the z- and x-components of the wavevector in the vacuum gap, respectively. They are related by $p=\sqrt{(\omega/c)^2-q^2}$, where ω/c is the amplitude of the wavevector. Summation is made to account for both s- and p-polarizations. The first term on the right-hand side of Eq. (4) corresponds to the far-field radiation contribution. Integration over q from 0 to ω/c accounts for all propagative waves and results in the Stefan–Boltzmann law. The second term represents the contribution of the near-field radiation to the total radiative heat flux. Integration over q from ω/c to infinity stands for the evanescent waves or the tunneling heat flux. It is evident that the amplitude of evanescent waves decreases exponentially as the distance d between the plates increases. The near-field term is negligible compared with the first term for large distance d [28]. Note that Eq. (4) includes integration over the azimuthal angle and accounts for interferences and polaritons coupling between the two media.

The Fresnel coefficients for s- and p-polarized electromagnetic waves incident from medium 3 (vacuum) on the interface with medium 1 are denoted by r_{31} and expressed, for s- and p-polarizations, as [50]

$$r^{\mathrm{s}}_{31}=\frac{p-s_1}{p+s_1}\ \text{ and }\ r^{\mathrm{p}}_{31}=\frac{\varepsilon_{r1}p-s_1}{\varepsilon_{r1}p+s_1} \quad (5)$$

where ε_{r1} is the complex dielectric constant of medium 1, while $s_1=\sqrt{\varepsilon_{r1}\omega^2/c^2-q^2}$ is the z-component of the wavevector in medium 1. Fresnel coefficients r^{s}_{32} and r^{p}_{32} between media 2 and 3 are obtained in a similar manner. Note that all these parameters depend on ω.

Finally, the net radiative heat fluxes $q''_{h\to\mathrm{PE}}$ and $q''_{\mathrm{PE}\to c}$ were computed from Eqs. (2)–(5) for distance d and temperature $T_{\mathrm{PE}}(t)$. Then, Eq. (1) was solved for the PE plate temperature $T_{\mathrm{PE}}(t)$ as a function of time.

3.4 Initial Conditions. The initial PE plate temperature at time $t=0$ was set to be $T_{\mathrm{PE}}(t=0)=(T_c+T_h)/2$. The PE plate oscillated at frequency f between hot and cold plates separated by a gap of 100 μm and maintained at constant temperatures T_h and T_c, respectively. The distances $d_{\mathrm{PE},h}$ and $d_{\mathrm{PE},c}$ were step functions of time and oscillated at a frequency f and were such that $L_t+d_{\mathrm{PE},h}(t)+d_{\mathrm{PE},c}(t)=100$ μm. Their minimum value was arbitrarily set at 100 nm, which has been achieved experimentally [42] while ensuring that the near-field radiative heat transfer dominates radiation transfer successively between the PE plate and the cold and hot plates. Note also that the PE plate oscillation can be achieved using conventional piezoelectric actuators [51]. Initially, the PE plate was positioned so that $d_{\mathrm{PE},c}(t=0)=100$ nm.

3.5 Constitutive Relations. Constitutive relationships for the dielectric constant ε_{ri} of each medium i are necessary in order to compute the Fresnel coefficients as a function of angular frequency ω given by Eq. (5). The Drude model is widely accepted to predict the complex dielectric constant of metals and is expressed as [50]

$$\varepsilon_r(\omega)=1-\frac{\omega_p^2}{\omega^2-i\gamma\omega} \quad (6)$$

where ω_p is the plasma frequency and γ is the relaxation frequency. On the other hand, the dielectric constant for dielectric materials is given by the Lorentz model [50],

$$\varepsilon_r(\omega)=1-\frac{\omega_p^2}{\omega_0^2-\omega^2-i\gamma\omega} \quad (7)$$

where ω_0 is the oscillator frequency. Multiple oscillators can be accounted for by adding terms similar to the second term on the right-hand side of Eqs. (6) and (7) with different oscillator, plasma, and relaxation frequencies. Here, the Drude model was used for aluminum with parameters $\omega_p=2.4\times10^{16}$ rad/s and $\gamma=1.25\times10^{14}$ rad/s [43]. The Lorentz model was used for SiO_2 with parameters $\omega_p=1.696\times10^{14}$ rad/s, $\omega_0=2.0\times10^{14}$ rad/s, and $\gamma=5.65\times10^{12}$ rad/s [50]. They were shown to accurately predict the optical properties of aluminum and SiO_2 in the frequency range of interest [43,50].

Simulations were performed for a single film of pyroelectric material of thickness $L_{\mathrm{PE}}=25$ μm sandwiched between two aluminum electrodes (Al) of thickness $L_{\mathrm{Al}}=1$ μm. Unless otherwise noticed, the Al electrodes were coated with a SiO_2 absorbing coating of thickness $L_{\mathrm{SiO_2}}=1.5$ μm to enhance the radiative heat flux, as previously discussed. Thus, the total thickness L_t of the composite PE plate was 30 or 27 μm with or without SiO_2 absorbing coating, respectively. The effective volumetric heat capacity $(\rho c_p)_{\mathrm{eff}}$ in the presence of absorbing layers was taken as

$$(\rho c_p)_{\mathrm{eff}}=\frac{1}{L_t}[(\rho c_p)_{\mathrm{PE}}L_{\mathrm{PE}}+2(\rho c_p)_{\mathrm{Al}}L_{\mathrm{Al}}+2(\rho c_p)_{\mathrm{SiO_2}}L_{\mathrm{SiO_2}}] \quad (8)$$

where $(\rho c_p)_i$ is the volumetric heat capacity of medium i, be it a pyroelectric element (PE), aluminum (Al), or silicon dioxide (SiO_2). For the PE plate made of 60/40 P(VDF-TrFE) with SiO_2 absorbing layers, $\rho_{\mathrm{PE}}=1930$ kg/m^3, $c_{p,\mathrm{PE}}=1200$ J/kg K [17], $(\rho c_p)_{\mathrm{eff}}$ was found equal to 2.31×10^6 J/m^3 K. In the absence of SiO_2 absorbing layers, $(\rho c_p)_{\mathrm{eff}}$ was equal to 2.33×10^6 J/m^3 K.

3.6 Method of Solution. The PE plate temperature $T_{\mathrm{PE}}(t)$ was determined by solving Eq. (1). The latter was solved numerically for $T_{\mathrm{PE}}(t)$ using a finite-difference method based on the forward-difference approximation for the time derivative. This yields the following explicit expression for T_{PE} at time $t+\Delta t$ knowing its value at time t,

$$T_{\mathrm{PE}}(t+\Delta t)=T_{\mathrm{PE}}(t)+\frac{q''_{h\to\mathrm{PE}}(T_h,T_{\mathrm{PE}}(t),d_{\mathrm{PE},h}(t))-q''_{\mathrm{PE}\to c}(T_{\mathrm{PE}}(t),T_c,d_{\mathrm{PE},c}(t))}{(\rho c_p)_{\mathrm{eff}}L_t}\Delta t \quad (9)$$

where Δt is the time step. The net radiation fluxes $q''_{h\to\mathrm{PE}}$ and $q''_{\mathrm{PE}\to c}$ were computed numerically at every time step according to Eqs. (2)–(5) where the integrals over frequency ω and over the x-component of the wavevector q were performed using the Simpson 3/8 rule. Integration over ω from 0 to infinity was performed up to $\omega=N_\omega k_BT_1/\hbar$, where k_B is the Boltzmann constant. Integration over q from ω/c to infinity was performed up to $q=N_q\omega/c$. Here, N_ω and N_q are the numbers of frequencies and wavevectors considered. Numerical convergence for $q''_{h\to\mathrm{PE}}$ and $q''_{\mathrm{PE}\to c}$ was es-

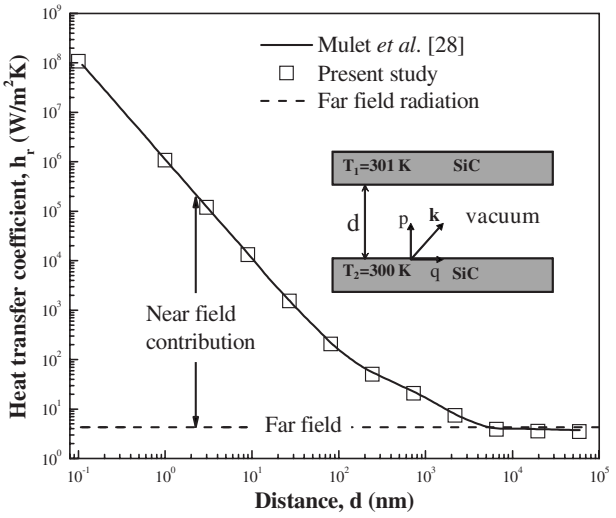

Fig. 2 Comparison between results obtained in the present study with results reported by Mulet et al. [28] for the heat transfer coefficient between two semi-infinite bodies of SiC at 300 K and 301 K as a function of distance *d* ($\lambda_{max} \simeq 10^4$ nm)

tablished by reducing $\Delta\omega$ and Δq and increasing N_ω and N_q by a factor of 1.3 until the numerical results did not vary by less than 0.1% for the heat fluxes $q''_{h\to PE}$ and $q''_{PE\to c}$. Numerical convergence for $T_{PE}(t)$ was established by reducing Δt by a factor of 1.6 until the results did not vary by less than 1% for all time steps.

When the gap is large ($\sim$100 μm), the SiO_2 thin films cannot be treated as opaque or semi-infinite. However, the net heat flux through the smaller gap is always much larger than that through the larger gap on the other side of the PE plate. In other words, heat transferred through the larger gap does not contribute significantly to the net total heat flux received by the PE plate and therefore has no effect on its temperature oscillation.

3.7 Validation. Validation of the computer program developed in this study was performed for identical plane-parallel semi-infinite solids separated by a vacuum gap of thickness *d*. The results were compared with those reported in the literature for both metallic and dielectric materials.

First, the radiation heat flux between two silver plates at temperatures 0 K and 273 K was computed using the Drude model with parameters $\omega_p = 1.4\times10^{16}$ rad/s and $\gamma = 2.5\times10^{13}$ rad/s [43]. The numerical results from the code developed in this study fell within 0.1% of those reported by Volokitin and Persson [47] for distances between 1 nm and 1 μm.

A radiative heat flux between dielectric materials at 300 K can be even larger than that for silver, as shown by Mulet et al. [28]. This is due to their dielectric constant, which enables a high coupling between the surface waves in the infrared part of the spectrum. Numerical calculations were performed for parallel semi-infinite plates of SiC at temperatures of 300 K and 301 K, respectively. The radiative heat transfer coefficient h_r was defined as $h_r(d) = \lim_{T_1\to T_2}[q''_{1\to2}(T_1,T_2,d)/(T_1-T_2)]$. The parameters for SiC used in the Lorentz model were $\omega_p = 2.72\times10^{14}$ rad/s, $\omega_0 = 1.49\times10^{14}$ rad/s, and $\gamma = 8.97\times10^{12}$ rad/s [52]. The radiative heat transfer coefficient at 300 K calculated from far-field radiation by the Stephan–Boltzmann law was also given for comparison purposes. The far-field radiation heat flux was expressed as $q''_{1\to2} = \sigma(T_1^4 - T_2^4)/(2/\alpha_1 - 1)$, where $\sigma = 5.67\times10^{-8}$ W/m^2 K^4 is the Stefan–Boltzmann constant and $\alpha_1 = \alpha_2$ is the total hemispherical emissivity of SiC at 300 K such that $\alpha_1 = 0.83$ [48]. Figure 2 shows the radiative heat transfer coefficient h_r between two semi-infinite bodies of SiC as a function of distance *d*. It is evident that the numerical results obtained agree well with those reported by Mulet et al. [28], and the heat flux is enhanced by several orders of magnitude compared with the far-field radiative heat flux when the gap size becomes smaller than $\lambda_{max} = 10^4$ nm.

3.8 Thermodynamic Efficiency of the Device. In order to assess the performance of the proposed pyroelectric device, the average thermodynamic efficiency over a cycle is defined as

$$\eta = \frac{\dot{W}_e - \dot{W}_p}{\dot{Q}_{in}} \tag{10}$$

where $\dot{W}_e$ is the electric power generated by the PE plate and $\dot{W}_p$ is the power provided by the piezoactuators, both per unit surface area of the PE plate and expressed in W/m^2. The heat flux (in W/m^2) provided by the hot plate to the PE plate over one cycle of period τ is denoted by $\dot{Q}_{in}$ and expressed as

$$\dot{Q}_{in} = \frac{1}{\tau}\int_0^\tau q''_{h\to PE}(T_h, T_{PE}, d_{PE,h}(t))\,d\tau \tag{11}$$

where $\tau = 1/f$ is the oscillation period.

In order to estimate the power $\dot{W}_p$, the pressure balance on the PE plate was performed. The main forces affecting the motion of the PE plate are (i) the gravitational force, (ii) the Casimir force, (iii) the van der Waals force, and (iv) the radiation pressure force.

Assuming that the oscillation is vertical, the gravitational force acting on the PE plate has to be overcome by the piezoelectric pillars. The gravitational force per unit surface area is given by $P_g = \rho_{eff} L_t g$, where g is the gravitational acceleration ($g = 9.81$ m/s^2). Given the PE plate thickness $L_t = 30$ μm and its effective density of $\rho_{eff} = 2.10$ g/cm^3, the gravitational pressure P_g was estimated to be about 0.6 Pa.

The Casimir force is an attractive force between surfaces caused by the quantum fluctuations in the zero point electromagnetic field [53]. In the present study, when the parallel plates get close to each other, the Casimir force, negligible at macroscale, becomes important. The attractive Casimir force per unit surface area for semi-infinite parallel metallic plates is expressed as $P_c = -\pi^2\hbar c/240d^4$ [51]. Thus, the Casimir force acting between two metallic plane-parallel plates distant by $d = 100$ nm amounts to 13 Pa. When the two plates are made of dielectric materials (e.g., SiO_2 and SiC), the Casimir force is typically smaller by one order of magnitude [54]. Moreover, if the two plates are not perfectly parallel and the closest distance between them is the same as the distance between parallel plates, the Casimir force will be even lower [55].

The van der Waals force is often responsible for the adhesion in microscale devices. For two parallel flat plates in vacuum, the van der Waals pressure is expressed as $P_v = -H/12\pi d^2$, where H is the Hamaker constant and d is the distance separating the two surfaces [56]. The Hamaker constant of most condensed phases with an interaction across the vacuum is found to lie in the range from 0.4 to 4×10^{-19} J [56]. In the present study, the minimum distance between the PE plate and the hot/cold plates was assumed to be 100 nm. Then, the adhesive pressure due to the van der Waals force was less than 1×10^{-6} Pa.

Moreover, the radiation pressure on the plates is given by $P_{rad} = \dot{Q}_{in}/c$ [57]. The magnitude of the average heat transfer rate $\dot{Q}_{in}$ is about 1 W/cm^2, corresponding to a radiation pressure around 10^{-5} Pa.

Consequently, both P_{rad} and P_v are negligible compared with P_g and P_c, and the time-averaged oscillation power $\dot{W}_p$ per unit surface area needed from the piezoelectric pillars can be expressed as

$$\dot{W}_p = \frac{2}{\tau}\int_{z_1}^{z_2} (P_g/2 + P_c)\mathrm{d}z \tag{12}$$

where τ is the oscillation period, and $z_1 = d_{\mathrm{PE},c}(t=0) = 0.1$ μm and $z_2 = d_{\mathrm{PE},c}(t=\tau/2) = 69.9$ μm are the minimum and maximum gaps between the PE plate and the cold plate. Note that the gravitational pressure P_g needs to be overcome only in the ascending motion of the PE plate.

The electrical energy density N_D is defined as the electrical energy generated per cycle and per unit volume of the pyroelectric material and can be determined experimentally by operating the Olsen cycle across the phase transition interval between temperatures T_{p1} and T_{p2} [6,10,17]. Then, according to Assumption 8, the electrical power density generated by the device at a given frequency can be estimated. If the thickness of the PE thin film is denoted by L_{PE}, the electrical power generated at frequency f per unit surface area of the PE plate is given by

$$\dot{W}_e = fL_{\mathrm{PE}}N_D \tag{13}$$

3.9 Maximum Efficiencies. The Carnot efficiency is the maximum thermodynamic efficiency that can be theoretically achieved by a power cycle consisting of reversible processes and operating between two thermal reservoirs at temperatures T_c and T_h. It is expressed as

$$\eta_{\mathrm{Carnot}} = 1 - \frac{T_c}{T_h} \tag{14}$$

Alternatively, the Curzon–Ahlborn efficiency η_{CA} represents the efficiency at the maximum power production of heat engines, which only considers the irreversibility of the finite rate heat transfer between thermal sources and working fluids (endoreversible engines) [58]. The Curzon–Ahlborn efficiency η_{CA} is expressed as [58]

$$\eta_{\mathrm{CA}} = 1 - \sqrt{\frac{T_c}{T_h}} \tag{15}$$

To assess the performance of the conceptual device, it is instructive to compare the efficiency of the device with both η_{Carnot} and η_{CA}.

4 Results and Discussion

4.1 Effect of Absorbing Layers. This section aims at assessing the effect of the SiO_2 absorbing layers on the device performance. The temperature oscillations of a PE plate consisting of a pyroelectric material 60/40 P(VDF-TrFE) film sandwiched between two aluminum electrodes were simulated with and without a 1.5 μm thick SiO_2 absorbing layers. The device was operated at $f=1$ Hz with the cold plate at $T_c=273$ K and the hot plate at $T_h=388$ K. Figure 3 shows the corresponding temperature variations of the PE plate as a function of time. It indicates that the PE plate with SiO_2 absorbing layers underwent a temperature swing of $\Delta T_{\mathrm{PE}}=63$ K, while that without absorbing layers reached 50 K. Therefore, the presence of SiO_2 absorbing layers enhanced the nanoscale radiative heat transfer from the cold and hot plates to the PE plate. This, in turn, increased the amplitude of the PE plate temperature oscillations. It also resulted in a higher operating frequency and a larger power density. Consequently, in view of these results, only the device with SiO_2 absorbing layers will be considered in the remaining part of the study.

4.2 Effect of Oscillation Frequency. As previously discussed, the energy density N_D is assumed to be a constant as long as the device is operated across the phase transition interval between temperatures T_{p1} and T_{p2}. Therefore, increasing the frequency of temperature oscillation in the PE plate will increase the power density of the device. On the other hand, the Olsen cycle using 60/40 P(VDF-TrFE) was experimentally performed across

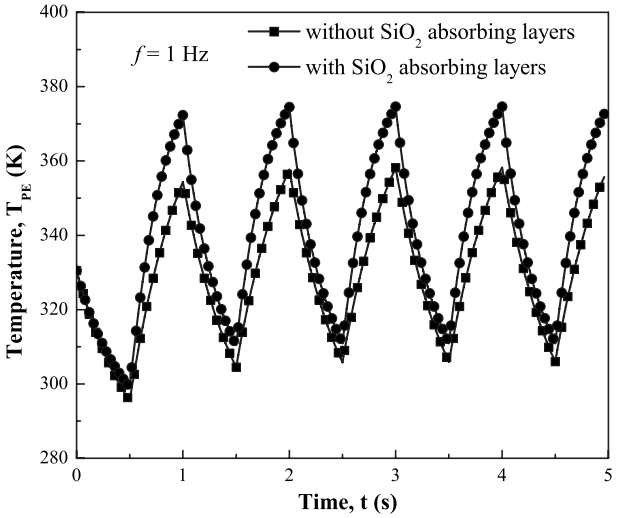

Fig. 3 Temperature oscillation of the PE plate made of 60/40 P(VDF-TrFE) as a function of time oscillating at 1 Hz between cold and hot plates at $T_c=273$ K and $T_h=388$ K, with and without SiO_2 absorbing layers

the phase transition occurring between temperatures $T_{p1}=313$ K and $T_{p2}=370$ K corresponding to $\Delta T_{\mathrm{PE}}=57$ K with $T_{\mathrm{Curie}}=348$ K and resulted in an energy density N_D of 279 J/l [17].

Figure 4(*a*) shows the PE temperature as a function of time at a frequency $f=0.6$ Hz for $T_c=273$ K and $T_h=388$ K. It indicates that the PE temperature oscillated between minimum and maximum temperatures $T_{\min}=297$ K and $T_{\max}=382$ K across the Curie temperature $T_{\mathrm{Curie}}=348$ K, ensuring a complete phase transition [17]. Similarly, Fig. 4(*b*) shows that the temperature oscillated between 315 K and 369 K at a frequency $f=1.2$ Hz. It is evident that the amplitude of the temperature oscillation decreased as the frequency increased. This result suggests that it is possible to achieve the desired temperature oscillation across the phase transition at a frequency ten times larger than that achieved by Olsen and co-workers using convective heat transfer [6].

In order to identify the largest frequency for which the temperature oscillation covers the phase transition, different frequencies were examined. Figure 5 shows the maximum and minimum temperatures reached by the PE plate made of 60/40 P(VDF-TrFE) with SiO_2 absorbing layers as a function of frequency. It indicates that for frequencies less than 1.2 Hz, the PE plate experienced temperature oscillations from below 313 K to above 370 K, thus covering the phase transition region [17]. According to Eq. (13), the maximum power output per unit surface area achieved was 0.84 $\mathrm{mW/cm^2}$ at 1.2 Hz. This is more than twice the power output reported by Kouchachvili and Ikura [17].

Alternatively, by choosing a material exhibiting a very strong electrocaloric effect, the power density can be further increased. For example, the composite thin film 0.9PMN-PT features a volumetric heat capacity of $(\rho c_p)_{\mathrm{PE}}=3\times10^6$ $\mathrm{J/m^3\,K}$ and an energy density of 432 J/l for a 10 K temperature variation from $T_{p1}=338$ K to $T_{p2}=348$ K [25,26]. Although such temperature interval is beyond the material Curie temperature of 333 K [26], it is still possible to generate a very large energy density due to the highly nonlinear behavior near that temperature. However, such composite films should be very thin in order to sustain very large electric fields and thus convert more heat into electric energy [25]. To achieve large power output per unit surface area with such a composite material, we considered a PE plate made of 100 layers of 300 nm 0.9PMN-PT thin films separated by 50 nm aluminum electrodes. The overall thicknesses of the pyroelectric material and aluminum electrodes were $L_{\mathrm{PE}}=30$ μm and $L_{\mathrm{Al}}=5$ μm, respectively. A 1.5 μm thick SiO_2 absorbing layer was also present

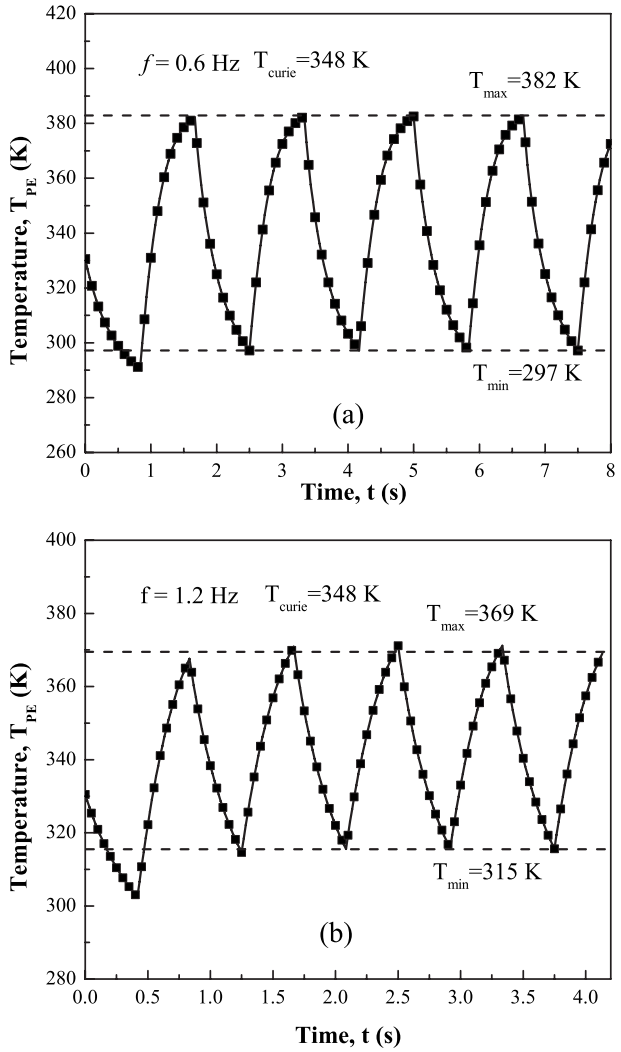

Fig. 4 Temperature oscillation of PE plate made of 60/40 P(VDF-TrFE) with SiO_2 absorbing layers as a function of time with T_c=273 K and T_h=388 K at frequencies of (*a*) *f*=0.6 Hz and (*b*) *f*=1.2 Hz

on both sides of the composite PE plate. Therefore, the overall PE plate thickness was $L_t=38$ μm, and the effective volumetric heat capacity was $(\rho c_p)_{\text{eff}}=2.82\times10^6$ J/m^3 K. The temperatures of the cold and hot plates were set as $T_c=283$ K and $T_h=383$ K, respectively, in order to achieve proper temperature oscillation. Figure 6 shows the maximum and minimum temperatures of oscillation as a function of frequency for the 0.9PMN-PT composite PE plate considered. Given the reported energy density $N_D=432$ J/l for 10 K temperature oscillations [25], the electrical power density $\dot{W}_e$ was estimated to be 6.5 mW/cm^2 at the working frequency of 5 Hz.

Finally, it is interesting to compare this power output with those of alternative technologies such as thermoelectric energy generators. A comparison was made between the PE device made of 60/40 P(VDF-TrFE) operating between $T_{\min}=313$ K and $T_{\max}=370$ K at 1.2 Hz, and thermoelectric generators operated between 313 K and 370 K. For example, Böttner et al. [59] achieved a power density of 0.06 mW/cm^2 at a temperature difference of 5 K at around 300 K using *n*-Bi_2Te_3 and *p*-$(Bi,Sb)_2Te_3$ materials. Assuming that the efficiency of a thermoelectric generator increases nearly linearly with temperature difference [60], the thermoelectric generator may achieve 0.7 mW/cm^2 between 313 K and 370 K. Thus, it is comparable to the power density of

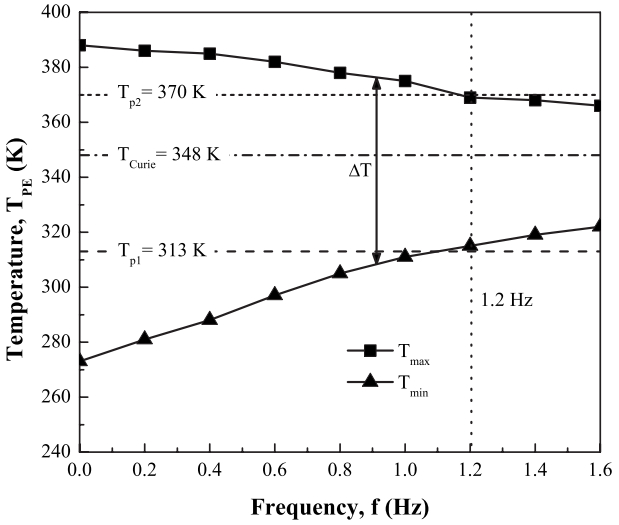

Fig. 5 Minimum and maximum temperatures of oscillation as a function of frequency for PE plate made of 60/40 P(VDF-TrFE) film with SiO_2 absorbing layers for T_c=273 K and T_h=388 K

0.84 mW/cm^2 obtained from the simulated results of the PE device using P(VDF-TrFE) for the same temperature difference.

4.3 Device Efficiency. To assess the device efficiency, the input power $\dot{W}_p$ consumed to oscillate the PE plate between the hot and cold sources was estimated. According to Eq. (12), the input oscillation power was estimated to be less than 10 μW/cm^2 for P(VDF-TrFE) at 1 Hz. This magnitude is also consistent with results reported in the literature for the piezoelectric material PZT [61]. Thus, the electrical power generated $\dot{W}_e$ was two orders of magnitude larger than the input power $\dot{W}_p$, which can thus be neglected. Similar results applied to the PE plate made of the 0.9PMN-PT thin film. Consequently, the maximum energy efficiency of the device η, defined by Eq. (10), could reach up to 0.2% at $f=1.2$ Hz for 60/40 P(VDF-TrFE). On the other hand, using the 0.9PMN-PT composite thin films resulted in an efficiency of 1.3% at $f=5$ Hz for a 10 K temperature difference. This is about 50 times larger than that estimated by van der Ziel [21].

Figure 7 shows the efficiency ratio $\eta/\eta_{\text{Carnot}}$ and η/η_{CA} as a

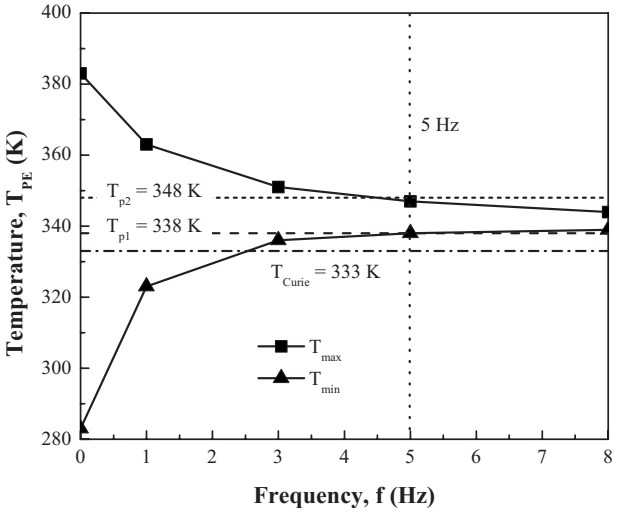

Fig. 6 Minimum and maximum temperatures of oscillation as a function of frequency for PE plate made of 0.9PMN-PT thin films with SiO_2 absorbing layers for T_c=283 K and T_h=383 K

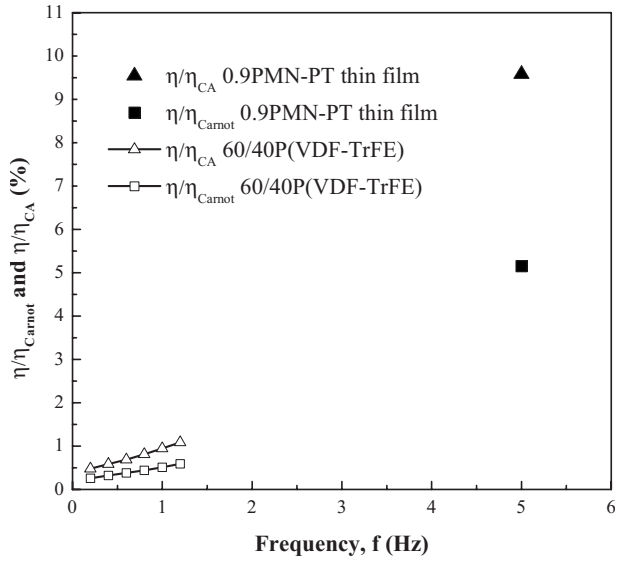

Fig. 7 Efficiency ratios η/η_{Carnot} and η/η_{CA} as a function of frequency for PE plates made (i) of 60/40 P(VDF-TrFE) for temperature oscillations shown in Fig. 5 and (ii) of 0.9PMN-PT ($T_{max}-T_{min}=10$ K) with SiO_2 absorbing layers

function of frequency for PE plates made of a single 60/40 P(VDF-TrFE) film and multiple films of 0.9PMN-PT with their electrodes. It suggests that by using the copolymer P(VDF-TrFE) at the operating frequency of 1.2 Hz with a 57 K temperature oscillation amplitude, up to 0.6% of the Carnot efficiency or 1.2% of the Curzon–Ahlborn efficiency can be achieved between $T_c=273$ K and $T_h=388$ K. As a reference, it is worth mentioning that Olsen and Bruno [6] experimentally obtained efficiencies that were about one magnitude smaller than the numerical results above using 73/27 P(VDF-TrFE) for the Olsen cycle between 296 K and 340 K. As for the 0.9PMN-PT composite plate, the efficiency at the operating frequency of 5 Hz for a 10 K temperature oscillation amplitude corresponds to 5% of the Carnot efficiency and 10% of the Curzon–Ahlborn efficiency for temperatures $T_c=283$ K and $T_h=383$ K.

4.4 Discussion. The 0.9PMN-PT composite thin film may feature an even larger energy density if the device was operated across the whole phase transition temperature interval, taking advantage of the nonlinear effect around the Curie temperature. Then, the device would reach a larger power output and higher efficiency. Alternatively, synthesis and processing of pyroelectric/ferroelectric materials with a larger energy density N_D should be explored. In addition, a multistage pyroelectric plate consisting of superimposed pyroelectric films with different Curie temperatures could be envisioned to harvest more energy through a wider phase transition region and to further increase the output energy density and efficiency of the device. A prototype of such a device should be experimentally assembled and operated to establish the feasibility of the concept investigated in this manuscript. Finally, a life cycle analysis of the device should also be performed to fully assess its usefulness.

Finally, note that (i) parallelism is not essential to the device operation and (ii) a gap smaller than 100 nm, if it can be achieved in practice, would result in larger temperature oscillations or operating frequencies for a given temperature swing. In turn, the power density and efficiency of the device would increase. Touching, however, would not be beneficial since heat transfer would then be by conduction, which is slow and limited by the thermal contact resistance between the PE plate and the cold or hot plates.

5 Conclusion

This paper combines, for the first time, nanoscale thermal radiation and pyroelectric energy conversion for harvesting low grade waste heat. The nanoscale radiation model was validated against results reported in the literature. The proposed device made use of the enhanced radiative heat transfer across a nanosize gap to achieve high operating frequencies or large temperature oscillations in a composite PE plate. The hot and cold plates were coated with a SiO_2 absorbing layer to further enhance the radiative heat fluxes. The maximum efficiency and power density for a PE plate made of 60/40 P(VDF-TrFE) operated between 273 K and 388 K were found to be 0.2% and 0.84 mW/cm^2, respectively. The PE plate made of the 0.9PMN-PT composite thin films achieved a higher efficiency and a larger power output, namely, 1.3% and 6.5 mW/cm^2, respectively, for a temperature oscillation amplitude of 10 K around 343 K at 5 Hz.

Nomenclature

c = speed of light in vacuum ($c=2.998\times10^8$ m/s)
c_p = specific heat (J/kg K)
d = distance between two parallel plates (μm)
$d_{PE,c}$, $d_{PE,h}$ = distance between the PE plate and the cold and hot plates, respectively (μm)
f = cycle frequency (Hz)
$\hbar$ = reduced Planck's constant ($\hbar=1.055\times10^{-34}$ J s)
h_r = radiative heat transfer coefficient (W/m^2 K)
H = Hamaker constant (J)
i = electrical current (A)
$I^0_{b\omega}$ = spectral blackbody radiation intensity (W/m^2)
k = thermal conductivity (W/m K)
k_B = Boltzmann's constant ($k_B=1.3806\times10^{-23}$ J/K)
L = film thickness (μm)
L_t = total PE plate thickness (μm)
N_q = numbers of wavevectors
N_ω = numbers of frequencies
N_D = energy density of pyroelectric material (J/l)
p = z-component of wavevector (rad/m)
p_c = pyroelectric coefficient ($\mu C/m^2$ K)
P_c = Casimir pressure (Pa)
P_g = gravitational pressure (Pa)
P_{rad} = radiation pressure (Pa)
P_v = van der Waals pressure (Pa)
q = x-component of wavevector (rad/m)
q'' = heat flux (W/m^2)
$\dot{Q}_{in}$ = average net heat flux from the hot plate to the PE plate (W/m^2)
r = Fresnel coefficient
s_1 = z-component of the wavevector in medium 1 ($s_1=\sqrt{\varepsilon_{r1}\omega^2/c^2-q^2}$)
t = time (s)
T = temperature (K)
T_{Curie} = Curie temperature (K)
$\dot{W}_e$ = average generated electrical power (mW/cm^2)
$\dot{W}_p$ = average input oscillation power (mW/cm^2)
x,z = transverse and longitudinal coordinates

Greek Symbols

$\alpha_{1,2}$ = total hemispherical emissivity
ε_0 = dielectric permittivity of vacuum ($\varepsilon_0=8.85\times10^{-12}$ F/m)
ε_r = dielectric constant

$\Phi_{12}(\omega,d)$ = spectral efficiency in radiation transfer between media 1 and 2
γ = relaxation frequency (rad/s)
η_{Carnot}, η_{CA} = Carnot and Curzon–Ahlborn efficiencies
λ = wavelength (μm)
ρ = density (kg/m^3)
σ = Stefan–Boltzmann constant ($\sigma=5.67\times10^{-8}$ W/m^2 K^4)
τ = cycle period ($\tau=1/f$) (s)
ω = angular frequency (rad/s)
ω_0 = oscillator frequency (rad/s)
ω_p = plasma frequency (rad/s)

Subscripts

1, 2, 3 = refers to media 1, 2, and 3
Al = Al electrodes
b = blackbody
c = cold plate
eff = effective properties of the PE plate
h = hot plate
p = phase transition
PE = PE thin film or plate
ω = refers to values at frequency ω

References

[1] Lawrence Livermore National Laboratory, 2008, "U.S. Energy Flow Trends—2002," https://eed.llnl.gov/flow/02flow.php
[2] Olsen, R., 1982, "Ferroelectric Conversion of Heat to Electrical Energy—A Demonstration," J. Energy, **6**(2), pp. 91–95.
[3] Olsen, R., Bruno, D., and Briscoe, J., 1984, "Cascaded Pyroelectric Energy Converter," Ferroelectrics, **59**(1), pp. 205–219.
[4] Olsen, R., Bruno, D., Briscoe, J., and Butler, W., 1981, "A Pyroelectric Energy Converter Which Employs Regeneration," Ferroelectrics, **38**(1–4), pp. 975–978.
[5] Olsen, R., and Brown, D., 1982, "High-Efficiency Direct Conversion of Heat to Electrical Energy-Related Pyroelectric Measurements," Ferroelectrics, **40**(1–2), pp. 17–27.
[6] Olsen, R., Bruno, D., and Briscoe, J. M., 1985, "Pyroelectric Conversion Cycle of Vinylidene Fluoride-Trifluoroethylene Copolymer," J. Appl. Phys., **57**(11), pp. 5036–5042.
[7] Olsen, R., Bruno, D., and Briscoe, J. M., 1985, "Pyroelectric Conversion Cycles," J. Appl. Phys., **58**(12), pp. 4709–4716.
[8] Ikura, M., 2002, "Conversion of Low-Grade Heat to Electricity Using Pyroelectric Copolymer," Ferroelectrics, **267**(6), pp. 403–408.
[9] Kouchachvili, L., and Ikura, M., 2007, "Pyroelectric Conversion-Effects of P(VDF-TrFE) Preconditioning on Power Conversion," J. Electrost., **65**(3), pp. 182–188.
[10] Olsen, R., and Bruno, D., 1986, "Pyroelectric Conversion Materials," *Proceedings of the 21st Intersociety Energy Conversion Engineering Conference*, pp. 89–93.
[11] Vanderpool, D., Yoon, J., and Pilon, L., 2008, "Simulations of a Prototypical Device Using Pyroelectric Materials for Harvesting Waste Heat," Int. J. Heat Mass Transfer, **51**, pp. 5052–5062.
[12] Nguyen, H. T., Navid, A., and Pilon, L., 2010, "Improved Pyroelectric Energy Converter for Waste Heat Energy Harvesting Using Co-Polymer P(VDF-TrFE) and Olsen Cycle," Appl. Therm. Eng., to be published.
[13] Lang, S. B., 2005, "Pyroelectricity: From Ancient Curiosity to Modern Imaging Tool," Phys. Today, **58**(8), pp. 31–36.
[14] Cravalho, E. G., Tien, C. L., and Caren, R. P., 1967, "Effect of Small Spacings on Radiative Transfer Between Two Dielectrics," ASME J. Heat Transfer, **89**(4), pp. 351–358.
[15] Polder, D., and Van Hove, M., 1971, "Theory of Radiative Heat Transfer Between Closely Spaced Bodies," Phys. Rev. B, **4**(10), pp. 3303–3314.
[16] Olsen, R., and Evans, D., 1983, "Pyroelectric Energy Conversion—Hysteresis Loss and Temperature Sensitivity of a Ferroelectric Material," J. Appl. Phys., **54**(10), pp. 5941–5944.
[17] Kouchachvili, L., and Ikura, M., 2008, "Improving the Efficiency of Pyroelectric Conversion," Int. J. Energy Res., **32**(4), pp. 328–335.
[18] Navid, A., Lynch, C. S., and Pilon, L., 2010, "Purified and Porous Poly(Vinylidene Fluoride-Trifluoroethylene) Thin Films for Pyroelectric Infrared Sensing and Energy Harvesting," Smart Mater. Struct., **19**, p. 055006.
[19] Clingman, W. H., and Moore, R. G., 1961, "Application of Ferroelectricity to Energy Conversion Processes," J. Appl. Phys., **32**(4), pp. 675–681.
[20] Fatuzzo, E., Kiess, H., and Nitsche, R., 1966, "Theoretical Efficiency of Pyroelectric Power Converters," J. Appl. Phys., **37**(2), pp. 510–516.
[21] van der Ziel, A., 1974, "Solar Power Generation With the Pyroelectric Effect," J. Appl. Phys., **45**(9), p. 4128.
[22] Itskovsky, M. A., 1999, "Pyroelectric Hysteresis Loop at Ferroelectric Phase Transition," J. Appl. Phys., **85**(8), pp. 4256–4258.
[23] Smolenskii, G. A., Krainik, N. N., Khuchua, N. P., Zhdanova, V. V., and Mylnikova, I. E., 1966, "The Curie Temperature of $LiNbO_3$," Phys. Status Solidi B, **13**(2), pp. 309–314.
[24] Gonzalo, J. A., 1976, "Ferroelectric Materials as Energy Converters," Ferroelectrics, **11**(1), pp. 423–430.
[25] Sebald, G., Pruvost, S., and Guyomar, D., 2008, "Energy Harvesting Based on Ericsson Pyroelectric Cycles in a Relaxor Ferroelectric Ceramic," Smart Mater. Struct., **17**(1), p. 015012.
[26] Mischenko, A. S., Zhang, Q., Whatmore, R. W., Scott, J. F., and Mathur, N. D., 2006, "Giant Electrocaloric Effect in the Thin Film Relaxor Ferroelectric $0.9PbMg_{1/3}Nb_{2/3}O_3$–$0.1PbTiO_3$ Near Room Temperature," Appl. Phys. Lett., **89**(24), p. 242912.
[27] Rytov, S. M., 1953, *Theory of Electrical Fluctuation and Thermal Radiation*, Academy of Science of USSR, Moscow.
[28] Mulet, J. P., Joulain, K., Carminati, R., and Greffet, J. J., 2002, "Enhanced Radiative Heat Transfer at Nanometric Distances," Microscale Thermophys. Eng., **6**(3), pp. 209–222.
[29] DiMatteo, R. S., Greiff, P., Finberg, S. L., Young-Waithe, K. A., Choy, H. K. H., Masaki, M. M., and Fonstad, C. G., 2001, "Enhanced Photogeneration of Carriers in a Semiconductor Via Coupling Across a Nonisothermal Nanoscale Vacuum Gap," Appl. Phys. Lett., **79**(12), pp. 1894–1896.
[30] Whale, M. D., and Cravalho, E. G., 2002, "Modeling and Performance of Microscale Thermophotovoltaic Energy Conversion Devices," IEEE Trans. Energy Convers., **17**(1), pp. 130–142.
[31] Zhang, Z. M., Fu, C. J., and Zhu, Q. Z., 2003, "Optical and Thermal Radiative Properties of Semiconductors Related to Micro/Nanotechnology," Adv. Heat Transfer, **37**, pp. 179–296.
[32] Hargreaves, C., 1969, "Anomalous Radiative Transfer Between Closely-Spaced Bodies," Phys. Lett., **30A**(9), pp. 491–492.
[33] Domoto, G. A., Boehm, R. F., and Tien, C. L., 1970, "Experimental Investigation of Radiative Transfer Between Metallic Surfaces at Cryogenic Temperatures," ASME J. Heat Transfer, **92**(3), pp. 412–417.
[34] Kittel, A., Wischnath, U. F., Welker, J., Huth, O., Ruting, F., and Biehs, S. A., 2008, "Near-Field Thermal Imaging of Nanostructured Surfaces," Appl. Phys. Lett., **93**(19), p. 193109.
[35] Pan, J. L., 2000, "Radiative Transfer Over Small Distances From a Heated Metal," Opt. Lett., **25**(6), pp. 369–371.
[36] Pan, J. L., Choy, H. K. H., and Fonstad, C. G., 2000, "Very Large Radiative Transfer Over Small Distances From a Blackbody for Thermophotovoltaic Applications," IEEE Trans. Electron Devices, **47**(1), pp. 241–249.
[37] Loomis, J., and Maris, H., 1994, "Theory of Heat Transfer by Evanescent Electromagnetic-Waves," Phys. Rev. B, **50**(24), pp. 18517–18524.
[38] Pendry, J. B., 1999, "Radiative Exchange of Heat Between Nanostructures," J. Phys.: Condens. Matter, **11**(35), pp. 6621–6633.
[39] Hu, L., Narayanaswamy, A., Chen, X., and Chen, G., 2008, "Near-Field Thermal Radiation Between Two Closely Spaced Glass Plates Exceeding Planck's Blackbody Radiation Law," Appl. Phys. Lett., **92**(13), p. 133106.
[40] Narayanaswamy, A., Shen, S., and Chen, G., 2008, "Near-Field Radiative Heat Transfer Between a Sphere and a Substrate," Phys. Rev. B, **78**(11), p. 115303.
[41] Narayanaswamy, A., Shen, S., Hu, L., Chen, X. Y., and Chen, G., 2009, "Breakdown of the Planck Blackbody Radiation Law at Nanoscale Gaps," Appl. Phys. A: Mater. Sci. Process., **96**(2), pp. 357–362.
[42] Shen, S., Narayanaswamy, A., and Chen, G., 2009, "Surface Phonon Polaritons Mediated Energy Transfer Between Nanoscale Gaps," Nano Lett., **9**(8), pp. 2909–2913.
[43] Biehs, S. A., Reddig, D., and Holthaus, M., 2007, "Thermal Radiation and Near-Field Energy Density of Thin Metallic Films," Eur. Phys. J. B, **55**(3), pp. 237–251.
[44] Biehs, S. A., 2007, "Thermal Heat Radiation, Near-Field Energy Density and Near-Field Radiative Heat Transfer of Coated Materials," Eur. Phys. J. B, **58**(4), pp. 423–431.
[45] Francoeur, M., Mengüç, M. P., and Vaillon, R., 2008, "Near-Field Radiative Heat Transfer Enhancement Via Surface Phonon Polaritons Coupling in Thin Films," Appl. Phys. Lett., **93**(4), p. 043109.
[46] Fu, C. J., and Tan, W. C., 2009, "Near-Field Radiative Heat Transfer Between Two Plane Surfaces With One Having a Dielectric Coating," J. Quant. Spectrosc. Radiat. Transf., **110**(12), pp. 1027–1036.
[47] Volokitin, A. I., and Persson, B. N. J., 2001, "Radiative Heat Transfer Between Nanostructures," Phys. Rev. B, **63**(20), p. 205404.
[48] Modest, M., 2003, *Radiative Heat Transfer*, Academic, San Diego, CA.
[49] Joulain, K., Mulet, J. P., Marquier, F., Carminati, R., and Greffet, J. J., 2005, "Surface Electromagnetic Waves Thermally Excited: Radiative Heat Transfer, Coherence Properties and Casimir Forces Revisited in the Near Field," Surf. Sci. Rep., **57**(3–4), pp. 59–112.
[50] Brewster, M. Q., 1992, *Thermal Radiative Transfer and Properties*, Wiley-Interscience, New York.
[51] Chan, H. B., Aksyuk, V. A., Kleiman, R. N., Bishop, D. J., and Capasso, F., 2001, "Quantum Mechanical Actuation of Microelectromechanical Systems by the Casimir Force," Science, **291**(5510), pp. 1941–1944.
[52] Bohren, C. F., and Huffman, D. R., 2004, *Absorption and Scattering of Light by Small Particles*, Wiley-Interscience, New York.
[53] Casimir, H. B. G., and Polder, D., 1948, "The Influence of Retardation on the London-van der Waals Forces," Phys. Rev., **73**(4), pp. 360–372.
[54] Serry, F. M., Walliser, D., and Maclay, G. J., 1995, "The Anharmonic Casimir Oscillator (ACO)—The Casimir Effect in a Model Microelectromechanical System," J. Microelectromech. Syst., **4**(4), pp. 193–205.

[55] Mostepanenko, V. M., and Trunov, N. N., 1997, *The Casimir Effect and Its Applications*, Oxford University Press, New York.
[56] Israelachvili, J., 1992, *Intermolecular and Surface Forces*, Academic, San Diego, CA.
[57] Nichols, E. F., and Hull, G. F., 1903, "The Pressure Due to Radiation," Astrophys. J., **17**(1), pp. 315–351.
[58] Curzon, F. L., and Ahlborn, B., 1975, "Efficiency of a Carnot Engine at Maximum Power Output," Am. J. Phys., **43**(1), pp. 22–24.
[59] Böttner, H., Nurnus, J., Gavrikov, A., Kühner, G., Jägle, M., Künzel, C., Eberhard, D., Plescher, G., Schubert, A., and Schlereth, K. H., 2004, "New Thermoelectric Components Using Microsystem Technologies," J. Microelectromech. Syst., **13**(3), pp. 414–420.
[60] Priya, S., and Inman, D. J., 2009, *Energy Harvesting Technologies*, Springer, New York.
[61] Jordan, T., Ounaies, Z., Tripp, J., and Tcheng, P., 1999, "Electrical Properties and Power Considerations of a Piezoelectric Actuator," Mater. Res. Soc. Symp. Proc., **604**, pp. 203–208.

An Experimental Study to Show the Effect of Thermal Stress on Thermal Contact Conductance at Sub-megapascal Contact Pressures

Prashant Misra

J. Nagaraju[1]
e-mail: solarjnr@isu.iisc.ernet.in

Department of Instrumentation,
Indian Institute of Science,
Bangalore 560012, India

Experimental studies are presented to show the effect of thermal stresses on thermal contact conductance (TCC) at low contact pressures. It is observed that in a closed contact assembly, contact pressure acting on the interface changes with the changing temperature of contact members. This change in contact pressure consequently causes variations in the TCC of the junction. A relationship between temperature change and the corresponding magnitude of developed thermal stress in a contact assembly is determined experimentally. Inclusion of a term called temperature dependent load correction factor is suggested in the theoretical model for TCC to make it capable of predicting TCC values more accurately in contact assemblies that experience large temperature fluctuations. [DOI: 10.1115/1.4001615]

Keywords: OFHC Cu, thermal contact conductance, thermal stress, load correction factor

1 Introduction

Ordinary materials (including metals) have a tendency to expand when heated and contract when cooled. These thermal strains are reversible in nature, meaning thereby that the material returns to its original shape when the temperature returns to its original value. Thermal stress is generated in a material if it is constrained and unable to expand freely under the influence of increasing temperature. Due to a uniform temperature increase (ΔT), a bar of length L, fixed between two rigid supports, is subjected to thermal stress (p_t), given by

$$p_t = E \cdot \alpha \cdot \Delta T \tag{1}$$

In case one of the supports yields by a small amount (a), the magnitude of generated thermal stress is reduced and is given by

$$p_t = (L \cdot \alpha \cdot \Delta T - a)\frac{E}{L}, \quad a \le L \cdot \alpha \cdot \Delta T \tag{2}$$

Thermal contact conductance (TCC) of a junction depends on a number of parameters such as contact pressure, material properties (thermal conductivity, hardness, etc.), surface topography, and interstitial medium. Over the decades, a number of experimental and theoretical investigations have been carried out by researchers in order to understand and formulate the influence of these parameters on TCC. According to Yovanovich [1], TCC across metallic contacts is given by

$$h_c = 1.25k\frac{m}{\sigma}\left(\frac{P}{H}\right)^{0.95} \tag{3}$$

It is evident in Eq. (3) that the temperature dependence of TCC is handled by the thermal conductivity (k) and microhardness (H) of the material. For metals, in general, both thermal conductivity and hardness are weak functions of temperature. Hence, it is expected according to Eq. (3) that TCC is not significantly affected by the temperature of the contact. However, temperature variations cause thermal stresses in a closed contact assembly, which affect the contact pressure acting on the interface. Since the TCC of a junction is a strong function of the contact pressure, even a small change in contact pressure can have a considerable effect on the TCC. Consider a closed contact in which the contact pressure is maintained at a fixed value so as to get the optimum performance. Now, suppose that the temperature in the contact assembly increases during operation. Being unable to expand freely, various components of the assembly experience thermal stresses, and as a result the overall contact pressure acting on the interface is increased. Consequently, the TCC of the interface will also be increased. Because of this unexpected increase in contact pressure, the value of TCC predicted by Eq. (3) will be much lower than the actual value. Hegazy [2] collected TCC data for various contacts and found that at low contact pressures, the models underpredicted the TCC values for all materials and roughness levels. The low contact pressure range is when the ratio $P/H < 5 \times 10^{-4}$ approximately. Other researchers [3–6] have also reported similar types of behavior, and the primary reason behind this is widely speculated to be the effect of thermal stresses.

In this article, we describe an experimental study to show the presence of thermal stress in contacts and its effect on TCC. The increase in contact pressure with increasing temperature is measured in situ with the help of a load cell. Experimental data are compared with the theoretical model, and a possible correction is proposed to make the models capable of handling the effect of thermal stresses at small contact loads.

2 Experimentation

The test facility developed for simultaneously measuring electrical contact resistance, and TCC [7] is used for the experimentation. However, only TCC measurements are made in the present study. The test column assembly that holds the contact specimens is shown in Fig. 1. The hydraulic loading system is replaced with a screw-jack system with which a desired contact load is applied. The axial contact load acting on the specimens is measured with the help of a compression type load cell placed at the bottom. Steady state temperature data obtained with the help of thermocouples at various locations in the test column are used for heat flow rate and interface temperature drop estimations. A detailed description of the setup, its functioning, and the methodology used for TCC measurements is provided elsewhere [7].

All the experiments are conducted on oxygen free high conductivity (OFHC) Cu specimens for which

$$k(T) = 385.10 - (0.19252)T, \quad 20 < T < 180\ ^\circ\mathrm{C} \tag{4}$$

Cylindrical specimens of 40 mm length and 16 mm diameter are prepared from a single bar stock of material to ensure identical material properties. To insert the thermocouples, three holes (1.2 mm diameter, 8 mm deep, and 10 mm apart) are drilled in each specimen along its length. Contact surfaces are polished and then thoroughly cleaned to ensure a better metal to metal contact. Prior to conducting experiments, the surface topography and microhardness of contact surfaces are measured, and the values are listed below:

$$\sigma = 0.283\ \mu\mathrm{m}, \quad m = 0.003, \quad H = 1.59 \times 10^9\ \mathrm{N/m^2}$$

Prior to actual experiments, the specimens are subjected to at least

[1]Corresponding author.

Contributed by the Heat Transfer Division of ASME for publication in the JOURNAL OF HEAT TRANSFER. Manuscript received July 3, 2009; final manuscript received March 1, 2010; published online June 29, 2010. Assoc. Editor: Ofodike A. Ezekoye.

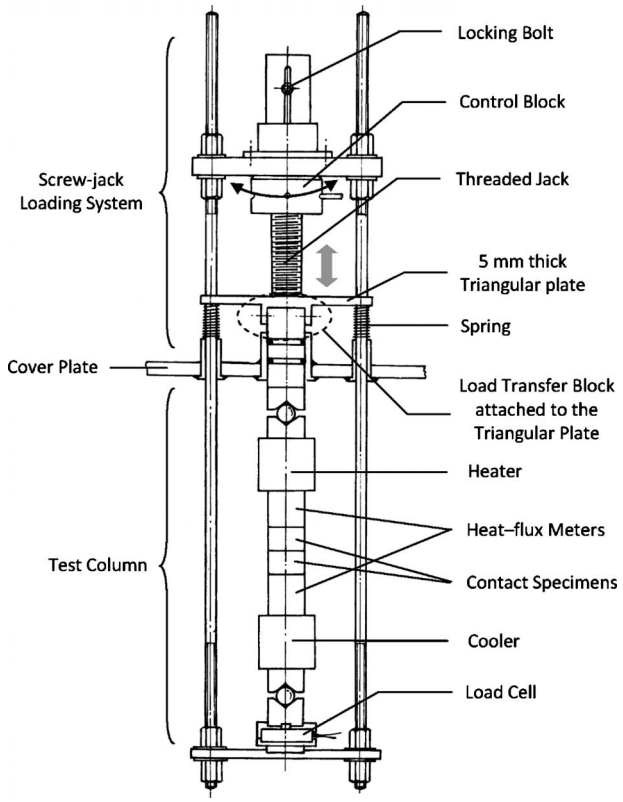

Fig. 1 Test column assembly

five loading-unloading cycles over the entire contact load range to minimize the effect of hysteresis on successive measurement cycles.

In the first part of the experiment, the applied contact pressure is fixed at some minimum value. This contact pressure is not changed manually hereafter in this part. The temperature of the contact is increased in steps, and TCC measurements are made at each step. With the rising temperatures in the test column, thermal stresses set in, and as a result the compressive load in the column increases. This increase in contact load is sensed by the load cell connected in series with the column. By measuring the interface temperature and the contact load at every step, a linear relationship (Eq. (5)) is obtained between the temperature change and the corresponding change in the contact pressure. In the second part of the experiment, the interface temperature is kept unchanged. The contact load is manually increased in steps, and the TCC measurements are again taken at every step. The contact load values (steps), at which the measurements are made, are calculated from the corresponding values of change in temperature recorded in the first part (using Eq. (5)).

The experiments are conducted in three different environments (vacuum, argon, and nitrogen) on the same pair of specimens. In case of gaseous environments, the gas pressure is maintained at 2 bars. The uncertainty in TCC measurements is $\pm 6\%$. A detailed uncertainty analysis is given in Ref. [8].

3 Results and Discussion

Figure 2(*a*) shows the variation in compressive load (contact pressure) in the test column with interface temperature. It can be observed in Fig. 2(*a*) that the contact pressure always increases linearly with increasing interface temperature. Furthermore, this variation in contact pressure with interface temperature is more or less the same in all the environments. Expectedly, the environment has no effect on the generated thermal stress in the test column as it purely depends on the temperature change and the properties of test column materials. Figure 2(*b*) shows the change in contact pressure (ΔP) plotted against the change in interface temperature (ΔT) for the three environments. The data are fitted in the form of a linear correlation in such a way that the fitted line is forced to pass through the origin (the change in contact pressure must be zero when there is no change in the interface temperature). The correlation for calculating the thermal stress in the test column is

$$\Delta P = p_t = 14.44 \Delta T \tag{5}$$

Using Eq. (5), the magnitude of thermal stress in the test column can be calculated for a known interface temperature change, without any prior knowledge of the initial contact pressure. Ideally, thermal stress can also be calculated from the temperature change and material properties of the individual components of the test column by using the general relationship of Eq. (1). However, the

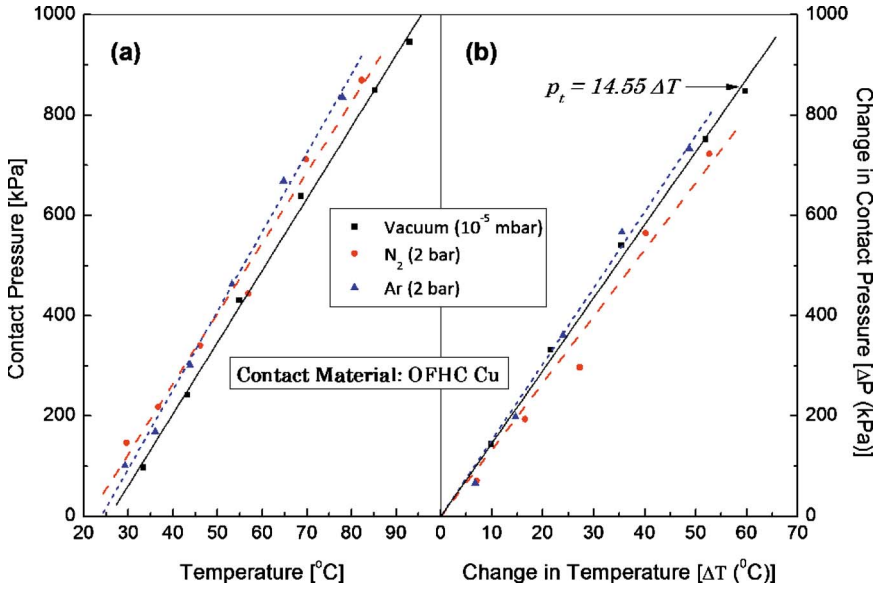

Fig. 2 (*a*) Variation in contact pressure with interface temperature. (*b*) Variation in thermal stress with change in interface temperature.

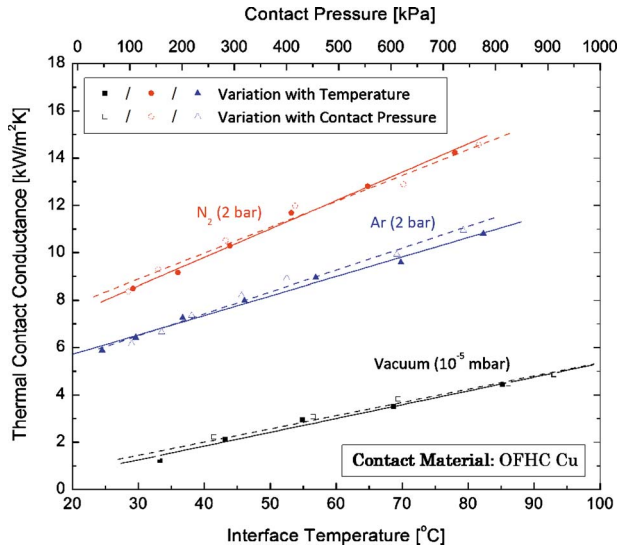

Fig. 3 Comparison of TCC measurements made by increasing the temperature and by increasing the contact pressure in vacuum, nitrogen, and argon environments

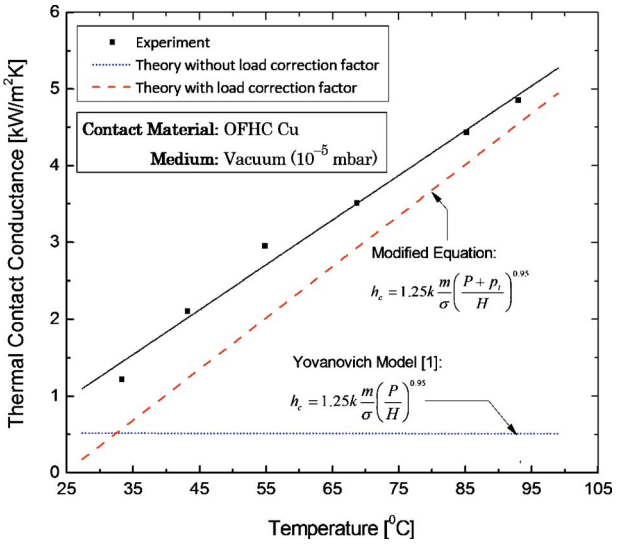

Fig. 4 Comparison of experimental data with the theoretical model (with and without modification)

magnitude of thermal stress calculated in this way comes out to be much higher than the experimentally measured one. This is because of the relaxation of generated thermal stresses due to the following possible reasons. The test column is not a single continuous piece of material but a stack of components. Interfaces between various components and the presence of relatively soft and compressible materials such as mica and heat sink compound [7] at some of the interfaces contribute toward stress relaxation. These interfaces provide some room for the thermal expansion of components, which causes a relaxation of thermally generated stresses, as suggested by Eq. (2).

Figure 3 shows the comparison of TCC values measured during the two parts of the experimentation in vacuum, N_2, and Ar environments. The values of TCC in gaseous environments are significantly higher than that in vacuum because of the enhanced thermal gap conductance. N_2 being the gas of higher thermal conductivity exhibits higher TCC compared with Ar. It can be observed that in all the environments, the TCC values measured in the first part when the temperature was varied (at constant contact pressure) are very close to those measured in the second part when the contact pressure was varied (at constant interface temperature). This observation confirms that the sharp change witnessed in the TCC values with increasing temperature is a result of generated thermal stress in the contact assembly.

As discussed earlier, the theoretical model (Eq. (3)) underpredicts the TCC values at small contact pressures because of thermal stresses. The provision for thermal stress can be made in the model by introducing a new parameter called temperature dependent load correction factor (p_t). p_t is nothing but the estimated thermal stress in the contact assembly for a given temperature change, which is added to the applied contact pressure. The modified version of Eq. (3) can be written as

$$h_c = 1.25k\frac{m}{\sigma}\left(\frac{P+p_t}{H}\right)^{0.95} \tag{6}$$

The changes in TCC due to thermal stresses become noticeable when the magnitude of applied contact pressure is small (comparable to the generated thermal stress). At sufficiently high contact pressures, the effect of thermal stress is suppressed by the applied contact pressure. When $P \gg p_t$, Eq. (6) becomes equivalent to Eq. (3). Experimental TCC data measured in vacuum are compared with the modified theoretical model (Eq. (6)) in Fig. 4 (represented by a dashed line). TCC values are plotted as a function of temperature. Yovanovich's model in its original form (Eq. (3)) is also plotted in the same figure (represented by dotted line). It is observed that after the introduction of the load correction factor, the TCC values predicted by the model are in better agreement with the experimental data.

It is worth mentioning here that the load correction factor for a contact assembly has to be determined experimentally, and it is unique to a particular assembly. As a consequence of stress relaxation, in multicomponent contact assemblies the net magnitude of thermal stress depends not only on elastic and thermophysical properties of component materials but also on the arrangement of different components in the assembly.

It also needs to be emphasized here that thermal stress can affect contact resistance only by altering the applied contact load, and an accurate prediction of data is possible by correcting the value of the contact load in the existing models. The anomalies between experimental data and TCC models at low contact pressures observed by various researchers may not always be entirely due to the presence of thermal stresses. A recent study by Milanez et al. [9] reports that the incorrect assumption of surface asperity height distributions being Gaussian causes the TCC models to underpredict the experimental data. Existing TCC models assume a Gaussian height distribution that does not remain true because of the truncation of highest asperities leading to the enhancement of thermal contact conductance.

4 Conclusions

The present study showed experimental evidence to support the idea that the disagreement between experimental and theoretical TCC values at low contact pressures is due to the effect of thermal stress. A comparison with experimental data showed that the introduction of a temperature dependent load correction factor in the theoretical model predicts more accurate TCC values in contact assemblies experiencing thermal stresses due to temperature variations. Fortunately, the effect of thermally generated stresses on TCC is generally diminished because of stress relaxation in contact assemblies due to reasons such as the presence of interfaces and the nonrigid nature of loading supports. But on the flip side, this stress relaxation makes it impossible to estimate the magnitude of thermal stress in a contact assembly from the temperature change and material properties of components.

Nomenclature

E = Young's modulus (N/m^2) (for OFHC Cu: $E = 115 \times 10^9$ N/m^2)
H = Vickers microhardness (N/m^2)
h_c, TCC = thermal contact conductance (W/m^2 K)
k = thermal conductivity (W/m K)
L = length (m)
m = combined average asperity slope
P = contact pressure (kPa)
p_t = thermal stress (kPa)
T = temperature (°C)
α = coefficient of thermal expansion (K^{-1}) (for OFHC Cu: $\alpha = 16.5 \times 10^{-6}$ K^{-1})
σ = combined rms roughness (μm)

References

[1] Yovanovich, M. M., 1981, "New Contact and Gap Correlations for Conforming Rough Surfaces," *Proceedings of the AIAA—16th Thermophysics Conference*, Paper No. AIAA-81-1164.

[2] Hegazy, A. A., 1985, "Thermal Joint Conductance of Conforming Rough Surfaces: Effect of Surface Micro-Hardness Variation," Ph.D. thesis, University of Waterloo, Waterloo, ON, Canada.

[3] Milanez, F. H., Culham, J. R., and Yovanovich, M. M., 2002, "Experimental Study on the Hysteresis Effect of Thermal Contact Conductance at Light Loads," *Proceedings of the 40th AIAA Aerospace Science Meeting Exhibit*, Reno, NV.

[4] Sridhar, M. R., and Yovanovich, M. M., 1996, "Thermal Contact Conductance of Tool Steel and Comparison With Model," Int. J. Heat Mass Transfer, **39**(4), pp. 831–839.

[5] Nho, K. M., 1990, "Experimental Investigation of Heat Flow Rate and Directional Effect on Contact Conductance of Anisotropic Ground/Lapped Interfaces," Ph.D. thesis, University of Waterloo, Waterloo, ON, Canada.

[6] DeVaal, J. W., 1988, "Thermal Joint Conductance of Surfaces Prepared by Grinding," Ph.D. thesis, University of Waterloo, Waterloo, ON, Canada.

[7] Misra, P., and Nagaraju, J., 2004, "Test Facility for Simultaneous Measurement of Electrical and Thermal Contact Resistance," Rev. Sci. Instrum., **75**(8), pp. 2625–2630.

[8] Misra, P., 2009, "Simultaneous Studies of Electrical Contact Resistance and Thermal Contact Conductance Across Metallic Contacts," Ph.D. thesis, Indian Institute of Science, Bangalore, India.

[9] Milanez, F. H., Yovanovich, M. M., and Culham, J. R., 2003, "Effect of Surface Asperity Truncation on Thermal Contact Conductance," IEEE Trans. Compon. Packag. Technol., **26**(1), pp. 48–54.

Heat Flux and Temperature Field Estimation Using Differential Interferometer

S. Prasanna
Research Scholar

S. P. Venkateshan[1]
Professor
e-mail: spv@iitm.ac.in

Department of Mechanical Engineering,
Heat Transfer and Thermal Power Laboratory,
IIT Madras,
Chennai 600036, India

A new methodology based on least-squares approach has been developed to estimate the temperature field from an interferogram recorded using a Differential interferometer (DI). The interferograms are digitally evaluated using two dimensional Fourier transforms to retrieve the temperature gradient field. Temperature field is constructed by fitting a cubic spline to the first derivatives data. The methodology has been applied to both experimental and synthetic interferograms. Both convective heat flux and temperature field were predicted accurately. The role of image noise and errors in the temperature measurements on the temperature field estimation have been studied with the aid of synthetic interferograms. [DOI: 10.1115/1.4001630]

Keywords: differential interferometer, digital analysis, thermal visualization

1 Introduction

Interferometry is a nonintrusive optical method used to make quantitative heat transfer measurements. It is based on the principle of superposition of two coherent light beams, which have different optical path lengths, caused while they traverse a medium with nonuniform refractive index n, which itself is brought about by a nonuniform temperature field. When two coherent beams of intensity i_1 and i_2 with relative phase difference ϕ superimposed, the resultant intensity field would be [1]

$$i_r = i_1 + i_2 + \sqrt{i_1 i_2}\cos(\phi) \tag{1}$$

which forms a fringe field. For a Differential interferometer (DI), the fringes are lines of constant density gradient (and hence, constant temperature gradient). If the flow field is assumed to be two dimensional, the optical path difference of the light rays traveling through the test section of length L would be $2L\Delta n$, and the relation between the optical path difference (OPD) and phase difference ϕ is

$$\phi = \frac{OPD}{\lambda}2\pi = \frac{2L\Delta n}{\lambda}2\pi = 2\pi m \tag{2}$$

where m is the fringe shift factor [2]. By estimating the phase field from an interferogram, heat flux from surfaces can be determined [2]. Nevertheless, the estimation of the temperature field would throw light on the *qualitative* nature of the flow and thermal fields. In heat transfer applications, it is important to know the entire temperature field since the temperature level plays a crucial role in deciding on the suitable design parameters. The present paper intends to present a method to estimate the temperature field from a *single* interferogram using a completely automated digital analysis.

2 Fringe Analysis

The working principle and construction details of DI (Fig. 1) are given in Ref. [2] and will not be repeated here. The intensity distribution of a typical interferogram can be represented as

$$i_r(x,y) = a(x,y) + b(x,y)\cos[\theta(x,y)] + \text{noise} \tag{3}$$

The interferograms captured contains Gaussian noise due to the limitations of the digital camera and are eliminated by selecting a suitable low pass filter. The main issue in the retrieval of the phase map from an interferogram is that a, b, and θ are unknown, and more than one interferograms would be necessary to estimate the unknowns. This is not favorable for heat transfer research, especially for transient problems. Therefore, it is necessary to estimate the phase field from a single interferogram. In the present paper, phase field is obtained from a single interferogram employing carrier frequency method [3]. A high frequency phase is added to the original wavefront, so that the phase map stored in the interferogram corresponds to $\theta(x,y) = 2\pi f_x x + 2\pi f_y y + \phi(x,y)$, where f_x and f_y are the frequencies of the phase added in the x- and y-directions, respectively. Equation (3) can be conveniently expressed as

$$i_r(x,y) = a(x,y) + \frac{b(x,y)}{2}[e^{i\theta(x,y)} + e^{-i\theta(x,y)}] \tag{4}$$

With the aid of Fourier transform, the components corresponding to the image background a and one of the two conjugates (b) are removed to obtain

$$i_r(x,y) = \frac{b(x,y)}{2}e^{i\theta(x,y)} \tag{5}$$

The wrapped phase θ is then determined from the image as

$$\theta(x,y) = \tan^{-1}\left[\frac{\text{Im}(i_r)}{\text{Re}(i_r)}\right] \tag{6}$$

The phase obtained from the above equation lies between $-\pi$ and π due to the periodic nature of the trigonometric function. The correct phase is then determined by performing two dimensional unwrapping [4].

The resultant phase map includes the carrier frequency information and has to be filtered to obtain the actual phase ϕ due to thermal density variations. The carrier frequency is independently determined from a reference interferogram, captured without temperature variation, and is then subtracted from θ to obtain the actual phase field ϕ.

3 Temperature Estimation

As refractive index and temperature are related, this section would discuss the estimation of n alone. The relation between n and the phase is

$$n_{y+\Delta s} - n_y = \frac{\lambda}{4L\pi}\phi(y) \tag{7}$$

where Δs is shear distance [2]. The retrieval of n from the phase is a boundary value problem, where n in the entire domain that has to be constructed based on the available temperature (surface and ambient fluid) measurements and the retrieved phase data. References [5–7] performed direct integration on the difference data, which, in principle, should give the desired function, but the noise in the phase field accumulates to produce physically meaningless results (Fig. 2). In order to control the error propagation, a least-

[1]Corresponding author.

Contributed by the Heat Transfer Division of ASME for publication in the JOURNAL OF HEAT TRANSFER. Manuscript received October 13, 2009; final manuscript received March 7, 2010; published online June 30, 2010. Assoc. Editor: Yutaka Asako.

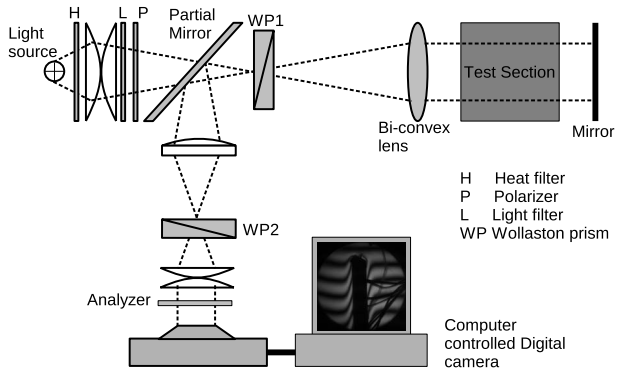

Fig. 1 Schematic diagram of DI

squares approach is used, wherein the refractive index field is represented by a suitable parametric curve such that the following objective function is minimized:

$$\text{Minimize:} R = \sum \left[n_{y+\Delta s} - n_y - \frac{\lambda}{4L\pi}\phi(y) \right]^2 + \alpha \sum \left[n_{y+\Delta y} - 2n_y + n_{y-\Delta y} \right] \quad (8)$$

where Δy is the pixel width and α (fixed at 0.10 here) is the smoothing parameter [8]. The second term in Eq. (8) is a second order regularization term. n is represented by a cubic spline [9], which is locally flexible, and the boundary conditions can be represented properly (first derivative at the boundaries are known from phase measurements). The control points of the spline are uniformly distributed, row wise, over the domain. The refractive indices at the control points have to be estimated such that the residual given by Eq. (8) is minimum. The above procedure is performed on each row of the interferogram to obtain the refractive index distribution in the entire domain. A numerical code for the above methodology has been developed using MATLAB 7.

Figure 2 shows the comparison of the temperature profiles retrieved using direct integration [5–7], cubic polynomial [10], and cubic spline fit. Temperature at the wall and ambient are known a priori or measured in an experiment. Both direct integration and cubic polynomial fit perform poorly (error more than 10%).

4 Results and Discussion

4.1 Experiments. Laminar free convection from an isothermal vertical plate is a benchmark problem with extensive experimental and numerical validations [11], and hence, to test the ability of the present method, experiments have been conducted on a heated aluminum plate. The details of the experimental setup can be found in Ref. [2]. The length (optical) of the plate is 0.25 m. Temperature measurements on the plate and the ambient have been done with the help of calibrated K-type thermocouples, with an uncertainty of $\pm 0.1\,^{\circ}$C. The measured temperatures at the wall and ambient are provided as boundary conditions. The regions with parallel fringes have been identified as the "ambient" [2]. Figure 3 shows the parity plot between the predicted Nusselt number and Ostrach solution, and there is an excellent agreement for all x. It is also found that the temperature profile matches with the theoretical profile very well, as shown in Fig. 4. Figure 5 shows the temperature field over the entire domain, estimated for the heated vertical polished aluminum plate for a plate Grashoff number of 1.5×10^6. The temperature field near the leading edge cannot be resolved properly.

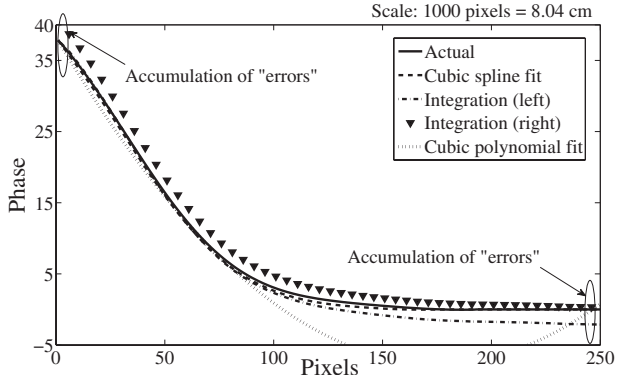

Fig. 2 Comparison of phase (temperature) retrieved by various methods with the Ostrach solution for the heated vertical plate

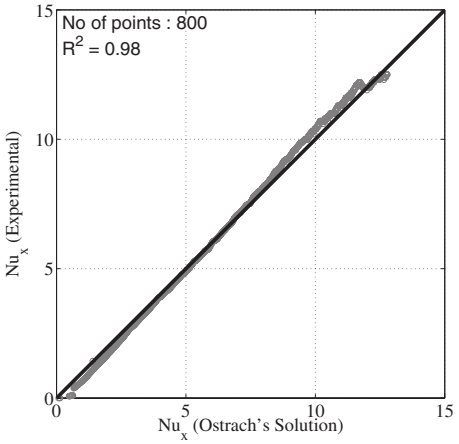

Fig. 3 Parity plot between the Nusselt number predicted experimentally and the Ostrach solution for a heated vertical aluminum plate (Local Grashoff number, $Gr_x<1.5\times10^6$)

4.2 Numerical Simulation. Though the method seems to compare well with theoretical solutions, it is necessary to quantify

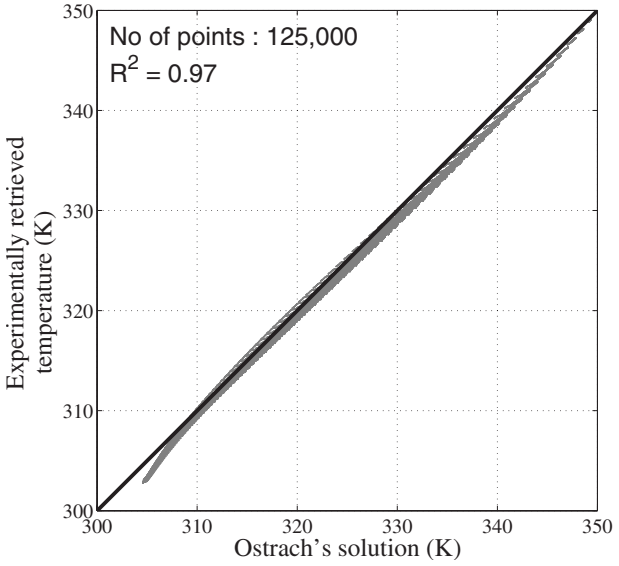

Fig. 4 Parity plot between temperature profiles—Experimental and Ostrach for the aluminum (Local Grashoff number, $Gr_x<1.5\times10^6$)

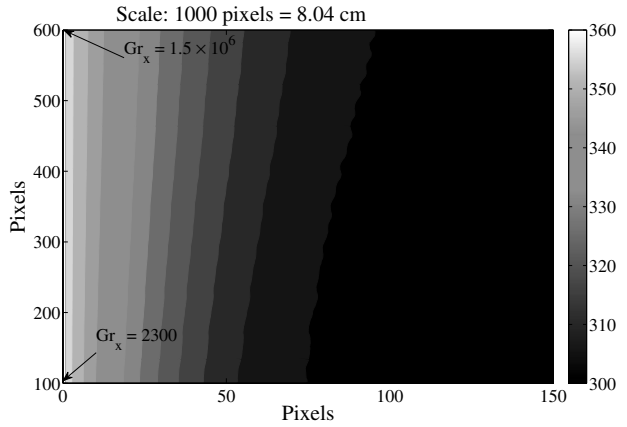

Fig. 5 Retrieved two dimensional temperature field clearly showing the thermal boundary layer adjacent to the heated aluminum plate (Local Grashoff number, $Gr_x < 1.5 \times 10^6$)

the accuracy of the methodology. Hence, the present analysis has been applied to a set of synthetic interferograms with artificial noise and error in the temperature measurement. The temperature field has been constructed based on the theoretical solution [11] and subsequently converted to an equivalent phase field modulated with a carrier frequency f_x and degraded with artificial Gaussian noise and background variation. The noise in the interferogram is estimated as the ratio of the noise amplitude to the mean intensity of the interferogram. Figure 6 shows a sample interferogram simulated for a plate Grashoff number of 5×10^6 with $\pm 5\%$ noise, wrapped phase map, unwrapped phase map, and the final phase field after eliminating the carrier frequency.

The error in the phase field measurement and hence, the heat flux, increased with the addition of noise. The average error in the phase measurement with $\pm 5\%$ random noise was found to be about ± 0.5 rad, which amounts to less than $\pm 2\%$ error in the heat flux measurement. The temperature field has also been estimated for different levels of noise. The error in the temperature estimation also increased with noise. The maximum error for the temperature estimates for the cases considered were less than $\pm 2\%$.

The analysis has been extended to incorporate the effect of error in the temperature measurement, which is of practical importance. Cases with $\pm 0.1°C$, $\pm 0.5°C$, and $\pm 1°C$ uncertainties in the wall temperature measurement have been considered. The analysis was performed by adding the uncertainty to the temperature of the wall alone. Table 1 shows the error in the heat transfer and temperature estimated with image noise and uncertainty in the temperature measurement. The above analysis shows that uncertainty in the temperature measurement has significant influence on the heat flux and temperature estimations.

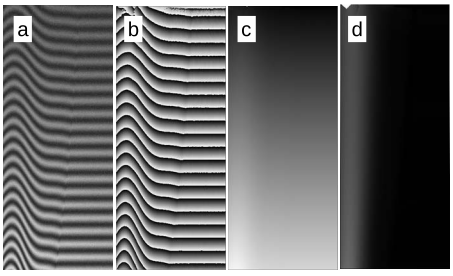

Fig. 6 Interferogram analysis on a simulated interferogram for $Gr = 5 \times 10^6$: (*a*) sample simulated interferogram, (*b*) wrapped phase (*c*) unwrapped phase and (*d*) phase map after eliminating carrier frequency

Table 1 Maximum error in the heat flux and temperature measurements

Noise (%)	Wall temperature uncertainty (°C)	Error in Heat flux (%)	Error in Temperature (°C)
0	0.0	0.5	0.8
0	0.1	2.6	1.4
0	1.0	7.3	2.3
1	0.0	1.2	1.1
1	0.1	2.9	1.7
1	1.0	8.1	2.4
5	0.0	1.5	1.6
5	0.1	3.4	1.9
5	1.0	9.3	2.8

All error estimates have been rounded to one significant digit after the decimal point

Temperature retrieval from noise free interferogram with no wall temperature uncertainty is not error free and indicates the limitations of phase estimation using Fourier transforms. The Fourier transform technique adds spurious noise to the phase map [12,13]. Also, the methodology fails near the leading edge mainly because of high temperature gradients. However, this is the inherent limitation of all interferometric techniques. The limitation arises because of the resolution of the digital camera. The resolution of the camera should be such that it can resolve two fringes clearly, i.e., the distance between the two dark (or bright) bands should be more than two pixel width. Also, the Fourier transform technique requires the variation in the actual phase to be small compared with that of the carrier frequency, which is not the case near the leading edge. Also, the high temperature gradients near the leading edge can influence refraction strongly. However, the present methodology captures the thermal image satisfactorily and can be a useful tool for thermal visualization.

5 Conclusion

A new methodology to estimate heat flux and temperature fields from a single interferogram with the aid of completely automatic digital optical analysis has been proposed. The methodology has been applied to both synthetic and experimental interferograms. The heat flux and temperature predictions were found to be extremely good in comparison with the available solution. The maximum deviation in the heat flux is approximately $\pm 5\%$, while the maximum deviation in the temperature is about $1°C$ as compared with the Ostrach solution. Also, the effects of image noise and uncertainty in the temperature measurement on heat transfer predictions have been studied. This establishes the ability of the digital fringe analysis along with the method for temperature retrieval to resolve the temperature field accurately.

References

[1] Born, M., and Wolf, E., 1999, *Principles of Optics: Electromagnetic Theory of Propagation, Interference and Diffraction of Light*, Cambridge University Press, Cambridge, England.
[2] Krishna Sabareesh, R., Prasanna, S., and Venkateshan, S., 2010, "Investigations on Multi-Mode Heat Transfer From a Heated Vertical Plate," ASME J. Heat Transfer, **132**(3), p. 032501.
[3] Takeda, M., Ina, H., and Kobayashi, S., 1982, "Fourier-Transform Method of Fringe-Pattern Analysis for Computer-Based Topography and Interferometry," J. Opt. Soc. Am., **72**, pp. 156–160.
[4] Spottiswoode, B., 2008, "2D Phase Unwrapping Algorithms," MATLAB Central, File Exchange No. 22504, URL http://www.mathworks.com/matlabcentral/fileexchange/22504
[5] Carlomagno, G., and Rapillo, A., 1986, "A Wollaston Prism Interferometer Implemented With a Digitizer," Exp. Fluids, **4**(6), pp. 332–336.
[6] Waldner, S., 1996, "Removing the Image-Doubling in Shearography by Reconstruction of the Displacement Field," Opt. Commun., **127**(1–3), pp. 117–126.
[7] Woisetschläger, J., Pretzler, G., Jericha, H., Mayrhofer, N., and Pirker, H.,

1998, "Differential Interferometry With Adjustable Spatial Carrier Fringes for Turbine Blade Cascade Flow Investigations," Exp. Fluids, **24**(2), pp. 102–109.
[8] Tikhonov, A., Arsenin, V., and John, F., 1977, *Solutions of Ill-Posed Problems*, V. H. Winston, Washington, DC.
[9] De Boor, C., 2001, *A Practical Guide to Splines*, Springer-Verlag, Berlin.
[10] Rammohan Rao, V., 1992, "Interferometric Study of Interaction Between Radiation and Free Convection in Fins and Arrays," Ph.D. thesis, Indian Institute of Technology Madras, Chennai, India.
[11] Ostrach, S., 1952, "An Analysis of Laminar Free-Convection Flow and Heat Transfer About a Flat Plate Parallel to the Direction of the Generating Body Force," Lewis Flight Propulsion Laboratory, NACA, Technical Report No. NACA-TN-2635.
[12] Kujawinska, M., and Wojciak, J., 1991, "High Accuracy Fourier Transform Fringe Pattern Analysis," Opt. Lasers Eng., **14**, pp. 325–339.
[13] Roddier, C., and Roddier, F., 1987, "Interferogram Analysis Using Fourier Transform Techniques," Appl. Opt., **26**(9), pp. 1668–1673.

On the Mechanism of Dropwise Condensation of Steam on Ion Implanted Metallic Surfaces

Michael H. Rausch

Alfred Leipertz
e-mail: sek@ltt.uni-erlangen.de

Andreas P. Fröba[1]
e-mail: apf@ltt.uni-erlangen.de

Lehrstuhl für Technische Thermodynamik (LTT),
Universität Erlangen-Nürnberg,
Am Weichselgarten 8,
D-91058 Erlangen, Germany

Our recent experimental studies indicate that nanostructured, chemically inhomogeneous surfaces are the origin of dropwise condensation of steam on ion implanted metals. Yet, the underlying microscopic mechanism governing this special condensation form is still not clear. We suggest a condensation model based on droplet nucleation and growth on elevated precipitates, resulting in short-term steam entrapment after droplet coalescence. According to the wetting theory, this transition state yields increased macroscopic contact angles. Condensation phenomena such as enlarging dropwise condensation areas in spite of increasing condensation rate become comprehensible by our model. Furthermore, it points out that for this special surface type, contact angles and surface free energies measured under ambient air conditions are not usable for predicting the condensation form of steam. Although the suggested microscopic model cannot be directly proved by experiment, its validity is supported by its capability of explaining experimental observations colliding with previous theoretical approaches. [DOI: 10.1115/1.4001646]

Keywords: dropwise condensation, nucleation, microscopic mechanism, wetting, ion implantation

1 Introduction

About 80 years ago, Schmidt et al. [1] found that the promotion of dropwise condensation of steam can distinctly enhance the condensation heat transfer coefficient compared with filmwise condensation. It is obvious that strongly hydrophobic coatings are predestined for inducing permanent dropwise condensation, but their use is connected with additional heat transfer resistances and, at least in many cases, mechanical instability [2]. These disadvantages are not valid for the direct modification of metallic surfaces by ion implantation, which was proved to induce dropwise condensation of steam in the late 1980s [3]. To date, however, it is not clear which surface modifications governed by ion implantation are responsible for this effect. Approaches solely based on the reduction in surface free energy by ion implantation [4] turned out to be contradictory to many of our recent experimental results [5,6], which will be summarized in the following.

For titanium grade 1, aluminum alloy Al 6951, and stainless steel AISI 321, dropwise condensation of steam could be induced by ion beam implantation technology, although distinctly reduced contact angles and increased surface free energies were measured for most of the samples. Here, N^+, C^+, or O^+ doses of 10^{16} cm^{-2}, and an implantation energy of 20 keV were applied. For the AISI 321 sample exemplarily shown in Fig. 1(*a*), the surface free energy was increased from 30.0 $mN\,m^{-1}$ to 39.2 $mN\,m^{-1}$ by C^+ implantation. On the same steel and Hastelloy C-276, gradual spreading of dropwise condensation over untreated areas was observed. Some commercially available thin plates made of other high-alloyed materials even instantly exhibited stable dropwise condensation without any treatment. For a Hastelloy C-2000 sample, this behavior exemplarily depicted in the right part of Fig. 1(*b*) was stable for about 2 months, although a quite low contact angle for water was measured. On the left part of the sample, plasma ion implantation with nitrogen ions unexpectedly induced filmwise condensation accompanied by an increased contact angle for water.

Our recent condensation experiments and surface analyses [5,6] reveal a correlation between nanostructured, chemically inhomogeneous surfaces and the appearance of dropwise condensation of steam on metals. Such surface characteristics can be caused by the precipitation of particulate compounds, which are formed from the base material and the implanted elements exceeding the solubility of the substrate. For some untreated high-alloyed materials, oxidation and erosion effects occurring during condensation proved to gradually produce similar surfaces suitable for dropwise condensation. Such surfaces may also be established by manufacturing processes for sheet metals enabling instant dropwise condensation such as on the untreated Hastelloy C-2000 surface given in Fig. 1(*b*). Here, the transition to filmwise condensation by ion implantation could be governed by sputtering effects destroying the characteristics responsible for dropwise condensation.

Further condensation experiments were performed with a titanium sample implanted with a comparatively low N^+ ion dose of 10^{15} cm^{-2} at 20 keV [6]. The sample showed a mixed pattern of filmwise and dropwise condensation. The dropwise condensation areas enlarged with increasing subcooling. Assuming that dropwise condensation is only an effect of low wettability, inverse behavior would have been expected because of the increased condensation rate for increased subcooling. A comparison of our experiment with former studies [7,8] suggested a nucleation mechanism with an increasing number of nucleation sites being activated by increasing subcooling [6]. The surface structures found for ion implanted and otherwise modified metal surfaces feature potential nucleation sites for such a mechanism. However, the surfaces examined in the former studies [7,8] showed dropwise condensation all over the condensation areas due to their high hydrophobicity. Thus, the question arises on how increasing subcooling and condensation rates could prevent more and more of the titanium surface treated with low ion dose from being wetted by the condensate. In addition, it remains unclear why in many cases wettability parameters such as contact angles and surface free energies cannot be used for predicting the condensation form on metals. Following up these questions, a model for the microscopic mechanism of dropwise condensation of steam is suggested and discussed in this work. It is based on the new knowledge on the surface characteristics of modified metals showing this condensation form and the experiment hinting at nucleation effects.

2 Microscopic Mechanism of Dropwise Condensation

We postulate the initial droplet formation on elevated locations such as precipitates or oxidation products. The small droplets on the nucleation sites grow by condensation. According to our former studies summarized above [5,6], the diameter and the height of these sites usually range from 20 nm to 100 nm, and from 10 nm to 50 nm. In case of sufficiently small distances between the nucleation sites and adequately large microscopic contact angles between the nucleation site and the condensate, neighboring droplets can contact and coalesce before the three

[1]Corresponding author.

Contributed by the Heat Transfer Division of ASME for publication in the JOURNAL OF HEAT TRANSFER. Manuscript received December 1, 2009; final manuscript received April 13, 2010; published online July 15, 2010. Assoc. Editor: Louis C. Chow.

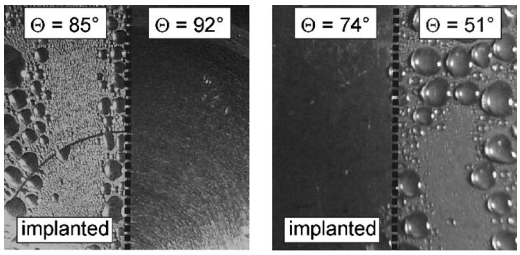

Fig. 1 Condensation forms of steam at about 1 bar and small subcooling (<1 K) and contact angles Θ for water measured under ambient conditions: (*a*) stainless steel AISI 321, ion beam technology, C^+ ions, 10^{16} cm^{-2}, and 20 keV; (*b*) Hastelloy C-2000, plasma ion implantation, nitrogen ions, 10^{17} cm^{-2}, and 40 keV

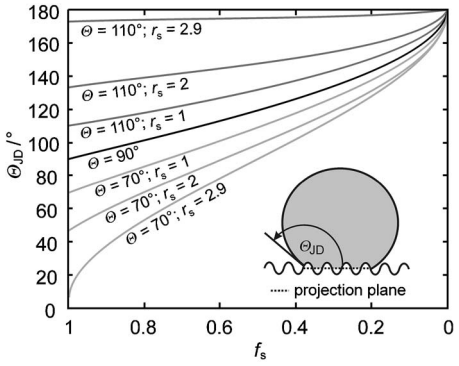

Fig. 3 Effect of gas entrapment and surface roughness on the macroscopic contact angle according to the model suggested by Johnson and Dettre [10]

phase contact line reaches the base of the nucleation site; see Fig. 2. Depending on the geometry of the nucleation sites, this behavior is possible for microscopic contact angles considerably smaller than 90 deg.

Fostered by the fast droplet coalescence [9], short-term steam entrapment can occur in the cavities between the nucleation sites. The resulting transition state corresponds with the contact angle model

$$\cos \Theta_{JD} = r_s f_s \cos \Theta - f_g \quad (1)$$

suggested by Johnson and Dettre [10]. It combines the approaches by Wenzel [11] and Cassie and Baxter [12]. The macroscopic contact angle Θ_{JD} depicted in Fig. 3 describes the wetting behavior of rough surfaces, including gas entrapment in cavities. This angle results from the contact angle Θ, according to Young's equation [13] for an ideal surface consisting of the nucleation site material in our case. Laying a projection plane through the three phase contact lines, f_s describes the area fraction cutting the nucleation sites. f_g is the remaining fraction where the liquid and gas phases are in contact ($f_g = 1 - f_s$). The roughness parameter r_s represents the ratio of the real and the projected solid surface area in contact with liquid. It includes all scales of surface roughness. As illustrated by Fig. 3, gas or steam entrapment enhances the macroscopic contact angle, and thus increases the tendency for stable dropwise condensation.

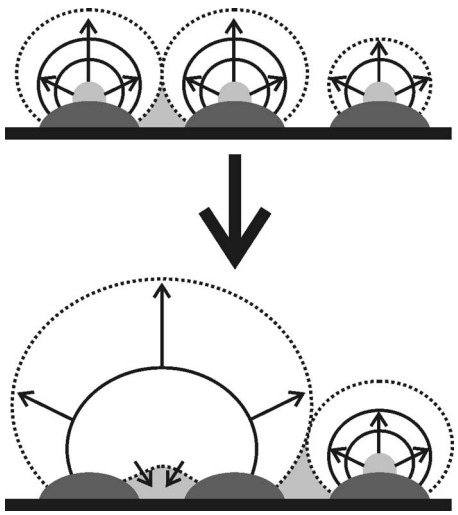

Fig. 2 Steam entrapment in cavities between elevated nucleation sites due to fast droplet coalescence

3 Discussion

The initial droplet formation on elevated locations postulated for the model is in contrast to theoretical considerations indicating preferred nucleation in cavities of homogeneous materials [14]. The surfaces regarded here, however, are highly inhomogeneous, and heterogeneous nucleation for condensation on such complex surfaces is not completely understood. Thus, effects of nanoscale surface roughness and differing surface free energies of the surface components could allow the assumed behavior.

The continuous collapse of entrapped steam at the cooled condensation wall seems to be of minor importance with respect to stability of dropwise condensation. This can be attributed to permanent new steam entrapment at the boundaries of the rapidly growing droplets, which apparently affects the resulting macroscopic contact angle more strongly. Nevertheless, the mechanism can only be maintained if the condensate present in the cavities is removed as soon as the corresponding droplets depart or are entrained by other droplets. This requirement is fulfilled in case the assumed formation of initial droplets on the elevated nucleation sites due to, e.g., preferred wettability is correct. It should be noted that extremely thin water films are usually adsorbed on metal surfaces, even at atmospheric conditions. Such films may not perturb the mechanism as they do not necessarily take part in the condensation process [15,16]. Remaining condensate on the nucleation sites could even speed up the condensation process because no new droplet nucleation was necessary.

Successful promotion of dropwise condensation of steam on rough and polished titanium and AISI 321 surfaces [5,6] indicated that the suggested mechanism was not strongly affected by macroscopic surface roughness. This can be explained by the discussed nanoscale surface characteristics overlaying micro- or macroscale surface roughness. However, condensate retention due to hysteresis of the macroscopic contact angle has to be minimized in order to avoid spreading of a condensate film over the nanostructures. This can be seized by polishing the condenser surfaces. For the unpolished samples given in Fig. 1, the macroscopic surface roughness seems to be of minor importance. This can be attributed to the small subcooling <1 K adjusted in our condensation chamber for long-term experiments [17], which results in a very low frequency of droplet departure.

According to the proposed model, relevant vapor entrapment cannot occur if the three phase contact line reaches the base of the nucleation sites prior to droplet coalescence. In this case, dropwise condensation can only be maintained if the base material is very poorly wetted by the condensate. No vapor entrapment is possible for very small microscopic contact angles between the nucleation site and condensate, which can be expected for working fluids with low surface tension such as refrigerants. In addition, sufficiently high nucleation site densities are required for

vapor entrapment. For promoting dropwise condensation of steam by ion implantation, ion doses initiating the precipitation of a satisfactory areal density of particulate compounds have to be applied. The titanium sample implanted with low N^+ dose discussed in Sec. 1 seems to represent a limiting case concerning the nucleation site density as it showed a mixture of filmwise and dropwise condensation. This was substantiated by AFM analysis in our recent work [6]. More precipitates were found in the areas showing permanent dropwise condensation than in those with changing condensation form or permanent filmwise condensation. The suggested mechanism provides an explanation for the effect of growing dropwise condensation areas with increasing subcooling observed for this sample. Increasing the cooling power accelerates the collapse of entrapped steam, but it also speeds up the formation of new entrapment at the droplet boundaries by increasing the condensation rate. For the titanium sample, it seems that the effect on the formation of new steam entrapment is dominating, which results in expanding dropwise condensation areas.

The contradictions between the condensation form and measured contact angles and surface free energies for a number of metallic samples can also be explained by the suggested model. For measuring contact angles, single droplets are placed on the dry sample and enlarged by adding liquid for the acquisition of advancing contact angle data. The liquid gradually wets the microscopic roughness, which results in macroscopic contact angles Θ_W described by Wenzel's equation [11]

$$\cos \Theta_W = r_s \cos \Theta \tag{2}$$

Contact angles measured for several reference fluids are used for the calculation of the surface free energy of the studied material. Thus, the discussed increase in macroscopic contact angles due to steam entrapment during the condensation process cannot be evaluated. Accordingly, the wettability parameters determined at dry conditions are not capable of predicting condensation forms on surfaces suitable for the suggested condensation mechanism.

Finally, the postulation of the initial droplet formation on elevated nucleation sites should be revisited. If this assumption is wrong and droplet formation starts in cavities, no steam entrapment would be possible. Consequently, Wenzel's equation should be able to describe the wettability of the surface for the condensation process. As many of our experimental results show that this is not the case, the above postulation seems to be realistic.

4 Conclusions

In the present work, a microscopic mechanism for dropwise condensation of steam on nanostructured and chemically inhomogeneous metallic surfaces with limited hydrophobicity is proposed. It is based on droplet nucleation and growth on elevated locations, resulting in short-term steam entrapment after droplet coalescence. This transition state implies distinctly increased contact angles, which enable stable dropwise condensation. Consequently, contact angles and surface free energies measured under atmospheric conditions fail to predict the condensation form on surfaces suitable for the suggested mechanism. Although the model cannot be directly proved due to the microscopic scale of the underlying processes, it is supported by its ability to explain condensation phenomena which are in contradiction with former theoretical approaches.

Acknowledgment

We gratefully acknowledge the financial support by the German Research Foundation (Deutsche Forschungsgemeinschaft, DFG).

Nomenclature

f = areal fraction
r = roughness parameter

Greek Symbols

Θ = contact angle (rad)

Subscripts

g = gas
JD = according to Johnson and Dettre
s = solid
W = according to Wenzel

References

[1] Schmidt, E., Schurig, W., and Sellschopp, W., 1930, "Versuche über die Kondensation von Wasserdampf in Film-und Tropfenform," Forsch. Ingenieurwes., **1**(2), pp. 53–63.
[2] Rose, J. W., 2002, "Dropwise Condensation Theory and Experiment: A Review," Proc. Inst. Mech. Eng., Part A, **216**, pp. 115–128.
[3] Zhao, Q., Zhang, D., and Lin, J., 1988, "A Study of Surface Materials Achieving Dropwise Condensation," *Proceedings of the First International Conference on Heat Transfer in Energy Conservation*, Shenyang, Vol. 1, pp. 177–179.
[4] Zhao, Q., and Burnside, B. M., 1994, "Dropwise Condensation of Steam on Ion Implanted Condenser Surfaces," Heat Recovery Syst. CHP, **14**(5), pp. 525–534.
[5] Rausch, M. H., Leipertz, A., and Fröba, A. P., 2010, "On the Characteristics of Ion Implanted Metallic Surfaces Inducing Dropwise Condensation of Steam," Langmuir, **26**(8), pp. 5971–5975.
[6] Rausch, M. H., Leipertz, A., and Fröba, A. P., 2010, "Dropwise Condensation of Steam on Ion Implanted Titanium Surfaces," Int. J. Heat Mass Transfer, **53**, pp. 423–430.
[7] Erb, R. A., 1968, "Heterogeneous Nucleation in Dropwise Condensation," *Surface Phenomena of Metals*, Society of Chemical Industry, London, Vol. 28, pp. 383–405.
[8] McCormick, J. L., and Westwater, J. W., 1965, "Nucleation Sites for Dropwise Condensation," Chem. Eng. Sci., **20**, pp. 1021–1036.
[9] Rose, J. W., 2004, "Surface Tension Effects and Enhancement of Condensation Heat Transfer," Chem. Eng. Res. Des., **82**(4), pp. 419–429.
[10] Johnson, R. E., and Dettre, R. H., 1964, "Contact Angle Hysteresis. I. Study of an Idealized Rough Surface," *Contact Angle, Wettability, and Adhesion, Advances in Chemistry Series*, F. M. Fowkes, ed., American Chemical Society, Washington, DC, Vol. 43, pp. 112–135.
[11] Wenzel, R. N., 1936, "Resistance of Solid Surfaces to Wetting by Water," Ind. Eng. Chem., **28**, pp. 988–994.
[12] Cassie, A. B. D., and Baxter, S., 1944, "Wettability of Porous Surfaces," Trans. Faraday Soc., **40**, pp. 546–551.
[13] Young, T., 1805, "An Essay on the Cohesion of Fluids," Philos. Trans. R. Soc. London, **95**, pp. 65–87.
[14] Kast, W., 1964, "Bedeutung der Keimbildung und der instationären Wärmeübertragung für den Wärmeübergang bei Blasenverdampfung und Tropfenkondensation," Chem.-Ing.-Tech., **36**(9), pp. 933–940.
[15] Eucken, A., 1937, "Energie-und Stoffaustausch an Grenzflächen," Naturwiss., **25**, pp. 209–218.
[16] Yongji, S., Dunqi, X., Jifang, L., and Siexong, T., 1991, "A Study on the Mechanism of Dropwise Condensation," Int. J. Heat Mass Transfer, **34**(11), pp. 2827–2831.
[17] Rausch, M. H., Fröba, A. P., and Leipertz, A., 2008, "Dropwise Condensation Heat Transfer on Ion Implanted Aluminum Surfaces," Int. J. Heat Mass Transfer, **51**(5–6), pp. 1061–1070.